GEOWISSENSCHAFTLICHE MITTEILUNGEN

Heft Nr. 79, 2007

Proceedings of the 18th European VLBI for Geodesy and Astrometry Working Meeting

12-13 April 2007

edited by
Johannes Böhm, Andrea Pany, and Harald Schuh

Veröffentlichung
des Instituts für Geodäsie und Geophysik

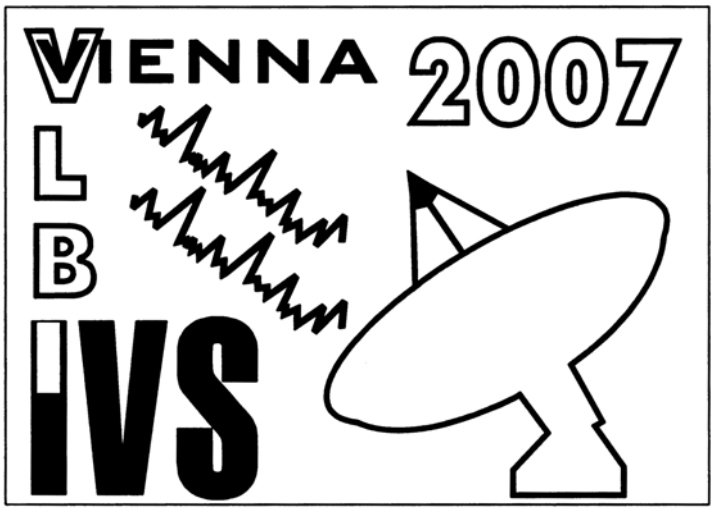

ISSN 1811-8380
Schriftenreihe der Studienrichtung VERMESSUNG UND GEOINFORMATION
TECHNISCHE UNIVERSITÄT WIEN

2007
Published by the Institutes of the Course on 'Geodesy and Geoinformation'
of the Vienna University of Technology
Gußhausstraße 27-29
A-1040 Wien

Responsible for this Issue: Johannes Böhm, Andrea Pany, and Harald Schuh
Printed by: Grafisches Zentrum

Auflage: 200 Stück

ISSN 1811-8380

Table of contents

Preface

The 18th European VLBI for Geodesy and Astrometry (EVGA) Working Meeting was held in Vienna, Austria from 12-13 April 2007 at the Federal Office of Metrology and Surveying (BEV). 69 scientists from all over the world (20 countries) came to Vienna to present and discuss results of recent research in geodetic and astrometric VLBI; in total, 40 oral and 12 poster presentations were delivered by the participants. On Saturday, 14 April 2007 the 8th IVS Analysis Workshop, and on Sunday, 15 April 2007 the 2nd VLBI2010 face-to-face meetings were held in Vienna, too.

Picture: The participants of the 18th European VLBI for Geodesy and Astrometry (EVGA) Working Meeting.

The oral presentations are collected at the webpage of the EVGA (http://www.evga.org/) and can be downloaded there. The electronic version of the Proceedings and further information concerning the meeting can be found at:

http://www.hg.tuwien.ac.at/~evga/

The online version also provides pdf files for colour printing. The papers of this publication should be cited as:

{Authors}, {Title} (2007), Proceedings of the 18th European VLBI for Geodesy and Astrometry Working Meeting, 12-13 April 2007, edited by J. Böhm, A. Pany, and H. Schuh, Geowissenschaftliche Mitteilungen, Heft Nr. 79, Schriftenreihe der Studienrichtung Vermessung und Geoinformation, Technische Universität Wien, ISSN 1811-8380.

Acknowledgements

We would like to thank all the authors for preparing and submitting their papers in such a short time facilitating a rapid publication of the excellent results of the various groups.

We are very grateful to the Federal Office of Metrology and Surveying (BEV) for providing the rooms and facilities for the meeting.

Thanks to all members of the research group 'Advanced Geodesy' of the Institute of Geodesy and Geophysics of the Vienna University of Technology for helping in the preparation and organization of the meeting; in particular, we'd like to thank Jörg Wresnik who was burdened with most of the organizational work.

Johannes Böhm, Andrea Pany, and Harald Schuh
Editors
Vienna, July 2007

Status of Geodetic Application Research in KASI

Y. Kwak
Space Geodesy Division, Korea Astronomy and Space Science Institute, Daejeon 305-348, Korea
Ajou University, Suwon 442-749, Korea

J. Cho, J. Park
Space Geodesy Division, Korea Astronomy and Space Science Institute, Daejeon 305-348, Korea

Abstract. The Space geodesy division of KASI (Korea Astronomy and Space science Institute), investigated the geodetic applications of KVN (Korean VLBI Network) as one of the institute projects in 2006. We simulated the global and local scale contribution of KVN to geodetic VLBI networks when KVN participates in the geodetic observations and performed the preliminary study for plate motion in Korean peninsula using KVN. Through these studies, we could expect prospective role of KVN in space geodesy field in Korea.

Keywords. KASI, Space geodesy, KVN, VLBI

1 Introduction

KASI will have three VLBI stations (Korean VLBI Network:KVN) for astronomical and geodetic purposes till next year, 2008. Three 21m antennas will be located in Seoul, Ulsan and Jeju, (Minh et al, 2003).

Space geodesy division of KASI investigated the geodetic applications of KVN in 2006. We evaluated the impact of KVN to geodetic VLBI network. We designed two networks, KVN-Asia and KVN-Pacific, to distinguish the impacts of KVN on global and local scale networks. We estimated the precision of station coordinates and EOP as evaluating indices. We also performed simulations for determining the plate motion in Korean peninsula. We estimated the precision of the plate motion parameter, plate angular velocity, using KVN and additional Suwon mobile VLBI site coordinates

We also started operating CALC/SOLVE and OCCAM with two server class computers for geodetic analysis works.

2 Geodetic Applications for KVN

2.1 KVN Contribution to Geodetic Researches

Figure 1 shows the network design of our simulation for the contribution of KVN to analysis of station coordinates and EOP (Earth Orientation Parameters) when KVN is included in existing geodetic VLBI networks. The purpose of this simulation is to evaluate impacts of KVN to existing geodetic VLBI networks (Cho et al., 2006). We designed two networks to distinguish the impacts of KVN on global and local scale networks. One is a global network which comprises over 6,000km-long inter-continental baselines called KVN-Pacific. The other is a local network which comprises East-Asian geodetic VLBI stations called KVN-Asia. The key parameters of the simulation are formal errors of station coordinates and EOP. The resultant formal errors were shown in Figure 2 and Figure 3.

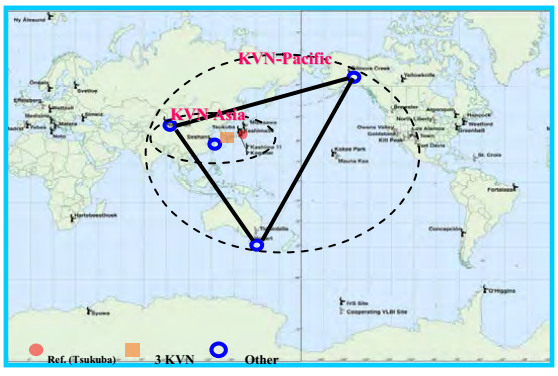

Fig. 1 The design of the simulation of KVN contribution to existing geodetic VLBI networks. (KVN-Pacific consist of Seshan, Nanshan, Gilcreek, Hobart and KVN as a global network; KVN- Asia consist of Seshan, Nanshan and KVN as a local network)

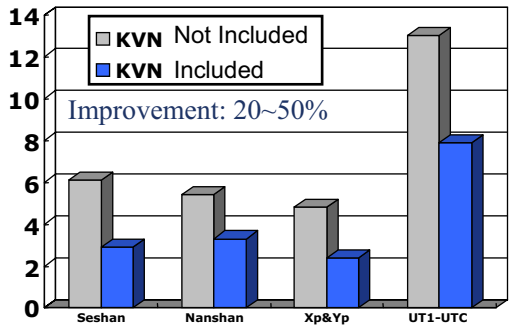

Fig. 2 The formal errors of station coordinates and EOP analysis for KVN-Asia (Unit : 3-D coordinates(mm), Xp&Yp(μas*100), UT1-UTC(μs)).

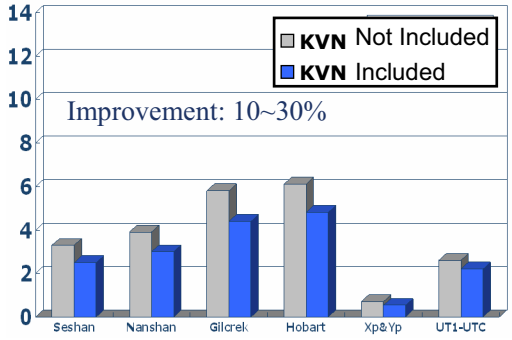

Fig. 3 The formal errors of station coordinates and EOP analysis in KVN-Pacific (Unit : 3-D coordinates(mm), Xp&Yp(μas*100), UT1-UTC(μs))

In the case of KVN-Asia, the estimation precision of EOP was improved by 40~50% and the estimation precision of the coordinates was improved by 20~50%. However the improvement of EOP is meaningless since the absolute value of the error is still big compared with IVS solution, 50μas for polar motion and 5μs for UT1-UTC(Niell et al., 2004).

In the case of KVN-Pacific, the estimation precision of EOP was improved by 10~20% and the estimation precision of the coordinates was improved by 10~30%. Even though the improvement of the formal errors of EOP is small, the absolute value is meaningful compared with IVS solution.

We could expect that KVN is able to be applied on various space geodetic research fields based on the results from KVN simulation. Korean Peninsula is located in circumference of the Eurasian plate (EU) and ocean tide of west sea of Korea is variable. Therefore the denser array of East-Asian VLBI including KVN is locally able to be applied on monitoring plate motion and ocean loading of Korean Peninsula. Moreover, if KVN participates in global scale East-West baseline observation rather than South-North baseline observation, KVN can globally contribute to improving estimation precision of UT1-UTC.

2.2 Plate Motion in Korean Peninsula

Korean Peninsula has been postulated to be in circumference of EU. On the other hand, recent seismological and GPS researches suggest that it is on a separate plate called the Amurian plate (AM). However, the previous GPS research results for AM are inconsistent with each other beyond the estimated statistical errors. Moreover, the estimated plate motion parameter which we obtained from the velocity data of six Korean GPS stations was not agreeing with any existing results (Kwak et al., 2006). Therefore, independent measurements are required to distinguish those results.

We performed a simulation of determining the plate motion parameter using measured velocities of several VLBI stations in North America. The results of the simulation showed that even small VLBI arrays are able to well determine the plate motion parameter, if the arrays are located in stable area (Kwak et al., 2006). Therefore the compact KVN is capable of achieving good determination of the plate motion parameters if it is verified to be located on stable sites.

We estimated the precision of the AM motion parameters with coordinates and assumed velocity precision of KVN and additional Suwon mobile VLBI site based on above simulation results (Table 1). The estimation results showed that the Korean VLBI array would verify the existence of the AM, as far as the observation precision of 0.2 - 0.5 mm/yr for station velocities is achieved.

Table 1. Estimation precision of the plate angular velocity of AM relative to ITRF using KVN and additional Suwon mobile VLBI site coordinates

Velocity error(mm/yr)	Plate angular velocity precision(deg/Myr)
0.5	0.0240
0.2	0.098

2.3 Analysis S/W

Table 2. The specifications of analysis server computers

	Calc/Solve 10	OCCAM6.2
O/S	Red Hat Enterprise Linux WS release 4, Kernel Ver. 2.6.9	MS Windows XP Professional
CPU	Intel(R) Pentium(R) D Processor 940 (3.20GHz/800MHz/2 x2MB w/VT)	Intel(R) Pentium(R) D Processor 940 (3.20GHz/800MHz/2 x2MB w/VT)
RAM	4GB	2GB
HDD	1TB	1.5TB

We started operating CALC/SOLVE 10 and OCCAM 6.2 with two server class computers for geodetic analysis of IVS observation data and local observation data of KVN. Table 2 shows the specification of the computers.

3 Future Works and Outlook

The construction of KVN antennas will be finished and the first geodetic observation of KVN will be performed in 2008. Therefore we will secure operation techniques for geodetic sessions of KVN before then.

We will also continue analysis works. Several IVS sessions will be analyzed using Calc/Solve and OCCAM program and the analyzed results between them will be compared.

We could expect that KVN will be applied on various space geodetic research fields based on the results from KVN simulation. The denser East-Asian VLBI array including KVN is locally able to be applied on monitoring plate motion, especially verifying AM existence, and ocean loading of Korean Peninsula. KVN is also able to globally contribute to improving estimation precision of UT1-UTC.

References

Cho, J., J. Park, P. Park (2006). Analysis on Impacts of KVN to geodetic VLBI Network. Journal of Astronomy and Space Science (in Korean), Vol. 23, No. 4, pp.337-344.

Kwak, Y, J. T. Sasao, J. Cho, J. Park, T. Kim (2006). Preliminary Study on the Plate Motion in Korean Peninsula with new Korean VLBI Array Journal of Astronomy and Space Science (in Korean), Vol. 23, No. 4, pp.345-354.

Minh, Y., D. Roh, S. Han, H. Kim (2003). Construction of the Korean VLBI Network (KVN). ASP Conference Series. Y. Minh(ed.) Vol. 306, ASP, San Francisco, pp. 373-381.

Niell, A., A. Whitney, B. Petrachenko, W. Schlueter, N . Vandenberg, H. Hase, Y. Koyama, C. Ma, H. Schuh, G. Tuccari (2004). VLBI2010: Current and Future Requirements for geodetic VLBI systems, IVS Memorandum 2006-008v01, p.8.

Medicina and Noto VLBI Radiotelescopes: gravitational deformations evaluated with terrestrial laser scanning

S. Montaguti, L. Vittuari
DISTART – University of Bologna, via Risorgimento, 2 40136 Bologna (Italy)

P. Sarti, M. Negusini
Institute of Radioastronomy – INAF, via P. Gobetti, 101 40129 Bologna (Italy)

Abstract. The Medicina and Noto VLBI antennas are Az-El telescopes that experience gravitational deformations as they move in elevation. The ideal parabolic shape of the primary mirrors is therefore perturbed and the dishes are deformed according to the elevation pointing position of the antenna. Receivers at different frequencies, in particular the S/X geodetic receivers, are placed on the quadrupode, at the primary focus position; they also experience a displacement due to gravitational forces as the elevation changes. A third effect induced by gravity is the sag which might be possibly experienced by the dish as the elevation changes.

The determination of the contribution and magnitude of all the different effects are of primary importance. The realization of an elevation dependent gravitational deformation model that can be implemented in the VLBI data analysis is our target; it would allow to quantify and correct any bias of gravitational origin which affects the observations.

In order to face this complex task, terrestrial laser scanning and terrestrial observations have been applied to the antenna of Medicina and Noto.

The VLBI dishes' movements in elevation prevent full visibility of the inner part of the parabola from the ground: *ad hoc* supports were therefore installed nearby the antenna secondary focus allowing a complete laser coverage of the inner dish surface at different elevations.

The raw data acquired with the laser scanner intrinsically define clouds of points expressed with respect to an instrumental reference system; in order to connect the observed points to an external reference system, it is necessary to relatively align the different clouds using tie points and moreover ad hoc terrestrial surveys are required to frame the laser survey in to the external reference system.

The surveys and their results will be presented, along with the data analysis procedure and the most recently estimated deformations.

Keywords. Gravitational deformations, laser scanning, VLBI radiotelescope, terrestrial surveying.

1 Introduction

In order to determine the gravitational deformations that affect the dish when the VLBI telescope is moved in elevation, a test campaign concerning the use of terrestrial laser scanning was carried out at Medicina and Noto radioastronomical observatories. The primary mirror of the antenna is not visible from the ground, except for very low elevations. This certainly poses serious limits to the application of terrestrial methods for structure's topology reconstruction. The approach of external elevated platforms usually adopted in photogrammetry cannot be used in laser scanning surveys since there is a need of continuously stable supports. Therefore ad hoc manufactured supports were fixed close to the antenna secondary focus for a complete laser scanning of the dish surface at any elevation. The pulse laser used in these experiments has a resolution in range of about 1.5 mm at 50m. Both Noto and Medicina antenna's surface have been scanned at different elevation's positions of the dish. At both observatories, the entire surface of the primary mirror was completely retrieved merging the partially overlapping scans performed at two different standpoints: a number of technical and operational difficulties prevented the identification of a unique location from where the laser scanner could scan the entire surface of the dish in one unique run. Section 2 gives an overview of the peculiarities and common characteristics of

the Medicina and Noto VLBI radiotelescopes. Section 3 summarises the field operations and the technical solutions that were adopted for the laser scanning survey; the data processing and related results follow in section 3.1. The topographic survey that was performed along with the scanning of the dish is described in section 4.

2 Medicina and Noto VLBI radiotelescopes

The radiotelescope of Medicina (Fig. 1) and Noto are formed by a primary parabolic mirror and a secondary hyperbolic mirror, or sub reflector, which is positioned approximately 9 meters apart from the primary one; the receivers used in the geodetic observations are located in the same position as the sub reflector (primary focus). The sub reflector is capable to move through a mechanism that slides forth and back according to the configuration adopted in the observations: when geodetic observations are performed, the sub-reflector is moved back and the S/X receivers placed on the quadrupode are precisely positioned in the primary focus.

Fig. 1 The VLBI Medicina antenna

The Noto VLBI antenna differs from the Medicina radiotelescope for its active surface. (Orfei et al. 2004). The active surface concept aims at compensating gravitational deformation effects of the antenna backup structure by moving the panels forming the antenna primary mirror. The deformation of the surface reduces the overall antenna gain and the effect is worse at higher frequencies.

The surface of the primary mirror can be represented by the equation of a generic rotational paraboloid having its vertex in the point (0,0,0) and its focus on the z axis (1).

$$z = \frac{x^2 + y^2}{4f} \quad (1)$$

If the antenna structure is deformed by gravity, the paraboloid might change its shape, position and orientation.

2.1 Radiotelescope's deformations

Temperature variation, wind and gravity can induce remarkable deformations of the ideal radiotelescope structure and might not be negligible. Therefore, it is important to try to quantify the amount and magnitude of each perturbation and account for their contribution into the geodetic observations (Clark and Thomsen, 1988).

Thermal deformations can be monitored through temperature sensors positioned at different heights on the structure of the antenna.

All kind of deformations can be investigated with finite element modelling of the structure of the telescope; this approach has been tested by Clark and Thomsen (1988) and necessarily requires the availability of a reliable model of the antenna.

An alternative approach to investigate gravitational deformations is based on high precision terrestrial surveying. In particular we have simultaneously applied classical geodetic surveying (trilateration and triangulation) along with laser scanning, in order to investigate and quantify the amount of deformation that affect the dish and its structure when moving the telescope in elevation. The effects of gravity are assumed to be azimuth independent: therefore, only elevation movements have been applied to the structure explicitly assuming a deformation symmetry for any azimuth position.

3 Laser scanning surveys carried out in the Medicina and Noto observatories

The instrument that was used for this survey (Fig. 2) is a Trimble Mensi GS200 pulse laser: it is capable to acquire about 5000 points per second with a resolution of approximately 1.5 millimetre at 50 meters, using the time-of-flight method for

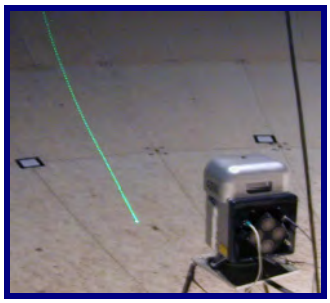

Fig. 2 The Trimble Mensi GS200 Laser System

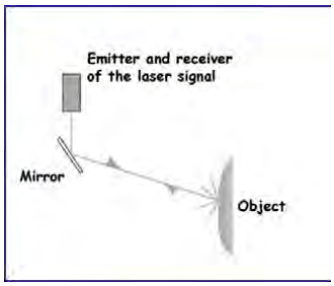

Fig. 3 The scheme of time-of-flight method

determining points positions (Fig. 3). In this case the laser beam hits the object, varying the azimuth and zenith angles.

The distance between the instrumental centre and the first reflecting point hit by the beam is determined by the measurement of the time-of-flight elapsing between the emission and the reception. This distance, combined with the two known output angles of the beam, allows determination of positions of the surveyed point. These coordinates are provided to the users in a Cartesian system (X, Y, Z), with its origin at the instrumental centre

The surveys were realized by moving the VLBI radiotelescopes at different elevations: 90, 75, 60, 45, 30 and 15 deg, with the scanning realized during the night, in order to reduce the effects induced by air refractivity (Fig. 4).

The surveys were carried out by placing the laser system inside the primary mirror on two standpoints (F1, F2) located near the secondary focus (Fig. 5). The technical characteristics of the instrument allowed a complete surveying of the whole surface of the primary mirror through a single standing; however, the lack of suitable standpoint locations, forced us to choose two different standpoint positions and to scan the dish in two separate, though overlapping, sessions.

A 2 cm sampling rate was adopted for the primary mirror while a 3 mm sampling rate was used on the 6 spherical targets that were positioned and surveyed as common points for the two different scans (Figs. 4 and 5).

3.1 Laser scanning data processing, post-processing and results

The acquired data sets were roughly cleaned by manually removing all the points that do not belong to the paraboloid. This was necessary since the primary mirror does not form a continuous surface: it is formed by panels that are separated by small gaps. Therefore, the laser beam occasionally passed through the gaps and hit the ground or parts of the

Fig. 4 The scanning session realized during the night

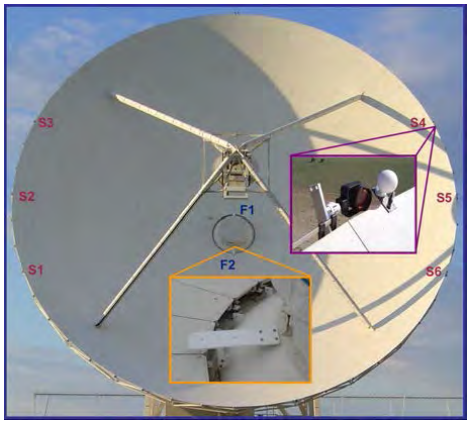

Fig. 5 Standpoints and target particular

lower structure of the antenna; these points had to be identified and removed.

The single scanning sessions (Fig 6) were aligned (Fig. 7) through six spherical targets serving as common points: they were placed on the external edge of the paraboloid (identified with the letter "S", Fig. 5).

In order to obtain a single cloud in the instrument's reference point, the two scanning sessions have been merged (Fig. 8).

Moreover, in order to determine the deformations of the primary mirror induced by gravity at different elevations, it is necessary to compare the different laser scanning sessions.

The best-fit paraboloid was computed, for each laser cloud acquired at varying elevations, writing a code in FORTRAN90; it can perform an estimation of:

- 3 translations which allow to place the origin of the frame into the vertex of the paraboloid.
- 2 rotations related to the x and y axes;
- the focal length of the best-fit paraboloid;
- the variance-covariance matrix and the correlation coefficients of the parameters;
- the residuals.

Such residuals were analyzed and used for selecting a better working data set on which the analysis was repeated.

The estimated parameters were used for roto-translating the clouds in a common frame where the vertex is placed in (0,0,0) and the Z-axis coincides with the axis of rotation. In this common frame we have computed the differences between the scannings carried out at different elevations.

Figure 9 shows the deformations between the scanning at 90 degrees and the one at 15 degrees for Medicina and Noto radiotelescopes. It has to be highlighted that for the Noto VLBI telescope, the active surface was permanently disabled during the scans.

The best-fit focal length varies as the elevation changes. The values determined for the radiotelescope of Medicina and Noto are shown in figure 10: the focal length decreases with elevation, suggesting an inward folding of the primary mirror

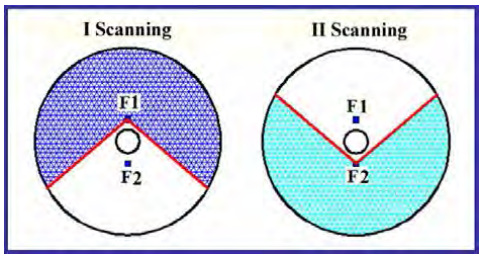

Fig. 6 The two scanning sessions

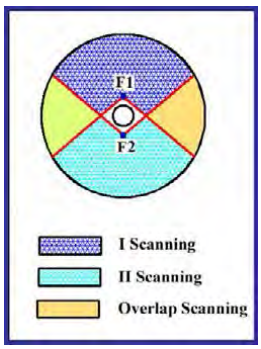

Fig. 7 Alignment Phase

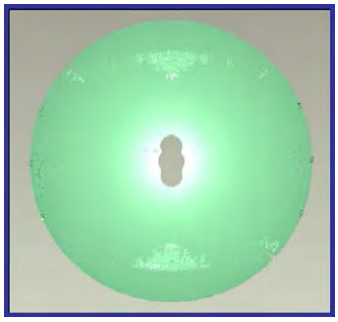

Fig. 8 Merge Phase

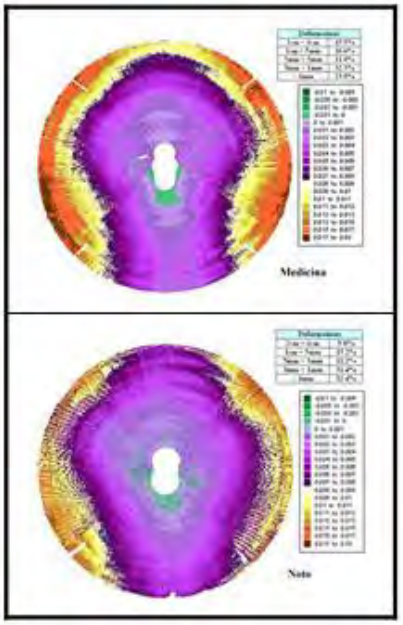

Fig. 9 The deformations between the scanning at 90 degrees and the one at 15 degrees

corresponding to an increasing concavity of the surface at lower elevations.

The differences of the best-fit focal lengths with respect to the theoretical length vary between 1.8 and 2.2 cm and almost 4 cm when the antenna is at 15 deg elevation, respectively for Medicina and Noto VLBI telescopes (Fig. 11).

4 Terrestrial surveys carried out in the Medicina and Noto observatory

In order to connect and frame the laser scanned surfaces to an external topocentric reference frame, common points were observed through a terrestrial survey (Fig. 12). A coupling of spheres and retro-reflecting prisms allowed the observation of common points with both laser and triangulation so as to derive transformation parameters. These common points were physically placed on the external part of the VLBI dish. Sphere's centres can be surveyed by the laser system. Spheres'centres can also be located with total stations using triangulation and symmetry considerations. Simultaneously, retro-reflecting prisms can also be surveyed with total stations. A detail of the couple sphere-prism is shown in Figure 12.

A complete survey of the network as well as the external surveying of the prisms at the different scanning elevations was performed (Figure 13). The terrestrial data were adjusted with the "STAR*NET" (Sawyer, 2001), a least squares analysis software that outputs estimated coordinates as well as a full variance-covariance matrix.

The positions of the retro-reflecting prisms at different elevation allowed the computation of transformation parameters that were applied to the sphere in order to translate the laser clouds into the topocentric frame (Fig. 14); this could realize a direct link between the local ground control network and the laser survey.

In the external reference frame and for different elevations of the VLBI dish the position in space of the vertex of the best fitting paraboloids were computed. Figure 15 shows the position of the best fit vertex in the local frame for the Medicina antenna.

5 Discussion

The laser technique that was adopted for the Medicina and Noto VLBI antennas supplied interesting results that must be combined with information derived by other observing approaches (see e.g. Bolli et al. 2006). In particular, the deformation determined with topographic surveys exploited both with terrestrial and GPS observations

Elevation (deg)	Focal Length of the best-fit paraboloid (m)	
	Medicina	Noto
90	10.2411 ± 0.0001	10.2373 ± 0.0001
75	10.2398 ± 0.0001	-
60	10.2383 ± 0.0001	-
45	10.2334 ± 0.0001	10.2304 ± 0.0001
30	10.2262 ± 0.0001	10.2268 ± 0.0001
15	10.2162 ± 0.0001	10.2190 ± 0.0001

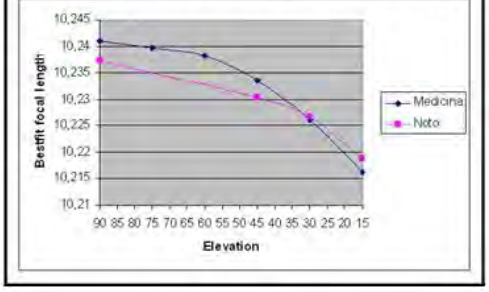

Fig. 10. The variation of the Best-fit Focal length (m) respect to the elevation (deg)

Theoretical Focal Length (m)	Elevation (deg)	Differences with Best-Fit Focal Length(m)	
		Medicina	Noto
10.2590	90	0.0179	0.0217
	75	0.0192	-
	60	0.0207	-
	45	0.0256	0.0286
	30	0.0328	0.0322
	15	0.0428	0.0401

Fig. 11 The differences of the best-fit focal lengths with respect to the theoretical length

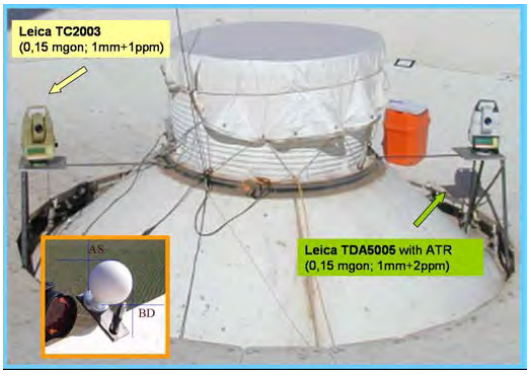

Fig. 12 Total station self centering system for the connection of the targets (spheres) to the local frame

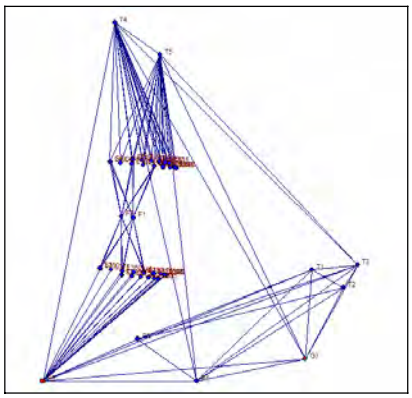

Fig. 13 The local ground control network, F1 and F2 standpoints in the dish and the retro-reflecting prisms surveyed at different elevations.

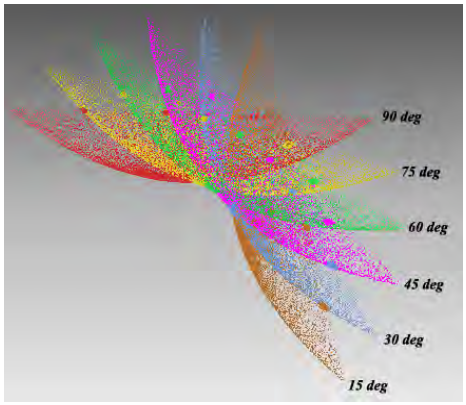

Fig. 14 Medicina scanning session inserted in the external reference system

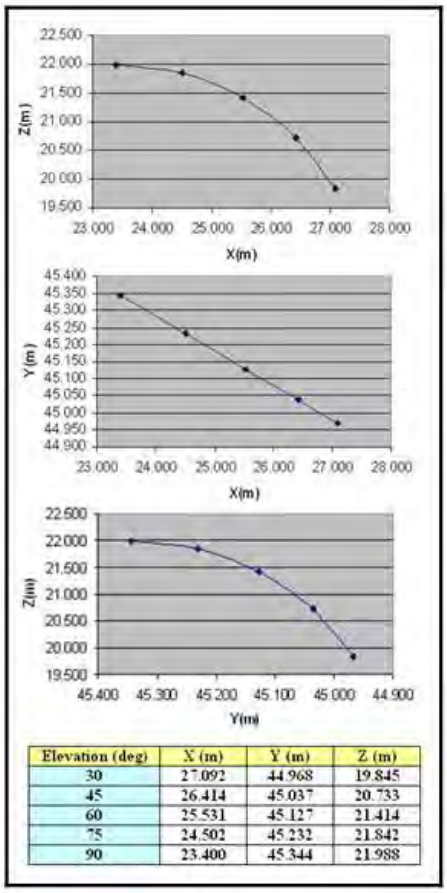

Elevation (deg)	X (m)	Y (m)	Z (m)
30	27.092	44.968	19.845
45	26.414	45.037	20.733
60	25.531	45.127	21.414
75	24.502	45.232	21.842
90	23.400	45.344	21.988

Fig. 15 Medicina antenna: the vertex of the different best fit paraboloids in the external reference system

represent a set of measurement with which the laser scanning results must be integrated. Furthermore, telescope dependent parameters coming from self-calibrating procedures based on astronomical observations must also be integrated and serve as touchstones that must be referred to and compared: this might represent an effective way to link the physical observing point to the theoretical/geometrical reference point. In particular, the focal length variation and its effect on geodetic data processing is a parameter that must be carefully investigated. The combination of the laser scanning results with the topographic results is a complex, though necessary, task in order to obtain a wider view on the deformations that affect the VLBI radiotelescope, quantify their contributions and try to meet the challenging 1-mm accuracy target.

References

Bolli P, Montaguti S, Negusini M, Sarti P, Vittuari L, Deiana GL (2006). Photogrammetry, laser scanning, holography and terrestrial surveying on the Noto VLBI dish. *Int. VLBI Service for Geodesy and Astrometry 2006 General Meeting Proc.* edited by Dirk Behrend and Karen Baver, NASA/CP-2006-214140, 172-176.

Clark T. A, P. Thomsen (1988). Deformations in VLBI Antennas. *Nasa Technical Memorandum 100696.*

Orfei A, M. Morsiani, G. Zacchiroli, G. Maccaferri, J. Roda, F. Fiocchi (2004). An active Surface for Large Reflector *Antennas. IEEE Antennas and Propagation Magazine*, 46, 4, 11 – 19.

Sawyer R. (2001). STAR*NET-PRO V6 least squares survey network adjustment. *Program reference manual*. Oakland, CA.

IAA RAS Radio Telescope Monitoring System

Dr. Andrey Mikhailov, Alexey Lavrov.
Institute of Applied Astronomy of the Russian Academy of Sciences, 10 Kutuzova emb., St.-Petersburg, 191187, Russia

Abstract. Institute of Applied Astronomy of the Russian Academy of Sciences (IAA RAS) has three identical radio telescopes, the receiving complex of which consists of five two-channel receivers of different bands, six cryogen systems, and additional devices: four local oscillators, phase calibration generators and IF commutator.

The design, hardware and data communication protocol are described.

The most convenient way to join the devices of the receiving complex into the common monitoring system is to use the interface which allows to connect numerous devices to the data bus.

For the purpose of data communication regulation and to exclude conflicts, a data communication protocol has been designed, which operates with complex formatted data sequences. Formation of such sequences requires considerable data processing capability. That is provided by a microcontroller chip in each slave device.

The test version of the software for the central computer has been developed in IAA RAS. We are developing the Mark IV FS software extension modules, which will allow us to control the receiving complex of the radio telescope by special SNAP commands from both operator input and schedule files. We are also developing procedures of automatic measurements of SEFD, system noise temperature and other parameters, available both in VLBI and single-dish modes of operation.

The system described has been installed on all IAA RAS radio telescopes at “Svetloe”, “Zelenchukskaya” and “Badary” observatories. It has proved to be working quite reliably and to show the perfonmance expected.

Keywords. Monitoring system, data communication protocol, radio telescope parameters measurement.

1 Introduction

It is a common task for all the sites of the IVS network to interface their unique devices to the Mark IV FS control computer. There are several approaches to solve this problem.

Some complex systems like antenna engine control has its own control computer and it may, for example, are interfaced to the Mark IV FS computer by LAN. Relative simple systems based on the internal controller may be interfaced to the Mark IV FS computer directly with USB or RS232 (depending on the data rate required), without any additional computer.

Our tasks were to design a monitoring system which should interface different devices of the radio telescope to the Mark IV FS computer and to develop software which could enable us to control devices and perform automatic measurements of radio telescope parameters.

The monitoring system described below is the third generation of the IAA radio telescope monitoring system and therefore it is named “G3”.

2 Devices to be controlled

The radio telescope receiving complex consists of ten radio receivers of Kq, X, S, C and L bands. For each band there are RCP and LCP receivers. In the secondary focus cabin, there are also 4 phase-locked local oscillators, the phase calibration system for S/X bands and the IF commutator.

Six cryogen systems (Fig. 1) are situated in the azimuth cabin of the radio telescope.

All the devices mentioned above have the relative simple control logic. This means that the number of specific instructions for the device is not approximately greater than 50, and the device parameters data are about 20 bytes.

The estimation of the data rate required gives us about 4000 baud.

Taking these properties of the devices into account, the most convenient way to join all these devices into the control system is to use the common serial bus.

3 Serial data bus implementation

In Fig. 1, the distances between the radio telescope rooms are shown. The RS485 interface was chosen for the data bus because it is well suited to connect numerous devices with low data rate and it is able to work with long cable lines.

Devices should be galvanicaly insulated from long cables for the electrical damage protection. We have designed a special structure of the serial data bus and special repeaters with galvanical insulation. Each repeater provides galvanical insulation from long cable line and its output distributes the data bus among a group of devices without insulation.

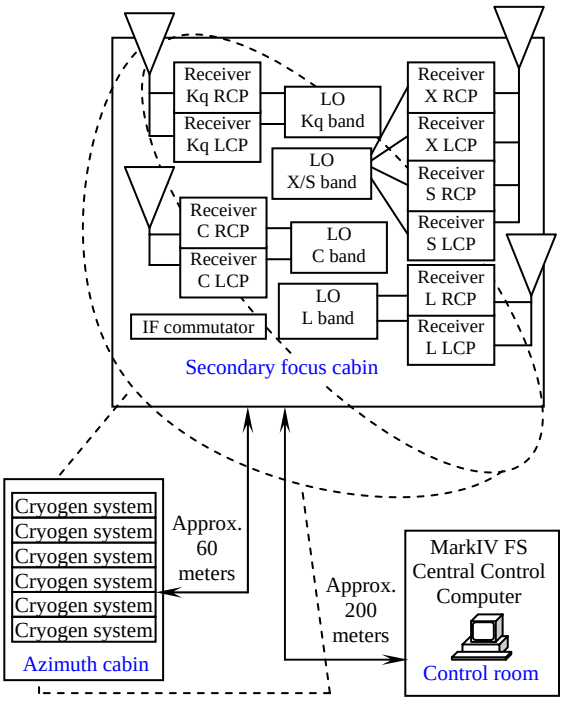

Fig. 1. Devices of the radio telescope receiving complex and their placement in the radio telescope

4 Data communication protocol

A data communication protocol should be designed in order to avoid conflicts between the devices during the data transmission.

The hierarchy of data communication is the following: the Mark IV FS computer is the master device as it always initiates the data communication, other devices are slaves.

According the hierarchy the sequence of data communication can be described with the following example. The master device sends out a two-byte packet. The first byte contains the slave device unique address, and the second byte contains the instruction code. The most significant bits of both bytes in the packet are the markers. They are 1 for the first byte and 0 for the second one. The bytes with wrong markers should be ignored.

Seven less significant bits of each byte can carry the slave address and instruction code.

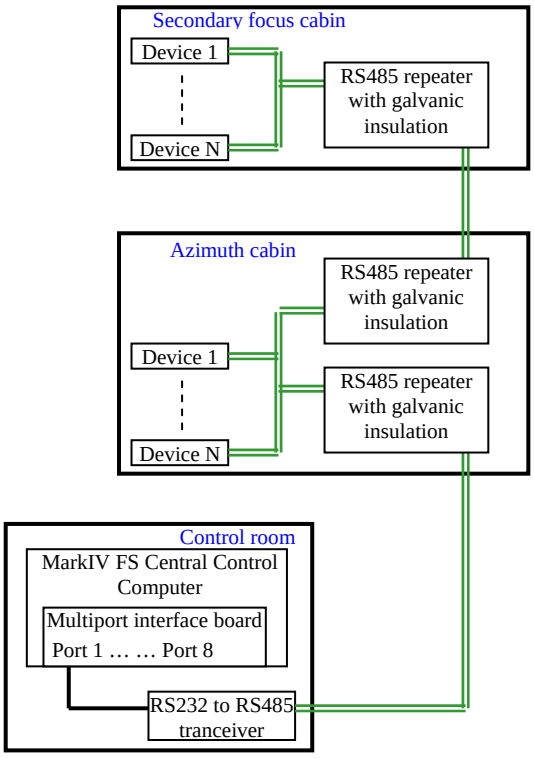

Fig. 2. Serial data bus implementation.

When the slave device receives a two-byte packet with its own address specified, it sends out an echo message. The echo message is a simple text string, containing the slave device address and the code of the instruction received. The time-out for the echo message is 200 milliseconds.

If the echo message is received by the master device and is correct, the master device sends out a two-byte packet similar to the above, but with the confirmation instruction.

When the slave device receives packet with its own address and the confirmation instruction, it executes the instruction specified in the previous packet and sends out an acknowledgement message. The acknowledgement message is a simple text string containing the slave device address and the code of an error occurring during the execution of the instruction. If the instruction specified in the previous packet was “send state”, the slave device must send a state message. The state message is a simple text string containing the slave device address, the device type and the list of the device parameters, separated by spaces and followed by the 8-bit checksum. If the instruction specified in the previous packet was “send version”, the slave devise must send out a version message. The version message is a simple text string containing the slave device address and its firmware version description followed by the 8-bit checksum.

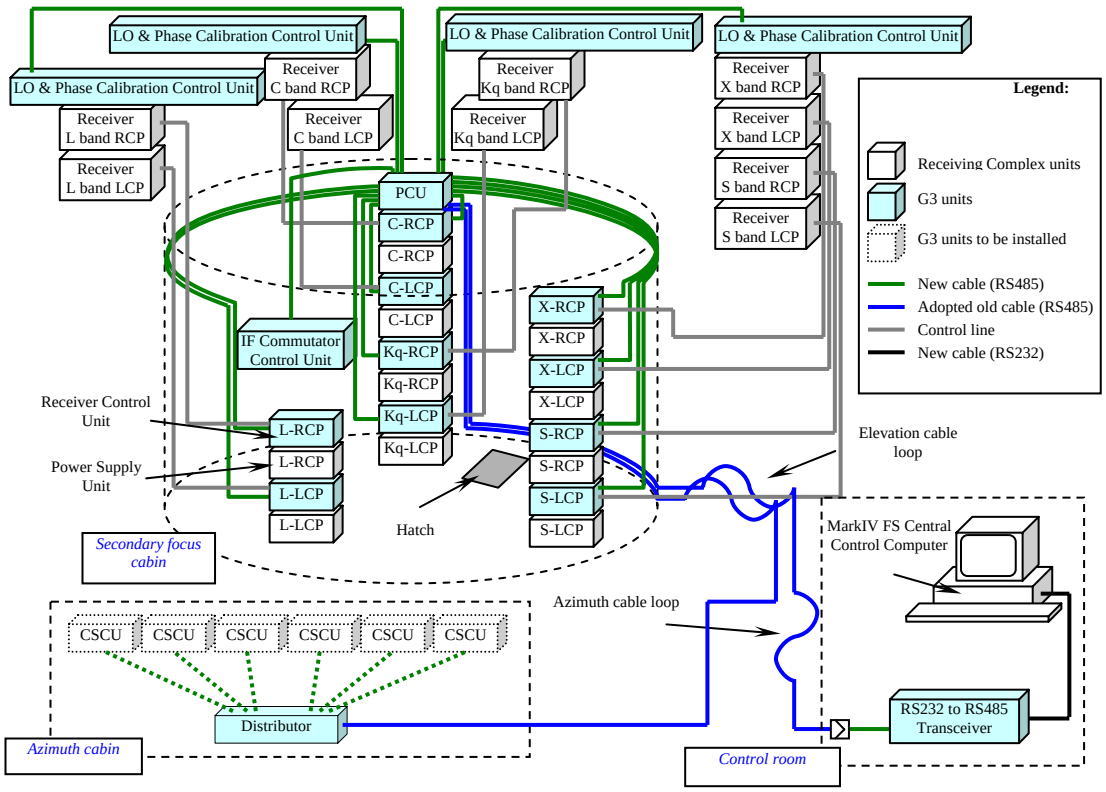

Fig. 3. Location of the G3 monitoring system units on the IAA RAS radio telescope.

The 127 address is common for all the slave devices. It means that the instructions may be sent to all the slave devices simultaneously. If it is the case, no messages from the slave devices must be sent.

The data communication protocol described enables to regulate data communication of 126 slave devices with 127 different instructions for each of them. Only one master device is allowed.

5 G3 system hardware

Fig. 3 shows the IAA RAS radio telescope monitoring system G3 consisting of: the RS232 to RS485 Transceiver, the Power Control Unit (PCU), up to 16 Receiver Control Units (RCU), the Distributor and up to 8 Cryogenic System Control Units (CSCU). Each control unit contains Atmel ATmega8535 Single-chip Microprocessor with an integrated serial port, 4 digital I/O ports and a 10-bit analog-digital converter.

The Power Control Unit distributes the common data bus among the Receiver Control Units and other devices in the secondary focus cabin of the radio telescope. It also controls the power-on commands of the Receiver Control Units.

The Transceiver, the PCU and the Distributor provide optical insulation of up to 1000 V from the long cables.

The Receiver Control Unit controls the receiver and collects the parameters of the receiver operation: the receiver parts operation mode, the power supplies status and cryogen temperatures. The cryogen temperatures dynamic range is 15°K through 273°K with 1°K resolution for the less precise scale and 15°K through 35°K with 0,1°K resolution for the precise scale.

The Cryogen System Control Unit controls the cryogen system and collects the parameters of its operation: the compressor and micro coolers “on” and “off” state, compressor temperatures, and pressure of the cooling agent in different parts of the cryogen system.

Fig. 3 shows the location of the G3 system parts in the IAA RAS radio telescope.

We plan to use the common bus and protocol designed for the G3 as standard facility for the development of the control interfaces for different devices in the radio telescope. Some examples of ongoing projects to be mentioned now are the LO and Phase Calibration Control Unit and R1000 DAS.

6 Special features

The G3 system design has two special features worth of mentioning.

The RS485 "smart" repeater. This repeater provides galvanic insulation in the PCU and the Distributor. There are 2 repeaters in the PCU and one in the Distributor (see Fig. 2). Therefore, we have designed a versatile repeater that can operate in both directions. The repeater has the simple logic circuit which automatically enables and disables RS485 driver of non-insulated output.

Using a pair of such repeaters, connected as the repeaters in the PCU, we can extend the G3 bus for all the desirable number of non-insulated segments.

The Receiver Control Unit power latch feature. The RCU power-on sequence is the following. First, the Mark IV FS computer commands the PCU to generate a power-on signal. If the power-on line stays low, the RCU stays on.

Second, the Mark IV FS computer commands the RCU to set the power latch. The power-on line from the PCU and the power latch are processed with "OR" circuit. Thus, the RCU can only be powered off by commanding both the RCU and PCU, and in case of the PCU power failure the receivers will still be powered on and operating in the mode selected earlier.

7 Mark IV FS software extension

The G3 monitoring system control software has been integrated into the station software in the Mark IV FS central control computer.

The control software for the manual operation has been developed and installed.

We are developing a complete set of the additional SNAP commands, which will allow us to operate the G3 system from the schedule files.

8 Radio telescope parameters measurement

The measurement of the radio telescope parameters is required before an observation session. This measurement can be performed by the operator either manually, or automatically (by the Mark IV FS software).

The Mark IV FS software has built-in procedures for the automatic measurements of the radio telescope parameters for non-modulated signals. But the IAA RAS radio telescopes operate both in modulated and non-modulated modes.

The operators make all the measurements of the radio telescope parameters manually. In order to increase the accuracy of the measurements and exclude the human factor, we are presently developing the software for the automatical measurements of the radio telescope parameters: SEFD, system noise temperature, sensitivity, etc. These procedures are based on well-known algorithms of radio telescope parameters measurement. The fluxes of calibration sources or known calibration noise signals of the receivers will be used as a reference.

9 Future work

Remote monitoring. IAA RAS has two of its three observatories connected to the Internet through high-speed fiber optical lines. The Badary station will be connected as soon as possible.

The goal of our future work is to develop a software, which will allow us to operate the radio telescopes remotely, from IAA RAS in St.-Petersburg. This remote monitoring should be complete as far as possible, i.e. we should be able to apply any possible command to the receiver (for example), and observe the resulting change of the output.

Thus, it will enable us to carry out complex measurements and adjustments remotely without a specialist having to travel to the station.

The G3 extension. The G3 monitoring system is designed to be an easily extendible system. Adding new hardware to the G3 monitoring system will allow us to monitor different parameters of the radio telescope equipment operation, namely: azimuth and secondary focus cabins internal temperature, cryostats vacuum, etc. The new 7 mm band receiver will also be connected to the G3 monitoring system.

10 Conclusion

The G3 monitoring system has been developed and installed into all the IAA RAS radio telescopes. The G3 system is a highly reliable, versatile, easily extendible monitoring system which can be easily adapted to another radio telescope.

The simple multi-address data communication protocol for small data rates has also been developed which can be used in similar systems.

The G3 monitoring system and the additional Mark IV FS software provides an ability to control the radio telescope equipment and carry out measurements of the radio telescope parameters

both on-station and remotely (from IAA RAS in St.-Petersburg, using Internet connections through high-speed optic fiber lines).

References

MAX1480A/B/C, MAX1490A/B. Complete, isolated RS-485/RS-422 data interface. 2003. Maxim Integrated Products. http://www.maxim-ic.com

Recent Developments at the EVN Mk IV Data Processor at JIVE

R.M. Campbell, A. Szomoru *
Joint Institute for VLBI in Europe, Oude Hoogeveensedijk 4, 9771 PD Dwingeloo, the Netherlands

Abstract. We review the fundamental capabilities of the EVN Mk IV Data Processor at JIVE in terms of both spectral and output capacity, discussing the situation that currently pertains and looking forward to the improvements under development. We briefly touch on operations of the correlator with EVN observations, and describe initial fringe tests to two aspiring EVN stations (Evpatoria and Irbene). The greatest strides in the past two years have been made in the realm of *e*-VLBI and progress towards an operational real-time *e*-EVN network. There have been 11 proposal-driven real-time science experiments in the past year, and developments to improve the sustainable data transfer rates and network size are gaining momentum.

Keywords. VLBI, EVN, correlation, e-VLBI

1 Current Capabilities

The EVN Mk IV data processor can correlate simultaneously up to 16 stations with 16 channels per station, each having a maximum sampling rate of 32 Msamples/s (thus a total of 1 Gbps per station for 2-bit recordings). We can currently correlate/provide:

- 1- and 2-bit sampling (all but a handful of experiments use 2-bit sampling).
- parallel- and cross-hand polarization products as desired in dual-polarization observations.
- up to 2048 frequency points per baseline/subband/polarization (*cf.* § 1.1).
- full-correlator integration times down to 0.25 s (*cf.* § 1.2).
- oversampling at 2 or 4 times the Nyquist frequency, in order to provide subband bandwidths down to 500 kHz (the maximum Nyquist-sampled $BW_{\rm sb}$ is 16 MHz).
- multi-pass correlation (*e.g.,* for observations having >16 stations at any given time).
- real-time *e*-VLBI operation (*cf.* § 4).

We can now extract phase-cal tones from data streams; work continues to incorporate these into the standard distribution product (IDI FITS files). Development of recirculation and Mark 5A+ & Mark 5B playback is underway; each of these should increase the spectral resolution of the correlator (see § 1.1).

1.1 Correlator Capacity

The total correlator capacity can be expressed as:

$$N_{\rm sta}^2 \cdot N_{\rm sb} \cdot N_{\rm pol} \cdot N_{\rm frq} \leq 131072 \qquad (1)$$

Here, $N_{\rm frq}$ is the number of frequency points per baseline/subband/polarization. $N_{\rm pol}$ is the number of polarizations in the correlation (1, 2, or 4). $N_{\rm sb}$ represents the number of different subbands, counting lower- and upper-sidebands from the same VC as distinct subbands. The value to use for $N_{\rm sta}$ is "granular" in multiples of 4: for example, if you have 5–8 stations, use "8". Independent of equation 1, the maximum number of input channels ($N_{\rm sb} \cdot N_{\rm pol_{\parallel}}$) is 16, and the maximum $N_{\rm frq}$ is 2048 (a single interferometer must fit onto a single correlator board). The minimum $N_{\rm frq}$ is 16. Table 1 shows some configurations that would use the full correlator capacity. You can now evaluate interactively whether your experiment adheres to equation (1) via the EVN calculator (via the Users' Guide on the EVN web site `www.evlbi.org`).

*on behalf of the EVN Data Processor Group at JIVE

Table 1. Examples of "maximal" correlator configurations (local validity).

$N_{\rm sta}$	$N_{\rm sb}$	$N_{\rm pol}$	$N_{\rm frq}$	comment
8	1	1	2048	EVN spectral-line
9	1	1	512	$9^{\rm th}$ sta: $N_{\rm frq} \rightarrow N_{\rm frq}/4$
16	8	4	16	global cross-polarization
16	2	2	128	re-arranging N's
8	16	1	128	How $N_{\rm sta}$ increase can
12	7	1	128	be absorbed by $N_{\rm sb}$
16	4	1	128	(not necessarily 2^n)

There are two independent developments that would effectively increase the correlator capacity as seen by a user. Recirculation is a means of time-sharing the correlator chips for observations that don't use the maximum bandwidth per subband (the correlator always runs at 32 MHz). This would increase the right-hand side of equation (1) by a factor $\mathcal{R} = 16\,{\rm MHz}/BW_{\rm sb}$ up to a maximum of 8. However, the maximum $N_{\rm frq}$ would remain 2048, as discussed above. The most significant benefit of recirculation would be increased spectral resolution for narrow-band global spectral-line observations; these could get $N_{\rm frq} = 2048$ just as 8-station experiments can now achieve. The second net correlator capacity increase comes when we can use Mark 5B recordings. Whether played back via Mark 5A+ or Mark 5B, the output data format would not have data-replacement headers. Up to now, we have been using local-validity, which tracks a separate validity bit per sample through the correlator. This avoids problems ensuing from Mk IV-format data-replacement headers correlating against each other when the *a priori* delay is close enough to a multiple of a tape-frame length times the fan-out ratio — but at the expense of doubling the correlator resources needed in a given configuration. Being able to avoid the data-replacement headers would thus multiply the right-hand side of equation (1) by 2, including increasing the maximum $N_{\rm frq}$ to 4096.

1.2 Output Capacity

The minimum $t_{\rm int}$ for a configuration using the whole correlator is now 1/4 s. Recent tests suggest that $t_{\rm int}$ of 1/8 are achievable for configurations that use less than half the correlator. However, should recirculation be used, the minimum integration time would be increased by a factor of $\mathcal{R}$ from its nominal value.

These low integration times, together with the fine spectral resolution afforded by large $N_{\rm frq}$, will provide the possibility to map considerably wider fields of view through reduced bandwidth- and time-smearing effects in the u-v plane For example, the fields of view having $\leq 10\%$ decrease in the response to a point source arising from each of these two effects are (Wrobel (1995), § 21.7.5):

$$\begin{aligned} FoV_{\rm BW} &\sim 49'' \, \tfrac{1}{B} \, \tfrac{N_{\rm frq}}{BW_{\rm sb}}; \\ FoV_{\rm time} &\sim 18'' \, \tfrac{\lambda}{B} \, \tfrac{1}{t_{\rm int}}. \end{aligned} \qquad (2)$$

Here, B is the longest baseline length in units of 1000 km, λ is in cm, and $BW_{\rm sb}$ is in MHz. The EVN calculator also evaluates time- and bandwidth-smearing fields of view in accordance with equation (2). Of course, one potential drawback to such wide-field correlations (with the short $t_{\rm int}$ and large $N_{\rm frq}$ they require) is the rapid growth of the size of the FITS file seen by the user — reaching about 7–10 GB per hour of observation at our current maximum output rate. The current record for output FITS files for a single experiment in one session stands at 674.9 GB.

There is also the perhaps non-intuitive conflict between Gbps recordings and $FoV_{\rm BW}$ — in order to achieve Gbps data rates, $BW_{\rm sb}$ will be 16 MHz, and $N_{\rm sb} \cdot N_{\rm pol}$ in equation (1) will be 16 (no cross-pols) or 32 (with cross-pols). Thus an 8-station Gbps experiment can get at most $N_{\rm frq} = 128$ in a single correlator pass, and $FoV_{\rm BW} \sim 6\farcm6/B$, with B still in units of 1000 km ($N_{\rm frq}$, $FoV_{\rm BW}$ halved if using cross-pols). This of course will have consequences for combining sensitivity and wide-field surveying in an optimal way.

2 Operations & Data Flow

We have 16 Mk5A playback units, and two working tape DPUs remain in place. All sessions starting from June 2006 have been recorded entirely on disk (including NRAO stations in global experiments). We operate the correlator an average of 67 hours per week (a three-week cycle in which there are two weeks of night shifts). Correlation of "long" jobs has become more stable and reliable. Our current record for a single job stands at $9^{\rm h}18^{\rm m}$ (in a 32 Mbps spectral-line experiment). Six-hour jobs in 128 Mbps experiments from the March 2007 session have become

routine (each of the continuum and line passes for a whole experiment done in one job).

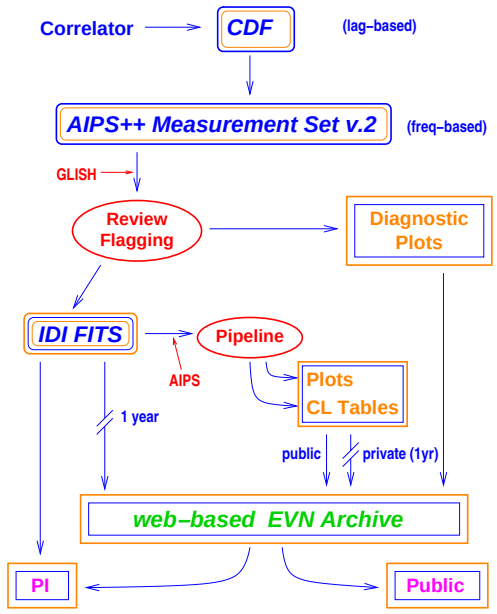

Figure 1. Post-correlation review process for an experiment.

Our internal data review process (figure 1) begins by transforming the lag-based correlator output into an AIPS++ Measurement Set (MS). From the MS, slices of the correlation functions in both time and frequency can be investigated, allowing us to detect and diagnose various problems with the recorded data or the correlation itself. We can also extract information more suited to providing feedback to the stations rather than to the PI (*e.g.,* sampler statistics). We apply various corrections to the correlated data at this stage, such as 2-bit van Vleck and fractional bit shift corrections, and flag subsets of the data for low weights and other known problems resulting in spurious correlation amplitudes and/or phases. Finally, we convert the final MS into IDI FITS files, which can be read into (classic) AIPS directly using `FITLD`. At this stage, the support scientist sends e-mail to the PI describing the correlation and any points of interest noticed during our data review. Distribution of the FITS data now occurs typically via the EVN Archive, but can still be done on physical media (DAT, DVD) as per the PI's preference.

During the course of the post-correlation review, we begin populating the EVN Archive (`www.jive.nl/archive/scripts/listarch.php`) for the experiment. Feedback from the stations and the diagnostic plots from the MS-based data review go into the archive immediately to allow the PI to get an idea about the success of the correlation even before receiving the data. The FITS files also go to the archive, but are kept private for a one-year proprietary period (see the *EVN Data Access Policy* in the EVN Users' Guide for more details).

Once we receive calibration information from the stations, the pipelining of the experiment can begin. The pipeline flags data known to be invalid (*e.g.,* antenna off-source), applies an *a priori* amplitude calibration, fringe-fits sources, makes preliminary CLEAN images using a fixed scheme for phase and amplitude self-calibration, and creates a set of AIPS tables from various stages of the calibration/fringe-fitting process that the PI can later apply directly to the raw data, if desired. A variety of plots are saved during the above process (*e.g.,* `POSSM`s, `VPLOT`s, dirty maps), which can provide more information with which to assess antenna performance. Plots specifically associated with sources identified by the PI as private are also password protected for the one-year proprietary period. The resulting AIPS tables help to simplify the initial stages of the analysis. The quality of the preliminary images may be affected by the lack of interactive data editing inherent in the pipeline concept. More details about the EVN pipeline can be found in `www.evlbi.org/pipeline/user_expts.html`.

3 Aspiring EVN Stations

In the second half of 2006, there were initial EVN fringe tests to two aspiring EVN stations: Evpatoria in the Crimea, Ukraine, and Irbene, near Ventspils, Latvia. Both tests used the DBBCs being developed in Noto, were recorded onto PC-EVN, and were translated into Mk4 format on Mark5 disk packs for correlation. Each test used an array of three stations, and observed about an hour per day over two days.

The Evpatoria test took place on 3–4 August, with Medicina and Westerbork also participating. Good fringes were seen in the baselines to Evpatoria in the expected subbands/polarizations (they recorded LCP into

both polarization channels of 4 out of the 8 subbands). Figure 2 shows the amplitude and phase across the bands for part of a scan.

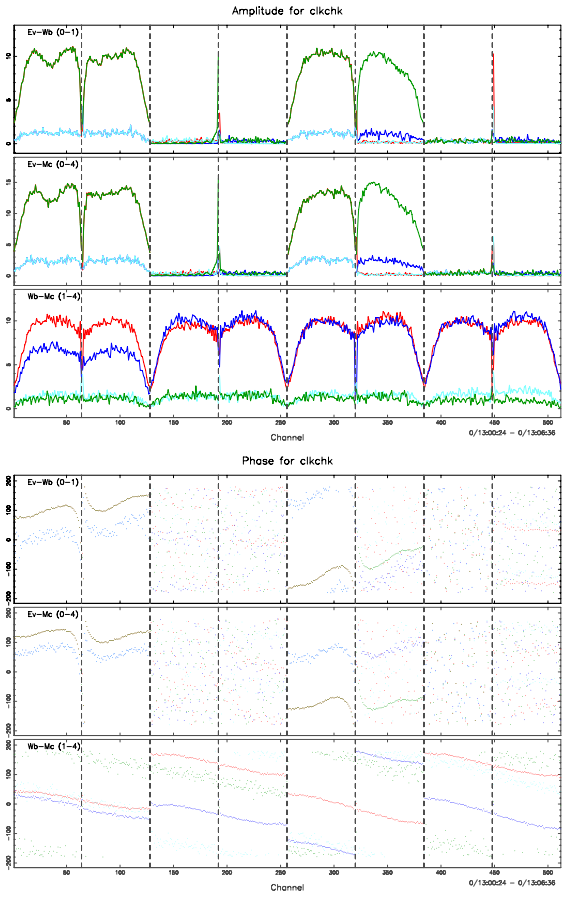

Figure 2. Amplitude and phase across the bands during the Evpatoria fringe test. The polarization color-coding is: Red = LL, Blue = RR, Cyan = LR, and Green = RL.

The Irbene test occurred on 13–14 November, with Noto and Torun also participating. Observations took place at 12 GHz, which was the only receiver available at Irbene. This covers emission from a methanol-maser transition, but is not a standard EVN observing band. The Irbene autocorrelation shows the correct trace for the methanol-maser emission in frequency and shape (figure 3). Separate receiver/observing problems at the other two participating stations meant that this was the strongest statement of success that could be concluded from these observations.

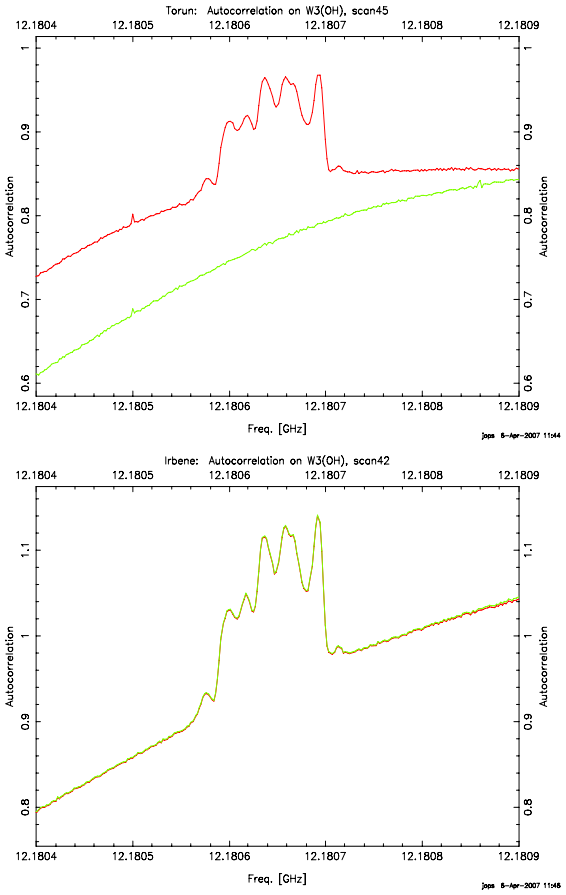

Figure 3. Portion of the Torun and Irbene autocorrelations in the vicinity of methanol-maser emission in W3(OH). The polarization color-coding is: Red = LL, Green = RR.

Many people associated with the EVN and the aspiring stations were indispensable in order to carry out these first tests: W. Baan & W. Alef to initiate the process; G. Tuccari & A. Mujunen to conduct the observations and provide the data in a straightforwardly correlatable format; and staff at the stations to express interest in collaboration with the EVN and to communicate local information necessary for correlation: O. Ul'yanov, A. Konovalenko, V. Shepelev, V. Kulishenko, and A. Nabatov at Evpatoria and I. Shmeld, G. Ozolins, D. Bezrukov, and J. Zagars at Irbene.

4 *e*-VLBI Overview

One of the highlights at JIVE over the past two years has been the funding and commencement

of EXPR*e*S (Express Production Real-Time *e*-VLBI Service). This is a 3-year I3 (Integrated Infrastructure Initiative) project funded by the EC (DG-INFSO), with the broad goals of enabling an operational real-time *e*-VLBI network and looking beyond the current 1 Gbps recording/correlation environment. The project website `www.expres-eu.org` provides the most up-to-date information.

Since March 2006, there have been regular *e*-VLBI experiments, occurring approximately monthly outside of the usual EVN sessions. These experiments are driven by open calls for proposals, in a fashion equivalent to traditional EVN observations. Such real-time *e*-VLBI observations are most attractive to projects that can take advantage of the rapid turn-around time (*e.g.,* adaptive scheduling on a set of flaring sources, when it is not known *a priori* which specific sources may be bright at the beginning of the observations). The more frequent observations also allow more opportunities for a group to obtain VLBI observations (nearly) simultaneously with other observations they may have arranged at other frequencies, *e.g.,* simultaneous VLBI and X-ray observations of micro-quasars at different points in their jet-disc coupling cycles (Fender et al., 2004).

So far, there have been 11 real-time *e*-VLBI experiments. The current "default" array comprises six stations (Jodrell Bank, Cambridge, Westerbork, Onsala, Medicina, Torun), and the reliably sustainable recording rate began at 128 Mbps, and has been 256 Mbps since October 2006. The first two publications resulting from *e*-VLBI EVN observations have already appeared: Rushton et al. (2007) and Tudose et al. (2007).

Increasing the size and recording-rate of the *e*-VLBI network is vital to make the technique attractive to a broader class of experiments. During tests, we have achieved rates of 512 Mbps from each of these stations, and also from Metsähovi in separate K-band tests using a smaller array. Figure 4 graphically summarizes the time evolution of the network size at different data rates for which *e*-VLBI fringes have been seen in scientific observations or tests.

Reliable *e*-VLBI operation has also required considerable software modifications to our control system to ensure the ROT synchronizes to the in-streaming recordings, as opposed to the usual mode in which the playback synchronizes to the ROT. We have also made hard-

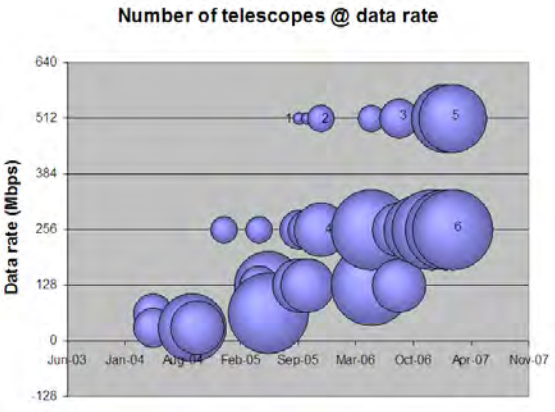

Figure 4. Time evolution of the network size at various recording rates. The diameters of the bubbles corresponds to the number of participating stations.

ware upgrades to the Mark 5A playback units (motherboard upgrades), which were necessary to achieve 512 Mbps recording rates. Similar hardware upgrades to the stations' Mark 5 units have similarly been required. In collaboration with SURFnet (the Dutch NREN), the network at JIVE has been completely redesigned, allowing up to 16 1 Gbps lightpaths and one 10 Gbps IP-switched lambda into JIVE. In the future, this could be upgraded to 16 5 Gbps connections.

One powerful advantage of real-time *e*-VLBI lies in the ability to monitor station performance continually and to provide instantaneous feedback to them. To this end, we have developed a suite of graphical data-quality and fringe monitoring tools, tabular network monitoring and configuration tools, and some utilities to control the Mark 5 units at the participating *e*-VLBI stations.

Seven EVN stations currently have connections at 1 Gbps or better: Jb, Cm, Wb, On, Mc, Tr, and Mh. Sheshan is connected at 1 Gbps through to Hong Kong, and there is currently 622 Mbps available from there to GÉANT (the pan-European research network). Arecibo has a 155 Mb/s connection (and had participated in 64 Mbps pilot *e*-VLBI experiments prior to the commencement of EXPR*e*S), and is working towards a 1 Gbps connection. Effelsberg should be connected at 1 Gbps or more by the end of 2007, and the new Yebes telescope will be connected at 1 Gbps by the time it is ready to participate in EVN observations (a status shared by the aspir-

ing Irbene station). Hartebeesthoek and Tigo are also participating in EXPR*e*S; they are working on improving their connections from their current maxima of 75 & 50 Mbps to 180 & 310 Mbps. Fibre paths from the other Chinese stations exist from the telescopes to nearby cities, but full access to the connection to GÉANT needs to be worked out. The connection from Noto has the bottleneck of getting off Sicily, and the new Sardinia telescope under construction has a similar issue.

Future developments aim towards getting away from the pre-scheduled *e*-VLBI dates and building truer on-the-fly schedule modification techniques to provide a more powerful rapid-response/target-of-opportunity capability. EVN observations of the recent outburst of the recurrent nova RS Ophiuchi (O'Brien et al., 2006) illustrate the importance of highly sensitive (512 Mbps or 1 Gbps) full-EVN observations that can be be carried out at times "demanded" by interesting activity in sources.

5 Software correlation

We have been inserting ftp scans into the standard Fringe-Test and Network Monitoring Experiments during EVN sessions for some time. We process these ftp scans using the NICT Software Correlator `fx_cor` Kondo et al. (2004). We run the this on an 8-node dual-processor PC cluster, where independent baselines are assigned to different nodes/processors. An automatic-ftp feature added to the Field System has been exercised in the November 2006 and March 2007 EVN sessions. This automatically copies a specified portion of a scan from the Mark 5 disk to a linux file and ftp's it directly to the cluster at JIVE, where a script detects the arrival of new data, performs the correlation, and posts the results to a web page available to the stations. NICT has provided responsive support to enable correlation of new recording modes that they would not normally handle. The ftp fringe tests themselves have been very successful in identifying problems early enough to allow stations to repair them before user experiments would have been affected.

Software correlation also forms a focus of the Joint Research Activity under the EXPR*e*S project. Specifically, this looks at workflow management and correlation algorithms that can be applied to a real-time GRID-based correlator. A workflow manager application prototype, to route data to cluster computers such that the network keeps up with the incoming data, has been developed by EXPR*e*S partners at Poznań Supercomputing and Networking Center (PSNC). We have adapted the correlator algorithms developed for the observations of the Huygens descent onto Titan (Pogrebenko et al., 2003)[1] for wide-field applications. The resulting multi-process XF software correlator has produced fringes on astronomical data, and a first version has been provided to PSNC.

References

Fender, R.P., T.M. Belloni, & E. Gallo (2004). Towards a Unified Model for Black Hole X-Ray Binary Jets. *M.N.R.A.S.*, 355, pp. 1105–1118.

Kondo, T., Y. Koyama, H. Takeuchi, & M. Kimura (2004). Current Status of the K5 Software Correlator. *IVS NICT-TDC News*, 25, pp. 23–27.

O'Brien, T.J., M.F. Bode, R.W. Porcas, T.W.B. Muxlow, S.P.S. Eyres, R.J. Beswick, S.T. Garrington, R.J. Davis, & A. Evans. An Asymmetric Shock Wave in the 2006 Outburst of the Recurrent Nova RS Ophiuchi. *Nature*, 442, pp. 279–281.

Pogrebenko, S.V., L.I. Gurvits, R.M. Campbell, I.M. Avruch, J.-P. LeBreton, & C.G.M. van't Klooster (2003). VLBI Tracking of the Huygens Probe in the Atmosphere of Titan. In: *Proc. of Planetary Probe Atmospheric Entry and Descent Trajectory Analysis & Science*, Lisbon, October 6–9. `www.mrc.uidaho.edu/entryws/presentations/Papers/Pogrebenko.pdf`.

Rushton, A., R.E. Spencer, M. Strong, R.M. Campbell, S. Casey, R.P. Fender, M.A. Garrett, J.C.A. Miller-Jones, G.G. Pooley, C. Reynolds, A. Szomoru, V. Tudose, & Z. Paragi (2007). First e-VLBI Observations of GRS 1915+105. *M.N.R.A.S.*, 374, pp. L47–L50.

Tudose, V., R.P. Fender, M.A. Garrett, J.C.A. Miller-Jones, Z. Paragi, R.E. Spencer, G.G. Pooley, M. van der Klis, & A. Szomoru (2007). First e-VLBI Observations of Cygnus X-3. *M.N.R.A.S.*, 375, pp. L11–L15.

Wrobel J.M. (1995). VLBI Observing Strategies. In: *VLBI and the VLBA*, eds. J.A. Zensus, P.J. Diamond, & P.J. Napier, ASP, San Francisco, pp. 411–427.

[1] *cf.* also `www.jive.nl/docs/resnotes`

The Bonn Mark IV Correlator for Astronomy and Geodesy

W. Alef
Max Planck Institute for Radioastronomy Bonn, Germany
A. Bertarini
Institute for Geodesy and Geoinformation Bonn, Germany
A. Müskens
Institute for Geodesy and Geoinformation Bonn, Germany

Abstract. We describe the status of the Bonn Correlator. We introduce the astronomy and geodesy teams, describe the correlator, give an overview of the operations and introduce the upgrades that happened during the past six months.

Keywords. correlator, VLBI, eVLBI

1 Introduction

The Mark IV correlator in Bonn, is jointly owned and operated by the Max Planck Institute for Radioastronomy (MPIfR), the Federal Agency for Cartography and Geodesy (BKG) and the Institute for Geodesy and Geoinformation of Bonn Univerity. It is one of the major correlators for the International VLBI Service (IVS) and it covers an important role in the correlation of millimetre-wavelength astronomy. The Bonn correlator has been constantly upgraded both in software and hardware to keep the pace with the new technology and engineering developements common to the VLBI world, such as the Mark 5B playback system and electronic VLBI (eVLBI).

2 The Team

The correlator is operated by two closely cooperating groups led by Walter Alef for astronomy and Arno Müskens for geodesy. The table names of the members of the two groups and describes their major tasks at the correlator.

3 Correlator Capabilities

The capabilities of the Bonn Correlator can be summarized as:

- 1 standard Mark IV correlator
  - 16 correlator modules
  - 16 inputs
- 7 tape playback units (will be removed this year)
- 9 station units (SU)
- 8 Mark 5A playback units connected via SUs
- 1 Mark 5A (upgrade to Mark 5B in house)
- 3 Mark 5B
- 4 correlator interface boards (CIB)
  - 8 CIBs under construction

We aim to have 12 disk playback units, which initially will be eight Mark 5A plus four Mark 5B. (see Fig. 1).

4 Correlator Operations

Almost 40 % of the total IVS correlation is performed at the Bonn correlator. In 2006 we correlated about 60 geodetic observations including IVS-R1, IVS-T2, Europe, IVS-OHIG and a few test experiments. In the current year all the IVS-R1 sessions will be correlated in Bonn.

The total processing time for 2006 is of about 7200 h.

MPIfR	Geodesy
Walter Alef (department head, correlator software support)	Arno Müskens (group leader)
Alan Roy (deputy department head, astronomer)	Alessandra Bertarini (correlator analyst)
David Graham (support scientist)	Simone Bernhart (correlator analyst)
Heinz Fuchs (correlator operator)	Christian Dulfer (eVLBI support)
Herman Sturm (correlator operator)	7 students (correlation support during weekends and nights)
Michael Wunderlich (electronic engineer)	
Rolf Maertens (electronic technician)	

Table 1. Correlator team.

Figure 1. Correlator at Bonn. Racks with (from left to right): two SUs + two Mark 5A, two Mark 5A + the space for four CIBs and two Mark 5B + the space for four CIBs.

The correlator has been running unattended for experiments with bit-rates less than 512 Mb/s. Sometimes problems with the SUs and the station unit interface modules (SUIMs) affected the results and a consequent recorrelation was needed.

Currently we are awaiting the first release of the Mark 5B correlator software.

Toward the end of 2007 the tape drives will be decommissioned to make space for the computer cluster that is going to become the software correlator (see also Alef at al. in this same conference proceedings).

5 Correlator Upgrades

Haystack Observatory and MPIfR agreed in December 2005 to upgrade the existing Mark IV correlator with:

- Linux-based control computer
- software for Mark 5B support
- extension to 12 stations
- support the correlation of data recorded at 2 Gb/s.

The transition to Linux has already started and two Linux computers (two dual core processors) are actively used in parallel with the old HP machines. To increase the data storage capacity a 10 TB RAID has been connected to a file server through fibre channel. An extra 7 TB storage capacity has been ordered and will serve as storage space for eVLBI data and software correlator input data. Two extra Linux computers are used to monitor the Mark 5 and to deal with the tape library. In the computer pool there is also a dedicated server for eVLBI with 4 TB disk space.

All the Linux machines are connected with Gb ethernet cards (GE).

6 eVLBI Status

The MPIfR is installing a private fibre connection (both 10 GE and 1 GE) between the Effelsberg telescope and the institute in Bonn. The work should be finished by October 2007.

Currently MPIfR has a dedicated 1 Gbps line to Internet for testing eVLBI, although this is a temporary solution.

MPIfR is moving toward a contract with the *Deutsches Forschungsnet* (DFN – german research net) to use the German X-WiN backbone located at the University of Bonn and secure 1 Gbps connectivity for eVLBI.

We plan also to connect the institute to The Netherlands at 10 Gbps for the eVLBI and Low Frequency Array (Lofar).

7 Conclusion

We have given a snapshot of the staus of the Mark IV correlator in Bonn as of April 2007, introducing the people, the hardware capability and recent upgrades for improved disk-based playback and eVLBI. The correlator continues to be a cornerstone of the IVS.

Software Correlator at MPIfR: Status report

W. Alef, D.A. Graham, H. Rottmann, A.L Roy
Max Planck Institute for Radio Astronomy, Bonn, Germany

A. Bertarini
Institute for Geodesy and Geoinformation, University of Bonn, Germany

A.T. Deller, S.J. Tingay
Swinburne University/CSIRO Australia Telescope National Facility

Abstract. We discuss the advantages and disadvantages of soft- versus hardware correlators for VLBI networks. We summarize the features of the DiFX software correlator and its performance. We report first results of a small test installation of DiFX at the MPIfR, the status of a geodetic evaluation of DiFX, and our plans for installing DiFX on a medium sized cluster as a successor to the present Mark IV hardware correlator.

Keywords. VLBI, techniques: interferometric, instrumentation: interferometers

1 Introduction

VLBI has been a main research area at the Max Planck Institute for Radio Astronomy in Bonn since the early seventies. The institute has been operating VLBI correlators since 1977. All correlators have been realized in hardware. The present Mark IV correlator was installed at the beginning of 2000 after seven years of development work by an international consortium.

Digital technology has advanced rapidly in the last few years. Data recording and processing can now be done at much higher rates, which are beyond the capabilities of the Mark IV hardware correlator. The advantages of its enormous integer computing power are at the same time the cause of its inflexibility to adapt to new developments and requirements.

Compared to the performance of computers which roughly doubled every 18 months, the growth for VLB-Interferometers, both in size and recording datarate, was slow. Hence today medium sized computer clusters have already enough computing power to correlate present day VLBI observations.

2 Hard- versus Software Correlator

Both hardware and software correlators have advantages and disadvantages. For hardware correlators the development dominates the overall costs. The development takes several years and typically freezes the state of the art technology of the time of the design into the machine, which is somewhat out-dated at the time of the realization. Nevertheless it delivers the most compute power per hardware and requires moderate amounts of power and cooling.

A sort of hybrid between a hardware and a software correlator can be built with FPGAs (field programmable gate arrays), which have seen an enormous increase in speed and capacity in the last few years. The development effort is less for an FPGA-based correlator, but the power consumption is higher.

A software correlator is a program running on a supercomputer or cluster. It can be written by a capable programmer in less than one or two years. Unlike hardware correlators the software is unclocked and can run faster or slower than real time depending on the observation to be correlated and the computing resources available. The channel and integration restrictions of hardware correlators are not present. The calculations are done in floating point arithmetic and are hence more precise. The code can relatively easily be modified and if more correlation power is needed, more modern computers can be added to a cluster. Big disadvantages of a software correlator are the high costs for running and cooling the cluster. The investment costs are at present less than 500 k€ with the prospect of decreasing by 50 % every 18 months.

At present for a VLBI array of up to 20 antennas both hardware and software correlators can be a reasonable choice, but given the above pros and cons MPIfR has decided for a software

correlator as a replacement for the Mark IV correlator.

At least four software correlators have been developed recently, most probably triggered by the advances in computer performance. At MPIfR we chose to investigate DiFX (Distributed FX software correlation) (Deller et al., 2007) as a possible successor of the Mark IV correlator for geodetic and astronomical VLBI observations. The correlator was developed by A. Deller (Centre for Astrophysics and Supercomputing, Swinburne, Australia) in less than a year. The correlator was successfully verified against the Australian S2 correlator and the VLBA correlator. DiFX was also chosen by NRAO as a possible successor for the VLBA correlator.

For test purposes DiFX was installed on a small cluster at MPIfR to investigate the as yet untested suitability of DiFX for geodetic observations. It should be noted that the developers of DiFX are also interested in adapting DiFX for Australian geodetic VLBI. Synergies will probably result from the collaborative development efforts of three institutions: Swinburne, NRAO, MPIfR.

3 Features of DiFX

As the name indicates, DiFX applies a Fourrier transform to the data followed by cross-multiplication. It is written in C++ and can use the Intel performance library. The correlator model is generated via CALC 9. The software uses MPICH (message passing interface) for parallelisation. Data can be read from disk files or network sockets. Perl scripts exist for creating control files for the correlator from VEX (VLB exchange) files. For geodesy style correlation A. Deller implemented scripts for scan-based correlation and extraction of the correlator model for data export. Data export is in RPFITS file format which can be read into AIPS, where the data can be analysed in the same way as is done for geodetic observations correlated at the VLBA correlator.

An overview of the software correlator architecture is given in figure 1. Correlation belongs to the class of "embarrassingly parallel" problems. To balance I/O and CPU limitations the correlation process can in the first stage of operation be split by antenna, and in the second stage by baseline. In addition every time chunk can be correlated independently of each other.

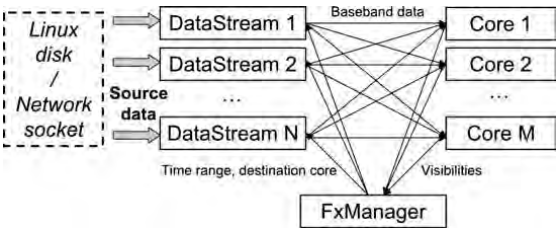

Figure 1. Overview of software correlator architecture. Data are loaded into memory from a disk or network connection by data-stream nodes. These nodes are directed by a master node (FxManager) to send data from given time ranges (typically several ms) to the processing elements (core nodes). The processed data are sent to the FxManager node for long-term accumulation and storage to disk. (Deller et al., 2007)

A cluster is a versatile machine and can be used for other computing intensive tasks during its idle time. At MPIfR we expect to use it above all as a local backend for the Effelsberg LOFAR station (Rottgering, 2007), for pulsar search, as a high resolution spectrometer for a digital receiver, or for radio astronomical simulations.

4 DiFX Performance

We used the test installation on 10 Dual-core processors to correlate 50 % of R1240. This is a five-station observation with 256 Mb/s datarate. The data resided on a fibre channel RAID which was connected to the small cluster with 1 Gb ethernet. Depending on the number of stations in a scan (two to five) we achieved a correlation factor of three to five (correlation time over observe scan length), which is slower than the processing factor of 1 of the Mark IV correlator. This is consistent with benchmarks performed at Swinburne and NRAO.

The extrapolated benchmark in figure 2 indicates that for the correlation parameters 64 MHz bandwidth, 8 sub-bands, 2-bit sampling, 256 spectral points a replacement for the full 16-station Mark IV correlator would require about 200 compute cores. It is expected that the requirements scale linearly with bitrate, so that for a 1 Gb/s observation about 800 cores would be needed to correlate close to real-time. For MPIfR a cluster with initially about 200 compute cores seems to be a good choice.

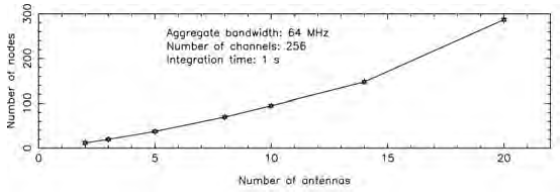

Figure 2. Benchmark data showing the computational requirements of DiFX to correlate in real time. The nodes are single-core 3.2 GHz Pentium processors with 1 Gbyte RAM, 64 MHz of total bandwidth per station was correlated with a 1 s integration period. The figure shows the scaling of computational requirements with number of antennas, using 256 spectral points per 8 MHz subband. (Deller et al., 2007)

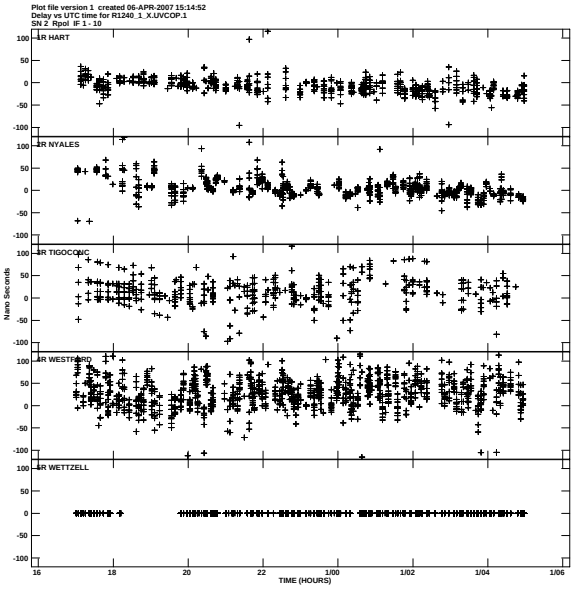

Figure 3. Delay residual in X-band of a single-channel antenna-based fringe fit. The reference station Wettzell has fixed zero delay. Due to the low SNR the scatter in the delay solutions is fairly high.

5 Status of the Geodetic Evaluation of DiFX

The correlated data of R1240 was read into AIPS with a ParselTongue script[1] and an initial single-channel station-based fringe-fit was performed. As an example the station-based delays are shown in figure 3.

The scheduled scan lengths of R1240 are sufficient for detecting the fringes on each baseline with SNR about 20 in a multi-channel fringe fit. In single-channel fringe-fitting in X-band the SNR is typically $\sqrt{8} = 2.8$ times lower which is above the detection threshold only by a small amount. A multi-channel fringe-fit will be performed as one of the next steps.

The CALC/SOLVE analysis of R1240 correlated with DiFX and with the Mark IV correlator are the final aims of our verification.

6 Implementation Plan

At present a proposal is being prepared for the acquisition of a medium sized cluster. The submission deadline is in June of 2007. Specifications have been defined in collaboration with A. Deller and S. Tingay. The funds will be raised by the Max Planck Society. A substantial contribution will come from the BKG (Bundesamt für Kartographie und Geodäsie). A first, small part of the cluster will be installed in late autumn of 2007. It will be used to better determine the requirements for the full cluster, which is projected for 2008. Further improvements to develop DiFX to a full production system which can replace the Mark IV correlator are the following:

- Phase-cal extraction will be needed if non Mark 5B playbacks are used.
- Output to HOPS format, so that the Mark IV fringe fitting software 'fourfit' can be used plus the standard export path via DBEDIT.
- A queue manager.
- Direct input from Mark 5A and 5B playback units. The solution here might be the 'file system' Conduant is developing for Mark 5.
- Output in IDI-FITS format which is more convenient for astronomical data reduction than the present RPFITS format.
- An improved GUI which can handle scan-based correlation.

References

Deller, A.T., Tingay, S.J., Bailes, M. & West, C. 2007, PASP, 119, 318-336

Rottgering, H., 2007, LOFAR - *Opening up a New Window on the Universe*, American Astronomical Society Meeting Abstracts, 210, 66.04

[1] http://www.radionet-eu.org/rnwiki/ParselTongue

e-VLBI data transfer from Onsala and Metsähovi to the Bonn correlator

R. Haas
Chalmers University of Technology, Onsala Space Observatory, SE-439 92 Onsala, Sweden

J. Wagner, A. Mujunen, J. Ritakari
Helsinki University of Technology, Metsähovi Radio Observatory, FIN-02540 Kylmälä, Finland

A. Müskens, C. Dulfer, A. Bertarini
University Bonn, Institute for Geodesy and Geoinformation, Nußallee 17, DE-53115 Bonn, Germany
at Max Planck Institut for Radioastronomy, Auf dem Hügel 69, DE-53121 Bonn, Germany

Abstract. During autumn 2006 and spring 2007 we performed a series of e-VLBI data transfer experiments from the Onsala Space Observatory (Sweden) and the Metsähovi Radio Observatory (Finland) to the VLBI correlator at the Max Planck Institute for Radioastronomy in Bonn (Germany). We used the Tsunami protocol for data transfer both in off-line and real-time mode and successfully transferred VLBI data with data-rates of up to 800 Mbit/s (off-line) and 256 Mbit/s (real-time). Detailed comparisons of the e-VLBI transferred data with traditionally shipped data show that the e-VLBI data transfer is reliable. We describe a new strategy for operational e-VLBI data transfer.

Keywords. e-VLBI, optical fibre networks, Tsunami protocol, correlation

1 Introduction

The turn-around time for VLBI experiments in the IVS rapid series R1 and R4 today is still on the order of several days. One of the main reasons is that the VLBI observational data are still recorded on Mark5 modules that are later shipped via mail services to the correlators. Even inside Europe the shipment of Mark5 modules takes several days, e.g. about 3-4 days from the Onsala Space Observatory, Sweden, to the correlator at the Max Planck Institut for Radioastronomy in Bonn, Germany. To improve the timeliness of geodetic VLBI results, the time needed for the data transfer from the observing stations to the correlators needs to be reduced.

One attractive option is to use electronic data transfer via optical fibre networks, so-called e-VLBI data transfer. An operational use of e-VLBI data transfer would speed up the turn-around time for VLBI experiments and additionally avoid expenses for the shipment of Mark5 modules, both from the observing sites to the correlators, and back.

During the last couple of years several VLBI stations have been connected to high-speed optical fibre networks. Already in 2003 Onsala and Metsähovi were connected to high-speed optical fibre backbones, and recently also the Bonn correlator was connected. To exploit these existing high-speed connections we started in the fall of 2006 a series of test-experiment for e-VLBI data transfer from the VLBI stations Onsala and Metsähovi to the Bonn correlator. Different data transfer options were tested and we developed a strategy that can be used for routine application of e-VLBI data transfer. This work also prepares for near real-time VLBI observations, e.g. for Earth rotation observations.

2 Equipment and network for the e-VLBI data transfer tests

The two VLBI stations Onsala and Metsähovi are connected by 1 Gbit/s and 10 Gbit/s, respectively, to their national university networks SUNET (SUNET, 2007) and Funet (Funet, 2007). These are connected via the NORDUnet IP backbone network (NORDUnet, 2007) to the pan-European multi-gigabit data communications network GÉANT (GÉANT, 2007). The optical fibre from Onsala to Chalmers University of Technology is equipped with a coarse wavelength division multiplexer (CWDM) and has been described in Haas & Elgered (2006). The CWDM allows a shared use of the optical fibre with different wavelength, different MTU buffer sizes and different data rates, and efficiently separates the VLBI data transfer from other obser-

vatory traffic. Figure 1 shows schematically the connection from the VLBI computers at Onsala to the computers at the correlator at the Max Planck Institute for Radioastronomy in Bonn. A similar graph could of course also be shown for the connection between Mestähovi and Bonn but is omitted here in order to save space.

Onsala and Metsähovi are both equipped with

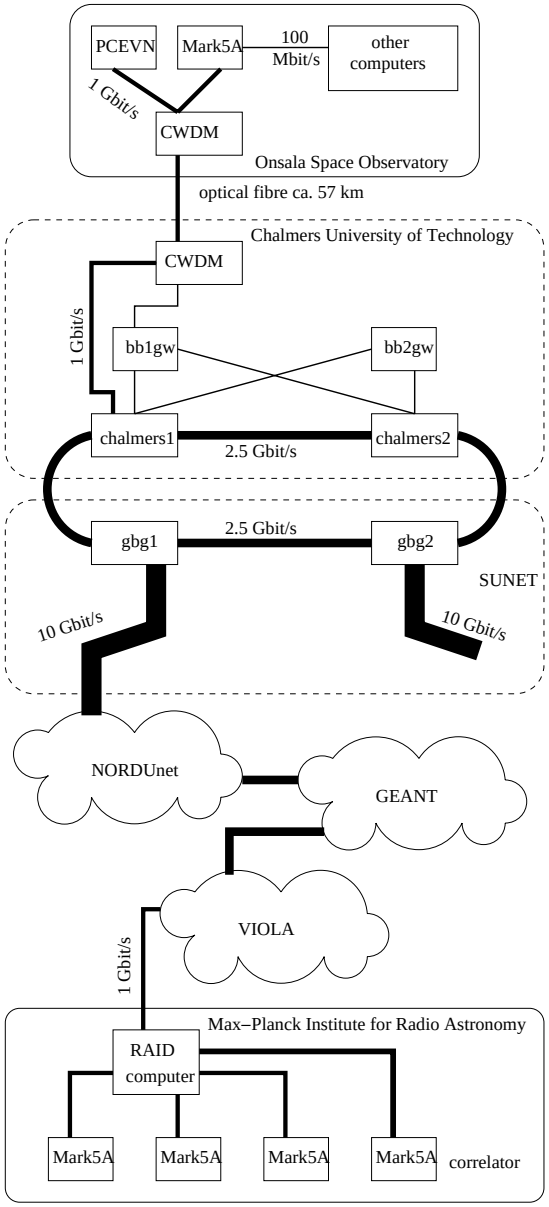

Figure 1. Schematic visualization of the connections from the VLBI computers at the Onsala Space Observatory to the computers of the correlator at the Max Planck Institute for Radioastronomy in Bonn.

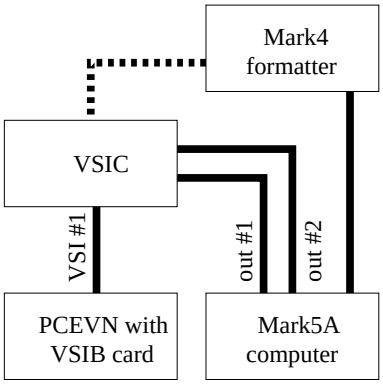

Figure 2. Connection of the PCEVN computer to the Mark4 formatter using the VSI converter.

Mark5 data acquisition systems and one (Onsala) or several (Metsähovi) PCEVN computers (Ritakari & Mujunen, 2002). The PCEVN at Onsala has a RAID system with a capacity of 1 TB, while the PCEVN computers at Metsähovi have RAID systems with capacities of up to 1.5 TB. For our e-VLBI data transfer tests the PCEVN computers were daisy-chained via a VSI-converter (Ritakari & Mujunen, 2002) to the Mark5A computers (solid lines in Fig. 2). This allows simultaneous parallel recording of VLBI data on both the Mark5 modules and the PCEVN RAID system, and real-time data-streaming with the PCEVN. The VSIC may be connected directly to the Mark4 formatter, too (dotted line in Fig. 2), thus bypassing the need for a Mark5 computer entirely.

Since mid 2006 the Bonn correlator has a 1 Gbit/s connection to the German research network VIOLA (VIOLA, 2007) that is connected to the European backbone network GÉANT. At Bonn there is a RAID-PC with a capacity of several TB, and several Mark5A computers for the actual correlator.

3 The Tsunami protocol for high-speed transfer of VLBI data

The Tsunami protocol (Tsunami UDP protocol, 2007) is an open-source protocol for data transfer that was initially developed by Indiana University and then successfully adapted by the Metsähovi group to support realtime and non-realtime VLBI applications. It combines Transmission Control Protocol (TCP) and User Datagram Protocol (UDP) data transfer to allow

high-speed transfer of large amount of data.

Figure 3 schematically describes how the data transfer with the Tsunami protocol works. A low bandwidth TCP control connection establishes the connection between client and server, requests file transfer, controls the file transfer and feeds back the link quality. A high bandwidth UDP connection carries the actual user data, e.g. for our application the VLBI observational data. The client controls all aspects of the data transfer and determines whether data needs to be re-transmitted, or not. This makes the data transfer very fast and reliable. In off-line applications the client can control the protocol to be effectively loss-less. In real-time applications, there are timing and RAM buffer constraints that limit re-transmission effectiveness. Depending on the severity and duration of network congestion some data loss may, though need not, occur. Small amounts of data loss are often considered common and acceptable in real-time e-VLBI (Spencer et al., 2004).

Pre-requisites for an effective use of the Tsunami protocol for high-speed transfer of VLBI data are that the observatories are equipped with commodity PCEVN hardware with integrated 1 Gbit/s Ethernet and a VSIB PCI card. The correlator needs a fast receiving PC with a RAID system. The observatories and the correlator need of course to be connected to high-speed optical fiber networks. The computers on both sides (observatory and correlator) have to be time-synchronized by the Network Time Protocol (NTP, 2007) for real-time Tsunami applications.

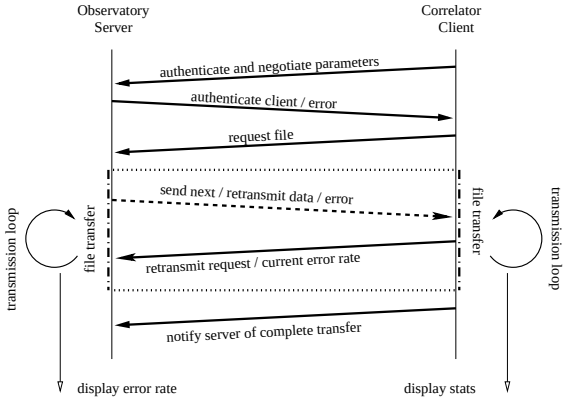

Figure 3. Schematic description of data transfer with the Tsunami protocol. See text for further explanations. Solid and dashed arrows depict TCP and UDP data transfer, respectively.

In off-line mode, a Tsunami server is started at the observatory, and a Tsunami client at the correlator. The Tsunami client connects to the server, starts the data transfer and receives the data that are stored on the RAID system of the sending PCEVN. The client can be called from scripts.

In real-time mode, a Tsunami client is started at the observatory. The server reads VSI bus data directly from the VSIB board of the PCEVN. The Tsunami client at the correlator requests experiment scans from the observatoriy using EVN Filenaming Convention compliant file names that contain auxiliary information about the desired scan. At the requested start time the server begins to stream the required amount of data to the client. The necessary Tsunami client scripts can be generated with a Metsähovi-provided snap-file transform script that reads the usual snap-files created when drudging the VLBI schedule files.

Data loss in real-time Tsunami applications can occur when the network link cannot reliably support the necessary data rates, or if the client PC is not capable of writing to the RAID system at the requested data rate. At high transfer speeds these effects can be more pronounced, but at slow speeds such as 128 and 256 Mbit/s they are usually not a problem. Short duration network congestion can be overcome by buffering of data in the RAM on the server side. The server is re-using the RAM ring buffer that is transparently provided by the VSIB card driver and has a typical size of 144 Mbytes.

4 Experience with e-VLBI data transfer to the Bonn correlator

During autumn 2006 and spring 2007 we performed a series of e-VLBI data transfer tests, see Table 1.

For the very first test we used the EGAE-software (EGAE, 2007) together with the Big Block File Tranfer Protocol (bbFTP, 2007), a file transfer software that is optimized for large files (> 2 GB), and transferred the Euro.84 data from Onsala to Bonn. The EGAE software first read out the data from the Mark5 module and saved them on the internal system hard-disk of the Mark5 computer. Then the data were transferred with bbFTP to the Bonn correlator. Once

Table 1. Experiments in fall 2006 and spring 2007 with e-VLBI data transfer to the Bonn correlator.

Session	data-transfer	station	
Euro.84	off-line EGAE-BBFTP	On	
Euro.85	off-line Tsunami	On	Mh*
T2.047	off-line Tsunami		Mh
T2.048	off-line Tsunami	On	
T2.049	off-line Tsunami	On	
Euro.87	off-line Tsunami		Mh
R1.258	real-time Tsunami	On	
R1.262	real-time Tsunami	On	
R1.263	real-time Tsunami	On	
R1.265	real-time Tsunami	On	

(*) partly real-time

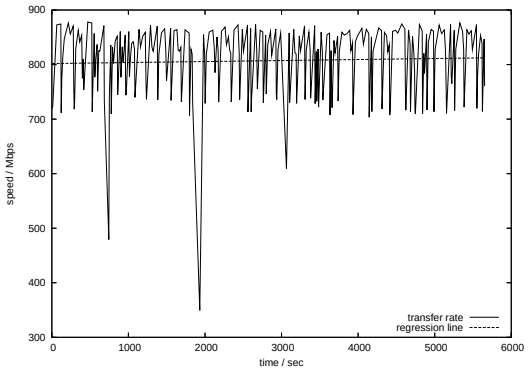

Figure 4. Euro.85 data transfer from Metsähovi to the Bonn correlator using the Tsunami protocol in off-line mode. The total amount of 572 GB were transferred in less than 1 hour and 40 minutes, with an average throughput of 806 Mbit/s.

a scan was successfully transferred, it was deleted from the system hard-disk of the Onsala Mark5 computer, and the next scan was read out from the Mark5 module. This procedure turned out to be restricted by the repeated read-write processes in connection with the data transfer from the Mark5 module to the system disk, and the bbFTP protocol. Thus, this test was quite slow and the effective throughput was only about 94.7 Mbit/s.

For the next tests we used the Tsunami protocol in off-line mode. Data were first recorded on the RAID system of the PCEVN computers at Onsala and/or Metsähovi, simultaneously to the data recordings on the Mark5 modules at the stations. For this purpose the PCEVN computers were daisy-chain connected to the Mark5A-computers, as described in Section 2. After the experiment the data were transferred with Tsunami protocol in off-line mode to the RAID-computer at the Bonn correlator. Data rates of up to 800 Mbit/s were achieved, see Fig. 4. Actually, some scans of Euro.85 were transferred with real-time Tsunami from Metsähovi, and the rest off-line.

After the off-line tests we tested also data transfer with the Tsunami protocol in real-time mode, from Onsala to Bonn. We tested this for a couple of R1-experiments that have a data rate of 256 Mbit/s. Additionally to the real-time streaming, we also recorded the data on the RAID system of the PCEVN computer at Onsala. However, due to capacity restrictions of currently 1 TB, we could only record every second scan on the PCEVN. With the real-time streaming we achieved average throughputs during the 24 hours of observations that were very close to the nominal data rates, see Fig. 5. Only a small amount of data lost due to congestion problems. The missing data were identified and then transferred after the experiment with off-line Tsunami from the PCEVN, or in case the missing data were not saved on the PCEVN, they were read out from the Mark5 module with the command 'disk2file' to the PCEVN and then transferred with off-line Tsunami.

The transferred data were first recorded on the RAID-computer at the Bonn correlator, and then transferred to Mark5 modules, using the

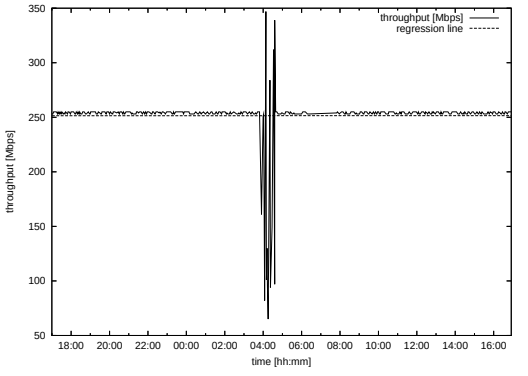

Figure 5. R1.265 real-time data transfer from Onsala to the Bonn correlator using the Tsunami protocol in real-time mode. The experiment had a data rate of 256 Mbit/s. Some data loss occured around 4:00 UT and an average throughput of 251 Mbit/s was achieved.

EGAE-software. For all experiments we also shipped the corresponding Mark5 modules to the Bonn correlator to allow a detailed investigation of the data transfer and comparison of the data. Figure 6 shows a comparison of scan-lengths from an autocorrelation of the two data sets. Positive values indicate that the Mark5-scans are longer, negative values indicate that the PCEVN-scans are longer. It appears that the PCEVN recorded, e-VLBI data transferred scans in general are slightly longer. The reason is that the recording on the PCEVN and the Tsunami transfer are independent from the Field System computer. PCEVN recording and transfer are triggered at the first 1 PPS and continue until the precise amount of requested scan data has been captured. The Mark5 recording in contrast lacks 1 PPS triggering and is dependend on the Field System computer communication and all station related procedures (e.g. preob) that are executed before the actual data recording on the Mark5 modules. These add a varying start-up delay to Mark5 recordings.

Figure 7 shows an example of a fringe plot obtained with e-VLBI transferred Onsala data for Euro.85.

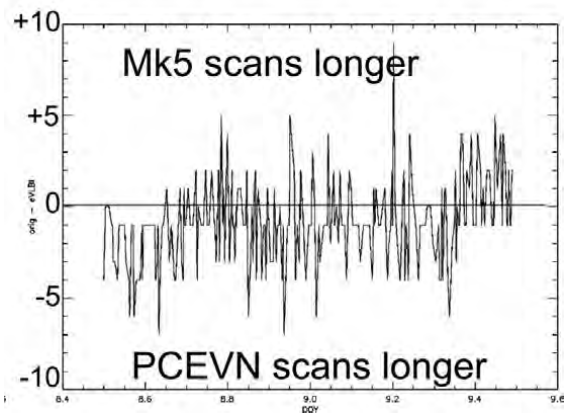

Figure 6. Comparison of scan-length from autocorrelation of data that were recorded on Mark5 modules and shipped to the Bonn correlator, and data that were transferred with the Tsunami protocol to the Bonn correlator.

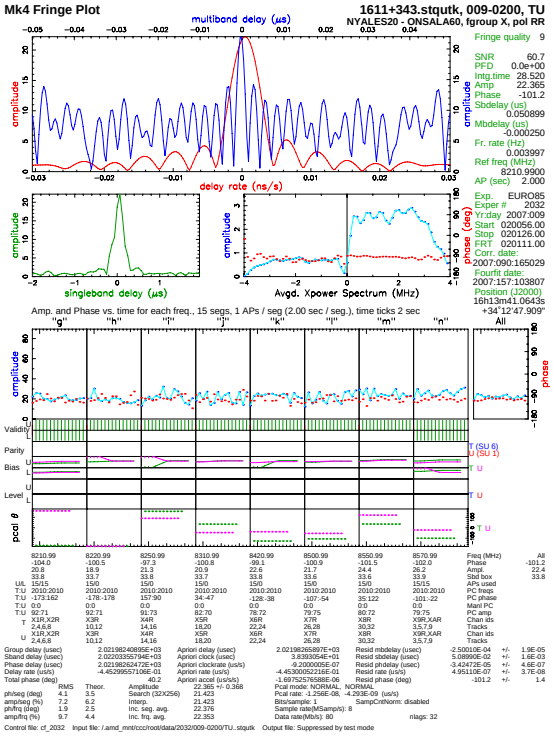

Figure 7. Fringe plot with e-VLBI transferred Onsala data for Euro.85.

5 New strategy for operational e-VLBI data transfer

Based on our experience with e-VLBI data transfer from Onsala and Metsähovi to the Bonn correlator using PCEVN and the Tsunami protocol, we propose a new strategy for operational e-VLBI data transfer. This strategy can and should be used for operational VLBI within the IVS and also prepares for possible near real-time correlation. The strategy involves:

1. real-time data transfer with the Tsunami protocol from the observing station to the correlator
2. simultaneous recording of the data on the PCEVN (backup-1)
3. recording of VLBI data on Mark5 modules (backup-2)

The correlator checks either at the end of the observing session or already during the session whether the real-time data transfer was successful and no data loss occurred. These checks of data completness can be done by scripts that e.g. compare the expected size of the files to be transferred and recorded at the correlator with the size of the actually recorded files at the correlator. Such scripts have been developed at the

Bonn correlator. In case that some data loss is detected, the incomplete or missing scans can be transferred off-line after the session with the Tsunami protocol directly from backup-1 on the PCEVN RAID system. In case there should be any problem with backup-1 on the PCEVN, there is backup-2 on the Mark5 module. In this case the data can be read out from the Mark5 module using the 'disk2file' command and then transferred off-line to the correlator. In the absolutely worst case that the network connection between the observing site and the correlator is completely broken and no data can be transferred electronically at all, the complete Mark5 module could be shipped traditionally via mail to the correlator. As soon as the correlation is completed, both backups can be removed, i.e. the files on the PCEVN RAID system can be deleted and the Mark5 module can be erased, re-conditioned and re-used for the next session.

6 Conclusions and outlook

The e-VLBI data transfer experiments performed in the fall of 2006 and the spring of 2007 with Onsala, Metsähovi and Bonn show that this approach to send geodetic VLBI data to a correlator works well. The data transfer, in particular with the Tsunami protocol, performed very well. Our tests show that it is possible to transfer a 24 h geodetic VLBI experiment to the correlator either in real-time or within two hours after the end of the experiment.

With standard 1 Gbit/s connections to the optical fibre backbone and standard Maximum Transmission Unit (MTU) size of 1500 a throughput of up to 800 Mbit/s was reached with off-line Tsunami. Real-time Tsunami worked reasonably well for several hours with data rates of 256 Mbit/s. Some data loss due to network congestion was still observable. However, we anticipate that this data loss can be avoided when using 10 Gbit/sec connections or light-paths.

Onsala is currently in a process of upgrading its network connection from 1 Gbit/s to 10 Gbit/s. Furthermore, does Onsala consider a possible upgrade of the capacity of the PCEVN RAID system from currently 1 TB to 2 TB. This will allow to record complete R1- and R4-experiments on the PCEVN. These R-experiments currently have typically 1.5 TB of observational data per station. Onsala aims at sending all VLBI data that is going to be correlated at the Bonn correlator via e-VLBI and not to ship any Mark5 modules to Bonn anymore.

Many VLBI stations in Europe and other parts of world have already today PCEVN equipment and are connected to high-speed optical fibre backbones. Thus, we propose to start the operational use of e-VLBI data transfer. A new strategy for an operational e-VLBI data transfer for the IVS sessions was described here.

Acknowledgment

We acknowledge that this work was partly funded by EXPReS. EXPReS is an Integrated Infrastructure Initiative (I3), funded under the European Commission's Sixth Framework Programme (FP6), contract number 026642 EXPReS.

References

bbFTP (Big Block File Tranfer Protocol), `http://doc.in2p3.fr/bbftp/`

EGAE (Experiment-Guided Adaptive Endpoint software), `http://evlbi.haystack.mit.edu/twiki/bin/view/EVLBI/EGAE`

Funet (Finnish University and Research Network), `http://www.funet.fi`

The GÉANT network, `http://www.geant.net`

Haas, R., and Elgered, G., 2006, The IVS network station at the Onsala Space Observatory, In: D. Behrend and K. D. Baver (eds.): *IVS 2005 Annual Report*, NASA/TP-2006-214136, 111–114.

NORDUnet IP Network `http://www.nordu.net`

NTP: The Network Time Protocol, `http://www.ntp.org/`

Ritakari, J., and Mujunen, A., 2002, A VSI-H Compatible Recording System for VLBI and e-VLBI, In: N.R. Vandenberg and K.D. Baver (eds.): *IVS 2002 General Meeting Proceedings*, NASA/CP-2002-210002, 128–131.

Spencer, R., Hughes-Jones, R., Mathews, A., and O'Toole, S., 2004, Packet Loss in High Data Rate Internet Data Transfer for eVLBI, In: R. Bachiller, F. Colomer, J.-F. Desmurs, P. de Vicente (eds.): *Proc. of the 7th European VLBI Network Symposium*, 261–264, `http://arxiv.org/abs/astro-ph/0501018`

SUNET (Swedish University Computer Network), `http://www.sunet.se`

Tsunami UDP protocol, `http://tsunami-udp.sourceforge.net/`

VIOLA (Vertically Integrated Optical Testbed for Large Applications in DFN), `http://www.viola-testbed.de/`

The Mark 5 VLBI Data System

Alan R. Whitney
MIT Haystack Observatory
Westford, MA 01886 USA

Abstract. The Mark 5 VLBI data system is a disk-based data-recording and playback system for high-data-rate VLBI observations, and has been adopted worldwide for VLBI observations.

Approximately 150 Mark 5A systems, capable of recording/playback at 1024 Mbps, are now deployed around the world, directly replacing the Mark 4/VLBA tape-based systems which were prevalent for over 25 years. The Mark 5A system records to an 8-disk removable module which is normally transported to a central correlator facility for processing.

The Mark 5B VLBI data system is designed to support the VSI-H international specification and is now being deployed. It is based on the same physical platform and uses the same disk-modules as the Mark 5A; it also supports the same maximum data rate of 1024 Mbps. Data formatting and time-tagging is done internally within the Mark 5B, eliminating the need for external formatters. Backwards playback compatibility with Mark 5A is accomplished by an upgrade to the Mark 5A. An upgrade of the Mark 5B system, dubbed Mark 5B+, is now also available and capable of sustained recording at 2 Gbps.

The Mark 5C system, currently in development, accepts sampled data through a standard 10 Gigabit Ethernet OSI Layer 2 interface and will support sustained recording up to 4 Gbps. The Mark 5C will support a recording mode which is backwards compatible with the Mark 5B system for playback; Mark 5C is expected to be available in early 2008.

Keywords. Very Long Baseline Interferometry, VLBI, radio astronomy, real-time data-acquisistion

1 Introduction

Data from Very-Long Baseline Interferometer (VLBI) observations have been traditionally captured on magnetic tape, starting in 1967 on 12" open-reel 7-track computer tape at 760 kbps. Extraordinary development efforts over the following 30 years by a number of institutions continually pushed special-purpose VLBI tape-based systems to higher and higher data rates, culminating in systems that approached or equalled 1Gbps sustained rates (Whitney (1993)). Unfortunately, these systems tended to push the technology to the very edge, were extremely expensive both to own and maintain, and were often unreliable as well.

In 2001 Haystack Observatory demonstrated a 'breadboard' disk-based VLBI data system at 256 Mbps based primarily on commercial-off-the-shelf (COTS) technology. This led to the development of the Mark 5A disk-based VLBI data system (see Figure 1), released in 2003, capable of 1024 Mbps sustained data rate. This system was designed as a plug-compatible replacement for the widely used Mark4/VLBA tape systems. Since then, nearly all of the VLBI world has shifted to disk-based systems, most of which are Mark 5A.

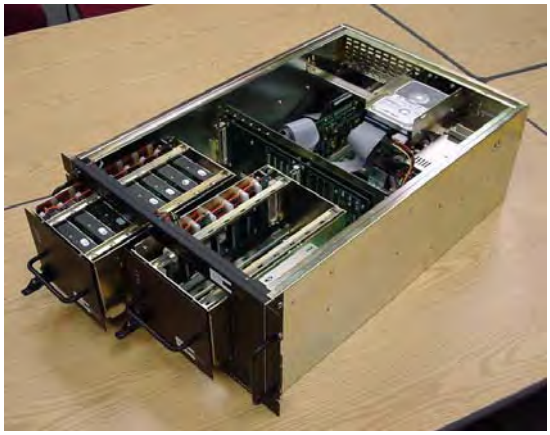

Figure 1: Mark 5A VLBI data system

In early 2006, the Mark 5B system was made available to the VLBI community. The Mark 5B also support 1024 Mbps and uses the same basic platform and disk modules of the Mark 5A, but

implements the internationally agreed VSI-H interface to increase compatibility with equipment developed by other institutions. Also in 2006, the Mark 5B+ system, a slight variant of the Mark 5B to support 2 Gbps, was released and is now also in general use.

In the last few years, with the advent of high-speed network interfaces, and in particular with the introduction of economical 10 Gigabit Ethernet interfaces, the attraction of adapting the Mark 5 system to 10 GigE has grown. As a result, the development of the next-generation Mark 5 system, dubbed 'Mark 5C', is now underway to take advantage this new high-speed interface. The Mark 5C will support a sustained data rate of 4Gbps to a suite of 16 disks through a 10GigE data interface. We expect that the Mark 5C to be available sometime in 2008.

The advent of the disk-based VLBI data systems, but in particular the Mark 5 family of systems, has also helped to rapidly propel the pace of VLBI development, including fully digital back-end systems and transmission of VLBI data over global high-speed fiber networks.

2 Mark 5 System Goals

At the outset of the development of the Mark 5 data system in 2001, a set of general goals was set to guide development. In particular, the goals are:

1. Low cost
2. Based primarily on unmodified COTS components
3. Modular, easily upgradeable
4. Robust operation, low maintenance cost
5. Easy transportability
6. Conformance to VSI-H specification (VSI-H (2000))
7. Compatibility with existing VLBI systems during transition
8. Flexibility to support e-VLBI
9. Minimum of 1 Gbps data rate
10. 24-hour unattended operation at 1 Gbps

The Mark 5A system achieved all of these goals except number 6 and number 10. The Mark 5B system also meets goal number 10, and the recent introduction of 750 GB disks also satisfies goal number 10. Using two 8-disk modules comprised of 750 GB disks, an unattended Mark 5 system can record at 1 Gbps for 26 hours.

3 Mark 5B Data System

Mark 5B Design

The Mark 5B data system was designed to have the following characteristics:

- Uses the same chassis and disk packs as the Mark 5A (Mark 5A (2003))
- Implements the VSI-H Interface Standard
- Maximum record/playback data-rate is 1024 Mbps (same as Mark 5A)
- Requires new Mark 5B I/O card, currently under design
- Eliminates the need for an external formatter (but requires mating VSI-H interfaces)
- With a 14-BBC Mark 4, up to 1792 Mbps can be recorded with two parallel Mark 5B systems
- Mark 4 Station Unit capabilities are designed into the Mark 5B so that Mark 5B systems can be connected to Mark 4 correlators without the use of a Mark 4 Station Unit.
- Built-in phase-cal extraction and state-counting during recording and playback
- Xilinx FPGA design is updateable via software download from PC (Mark 5A FPGA requires programming from a separate external source)
- Upgrade from Mark 5A to Mark 5B requires only replacement of Mark 5A I/O interface card with a Mark 5B I/O interface card

The Mark 5B can be configured as either a Data Input Module (DIM) or Data Output Module (DOM) via software control, which loads the selected personality into the on-board FPGA. We will describe the DIM and DOM separately.

Data Input Module (DIM)

The DIM is responsible for accepting the data on the VSI-H input connector, properly time-tagging it, and sending it to the Mark 5 disk module. A simplified block diagram of the DIM is shown in Figure 2.

DIM functionality is a straightforward implementation of the VSI-H specification. 32 data bit-streams (BS_n) accompanied by corresponding CLOCK, 1PPS and PVALID signals arrive on an MDR-80 connector carrying LVDS signals. The 1PPS signal is used just once (on command) to

synchronize the internal Data Observe Time (DOT) clock, which thereafter keeps time solely by counting CLOCK cycles. Two alternate external 1pps inputs are also available for synchronization, labeled ALT1PPS and ALT2PPS. ALT1PPS is carried on a VSI-H-specified MDR-14 connector with LVDS levels; ALT2PPS is available as a TTL-level SMB connector on the board. Only one of these 1pps signals may be selected to initialize the DOT clock. After DOT clock initialization, the external 1pps signal is not used by the DIM.

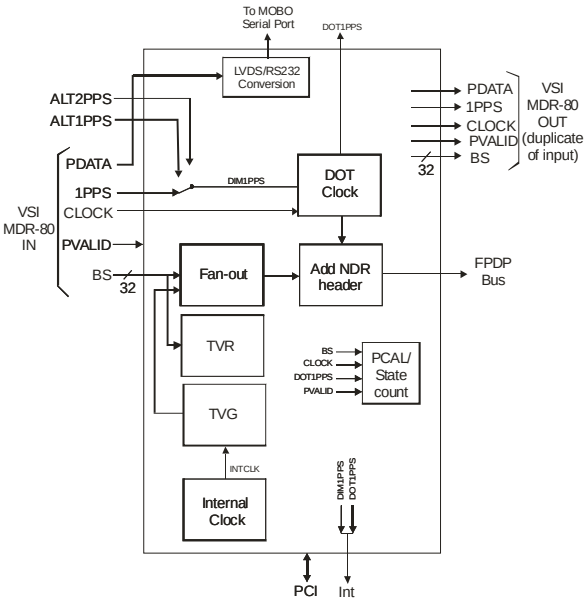

Figure 2: Block diagram of Mark 5B DIM

The number of active bits streams to be recorded may be 1, 2, 4, 8, 16 or 32, as per the VSI-H specification. The selected bit-streams are multiplexed, as necessary, before writing to the 32-bit wide FPDP bus which drives the writing of the disks. The disk data are divided into sequential 10,000 byte Disk Frames (DF), each of which is preceded by a 16-byte non-data-replacement Disk Frame Header (DFH) and includes a sync-word, a DF sequence number, and time encoded in the same format as a VLBA tape frame header, including an accompanying 16-bit CRCC code. The DF frame number resets to 0 at every second tick.

Also included in the DIM is a standard VSI test-vector generator (TVG) and test-vector receiver (TVR). The TVG data can be written to disk for analysis either by software, or may be played back to a TVR in a DOM.

An on-board phase-cal processor can extract 16 tones from each of 16 channels of data, as well as state counts for each channel (Cappallo (2004)). Both the phase-cal and state-count information may be read every second; the state-count information may be used to dynamically adjust signal levels coming into the data-acquisition system in order to optimize the signal-to-noise ratio of 2 bit/sample data.

The PDATA signal is converted to RS-232 and sent to an on-board RS-232 connector, where it may be interfaced to a serial input port on the host PC for processing.

A 'cascade' mode of operation of the Mark 5B is supported so that the signals received on the VSI-H MDR-80 connector are replicated on a VSI-H MDR-80 output connector. This feature may be used to 'daisy-chain' Mark 5B systems together to extend the total unattended observing time.

Data Output Module (DOM)

The DOM is responsible for accepting data that has previously been recorded on disk, then reconstructing replicas of the original data streams and timing signals on the VSI-H MDR-80 output connector. A simplified block diagram of the DOM is shown in Figure 3.

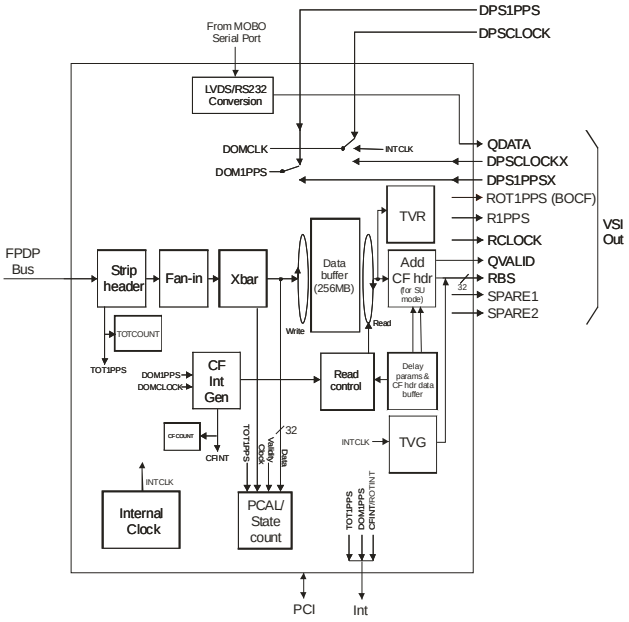

Figure 3:Block diagram of Mark 5B DOM

When operating in standard VSI DOM mode, operation is quite straightforward. External timing

reference signals DPS1PPS and DPSCLOCK, normally generated by the correlator to which the DOM is interfaced, assure that the data output of the DOM is correct in epoch and rate. The data arriving from the disks via the FPDP bus are stripped of Disc Frame Headers, de-multiplexed as necessary, and a crossbar is used to restore the bit-streams to their original positions in the bit-stream mask. The data are then regenerated with a delay (wrt to the DPS1PPS and ROT1PPS ticks) according to user specification. The signals emerging from the VSI-H output MDR-80 connector are a mirror of the signals which were input into the DIM at the time of the recording. An on-board phase-cal processor can extract 16 tones from each of 16 channels of data, as well as state counts for each channel; the processing results are read periodically and transmitted to the correlator.

The DOM also includes both a TVG and a TVR for testing purposes.

Station Unit Emulation Capability

Configured as a DOM, the Mark 5B can act as a replacement for the Mark 4 Station Unit (Whitney (2004)) so that it can interface directly to a Mark 4 correlator. Operating in DOM station-unit mode, the Mark 5B has several functions:

- Delays the data according to a fifth-order spline polynomial supplied to the Station Unit before presentation to the correlator proper
- Inserts headers into the data stream with model information to be used by the correlator proper
- Extracts up to 16 phase-calibration signals from each channel
- Counts state statistics to properly normalize correlation coefficients

The implementation of these functions is aided by an on-board 256 MB memory module which allows rapid dynamic changes in the data-delay at intervals specified by the controlling delay model.

Mark 5B I/O Interface Board

An annotated photo of the Mark 5B I/O board is shown in Figure 4. Note that there are separate MDR-80 connectors for VSI-H input and output. Also note the 256MB memory module that is piggybacked onto the board to support operation of the Mark 5B in ‘station unit’ mode.

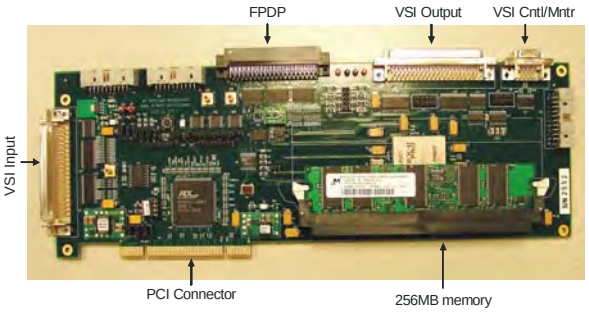

Figure 4: Mark 5B I/O Interface Board

Playback Compatibility with Mark 5A

The Mark 5B data format is designed so that disk modules recorded on a Mark 5B in all commonly-used modes can be played back on a Mark 5A unit which has enhanced FPGA code installed. The playback format of the Mark 5A+ unit when reading Mark 5B disks is standard VLBA track format. This ‘compatibility’ mode allows data recorded on Mark 5B systems to be correlated on existing Mark 5A correlators during the transition period to Mark 5B.

Mark 5B+ (2048 Mbps)

The Mark 5B system has been enhanced to support recording at 2048 Mbps across 16 disks. This system, dubbed ‘Mark 5B+, is identical to Mark 5B except for an updated version of the StreamStor disk-interface card, dubbed ‘Amazon’, from Conduant Corporation. The Amazon interface supports a clock rate of 64 MHz across a 32-bit bus, compared to 32 MHz for the original StreamStor card. The Mark 5B I/O interface card was designed from the outset to support a 64 MHz clock, so in combination with the Amazon board, the Mark 5B+ supports 2048 Mbps across either one disk-module (8 disks) or two disk-modules (16 disks). The Mark 5B+ is in all other respects identical to the Mark 5B. The Mark 5B+ DOM still only supports a maximum playback rate of 1024 Mbps, commensurate with the maximum rate that can be accepted by the Mark 4 VLBI correlator (Whitney (2004)). This means that data recorded at 2048 Gbps data is limited to a correlation rate of 1024 Mbps.

4 Mark 5C Data System

The expected ubiquity of low-cost 10 Gigabit Ethernet-compatible hardware in the marketplace in the near future, as well as its excellent match to next-generation VLBI data rates, has led us to begin

development of a next-generation Mark 5 system which will take advantage of this interface.

The Mark 5C will be implemented in hardware using the existing Amazon disk-interface card with a new 10GigE-specific interface daughterboard being designed by Conduant Corp. Unlike the Mark 5A and Mark 5B, no separate specialized I/O card will be necessary. In addition, the Mark 5C will have the following characteristics:

- The 10GigE interface on the Amazon card will be receive-only, OSI Layer 2, optimized for real-time streaming and recording of data up rates of 4Gbps. Data playback will be only through the host PC, consistent with the rapid move to software correlators; an expected upgrade of the Amazon card to support the PCI-e bus should enable substantially higher transfer rates.
- The data payload from each arriving Ethernet packet will be recorded to disk in the order received. In this sense, the Mark 5C is entirely 'formatless'; i.e. all data formatting must be done by the data source. This allows the user to format the recorded data according his/her needs.

The obvious implication of these Mark 5C characteristics is that the data source is responsible for all data time-tagging, formatting and creation of OSI Layer 2 Ethernet packets.

The data format being designed for standard VLBI use has the following characteristics:

- All Ethernet packets within a single scan must be of the same length but, within certain limits, the packet length can be chosen by the user. Packet lengths up to 9000B will be supported.
- Every Ethernet packet contains a data payload which corresponds to a single Disk Frame (DF)
- Each DF is self-identifying with a 16-byte header field, which contains time-code and ID information; the header field is followed by sample data.
- Since each DF has an embedded time code, the data may be discontinuous in time from packet to packet (advantageous, for example, when recording pulsar data).
- Every Ethernet packet contains data from a single VLBI frequency channel, identified in the DF header.
- A 'backwards-compatible' Mark 5B format will be supported that will allow disk modules written by the Mark 5C in this format to be replayed on standard Mark 5B/5B+ systems.

A new generation of digital backend systems is now being designed that will create Ethernet packets according to these specifications. We expect that the Mark 5C and new digital backend systems will be available sometime in 2008.

5 Summary

After more than 30 years of pushing magnetic-tape technology to its limits, the advent of the modern inexpensive consumer-grade disks has allowed new VLBI data recording systems to be created which are far less expensive, far more reliable, and which allow performance levels unachievable with tape. The Mark 5 series of disk-based VLBI data systems has, in less than 4 years, been deployed to the vast majority of the world's VLBI observatories, and magnetic tape has quickly become a thing of the past. Furthermore, since the introduction of the 1-Gbps Mark 5A system in 2003, data rate capability has doubled to 2 Gbps with the Mark 5B+, and will be doubled again to 4 Gbps with the expected introduction of the Mark 5C in 2008. This performance improvement has been achieved by economical incremental upgrades of the original Mark 5A system, and has maintained backwards compatibility from generation-to-generation.

We wish to acknowledge important support from BKG (Germany), JPL (USA), KVN (S. Korea), MPI (Germany), NASA (USA), JIVE (Netherlands), NRAO (USA) and USNO (USA) in the early development of the Mark 5 systems. We also wish to acknowledge the important contributions of Conduant Corporation of Longmont, CO, who developed the StreamStor real-time technology and who have worked closely with MIT Haystack Observatory in the development of the Mark 5 systems.

References

Cappallo, R.J. “Phase Cal Extraction for the Mark 5B”, ftp://web.haystack.edu/pub/mark5/021.pdf, 2004.

Mark 5A: “Mark 5A User’s Manual”, http://www.haystack.edu/tech/vlbi/mark5/docs/manual5a.pdf, 2003.

Mark 5B: “Mark 5B User’s Manual”, http://www.haystack.edu/tech/vlbi/mark5/docs/Mark%205B%20users%20manual.pdf, 2006.

Whitney, A.R. "The Mark IV VLBI Data-Acquisition and Correlation System", I.I. Meuller and B. Kotaczek (eds.), Developments in Astrometry and Their Impact on Astrophysics and Geodynamics, 151-157, 1993.

Whitney, A.R., Cappallo, R., Aldrich, W., Anderson, B., Bos, A., Casse, J., Goodman, J., Parsley, S., Pogrebenko, S., Schillizzi, R., Smythe, D., “The Mark 4 VLBI Correlator: Architecture and Algorithms,” *Radio Science*, **39**, RS1007, 2004.

VSI-H: “VLBI Standard Hardware Interface Specification – VSI-H”, http://dopey.haystack.edu/vsi/index.html, 2000.

Wide-Bandwidth Digital Backend System for VLBI

Alan R. Whitney
MIT Haystack Observatory
Westford, MA USA

Abstract. Modern digital electronics now allow the replacement of aging VLBI analog backend systems with fully digital systems to provide numerous benefits, including: 1) uniform, repeatable, predictable performance, 2) low cost, 3) increased flexibility, 4) easy expandability, 6) easy transportability, and 5) flexible and rapid implementation through use of modern FPGA devices. A first-generation Digital Backend (DBE) system, based on a polyphase-filter-bank approach that can process four 500 MHz-bandwidth IF signals, has been built (for <$15K), tested, and exercised in real-world VLBI experiments at rates to 4 Gbps/station. Tests at 8 Gbps/station are planned. A second-generation DBE system to process four 1 GHz-bandwidth IFs is now in development in collaboration with UC Berkeley and National Radio Astronomy Observatory; the cost of this system is expected to <$10K.

Keywords. Very Long Baseline Interferometry, VLBI, radio astronomy, signal processing, digital backend systems

1 Introduction

The introduction of digital signal processing into wideband radio-astronomy backend systems is bringing dramatic improvements to the practice of very-long baseline Interferometry (VLBI). Digital backends (DBEs), as they are generically called, provide a host of advantages over old analog equipment:

- Replace nearly a rack full of currently used analog backend equipment
- Extend the output data rate by a factor of at least 4 - to 4Gbps or more; use of multiple parallel DBE's will allow data rates to easily extend to 8 or 16 Gbps
- Provide absolute predictability, uniformity and stability unattainable by analog systems
- Interface directly with the new generation of high-data-rate VLBI data systems, including the Mark 5B/B+/C disk-based systems [Whitney (2007)] developed at Haystack Observatory, as well as other compatible data systems developed elsewhere.
- Cost <10% of the current analog backend system

Coupling these next-generation VLBI backend systems with the most sensitive cm and mm/submm wavelength telescopes will result in radio arrays with aggregate sensitivities that far exceed those possible today – an increase in capability normally associated with the construction of an entirely new telescope.

The new DBE technology has already been used in several successful experiments at data rates as high as 4 Gbps, including mm-wavelengths experiments and geodetic-VLBI experiments. Plans are in progress to extend observations to 8 Gbps for sustained recording. A new 'burst-mode' capability is under development which will use DBEs to create data streams at rates of 16 to 32 Gbps that will be captured into high-speed RAM for a limited amount of time (order 30 seconds or so) and then 'dribbled' at a lower rate of 4 or 8 Gbps to disk-based recording systems. This burst-mode capability is useful for several types of observations: 1) ultra-high bandwidth geodetic observations that record short bursts of on-source data which stream to a recorder at lower rates while the antenna is moving to the next source, 2) observations at mm-wavelength where atmospheric turbulence limits the coherence length of observations to ~30 seconds, and 3) efficient high-bandwidth pulsar observations which record data only during the active part of each pulse.

Implementation of this new technology in the U.S. has been a cooperative venture between MIT Haystack Observatory and the Space Sciences Laboratory at UC Berkeley, with Berkeley providing a generalize-purpose FPGA-based hardware platform for radio-astronomy signal processing, and Haystack and Berkeley working together to implement and test the specific FPGA code for the DBE application.

Once the DBE technology is proven, the technology of the DBE system will be transferred to industry for replication and be made available to the global VLBI community.

2 Current Analog Instrumentation

The current generation of VLBI backend systems had their origins largely in the 1970's and early 1980's, resulting in the systems that are still in use for the majority of the world's VLBI observing. A block diagram of a typical current-generation VLBI backend system, such as Mark 4 or VLBA [Thompson et al (1995)] is shown in Figure 1. An IF signal in a fixed range of 500-1000 MHz is processed through a suite of up to 16 analog baseband-converter (BBC) modules; each BBC module selects a small slice, typically up to 16 MHz wide, of the IF and translates it to a pair of adjacent USB/LSB channels. Each of the output channels is then digitally sampled at the Nyquist rate, formatted and time-tagged by a 'formatter'; the formatter is typically limited to an aggregate data rate of 1024 Mbps or less. The data are then recorded onto magnetic disks or, more recently, may be directly transmitted to a correlator through high-speed global networks.

Though this analog backend system, or small variants, has been the mainstay of VLBI observations for several decades, it suffers from several serious drawbacks:

- Fixed IF-frequency input range: Even current Mark 4 and VLBA systems use different IF ranges, and many modern RF-IF systems, particularly those at shorter wavelengths, employ IF frequencies ranges that extend as high as ~12 GHz; in addition, the proposed broadband (~2-13 GHz) system for geodetic VLBI requires flexibility in the placement of observing-frequency windows.
- High cost: Each of the Mark 4/VLBA BBC modules costs ~$25K, and some parts are obsolete and nearly impossible to obtain. Similarly, the formatter module costs ~$50K and also contains obsolete parts.
- Non-uniformity of channel bandpasses: Due to the analog nature of the BBC electronics, channel-to-channel differences may be significant. Analog-filter variations of up to ~2.5% can produce phase errors up to several degrees.
- Lack of expandability: Expanding data rates beyond 1024 Mbps is a practical impossibility due the high cost and non-availability of the needed components.
- Physical bulk: The current system of IF distribution, analog BBC's and formatters requires nearly a rack full of equipment, which is very expensive and fragile to transport.

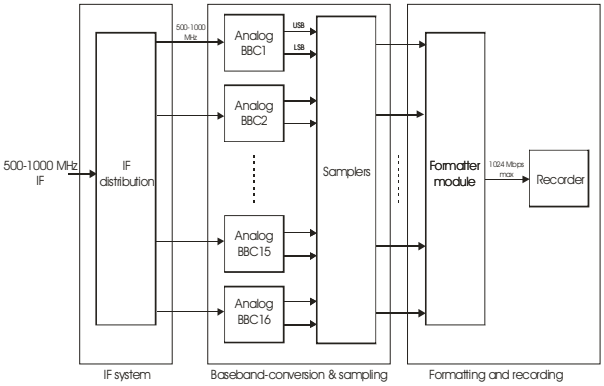

Figure 1: Diagram of legacy analog backend system

3 Design of new DBE system

We have developed a first-generation DBE system which addresses the aforementioned drawbacks of current systems and provides a dramatic increase in capability for VLBI observations. Figure 2 shows a simplified view of the new DBE 'module' with attached Mark 5B+ recording systems; normally, two of these DBE modules are packaged into a single 'DBE chassis'. The primary features of a DBE module are:

- Dual polyphase filter bank (PFB): A dual-port sampler accepts two 500 MHz-wide IF signals and splits each into 2^n-1 contiguous frequency channels of bandwidth $512/2^n$ MHz.
- Dual VSI output interfaces: Two standard data outputs conforming to the VSI-H specification [VSI-H (2000)] can support a total data rate of up to 4 Gbps (Nyquist sampled at 1024 S/sec, 2 bits/sample) from the two independent 500 MHz-wide IF channels. Recording is normally done on a pair of Mark 5B+ systems, though other VSI-H-compliant recording systems may be used.
- Flexibility: The signal-processing algorithm is implemented in an FPGA device which can be easily modified in the field for different channel bandwidths and different bandpass shapes. A fully compatible digital version of the analog BBC could also be implemented for a limited number of channels, though we have not yet created such a design.
- Low cost: The cost of the new DBE module is ≤$7K. Furthermore, the need for a separate formatter is eliminated since the Mark 5B+ recording system formats all data internally.

– Easy expandability: The low-cost and small physical volume of the DBE module allows easy expansion in increments of 4 Gbps. Normally, two DBE modules are packaged into a single chassis for 8 Gbps capability.

– Easy transportability: A full 8 Gbps DBE system, including two Mark 5B+ units, occupies ~63 cm of standard rack space. A complete 16 Gbps system with 8 Mark 5B+ units occupies only a modest-sized rack.

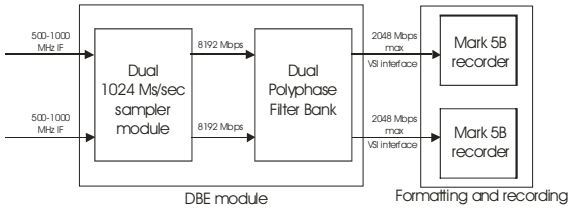

Figure 2: Simplified block diagram of DBE module with attached recorders

3.1 Details of DBE design

Figure 3 shows a more detailed block diagram of a DBE module. The data from the two IF's are sampled at 1024 Ms/sec at 8 bits/sample by dual samplers in a single chip; the sample clock is supplied externally and is phase-locked to the station hydrogen-maser frequency standard. The sample data are processed by two FPGA-based PFB's to segment each 500 MHz IF into 2^n-1 adjacent frequency channels spanning the 500 MHz IF bandwidth (for example – for continuum observations, fifteen 32 MHz channels; a 16th potential channel is unavailable due to the PFB algorithm implemented in the FPGA. Only 16 and 32 MHz channel-bandwidths are currently implemented, but it is straightforward to support other channel bandwidths, either smaller or larger.

An externally-generated station 1PPS signal, also locked to the station hydrogen-maser frequency standard, provides a one-time reference tick to the initiate a module-based 1 pps generator. An on-board Test Vector Generator (TVG) provides test signals for verification of the VSI interfaces to the recording system. An externally generated channel-gain control, normally derived from sample-state-statistics accumulated in the Mark 5B+, can be used to adjust individual channel signal gains in the DBE (through a serial port) for optimal signal-to-noise ratio in correlation processing.

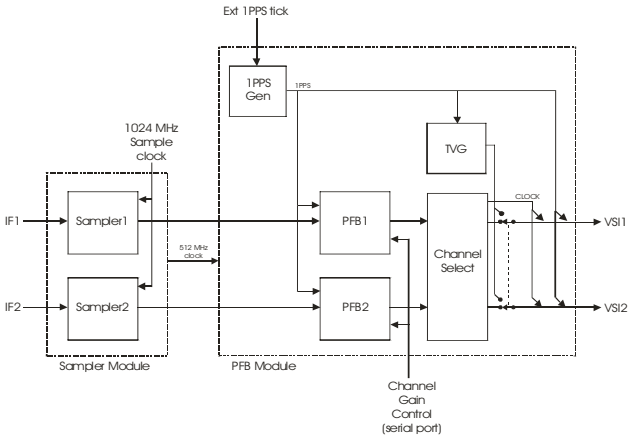

Figure 3: Simplified block diagram of sampling and baseband-conversion modules

3.2 Physical Realization of DBE

The DBE module is implemented on a hardware platform, dubbed 'iBOB', developed at the Space Sciences Laboratory at UC Berkeley as part of its NSF-sponsored CASPER project [CASPER] to provide general-purpose hardware platforms for radio-astronomy signal processing. The CASPER project also provides FPGA library modules for signal-processing functions that can be used as a basis for implementing specific solutions to a variety of radio-astronomy signal-processing problems. The design used in the DBE was jointly developed and tested by MIT Haystack Observatory and the CASPER project.

Figure 4 shows a single iBOB board along with two attached sampler boards (though we use only one sampler board). Figure 5 shows a DBE chassis which includes two iBOB boards along with a common sampler-clock/1pps generator board. The completed DBE chassis accepts four 500 MHz-wide IF signals and processing then into four VSI-H outputs at 2 Gbps each for an aggregate output rate of 8 Gbps at a cost of <$15K.

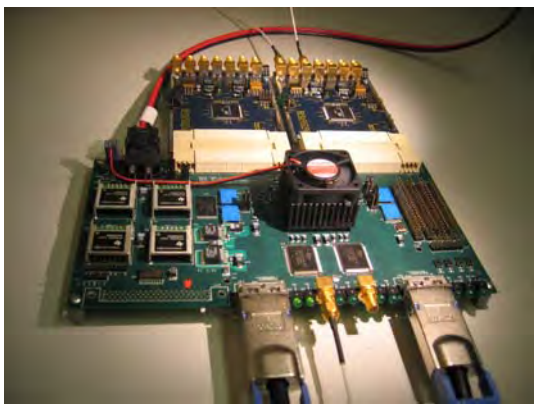

Figure 4: iBOB board with two attached sampler-module boards

Figure 5: DBE chassis with two iBOB boards plus sample-clock synthesizer board

3.3 Compatibility Issues

The PFB algorithms used in the DBE are designed to achieve the widest processed VLBI bandwidth at the lowest cost. This approach is not fully compatible with the old analog BBC systems, which have considerable flexibility in placement of individual frequency bands. However, for major classes of experiments where the maximum processed bandwidth is desired at the lowest cost, outfitting all participating stations with these DBE systems is very cost effective. This is the approach we have taken in all experiments carried out with the DBE system. The FPGA chips can also be re-programmed to emulate the old analog BBC, but considerably more hardware is required since only a few digital BBCs can be implemented on each iBOB board.

4 Experience with the DBE system

Several experiments have been conducted in 2006 and 2007 with the DBE system. As an example of the performance of the DBE system, Figure 6 shows the results of a single 295-second scan taken 4 May 2006 on source 4C39.25 on a baseline from Westford, MA (18m diameter antenna) to NASA/GSFC, MD (9m diameter antenna) spanning 8640 to 9088 MHz at an aggregate data rate of 2048 Mbps. The correlation amplitude and residual phase vs. time are shown for each of the fifteen 32-MHz wide channels, broken into 13-second data segments (amp is lower trace; phase is upper trace). The amplitude and phase of the upper 7 channels are adversely affected by the amplitude and phase rolloff of the receiver in front of the DBE, but the lower 8 channels show virtually 'flat' channel-to-channel phase (phase fluctuations with time are due primarily to atmospheric turbulence phenomena and are largely common from channel to channel). No phase-calibration information has been used in this processing. The corresponding plots for the lower 8 channels processed separately are shown in Figure 7; the RMS channel-to-channel phase variation for the integrated scan is measured to be ~2.5 degrees; this is compared to ~1.0 degrees theoretically obtainable for the SNR of the observation, which is comparable to the best performance that has ever been observed with the analog backend system.

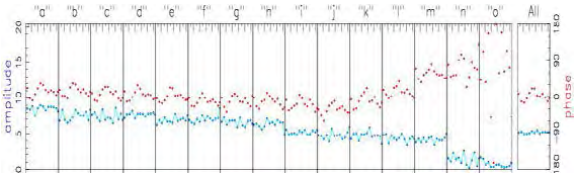

Figure 6: Correlation amplitude and phase vs. time for each of 15 processed frequency channels of sample observation taken with DBE (see text)

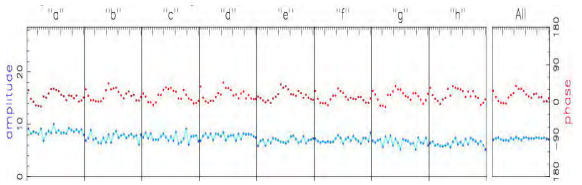

Figure 7: Correlation amplitude and phase vs. time for first 8 channels of observation in Figure 6.

A mm-wavelength astronomy VLBI experiment was conducted in April 2007 at 230 GHz using stations SMTO (AZ), CARMA (CA), and JCMT (Mauna Kea, HI). Two 500 MHz IFs were processed for a total aggregate data rate of 4 Gbps recorded to two Mark 5B+ recorders at each site. This experiment is in processing as of this writing, but the preliminary results show good fringes on all target mm-wavelength sources. The primary purpose of this experiment is to study the black hole at the center of our Milky Way galaxy.

An experiment is planned for fall 2007 using prototype equipment for the next-generation VLBI2010 geodetic-VLBI receiver system which spans ~2-13 GHz. Four 500-MHz frequency windows from each of two linear polarizations will be selected as inputs to the DBE system. The DBE system itself will be modified to select only every other 32MHz-wide frequency channel from each PFB, leading to an aggregate data rate of 8 Gbps/station spread to four Mark 5B+ systems.

5 Next-generation DBE system

A next-generation DBE system (dubbed 'DBE2') is currently under development at Haystack Observatory in collaboration with UC Berkeley and National Radio Astronomy Observatory. The system will utilize an 'iBOB2' hardware platform with enhanced capabilities. Haystack Observatory will develop the FPGA code to implement dual-PFB of two 1000 MHz bands, yielding an aggregate rate

of 8 Gbps streamed to one or two 10 Gigabit Ethernet output connectors. A next-generation Mark 5C recording system is being developed by Haystack Observatory to record 4 Gbps from a single 10 Gigabit Ethernet data stream. Two iBOB2 boards will be packaged into a single DBE2 chassis, enabling the processing of four 1000 MHz frequency bands for an aggregate data output rate of 16 Gbps. DBE2 is expected to be available in prototype version by end 2007 and will be used as the basis for the backend signal processing for a full-up prototype VLBI2010 geodetic-VLBI system. NRAO will develop the FPGA code to implement 4 to 8 digital downconverters that are fully compatible with the existing Mark 4/VLBA analog BBCs. Since the hardware platform for these individual FPGA implementations is the same, the FPGA code can be easily shareable to tailor the DBE to the needs of the user.

6 Dual-channel IF conversion module

In order to convert the output from the telescope or array receiver we are building a flexible IF conversion unit to translate any telescope IF band in the range 0.1 to 12 GHz to a 500 MHz wide band centered at 750 MHz, which is compatible with the DBE system. The center frequency of 750 MHz is convenient since the 1024 Ms/sec sample rate for the A/D converter will be alias-sampled to cover a baseband from 8 to 508 MHz. The sample rate of 1024 MHz, rather than an even 1000 MHz, is needed for the PFB in order to provide the standard 16 MHz (32 Ms/sec) and 32 MHz (64 Ms/sec) VLBI channels. The filter sharpness allows 14 channels of 32 MHz bandwidth with full flatness, plus two outer-edge channels with somewhat reduced flatness (i.e. a total of 2048 Mbps output from each PFB for each IF input signal).

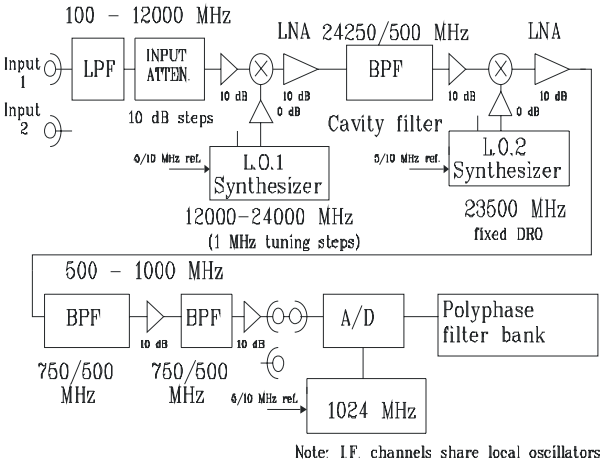

Figure 8: Block diagram of IF-to-baseband converter module (also shows attached A/D converter and PFB)

Figure **8** shows a simplified block diagram of the converter module. The converter will process two IF channels which share both LO1 and LO2. Table 1 lists the preliminary specifications. The estimated replication cost for a dual-channel IF converter is ~10K$.

IF input range	100-12000 MHz
Number of input channels	2
Gain	0-60 dB in 10 dB steps
Output	508-1024 MHz
Flatness	+/- 2 dB
LO phase noise	< 5 deg rms
LO temp Co	< 1 ps/degC
LO frequency resolution	1 MHz
Spurious-signal rejection	< -100 dBc
Image rejection	better than 60 dB
Nominal output level	0 dBm
IIP2	> 40 dBm
IIP3	> 10 dBm

Table 1: Preliminary specifications for IF-to-baseband converter module

7 Future Projects with High Bandwidth Global VLBI Arrays

Besides dramatic improvements in geodetic-VLBI, implementation of DBE technology on global VLBI arrays will significantly broaden the scope of other scientific investigations. A sample of such areas enabled by high sensitivity VLBI includes:

- Launching AGN Jets: Relativistic jets in AGN are powerful cosmic accelerators, but detailed mechanisms for their generation and high degree of collimation are poorly understood. High sensitivity VLBI polarimetry can address the important question of whether magnetically accelerated and focused jets originate near a Massive Black Hole or many parsecs downstream.
- Kinematics of the Milky Way and the Local Group: High precision astrometric observations of interstellar masers, pulsars, and binary systems with high bandwidths will increase reference frame accuracy by factors >6 for our Galaxy, and constrain the mass content and distribution within the Local Group, including the dark matter halo.
- Detailed Images of GRB and SN Explosions: The ability to make high

fidelity and high angular resolution images of these events as they evolve in time will provide new constraints on theoretical models including burst energetics and composition of the surrounding medium.

- Spacecraft Navigation: Accurately locating spacecraft that are many AU from Earth is a critical mission of the NASA Deep Space Network. High sensitivity VLBI increases positional accuracy by allowing weaker quasars, located closer to the spacecraft, to be used as reference points.

8 Summary

The promise of the modern digital electronics to replace existing analog backend systems for VLBI has been demonstrated. Low-cost digital backend (DBE) units have been designed, verified and used in real-world VLBI experiments at aggregate data rates to 4 Gbps/station, with 8 Gbps/station expected in 2007. A next-generation DBE system is under development which will extend this to 16 Gbps. These systems are finding immediate use in new broadband geodesy and astronomy VLBI systems and will likely completely replace the existing analog systems within a few years.

References

CASPER: Center for Astronomy Signal Processing and Electronics Research, http://casper.berkeley.edu/

Thompson, A.R., (1995) The VLBA Receiving System: Antenna to Data Formatter, in *Very Long Baseline Interferometry and the VLBA*, J.A. Zensus, P.J. Diamond, and P.J. Napier, Eds., Astron. Soc. Pacific Conf. Ser., **82**, 73-92.

VSI-H: (2000) VLBI Standard Interface Specification – VSI-H, http://www.haystack.edu/tech/vlbi/vsi/index.html

Whitney, A.R., (2007) The Mark 5 VLBI Data System, a companion paper in this compilation of EVGA 2007 papers.

DBBC – A Flexible Environment for VLBI and Space Research: Digital Receiver and Back-end Systems

G. Tuccari, S. Buttaccio, G. Nicotra
Istituto di Radioastronomia,
INAF, Contrada Renna, 96017 Noto (Sr), Italy

W. Alef, R. Keller, M. Nalbach, M. Wunderlich
Max Planck fuer Radioastronomie,
Auf dem Huegel, D-53121 Bonn, Germany

Abstract. The Digital Base Band Converter project produced a general method and a class of boards giving the possibility to build a general purpose radio system for VLBI or single-dish observational activities. Moreover it is evident as disposing of elements able to operate in a frequency range of few gigahertz, the same parts can be adopted for the direct sampling of radio frequency bands, and not only for intermediate frequency stages. Such approach suggests the realization of what can be defined a 'digital radio system', where such definition would include receivers with conversion not realized with analogue techniques, while still maintaining only amplification stages in the analogue domain in order to satisfy requirements for the analogue to digital conversion unit.

This paper presents a description of the elements developed in the DBBC project, with their use in different environments, in order to realize different instruments. The flexibility of the system is then evident because an appropriate distribution and assembly of parts is able to satisfy more requirements.

The description includes also the upgrade program where new elements with improvements are introduced for additional functionalities and optimization of the general performance.

Keywords. Digital radio, digital back-end, FPGA.

1 Introduction

The DBBC system is a complete environment able to handle data processing for a variable number of radio frequency bands in order to produce a very general data output under different types of physical supports.

It is showed in the bibliography the evolution of the development that has been realised as an European VLBI Network project.

At the present time few other similar developments are under way, with pretty different elements in the architectural aspect. Indeed what is still keeping unique such project is the flexibility in joining different elements for getting a variable number of radio bands available for producing a large number of high data rate output signals. Such variability, that is reflected in an appropriate use of elements with their related cost, produce an high degree of flexibility.

The different elements can be placed in a multitude of hardware architectures, that adding the flexibility due to the FPGA elements in terms of 'internal' hardware realization, allows to achieve a very high degree of freedom for producing data processing of the signals detected by the receivers placed in the radio telescope.

Example of implementation are pointed-out in terms of different flavours of digital back-ends and digital receivers.

2 System components

2.1 The ADBoard1

An analogue signal coming from the receiver in order to be processed in numerical format needs to be converted in the digital domain. To realize such functionality the ADBoard1 is adopted.
Input and clock signals can be entered as single-end or differential. Moreover a differential reset input is available to be used to synchronize more boards when operating in the same environment. A picture of this system component is showed in the fig.1.

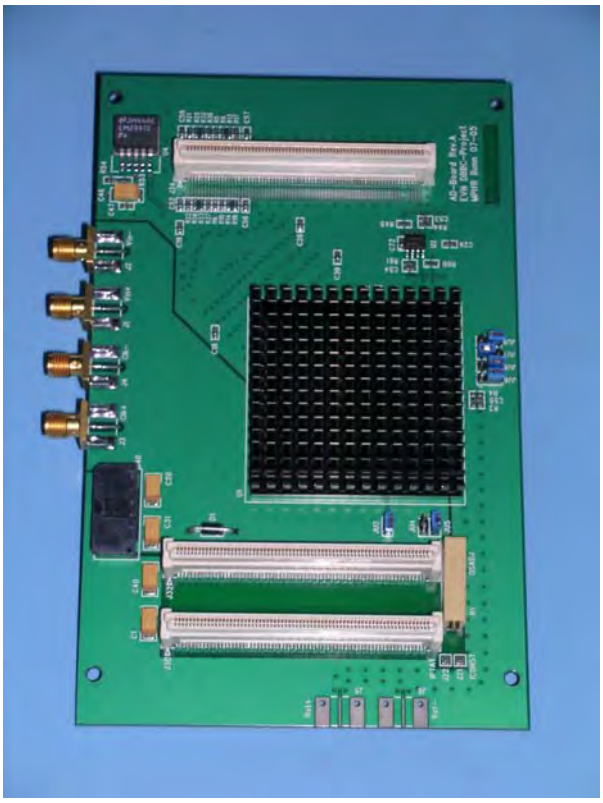

Fig. 1 Analog to digital conversion board ADB1.

The ADB1 is producing a digital representation of an analog signal entering the system up to a maximum frequency of 2.2 GHz, sampled at a maximum rate of 1.5 GHz with a 8-bit representation. In order to reduce the output data rate a 2x8-bit de-multiplexed version of two consecutive samples is produced in double data rate at a quarter of the sampling frequency. Additional functionalities are possible to take into account possible voltage offset present within the analog signal, so as different representation schemes.

2.2 The Conditioning Module

The analogue signal as coming from the receiver is not in general appropriate to enter the ADB1 because more elements need to be properly taken into account. Indeed the amplitude should be limited in order to avoid any over range that would introduce additional unwanted noise to the proper noise band. In the same time levels should be not too low so to optimize the signal representation in the conversion domain. In terms of frequency domain the AD device is able to sample data in multiple adjacent Nyquist zones, so the effective sampling frequency will be a limitation for the instantaneous bandwidth while maintaining the possibility to explore different regions of the spectrum for multiple higher frequency portions of such bandwidth. Such opportunity obliges to define which Nyquist zone to address to the AD to avoid superimpositions of simultaneous portions of the entire band satisfying the same requirements, with introduction of unwanted additional noise to the wanted part of spectrum.

A total power measurement needs to be available to the user for several reasons, such as real measurement for scientific purposes, signal level control, automatic gain control.

To accommodate all these functionalities the Conditioning Module has been developed able to take care of such aspects. An image of the first version is showed in the figure 2.

This unit is able to operate in the range 0.01-2.20 GHz as required by the ADB1 and can support a selection of one between four input channels. An active amplitude control in the range +-16dB assures

Fig. 2 Conditioning Module

a proper level control for the ADB1 and a selection is possible between four band definition filters, inserted in such unit.

Total power measure is available in the entire range and readable trough a digital interface, used also for all the other functionalities required to have a control related to the PCSet, a computer system, part of the DBBC components.

2.3 The CoreBoard1

Data coming from a maximum of four ADB1 boards are available to the processing elements, named CoreBoard1. A number of such boards can share the same group of sampled data, to produce a number of 64 processed channels. The output data channels could on the other hand be produced by different groups of sampled data, giving the possibility to produce a mix of channels coming from more than 4 input analogue channels.

The processing board adopts a large FPGA and is showed in the figure 3. With its the very general structure it's possible to process data injected into the board in a really great numbers of modes. So the output channels produced by one or more of such board will follow the mathematical sequence of operations internally programmed.

An output bus is carrying the 64 differential data channels, related clock and timing signals, while a further bus is adopted for service functionalities, like the dialogue with the PCSet, Jtag programming chain, digital to analog monitoring channel, an so on.

2.4 FiLa Board

The First/Last board of the system is named FiLa Board and accomplishes all the functionalities that are related to the communication with the external world. So the first board is able to act as a link between the PCSet and the elements of the system, to connect the Jtag programming interface, to insert 1PPS timing signals and other ancillary control functions. The last board is supporting two VSI interfaces with equalization control for adapting particularly long cables, includes a DA converter for monitoring functions, and support Jtag additional elements in the chain. An image is shown in figure 4. A set of external connections is available in order to support the monitoring of system 1PPS and the 80Hz synchronization signal for continuous Tcal measurements.

Fig. 3 The processing board CoreBoard1.

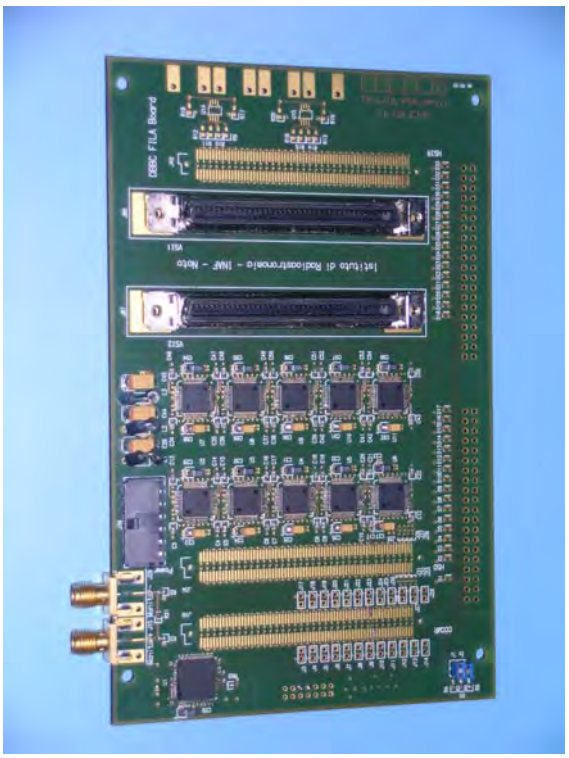

Fig. 4 The FiLa Board.

3 Upgrade

An upgrade process is under way in order to produce a new class of components to increase the performance. A description of the main elements is reported.

The ADB2 still maintaining compatibility with the ADB1 is able to sample signal up t 3.5 GHz with a sampling clock until 2.2 GHz. So the instantaneous bandwidth is up 1.1 GHz and in about three Nyquist zones the entire range can be covered. Output of this board can be slowed up to four 8-bit bus for feeding the Core processing boards. Several output modes are available depending on the clock rate adopted.

A piggy-back board can be attached to the ADB2 to extract data or inject in the sampled data chain, giving the possibility to adopt a different transfer method. In this connection the full 10-bit representation is available.

Such connection is for example used by the FiLa10G board, a second upgrade for the system. Such element is acting in a triangle connectivity in order to relate the output of the ADB2 or the input of the data samples bus with a 10Gbps bidirectional optical connection and with a set of two input and two output VSI connectors. In practice it's possible to interconnect sampled data with a 10Gbps link for a remote placement of the ADB2 and still use the same board for receiving data from a remote source. What described is a 'first stage type' functionality, but the FiLa10G is a first/last type board, so the last functionality is related to the ability to transfer processed data (coming from the last part of the chain), because VSI data can be transferred in bidirectional fashion using the optical link, so as the sampled data can be forwarded to the VSI connections. All the triangle bidirectional functionality is allowed.

The third main upgrade is related to the CoreBoard2. The new processing board is adopting a last generation FPGA device with much improved performance in terms of number of gates available and as operating clock frequency. In the down-converter functionality for instance a single CoreBoard2 is able to replace four CoreBoard1. Then the calculation density is much improved giving the additional chance to accommodate more units in a same box, with related reduction of general cost and cooling needs.

The CoreBoard2 is able, similarly to the ADB2, to support a piggy-back module, that can for example used to add a great quantity of memory to the system. This could be useful in a number of operations such as the de-dispersion functionality in the pulsar research field. Further uses can be related to a peculiar redistribution of data or correlation functions.

4 Different functionalities

With the elements described above a number of different functionalities involving a pretty variable number of input and output sources can be realized.

Three examples are described for representing the potential aspects that can be covered within the same instrument with the simple change of firmware or with the different assembly of the same parts. The first is represented by the most obvious VLBI back-end resembling the MK4/VLBA terminals. A complete system is obtained with the functionality of 8/16 independent base band converters adopting a chain as shown in the figure 5 for 8 bbcs, where a chain of a first FiLa Board, four ADBoard1, eight CoreBoard1, a last FiLa Board are placed coupled to produce a system with a maximum output data rate of 4 Gbps with two VSI connectors to supply a VSI recorder.

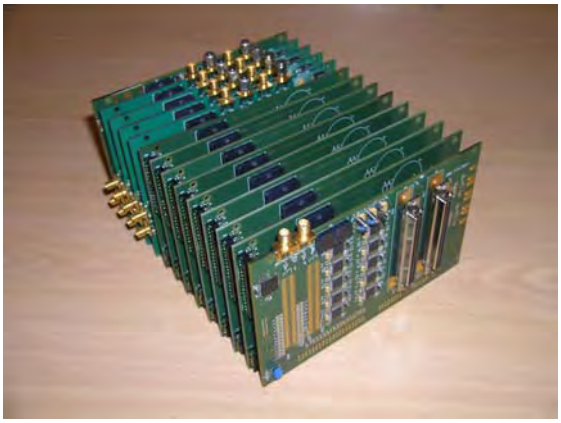

Fig. 5 System chain for a VLBA equivalent system (without conditioning Modules and PCSet).

With a simple sequence of two Fila, two ADB1, one Core1, Fila, is possible to realize a digital receiver. Such new concepts rely on the possibility to directly sample the RF signal band coming fro the front-end and, in appropriate way amplified, in order to satisfy the Conditioning Module and ADB1 requirements. MPI and IRA are developing two L-band receivers adopting this method and a direct recording is realized to produce sequence of data files to produce a direct data processing, such as VLBI cross correlation, or any other software data

reduction. Particular efforts need to be taken into account due to the fact that such system is part of the very sensitive receiver area, because placed inside the receiver body So it needs to adopt appropriate shielding methods, today under testing in MPI.

A third example is due to the multi-feed K band receiver developed in IRA that requires a general purpose backend for single-dish and VLBI operations. The system is particularly complex due to the presence of 14 different IFs (7 feeds in two polarizations). To handle the large quantity of IFs and to support the process to calculate total power in the digital domain, to realize the spectrometer functionality with 32K channels, to handle pulsar observations, to allow polarimetry measurements, etc., a sequence of a chain composed by a FiLa Board, two ADB1, one CoreBoard2, two ADB2, one CoreBoard2, ..., a FiLa Board, is adopted.

Other architectures can be assembled taking into account the needs of data processing capability and the number of input and output channels to support.

References

Tuccari, G., (2004). Development of a Digital Base Band Converter: Basic Elements and Preliminary results. Astronomical Society of the Pacific Conference Series, vol. 306, pp 177-192.

Niell, A., Whithney, A., Petrachenko, B., Schluter, W., Vandenberg, Hase, H., Koyama, Y., Ma, C., Schuh, H., Tuccari, G. (2005). VLBI2010: Current and Future Requirements for Geodetic VLBI Systems, Report of Working Group 3 to the IVS Directing Board, September 16, IVS Memorandum 2006-008v01.

Tuccari, G., Whitney, A., Hinteregger, H., Koyama, H., Kondo, T., (2006) IVS-WG3 Report on Backend Systems, IVS Memorandum 2006-003v01.

Tuccari, G., (2006) VLBI Backend System - Perspectives in 2012, Book of Abstracts of the meeting VLBI-2012 for astrometry, geodynamics, and astrophysics - VLBI-2012, held in St. Petersburg, September 2006, pp 85-90.

Effect on Geodetic-VLBI Measurables due to Polarization Leakage in the Receivers

A. Bertarini
Institute for Geodesy and Geoinformation, Bonn, Germany
W. Alef
Max Planck Institute for Radioastronomy, Bonn, Germany
B. E. Corey
Haystack Observatory, MIT, USA
A. Nothnagel
Institute for Geodesy and Geoinformation, Bonn, Germany
R. C. Walker
National Radio Astronomy Observatory, Socorro, USA

Abstract. Geodetic VLBI delivers baseline length and Earth orientation parameter measurements, which offer the most viable and precise way to study Earth crustal and core dynamics and to support space navigation. Precision is presently at the 6 mm level, of which 1.5 mm to 4 mm uncertainty comes from polarization leakage in the stations. The knowledge of the polarization leakage and the subsequent calibration during data analysis to remove its effect will enhance the precision of the geodetic measurables. The aim of the presentation is to make the audience aware of the project that we have successfully proposed to the International VLBI Service (IVS) and Very Long Baseline Array (VLBA) in which we will determine the leakages and will apply the corrections to the post-correlation data.

Keywords. polarimetry, VLBI

1 Introduction

Polarization leakage is one of the biggest of the instrumental error sources in the determination of multi-band delay (MBD) and hence in the determination of baseline length and Earth orientation parameters (EOP). Leakage occurs due to the electrical properties and shape of the polarizer and varies with frequency. Assuming a theoretical value of polarization leakage of -15 dB one expects a MBD error of 14 ps (Rogers 1991). Measured values of MBD errors due to polarization leakage are tipically between 2 ps and 9 ps at 8.4 GHz (Corey & Titus 2006).

By correcting the polarization leakages, the root mean square (rms) uncertainty in the delay measurement due to instrumental error should drop from 17 ps (estimated by Rogers 1991) to a range between 16 ps (adopting the median measured MBD error due to leakage from Corey & Titus 2006) to 10 ps (adopting the theoretical MBD error due to leakage from Rogers 1991). By calibrating the intrinsic source polarization the rms should further improve (Rogers 1991).

2 Instrumental Effects

We will describe how leakage occurs, using as an example, the septum polarizer (see Fig. 1).

We will, for simplicity, consider the incoming radiation as pure right circular polarization (RCP), thus having the same amplitude in the x and y directions and a 90° phase shift.

The wave encounters the polarizer, which in the case of a septum polarizer is a metal fin within the waveguide as shown in Fig. 1.

The component of the electric field perpendicular to the fin (E_x) is divided, due to the boundary conditions on the conducting fin, in two electric field regions which have the same intensity and orientation as E_x. The component of the electric field parallel to the fin (E_y) is divided, due to the boundary conditions on the conducting fin, in two electric field regions which have the same intensity as E_y but the orientations are rotated into the horizontal plane in the clockwise direction in one region and in the counterclockwise direction in the other region. The phase velocities of the E_x and E_y components differ from each other while propagating from the polarizer input to the dipole because the septum divides the waveguide into regions that have different dimentions in the x and y directions (x is halved, y remains the same). These dimen-

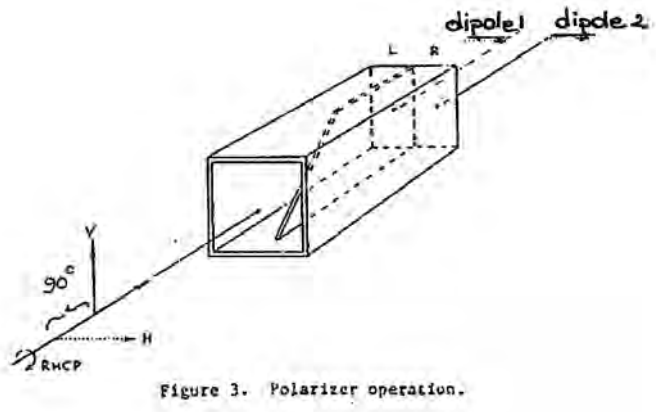

Srikanth, S. "EVLA Feed/FE PDR", 2002

Figure 1. Schematic diagram of a septum polarizer. Courtesy of S. Srikanth.

tions and the length of the septum are chosen to introduce a 90° phase shift between the E_x and E_y components. When those fields (i.e. E_x and the rotated E_y fields with 90° phase shift) superimpose at the dipoles, they interfere constructivly at one dipole and destructively at the other dipole. This logic can be exactly repeated for pure left-circular polarization (LCP) having though the output at the other dipole. The general case would be a mixture of RCP and LCP input which will be separated to produce outputs on both dipoles. In the ideal case of pure RCP or LCP there will be an electric field present at only one dipole whilst the other will have zero output. In the real case, a band of frequencies is observed and, as developed in Fig. 2, the theoretical difference between the two linear polarizations measured at one output (e.g. one of the two dipoles in Fig 1) is an accurate 90° only at two frequencies (Fig. 2). In this broad-band case, the septum polarizer will not separate the two polarization with perfect purity and some contamination from the unwanted polarization will add algebraically to the signal.

3 Effects on the Geodetic Measurables

The effect of leakage is to perturb the visibility phase in one polarization with a small amount of signal leaking from the other polarization. The leakage and hence the phase perturbation is frequency dependent and so perturbs the delay (Eq. 1) and will not close around a triangle of baselines (Massi & Aaron 1997), (Massi 1997).

$$\frac{d\phi}{d\nu} = \tau \qquad (1)$$

Past studies had either estimate (Rogers 1991) or measured (Corey & Titus 2006) an unwanted left-circular polarization response between -20 dB to -15 dB (which correspond to a power leakage of about 1 % to 3 % of one polarization into the other). The leakage leads to delay errors up to 3 mm at 8.4 GHz and up to 13 mm at 2.3 GHz (Corey & Titus 2006). Those studies measured the leakage with only low precision, because the calibrators were assumed to be unpolarized, the sources were not mapped, the bandwidth spanned for the geodetic antennas was only 360 MHz of the 720 MHz available at X-band (Corey & Titus 2006), or too few scans were observed in dual- polarization mode.

4 Strategy

During the course of this project we will determine the leakage by imaging the sources to remove the effects of the intrinsic polarization and by spanning the whole 720 MHz at X-band.

Leakage is detected by cross-correlation between right-hand circular polarization (RCP) at one antenna and left-hand circular polarization (LCP) at the other antenna. Geodetic stations mostly have only RCP, but measurements of the leakage for these stations are still possible if the antenna at the other end of the baseline has dual-polarization receivers.

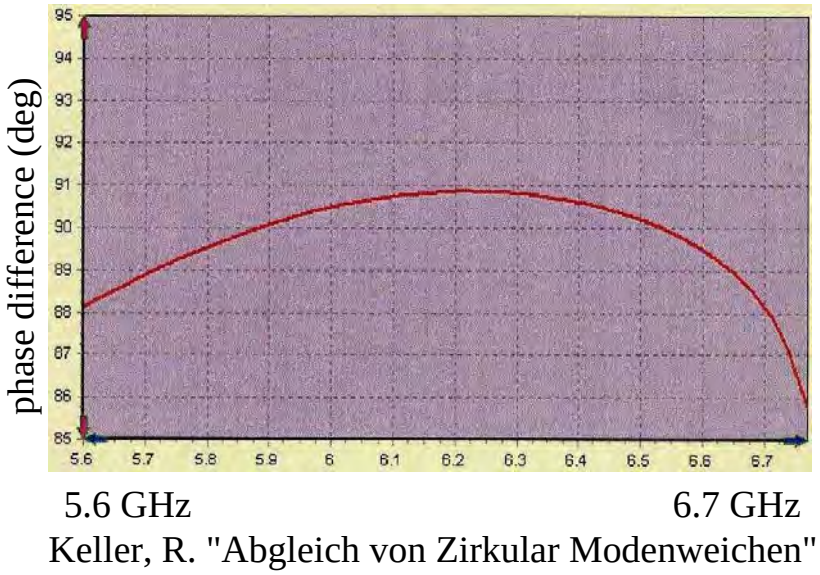

Figure 2. Phase response of an MPIfR septum polarizer vs frequency. Courtesy R. Keller. Shown is the phase difference of S_{12} for the x and y fields, that is the relative phase of the E_x and rotated E_y field components at the dipole, given E_x and E_y fileds injected in phase with eachother at the polarizer input. A perfect system should deliver 90°, however deviations of up to 4° are caused by the changing wavelength across the band causing imperfect 90° phase shift. The curvature allows one optimize the design to produce a 90° phase shift at two frequencies. The larger fractional bandwidth achievable with such polarizer is 16 %.

We will measure the polarization leakage at geodetic and VLBA stations at many closely-spaced frequencies spanning the 2.3 GHz and 8.4 GHz bands. To obtain the most complete coverage possible of the front-end RF bandwidth we will switch in frequency to obtain a polarization leakage measurement every 8 MHz with some gaps due to frequency limitations in the intermediate frequency (IF) distributors at the stations with Mark 4 terminals.

After the correlation, the data will be reducued and imaged using AIPS (Astronomical Image Processing System).

The leakage measurements obtained will be used to develop and validate a calibration scheme for geodetic observations.

5 Conclusion

We have desribed a typical polarizar used in a VLBI station and shown typical limits on the polarization purity. We described a project to measure the polarization leakage at geodetic VLBI stations. This will result in reliable corrections over most of the S-band and X-band for the stations in the observation including the VLBA. The corrections will be useful for geodetic analysis and astronomical polarimetric observations and should reduce the uncertainty on geodetic observables.

Acknowledgment

We thank Reinhard Keller, for technical help and support during the writing of this proceeding.

References

Rogers, A.E.E., 1991, Instrumentantion Improvements to Achieve Millimeter Accuracy, in Proceedings of the AGU Chapman Conference on Geodetic VLBI: Monitoring Global Change, NOAA Technical Report NOS 137 NGS 49, 1-6.

Corey, B., Titus, M., 2006, Antenna Cross-Polarization Characteristics at Geodetic VLBI Stations, IVS 4th General Meeting Proceedings. Concepcion Chile. Ed D. Behrend and K.D. Baver.

Massi M., Aaron, S., 1997, Stability of EVN D-terms, EVN Doc no.77.

Massi, M., Rioja, M., Gabuzda, D., Leppänen, K., Sanghera, H., Ruf, K., Moscadelli, L., 1997, Baseline errors in European VLBI Network measurements III. The dominant effect of instrumental polarization, A&A, 318, L32.

SATTRACK A Satellite Tracking Module for the VLBI Field System.

M. Moya Espinosa and R. Haas
Chalmers University of Technology, Department of Radio and Space Science, Onsala Space Observatory
SE-439 92 Onsala (Sweden)

Abstract. We present the new satellite tracking module SATTRACK for the VLBI Field System (FS) (VLBI Field System, 2007). This module has been successfully integrated into the FS and allows to track low earth orbiting (LEO) satellites directly from the FS operator input window. The orbital calculations are based on NORAD Two Line Elements (TLE, 2007) and the Simplified General Perturbation 4 model (Hoots & Roehrich, 1998). SATTRACK has been tested successfully both at Onsala Space Observatory (Sweden) and at Observatorio Geodesico in TIGO Concepción (Chile).

Keywords. VLBI, antenna pointing, satellite orbit calculation, satellite tracking

1 Introduction

One pre-requisite for successful VLBI observations is that the involved radio telescopes point correctly to the radio sources that are going to be observed. 'Correctly' means here both in time, i.e. the observations need to be simultaneous, and in space, i.e. the radio telescopes involved in the observation have to point to the same direction. Usually, radio telescopes have mechanical anomalies, are affected by gravitational deformations and are influenced by environmental parameters like temperature and humidity. Thus, the telescopes have so-called pointing models that shall take care of these effects and shall guarantee that the radio sources that the telescopes point at really lie within a small fraction of the telescopes' main lobes.

VLBI stations usually perform antenna pointing tests before doing geodetic VLBI observations. These tests are done to check that the respective pointing models are correct. Relatively strong and point-like radio sources are used for the pointing tests. The tests are controlled via the VLBI Field System (FS) (VLBI Field System, 2007) using the command 'fivept'. This command performs a series of intensity measurements at a number of positions distributed along two perpendicular coordinate axes with respect to the nominal position of the radio source. A Gaussian fit in two dimensions is calculated based on these measurements and possible offsets in the two coordinate axes (e.g. azimuth and elevation) are determined from the fit. In case significant offsets are detected, the corresponding telescope pointing model could be updated.

In the Northern hemisphere often the strong radio source Cassiopeia A is used for pointing test on X-band. This radio sources is not visible in the Southern hemisphere and there are no other strong X-band radio sources that are suitable for small radio telescopes. This is a problem for the small 6-m radio telescope TIGO at Concepción (Chile). Thus, TIGO lacks the possibility to do pointing tests.

A possible solution for TIGO is to use strong artificial radio sources for pointing measurements. Such radio sources exist as low Earth orbiting (LEO) satellites that broadcast on X-band. Currently, there are two earth observing satellites, TERRA (TERRA, 2007) and AQUA (AQUA, 2007), that are in LEO polar orbits and continuously broadcast their observational data on X-band, at 8212.5 MHz and 8160.0 MHz, respectively. These frequencies lie within the usual X-band frequency band used for geodetic VLBI. The direct broadcast of TERRA and AQUA is only interrupted in case the Deep Space Network (DSN) tracks space probes on X-band and the satellites are visible from the DSN ground network.

Thus, we started a project to implement a satellite tracking module called SATTRACK directly into the VLBI FS in order to allow pointing measurements using TERRA and AQUA.

2 Satellite orbit calculations

The equation of motion for a satellite can for most applications be described as a two-body problem with a central body and the satellite itself. A second order differential equation can be formulated and described with six orbital elements, the satellite's Kepler elements. With these six elements the position of the satellite can be calculated in an Earth centered inertial reference frame. A transformation of this position into the local topocentric reference frame results in a directional vector in terms of azimuth and elevation of the satellite. Latter can be used to steer a telescope to track the satellite.

However, the description of a satellite orbit with six Kepler elements is a simplification and does not take into account disturbing forces other bodies (e.g. the Moon), variations in the geopotential field, solar radiation pressure, atmospheric drag, etc. Thus, the Kepler elements change with time.

Models have been developed to describe the orbital perturbations and to allow calculation of perturbed satellite orbits. On of the models is the so-called Simplified General Perturbation 4 model (Hoots & Roehrich, 1998). This model uses perturbation theory to incorporated the gravitational and atmospheric perturbing forces. It is described by closed algorithms that are expressed in a series of mathematical equations and do not need any numerical integration to achieve accurate results. SGP4 is valid for low Earth orbiting (LEO) satellites with orbiting period less than 225 minutes. There is also a variant valid for medium Earth orbit (MEO) satellites, called SDP4.

These models are used by the North American Aerospace Defence Command (NORAD, 2007) to analyze radar observations of Earth orbiting satellites. NORAD tracks all Earth orbiting satellites with radar and determines the respective satellite orbits. The orbital parameters are published via the Celestrak website (Celestrak, 2007) in the form of so-called Two-Line Elements (TLE, 2007). The TLE are two ASCII lines that include information about the satellite, its orbital parameters and their perturbations. TLE are updated continuously, for some low orbiting objects several times per day. Table 1 gives as an example TLE for the two satellites TERRA and AQUA that both have orbital periods of roughly 100 minutes.

3 Concept of SATTRACK

The aim of the SATTRACK module was to allow tracking of satellites with VLBI telescopes directly from the VLBI Filed System. It should be able to calculate for a specified prediction epoch whether the chosen satellite is above or below the horizon, give information about when the satellite rises and sets, and when the satellite has its overpass peak. Figure 1 visualizes the concept of an overpass. Furthermore was the SATTRACK module meant to be easy to use, should allow tracking of as many satellites as possible, and be flexible for future updates. SATTRACK uses TLE and the SGP4 model for orbit calculations. The TLE data are downloaded automatically at least once per day from the Celestrak website. We defined four basic commands for SATTRACK:

file This command checks whether there is a TLE file available on the FS computer and what the epoch of this file is.

overpass This command gives rise and set time and direction of the next overpass trajectory.

predict This command gives a detailed list with time and direction for a predicted overpass trajectory.

track This command starts the actual tracking of the next coming overpass and send the corresponding prameters to the antenna control unit (ACU).

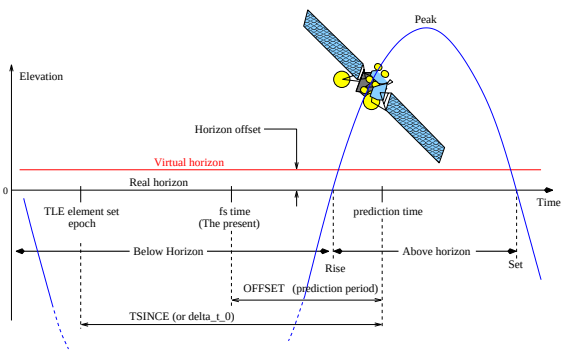

Figure 1. SATTRACK concept: Definition of rise, peak and set of a satellite overpass.

Table 1. Examples of TLE for the satellites TERRA and AQUA. The satellite identification numbers are given as second element in each of the lines. The first lines give information like epoch year (last two digits of year) day of the year and fractional portion of the day, first time derivative of the mean motion, second time derivative of mean motion (decimal point assumed), and BSTAR drag term (decimal point assumed) as elements 7–11. The second lines give information like inclination (degrees), right ascension of the ascending node (degrees), eccentricity (decimal point assumed), argument of perigee (degrees), mean anomaly (degrees), mean motion (revolutions per day) as elements 3–8.

```
TERRA
1 25994U 99068A   06300.81371596  .00000052  00000-0  21531-4 0  8936
2 25994 098.2019 013.3688 0000980 097.6945 262.4353 14.57100321364862
AQUA
1 27424U 02022A   06300.21551320  .00000094  00000-0  30992-4 0  9825
2 27424 098.2089 239.1639 0000459 093.6439 266.4821 14.57119255238385
```

4 Implementation of SATTRACK into the VLBI Field System

The VLBI FS consists of a number of memory resident programs on a Linux PC that are used to control most of the operations needed for VLBI operations (VLBI Field System, 2007). For the implementation of SATTRACK into the FS we needed to interact with the FS operator interface window (*oprin*) to issue a corresponding command, and to interact with the station quick response (*stqkr*) module to pass the information to the antenna control module (*antcn*). All details of the implementation are described in Moya Espinosa (2007).

Figure 2 shows schematically how and where the SATTRACK module was integrated into the FS structure. A new 'case 8' was added to the *antcn* module and handles the commands of SATTRACK.

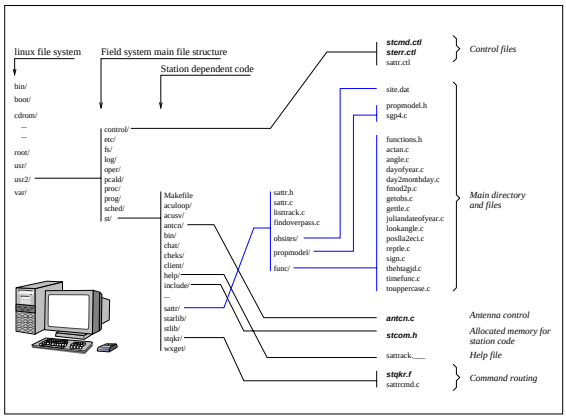

Figure 2. Schematic description of the integration of SATTRACK into the structure of the VLBI Field System.

Figure 3 shows schematically how SATTRACK was integrated to *antcn*.

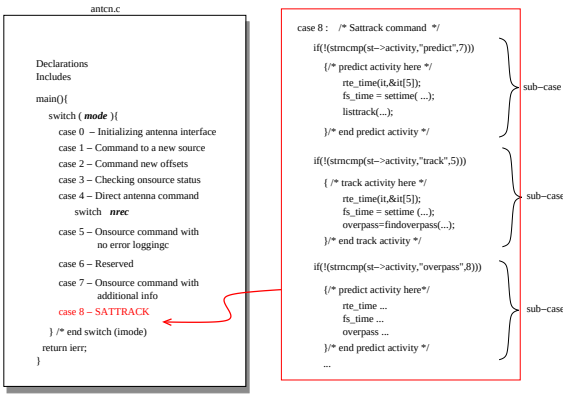

Figure 3. Schematic description of the new 'case 8' in *antcn* that handles the SATTRACK commands.

In case of the SATTRACK *track* command, first the tracking epoch and direction are calulated, and then the actual tracking commands are sent to the ACU via the FS module *antcn*. Since ACUs are different at different radio telescopes, this communication was implemented in a flexible way. For the Onsala 20 m telescope tracking with right ascension and declination of the satellite was implemented, while for TIGO tracking with azimuth and elevation was implemented.

5 SATTRACK orbit prediction accuracy

After development and integration of SATTRACK into the VLBI FS we addressed also the accuracy of orbit prediction with SATTRACK. We compared the SATTRACK results to results of a satellite overpass predictor available on the internet (NASA Satellite Overpass Predictor, 2007). As a measure of disagreement between the two predictors we defined the magnitude of the difference between the two directional vectors from a observer to the predicted satellite position. Figure 4 shows these prediction errors for TERRA and AQUA, respectively, derived from the analysis of 28 and 19 overpasses.

From these comparisons, the prediction errors for both satellites were determined to be on the order of 0.15°. However, probably can large parts of these discrepancy be explained by inaccuraciies in the NASA satellite overpass predictor, as discussed via email with Mike Heney at NASA Goddard Space Flight Center (Heney, 2007). Thus, only actual satellite tracking tests could prove whether SATTRACK worked as expected.

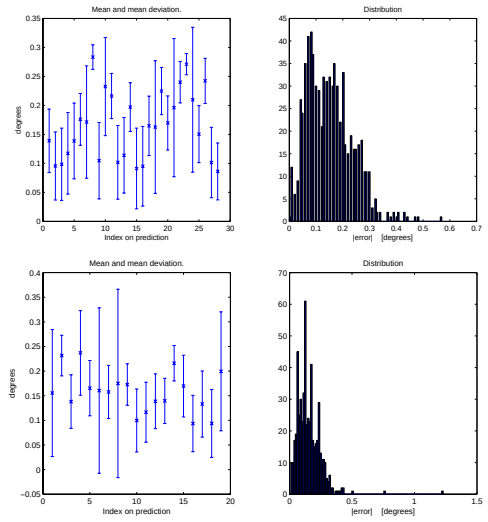

Figure 4. Statistics on prediction errors for TERRA (top) and AQUA (bottom) based on 28 and 19 overpasses, respectively, and comparison to corresponding predictions by the NASA overpass predictor. The left graphs show mean values and standard deviations, while the right graphs show the error distribution over all passes.

6 Satellite tracking tests at Onsala (Sweden) and TIGO (Chile)

Satellite tracking tests with SATTRACK were carried out during June and July of 2006 at Onsala Space Observatory in Sweden and January 2007 at Observatorio Geodesico TIGO in Concepción in Chile. Onsala is located in the Northern hemisphere at latitude 57.4^o North and longitude 11.9^o East, while TIGO is located in the Southern hemisphere at latitude 36.8^o West and longitude 73.0^o South. At X-band these two telescopes have half-power beam-widths of 0.1° and 0.35°, respectively. The telescopes have diameters of 20 m and 6 m, respectively.

The downlink frequencies for TERRA and AQUA are 8212.5 MHz and 8160.0 MHz. The local oscillator for X-band observations at Onsala and TIGO have a frequency of 8080.0 MHz. This means that the signals of the two satellite are observable after down-conversion at frequencies 132.5 MHz and 80.0 MHz. However, TIGO has and additional upconverter with a frequency of 479.90 MHz. Thus, for TIGO the TERRA signals are observable at 612.4 MHz (upper side band) and 347.4 MHz (lower side band) and the AQUA signals at 399.9 MHz (lower side band) and 550.9 MHz (upper side band).

We used SATTRACK at Onsala and TIGO and connected a spectrum analyzer to the output of the VLBI rack. Figure 5 and Figure 6 show the corresponding spectra of the tracking events at Onsala and TIGO. In both figures the upper graph show reference spectra when no satellite was tracked. The middle and lower graphs show the spectra when TERRA and AQUA were tracked, respectively. These graphs prove clearly that the SATTRACK module works as expected and successfully tracked the satellites.

Figure 7 shows a series of spectra observed during a TERRA pass at Onsala. Clearly the TERRA signal at 132.5 MHz is visible thoughout the 19 minutes long overpass.

A corresponding figure with a series of spectra during an overpass at TIGO could unfortunately not be created. The TIGO ACU did stop the tracking after sending a small number of tracking parameters. This bug in the ACU control software made it impossible to track a whole overpass. Currently, work is in progress at TIGO to fix this ACU problem. Once this problem is fixed, first pointing tests at TIGO can be performed.

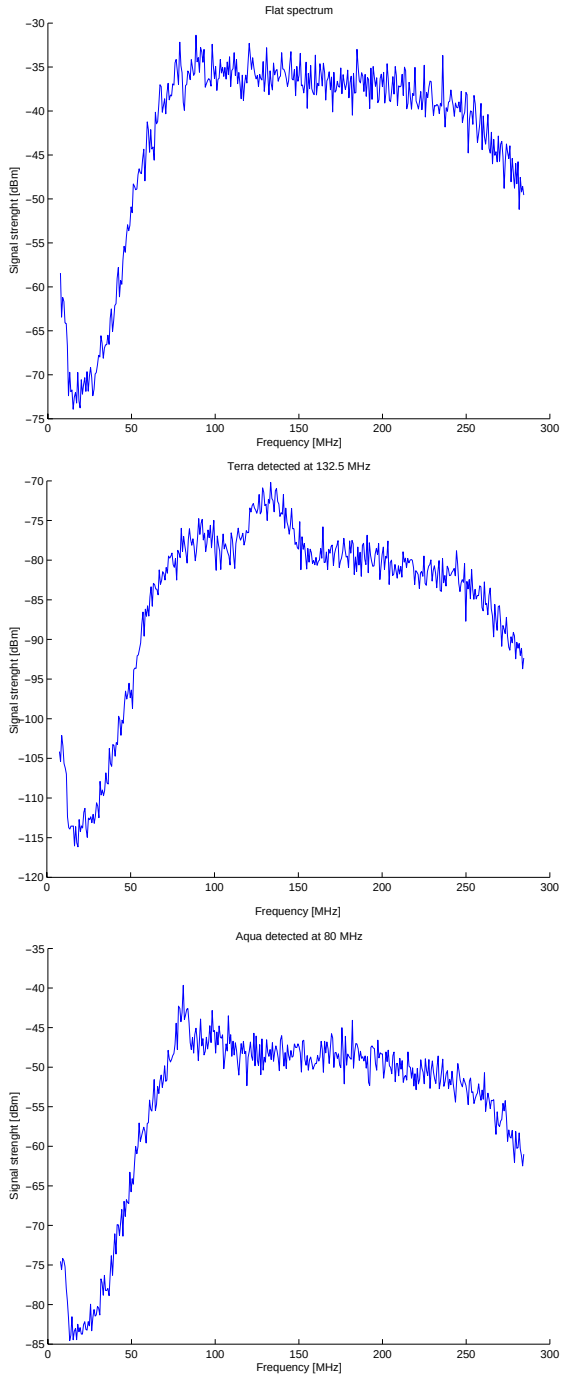

Figure 5. Spectra observed at Onsala. Top: A reference spectrum with no Satellite signal present. Middle: A signal from TERRA at frequency 132.5 MHz is detected. Bottom: A signal from AQUA at frequency 80.0 MHz is detected.

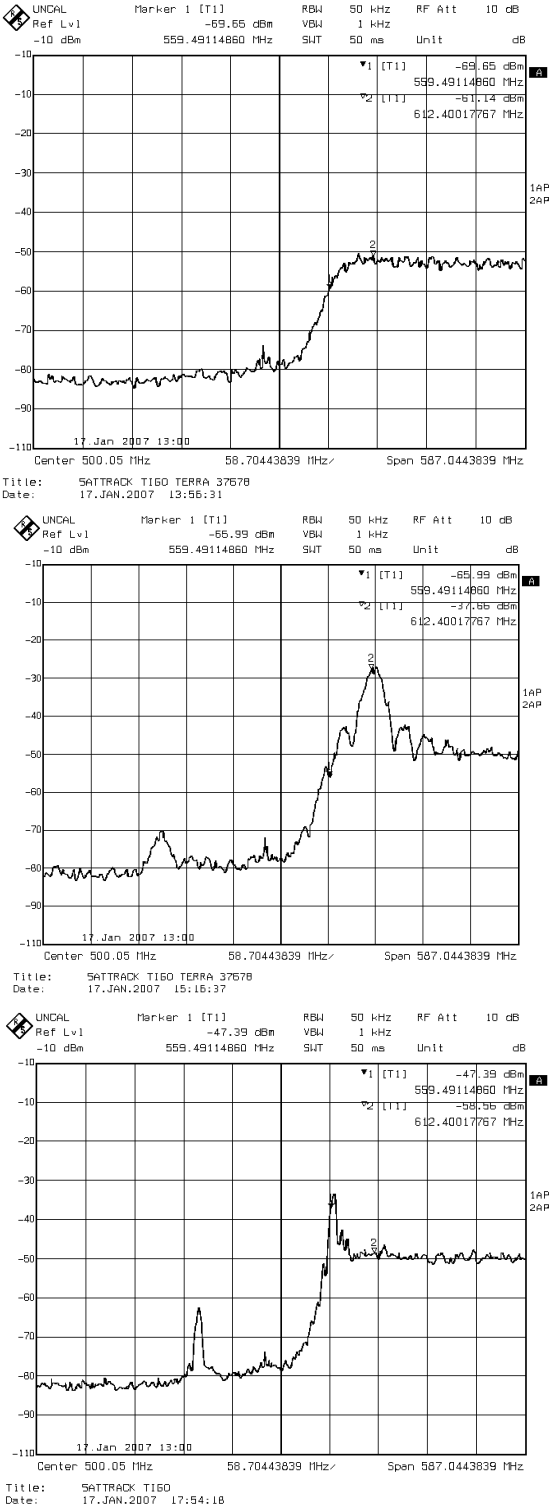

Figure 6. Spectra observed at TIGO. Top: A reference spectrum with no Satellite signal present. Middle: Signals are detected for the TERRA satellite at 347.4 MHz and 612.4 MHz. Bottom: Signals are detected for the AQUA satellite at 399.9 MHz and 550.9 MHz.

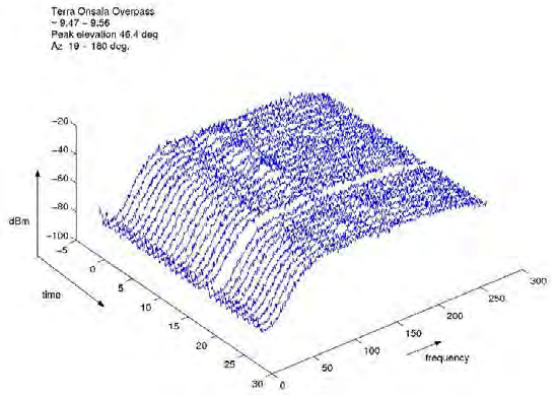

Figure 7. Spectra of a 19 minutes long overpass of TERRA at Onsala.

7 Conclusions and outlook

We developed a new satellite tracking module SATTRACK for the VLBI Field System. SATTRACK was successfully tested at the Onsala Space Obseratory (Sweden) and at TIGO Concepción (Chile). The module allows to issue satellite tracking commands easily from the FS operator input window. The module uses TLE satellite orbit information and the SGP4 orbit calculation model that is valid for LEO satellites. A future inclusion of other orbit calculation models, for example to track satellites in higher orbits, is possible and planned. This could be a step towards VLBI using artificial radio sources Kawano et al. (2006), Sekido & Fukushima (2006). Such observations could be used to tie kinematic and dynamic reference frames. We also plan to implement tracking possibility of GNSS satellites based on predicted orbit provided by the International GNSS Service (IGS). We hope that SATTRACK in the near future will be included in the official release of the VLBI FS.

References

AQUA (2007), `http://aqua.nasa.gov/`

Celestrak website, `http://www.celestrak.com`

Heney, M. K. (2007), comments about the accuracy of the NASA Satellite Orbit Predictor, personal communication via email 2007-01-23.

Hoots F.R., Roehrich R.L. (1998), SPACETRACK REPORT NO. 3. Models for Propagation of NORAD Element Sets, December 1980, Package Compiled by TS Kelso 31 December 1988.

Kawano M., Hanada H. Matsumoto K. (2006), *International VLBI Tracking of SELENE*, in: D. Behrend and K. Baver (Eds.): *IVS 2006 General Meeting Proceedings*, NASA-CP-2006-214140, 47–51.

Moya Espinosa, M. (2007), SATTRACK Satellite Tracking Availability for the VLBI Field System, Master of Science Thesis, Department of Radio and Space Science, Chalmers University of Technology.

NORAD (North American Aerospace Defence Command), `http://www.norad.mil/`

NASA Earth Observatory Satellite Overpass Predictor (2007), `http://earthobservatory.nasa.gov/MissionControl/overpass.html`

Sekido M., Fukushima T. (2006), A VLBI delay model for radio sources at finite distance, Journal of Geodesy, DOI: 10.1007/s00190-006-0035-y.

TERRA (2007), `http://terra.nasa.gov/`

TLE (NORAD Two-Line Elements), `http://celestrak.com/NORAD/elements/`

VLBI Field System Documentation, `http://lupus.gsfc.nasa.gov/software_fs_main.html`

GINS: a new tool for VLBI Geodesy and Astrometry

G. Bourda[1], P. Charlot[1], R. Biancale[2]
(1) Observatoire Aquitain des Sciences de l'Univers - Université Bordeaux I
Laboratoire d'Astrophysique de Bordeaux - UMR5804/CNRS - Floirac, France
(2) Centre National d'Etudes Spatiales - Groupe de Recherche de Géodésie Spatiale
Toulouse, France

Abstract. In the framework of the Groupe de Recherches de Géodésie Spatiale (GRGS), a rigorous combination of the data from five space geodetic techniques (VLBI, GPS, SLR, LLR and DORIS) is routinely applied to simultaneously determine a Terrestrial Reference Frame (TRF) and Earth Orientation Parameters (EOP). This analysis is conducted with the software package GINS which has the capability to process data from all five techniques together. Such a combination at the observation level should ultimately facilitate fine geophysical studies of the global Earth system. In this project, Bordeaux Observatory is in charge of the VLBI data analysis, while satellite geodetic data are processed by other groups. In this paper, we present (i) details about the VLBI analysis undertaken with GINS, and (ii) the results obtained for the EOP during the period 2005–2006. We also compare this EOP solution with the IVS (International VLBI Service for geodesy and astrometry) analysis coordinator combined results. The agreement is at the 0.2 mas level, comparable to that of the other IVS analysis centers, which demonstrates the capability of the GINS software for VLBI analysis.
Keywords. astrometry, geodesy, reference systems, Earth rotation, VLBI

1 Introduction

The software package GINS (Géodésie par Intégrations Numériques Simultanées) is a multi-technique software initially developed by the GRGS/CNES (Groupe de Recherches de Géodésie Spatiale – Centre National d'Etudes Spatiales, Toulouse, France) for analysing satellite geodetic data, and extended at later stages for analysing data from other space geodetic techniques (Meyer et al., 2000). Currently, GPS (Global Positionning System), DORIS (Doppler Orbitography and Radio-positioning Integrated by Satellite), SLR (Satellite Laser Ranging), LLR (Lunar Laser Ranging) and VLBI (Very Long Baseline Interferometry) observations can be processed with GINS. The parameters that can be estimated comprise satellite orbits around the Earth or another body of the solar system, gravity field coefficients, Earth Orientation Parameters (EOP), station coordinates, or other geophysical parameters. The well-known GRIM5 and EIGEN gravity field models were produced with GINS in particular (Biancale et al., 2000; Reigber et al., 2002).

A rigorous combination of all the above space geodetic data has been developed to estimate station coordinates and EOP simultaneously from all techniques in the framework of the IERS (International Earth Rotation and Reference Systems Service) multi-technique combination pilot project. In this analysis, observations of the different astro-geodetic techniques (VLBI, GPS, SLR, LLR and DORIS) are first processed separately using GINS. The weekly datum-free normal equation matrices derived from the analyses of the different techniques are then combined to estimate station coordinates and EOP (Coulot et al., 2007; Gambis et al., 2007). Results are made available to the IERS in the form of SINEX files. In this project, the VLBI data are analysed in Bordeaux, while the satellite geodetic data are processed either in Toulouse (for GPS, DORIS and LLR) or Grasse (for SLR), with the final combination produced at Paris Observatory (see Figure 1 for more details about the project organization).

The strength of the method is in the use of a unique software for all techniques with identical and up-to-date models and standards, ensuring homogeneous and reliable combined products. In addition, the solution benefits from complementary constraints brought by the various techniques.

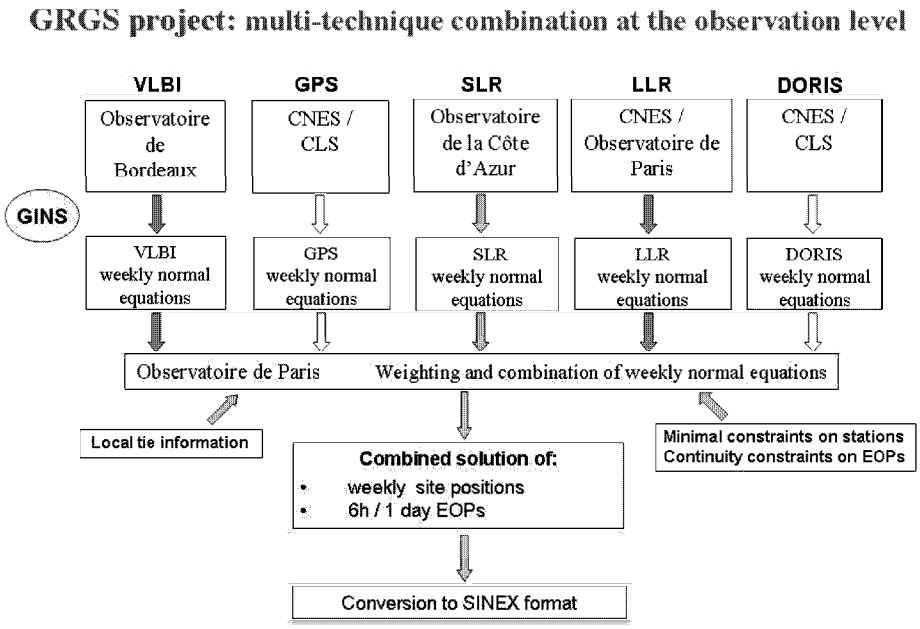

Figure 1. Organization of the coordinated project of the GRGS for multi-technique combination at the observation level. CLS (*Collecte Localisation Satellite*) is a private company funded in particular by the CNES.

In this paper, we present an overview of the analyses undertaken with this new VLBI software, the results obtained for the EOP from 2005 to 2006, and the comparisons made with the IVS (International VLBI Service for geodesy and astrometry) analysis coordinator combined results. These comparisons indicate that GINS is at the level of the other VLBI analysis software packages.

2 VLBI analysis with GINS: data and modeling

Since 2005 the regular weekly VLBI data acquired by the IVS have been routinely processed with the GINS software in order to estimate the EOP and the VLBI station positions. These data include both the IVS intensive sessions (i.e. one-hour long daily experiments) and the so-called IVS-R1 and IVS-R4 sessions (i.e. two 24-hour experiments per week). Overall, a total of 20 stations have been used in such sessions.

Based on these data, weekly normal matrices are produced for combination with the data acquired by the other space geodetic techniques (GPS, SLR, LLR and DORIS). The free VLBI parameters include station positions and the five EOP (X_p, Y_p, $UT1 - UTC$, $\mathrm{d}\psi$, $\mathrm{d}\epsilon$) along with clock and troposphere parameters. The clocks are modeled using piecewise continuous linear functions with breaks every two hours. The tropospheric zenith delays are modeled in a similar way except that breaks are applied every hour. Continuity constraints of 10 μs and 10 cm are applied to the clock and troposphere breaks, respectively. The a priori EOP series used is the IERS C04 series, the a priori Terrestrial Reference Frame (TRF) is VTRF2005 (Nothnagel, 2005), while the celestial frame is fixed to the ICRF (International Celestial Reference Frame; Ma et al., 1998; Fey et al., 2004).

The following tidal and atmospheric models are also used in the analysis:

- IERS Conventions 2003 for solid Earth tides and pole tide models (McCarthy and Petit, 2003),
- FES2004 for oceanic tides and oceanic loading models (Lyard et al., 2006),
- 6h-ECMWF (European Center for Mete-

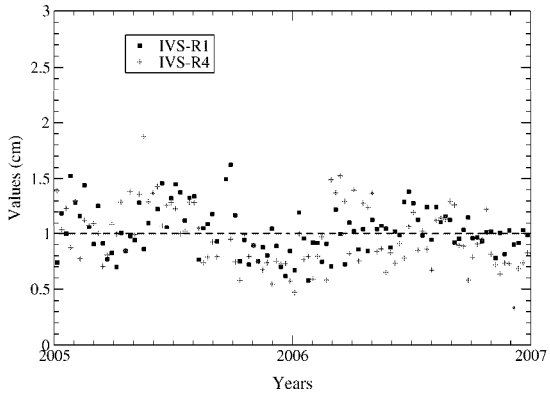

Figure 2. Post-fit weighted RMS delay residuals with GINS for the IVS-R1 and IVS-R4 sessions conducted in 2005-2006.

orological Weather Forecast) atmospheric pressure fields only over continents (inverse barometer hypothesis) for atmospheric loading model,

- Niell tropospheric mapping functions (Niell, 1996).

3 VLBI analysis with GINS: results and comparison

In this section, we present the VLBI-only EOP results obtained based on a fixed TRF (VTRF2005) and compare these to the IVS combined EOP series. One set of EOP (X_p, Y_p, $UT1 - UTC$, $d\psi$, $d\epsilon$) was estimated for every 24-hour session.

Figure 2 shows the post-fit weighted RMS (Root Mean Square) delay residuals obtained with GINS for the IVS-R1 and IVS-R4 sessions in 2005–2006. The RMS average over this period is 1.08 cm (i.e. 36 ps) for the IVS-R1 sessions, and 0.97 cm (i.e. 32 ps) for the IVS-R4 sessions.

Figure 3 shows the EOP series as derived with GINS, on the basis of the analysis described in the previous section. The results are plotted with respect to the IVS combined series (ivs06q3e.eops; see http://vlbi.geod.uni-bonn.de/IVS-AC/combi-eops/QUAT/HTML/start_q.html). Table 1 summarizes the statistics for these series, plus those with respect to the IERS C04 series. Our current VLBI-only EOP results agree with the IVS combined series at the following levels (see RMS values in Table 1):

- 0.20 mas for the polar motion coordinates,
- 0.15 mas for the celestial pole offsets, and
- 10 μs for the Earth's angle of rotation.

These differences may partly arise from using different TRF in the two analyses: the IVS analysis coordinator used ITRF2000, whereas we fixed the TRF to VTRF2005. Another point to highlight is that these comparisons used non-weighted RMS to evaluate the differences between the EOP series obtained with GINS and those published by the IVS analysis coordinator. Such values are generally larger that the more common "weighted RMS".

4 Conclusions and prospects

GINS is a new VLBI analysis software in the IVS community. We showed that VLBI analyses undertaken with GINS lead to EOP results that agree at the level of 150–200 μas with respect to the IVS combined series results. This is comparable to the other IVS analysis centers, which demonstrates the capability of the GINS software for VLBI-only analysis.

Another strength of GINS is the possibility of analysing observations of five space geodetic techniques (VLBI, GPS, LLR, SLR and DORIS) alltogether. Such a combination at the observation level is one of the goals of the IAG (International Association of Geodesy) project GGOS (Global Geodetic Observing System; Rummel et al., 2002).

In the future, further developments and investigations are planned to refine such VLBI analysis with GINS:

- To improve the relative weighting of the VLBI observations.
- To adjust tropospheric gradients, together with zenithal tropospheric delays.
- To validate the underlying models in GINS by carrying out detailed comparisons with those implemented in the JPL (Jet Propulsion Laboratory) VLBI software MODEST (Sovers and Jacobs, 1996).
- To submit to the IVS analysis coordinator the EOP results obtained with GINS for further evaluation.

Table 1. Mean and RMS differences for each of the five EOP series (X_p, Y_p, $UT1-UTC$, $\mathrm{d}\epsilon$, $\mathrm{d}\psi \sin\epsilon$) derived with GINS when compared to (1) the IERS C04 series, and (2) the IVS combined series.

	EOP wrt	X_p μas	Y_p μas	$UT1-UTC$ μs	$\mathrm{d}\epsilon$ μas	$\mathrm{d}\psi \sin\epsilon$ μas
Mean	C04	-201	343	3.4	49	7
	IVS	47	-95	2.3	36	-62
RMS	C04	216	215	9.9	150	139
	IVS	212	211	10.2	145	139

- To adjust the radiosource coordinates to investigate the source position variability and ultimately to produce a celestial reference frame with GINS.

Acknowledgements

G. Bourda is grateful to the CNES (Centre National d'Etudes Spatiales, France) for the postdoctoral position granted at Bordeaux Observatory. She wishes also to the Advisory Board of the Descartes-Nutations prize for supporting the journey to Vienna in order to present this work.

References

Biancale R., Balmino G., Lemoine J.-M., Marty J.-C., Moynot B., Barlier F., Exertier P., Laurain O., Gegout P., Schwintzer P., Reigber C., Bode A., Konig R., Massmann F.-H., Raimondo J.-C., Schmidt R. & Zhu S. Y., 2000, "A new global Earth's gravity field model from satellite orbit perturbations: GRIM5-S1", Geophys. Res. Lett., 27, 3611–3614

Coulot D., Berio P., Biancale R., Loyer S., Soudarin L. & Gontier A.-M., 2007, "Toward a direct combination of space-geodetic techniques at the measurement level: Methodology and main issues", J. Geophys. Res., 112, 10.1029/2006JB004336

Fey A.L., Ma C., Arias E.F., Charlot P., Feissel-Vernier M., Gontier A.-M., Jacobs C.S., Li J. & MacMillan D.S., 2004, "The Second Extension of the International Celestial Reference Frame: ICRF-EXT.1", AJ, 127, 3587–3608

Gambis D., Biancale R., Carlucci T., Lemoine J.-M., Marty J.-C., Bourda G., Charlot P., Loyer S., Lalanne T. & Soudarin L., 2007, "Combination of Earth Orientation Parameters and terrestrial frame at the observational level", IAG Springer Series (submitted)

Lyard F., Lefèvre F., Letellier T. & Francis O., 2006, "Modelling the global ocean tides: a modern insight from FES2004", Ocean Dynamics, 56, 394–415

Ma C., Arias E.F., Eubanks T.M., Fey A.L., Gontier A.-M., Jacobs C.S., Sovers O.J., Archinal B.A. & Charlot P., 1998, "The International Celestial Reference Frame as Realized by Very Long Baseline Interferometry", AJ, 116, 516–546

McCarthy D.D. & Petit G., 2003, "IERS Conventions (2003)", IERS Technical Note 32, Frankfurt am Main: Verlag des Bundesamts fr Kartographie und Geodsie, paperback, ISBN 3-89888-884-3 (print version)

Meyer U., Charlot P. & Biancale R., 2000, "GINS: A new Multi-Technique Software for VLBI Analysis", International VLBI Service for Geodesy and Astrometry 2000 General Meeting Proceedings, edited by Nancy R. Vandenberg and Karen D. Baver, NASA/CP-2000-209893

Niell A.E., 1996, "Global mapping functions for the atmosphere delay at radio wavelengths", J. Geophys. Res., 101, 3227-3246, 10.1029/95JB03048

Nothnagel A., 2005, "VTRF2005 - A combined VLBI Terrestrial Reference Frame", Proceedings of the 17th Working Meeting on European VLBI for Geodesy and Astrometry, Noto, Italy

Reigber Ch., Balmino G., Schwintzer P., Biancale R., Bode A., Lemoine J.-M., Koenig R., Loyer S., Neumayer H., Marty J.-C., Barthelmes F., Perosanz F. & Zhu S.Y., 2002, "A high quality global gravity field model from CHAMP GPS tracking data and Accelerometry (EIGEN-1S)", Geophysical Research Letters, 29(14), 10.1029/2002GL015064

Rummel R., Rothacher M. & Beutler G., 2005, "Integrated Global Geodetic Observing System (IGGOS) – science rationale", Journal of Geodeynamics, 40(4–5), 357–362, 10.1016/j.jog.2005.06.003

Sovers O.J. & Jacobs C.S., 1996, "Observation Model and Parameter Partials for the JPL VLBI Parameter Estimation Software *MODEST*", JPL Publication 83-39, Rev. 6, August 1996

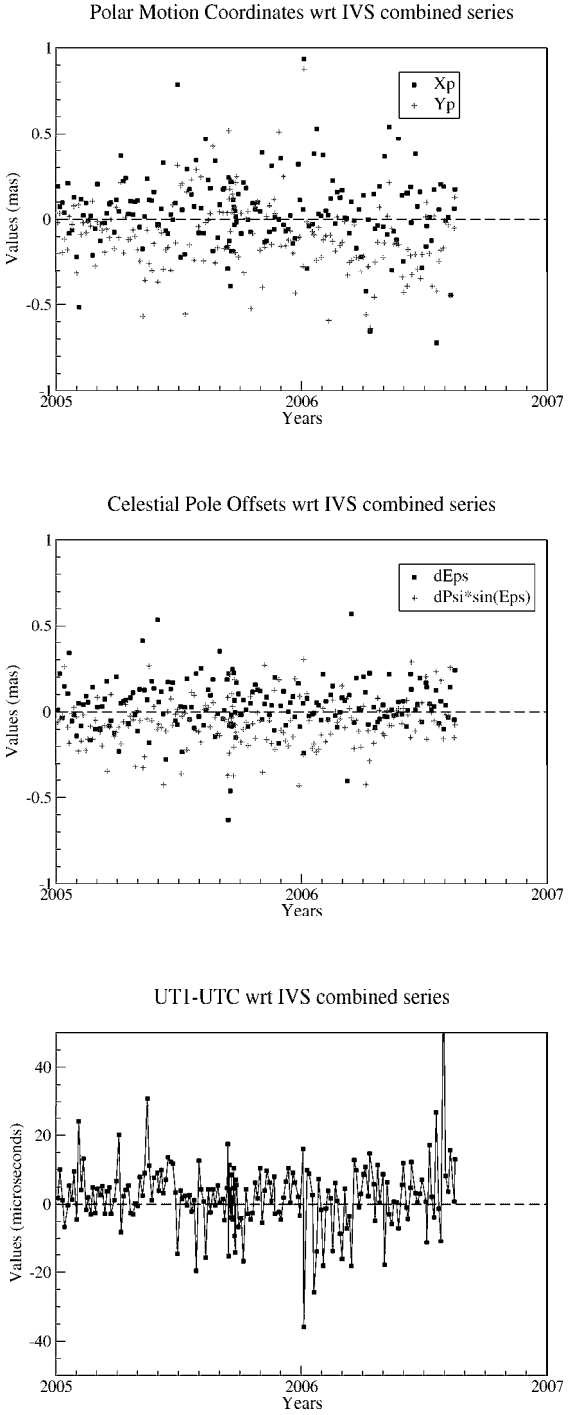

Figure 3. VLBI Earth Orientation Parameters (X_p, Y_p, dϵ, dψ sin ϵ, $UT1-UTC$) estimated with GINS, compared to the IVS analysis coordinator combined series (ivs06q3e.eops) between 2005 and 2006.

Baseline length repeatability

O. Titov
Geoscience Australia, GPO Box 378, Canberra, ACT, 2601, Australia

Abstract. The goal of this paper is to introduce a more effective approximation for the "repeatability – baselength" relationship that is used to evaluate the quality of geodetic VLBI results. Traditionally this relationship is approximated by linear function of baselength for all possible situations. The new model incorporates the mean number of observations of reference radio sources made by each baseline. It is shown that it provides a better approximation of geodetic VLBI results than the traditional linear model. A long baseline performs a fewer number of observations than a shorter baseline. Two baselines of the same length perform a different number of observations if one of them is made by slow slewing radio telescopes, and the other by fast slewing ones. Further development of the new approach comes down to modelling of the repeatability as a function of two parameters: baseline length and baseline slewing rate. This last model can be useful for simulation purposes.

Keywords. VLBI, Geodetic Data Analysis, Baseline Time Series Repeatability

1 Introduction

The baseline length repeatability is used as a measure of the quality of geodetic VLBI data. Traditionally it is fitted by linear model as a function of baseline length. However, studies in the last few years have shown that the simple linear regression does not fit long baselines properly. Longer baselines should provide worse results than shorter baselines due to less number of observations (see, for example MacMillan et al., 2006; Lambert, 2006; Searle, 2006). Mendes Cerveira et al., (2006) applied a quadratic model instead of a linear one. They stated that it can be explained by a reduction of common sky zone at large distance and, correspondingly, a smaller number of observations. This intuitive explanation is correct, but, no appropriate analytical model has been proposed.

In this paper we develop a more advanced analytical expression taking into account the mean number of observations made by each baseline.

2 Definition of the new approach

The daily baseline length values derived from VLBI data analysis produce the time series of baseline evolution which can be approximated by a linear model. The weighted post-fit residuals are used to calculate the baseline length repeatability R. In accordance with Niell (2005) for the baseline length L the repeatability R can be expressed in terms of vertical and horizontal uncertainties of the positions of both antennas σ_v σ_h , respectively

$$R^2 = 2 \cdot [1 - (L/2R_e)^2 \sigma_h^2 + (L/2R_e)^2 \sigma_v^2] \qquad (1)$$

Here R_e - the Earth radius.
In other words

$$R^2 = a'L^2 + b' \qquad (2)$$

so that the coefficients a' and b' are given by

$$a' = \frac{\sigma_v^2 - \sigma_h^2}{2R_e^2} \qquad (3)$$

$$b' = 2\sigma_h^2 \qquad (4)$$

Theoretically, only the quadratic form (2) provides an accurate model. However, for many applications the linear model

$$R = aL + b \qquad (5)$$

is used instead of (2), although it is not absolutely correct.
A global VLBI solution based on data from 1979 till 2006 was used to estimate the empirical parameters. All data were processed using the OCCAM software (Titov et al. 2001) by a least squares collocation method (Moritz, 1980; Titov 2000, 2004). This solution comprises the 212 ICRF

'defining' radio sources (Ma et al. 1998) as global parameters with NNR constraints and 102 'other' radio sources as 'arc' parameters. The remaining radio sources are treated as global parameters without NNR-constraints.

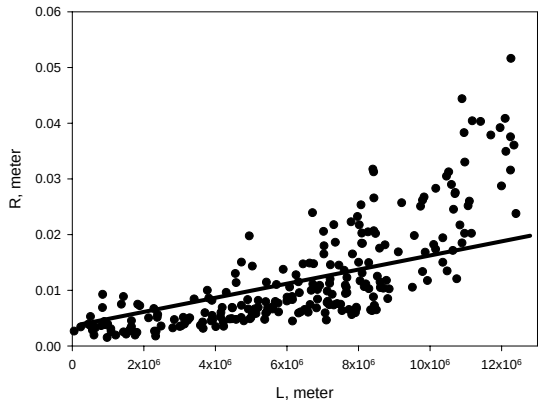

Fig. 1 Repeatability and its modeling by linear function.

Daily positions of VLBI sites are estimated to provide the time series of baseline length. In a statistical analysis, we use the time series for 31 VLBI sites only, to mitigate the effect of the sites with a short observational history.

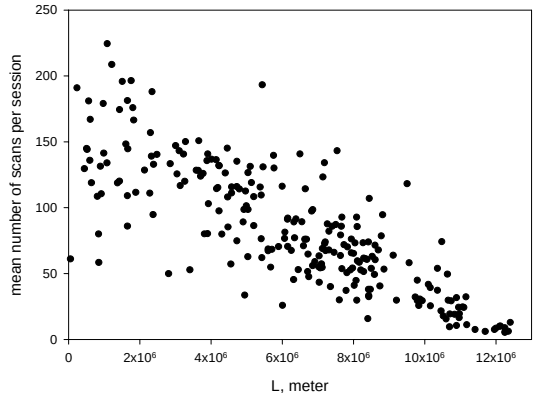

Fig. 2 The mean number (N) of the reference radio source scans for each baseline vs baselength L.

Fig 1 shows approximation by the linear model (5) of the baseline repeatability values calculated from the global VLBI solution. It is obvious that the linear model does not approximate long baseline values. Fig 2 shows the mean number N of observations of reference radio sources with respect to the baseline length. These numbers gradually decrease for long baselines, therefore, it is assumed that the disadvantage of the model (5) is statistical in nature and a new model for repeatability must include this parameter N as follows

$$R = A\frac{L}{\sqrt{N}} + B\frac{1}{\sqrt{N}} \qquad (6)$$

Fig 3 shows an approximation of the repeatability values by the new model (6). It fits observed data better than the traditional linear model (5). Post-fit residuals of the approximation of the model 4 are shown in Fig. 4

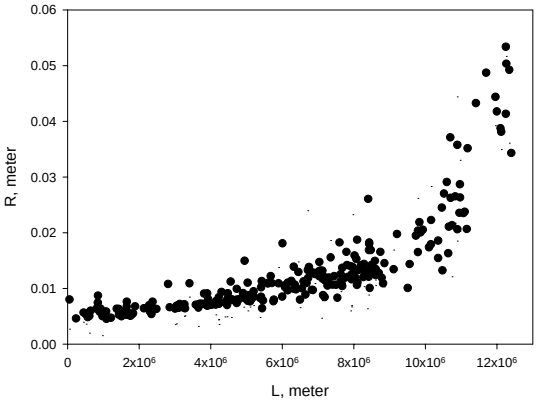

Fig. 3 Repeatability modeling by (6).

A set of VLBI data should be processed to obtain the parameter N for model (6) implementation. However, for the purpose of simulation it is necessary to assess the repeatability without data analysis. To realize this approach one has to model the parameter N as a function of baselength L and slewing rate of the VLBI antenna V. Fig 2 demonstrates that the N linearly decreases to the long baseline area. Empirically, we establish that the function $N(L,V)$ for each baseline is given by

$$N = \sqrt{V}(C - DL) \qquad (7)$$

where C, D are the coefficients to be estimated by the least squares method; $V = \min(V_1, V_2)$, here V_1, V_2 is the slew rate values for the both stations of one baseline. Fig 5 shows the post-fit residuals after approximation of the data on Fig 2 by model (7).

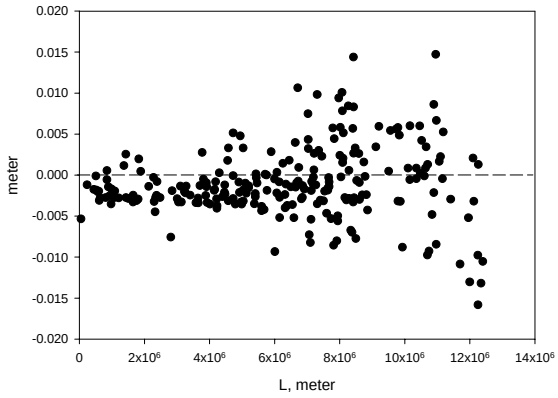

Fig. 4 Post-fit residuals for model (6).

3 Solution statistics

The combination of (6) and (7) provides the following expression for repeatability

$$R = \frac{AL + B}{V^{0.25}(C - DL)} \qquad (8)$$

The repeatability R here is a function of two parameters – baselength L and slewing rate V. Unfortunately, (8) is non-linear, therefore, four empirical parameters can be estimated by least squares method separately from (6) and (7). Then these estimates can be combined to generate the final expression for repeatability (8).
Table 1 shows the estimates for equation (8) coefficients. Using these values one can approximate the repeatability R for any baseline with length L and slewing rate V.

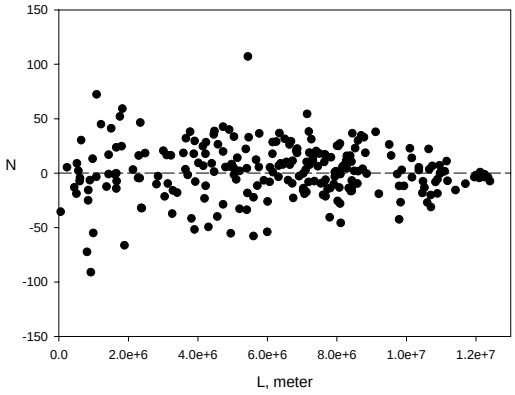

Fig. 5 Post-fit residuals for model (7) fitted to the data on Fig 2.

Table 1. Estimates of the parameters of model (8)

Param.	Estimate	Unit
A	(3.9 +/- 0.5)·10-9	ppb
B	0.065 +/- 0.004	meter
C	14.5 +/- 0.3	min/deg
D	(1.09 +/- 0.05)·10-6	min/(deg*meter)

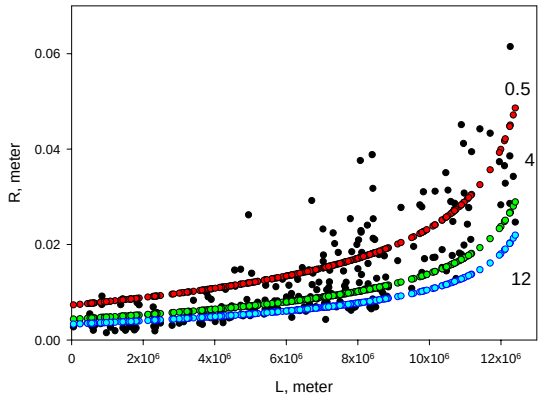

Fig. 6 Fitting observation (black dots) by the model (8) with different slewing rates (0.5, 4 and 12 degrees/second).

Fig 6 demonstrates the curves for three different slewing rates (0.5, 4 and 12 degrees/second). The increase of slewing rate from 0.5 to 4 degrees/second improves repeatability for all baselines, especially for long baselines (about 50%). The increase of slewing rate from 4 to 12 degrees/second results in moderate improvement for long baselines and marginal improvement for short baselines. Therefore, the slewing rates about 5-6 degrees/second seem to be optimal for existing configurations of the global VLBI network.

4 Discussion

This new estimator (6) can be applied if solutions with different number of observations for the same baseline are compared. One instance is the study of the effect of reference radio source selection (Feissel, 2003; Titov, 2007). Another application is comparison of VLBI network performance at different data rates. In both situations the conventional estimator (5) is not sufficient.

The traditional expression (5) produces the following estimates for a = 1.3 ppb and b = 3.0 mm (Fig 1). Equivalent horizontal and vertical uncertainties are shown at Table 2. New parameters A, B in (6) are tied with the old ones a, b in (5) as follows

$$a = \frac{A}{\sqrt{N}}; \quad b = \frac{B}{\sqrt{N}} \tag{9}$$

where N is the number of observations for each baseline. It means that the repeatability for each baseline should be also calculated on an individual basis. For $A = 3.9 \cdot 10^{-9}$ (Table 1) and a short baseline with typical N=200 (Fig 2), a = 0.27 ppb, for a medium baseline (N=100), a = 0.39 ppb, and for a long baseline (N=25), a = 0.78 ppb. From (3), (4) and (9), we can state the equivalent horizontal and vertical uncertainties as follows

$$\sigma_h \approx \frac{b}{\sqrt{2}} = \frac{B}{\sqrt{2N}} \tag{10}$$

$$\sigma_V \approx \sqrt{2a^2 R_e^2 + \frac{b^2}{2}} = \sqrt{\frac{2A^2 R_e^2}{N} + \sigma_h^2} \tag{11}$$

Using the A and B meanings from Table 1 the uncertainties are calculated (Table 2)

Table 2. Equivalent horizontal and vertical uncertainties for the traditional fit (5) (first row) and new fit (6) for different N

N	σ_h, mm	σ_v, mm
any	2.4	12.0
25	9.2	11.5
100	4.6	5.8
200	3.3	4.1

Finally, from (7), (10) and (11) the uncertainties can be expressed as a function of baselength and slewing rate. Fig 7 shows the uncertainties with respect to baselength for V = 120 deg/min

$$\sigma_h \approx \frac{B}{\sqrt{2(C - DL)\sqrt{V}}} \tag{12}$$

$$\sigma_V \approx \sqrt{\frac{2A^2 R_e^2}{\sqrt{V}(C - DL)} + \sigma_h^2} \tag{13}$$

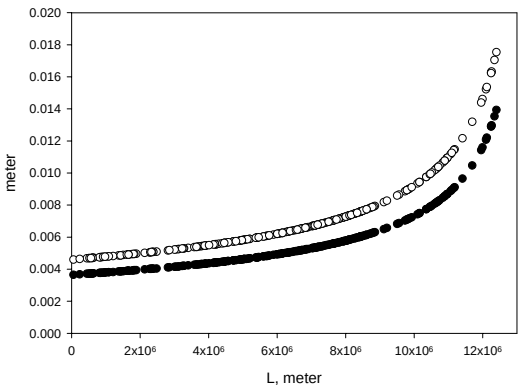

Fig. 7 Vertical (open circles) and horizontal (close circles) uncertainties for slew rate V = 120 deg/min.

With the traditional approach the vertical uncertainty exceeds the horizontal one by a factor of five. With the new approach, as shown in Table 2 the vertical uncertainties exceed the horizontal uncertainties, although the difference between them is small (less than 3 mm). We can conclude that an accuracy of the estimates of geodetic VLBI site positions is almost equal for both components. However, for more accurate estimation of these uncertainties equation (2) should be applied instead of (5).

5 Conclusion

It is shown that the repeatability of individual baseline length estimate measured by VLBI is not only a function of baseline length, but also a function of the mean number of observations made during a typical 24-hour session. This dependence manifests itself through the actual "repeatability – baselength" plot. Subsequently the number of observations is a function of baseline length and baseline slewing rate. It is suggested that the conventional "repeatability – baselength" model that has been used for many years should be revised.

Two new empirical models for approximation of the "repeatability – baselength" relationship have been proposed. They can be applied for the comparison of solutions with different numbers of observations. The first model includes the actual number of the observations of reference radio sources along with a baseline length. The second model includes a baseline length and a baseline slewing rate. This model can also be used for simulation purposes.

Revised estimates of the vertical and horizontal uncertainties are shown with implementation of the new approach. Each set of (vertical, horizontal) estimates are quite close. A more detailed consideration should verify these findings.

References

Boehm, J., H. Schuh (2007) Troposphere gradients from the ECMWF in VLBI analysis. *Journal of Geodesy*, doi:10.1007/s00190-007-0144-2.

Feissel-Vernier, M. (2003) Selecting stable extragalactic compact radio sources from the permanent astrogeodetic VLBI program. *Astron Astroph*, 403, pp. 105-110.

Ma, C., E. F.Arias, T.M. Eubanks, A.L. Fey, A.-M. Gontier, C. S. Jacobs, O. J. Sovers, B. A. Archinal, P. Charlot (1998) The international celestial reference frame as realised by very long baseline interferometry. *Astron J*, 116 pp. 516-546.

Lambert, S. (2006) Baseline and Site Repeatability in the IVS rapid Network. In: *Proc of IVS 2006 General Meeting*. Vandenberg N, Baver K D (eds), NASA/CP-2006-214140, pp. 296-299.

MacMillan, D., D. Behrend, D. Gordon, C. Ma (2006) First Results from CONT05, In: *Proc of IVS 2006 General Meeting*. Vandenberg N, Baver K D (eds), NASA/CP-2006-214140, pp. 269-273.

Mendes Cerveira, P. J., R. Henkeilmann, J. Boehm, R. Weber, H. Schuh (2006) Contribution of GPS and VLBI for understanding station motions. *Journal of Geodynamics*, 41, pp. 87-96.

Moritz, H. (1980) *Advanced Physical Geodesy*, Herbert Wichmann Verlag, Karlsruhe.

Niell, A. (2005) Baseline length repeatability as evaluator. East Coast Geodetic VLBI meeting, *in GSFC VLBI Memos, http://lupus.gsfc.nasa.gov/docs_memos.htm*

Searle, A. (2006) E3 Network Results. In: *Proc of IVS 2006 General Meeting*. Vandenberg N, Baver K D (eds), NASA/CP-2006-214140, pp. 330-334.

Titov, O. (2000) Estimation of subdiurnal tidal terms in UT1-UTC from VLBI data analysis. *IERS Technical Note*, 28, Observatoire de Paris, Paris, pp. 11-14.

Titov, O., V. Tesmer, J. Boehm (2001) OCCAM 5.0 User Guide. *AUSLIG Technical Note*, 7, AUSLIG, Canberra.

Titov, O. (2004) Construction of a Celestial Coordinate Reference Frame from VLBI data. *Astron Reports*, 48, pp. 941-948.

Titov, O. (2007) Effect of the selection of reference radio sources on geodetic estimates from VLBI observations. *Journal of Geodesy*, doi:10.1007/s00190-007-0145-1.

ERP time series with daily and sub-daily resolution determined from CONT05

T. Artz, S. Böckmann, A. Nothnagel
Institut für Geodäsie und Geoinformation der Universität Bonn, Nußallee 17, D-53115 Bonn, Germany

V. Tesmer
Deutsches Geodätisches Forschungsinstitut, Alfons-Goppel-Straße 11, D-80539 München, Germany

Abstract. From time to time, continuous VLBI campaigns take place under the direction of the IVS. Even though these observations are continuous over two weeks, the standard VLBI analysis procedure leads to independent daily datasets. In this paper, an alternative approach is presented to estimate earth rotation parameters with different temporal resolutions. By stacking the single sessions to a two-weekly solution on the normal equation level, a consistent time series is produced over the whole CONT05 period. Stacked parameters are station positions which are estimated in a 'global' approach and borders of time dependent parameters e.g. zenith wet delay.

Analysis of the correlation matrix of estimated parameters gives an impression of the dependencies between them. Furthermore, it is demonstrated how these dependencies depend on the type of datum used. E.g. correlations between earth rotation parameters (ERP) and tropospheric zenith delay of certain VLBI sites have been detected.

The ERP time series resulting from the stacking approach turned out to be more consistent over the fortnightly time span. In particular, time series of hourly ERP exhibit a better behaviour at the session boundaries, since the discrepancies at session borders due to poorly determined intervals is minimized.

Keywords. Earth rotation, VLBI, CONT05, normal equations

1 Introduction

VLBI is one of the fundamental techniques to observe earth orientation parameters, i.e. polar motion (x_p, y_p), phase of rotation $(UT1 - UTC)$ and nutation $(d\psi, d\epsilon)$. In particular, continuous observation campaigns with a quasi identical network are of great importance for the determination of sub-daily ERP with a high temporal resolution. The latest of these campaigns took place in September 2005 with an observation network of 11 globally distributed antennas (Fig. 1). One of the goals of CONT05 was to describe the discrepancies between sub-daily ERP tidal models and observed sub-daily ERP. (MacMillan et al., 2006)

Figure 1. CONT05 observing network (MacMillan et al., 2006).

Due to the standard analysis procedure in the Mark IV analysis chain, this fortnightly time span with approximately 90.000 observations is divided into 15 independent datasets. Each day of CONT05, starting and ending at 17h (UTC), has been correlated for itself with one of the three Mark IV correlators at USNO (Washington D.C.), MIT Haystack observatory (Westford, MA, USA) and MPIfR/BKG (Bonn, Germany). Consequently, the correlated data has been fringe fitted and stored for each day independently. Therefore, parameters that are estimated with sub-daily resolution occur twice at the same epoch (i.e. at the end of one and the beginning of the successive session) often differing by more than 1 mas in polar motion.

In this paper, an alternative analysis approach

is presented, which is more convenient for continuous campaigns. On the normal equation level, the individual sessions are accumulated to a two-weekly solution. The accumulation is realized by estimating station positions in a 'global' approach and by stacking of the time dependent parameters (e.g. zenith wet delay) at the session borders.

In this paper, the investigations are limited to parameters of polar motion and UT1, as there is mathematical correlation between a retrograde diurnal term of polar motion and offsets in the two nutation components (Moritz & Mueller, 1987).. As shown by (Tesmer et al., 2001) and (Thaller et al., 2006), nutation could be fixed to the best model values available to overcome such correlation, if ERP are estimated with a sub-daily resolution.

2 Solution procedure

For the initial step of the VLBI analysis, the CALC/SOLVE analysis software (Petrov, 2006) was used in the so-called independent mode. Reductions of observations have been applied in correspondence with the IERS Conventions 2003 (McCarthy & Petit, 2004). Particularly, high frequency polar motion due to ocean tides as well as the influence of nutation on the ERP have been applied according to chapter 5.4.2 of IERS Conventions 2003. Furthermore, the ocean tide model FES2004[1] as well as atmospheric pressure loading time series[2] have been used. If ERP are estimated with a sub-daily resolution, nutation has been fixed to the IAU2000A model with additional corrections reported in IERS 05 C04 series (Bizouard & Gambis, 2005).

In the next step, the completely unconstrained normal equation (NEQ) system, containing all estimated parameters, has been extracted from SOLVE and rate constraints have been applied to clocks, atmospheres and gradients.

The final solution step was performed for three solution types with the DOGS-CS software provided by DGFI (Gerstl et al., 2001). On the one hand, there are two solutions where each session is solved independently, with either the station coordinates fixed to their a priori values, or no-net-rotation and no-net-translation (NNR/NNT) conditions applied. On the other hand a complete solution was calculated by accumulation of the single NEQ systems. Stacking of NEQ means that row and column of a parameter, which occurs twice or more at the same epoch in different normal matrices, are added. In general, these will be the sub-daily estimated parameters at the session boundaries. But NEQ elements of other parameters can also be added, after transformation to a common, specific epoch (Angermann et al., 2004). Therefore, station coordinates were transformed to the middle of the CONT05 period, thus it is possible to estimate coordinates with NNR/NNT condition only once for the whole time span.

As a consequence, one single equation system for the whole CONT05 campaign is solved. In this solution, all sub-daily parameters are estimated continuously over the whole time span. Only the clock parameters stay local for each session. Thereby, the closest approximation to one single CONT05 solution has been achieved.

3 Impact of datum definition on correlations

SOLVE allows to parameterize ERP either as offset and rate once per day or by linear splines. Therefore, the procedure described above can be performed with different temporal resolutions ranging from several minutes up to one day. Here, the daily resolution will be investigated first, to clarify the impact of the datum definition on ERP. Afterwards, the procedure will be applied to ERP estimated with hourly resolution.

If ERP as well as station coordinates are estimated from VLBI observations, the NEQ have a rank deficiency of six. To regularize the NEQ, NNR/NNT conditions may be applied to the equation system. Another possibility is to fix the station coordinates to their a priori values, as we are primarily interested in parameters of earth rotation.

3.1 ERP with daily resolution

A solution, in which earth rotation is parameterized by an offset and it's time derivative, leads to a clear view on the dependencies of estimated parameters. Comparing the correlation matrices of the three different solution types shows the

[1] derived from Automatic Ocean Tide Loading Service (http://www.oso.chalmers.se/∼loading) (Scherneck & Bos, 2002)

[2] provided by the Goddard VLBI group (http://gemini.gsfc.nasa.gov/aplo) (Petrov & Boy, 2004)

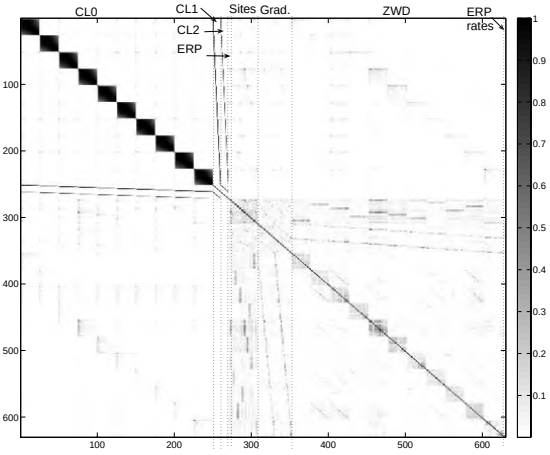

Figure 2. Correlation matrix of session 05SEP19XA with NNR/NNT conditions.

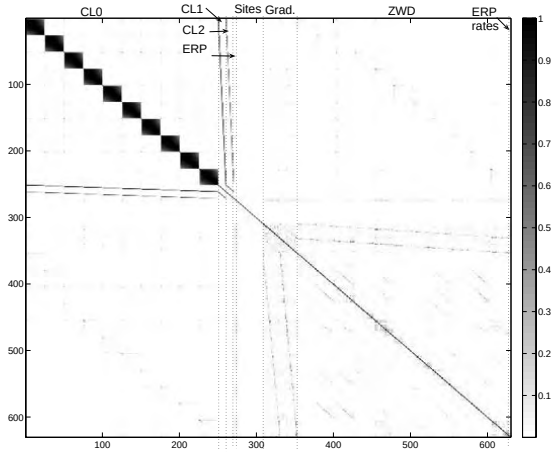

Figure 3. Correlation matrix of session 05SEP19XA with station coordinates fixed to a priori values.

impact of the datum definition on these dependencies. The correlation matrix is given by

$$\begin{aligned} \mathbf{R} &= \mathbf{F} \cdot D(\mathbf{x}) \cdot \mathbf{F}, \qquad (1) \\ \mathbf{F} &= diag(1/\sigma_1, ..., 1/\sigma_n), \end{aligned}$$

where $D(\mathbf{x})$ is the variance-covariance matrix of the estimated parameters, i.e. the inverse of the normal matrix, and σ_i are the square root of it's diagonal elements. In Figure 2, the correlation matrix of one single session from the CONT05 period is displayed. The rank deficiency has been cured by applying NNR/NNT conditions. Correlations of parameters modelled by linear splines, especially inside of the clock and troposphere blocks for each single station, can clearly be noticed. Furthermore, there are dependencies of station coordinates with all other parameters and those of troposphere gradients with the tropospheric zenith delays. Some correlations of clocks and tropospheric parameters at some stations also become obvious. Fixing station coordinates to their a priori values will lead to a different correlation matrix, as shown in Figure 3. It becomes obvious that nearly all correlations, besides the clocks, are reduced. This solution might be used for ERP solutions but fixing the stations to their coordinates from a linear model valid for a period of 20 years will lead to a certain degree of strain in the geometry of observing network which consequently influences the ERP, e.g. because of annual motion of the stations not explained by the correction models.

What happens if we accumulate the NEQ of the individual sessions to one big (complete)

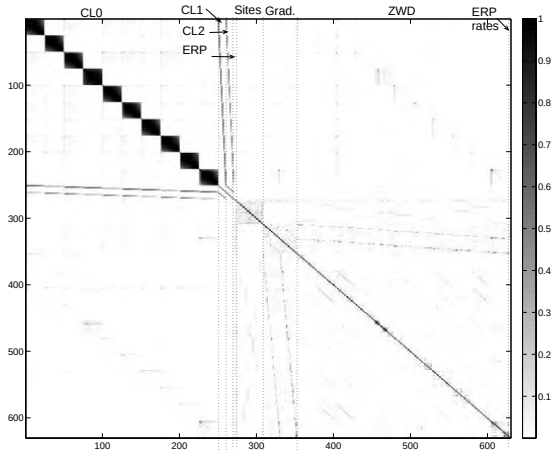

Figure 4. Correlation matrix of session 05SEP19XA of the complete solution with NNR/NNT conditions. Only an extract of parameters valid for this session is displayed.

equation system can be seen in Figure 4. In this figure, only an extract of parameters of a single session is shown. The only change to the independent solution with fixed stations (Fig. 3) is that there are some correlations inside the block of station coordinates. However, with fixed station coordinates they must be zero contrary to the case with estimated coordinates.

Now we have a look at all correlation coefficients of a single ERP with respect to all other parameters (Fig. 5). The correlations appearing in the individual NNR/NNT solution (gray) are reduced either by fixing sites (light gray)

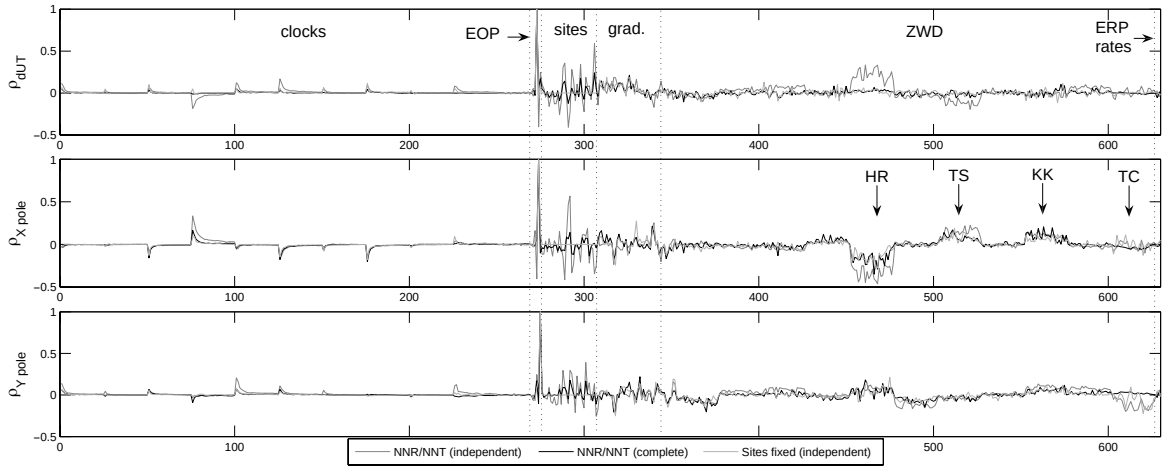

Figure 5. Coefficients of correlation with all other parameters for the three different solutions

or by calculating the complete solution (black). A really interesting fact is the correlation of ERP with the zenith wet delay (ZWD) of certain sites. This effect can be seen through all of the CONT05 sessions, though the set of sites that is affected alters. These sites are Tsukuba, Kokee Park, TIGO/Conc., and particularly Hartebeesthoek. Maybe this develops from estimating ZWD as well as gradients while observations are pointing mostly in a certain region of the sky. It might be mitigated by a better global distribution of the observing sites or by a different scheduling.

To conclude this investigations one can state that the way of stacking the NEQ over two weeks and estimating site positions once for the mid epoch is sufficient to de-correlate the equation system. The station variation decreases in comparison to a solution with NNR/NNT conditions since they are estimated only once. Consequently, the influence on ERP becomes less. Nevertheless, a variation of each site with respect to their a priori values (e.g. due to annual motion) is possible.

3.2 ERP with sub-daily resolution

In a solution, where ERP are modelled by linear splines with a temporal resolution of one hour, very similar correlations can be seen as in the previous case (Fig. 6). This Figure shows only the correlation matrix of a solution with NNR/NNT conditions. The changes to the correlation matrix of a solution with fixed sites or the complete approach are similar to the daily

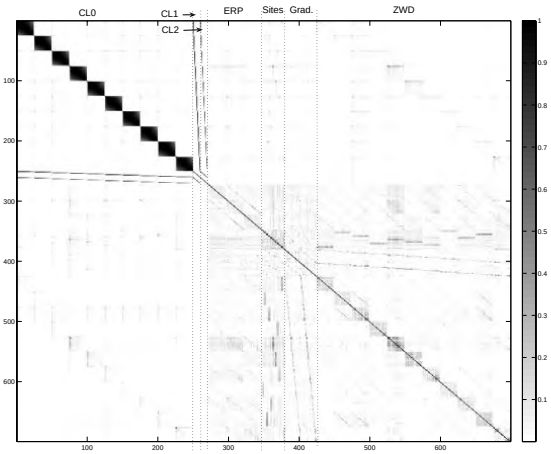

Figure 6. Correlation matrix of a solution with hourly ERP of a independent NNR/NNT solution. The changes to the correlation matrix of a solution with fixed sites or the complete approach are similar to the daily case (Fig. 3 and 4).

case (Fig. 3 and 4). Again, there are clear correlations between all sub-daily parameters when applying NNR/NNT conditions to each single session. These dependencies are reduced by either fixing sites or performing the complete solution, except for the clocks and the correlations of tropospheric gradients and ZWD. Furthermore, a correlation between ERP and tropospheric zenith delay is detectable again.

Therefore, all the conclusions drawn in the previous section are still valid.

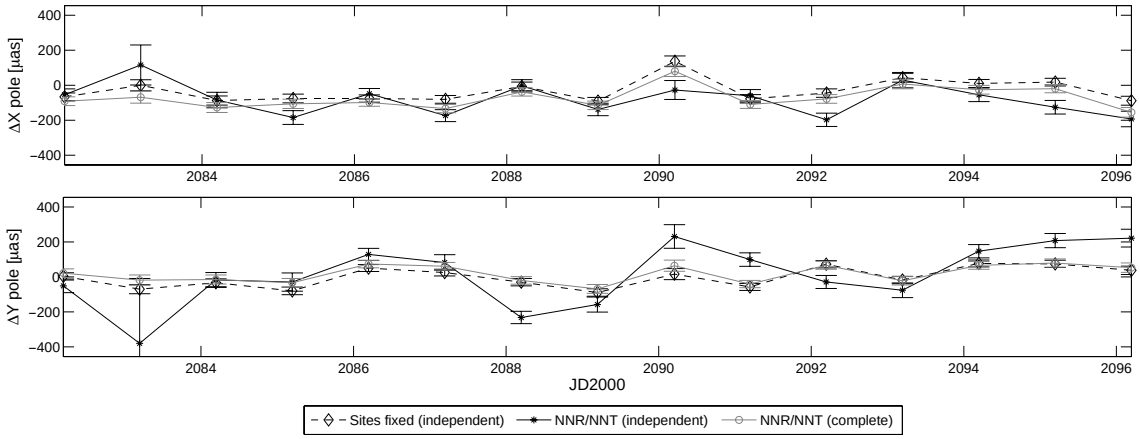

Figure 7. Daily estimated ERP w.r.t. reprocessed GPS series (Steigenberger et al., 2006).

4 Results

The time series resulting from the three approaches show exactly the behaviour one would expect from the cognitions of the previous section. The daily estimated ERP differ clearly depending on the method of defining the datum. An independent solution with NNR/NNT conditions depends heavily on the conditions of single stations. In case of trouble at one site, e.g. at TIGO/Conc. in the second session of CONT05, the estimated time series is corrupted due to correlations of ERP and site coordinates (Fig. 7). Apparently, the independent NNR/NNT solution produces nearly unreliable results. Compared to a reprocessed GPS series (Steigenberger et al., 2006) it is noisy and has differences of up to 300 μas to the other two solutions.

In contrast, the time series resulting from the independent solution with fixed sites and from the complete solution show a comparable behaviour. The offset between these two series results from the differences in TRF.

In the sub-daily time series in general the same effects can be seen. These effects, as far as they have been mentioned already, are mainly due to the datum definition. In addition, the influences of adding NEQ elements of parameters at the session boundaries become obvious. Looking at the transition between two sessions (Fig. 8) shows the benefit of the applied approach clearly. In the displayed X pole series, outliers at the session borders are considerably reduced by the complete solution. This optical impression is supported by the numerical values in table 1. The

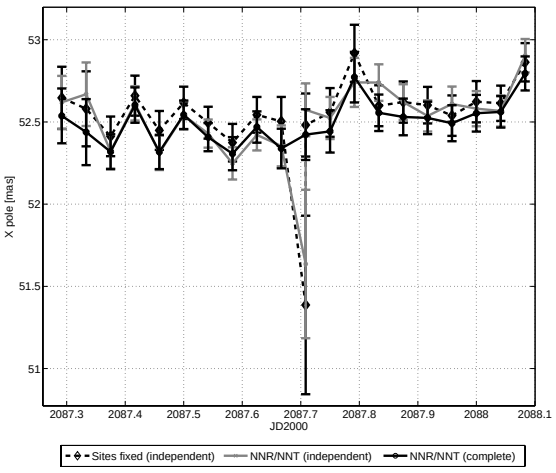

Figure 8. X pole with sub-daily resolution at a session border.

WRMS and RMS of the detrended time series w.r.t. the reprocessed GPS series becomes quite better by the complete solution. Especially the RMS demonstrates the effect of stacking ERP elements at the daily borders. In the Y pole series, an RMS improvement of about $\frac{1}{4}$, compared to the fixed solution can be detected. Hence, by the stacking procedure a consistent time series is generated over the whole CONT05 period.

5 Conclusions

Several investigations have been carried out with the CONT05 VLBI observations. Inspection of the correlation matrix of estimated parame-

Table 1. WRMS and RMS of the detrended sub-daily time series w.r.t GPS

Datum definition	X pole [μas]		Y pole [μas]	
	WRMS	RMS	WRMS	RMS
Fixed	204.3	251.6	231.4	326.0
NNR/NNT	212.0	271.3	295.1	369.5
Complete	200.7	216.5	230.1	246.0

ters demonstrated dependencies between several parameters. These dependencies differ due to the the definition of the datum. The comparison of the correlation matrix of a solution with NNR/NNT condition and a solution with fixed sites revealed that ERP are more independent from other parameters, if sites are fixed to their a priori values. Furthermore, it became clear that correlations can be reduced not only by fixing sites, but also by estimating sites just once for the fortnightly time span. Some interesting correlations between ERP and ZWD of certain VLBI sites have also been detected, but not yet explained. The correlations turned out to be comparable when either estimating ERP with a daily or a sub-daily resolution.

A third, so called complete solution, has been performed on the normal equation level. The NEQ of each individual session have been stacked. Therefore, parameters at the session borders, which exist twice at the same epoch, have been used. Furthermore, parameters of site coordinates have been transformed from the session epoch to the middle of the CONT05 period. Subsequently, the NEQ elements of site coordinates have been stacked, too. Thereby two major effects can be asserted: the correlations are comparable to the case of fixed sites and outliers in the sub-daily ERP time series are clearly reduced. The latter leads to an improvement of the RMS w.r.t. a GPS ERP series by about $\frac{1}{4}$. Thus, through the approach presented here a consistent solution has been created, which seems to be the optimal approach for continuous VLBI observations.

Acknowledgments. This research has been funded by the Deutsche Forschungsgemeinschaft (DFG) under the promotional references DFG Gz: No 318/2-1.

References

Angermann D., Drewes H., Krügel M., Meisel B., Gerstl M., Kelm R., Müller H., Seemüller W., Tesmer V., ITRS Combination Center at DGFI: A Terrestrial Reference Frame Realization, Verlag der Bayerischen Akademie der Wissenschaften, DGK Reihe B, Heft Nr. 313, 2004.

Bizouard C., Gambis D, The combined solution C04 for Earth Orientation Parameters consistent with International Reference Frame 2005, web document: http://hpiers.obspm.fr/eop-pc/products/combined/C04_05.guide.pdf (2007.02.25)

Gerstl M., Kelm R., Müller H., Ehrnsperger, DOGSCS Kombination und Lösung großer Gleichungssysteme, DGFI Interner Bericht Nr. MG/01/1995/DGFI, 2001.

McCarthy & Petit (Eds.), IERS Conventions (2003), IERS technical note No. 32, Verlag des Bundesamtes für Kartographie und Geodäsie, 2004.

MacMillan D., Behrend D., Gordon D., Ma C., First Results from CONT05, IN: D. Behrend & K.D. Baver: IVS 2006 General Meeting Proceedings, 269-273, 2006.

Moritz H., Mueller I.I., Earth rotation: Theory and Observation, Ungar Publishing Company, New York, ISBN 0-8044-4671-7, 1987.

Petrov L., Boy J.-P., Study of the atmospheric pressure loading signal in VLBI observations, J. Geophys. Res., 10.1029/2003JB002500, Vol. 109, No. B03405, 2004.

Petrov L., Mark-5 VLBI Analysis Software Calc/Solve, Web document http://gemini.gsfc.nasa.gov/solve/ (2006.12.15)

Scherneck H.-G. and Bos M., Ocean Tide and Atmospheric Loading, In: N. R. Vandenberg and K. D. Baver (Eds.): IVS 2002 General Meeting Proceedings, 205-214, NASA/CP-2002-210002, 2002.

Steigenberger P., Rothacher M., Dietrich R., Fritsche M., Rülke A., Vey S., Reprocessing of a global GPS network, J. Geophys. Res., 111, B05402, doi:10.1029/2005/JB003747, 2006.

Tesmer V., Kutterer H., Richter B., Schuh H., Reassesment of Highly Resolved EOP Determined with VLBI, In: A. Rius and D. Behrend (Eds.): Proceedings of the 15th Working Meeting on European VLBI for Geodesy and Astrometry, 83-90, 2001.

Thaller D., Krügel M., Rothacher M., Tesmer V., Schmid R., Angermann D., Combined Earth orientation parameters based on homogeneous and continuous VLBI and GPS data, Journal of Geodesy, DOI 10.1007/s00190-006-0115-z, 2006.

On dependence of EOP precision and accuracy on VLBI network

Z. Malkin
Central (Pulkovo) Astronomical Observatory RAS, St. Petersburg 196140, Russia

Abstract. In this paper, a new VLBI network geometry index, the volume of network, is examined as an indicator of the quality of the Earth rotation parameters (EOP) obtained from VLBI observations. It has been shown that both EOP precision and accuracy can be described by a power low $\sigma = aV^b$, where V is the volume of network, in a wide range of the network size from domestic to global VLBI networks. In particular, the dependence found in this study can be used for comparison of results obtained from different observing programs.

Keywords. VLBI, Earth Rotation Parameters, EOP precision, EOP accuracy, network geometry

1 Introduction

By the nature of the VLBI technique, the quality of the Earth rotation parameters (EOP) derived from the VLBI observations depends on network geometry that is its size and orientation. We can consider some network geometry indices, such as

- Network span: $(\Delta\varphi, \Delta\lambda)$, $(\Delta X, \Delta Y, \Delta Z)$.
- Network orientation: mean longitude, baselines directions.
- Number of stations.

Defining and quantification of dependence of the EOP precision and accuracy on network geometry is important for practical purposes, *e.g.* planning of VLBI network or comparison of EOP results obtained from different networks and observing programs. In the common case, such dependence can be expressed as a function of several network geometry indices. In this study we consider a new generalized index of VLBI network geometry, namely the volume of network, which allows us to find the dependence of the EOP quality on network geometry good enough for practical use. It was shown that both EOP precision and accuracy strongly follow to a power low w.r.t. the network volume.

Table 1. Volume of different VLBI networks. Smallest, largest and two latest CONT campaigns networks are shown.

Session	Volume, Mm^3
JD0610	9.925E-04
EURO35	5.285E-03
JD0610	5.285E-03
EURO56	1.761E-02
CONT02	9.221E+01
CONT05	2.654E+02
T2037	4.607E+02
T2038	4.723E+02
T2041	4.816E+02
T2043	4.871E+02

2 Dependence of the EOP quality on the network volume

We have computed the volume of network in the following way.

1. Compute the tetrahedron mesh for the network polyhedron by means of the Delaunay triangulation making use of the GEOMPACK package by B. Joe (Joe, 1991).
2. Compute the volume of each tetrahedron as scalar triple product: $[(\vec{r_2} - \vec{r_1})(\vec{r_3} - \vec{r_1})(\vec{r_4} - \vec{r_1})]$.
3. Compute the sum of volumes of the tetrahedrons.

Some examples of the volume of different IVS observing networks are shown in Table 1. For comparison, the volume of the Earth is 1083 Mm^3.

Table 2. Representation of the EOP precision by a power low $\log\sigma = a + b\,\log V$.

EOP	a	b
Xp	-0.340 ± 0.022	-0.351 ± 0.018
Yp	-0.342 ± 0.023	-0.373 ± 0.019
UT	-0.603 ± 0.043	-0.382 ± 0.036
Xc	-0.771 ± 0.016	-0.238 ± 0.013
Yc	-0.772 ± 0.016	-0.238 ± 0.013

Table 3. Representation of the EOP accuracy by a power low $\log\sigma = a + b\,\log V$.

EOP	a	b
Xp	-0.212 ± 0.045	-0.315 ± 0.038
Yp	-0.263 ± 0.049	-0.298 ± 0.041

We have performed the following computations for this study.

1. Compute EOP for all 24h sessions starting from 1996.5, which corresponds to the beginning of the IGS series used for further comparison.

2. Split EOP results into bins by the network volume V: $V<0.1$, $(\sqrt{10})^k \le V < (\sqrt{10})^{k+1}$, $k = -2, \ldots, 5$.

3. Compute for each bin:

   - average network volume,
   - average EOP uncertainty,
   - WRMS of the differences between the VLBI and IGS EOP series igs95p02.erp after removing trend (for pole coordinates only).

Then we have computed the parameters of the power low representing the dependence of the VLBI EOP precision (uncertainty) and accuracy (WRMS w.r.t. IGS) as $\log\sigma = a + b\,\log V$, where σ is the error value under consideration (uncertainty or WRMS for given type of EOP). Parameters a and b were computed by means of the least square linear fit with weighting dependent on number of sessions fallen into each bin. Results are presented in Fig. 1, 2 and Tables 2, 3. In the plots and tables Xp and Yp denote the terrestrial pole coordinates, and Xc and Yc denote celestial pole offset. One can see that the dependence of both EOP precision and accuracy is nicely described by a power low.

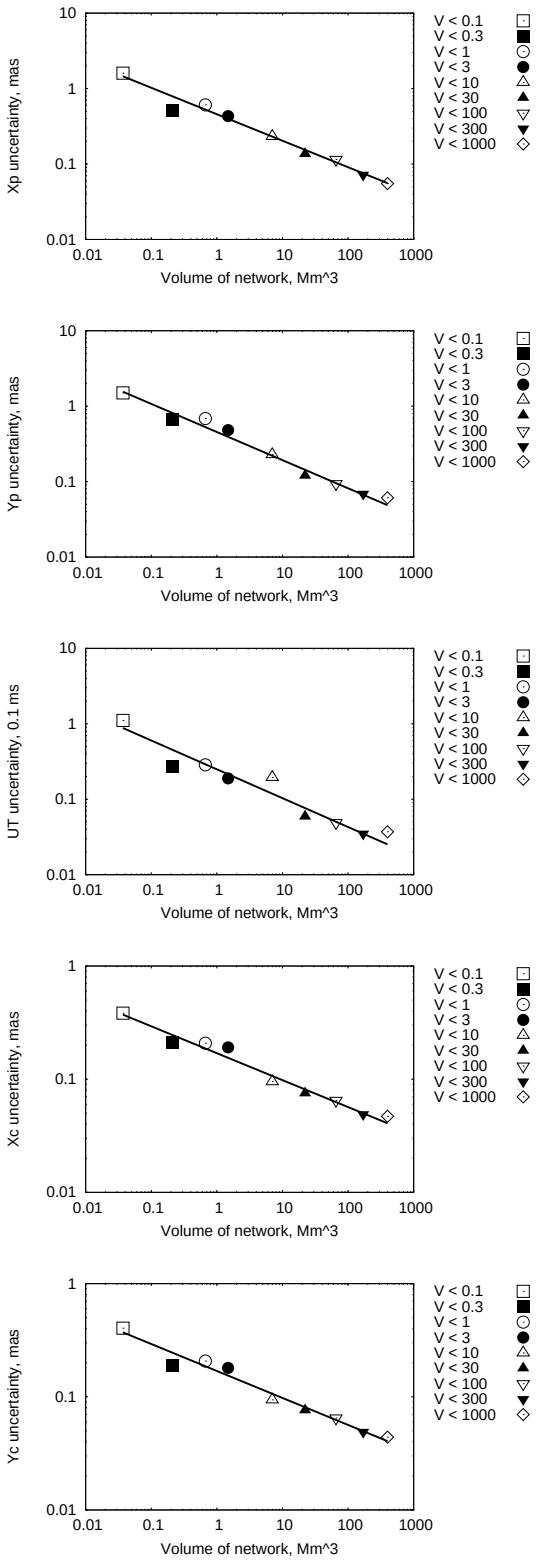

Figure 1. Dependence of the EOP precision on the network volume V. Solid line corresponds to the power low (Table 2).

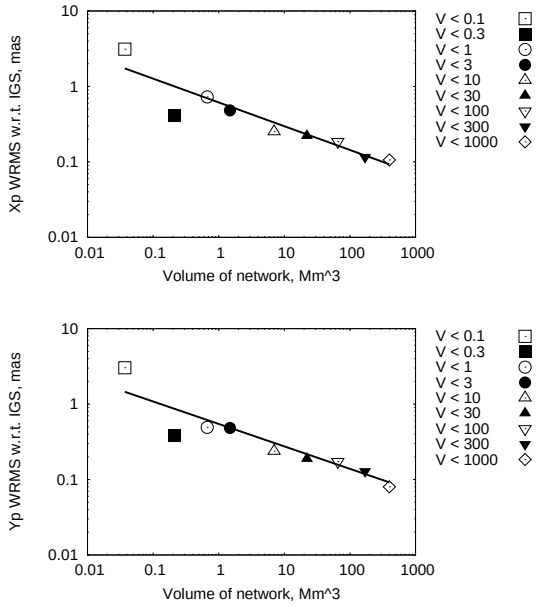

Figure 2. Dependence of EOP accuracy on the network volume V. Solid line corresponds to the power low (Table 3).

3 Comparison of observing programs

As an example of application of proposed method of estimation of the EOP quality depending on network geometry, we considered a comparison of EOP results obtained from different IVS observing programs. For this purpose, we have performed the same computations as described in the previous section, with only difference that EOP results were split into 13 observing programs: global networks R1, R4, RD, RDV, NEOS-A, CORE-A, CORE-B, CONT02, CONT05, T2, E3, and regional networks EURO, JADE. Results of computations are presented in Fig. 3 and 4. Solid lines on these plots correspond to the power low with parameters found above (Tables 2 and 3 for EOP precision and accuracy correspondingly).

Comparing results with ones obtained in the previous section, one can see that the scatter of the points in Fig. 3 and 4 is greater than one in Fig. 1, 2, which can be explained by the fact that, as a rule, networks of different size participated in the same observing program. It can be seen that scatter of EOP accuracy (Fig. 4) is much less than that of EOP precision (Fig. 3). This means that EOP accuracy follows more strongly to a power low than EOP precision.

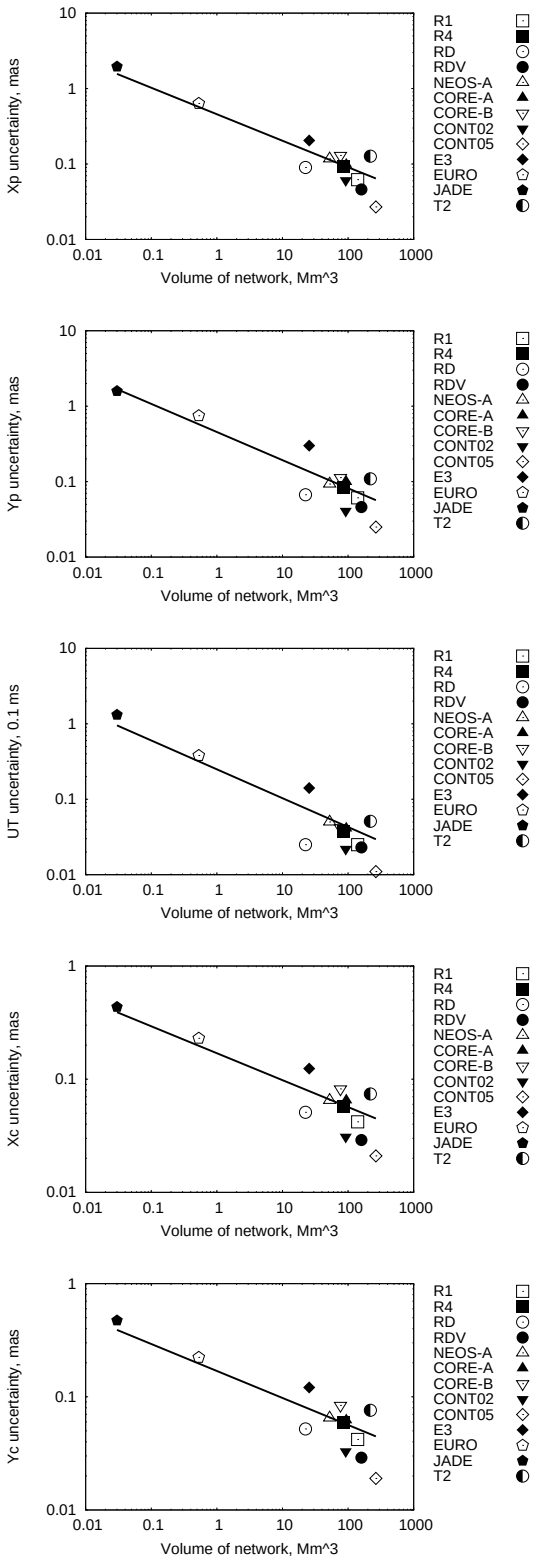

Figure 3. Dependence of the EOP precision on the network volume V for different observing programs. Solid line corresponds to the power low (Table 2).

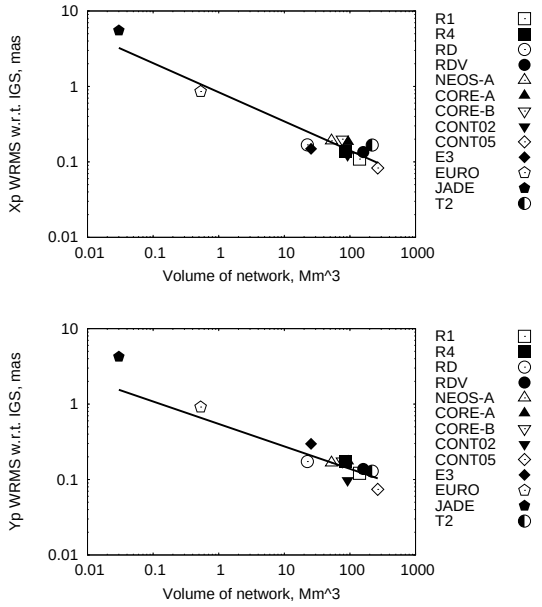

Figure 4. Dependence of the EOP accuracy on the network volume V for different observing programs. Solid line corresponds to the power low (Table 3).

Plots in Fig. 3 and 4 reveal some other interesting features, for instance:

- Somewhat better precision and accuracy of R1 program as compared with R4 may be a consequence of the difference in network size ($V^{R1}_{mean} = 140$ Mm^3, $V^{R4}_{mean} = 84$ Mm^3).
- E3 program observed with relatively small number of stations and low data rate shows relatively low precision but good accuracy at a level of Mk4 observations.
- Difference in the EOP quality of RD and R1 programs actively discussed by the IVS Observing Program Committee[1] also can be explained by large difference in the network volume ($V^{RD}_{mean} = 22$ Mm^3). From the plots, we can conclude that R4 program provides better EOP precision and accuracy than R1 after correction for this factor.

4 Conclusions

The volume of VLBI network can serve as a generalized index of network geometry. It allows us to get an effective estimate of both precision and accuracy of EOP for both global and regional networks in wide range of network size and schedule parameters. The dependence of the EOP quality on the network volume found in this study can be used for comparison EOP results obtained from different networks and observing programs. It also can be used in planning of new VLBI networks.

[1] http://ivscc.gsfc.nasa.gov/pipermail/ivs-opc/2007/

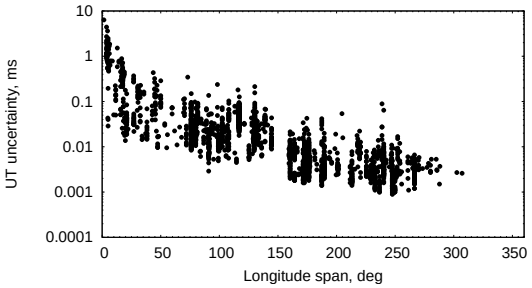

Figure 5. Dependence of the UT1 uncertainty on the longitude span.

Indeed, this method is applicable only to VLBI networks consisting of at least four stations. For 3-station network, it worth testing the area of the triangle as an index of network geometry.

We consider the method described in this paper as a convenient and accurate enough tool for investigation and prediction of the quality of EOP obtained from different VLBI network. Other dependencies can be used for specific purposes, *e.g.* dependence of UT1 results on longitude span (see Fig. 5).

It should be mentioned that the main conclusion drawn from this study is that EOP precision and accuracy obtained from VLBI observations can be well described by a power low w.r.t. the network volume. However, specific numbers shown in Tables 2, 3 may vary depending on the software used for analysis. For this reason, deriving of the power low parameters and further applications should be made making use of the same software and processing options.

References

Joe, B. (1991). GEOMPACK – a software package for the generation of meshes using geometric algorithms. *Adv. Eng. Software*, Vol. 13, pp. 325-331.

QUASAR software in IAA EOP service: Global Solution and Daily SINEX

S. Kurdubov
LSGER, Institute of Appiled Astronomy RAS, nab. Kutuzova 10, St.-Petersburg, Russia

Abstract. In this paper we briefly describe the QUASAR software for VLBI data processing created in IAA RAS. The estimation parameters and results of global solution obtained with QUASAR software are shown. The first results of involving QUASAR software into IAA EOP service for EOP and station positions calculation are discussed.

Keywords. astrometry, reference systems, VLBI

1 Introduction

Since March 2007 our analysis center has started to generate the following kinds of products: Terrestrial Reference Frame, Celestial Reference Frame and Daily Solution Files EOP+station coordinates (DSNX). For this purpose we use the new version of QUASAR software which was originally created in IAA by Igor Surkis and Vadim Gubanov. The software, reduction and estimation methods are described in this paper.

2 QUASAR software features

2.1 Reducton

Most of reduction calculations in QUASAR software are implemented according to the IERS Conventions (2003). The Vienna Mapping Function (VMF1) are used for the tropospheric delay calculation. Celestial Intermediate Pole (CIP) formalism are used for Celestial pole coordinates and derivations then we really estimate CIP-x and CIP-y instead of $d\psi$, $d\epsilon$. Also many changeable options are implemented in the software such as ocean loading model, mapping function for tropospheric delay, intraday variations of EOP, free core nutation, refraction, antenna axis offset and so on.

2.2 Estimation

QUASAR software supports both single and multi- session adjustment. There are wide list of parameters which have derivations and can be estimated. Every parameter can be estimated in different ways: as global, arc or stochastic. Every parameter can be represented as polynomial trend on the span of one session or all observation period.

In QUASAR software implemented different stochastic and dynamic estimation methods, but well tested and used at this moment is only Least Square Collocation (LSC) method. For covariance functions needed in this method we use mean correlation function for each stochastic signal and individual variance values for each station and signal.

3 Global solution

The main goal of processing all VLBI data in one global solution is to obtain more accurate Celestial and Terrestial Referencs Frames (CRF and TRF). We use the Least Square Collocation technique in QUASAR software to obtain the global solutions from all available VLBI data.

3.1 Parametrization

In the global solution presented we use following parametrization:

Global parameters: source coordinates right ascension and declination for all sources, coordinates and velocities for all stations, antenna axis offsets (axis offsets are estimated only in test solutions because in presented to the IVS solutions the only list recommended by Analysis Coordinator must be used)

Arc parameters: Earth orientation parameters (terrestrial pole coordinates Xp,Yp, univer-

Table 1. Transformation parameters from VTRF2005 to the catalogue obtained

Epoch	T1	T2	T3	D, 10^{-9}	R1	R2	R3
2005.0	4.6	−5.3	8.5	−1.9	27	−10	4
1997.0	4.7	−5.3	5.0	−1.55	−62	−90	−5

sal time UT1–UTC, celestial pole coordinates Xc,Yc), linear trend of wet zenith delay (WZD), troposphere gradient east and north, quadratic trend of station clock offset.

Stochastic parameters: intraday variations of WZD, clock offsets.

In order to eliminate the rang deficiency in normal equations these constraints was applied: no-net-rotation for 212 defining sources ICRF, no-net-rotation/translation for positions and velocities of 11 stations (KOKEE, WETTZELL, WESTFORD, ALGOPARK, NYALES20, ONSALA60, LA-VLBA, MATERA, FORTLEZA, NOTO, MK-VLBA), not estimated sources observed less than 15 times and stations velocities of less than one year observation period (soft constraints), sum of clock offsets is equal to zero in each session, soft constraint for EOP for sessions with low geometry.

3.2 Statistics

There are some statistics for the first global solution submitted to IVS: 3791 VLBI sessions from Aug 1979 to Jul 2006 were processed (4823609 delays). Coordinates and velocities of 132 stations and coordinates of 745 radio sources were estimated. For 14 stations discontinues motions were taken into account.

The CRF and TRF catalogues are obtained. Mean formal errors of radio source catalogue is 120 μas in right ascension and 150 μas in declination. Weighted differences between the obtained and ICRF-ext.2 catalogue are 200 μas in right ascension and declination (taken into account sources been observed more then 20 times more than in 3 sessions total 574).

Transformation parameters vs VTRF2005 (Nothnagel(2005)) are shown in Table 3.2

4 Daily SINEX

Our analysis center was first which started to obtain and submit DSNX files using filtering technique. Therefore there are some equations below to describe our approach.

4.1 Particular feature DSNX generation for LSC Method

The model of observation is:

$$\mathbf{l} = A\mathbf{x} + U\mathbf{s} + \mathbf{v} \tag{1}$$

where $\mathbf{l}$ — o-c vector, A — Jacobian matrix for unknown parameters, U — Jacobian matrix for stochastic parameters, $\mathbf{x}$ — vector of unknown parameters (EOP, EOP rates, WZD trend, WZD rates, tropospheric gradients, Clock-offset, Clock-offset rates and quadratic trend, station coordinates), $\mathbf{s}$ - vector of unknown stochastic signals (stochastic component of WZD, stochastic component of clock-offset). Q_{vv} - covariation matrix of residuals, Q_{ss} - covariation matrix of stochastic signals.

The Q_{vv} is diagonal matrix and diagonal elements can be obtained from the formal errors of observations. The Q_{ss} is non diagonal a priory defined matrix for all stochastic signals (WZD and clock for all stations)

The equation (1) can be written in the form:

$$\mathbf{l} = A\mathbf{x} + \mathbf{w} \tag{2}$$

where $\mathbf{w}$ is a new residuals vector with the covariance matrix $Q_{ww} = UQ_{ss}U' + Q_{vv}$. We can obtain the normal equation for (2):

$$A'Q_{ww}A\mathbf{x} = A'Q_{ww}\mathbf{l} \tag{3}$$

For equation (3) we can apply the constraints putting zero to the sum of clock offsets of all stations equal to (instead of selection base station). After that, clock and WZD parameters can be eliminated and we obtain the normal matrix, that will be outputted to SINEX.

In order to calculate WRMS of post fit residuals and another parameters for solution statistics block we apply no-net-rotation/translation constrains for station positions in system (3) and solve it. After that the stochastic signal vector $\mathbf{s}$ can be estimated by filtering it from $\mathbf{w}$:

$$\mathbf{s} = Q_{ss}U^T Q_{ww}^{-1}\mathbf{w} \tag{4}$$

where $\mathbf{w}$=$\mathbf{l}$ - A $\mathbf{x}$ and finally $\mathbf{v}$=$\mathbf{l}$ - A $\mathbf{x}$ - U $\mathbf{s}$ And this vector is used for the VTPV and WRMS calculation ($P = Q_{vv}^{-1}$).

4.2 Some Results

The DSNX files obtained for all daily sessions were sent to the IVS combination center and

Table 2. X-Pole residuals w.r.t 05C04. Statistics (1984 – now)

AC	BKG	DGFI	GSFC	IAA	COMBI
Offset [μas]	11.2	-10.7	6.2	11.3	11.3
WRMS [μas]	154.0	136.4	139.7	174.1	136.8

Table 3. Y-Pole residuals w.r.t 05C04. Statistics (1984 – now)

AC	BKG	DGFI	GSFC	IAA	COMBI
Offset [μas]	-42.5	-51.9	-50.7	-36.5	-42.4
WRMS [μas]	154.7	147.1	144.0	185.5	142.9

were approved by coordinators and included to the combination. In following tables 4.2, 4.2 presented examples of EOP series obtained from our results in comparison with another analysis centers. Data were taken from official IVS web site (IVS).

5 Conclusions

Thus the QUASAR software is fully operational and involved in the IAA VLBI service. It allows our analysis center to contribute in all IVS products include the TRF, CRF and daily solution for EOP and station coordinates.

I am very gratefull to my science advisor Vadim Gubanov for the discussions about all aspects of VLBI data processing, to creator of QUASAR software Igor Surkis for help in understanding it mechanics, to Elena Skurikhina for help in testing my results. And many thanks to the analysis coordinator Sarah Boeckmann for help in finding many bags in software.

References

McCarthy & Petit(2004), ed., IERS Conventions(2003)(IERS Technical Note No. 32), 2004, Frankfurt am Main: Verlag des Bundesamtes fuer Katrografie und Geodaesie, 127 pp., paperback, ISBN 3-89888-884-3.

Moritz H., Earth Rotation: Theory and Observation, 1987, Frederick Ungar, 617 pp.

V.S. Gubanov, Yu.L. Rusinov, I.F. Surkis, C.Y. Shabun, S.L. Kurdubov Project: Global Analysis of 1979–2004 VLBI Data In: International VLBI Service for Geodesy and Astrometry 2004 General Meeting Proceedings, NASA/CP-2004-212255, 2004, 315–319.

Nothnagel A. VTRF2005 — a combined VLBI Terrestrial Reference Frame. Proceedings of the 17th Working Meeting on European VLBI for Geodesy and Astrometry, Noto, Italy, April, 2005, 118–124.

International VLBI Service http://ivscc.gsfc.nasa.gov/.

Comparison and combination of consistent VLBI solutions

S. Böckmann, T.Artz, A. Nothnagel
Institut für Geodäsie und Geoinformation, Universität Bonn, Nußallee 17, D-53115 Bonn, Germany

V. Tesmer
Deutsches Geodätisches Forschungsinstitut, Alfons-Goppel-Strasse 11, D-80539 München, Germany

Abstract. For the official combination of the International VLBI Service for Geodesy and Astrometry (IVS) different analysis centres contribute their solutions analysed with different VLBI software packages.

In this paper results from two VLBI analysis software packages, Occam and Calc/Solve, have been compared to detect systematic differences. The comparisons have been carried out with station position time series and earth orientation parameter series calculated from standard solutions as used for the official IVS combination. In addition, the same studies have been done with consistent time series generated after a number of effects have been adapted to the same models in both software packages. Systematic differences mainly in the station height components have been detected and could be attributed to differences in the pole tide model.

Furthermore, a combination on the normal equation level and comparisons with IGS earth orientation parameters have been carried out. The results show that a combination can stabilise the results if the contributing solutions have no systematic differences and are of similar quality.

Keywords. Combination, pole tide, earth orientation, station coordinates, VLBI

1 Introduction

Different IVS Analysis Centres (ACs) analyse geodetic VLBI observations with different software packages and provide their solutions to the official IVS combined VLBI solution. All ACs calculate their solution with models and strategies selected to the best of their knowledge. However, these "solutions" are made available as datum-free normal equations in SINEX format. The final solution can then be set up with identical datum definitions of choice (Vennebusch et al., 2006). Systematic differences in the a priori models and parametrisation of the different software packages as well as the use of different geophysical constants result in systematic differences in the estimated parameters. A combination of different individual solutions can only stabilize the results, if the solutions solely differ normally distributed (not systematically). Thus, before combining different VLBI solutions or combining VLBI with other space geodetic techniques, systematic differences in the estimated parameters have to be detected and removed.

In this study two main areas are addressed. The first is the comparison of the results of two VLBI analysis software packages, Occam (Titov et al., 2004) and Calc/Solve (Petrov, 2002), to detect remaining systematic differences. Therefore, station position time series and long term earth orientation parameter (EOP) series have been calculated without and with adapting geophysical models and the parametrisation in the two programs.

The second is the combination on the basis of normal equations with a subsequent estimation of EOP and station coordinates for the two solutions without adaptations and for the two solutions with adaptations for a priori models and parametrisation.

2 Input data

The comparisons and combinations presented in this paper are based on time series calculated from 2752 daily unconstrained, pre-reduced normal equations of sessions between 1984 and 2006. These normal equations are given in four different versions. Two of them are results from Occam, both calculated at the German Geodetic Research Institut (DGFI), the other two are results from Calc/Solve, calculated at NASA

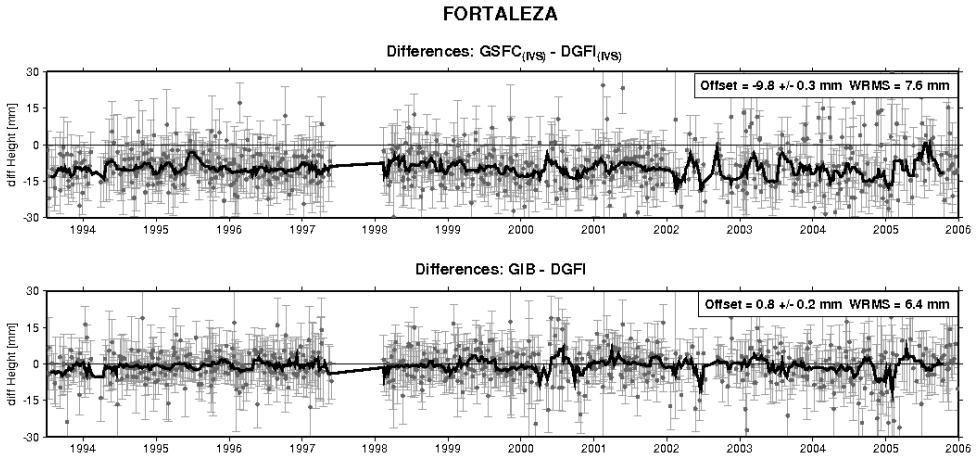

Figure 1. FORTALEZA height component

Goddard Space Flight Center (GSFC) and at the Institute of Geodesy and Geoinformation Bonn (GIB). To get comparable results, all solutions have been transformed to the same reference epoch and to an equal set of a priori values. Datum deficiencies have been removed by imposing an identical datum. Two types of solutions have been computed, one for EOP and one for station coordinate time series. EOP series have been estimated fixing all station coordinates to the ITRF2005. For the station position time series no-net-translation (NNT) and no-net-rotation (NNR) condition equations with respect to ITRF2005 have been applied. The source positions were fixed to ICRF and its extensions. Neither thermal deformation nor atmospheric loading was applied.

3 Comparisons

In this section, two comparisons of Occam and Calc/Solve results will be inter-compared. The first comparsion, $GSFC_{IVS}$ - $DGFI_{IVS}$, has been carried out with time series calculated from DGFI and GSFC normal equations as they are being used for the standard IVS combination. These solutions contain differences in some a priori models and parametrisation. One is the definition of the mean pole within the pole tide model. While the GSFC solution defines the mean pole as $X_0 = Y_0 = 0$, the DGFI solution uses a linear mean pole model as recommended in the IERS Conventions 2003 (McCarthy and Petit, 2004). In addition, a priori troposphere gradients were set to zero in the DGFI solution, whereas GSFC uses a priori gradients from the Data Assimilation Office (DAO) weather model. Tropospheric gradient rates were estimated in the GSFC solution only. Furthermore, different parametrisation for the troposphere parameters are used. The zenith wet delay piece-wise linear function is parametrised with a time-constant of one hour in the DGFI solution, in contrast to 20 minutes as it is done by GSFC.

The second comparison, GIB - DGFI, has been carried out with consistent handling of the models: In order to achieve an overall consistency, all a priori models and parametrisation have been adapted in the two software packages. After these software changes a new Occam solution was calculated at DGFI and a new Calc/Solve solution at GIB.

3.1 Comparisons of station position time series

For the four different solutions, station position time series of all VLBI sites have been computed and compared. Figure 1 illustrates the differences of the two solutions $GSFC_{IVS}$ and $DGFI_{IVS}$, exemplarily for the FORTALEZA height component as well as the differences between the two adapted solutions (GIB - DGFI). The differences for each single session (dots) are shown as well as a 70-day median computed every 7 days to better visualise the differences. A systematic disagreement between the $GSFC_{IVS}$ and the $DGFI_{IVS}$ solution is obvious. In contrast to this, the systematic bias is completely removed between the two consistent time series (below). Also the WRMS determined from the resulting

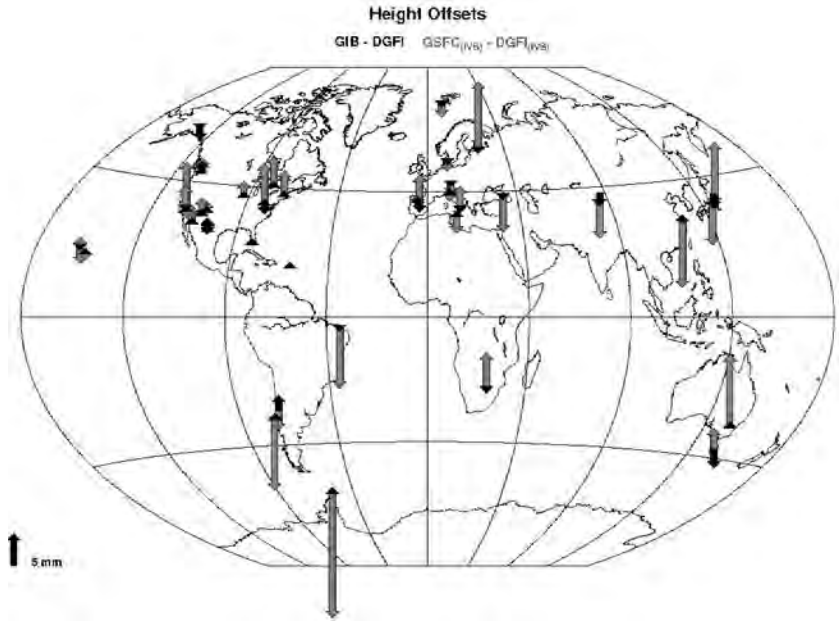

Figure 2. Height offsets of all VLBI stations, GIB - DGFI differences in black, GSFC(IVS) and DGFI(IVS) differences in grey

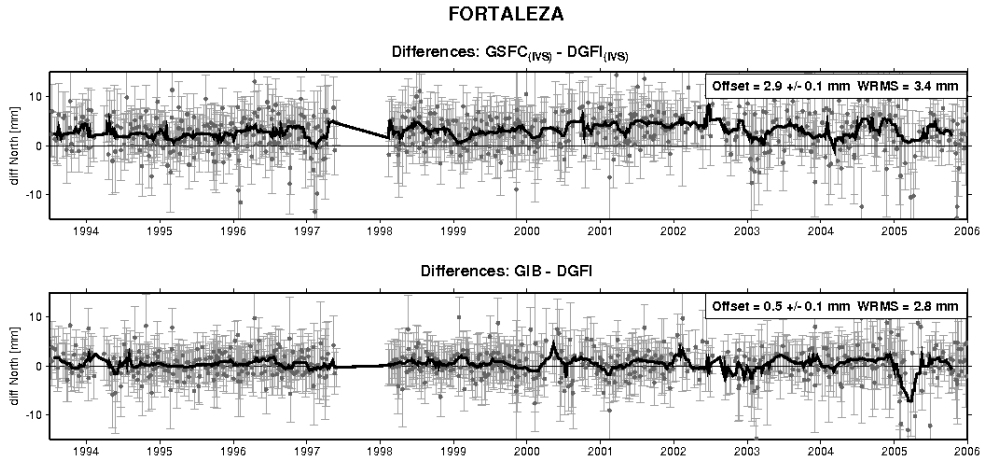

Figure 3. FORTALEZA north component

differences of all sessions including FORTALEZA between 1993 and 2006, is reduced from 7.6 mm ($GSFC_{IVS}$ - $DGFI_{IVS}$) to 6.4 mm (GIB - DGFI). Looking at the whole ensemble of VLBI sites in the world, significant height offsets are observable for a lot of stations. Figure 2 illustrates the height offsets for both comparisons of all VLBI stations participating in more than 30 sessions. On average the height offsets between $GSFC_{IVS}$ and $DGFI_{IVS}$ reach 5 mm with a clear systematic behaviour of the signs. The main reason for this is the different mean pole within the pole tide model (see Sec. 2). Unlike this, almost all offsets between the GIB and DGFI solutions are smaller than 1 mm.

Differences in the horizontal site components show a similar behavior as the differences in the height component. Regarding the differences in the FORTLEZA north component (Fig. 3) a clear offset of about 3 mm is detectable in the $GSFC_{IVS}$ - $DGFI_{IVS}$ differences. Again this offset is completely removed in the horizontal position time series differences of the two consistent solutions GIB and DGFI. The horizontal site offsets for

Figure 4. Horizontal offsets of all VLBI stations, GIB - DGFI differences in black, GSFC(IVS) and DGFI(IVS) differences in grey

all VLBI stations are shown in Figure 4. As for the height offsets, only horizontal offsets are plotted for stations taking part in more than 30 sessions. Especially for the Japanese stations and the Hawaiian stations considerable systematic differences are in evidence for the comparisons between $GSFC_{IVS}$ and $DGFI_{IVS}$. As expected, the differences are generally smaller in the comparison between the consistent time series with systematics being removed.

3.2 Comparisons of EOP series

Beside the station position time series, also long term EOP series from 1984 till 2006 have been computed and compared. Figure 5 summarises the results for polar motion, UT1-UTC and their rates of the two comparisons $GSFC_{IVS}$ - $DGFI_{IVS}$ and GIB - DGFI. The offsets as well as the WRMS values exhibit characteristics as expected. They are smaller for nearly every parameter when comparing the two consistent solutions instead of comparing the two IVS contributions.

Regarding the $GSFC_{IVS}$ - $DGFI_{IVS}$ Y-pole differences in detail, a clear signal with two main frequencies at 433 days with an amplitude of $\sim$27 μas and at 365 days with an amplitude of $\sim$12 μas is visible (Fig. 6a). As for the height offsets this is due to differences in the pole tide modelling: Beside the different definitions of the mean pole (c.f. Sec 2) an error in the computation of the latitude deformation in the Occam software was detected. Revising the software error significantly removed the signal (Fig. 6b), only normally distributed (none systematic) differences remain. However, the remaining scatter can be reduced even more, if all a priori models are adjusted in the two software packages (Fig. 6c). Nevertheless, it is questionable if the ultimate goal is to compute (and later combine) two exactly the same solutions.

4 Combination results

After removing the systematic differences in the GIB and DGFI contributions, a combination on the normal equation level has been carried out. Two different combined solutions have been estimated. One from the two standard IVS inputs, $GSFC_{IVS}$ and $DGFI_{IVS}$, the second from the two consistent solutions, GIB and DGFI. Long term EOP series have been estimated for all six solutions and compared with the IGS Final Combined Solution (igs00p03.erp, ftp://cddis.gsfc.nasa.gov/pub/gps/products). The results of the comparison between 1997 and 2006 are summarized in Table 1.

The combination ($COMBI_{IVS}$) of the two solutions $GSFC_{IVS}$ and $DGFI_{IVS}$ leads to smaller WRMS values with respect to IGS compared to each individual solution for most of the EOP components. In contrast to this, the WRMS

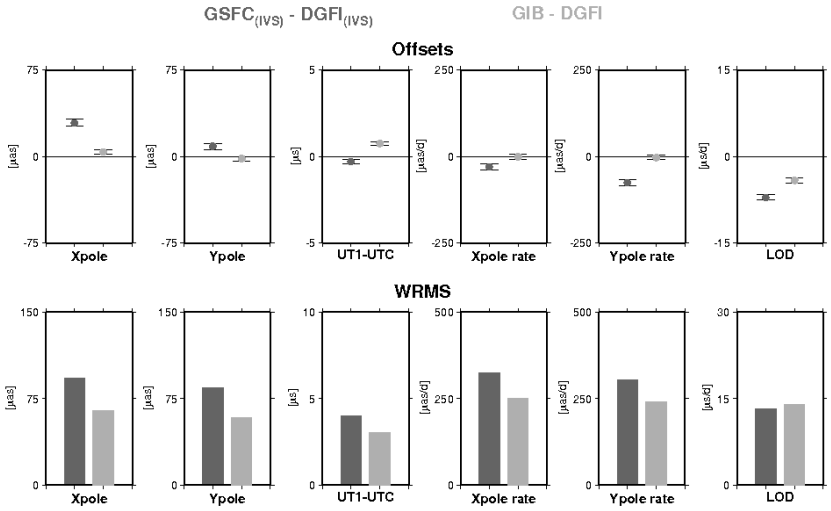

Figure 5. Results of EOP comparisons of the different VLBI solutions, offsets and WRMS for GSFC(IVS) - DGFI(IVS) differences (left column) and GIB - DGFI differences (right column)

Table 1. EOP differences from 1997 onwards with respect to IGS final combined solution

WRMS w.r.t IGS					
	X_p [μas]	Y_p [μas]	$X_p$rate [μas/d]	$Y_p$rate [μas/d]	LOD [μs/d]
$DGFI_{IVS}$	133.7	123.7	382.4	390.8	23.8
$GSFC_{IVS}$	142.0	119.7	358.6	339.0	21.8
$COMBI_{IVS}$	131.2	116.9	253.3	348.4	22.7
DGFI	128.5	121.9	357.6	348.7	22.7
GIB	135.9	128.2	388.3	375.0	26.6
COMBI	130.9	124.4	364.9	355.0	24.3

values of the combined results (COMBI) of the two adapted solutions display a mean of the two input solutions. Obviously, the DGFI solution shows a much better agreement with the IGS EOP solution than the GIB solution. This leads to the assumption that the combination of these solutions cannot stabilise the results due to the suboptimal quality of the GIB solution.

5 Summary and Outlook

The comparisons have shown that systematic differences exsist between the Occam and Calc/Solve results as they are used in the standard IVS combination exist. The most significant systematic differences in the results originate from differences in the pole tide modelling. These systematics are not appropriate for a combination, as they lead e.g. to unclear references for EOP. Adapting the two VLBI software packages to identical models and parametrisation we produced consistent solutions which do not show any systematic differences in the results.

Moreover, the combination yields EOP time series that agree better with the IGS EOP series than the single solutions, if the individual solutions do not show systematic differences in the estimated parameters and are of similar quality. Thus, for a combination of different VLBI solutions and especially for further combinations with other space geodetic techniques, it is necessary that for every single solution a priori models and parametrisation are used that do not lead to systematic differences in the estimated parameters between the single solutions. Most of these systematics can be avoided, if every AC uses the IERS standards.

Acknowledgements This research has been funded by the project "GEOTECHNOLOGIEN" of the German ministry of education and research (BMBF) under reference FKZ 03F0425D.

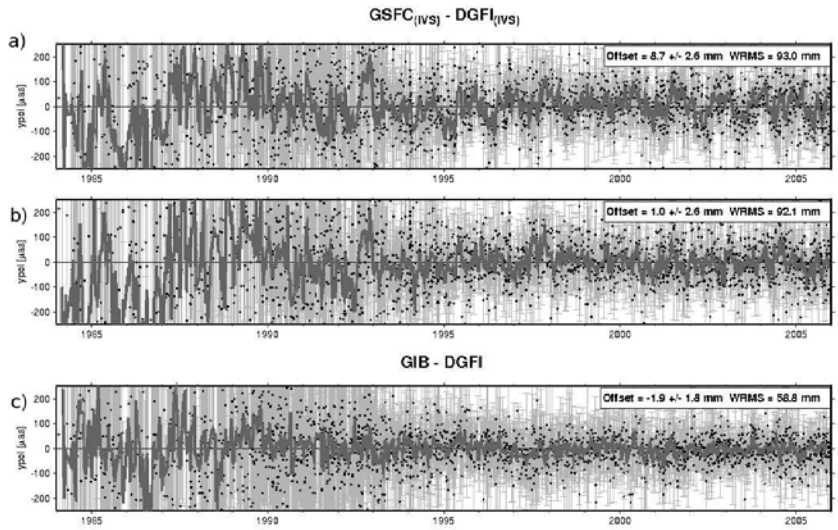

Figure 6. Y-pole differences between 1984 and 2006 **a)** GSFC(IVS) - DGFI(IVS), **b)** GSFC(IVS) - DGFI(IVS) after removing error in DGFI(IVS) solution, **c)** GIB - DGFI

References

Titov, O., V. Tesmer, J. Boehm (2004) OCCAM v.6.0 software for VLBI data analysis, IVS General Meeting Proceedings, NASA/CP-2004-212255, MD, USA pp 267-271

Petrov, L (2002), Mark IV VLBI analysis software Calc/Solve. Web document: http://gemini.GSFC.nasa.gov/solve

McCarthy, D and G. Petit (2004), IERS Conventions (2003) IERS Technical Note 32, Verlag des Bundesamtes fuer Kartografie und Geodaesie, Frankfurt

Vennebusch V., S. Böckmann, A. Nothnagel (2006), The contribution of Very Long Baseline Interferometry to ITRF2005, J Geodesy DOI10.1007/s00190-006-0117-x

Long-term trends of water vapour from VLBI observations

R. Heinkelmann, J. Böhm, H. Schuh
Institute of Geodesy and Geophysics,
Vienna University of Technology, Gusshausstrasse 27-29, A-1040 Vienna, Austria
rob@mars.hg.tuwien.ac.at

M. Schmidt
Deutsches Geodätisches Forschungsinstitut, Alfons-Goppel-Strasse 11, D-80539 Munich, Germany

Abstract. In this paper, we investigate the application of B-spline wavelets for the trend representation of zenith delay time-series. Linear trend estimates of combined long time-series of zenith delays (ZD) from IVS Analysis Centers (AC) are compared with those from IGS and ECMWF. In the presence of large noise, the B-spline wavelet representation of the trend of ZD allows to estimate significant linear trends. E.g. at GILCREEK the 1-σ standard deviation of the residual series decreases from 21 mm (no filtering) to 4 mm (wavelet-filtering). At a majority of sites linear trends of ZD obtained by various IVS AC agree well. Disagreement is mostly due to inhomogeneities of the atmosphere pressure data used for the VLBI data analysis.

Keywords. VLBI, zenith delays, B-spline wavelet, trend analysis

1 Introduction

In a project under the umbrella of the International VLBI Service for Geodesy and Astrometry (IVS, Schlüter et al., 2002) long time-series of zenith total delays (ZTD) and zenith wet delays (ZWD) of eight IVS Analysis Centers (AC) have been combined on the level of parameters. The combination procedure is described by Heinkelmann et al. (2007). Currently, the combined time-series are available for 50 network stations, covering 21 years, from the beginning of 1984 until the end of 2004. The combined long time-series are accessible from IVS Data Centers (e.g., IVS, 2007). Table 1 shows the number of sessions and stations, and the time-span covered by the specific IVS AC. Contributing AC are: Geoscience Australia, Canberra, Australia (AUS); Bundesamt für Kartographie und Geodäsie, Leipzig, Germany (BKG); Centro di Geodesia Spaziale, Matera, Italy (CGS); Deutsches Geodätisches Forschungsinstitut, Munich, Germany (DGFI); NASA Goddard Space Flight Center, Greenbelt, USA (GSFC), Institute of Applied Astronomy, St. Petersburg, Russia (IAA); Institute of Geodesy and Geophysics, Vienna, Austria (IGG); Main Astronomical Observatory, National Academy of Sciences, Kiev, Ukraina (MAO).

Table 1. IVS AC contributing to the long-term combination of zenith delays

AC	time-span	sessions	stations
AUS	1979 - 2005	3348	54
BKG	1984 - 2005	3226	60
CNR	1987 - 2005	1009	75
DGFI	1984 - 2004	2613	49
GSFC	1979 - 2005	3873	149
IAA	1979 - 2004	3443	127
IGG	1984 - 2005	2728	50
MAO	1980 - 2005	2905	80
combined IVS	1983 - 2004	3477	50

2 Analysis of zenith delay signals

Zenith delay time-series y_t can be considered as linear combination of a constant mean, a trend component, one or more cycles, extreme events or outliers, and a noise component

$$y_t = mean + trend + cycle + extrema + noise\ . \quad (1)$$

The outliers can either be removed by visual inspection, or – more objectively – by robust estimation (see Heinkelmann et al., 2007).

2.1 Fourier expansion of cyclic component in zenith delay signals

We identify the periods of cycles by spectral analysis. In contrast to Heinkelmann et al. (2007), we consider up to eight terms starting with annual periods:

$$y_t - mean - extrema = cycle$$
$$cycle = \sum_{i=1}^{8}\left[A_i \sin(2\pi f_i t) + B_i \cos(2\pi f_i t)\right] \quad (2)$$

In Equation (2) A_i and B_i are determined by least-squares method; see e.g. Koch (1997). The eight pairs of coefficients characterize amplitudes and phases of sinusoids with frequencies f_i corresponding to annual, semi-annual and six successive periods. The trend component does not have to be considered for the determination of cycles, since trend and cyclic components are sufficiently de-correlated due to the length of the time-series, covering about 20 years.

2.2 Trend representation using normalized quadratic B-splines wavelets

Linear and non-linear characteristics of a climate trend can be assessed and represented by wavelet modeling. Therefore, we apply the normalized quadratic B-spline function as one-dimensional scaling function. The normalized B-spline $N_{j,k}^{d}(x)$ of order d is defined recursively at equally spaced knots $t_0^j, t_1^j, ..., t_{m_j+d}^j$ ($m_j = 2^j + 2$) and represented in levels $j = 0,...,J$ of different resolutions with $k = 0,...,m_j - 1$ and $m = 1,...,d$ as

$$N_{j,k}^{m}(x) = \frac{x - t_k^j}{t_{k+m}^j - t_k^j} N_{j,k}^{m-1}(x) + \frac{t_{k+m+1}^j - x}{t_{k+m+1}^j - t_{k+1}^j} N_{j,k+1}^{m-1}(x) \quad (3)$$

and with initial values

$$N_{j,k}^{0}(x) = \begin{Bmatrix} 1 & if & t_k^j \le x < t_{k+1}^j \\ 0 & else & \end{Bmatrix}; \quad (4)$$

see e.g. Stollnitz et al. (1995). In general, the B-spline of order d is compactly supported, i.e. its values are different from zero only in a finite range on the real axis. Since we want to use this approach for regional modeling, we introduce the so-called endpoint-interpolated B-splines (Schmidt, 2007) of order d defined on the unit interval [0, 1[.

For our investigations we choose with $d = 2$ the normalized quadratic B-spline functions $N_{j,k}^{2}(x)$. In this case the knot sequence is given as

$$0 = t_0^j = t_1^j = t_2^j < t_3^j < t_4^j < ... < t_{m_j}^j = t_{m_{j+1}}^j = t_{m_{j+2}}^j = 1 \quad (5)$$

Figure 1 shows the normalized quadratic B-splines, for resolution level $j = 2$.

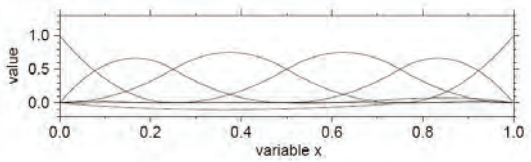

Fig. 1 Normalized quadratic B-splines, resolution level $j = 2$

Coefficients at the highest resolution level J are estimated by least-squares method (Koch, 1997). Then the coefficients related to the lower resolution levels $0 \le j < J$ can successively be expressed by linear combinations starting from the highest level J. This so-called pyramid algorithm is the basic tool of the decomposition of the input signal into frequency-dependent detail signals, which is known as the multi-resolution representation (Schmidt, 2007). The level-j approximation means the sum of the detail signals until resolution level j. The highest resolution level J is implicitly given such that the relation $m_J = 2^J + 2 < n$ holds, where n denotes the number of observations.

The detail signals of the seasonal reduced zenith wet delay time-series are exemplarily shown for station GILCREEK (Figure 2). Figure 3 displays the multi-resolution representation of the same time-series for various levels.

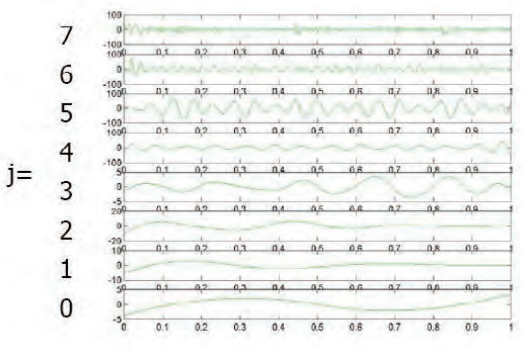

Fig. 2 Detail signals of seasonal reduced ZWD for resolution levels $j = 0,1,...,7$

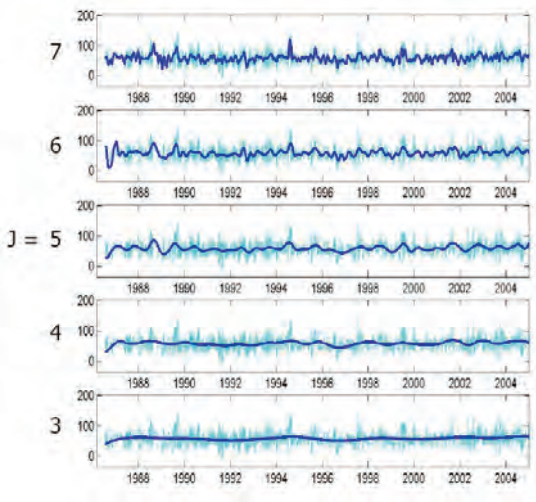

Fig. 3 Multi-resolution representation (blue) of seasonal reduced ZWD (cyan), maximal resolution level $J = 3$ to 7

When neglecting non-significant coefficients, the number of coefficients used for the representation of signals is usually reduced significantly. This can be interpreted as statistical data compression. The significance of the wavelet-coefficients can be assessed e.g. by hypothesis testing or thresholding.

We represent the trend component by wavelet modeling. For the comparison, we estimate a linear trend from the wavelet representation. The linear trends obtained from the wavelet approximations are more significant than the linear trends determined from un-filtered zenith delay time-series. E.g., for GILCREEK the 1-σ standard deviation of the unfiltered seasonal-reduced time series is 21 mm. Whereas 1-σ standard deviations of the wavelet-filtered seasonal reduced time series are between 12 mm ($J = 7$) and 4 mm ($J = 3$), depending on the maximal resolution level J.

3 Comparison of linear trends of zenith delays

3.1 Comparison of trends of ZWD between IVS AC

In general, there is good agreement between the various IVS AC solutions. In case of disagreement, e.g. at FORTLEZA, the reasons are discontinuities of the atmosphere pressure data used for the VLBI analysis. In particular the replacement of missing atmosphere pressure data by the IVS AC is done inhomogeneously. Table 2 shows linear trend estimates of the contributing IVS AC for some stations with long time-series.

3.2 Comparison of trends of ZTD between IGS and IVS combined series

The comparison with this IGS product covers only 8 years, because the combined IGS series are available since 1997, only. In general, the linear trends of IGS and IVS ZTD agree quite well. However, small differences can be found, which result from inhomogeneous analysis options and models applied for the computation of the IGS series (Table 3). In addition, the IGS solutions do not apply absolute antenna and satellite phase center calibrations. These differences of long-term trends get much smaller, when comparing with homogeneously re-processed GPS series (Steigenberger et al., 2007).

Table 3. Linear trends of ZTD of IGS and IVS combined series in mm/year

co-located site		IVS	IGS
IVS	IGS		
GILCREEK	**fair**	2.6 ± 0.2	2.8
WETTZELL	**wtzr**	-0.4 ± 0.1	-0.6
WESTFORD	**wes2**	3.3 ± 0.2	3.1
KOKEE	**kokb**	2.1 ± 0.1	1.8
FORTLEZA	**fort**	2.1 ± 0.1	2.2
HOBART26	**hob2**	-1.2 ± 0.3	-1.4

Table 2. Linear trends of ZWD of IVS AC and IVS combined series (last column) in mm/year

AC / site	AUS	BKG	CNR	DGFI	GSFC	IAA	IGG	MAO	IVS
GILCREEK	0.6	0.5	0.5	0.5	0.5	0.6	0.7	0.7	0.6
WETTZELL	0.1	0.4	0.4	0.4	0.5	0.4	0.2	0.5	0.4
WESTFORD	0.2	0.5	0.4	0.4	0.4	0.1	0.5	0.4	0.3
KOKEE	0.5	0.7	0.8	0.7	0.7	0.7	0.7	0.7	0.7
FORTLEZA	3.6	0.9	0.9	1.1	1.0	0.9	1.2	0.4	1.2
HOBART26	0.3	0.1	-0.1	0.0	0.7	0.2	0.4	1.1	0.3

3.3 Comparison of trends of ZWD between ECMWF and IVS combined series

Boehm and Schuh (2003) describe in detail, how ZWD can be derived from a numerical weather model (NWM), such as the 40-years re-analysis (ERA-40) of the ECMWF (European Centre for Medium-Range Weather Forecasts). Comparing our results with NWM is very valuable. At several stations the linear trends of zenith delays between ECMWF and IVS combined series do not match. At these stations, inhomogeneities can be found mostly in the in-situ meteorological data used for the IVS data analysis. If those inhomogeneities were detected and removed (see Heinkelmann et al., 2005), most of the trends agree much better. At stations where the disagreement remains, different long-term trends can be observed in the atmosphere pressure series between ECMWF and in-situ atmosphere data. We could adjust the observed trends of in-situ atmosphere pressure data to the trends given by the ERA-40 re-analysis. However, so far we have been hesitating to do so, since we are not convinced by the superiority of trends from re-analysis data sets. Considerable doubts that climate trends can be assessed from re-analysis data sets were also raised by Bengtsson et al. (2004).
Table 4 shows linear trends of ZWD at a subset of frequently observing stations. Here, the disagreement at FORTLEZA is for instance due to different trends of atmosphere pressure data sets. At WESTFORD, the inhomogeneous replacement of missing in-situ atmosphere pressure data contaminates the linear trends obtained from several IVS AC.

Table 4. Linear trends of ZWD of ECMWF and IVS combined series in mm/year

	IVS	ECMWF
GILCREEK	0.6 ± 0.1	0.6
WETTZELL	0.3 ± 0.1	0.5
WESTFORD	0.3 ± 0.2	-0.2
KOKEE	0.8 ± 0.1	0.3
FORTLEZA	1.4 ± 0.2	-1.9
HOBART26	-1.1 ± 0.7	-0.9

4 Conclusions

In the presence of large noise, the B-spline wavelet approximation of the trend component of ZD allows to estimate significant linear trends. E.g. at GILCREEK the 1-σ standard deviation of the residual series decreases from 21 mm (no filtering) to 4 mm (wavelet-filtering with J=3). At a majority of sites linear trends of ZD obtained by various IVS AC agree well. The combined ZD time-series can be compared with IGS and ECMWF series. Disagreement is mostly due to inhomogeneities of the atmosphere pressure data used for the VLBI data analysis. Small differences appear, if analysis options are inhomogeneous. If breaks of in-situ atmosphere pressure series were detected and removed, different linear trends of in-situ atmosphere pressure series are the main reason for remaining disagreement of observed trends of ZD.

It is not clear, whether observed trends of in-situ atmosphere pressure should be corrected, and whether re-analysis data sets, such as ERA-40, can be used as a reference for such a correction.

Acknowledgements

We greatly acknowledge the IVS and its components, in particular the AC providing data for the long-term combination. We also acknowledge the Zentralanstalt für Meteorologie und Geodynamik (ZAMG), Vienna, Austria, for providing access to the ECMWF data sets. The authors want to thank the Austrian Science Fund (FWF) for the financial support of our work within project P16992-N10 (VLBI for climate studies).

References

Bengtsson, L., S. Hagemann, K. I. Hodges (2004) Can climate trends be calculated from reanalysis data? Journal of Geophysical Research. Vol. 109(D11111), doi:10.1029/2004JD004536

Boehm, J. and H. Schuh (2003) Vienna Mapping Functions. In: *Proc. of the 16th working meeting of European VLBI for Geodesy and Astrometry*, W. Schwegmann and V. Thorandt (eds), Bundesamt für Kartographie und Geodäsie, Frankfurt/Leipzig, pp. 131-144

Heinkelmann, R., J. Böhm, H. Schuh (2005) Homogenization of surface pressure recordings and its impact on long-ter series of VLBI tropospheric parameters. In: *Proc. of the 17th working meeting of European VLBI for Geodesy and Astrometry*, M. Vennebusch and A. Nothnagel (eds) INAF- Istituto di Radioastronomia – Sezione di NOTO – Italy, pp. 74-78

Heinkelmann, R., J. Böhm, H. Schuh, S. Bolotin, G. Engelhardt, D. S. MacMillan, M. Negusini, E. Skurikhina, V. Tesmer, O. Titov (2007)

Combination of long time-series of troposphere zenith delays observed by VLBI. *Journal of Geodesy*. doi:10.1007/s00190-007-0147-z

IVS (2007) web-resource: ftp://ivs.bkg.bund.de/pub/vlbi/ivsproducts/trop/long_term/ivs2005a/

Koch, K. R. (1997) Parameterschätzung und Hypothesentests, *3rd edition, Dümmler*, Bonn

Schlüter, W., E. Himwich, A. Nothnagel, N. Vandenberg, A. Whitney (2002) IVS and its important role in the maintenance of the global reference frames. *Advances in Space Research*, Vol. 30, No. 2, pp. 145-150

Schmidt, M. (2007) Wavelet modeling in support of IRI. *Advances in Space Research*. doi:10.1016/j.asr.2006.09.030

Steigenberger, P., V. Tesmer, M. Krügel, D. Thaller, R. Schmid, S. Vey, M. Rothacher (2007) Comparison of homogeneously reprocessed GPS and VLBI long time-series of troposphere zenith delays and gradients. *Journal of Geodesy*. doi:10.1007/s00190-006-0124-y

Stollnitz, E. J., T. D. DeRose, D. H. Salesin (1995) Wavelets for computer graphics: A Primer. *Institute of Electrical and Electronics Engineering – Computer Graphics and Application*, Vol. 15(3), pp. 76-84 (part 1), and Vol. 15(4), pp. 75-85 (part2)

An analysis of celestial pole offset observations in the free core nutation frequency band

Z. Malkin, N. Miller
Central (Pulkovo) Astronomical Observatory RAS, St. Petersburg 196140, Russia

Abstract. In this study, three empirical Free Core Nutation (FCN) models developed to the present time, MHB2000, Malkin's and Lambert's ones, are compared on the basis of representation of variations of the FCN amplitude and phase predicted by these models. It is possible to conclude, that the model of the author provides the most realistic representation of the FCN variations. However, the specified models are based on representation about single FCN rotational mode. At the same time, some results of processing of the VLBI observations made during last years, specify possible presence of two close FCN periods. A theoretical explanation to presence of a second FCN frequency FCN has been given by G. Krasinsky in his theory of rotation of the Earth with two-layer liquid core, ERA2005. In the present work, for more detailed studying this phenomenon, the IVS time series of celestial pole offset, and also those predicted by the ERA2005 theory, have been investigated by means of several statistical methods which confidently show presence of two fluctuations in nutational movement of an Earth's rotation axis with the periods about −452 and −410 solar days.

Keywords. Earth rotation, nutation, free core nutation, VLBI

1 Introduction

Free Core Nutation (FCN) is the main factor limited the accuracy of coordinate transformation between terrestrial and celestial reference frames. On the other hand, investigation of the FCN parameters obtained from the Very Long Baseline Interferometry (VLBI) observations gives an important insight in the Earth structure and dynamics. Classical theory of Earth rotation predicts existence of a single FCN mode with period about −430 sidereal days (see e.g. Dehant, 2003; Hinderer, 2000). Making use of analysis of the VLBI observations to confirm this conclusion leads sometimes to contradictory results. Determination of the FCN period from the resonance effect gives a value close to the theory, whereas analysis of time series of differences between observed celestial pole coordinates and ones predicted by the IAU2000A precession-nutation model show substantial variations of the FCN period and phase (Malkin, 2003, 2004b; Vondrák, 2005).

In this paper, we analyze combined celestial pole offset series provided by the International VLBI Service for Geodesy and Astrometry (IVS) (Schlüter et al., 2002) by means of three methods of evaluation of harmonic components in time series: principal component analysis, spectral analysis and wavelet analysis. All the methods clearly show presence of two oscillations in the FCN frequency band, which may be a subject for further investigations.

2 Known empirical FCN models

To date, three empirical FCN models have been developed: MHB2000 (Herring, 2002), Malkin (ZM) (Malkin, 2003, 2004b), Lambert (SL) (McCarthy, 2005). Comparison of these models with results of VLBI observations shows that all three models allow one to account equally essentially for the FCN contribution. However, as can be seen from fig. 1, ZM model provides smooth and, apparently, more realistic representation of variations of the basic geophysical parameters, the FCN amplitude and phase.

It should be noted, however, that all models only approximate the observed variations in the celestial pole offset, without striking into the FCN physical properties. Further development of FCN model can be reached by consideration of a two-frequency FCN theory. Earlier, Malkin

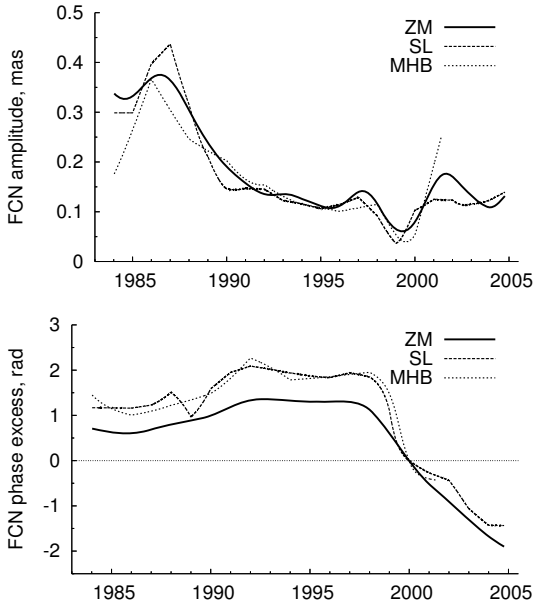

Figure 1. Variation of the FCN amplitude and phase in accordance with three FCN models.

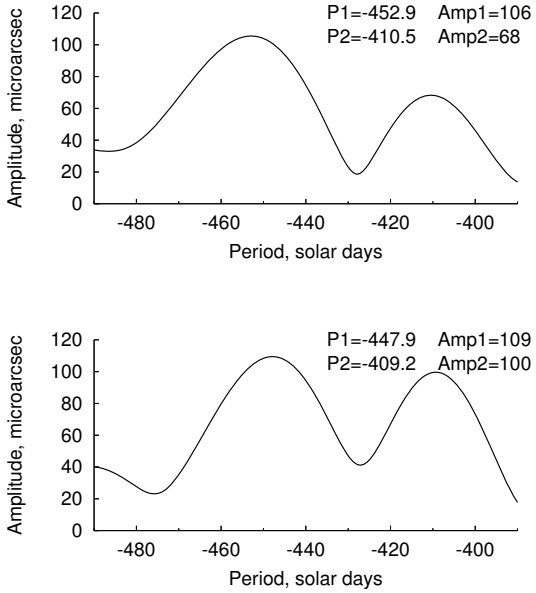

Figure 2. Spectra of the IVS (top) and ERA2005 (bottom) celestial pole offset series.

and Terentev (2003) revealed a second fluctuation with the period about 410 solar days in the celestial pole offset series. However, then this fact has not been given due value. Later, Schmidt et al. (2005) have shown the presence of two periods −435 and −410 days by means of the wavelet analysis with high frequency resolution. They supposed that observed variations in the FCN amplitude and phase are caused by beating between two oscillations with close periods. A theoretical explanation of this phenomenon has been given by Krasinsky (2006) in his numerical theory of rotation of the Earth, ERA2005, considering two-layer structure of the fluid core.

In this paper, we performed more detailed analysis of the celestial pole offset time series provided by the IVS for the period 1989–2006. Earlier observations were not analyzed in view of their relatively low accuracy, see Malkin (2003, 2004a). The smoothed differences between the observed celestial pole offset values and those predicted by the IAU200A model were used in our study.

3 Spectrum analysis

Firstly, we applied the discrete Fourier spectral analysis to the analyzed time series. We computed the Schuster periodogram for complex series $X + iY$. Usually for the spectrum analysis, the Fast Fourier Transform technique, which provides calculation of the spectrum estimations on a grid of frequencies, multiple to Nyquist frequency that does not provide the detailed frequency resolution, is used. To increase the frequency resolution, we used direct calculation of spectrum estimates, which allowed us to use any, as much as dense grid of frequencies (periods). Also, for increase of the frequency resolution, a frequency window was not applied, which does not lead to deterioration of results in this case, as initial data are smooth enough, and we study narrow enough band of a spectrum. The spectra of the differences between the IVS celestial pole offset time series and those predicted by the ERA2005 model are presented in Fig. 2, which shows reasonably good agreement of the ERA2005 theory and observations. Also in the investigated time series, the annual component is surely revealed, but with essentially smaller amplitude, than the FCN components.

4 Principal components analysis

The second method we used for investigation of the celestial pole offset series was Principal Component Analysis (PCA) also known as Singular

Spectrum Analysis. The "Caterpillar" software[1] developed at the St. Petersburg State University was used for computation. It should be mentioned that, except harmonic components, PCA allow one to isolate an actual long-term trend component not burdened by any assumption about its *a priori* model. Usually, the trend contribution in an analyzed time series as determined from the PCA is large enough (40.5% in our case), and it can distort the harmonic components under investigation.

To mitigate this effect, we performed the computations in two iterations. At the first iteration, all principal components were resolved, and at second one, the main trend components found at the first iteration were removed from the input time series. Fig. 3 shows the original time series and two principal components PC1 and PC2 found from the analysis. Three most valuable harmonic components are those with periods 452 solar days (the contribution is equal to 53.8%), 409 days (19.0%) and 366 days (6.8%). Specified period values were found from the spectral analysis made in the same way as described in the previous section.

5 Wavelet analysis

To investigate how the two FCN components vary with time, the wavelet technique was applied to the IVS celestial pole offset, two harmonic principal components found from the PCA and ERA2005 time series. The WWZ software[2] developed at the American Association of Variable Star Observers was used for analysis. The mathematical background of this method is described in (Foster, 1996). Results of the wavelet analysis are presented in Fig. 4. Two periodic components can be clearly seen at both observed and theoretical time series. For better comparison, we applied the wavelet with the same parameter σ=10 as was used in (Schmidt et al., 2005), which provides high frequency resolution. The time resolution is rather pure in such a case however. So, wavelet estimates, in fact, are averaged for several-year interval.

6 Discussion and conclusion

In this paper, we investigated the IVS celestial pole offset time series as well as theoretical

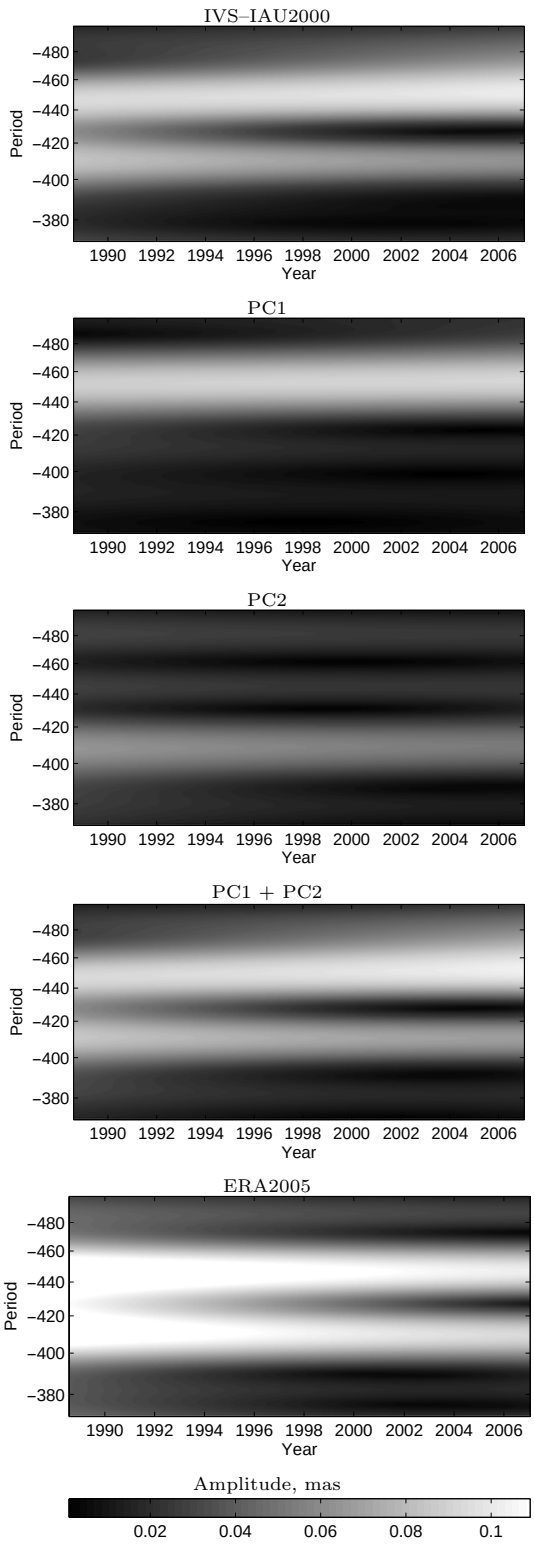

Figure 4. Results of the wavelet analysis of the input time series, its principal components and ERA2005 series.

[1] http://www.gistatgroup.com/cat/
[2] http://www.aavso.org/

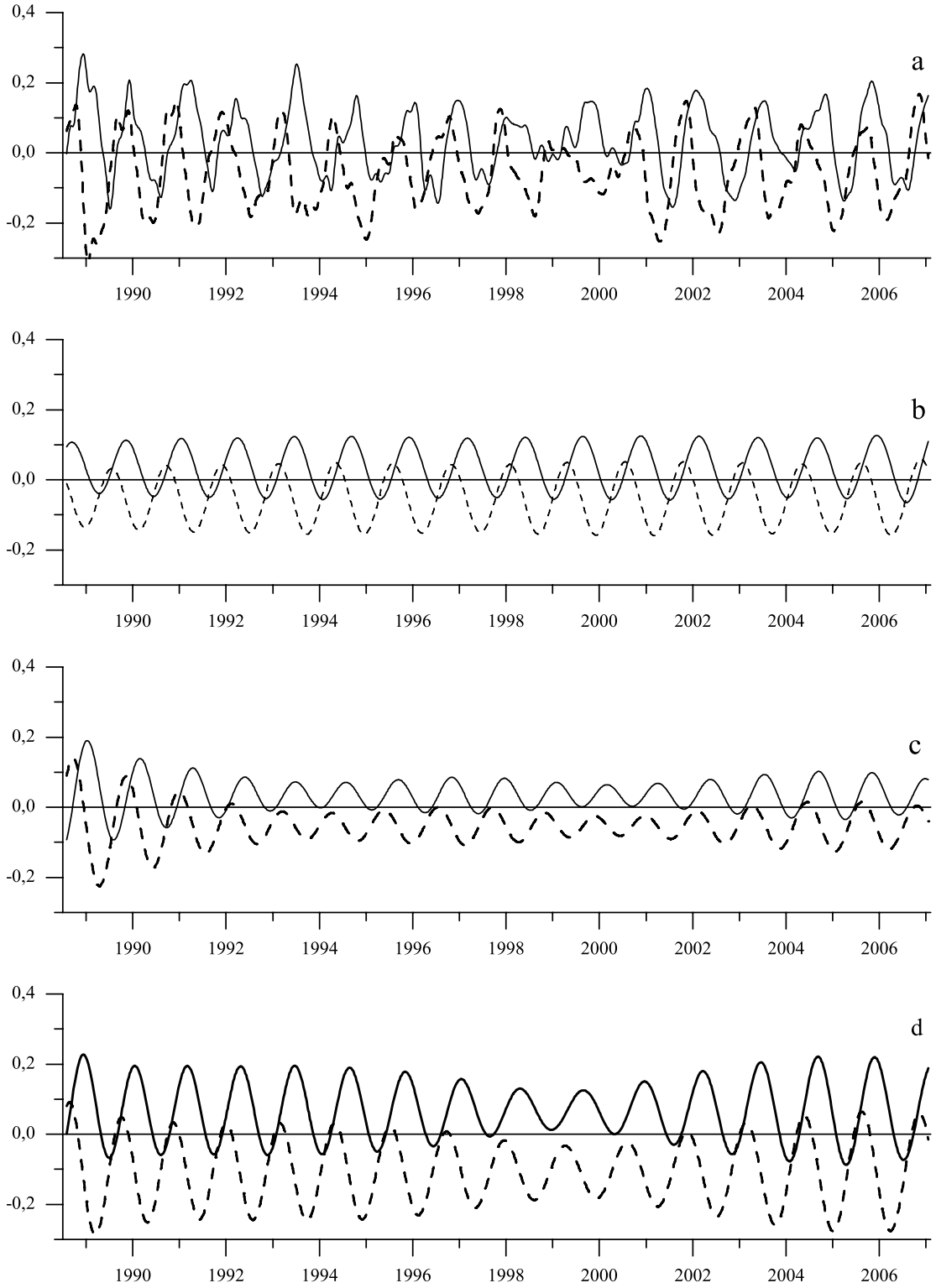

Figure 3. Input time series and main harmonic principal components obtained from the PCA (X — solid, Y — dashed): a — input, b — first principal component with period 452 days, c — second principal component with period 409 days, d — sum of two principal components.

ERA 2005 time series by means of three statistical tools, Discrete Fourier Transform, Principal Component Analysis and wavelet analysis, in the FCN frequency band. The results obtained with all the methods definitely show presence of two harmonic components with periods about −410 and −452 solar days, yet these methods are not fully independent.

This result confirms ones obtained in (Malkin, 2003; Schmidt, 2005) from VLBI data processing, and in (Krasinsky, 2006; Krasinsky and Vasilyev, 2006) in the framework of the ERA2005 theory. However, the values of the FCN component periods found here and obtained in the previous papers are substantially different. Moreover, supplement study has shown that the period of FCN components depend on the time span of data used for analysis. So, further investigations are needed before making a final conclusion. Also, it's important to compare these results with the resonance FCN period, see e.g. (Vondrák et al., 2005), in particular, considering a two-component resonance model.

Finally, there are grounds for hope that using two-component empirical FCN model, in case it is proved to be real, will allow us to predict the FCN contribution to the nutation series with better accuracy than existing models.

References

Dehant, V., K. Creager, S. Karato, and S. Zatman (eds.) (2003). The Earth's Core: Dynamics, Structure, Rotation. *AGU Geodynamics Series*, Vol. 31.

Foster, G. (1996). Wavelets for period analysis of unevenly sampled time series. *Astron. J.*, Vol. 112, pp. 1709-1729.

Herring, T.A., P.M. Mathews, and B.A. Buffet (2002). Modelling of nutation-precession: Very long baseline interferometry results. *J. Geophys. Res.*, Vol. 107, pp. 2069-2080.

Hinderer, J., J.P. Boy, P. Gegout, P. Defraigne, F. Roosbeek, and V. Dehant (2000). Are the Free Core Nutation parameters variable in time?, *Phys. Earth Planet. Int.*, Vol. 117, pp. 37-49.

Krasinsky, G.A. (2006). Numerical theory of rotation of the deformable Earth with the two-layer fluid core. Part 1: Mathematical model. *Cel. Mech. Dyn. Astr.*, Vol. 96, pp. 169-217.

Krasinsky, G.A., and M.V. Vasilyev (2006). Numerical theory of rotation of the deformable Earth with the two-layer fluid core. Part 2: Fitting to VLBI data. *Cel. Mech. Dyn. Astr.*, Vol. 96, pp. 219-237.

Malkin Z., and D. Terentev (2003). Preliminary analysis of the Free Core Nutation from VLBI data. In: *Proc. 16th Working Meeting on European VLBI for Geodesy and Astrometry*, Leipzig, Germany, 9-10 May 2003, pp. 227-235.

Malkin, Z.M. (2003). Comparison of VLBI nutation series with the IAU2000A model. In: *Proc. Journées Systèmes de Référence Spatio-temporels 2003*, St. Petersburg, Russia, 22-25 Sep 2003, Eds. A. Finkelstein, N .Capitaine, pp. 24-31.

Malkin, Z. (2004a). 5,000,000 Delays—Some Statistics. In: *IVS 2004 General Meeting Proc.*, Eds. N. R. Vandenberg, K. D. Baver, NASA/CP-2004-212255, pp. 47-51.

Malkin, Z. (2004b) A New Free Core Nutation Model with Variable Amplitude and Period. In: *IVS 2004 General Meeting Proc.*, Eds. N. R. Vandenberg, K. D. Baver, NASA/CP-2004-212255, pp. 388-392.

McCarthy D.D. (2005). The free core nutation. In: *Proc. Journées Systèmes de Référence Spatio-temporels 2004*, Paris, France, 20-22 Sep 2004, Ed. N. Capitaine, 2005, pp. 101-105.

Schlüter, W., E. Himwich, A. Nothnagel, N. Vandenberg, A. Whitney (2002). IVS and Its Important Role in the Maintenance of the Global Reference Systems. *Advances in Space Research*, Vol. 30, pp. 145-150.

Schmidt, M., V. Tesmer, and H. Schuh (2005) Wavelet analysis of VLBI nutation series with respect to FCN. *EGU 2nd General Assembly*, Vienna, Austria, 24-29 Apr 2005, Geophysical Research Abstracts, Vol. 7, 04555, SRef-ID: 1607-7962/gra/EGU05-A-04555

Vondrák, J, R. Weber, and C. Ron (2005). Free core nutation: direct observations and resonance effects. *Astron. Astrophys.*, Vol. 444, pp. 297-303.

On Comparison and Combination of Radio Source Catalogues

J.R. Sokolova
Institute of Geodesy and Geophysics, Vienna University of Technology, 1040 Gusshausstrasse. 27-29, Vienna, Austria
Central Astronomical Observatory at Pulkovo, Pulkovo Ch. 65/1, St. Petersburg 196140, Russia

Z.M. Malkin
Central Astronomical Observatory at Pulkovo, Pulkovo Ch. 65/1, St. Petersburg 196140, Russia

Abstract.
In this paper four methods of the representing RSC systematic differences have been examined by comparison of the residuals of the radio source positions between each pair of individual catalogues. Eight radio source catalogues, and the latest ICRF realization, ICRF-Ext.2, were used for comparison. After selection of the best method how representing differences representation we compute the systematic differences between each individual catalogue and the ICRF. Then, these differences were used in the procedure of construction of the combined radio source catalogue. In results, representation of the systematic differences between RSC with Legendre-Fourier functions is proven to be the most accurate method. Using this method, two combined radio source catalogues constructed. The first one provides a stochastic improvement of the ICRF, and the second one allows us to account also for possible systematic errors in the ICRF. Comparison of the celestial pole offsets obtained from processing of VLBI observations using ICRF and combined catalogue has shown improvement of the results obtained with the combined catalogue.

Keywords. VLBI, ICRF, catalogue comparison, catalogue combination

1 Introduction

In 1998, the International Celestial Reference Frame (ICRF) based on the positions of extragalactic radio sources was adopted by the International Astronomical Union (Ma et al. 1998). The first ICRF realization was based on the refined analysis of VLBI observations made at the Goddard Space Flight Center (Ma et al. 1998). In 1999 and 2004 two ICRF extensions ICRF-Ext.1 and ICRF-Ext.2 (hereafter referred to as ICRF) were issued. In those versions, the positions of 212 *defining* sources were kept the same as obtained in the first ICRF.

In the end of 2004, a joint pilot project of the IERS (International Earth Rotation and Reference Systems Services) and the IVS (International VLBI Service for Geodesy and Astrometry) was initiated (Ma 2004, Call for Participation). The goal of the project was to seek after ways to improve the existing ICRF.

In this paper we investigate a possibility of ICRF improvement by means of using advanced methods of comparison of the radio source catalogues (RSC) and RSC combination with the aim of mitigation of stochastic and systematic errors of individual RSC.

2 Input Catalogues

Input catalogues used in this study were submitted by eight IVS Analysis Centers: AUS (Geoscience Australia), BKG (Bundesamt für Kartographie und Geodäsie, Germany), DGFI (Deutsches Geodätisches Forschungsinstitut, Germany), GSFC (NASA Goddard Space Flight Center, USA), JPL (Caltech/NASA Jet Propulsion Laboratory, USA), MAO (Main Astronomical Observatory of National Academy of Sciences of Ukraine), SHAO (Shanghai Astronomical Observatory, China), USNO (U. S. Naval Observatory, USA). Brief description of the input catalogues is given in Table1.

Table 1. Input catalogues. (* - 199 stable sources from M. Feissel – Vernier stable list)

IVS Analysis Center	Software	Number of delays	Number of sources (total /references)
AUS	OCCAM	3208197	737 / 207
BKG	Calc/Solve	4031453	748 / 212
DGFI	OCCAM	3650771	686 / 199*
GSFC	Calc/Solve	4574189	954 / 212
JPL	MODEST	3575847	734 / 2
MAO	SteelBreeze	3773765	685 / 25
SHAN	Calc/Solve	4431503	813 / 212
USNO	Calc/Solve	4252684	943 / 207

For comparison of the catalogues, we used 196 ICRF *defining* sources present in all of the compared catalogues. Weighted root-mean-square (WRMS) differences of the radio source coordinates between the catalogues and the ICRF are shown in Fig. 1.

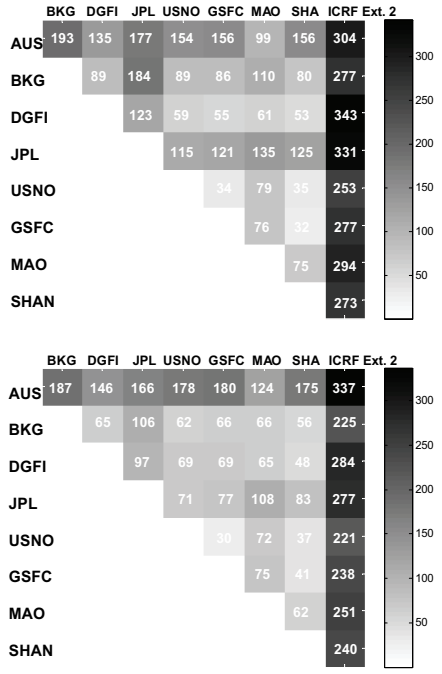

Fig. 1 WRMS differences between the input catalogues and the ICRF (μas). (Δα above, Δδ below).

One can see from Fig.1 that the WRMS differences have the least values for catalogues computed with Calc/Solve software, both for intercomparison of these catalogues and their comparison with the ICRF. The latter is most probably caused by the fact that the ICRF was constructed using the Calc/Solve software. Large WRMS differences between JPL and other catalogues may be caused by its orientation to the ICRF which has been defined by only two reference sources, unlike other catalogues, for which much longer lists of reference sources were used. Catalogue AUS shows the greatest differences with other catalogues, probably, because it is the only catalogue constructed using the Least Squares Collocation method, while other Analysis Centers used conventional Least Squares. One can see that the DGFI catalogue, also constructed using OCCAM software, but Least Squares version, does not stand out against other catalogues.

The most interesting fact is that all input catalogues demonstrate rather large differences with the ICRF, which may indicate significant systematic errors in the latter.

3 Analytical Representation of the systematic differences

In this section, we compare four methods of analytical representation of the systematic differences between RSC.

Simple Rotation. In this simplest method, the differences between catalogues are represented by three rotational angles A_1, A_2, A_3:

$$\Delta\alpha = A_1 \mathrm{tg}\delta \cos\alpha + A_2 \mathrm{tg}\delta \sin\alpha - A_3 \qquad (1)$$
$$\Delta\delta = -A_1 \sin\alpha + A_2 \cos\alpha$$

Rotation with Deformation. In this method currently used by the IERS, the systematic differences between two catalogues are approximated by

$$\Delta\alpha = A_1 \mathrm{tg}\delta \cos\alpha + A_2 \mathrm{tg}\delta \sin\alpha - A_3 + D_\alpha \delta \qquad (2)$$
$$\Delta\delta = -A_1 \sin\alpha + A_2 \cos\alpha + D_\delta \delta + B_\delta$$

Brosche's Method. In this method proposed by Brosche (1966), the differences between catalogues are represented via expansion in spherical harmonics:

$$\begin{Bmatrix} \Delta\alpha \\ \Delta\delta \end{Bmatrix} = \sum_{j=0}^{g} b_j Y_j(\alpha,\delta), \qquad (3)$$

where P_{nk}, are associated Legendre polynomials.

Legendre-Fourier Functions. Bien et al. (1978) proposed expansion in another set of orthogonal functions:

$$\begin{Bmatrix}\Delta\alpha\\ \Delta\delta\end{Bmatrix} = \sum_{j=0}^{g} b_{nkl} R_{nkl} L_n \, sin(\delta) F_{kl}(\alpha), \qquad (4)$$

where L_n are Legendre polynomials, F_{kl} are Fourier functions and R_{nkl} are normalizing functions.

All the four methods described above were applied to the differences between each of eight input catalogues and the ICRF. For this purpose, the coefficients of (1-4) were found by means of Least Squares adjustment. Then we computed the residuals between original differences and those computed by formulae (1-4). The results are presented in Table 2 and Fig. 2.

Table 2. WRMS residuals between the input catalogues and the ICRF before (Raw) and after approximation of the systematic differences (see notation of the methods in text). Unit: μas.

	AUS	BKG	DGFI	JPL	USNO	GSFC	MAO	SHA
				Δα				
Raw	304	277	343	331	253	277	294	273
R	301	271	342	308	249	274	286	271
RD	299	265	342	308	247	273	285	270
B	170	177	237	238	172	191	203	193
LF	**110**	**127**	**167**	**174**	**124**	**146**	**156**	**147**
				Δδ				
Raw	337	225	284	277	221	238	251	240
R	337	225	284	273	221	238	251	240
RD	333	224	283	273	221	237	251	239
B	180	159	178	182	152	158	169	166
LF	**111**	**115**	**116**	**131**	**109**	**111**	**136**	**117**

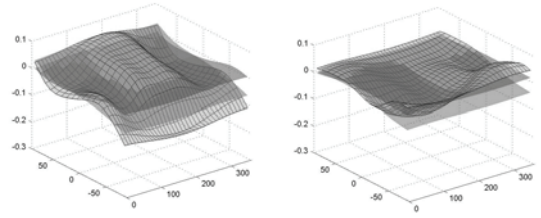

Fig. 2 Analytical representation of the differences between the input catalogues and ICRF: R (dark grey), RD (grey), LF (light grey). Original differences are shown in black lines. Horizontal axes show right ascension (*right*) and declination (*left*) in degrees. Unit: μas.

One can see that expansion in Legendre-Fourier functions provides the least residuals, it i.e. most accurate representation of the systematic differences between catalogues. Expansion in spherical functions (Brosche's method) gives worse accuracy. As to the first two methods, they seem to be not adequate to actual errors of modern RSC.

4 A Combined Catalogue in the ICRF system

At the next step, the systematic differences between the input catalogues and the ICRF found by the LF method were applied to all the input catalogues in order to transform them to the ICRF system. After that, the coordinates of all sources in transformed catalogues were averaged with weights depending on the formal errors of coordinates. In result, the combined catalogue RSC(PUL)07C01 was constructed. This catalogue contains all the 968 sources present in the input catalogues and can be considered as a stochastic improvement of the ICRF.

Fig. 3 shows the systematic differences between the combined catalogue RSC(PUL)07C01 and the ICRF. One can see that the catalogue RSC(PUL)07C01 represents the ICRF system at a level of about 10 μas.

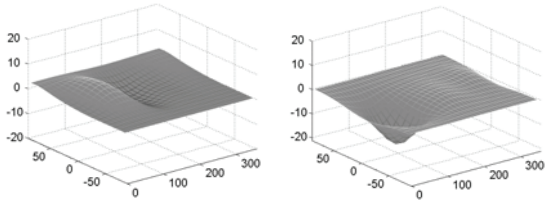

Fig. 3 Differences between RSC(PUL)07C01 and the ICRF. Horizontal axes show right ascension (*right*) and declination (*left*) in degrees. Unit: μas.

For construction of a final catalogue, systematic differences between the input catalogues and the ICRF were averaged with weights depending on the differences between input and combined catalogues. Final weights of the catalogues averaged over the sky are given in Table 3. Thus the computed average system was added to the catalogue RSC(PUL)07C01 to obtain the final combined

catalogue, RSC(PUL)07C02. It can be considered as both stochastic and systematic improvement of the ICRF. Result of comparison of RSC(PUL)07C02 and the ICRF presented in Fig. 4 leads us to the supposition that the ICRF may have significant systematic errors.

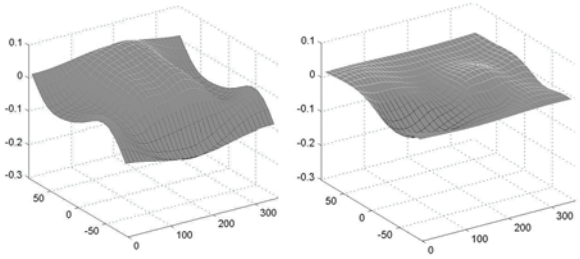

Fig. 4. Differences between RSC(PUL)07C02 and the ICRF. Horizontal axes show right ascension (*right*) and declination (*left*) in degrees. Unit: μas.

Table 3. Weights of the input catalogues applied during combination, averaged over the sky

	AUS	BKG	DGFI	JPL	USNO	GSFC	MAO	SHA
α	0.246	0.671	0.464	0.254	2.062	1.993	0.558	1.792
δ	0.205	1.220	0.586	0.446	1.927	1.921	0.541	1.459

6 Comparison with observation

To assess an actual accuracy of the combined catalogue, we have computed two celestial pole offset time series from processing of IVS R1 and R4 sessions observed in the period 2002–2006 with two RSC, ICRF-Ext.2 and RSC(PUL)07C02. Then we computed two estimates of the scatter for these time series. The first estimate is the WRMS difference between the computed celestial pole offsets and the IAU2000A model supplemented with the Free Core Nutation contribution. The second estimate was computed as weighted Allan deviation of the celestial pole (Malkin, 2007). The results of these tests presented in Table 4 show a clear improvement of the scatter of celestial pole offset estimates when using combined catalogue.

Table 4. Scatter of the celestial pole offset time series obtained with two catalogues. FCN column shows the scatter w.r.t. the FCN model, ADEV column shows Allan variance. Unit: μas.

CATALOGUE	FCN			ADEV		
	X	Y	Mean	X	Y	Mean
ICRF	103	101	102	113	109	111
RSC(PUL) 07C02	98	98	98	105	106	105

7 Conclusion

In this paper, we have examined four different methods of analytical representation of systematic differences between RSC. Expansion of the systematic differences in Legendre-Fourier functions is proven to be the most accurate method. Methods usually used for comparison of the VLBI CRF realizations based on axes rotation and rotation with deformation seem to be not suitable for the investigation of modern radio source catalogues

Two combined radio source catalogues have been constructed. The first of them, RSC(PUL)07C01 can be considered as stochastic improvement of the current realization of the ICRF. The final combined catalogue, RSC(PUL)07C02, provides both stochastic and systematic improvement of the ICRF.

Two tests based on analysis of the scatter of celestial pole offset time series computed using the ICRF and the combined catalogue have shown less scatter of the series based on the combined catalogue.

The results obtained in this paper allow us to make a conclusion that ICRF-Ext.2 may have significant systematic errors, most probably caused by fixing the coordinates of 212 *defining* sources in the successive ICRF realizations.

Acknowledgements. The authors greatly appreciate all IVS Analysis Centers that provided their radio source position catalogues used in this study.

Full version of this paper was submitted to *Astronomy and Astrophysics Journal.*

References

Bien, R., Fricke, W., Lederle, T. & Schwan, H. 1978, Veroff.. Astron. Rechen-Inst., Heidelberg, No. 29

Brosche, P. 1966, Veroff. Astron. Rechen-Inst., Heidelberg, No. 17

Ma, C., Arias, E.F., Eubanks, T.M., et al. 1998, AJ, 116, 516

Malkin, Z. 2007, Journal of Geodesy, submitted

Arias, E.F., Charlot, P., Feissel, M., Lestrade, J.-F. 1995, A&A, 303, 604

Arias, E. F. & Bouquillon, S. 2004, A&A, 422, 1105

Fey, A.L., Ma, C., Arias, E. F., et al. 2004, AJ, 127, 3587

Kur'yanova, A. N. & Yatskiv, Ya. S. 1993, Kinemat. fiz. nebesnyh tel, 9, 15

Ma, C. 2001, in Proc. 15th Working Meeting on European VLBI for Geodesy and Astrometry, ed. D. Behrend & A. Rius, 187

Schlueter,W., Himwich, E., Nothnagel, A., Vandenberg, N. & Whitney A. 2002, Advances in Space Research, 30, 145

Walter, H. G. & Sovers, O. J. 2000, Astrometry of fundamental catalogues. The evolution from optical to radio reference frames (Berlin: Springer-Verlag)

Yatskiv, Ya. S. & Kur'yanova, A. N. 1990, in: Inertial Coordinate System on the Sky, Proc. 141th IAU Symp., ed. J. H. Lieske & V. K. Abalakin, 295

Effect of various analysis options on VLBI-determined CRF

V. Tesmer
DGFI, Deutsches Geodätisches Forschungsinstitut, Alfons-Goppel-Strasse 11, 80539 München, Germany

Abstract. The next VLBI-determined realisation of the International Celestial Reference System (ICRS) is planned to be undertaken within the next few years. It will provide an important link between Earth and space oriented science via other celestial reference frames of very high precision, to be created in the next decade (e.g. satellite-based GAIA). This connection will be realised via the very stable VLBI observing network, referenced to the International Terrestrial Reference Frame (ITRF).

This paper analyses the effect of various analysis options on VLBI-determined Celestial Reference Frames (CRF), such as the choice of the tropospheric modelling, the choice of the data set (old sessions and VLBI Calibrator Survey sessions, VCS), the handling of sources that can presumably not be assumed to have time-invariant positions and the handling of the station network. The focus of this paper is to analyze their effect with best possible comparability, using exactly the same set of sessions (2847 sessions from 1984 till today) and analysis setup for the different solutions.

Keywords. International Celestial Reference Frame (ICRF), Very Long Baseline Interferometry (VLBI), geodesy, astrometry, radio source positions

1 Introduction

In January 1998, the VLBI-determined ICRF (608 radio positions of extragalactic objects, MA et al., 1998) replaced the optical FK5 as the celestial reference frame (the solution actually was computed 1995). Since then, it was extended twice, 1999 by 59 (ICRF-Ext1: IERS, 1999) and 2002 by 50 sources (ICRF-Ext2: FEY et al., 2004). To have homogeneity throughout the extensions, the same VLBI analysis setup was used as for the first solution. With continued applicable VLBI observations and improvements in analysis, a better realization of the ICRF is now possible and an even better realization is feasible in the foreseeable future. So the IAU, the IERS, as well as the IVS aim at a new realization of the ICRS in the next years. It is planned to be completed concurrent with the 2009 IAU General Assembly.

In this paper, several of the scientific points of the IVS/IERS Working Group on the second realization of the ICRF (www.iers.org/MainDisp.csl?pid=198-1100160) are discussed:

- the effect of tropospheric modeling on CRF (mapping function, gradient model, elevation dependent weighting),
- the effect of the choice of observation data (sessions before 1990 and 21 astrometric sessions),
- the effect of different parameterization of sources that may not be assumed to have time-invariant positions,
- the effect of different parameterization of the station network (estimate the station positions per session, as positions and velocities over ~20 years, or fix them to a priori values).

Many of these options had been investigated and discussed earlier by other scientists - references are given in the respective chapters. The purpose of this work is to analyse their influence on the estimated CRF with best possible comparability.

2 Solution setup and characteristics

2.1 Solution setup

13 CRF solutions were computed at DGFI with the least-squares method of the VLBI software OCCAM 6.1 (TITOV et al., 2004), using 2847 sessions from 1984 until 2006, with 52 telescopes observing 2769 sources (including 21 sessions of VLBI calibrator surveys VCS1-5, BEASLEY et al., 2002; FOMALONT et al., 2003; PETROV et al., 2005; PETROV et al., 2006; KOVALEV et al., 2007). Normal equations were set up per session with parameters of the CRF, Terrestrial Reference Frame (TRF) and the Earth orientation Parameters (EOP) in a common equation system. These session-wise normal equations were accumulated to one equation system with

DOGS-CS (GERSTL et al., 2001) and solved with NNT (no-net-translation) and NNR (no-net-rotation) conditions for 25 stations w.r.t. ITRF2000 (ALTAMIMI et al., 2000) and NNR conditions for the 199 'stable' sources (FEISSEL, 2003) w.r.t. ICRF-Ext1. Such setup yields 100% consistent and undeformed TRF, CRF and EOP (for a brief description of the procedure, see TESMER et al., 2004).

The compared variables are position differences (arc lengths), formal error differences (often the length of the vector spanned by the 2 components), and the differences of the absolute values of the correlations between the estimated declinations (DE) and right ascensions (RA). The figures illustrating position differences between two solutions contain moving medians, computed each 0.5° for values in a +-12.5° band, plotted as bold red line.

2.2 Solution characteristics

The spatial distribution of the 2769 sources in the solution is illustrated in figure 2.1.

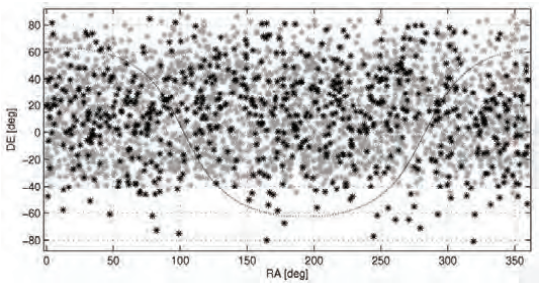

Fig. 2.1 Positions of the 2769 sources in the solution: 2070 sources only observed in one of the VCS sessions (grey) and 699 sources also used in standard VLBI sessions (black).

This big number of sources is dominated by the VCS data sets, only 837 sources were observed in more than 1 session and only 556 in more than 3. The maximum number of sessions, in which a source was observed, was 2711 (0552+398). 1712 sources were observed more than 50 times and 768 sources more than 100 times, the maximum number of observations per source was 235552 (0552+398).

In each single session, the observations of a source were only used, if the source was observed more than 3 times in that session. This restriction was applied to be able to compute session-wise source positions in other solution runs (2 parameters need 3 observations for bare redundancy).

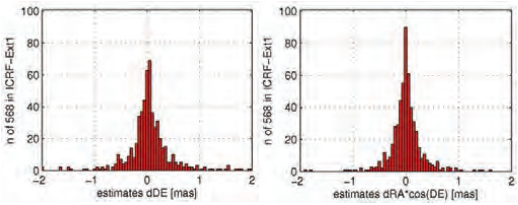

Fig. 2.2 Differences between the declination (left) and right ascension arc length (right) estimates of the solution and the ICRF-Ext1, plotted w.r.t. declination (for the 568 sources in the solution and the ICRF-Ext1).

Figure 2.2 compares the positions of the 568 sources, which are in the solution and in ICRF-Ext1, overall WRMS of the differences is 0.130 mas.

231 of the 2769 sources have formal errors that are smaller than 0.050 mas, for 576 they are between 0.050 and 0.200 mas and for 1496 between 0.200 and 0.500 mas. Figures 2.3, 2.4 and 2.5 illustrate that if sources have more than 100 observations or are observed in more than 3 sessions, they always have formal errors smaller than 0.500 mas and absolute values of the correlations between the two coordinate components smaller than 0.5.

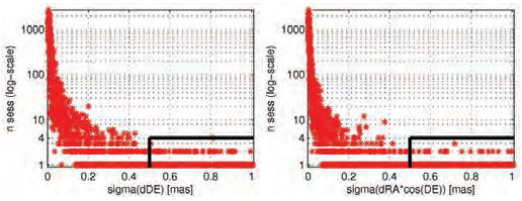

Fig. 2.3 Formal errors of the declination (left) and right ascension arc length (right) estimates of the solution (for all 2769 sources), plotted w.r.t. the number of sessions on a logarithmic scale; All sources with more than 3 sessions have formal errors smaller than 0.5 mas.

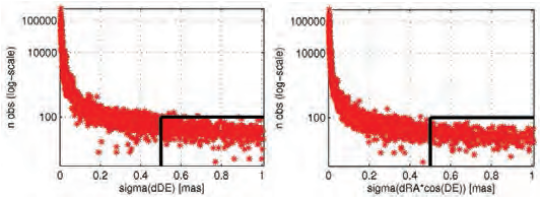

Fig. 2.4 Formal errors of the declination (left) and right ascension arc length (right) estimates of the solution (for all 2769 sources), plotted w.r.t. the number of observations on a logarithmic scale; Almost all sources with more than 100 observations have formal errors smaller than 0.5 mas.

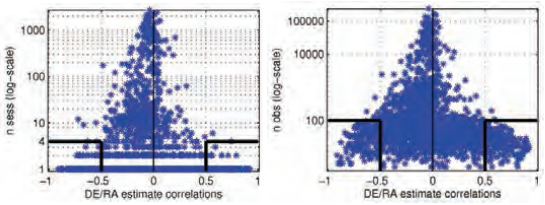

Fig. 2.5 Correlation coefficients between the declination (DE) and the right ascension (RA) estimates of the solution (for all 2769 sources). The left diagram displays the coefficients w.r.t. the number of sessions in which the sources were observed, the right w.r.t. the number of observations (both with logarithmic scale). Almost all sources with more than 100 observations or more than 3 sessions have DE/RA correlations with absolute values smaller than 0.5.

3 Effect of tropospheric modelling on CRF

This chapter analyses the effect of tropospheric analysis options, except for different types of a priori zenith delay, for which TESMER et al. (2006a) and HEINKELMANN et al. (2007) indicate that this does not significantly influence CRF solutions.

3.1 Mapping function

The differences between CRF solutions using the NMF (NIELL, 1996) and the VMF1 (BOEHM et al. 2006) are not big (see figure 3.1), with 0.007 mas WRMS of the differences. The effect of different tropospheric mapping functions on estimated CRF is discussed in more detail in TESMER et al. 2006b.

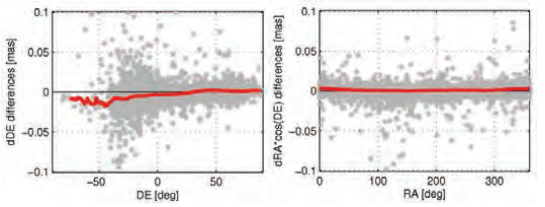

Fig. 3.1 Differences between 2769 declinations (left) and right ascension arc lengths (right) of two CRF solutions: using the VMF1 – using the NMF.

3.2 Gradient model

3.2.1 Gradients estimated or not

Estimating or not estimating tropospheric gradients has got a very significant influence on source positions, as shown by (MACMILLAN and MA, 1997). The WRMS of the differences is 0.251 mas, which is almost completely caused by the distinct ~0.500 mas "bow" in the DE component (figure 3.2). The formal errors of the estimates are smaller up to 0.200 mas if gradients are estimated (figure 3.3).

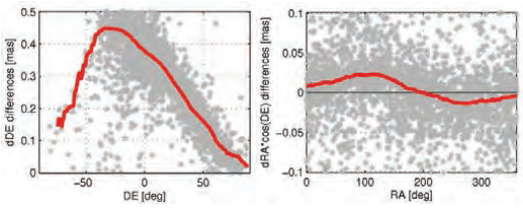

Fig. 3.2 Differences between 2769 declinations (left, plot has unusual scale) and right ascension arc lengths (right) of two CRF solutions: with no gradients estimated – with gradients estimated slightly constrained. The declination estimates are very much and systematically affected.

Fig. 3.3 Differences between the lengths of the vectors for the formal errors of two CRF solutions: with no gradients estimated – with gradients estimated.

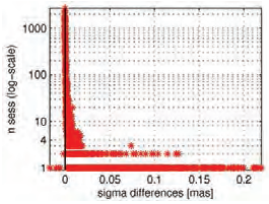

3.2.2 Constrained or unconstrained gradients

Because the gradient estimates are usually slightly stabilized by constraints, the estimated values depend on the a priori value and the amount (formal error) of the constraint. The results in figure 3.4 were derived comparing a fully unconstrained solution with one with an a priori value 0 with 0.2 mm precision (WRMS of the differences is 0.055 mas).

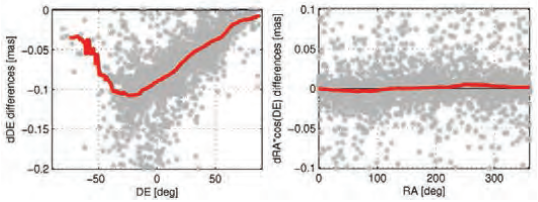

Fig. 3.4 Differences between 2769 declinations (left) and right ascension arc lengths (right) of two CRF solutions: with gradients estimated fully unconstrained – with gradients estimated slightly constrained. The declination estimates are affected with the same systematic "gradient" pattern as seen in figure 3.5, but considerably smaller.

3.2.3 A priori values for gradients

The effect of the a priori values (constrained with a certain precision) is illustrated in figure 3.5. Here, constant a priori gradient values (1990-95 mean

from the DAO weather model) were used instead of 0 (WRMS of the differences is 0.053 mas).

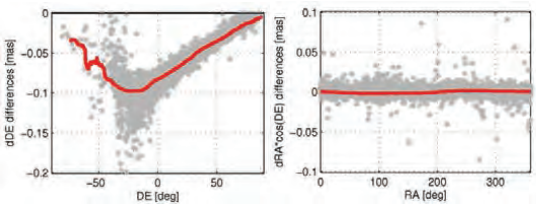

Fig. 3.5 Differences between 2769 declinations (left) and right ascension arc lengths (right) of two CRF solutions: using constant a priori gradient values which are 1990-1995 mean values from DAO weather model) – using 0 a priori gradient values. Although less scattered, the estimates show the same "gradient" pattern as in figure 3.4.

3.3 Elevation dependent weighting

Elevation dependent weighting (as part of a refined stochastic model, TESMER and KUTTERER, 2004) influences source positions (figure 3.6) and their stochastic properties (figure 3.7) with a WRMS of the differences of 0.036 mas.

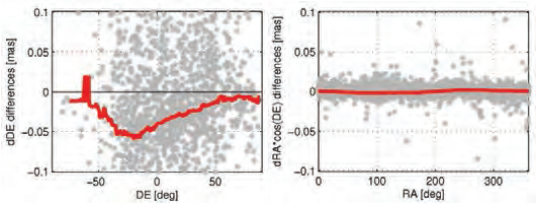

Fig. 3.6 Differences between 2769 declinations (left) and right ascension arc lengths (right) of two CRF solutions: using elevation dependent weighting – without using elevation dependent weighting. They also show the "gradient" pattern, but less strong in chapter 3.2, presumably because gradients are very sensitive for low elevations.

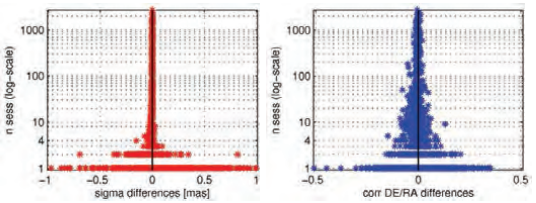

Fig. 3.7 Left: Differences between the lengths of the vectors for the formal errors of two CRF solutions; Right: Differences between the absolute values of the DE/RA correlation coefficients of two CRF solutions. Both display "using elevation dependent weighting – without using elevation dependent weighting" solution differences.

4 Effect of choice of observation data

4.1 VCS 1-5 sessions

The 21 sessions of the VLBI Calibrator Surveys 1 to 5 used here are a very precious data set, as they contribute 2070 sources to this solution. They were observed only using the station network of the VLBA (Very Long Baseline Array, www.vlba.nrao.edu). But, they were scheduled in a very special way, as each of the 21 sessions focussed on observing sources in one small region of the inertial frame. Only occasionally, sources in other directions are observed, which is necessary 1) to link the sources to the CRF with high precision, and 2) to be able to soberly estimate all other parameters of VLBI equation systems (clocks, troposphere etc.).

Nevertheless, using or not using these 21 sessions only marginally changes the other 699 sources (figure 4.1), which is reflected by the small WRMS of the differences of 0.017 mas. Also the stochastic properties of the 699 sources do not differ much, except for a small decrease of the formal errors of the sources observed in less than 4 sessions (figure 4.2).

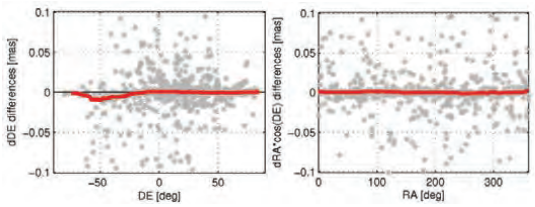

Fig. 4.1 Differences between 699 declinations (left) and right ascension arc lengths (right) of two CRF solutions: without using the 21 sessions of the VCS 1-5 – with using the VCS sessions.

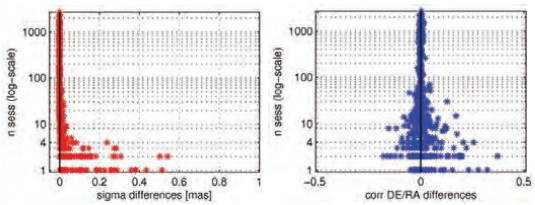

Fig. 4.2 Left: Differences between the lengths of the vectors for the formal errors of two CRF solutions; Right: Differences between the absolute values of the DE/RA correlation coefficients of two CRF solutions. Both display "without using the 21 sessions of the VCS 1-5 – with using the VCS sessions" solution differences.

4.2 Sessions before 1990

Another option to use or not use observation data is related to the old sessions. They are different than today's sessions, not only w.r.t. the number of observations, density and extension of the station networks, but also concerning the sources observed. In the early days, generally much less (~15) sources were observed than today (~60), some of them are today known to have apparent non-linear motion.

The WRMS of the differences between solutions using or not using e.g. the 534 sessions before 1990 is 0.028 mas. As illustrated in figures 4.3 and 4.4, most of the bigger differences are due to two early VCS sessions. It is assumed that in these sessions, some of the sources dominantly observed in the early days were used to link to the CRF. The differences do not exist for the 837 sources observed in more than 1 session (figure 4.4).

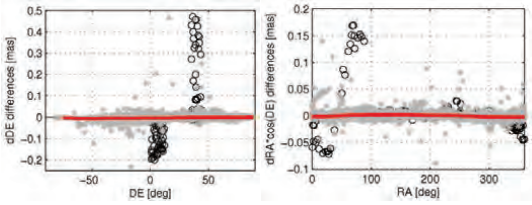

Fig. 4.3 Differences between 2769 declinations (left, plot has unusual scale) and right ascension arc lengths (right, plot has unusual scale) of two CRF solutions: without using the 534 sessions before 1990 – with using all 2847 sessions. Black circles mark 286 sources only observed in 2 early VCS sessions, 95JUL15XV and 96JUN07XV - they seem to have been observed with a suboptimal scheduling for geodetic data analysis.

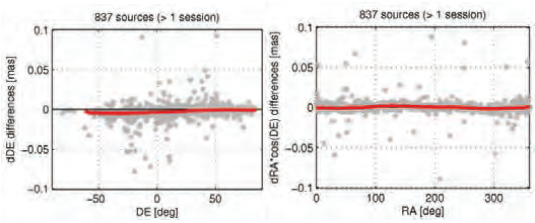

Fig. 4.4 Differences between 837 (for the 837 sources observed in more than one session) declinations (left) and right ascension arc lengths (right) of two CRF solutions: without using the 534 sessions of the before 1990 – with using them.

5 Effect handling of 'unstable' sources

5.1 'Unstable' according to Feissel, 2003

Estimating the 156 unstable sources (as declared by FEISSEL et al., 2003, via analysis of time series) as session-wise parameters (locally) or as one common position for the whole period (globally), changes some positions up to 0.5 mas (figure 5). Many of the sources with the biggest differences were only observed in one of the 21 VCS sessions. Nevertheless, as the sources with big differences are then estimated to have a comparably big formal error, the WRMS of the differences is 0.022 mas only. As shown in figure 5.2, the big differences are removed accounting only for the 407 sources observed in more than 3 sessions.

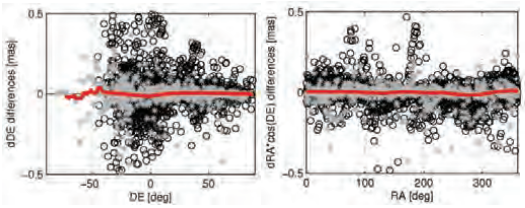

Fig. 5.1 Differences between 2613 declinations (left, plot has unusual scale) and right ascension arc lengths (right, plot has unusual scale) of two CRF solutions: estimating the 156 'unstable' sources local – estimating them global. The black circles mark 1872 sources that were only observed in one of the 21 VCS sessions. These sessions seem to have been observed with a scheduling, which was presumably especially sensitive to estimating a set of sources locally. But, if one accounts for the median formal errors of these 1872 sources (DE: 0.533, mas RE*cos(DE): 0.323 mas), these differences are only barely significant. The median formal errors for the 741 other sources are much bigger (DE: 0.136, mas RE*cos(DE): 0.084 mas). This is also illustrated by the small WRMS of the differences of 0.022 mas (see text).

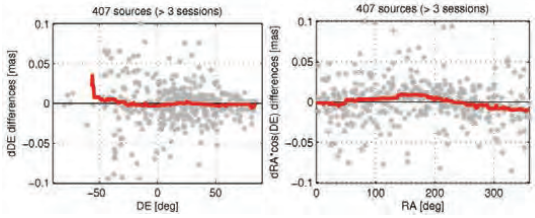

Fig. 5.2 Differences between 407 (for the 407 sources observed in more than three sessions) declinations (left) and right ascension arc lengths (right) of two CRF solutions: estimating the 156 'unstable' sources local – estimating them global.

5.2 Structure index 3&4 according to Charlot

The position differences due to estimating the 158 sources with structure indices 3 and 4 (as specified by CHARLOT, private communication, via analysis of source maps) as local or global parameters, reach up to 0.8 mas (figure 5.3). As for the 'stable' sources in 5.1, many of the sources with big differences were only observed in one of the 21 VCS sessions. Alike in 5.1, the sources with big differences are then estimated with big formal errors, so the WRMS of the differences is small (0.028 mas). Figure 5.2 shows that this effect does not exist for the 407 sources observed in more than 3 sessions.

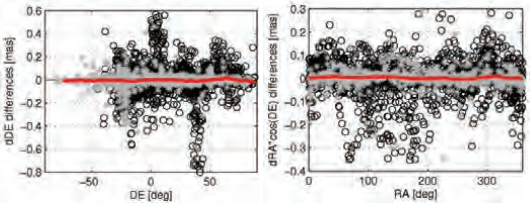

Fig. 5.3 Differences between 2611 declinations (left, plot has unusual scale) and right ascension arc lengths (right, plot has unusual scale) of two CRF solutions: estimating the 158 'structure index 3&4' sources local – estimating them global. The black circles mark 1872 sources that were only observed in one of the 21 VCS sessions, they seem to have been observed with a scheduling, especially sensitive to estimating a significant set of sources locally – But, if one accounts for the median formal errors of these 1872 sources (DE: 0.538, mas RE*cos(DE): 0.322 mas), these differences are only barely significant, as they are much bigger than the ones of the 741 other sources (DE: 0.133, mas RE*cos(DE): 0.080 mas). This is also illustrated by the small WRMS of the differences of 0.028 mas (see text).

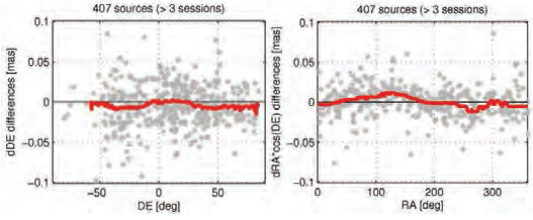

Fig. 5.4 Differences between 407 (for the 407 sources observed in more than one session) declinations (left) and right ascension arc lengths (right) of two CRF solutions: estimating the 158 'structure index 3&4' sources local – estimating them global.

6 Effect of handling of station position parameters on CRF

6.1 'Local' vs 'global' stations

The ICRF solutions were computed with all station positions estimated as local parameters, while today, one would probably use a global approach. Figure 6.1 illustrates the differences between two of such solutions, which do not show significant systematics (WRMS of the differences is 0.013 mas).

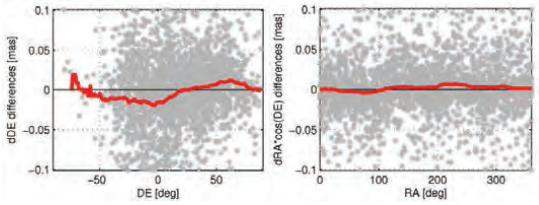

Fig. 6.1 Differences between 2769 declinations (left) and right ascension arc lengths (right) of two CRF solutions: estimating all stations locally – estimating them globally.

Fig. 6.2 Differences between the lengths of the vectors for the formal errors of two CRF solutions: estimating all stations locally – estimating them globally.

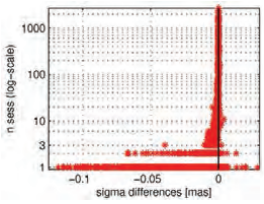

6.2 'Estimated' vs 'not estimated' stations

In this subchapter, the source positions from a solution with stations estimated globally are compared to such of a solution with stations fixed to values, estimated globally in a preceding solution run (thus any correlations with station parameters are suppressed). As illustrated in figure 6.3, this does almost not affect the estimated source positions at all (WRMS of the differences is 0.000 mas).

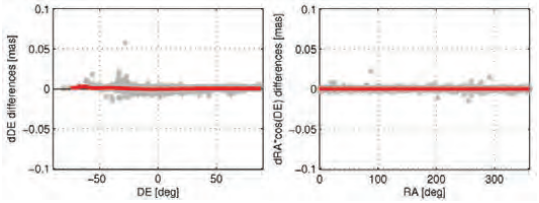

Fig. 6.3 Differences between 2769 declinations (left) and right ascension arc lengths (right) of two CRF solutions: fixing stations to 'own' TRF solution values – estimating all stations globally.

6.3 'Fix ITRF2005_preliminary' vs 'estimated' stations

Comparing source positions, which were estimated simultaneously with a TRF, to sources positions, which were derived with station positions fixed, e.g. to values of the ITRF2005, is an interesting test to assess the consistency of the specific TRF with the modelling in the own software. As the ITRF2005 is used here, it might also be considered as a measure for the consistency of the ITRF2005 (whose station positions are a combination of several techniques) with a TRF as realized by VLBI. Here, we used preliminary ITRF2005 solutions of the IGN (ALTAMIMI, private communication) and DGFI (ANGERMANN, private communication), which have no big differences w.r.t. the VLBI part of the final ITRF2005 solution (http://itrf.ensg.ign.fr/ITRF_solutions/2005/ITRF2005.php).

Figure 6.4 illustrates the differences between a solution fixing stations to the preliminary ITRF2005 solution of IGN and a solution estimating all stations globally. The differences show the same "gradient" pattern as found before in chapter 3.2 (WRMS of the differences is 0.059 mas). This suggests that one of the contributions to ITRF2005 used a different gradient model than the solution used as reference here. The same analysis done with the preliminary ITRF2005 solution of DGFI yields very familiar results, which suggests, that this effect is inherent to the ITRF2005 input data.

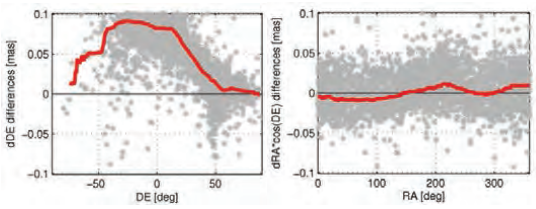

Fig. 6.4 Differences between 2769 declinations (left) and right ascension arc lengths (right) of two CRF solutions: fixing stations to a preliminary ITRF2005 solution – estimating all stations globally.

Fig. 6.5 Differences between the lengths of the vectors for the formal errors of two CRF solutions: fixing stations to a preliminary ITRF2005 solution – estimating them globally.

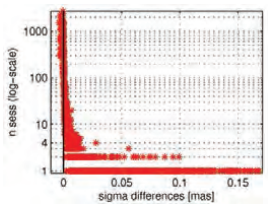

7 Summary and conclusions

The sensitivity of CRF estimates regarding analysis options can be summarized as follows:

- Most important is the gradient model in use, as different constraints and a priori values cause systematic effects between 0.100 and 0.500 mas. Elevation dependent weighting also causes systematic effects with the "gradient" pattern and a magnitude of 0.100 mas.
- The effect of using the VCS sessions is negligible, whereas the data before 1990 only affects some source positions related to two older VCS sessions significantly (up to 0.500 mas).
- Estimating the sources, assumed to have apparent non linear motion, as "local" parameters per session (rather than as "global" parameters), some estimated positions of sources observed in less than 4 sessions change by up to 0.500 to 0.800 mas. Especially sources of the VCS sessions are affected, although the differences are not significant regarding their formal errors.
- Globally or locally estimated station positions affect source positions by up to 0.100 mas, without systematic pattern. If the TRF is fixed to some a priori values while estimating a CRF, these values should be chosen carefully – in this analysis, fixing preliminary solutions of the ITRF2005 caused systematic differences comparable to the "gradient" pattern, with magnitude 0.100 mas, compared to a CRF with TRF estimated.

These results of the analyses yield the following conclusions/recommendations, which could be assumed to be discussed in the ICRF2 working groups:

- All contributing solutions should be homogenized concerning their gradient model, as differences would be systematic with magnitude up to 0.500 mas ("gradient" pattern).
- The ICRF2 documentation should describe the used gradient model in detail, and point out the necessity to also use it, if the results should be precise in the range of 0.100 to 0.500 mas.
- It should seriously be considered to use the observation data of the VCS sessions, as they do not affect the non-VCS position estimates, and the number of sources in ICRF2 could be expanded by a factor of at least 4. The sources

only observed in VCS sessions (which are generally only observed in 1 session) might be declared to be, e.g. “non-defining” sources.

- In order to keep the results as stable as possible (w.r.t. interconnection of all the contributing sessions’ CRF networks), it would be helpful if the number of sources not estimated as global parameters would be kept as few as justifiable.
- Formal position errors smaller than 0.500 mas and DE/RA correlations smaller than 0.5 in absolute value are achieved if sources are observed at least 100 times or in 4 sessions – this should be considered if further sessions are scheduled for the ICRF2 effort or at least for future VLBI realizations of the ICRS (e.g. for precise interconnection with optical frames).

Acknowledgement

This work made extensive use of the IVS VLBI observation data base – the author would like to pay great tribute to all the IVS components for their contributions and friendly, productive cooperation.

References

Altamimi Z, Sillard P, Boucher C: ITRF2000: A new Release of the International Terrestrial Reference Frame for Earth Science Applications. Journal of Geophysical Research 107 (B10) 2214 doi: 10.1029/2001JN000561, 2000

Beasley, A.J., D. Gordon, A.B. Peck, L. Petrov, D.S. MacMillan, E.B. Fomalont, C. Ma, "The VLBA Calibrator Survey - VCS1", Asrophys. J., Supp., vol. 141, p.13-21, 2002

Boehm J, Werl B, Schuh H: Troposphere mapping functions for GPS and very long baseline interferometry from European Centre for Medium-Range Weather Forecasts operational analysis data. Journal of Geophysical Research 111 (B2) B02406 doi: 10.1029/2005JB003629, 2006

Feissel-Vernier M: Selecting Stable Extragalactic Compact Radio Sources from the Permanent Astrogeodetic VLBI Program. Astronomy & Astrophysics, 403: 105-110, 2003

Fey, A.L., Ma, C., Arias, E.F., Charlot, P., Feissel-Vernier, M., Gontier, A. M., Jacobs, C.S., Li, J., & MacMillan, D., *Astronomical Journal*, 127, 3587, 2004

Fomalont, E., L. Petrov, D.S. McMillan, D. Gordon, C. Ma, "The second VLBA Calibrator Survey - VCS2", Astronomical Journal, 126 (N5), p. 2562-2566, 2003

Gerstl M., Kelm R., Müller H., Ehrnsperger: DOGSCS Kombination und Lösung großer Gleichungssysteme, DGFI Interner Bericht Nr. MG/01/1995/DGFI, 2001

Heinkelmann, R., J. Boehm, H. Schuh, V. Tesmer: The effect of meteorological input data on the VLBI reference frames. In: Bosch, W., H. Drewes (Eds.): Geodetic Reference Frames IAG Symposium Proceedings. Springer, submitted, 2007

IERS: First extension of the ICRF, ICRF-Ext.1. In: Gambis D (Ed.) 1998 IERS Annual report. Chapter VI, Observatoire de Paris: 87-114, 1999

Kovalev, Y., L. Petrov, E. Fomalont, D. Gordon, "The fifth VLBA Calibrator Survey - VCS5", *Astronomical Journal*, in press, 2007

Ma, C., F. Arias, M. Eubanks, L. Fey, A.-M. Gontier, C. Jacobs, O.J. Sovers, B. Archinal, P. Charlot: The International Celestial Reference Frame as Realized by Very Long Baseline Interferometry. The Astronomical J. 166, 516-546, 1998

MacMillan D, Ma C: Atmospheric Gradients and the VLBI Terrestrial and Celestial References Frames. Geophysical Research Letters, 24 (4): 453-456, 1997

Niell A (1996) Global Mapping Functions for the Atmosphere Delay at Radio Wavelength. Journal of Geophysical Research, 101(B2): 3227-3246

Petrov, L., Y. Kovalev, E. Fomalont, D. Gordon, "The third VLBA Calibrator Survey - VCS3", Astronomical Journal, vol. 129, p. 1163--1170, 2005

Petrov, L., Y. Kovalev, E. Fomalont, D. Gordon, "The fourth VLBA Calibrator Survey - VCS4", Astronomical Journal, vol. 131, 1872-1879, 2006

Tesmer V, Kutterer H, Drewes H: Simultaneous estimation of a TRF, the EOP and a CRF. In: Vandenberg N, Baver K (Eds.) IVS 2004 General Meeting Proceedings. NASA/CP-2004-212255: 311-314, 2004

Tesmer, V., H. Kutterer: An advanced stochastic model for VLBI observations and its application to VLBI data analysis. In: Vandenberg, N., K. Baver (Eds.): IVS 2004 General Meeting Proceedings. NASA/CP-2004-212255, 296-300, 2004

Tesmer, V., J. Boehm, R. Heinkelmann, H. Schuh: Impact of Analysis Options on the TRF, CRF and Position Time Series Estimated from VLBI. In: Behrend, D., K. Baver (Eds.): IVS 2006 General Meeting Proceedings. NASA/CP-2006-214140, 243-251, 2006a

Tesmer, V., J. Boehm, R. Heinkelmann, H. Schuh: Effect of different tropospheric mapping functions on the TRF, CRF and position time series estimated from VLBI. In: Schuh, H., A. Nothnagel, C. Ma (Eds.): VLBI special issue. Journal of Geodesy, DOI 10.1007/s00190-006-0126-9, 2006b

Titov O, Tesmer V, Boehm J: OCCAM v.6.0 software for VLBI data analysis. In: Vandenberg N, Baver K (Eds.) IVS 2004 General Meeting Proceedings. NASA/CP-2004-212255: 267-271, 2004

Linking Deep Astrometric Standards to the ICRF

S. Frey
Institute of Geodesy, Cartography and Remote Sensing (FÖMI), Satellite Geodetic Observatory
P.O. Box 585, H-1592 Budapest, Hungary
Hungarian Academy of Sciences, Research Group for Physical Geodesy and Geodynamics
P.O. Box 91, H-1521 Budapest, Hungary

I. Platais
Department of Physics and Astronomy, The Johns Hopkins University, Baltimore, MD 21218, USA

A. L. Fey
US Naval Observatory, 3450 Massachusetts Avenue, NW, Washington, DC 20392, USA

Abstract. The next-generation large aperture and large field-of-view optical telescopes will address fundamental questions of astrophysics and cosmology such as the nature of dark matter and dark energy. For a variety of applications, the CCD mosaic detectors in the focal plane arrays require astrometric calibration at the milli-arcsecond (mas) level. The existing optical celestial reference frames are insufficient to support such calibrations. To address this problem, deep optical astrometric fields are being established near the Galactic plane. In order to achieve a 5–10-mas or better positional accuracy for the Deep Astrometric Standards (DAS), and to obtain absolute stellar proper motions for the study of Galactic structure, it is crucial to link these fields to the International Celestial Reference Frame (ICRF). To this end, we selected 15 candidate compact extragalactic radio sources in the Gemini-Orion-Taurus (GOT) field. These sources were observed with the European VLBI Network (EVN) at 5 GHz in phase-reference mode. The bright compact calibrator source J0603+2159 and seven other sources were detected and imaged at the angular resolution of ~1.5–8 mas. Relative astrometric positions were derived for these sources at a milli-arcsecond accuracy level. The detection of the optical counterparts of these extragalactic radio sources will allow us to establish a direct link to the ICRF locally in the GOT field.

Keywords. VLBI, phase-referencing, differential astrometry, quasars, reference frames

1 Introduction

A new generation of imaging optical telescopes is designed to tackle fundamental questions of astrophysics and cosmology such as: How can we "see" the unseen part of the Universe in the form of dark matter? What is the nature of dark energy accelerating the expansion of Universe? How did the Galaxy form and is that process still on-going? One approach to these challenging questions is to use an observation system with extremely high étendue (the product of aperture, A, and field of view, Ω) reaching 250 m^2 deg^2. The premier near-term facility with such étendue is the 8.4-m Large Synoptic Survey Telescope (LSST; e.g. Tyson 2002), at the heart of which is a huge 3 Gigapixel CCD mosaic camera closely packed with several hundred chips enabling a large 10 deg^2 field of view. To probe dark matter and dark energy via gravitational weak lensing of distant galaxies, this camera must be calibrated astrometrically at the 5-mas level. Current optical celestial reference frames are clearly insufficient to support such calibrations.

The aim of the Deep Astrometric Standards (DAS) initiative is to establish four 10-deg^2-large deep astrometric fields near the Galactic plane for the calibration of LSST or any other large aperture facility (Platais et al. 2006). Currently available instruments capable of creating the DAS at optical wavelengths down to V=25^m are the US National Optical Astronomy Observatory (NOAO) 4-m telescopes, and the 3.6-m Canada-France-Hawaii Telescope (CFHT) which have the optimal aperture and well-calibrated CCD mosaic imagers (Platais et al. 2002).

A detailed description of the DAS and the science enabled by these observations is given by Platais et al. (2006). While the DAS concept primarily serves the needs of astrometric calibrations of large telescopes, the fields themselves can provide direct benefits to astronomy. Among others, potential applications of DAS include: constraining Galactic structure models, radial distributions of the thin and

thick disks; studying stellar populations of the Milky Way; providing the deepest stellar absolute proper motion data over large areas of the sky; and discovering new Kuiper Belt Objects in the outer Solar System.

The criteria for selecting the the first four DAS fields (Table 1) were the following: (1) diameter of 3.5º; (2) located near the celestial equator to ensure access from both hemispheres; (3) at least two directions separated by ~12^h in right ascension to ensure year-long access; (4) two pairs of fields similar in right ascension and located symmetrically to within ±20º on both sides of the equator to provide two fields at a time at a small and a higher zenith distance; (5) dominated by stars and not galaxies, i.e. near the Galactic equator; (6) free of bright (V<7^m) stars, dark clouds and emission nebulae; (7) uniform and not too dense distribution of stars across the field.

Table 1. The DAS field names are derived from the respective constellation names. The J2000 equatorial coordinates of the field centers are given.

Field name	Right ascension	Declination
Gem-Ori-Tau (GOT)	$6^h\ 00^m$	+21º 45′
Hya	$8^h\ 49^m$	−15º 25′
Oph	$17^h\ 44^m$	+11º 15′
Sgr	$19^h\ 20^m$	−20º 40′

All four DAS fields are planned to be observed multiple times in the next couple of years and then re-observed again around the year 2011 in order to obtain proper motions.

The purely optical realization of the DAS concept falls short in two aspects. First, the uncertainty in placing the positions onto the International Celestial Reference System (ICRS) could be a factor of 10 or more worse than the formal precision. Second, registering the positions of Galactic stars at various epochs would yield only relative proper motions which have a limited value. Only referencing them to extragalactic sources provides absolute proper motions, mandatory to the study of Galactic structure and populations. It is therefore crucial to establish a link between the DAS fields and the ICRS. Since the ICRS itself is established by the VLBI positions of compact extragalactic sources via the International Celestial Reference Frame (ICRF; Ma et al. 1998), we conduct radio observations to measure the ICRF positions of compact extragalactic sources in the DAS fields. From the standpoint of ground-based optical astrometry, the proper motions of these sources are zero and hence provide fiducials to obtain absolute proper motions of Galactic stars. Once both the optical and radio positions of these extragalactic objects are measured, the link of the DAS fields to the ICRS can be accomplished with high accuracy.

2 Sample selection

The first DAS field targeted with radio interferometric observations was the GOT field (Table 1). Note that the interstellar extinction is considerably higher in this field than in the others, making it the less favourable one for detecting the optical counterparts of the extragalactic radio sources.

As a first step in the radio, Very Large Array (VLA) observations were conducted at 2 cm and 6 cm wavelengths to measure the spectra and compactness of candidate radio–optical link sources on 2005 November 22. The initial sample was chosen from the 20-cm NRAO VLA Sky Survey (NVSS; Condon et al. 1998). The sources are located within 2° from the center of the GOT field. A total of 19 unresolved (θ<~20″) sources were chosen from the NVSS with flux density S>50 mJy. Nine of these sources with unresolved VLA structure at 6 cm and with reasonably flat spectra were selected for the VLBI observations. This sample was supplemented with five additional sources that are typically weaker in NVSS but have a flat spectrum and S>20 mJy at 6 cm according to the GB6 catalog (Gregory at al. 1996). Based on earlier experience (e.g. Mosoni et al. 2006), some of these latter sources were thought to have a good chance for being detected with VLBI as well.

3 Observations and data reduction

Phase-referencing observations at 5 GHz frequency (6 cm wavelength) were conducted with the European VLBI Network (EVN) on 2006 November 24. The nine participating radio telescopes were Effelsberg (Germany), Westerbork (The Netherlands), Jodrell Bank Mk2 (United Kingdom), Medicina, Noto (Italy), Toruń (Poland), Onsala (Sweden), Hartebeesthoek (South Africa) and Nanshan (P.R. China). The total observing time was

7 hours. The data were recorded with the data rate of 1 Gbit s^{-1}, in eight 8-MHz wide intermediate frequency channels in both left and right circular polarizations. The data were correlated with 2-s integration time at the EVN Data Processor at the Joint Institute for VLBI in Europe (JIVE), Dwingeloo, the Netherlands.

The quasar J0603+2159 was selected as the phase-reference calibrator source. It was the only known VLBI source (Fomalont et al. 2003) located within the field. At the time of the preparation of the experiment, its position was known with an accuracy of 2.7 mas only. However, the most recent release of the VLBI source position catalogue (Petrov 2007) involving new observations gives

$$\alpha = 06^h\,03^m\,51.557018^s \text{ and}$$
$$\delta = +21^\circ\,59'\,37.69867''$$

for J2000 right ascension and declination, with 0.27 mas and 0.53 mas formal errors, respectively.

Each program source (Fig. 1) was observed 5 times in ~130-s scans. The telescopes were nodding between the phase-reference calibrator and the target sources in 5–6.5-min duty cycles. Regular observations of three nearby (within 4°) bright and compact VLBI sources with well-known (<0.5-mas accuracy) ICRF positions were also scheduled, in order to verify the relative position of the primary phase-reference source and to help calibrating the data.

The ICRF positional accuracies achieved for the target sources that are detected in the experiment depend on the reference source position accuracy, the target–reference angular separation and the signal-to-noise ratio. For our snapshot observations with ~2.3° target–reference separations or less, these accuracies are better than 1 mas.

4 Results

The US National Radio Astronomy Observatory (NRAO) Astronomical Image Processing System (AIPS) package (e.g. Diamond 1995) was used for the initial data calibration. The visibility amplitudes were calibrated using the system temperatures measured at the antennas during the observations. Fringe-fitting was performed on the nearby secondary calibrator (J0550+2326, J0603+1742, J0604+2429) and strong fringe-finder (J0530+1331, J0555+3948) sources. Images of these sources were made with the Caltech Difmap program (Shepherd et al. 1994) employing the standard hybrid mapping procedure. In order to refine the amplitude calibration, the resulting antenna-based gain corrections were averaged and applied in AIPS before any further analysis.

As a next step, the delay, delay rate and phase solutions derived separately for each of the three secondary calibrators were interpolated and applied to the data of the primary phase-reference source J0603+2159. In all three cases, the position of its brightness peak agreed with the latest ICRF values (Petrov 2007) within the errors.

Fringe-fitting solutions were then derived for J0603+2159 itself in AIPS. An image of the source was made in Difmap. While the central radio ”core” shows a compact feature with a peak brightness of ~100 mJy/beam (Fig. 2), there is considerable extended emission detected to the N-NE at ~150 mas from the core (Fig. 3). Note that only about a quarter of the 5-GHz VLA flux density (1.3 Jy) is accounted for in the VLBI CLEAN components. Also, there seems to be present an extra correlated flux density on the shortest, most sensitive baseline between Effelsberg and Westerbork with respect to the source brightness distribution model derived from long-baseline measurements. This indicates that the brightness distribution of J0603+2159 is extended to the angular scales up to a few hundred mas. This structure could be imaged with the UK Multi-Element Radio Linked Interferometer Network (MERLIN).

The fringe-fitting was repeated using the CLEAN component model obtained for J0603+2159, to account for residual phase corrections due to the source brightness distribution. These solutions were then interpolated and applied to each of the faint target sources.

Table 2. The J2000 equatorial coordinates of the seven detected sources as derived from our phase-referenced EVN observations.

Source name	Right ascension h m s	Declination o ′ ″
J0554+2134	05 54 39.082744	+21 34 08.77722
J0557+2107	05 57 08.215333	+21 07 41.53847
J0558+2251	05 58 24.166092	+22 51 07.47746
J0559+2301	05 59 13.854134	+23 01 37.55485
J0601+2322	06 01 31.051556	+23 22 51.85210
J0602+2256	06 02 08.007727	+22 56 43.09517
J0605+2255	06 05 07.162366	+22 55 23.18172

Seven of the 14 target sources were detected (Fig. 1; Table 2), with peak brightness values ranging from ~5 to 46 mJy/beam. Self-calibration could be performed for four sources stronger than ~10 mJy. Some of the sources were resolved out at the longest inter-continental baselines to the Chinese and South African radio telescopes.

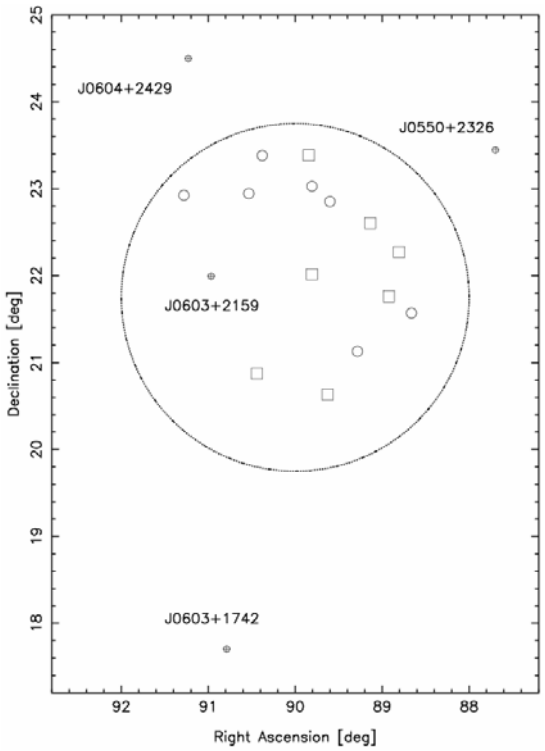

Fig. 1 Sky positions of the 14 candidate radio–optical link objects within 2º from the center of the DAS GOT field. The seven VLBI detections are marked with circles, the non-detections with squares. The positions of the primary phase-reference source J0603+2159 (within the field) and the nearby secondary calibrators are also indicated.

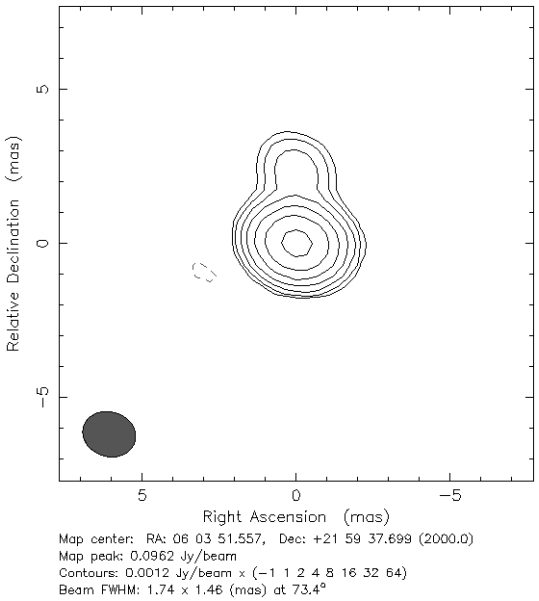

Fig. 2 5-GHz VLBI image of the compact core of the phase-reference calibrator quasar J0603+2159.

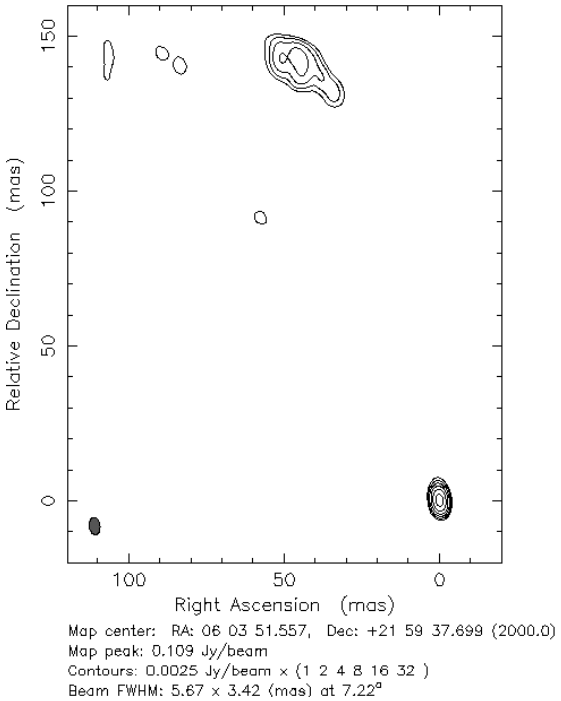

Fig. 3 Diffuse extended structure of J0603+2159 at ~150 mas angular scale in the 5-GHz VLBI image. For this image, a Gaussian taper (with the value of 0.5 at 50 mega-wavelength projected baseline length) was applied to weight down the measurements at the longest baselines.

5 Perspectives

Two additional DAS fields (Sgr and Hya; Table 1) are being observed with the VLA at 2 and 6 cm to look for potential compact flat-spectrum VLBI target sources. First-epoch optical observations of these fields have already been completed.

Acknowledgements. SF acknowledges support from the Hungarian Scientific Research Fund (OTKA T046097). IP gratefully acknowledges support from the US National Science Foundation through grant AST 04-06689 to Johns Hopkins University. This work has benefited from research funding from the European Community's sixth Framework Programme under RadioNet R113CT 2003 5058187. The EVN is a joint facility of European, Chinese, South African and other radio astronomy institutes funded by their national research councils.

References

Condon J.J., Cotton W.D., Greisen E.W., Yin Q.F., Perley R.A., Taylor G.B. and Broderick J.J. (1998). The NRAO VLA Sky Survey. *Astronomical Journal*, 115, pp. 1693-1716

Diamond P.J. (1995). VLBI Data Reduction in Practice. In: *Very Long Baseline Interferometry and the VLBA*, Zensus J.A., Diamond P.J., Napier P.J. (eds.), *ASP Conference Series*, 82, pp. 227-245

Fomalont E.B., Petrov L., MacMillan D.S., Gordon D. and Ma C. (2003). The Second VLBA Calibrator Survey: VCS2. *Astronomical Journal*, 126, pp. 2562-2566

Gregory P.C., Scott W.K., Douglas K. and Condon J.J. (1996). The GB6 Catalog of Radio Sources. *Astrophysical Journal Supplement Series*, 103, pp. 427-432

Ma C., Arias E.F., Eubanks T.M., Fey A.L., Gontier A.-M., Jacobs C.S., Sovers O.J., Archinal B.A. and Charlot P. (1998). The International Celestial Reference Frame as Realized by Very Long Baseline Interferometry. *Astronomical Journal*, 116, pp. 516-546

Mosoni L., Frey S., Gurvits L.I., Garrett M.A., Garrington S.T. and Tsvetanov Z.I. (2006). Deep Extragalactic VLBI-Optical Survey (DEVOS). I. Pilot MERLIN and VLBI observations. *Astronomy and Astrophysics*, 445, pp. 413-422

Petrov L. (2007). VLBI Source Position Catalogue, Solution 2007a, http://vlbi.gsfc.nasa.gov/solutions/2007a_astro

Platais I., Kuzhurina-Platais V., Girard T.M., van Altena W.F., Klemola A.R., Stauffer J.R., Armandroff T.E., Mighell K.J., Dell'Antonio I.P., Falco E.E. and Sarejidini A. (2002). WYIN Open Cluster Study. VIII. The Geometry and Stability of the NOAO CCD Mosaic Imager. *Astronomical Journal*, 124, pp. 601-611

Platais I., Wyse R.F.G. and Zacharias N. (2006). Deep Astrometric Standards and Galactic Structure. *Publications of the Astronomical Society of the Pacific*, 118, pp. 107-123.

Shepherd M.C., Pearson T.J. and Taylor G.B. (1994). Difmap: An Interactive Program for Synthesis Imaging. *Bulletin of the American Astronomical Society*, 26, pp. 987-989

Tyson A.J. (2002). Large Synoptic Survey Telescope: Overview. In: *Proc. SPIE*, 4836, pp. 10-20

On the role of differenced phase-delays in high-precision wide-field multi-source astrometry

I. Martí-Vidal, J.M. Marcaide, and J.C. Guirado
Dpt. Astronomia i Astrofísica, Universitat de València, Ed. Investigación Jeroni Muñoz, C/ Dr. Moliner 50, E-46100 Burjassot, València (SPAIN)

Abstract. Phase-delay is, by far, the most precise observable used in interferometry. In typical very-long-baseline-interferometry (VLBI) observations, the uncertainties of the phase-delays can be ∼100 times smaller than those of the group delays. However, the phase-delays have an important handicap: they are *ambiguous*, since they are computed from the relative phases of the signals of the different antennas, and an indeterminate number of complete 2π cycles can be added to those phases leaving them unchanged. There are different approaches to solve the ambiguity problem of the phase delays (Shapiro et al., 1979; Beasley & Conway, 1995), but none of them has been ever used in observations involving more than 2−3 sources. In this contribution, we will report for the first-time wide-field multi-source astrometric analysis that has been performed on a complete set of radio sources using the phase-delay observable. The target of our analysis is the S5 polar cap sample, consisting on 13 bright ICRF sources near the North Celestial Pole. We have developed new algorithms and updated existing software to correct, in an automatic way, the ambiguities of the phase-delay and, therefore, perform a phase-delay astrometric analysis of all the sources in the sample. We will also discuss on the impact of the use of phase-delays in the astrometric precision.

Keywords. Astrometry − techniques: interferometric − galaxies: quasars: general − galaxies: BL Lac objects: general − radio continuum: general

1 Introduction

Over the last years, we have carried out a series of VLBI observations, using the Very Long Baseline Array (VLBA) at 8.4, 15.4, and 43 GHz, aimed at studying the absolute kinematics of a complete sample of extragalactic radio sources using astrometric techniques. The target of our programme is the "S5 polar cap sample", consisting on 13 radio sources from the S5 survey (Kühr, Witzel, & Pauliny-Toth, 1981; Eckart, Witzel, & Biermann, 1986). All sources in this sample have flux densities larger than 0.2 Jy at the epoch of our observations and well defined ICRF positions. Table 1 shows the list of the S5 polar cap sample sources. Most of these sources have structures that evolve in time. For a reliable study of the absolute kinematics of their components we need to refer the source positions, and their possible changes in time and frequency, to stable (or *fixed*) points in the sky. The use of phase-delays allow us to refer the positions of the sources to the *phase centers* of the maps, providing a suitable reference in the source structure. In principle, the effect of the source structure can be also removed from the group delays, but the large and rapid changes of the phase structure for this observable makes this approach difficult (see the contribution of L. Petrov in these proceedings).

2 Observations

We observed the complete S5 polar cap sample at 15.4 GHz on 15 June 2000 using all the antennas of the VLBA for 24 hr (see Martí-Vidal et al., 2007, for details). The structures of the S5 polar cap sources for our epoch, and other epochs at 15.4 GHz and 8.4 GHz, were discussed by Pérez-Torres et al. (2004) and Ros et al. (2001).

3 The phase connection

We performed an astrometric analysis based on the phase-connection of the phase-delays, similar to previous analyses (e.g. Shapiro et al., 1979; Guirado et al., 1995), but with some substantial

Table 1. List of the S5 polar cap sample sources. Columns 2 and 3 are the ICRF positions (right ascension and declination in J2000.0, respectively) reported by IERS for year 2000.

Source	ICRF position (J2000.0)	
	α	δ
0153+744	$01^h\ 57^m\ 34.964908^s$	74° 42' 43.22998"
0212+735	$02^h\ 17^m\ 30.813365^s$	73° 49' 32.62180"
0454+844	$05^h\ 08^m\ 42.363503^s$	84° 32' 04.54402"
0615+820	$06^h\ 26^m\ 03.006188^s$	82° 02' 25.56764"
0716+714	$07^h\ 21^m\ 53.448459^s$	71° 20' 36.36339"
0836+710	$08^h\ 41^m\ 24.365236^s$	70° 53' 42.17328"
1039+811	$10^h\ 44^m\ 23.062554^s$	80° 54' 39.44303"
1150+812	$11^h\ 53^m\ 12.499130^s$	80° 58' 29.15451"
1749+701	$17^h\ 48^m\ 32.840231^s$	70° 05' 50.76882"
1803+784	$18^h\ 00^m\ 45.683911^s$	78° 28' 04.01854"
1928+738	$19^h\ 27^m\ 48.495214^s$	73° 58' 01.56997"
2007+777	$20^h\ 05^m\ 30.998513^s$	77° 52' 43.24766"

differences. Basically, our astrometric analysis can be described in three main steps:

- Step 1: Find a preliminary model of the phase-delays by fitting the clock drifts and the tropospheric zenith delays using the group-delay and delay rate data. Clock drifts are modelled with 3rd order polynomials and the tropospheric zenith delays at each site are modelled with piece-wise linear functions (one node every 6 hours).

- Step 2: Use the delay model obtained in the previous step to determine the number of 2π phase-delay cycles that must be added to the observed phase-delays in order to make them *unambiguous*.

- Step 3: Use the phase-delays obtained in the previous step for computing the *differenced phase-delays* between pairs of sources, and use both (differenced and undifferenced) delays in the astrometric fit.

By *differenced phase-delays*, we mean the difference of the delay corresponding to one source and the delay corresponding to another source, which is observed at a time very close to the observation of the first one. It can be shown that the *differenced phase-delays* between pairs of sources are almost free of antenna-based effects and, thus, their use allows higher precision of the estimates of source positions (Marcaide, Elósegui & Shapiro, 1994). Most of the difficulty in the use of the phase-delay astrometry is concentrated in step 2. The group-delays and delay rates are not precise enough for a correct prediction of the 2π cycles that must be added to the phase-delays of each baseline and time. Nevertheless, if the modelling of the delay rate is good enough for a correct prediction of the number of 2π cycles to be added between two consecutive scans of the same source, then the connection of the phase-delays will be succesful, regardless of possible overall ambiguities that could remain in the data (related to the ambiguities of the observations corresponding to the first scan of each source). In practice, the phase connection resulting from Step 2 will work as long as the residual delay rates obtained in Step 1 are lower than the delay corresponding to one phase cycle, divided by the time between two consecutive scans of the same source. In the case of the observations here reported, the residual rates should be smaller than $\sim$0.36 ps/s. We show in Fig. 1 the distribution of rate residuals resulting from the fit of Step 1. As we can see, most of the rate residuals fullfil this condition, but there is a small subset of relatively large residuals, which corresponds to observations for which unmodelled phase-delay cycles will surely remain after applying Step 2. In previous analyses (e.g. Shapiro et al., 1979; Guirado et al., 1995) these uncorrected phase cycles could be found by visual inspection, but with the amount of sources and antennas of our observations, such procedure is not practical. We had to develop an algorithm that automatically corrects the unmodelled phase-delay cycles that remain in the data after Step 2, allowing for a correct and definitive phase-connection of the phase-delays. This algorithm is part of the *University of Valencia Precision Astrometry Package*, which is presented in the next subsection.

3.1 The University of Valencia Precision Astrometry Package (UVPAP)

For the astrometric fits and the phase-connection process we used the *University of Valencia Precision Astrometry Package*, an extensively improved version of the VLBI3 program (Robertson, 1975). See also Ros et al. (1999), and references therein, for details of the VLBI3 model. The main improvements of UVPAP consist on the use of the JPL ephemeris binary tables and the upgrade of the relativistic effects of the Solar System bodies, computed using the Consensus

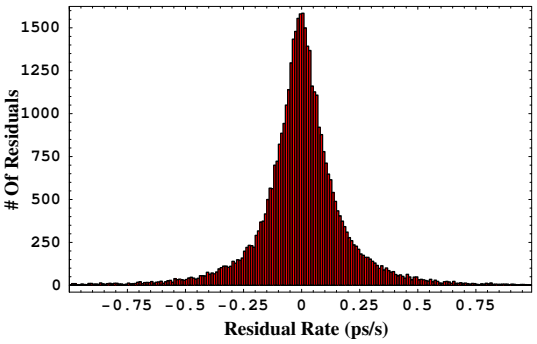

Figure 1. Distribution of residual delay rates for all the baselines, sources, and scans of our observations, after fitting the clock drifts and tropospheric zenith delays to the group-delay and delay rate data.

Model (Mc Carthy & Petit, 2003). The main advantage of UVPAP with respect to other softwares is the possibility of performing multi-source differenced phase-delay astrometric fits, which is the kind of analysis that we have performed.

With respect to the phase-connection, UVPAP uses a new, in-house developed, algorithm, which working within Step 2 of the previous section, detects the possible remaining unmodelled phase-delay cycles by imposing the nullity of the closure phases of all data[1]. This *automatic phase connector* is described in detail in Martí-Vidal et al. (2007). In addition to the phase-delay cycles that can be accounted for using the closure phases, there could also be other unmodelled cycles related to antenna-dependent effects (as it could be the case of fast changes in the tropospheric delays). These cycles would not affect the closure phases and, therefore, would be completely transparent to the *automatic connector algorithm*. Fortunately, such cycles introduce clear effects in the residuals of the differenced phase-delays; effects that can be easy visually detected, allowing for a later correction using an iterative bootstrapping process. This process, also described in Martí-Vidal et al. (2007), is called *smoothness criterion algorithm* and can be also automated. Once all the necessary corrections have been performed, the resulting phase-delays are completely connected, being unambiguous and susceptible of being used without any problem in our astrometric analysis.

[1] The closure phases of all data must be zero, given that we are taking into account the structures of the sources during all our astrometric analysis.

4 Phase-delay vs. group-delay

The standard deviation of the group-delay residuals of all data, after Step 1, is 0.74 ns. Once all the phase-connection process is performed, the standard deviation of the undifferenced phase-delay residuals, using all data, is only 0.03 ns. Thus, using phase-delays instead of group-delays decreases by a factor ∼25 the standard deviation of the residuals. This decrease directly translates into an important improvement of the χ^2 at the minimum and, accordingly, into a decrease of the statistical uncertainties of the adjusted source positions. In principle, the increase in astrometric precision should be roughly equal to the improvement of the value of the χ^2 at the minimum, but the real increase of the astrometric precisions can be even larger. The use of *differenced* phase-delays in the fit still improves the precision to the astrometry as we will see in the next section.

5 The role of differenced phase-delay observables in the fit

The use of differenced observables corresponding to a given pair of sources will increase the precision in the determination of the *relative* positions of such pair. In our observations, differenced observables for a total of 24 source pairs could be computed. This "network" of differenced observations introduces redundancies for sources that belong to more than one pair, which allow for an increase in the precision of their relative coordinatess. Therefore, the use of all our data in a unique fit gives us more robust results than a separate analysis of each particular source pair.

Since we are using differenced observables in our fit, the standard deviations of the separations of the 24 pairs are strongly dependent on the separation of the sources that form the pairs. This effect can be clearly seen in Fig. 2, which shows the uncertainties in the separations of the 24 source pairs as a function of such separations. The behavior is roughly linear, as predicted by the empirical formulae given by Shapiro et al. (1979) and corroborated by simulations of astrometric VLBA observations performed by Pradel, Charlot, & Lestrade (2006). However, our astrometric uncertainties are ∼10 times smaller than those estimated by Pradel, Charlot, & Lestrade (2006) for the typical declinations of the S5 polar cap sample sources. This large improvement in precision is probably due to the si-

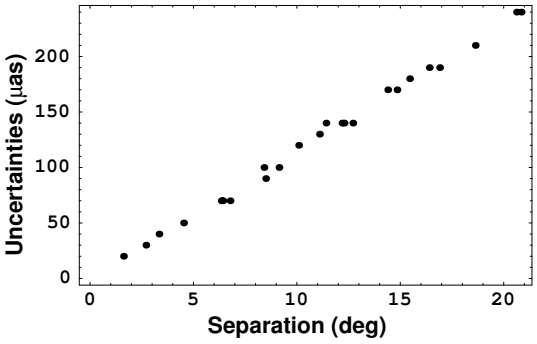

Figure 2. Uncertainties in the separations of all the pairs of sources as a function of such separations. Since the behavior of the uncertainties is roughly linear, the relative errors of the separations of the sources are similar, $\sim 3 \times 10^{-9}$.

multaneous analysis of the 13 sources, instead of using the usual two-source (target/reference) scheme. Hence, our global analysis brings more constraints to the positions of the sources, increasing the astrometric precision.

6 Differenced phase-delay astrometry vs. phase-reference mapping

The essence of our global differenced phase-delay astrometry is the same as that of the phase-reference astrometry (Beasley & Conway, 1995), since in both analyses the main observable used is the differenced phase (delay) between the signals coming from the different sources. Nevertheless, there is an important difference between our astrometric approach and the phase-reference technique that must be underlined: in the phase-reference astrometry, the coordinates of one source (the target source) are determined with respect to the coordinates of another source (the reference source). In our global analysis, we use data from all the 13 sources of the S5 polar cap simultaneously, in a unique fit, thus increasing by a factor $\sim$10 the precision of the solution, as we have shown in Sec. 5. Our astrometric corrections with respect to the coordinates shown in Table 1, taking the source 0454+844 as reference, can be visualized in Fig. 3. Of course, the corrections corresponding to sources with large separations from 0454+844 have relatively large uncertainties, but such sources will have more precise position estimates with respect to closer reference sources (see Fig. 2).

7 Conclusions

We have performed the first high-precision wide-field multi-source astrometric analysis using the phase-delay observable. We have developed new algorithms and updated existing software to create UVPAP, a package that allows us to solve automatically for the ambiguities of the phase-delays and perform multi-source a differenced phase-delay astrometric analysis.

We discuss on the impact of the use of phase-delays (and, in particular, differenced phase-delays) in the precision of the astrometry. Fitting the source positions with undifferenced phase-delays brings more than one order of magnitude higher precision than fitting the group-delays corresponding to the same set of observations. Using differenced phase-delays increases even more the achieved precision.

Other wide-field high-precision astrometric analyses, similar to that reported here, are currently under way and will eventually provide, when finished, spectral information and absolute kinematics of all sources in the S5 sample. Ultimately, we expect to provide a definitive test on the stationarity of the radio sources cores, checking with high-precision the stability of this subset of ICRF sources.

Acknowledgements: This work has been partially funded by Grants AYA2004-22045-E, AYA2005-08561-C03, and AYA2006-14986-C02 of the Spanish DGCYT. The National Radio Astronomy Observatory is a facility of the National Science Foundation operated under cooperative agreement by Associated Universities, Inc.

References

Beasley A.J. & Conway J.E., 1995, ASP Conf. Ser. 82: Very Long Baseline Interferometry and the VLBA, 82, 328

McCarthy D. D. & Petit G., 2003, The International Celestial Reference System: Maintenance and Future Realization, 25th meeting of the IAU, Joint Discussion 16, 22 July 2003, Sydney, Australia

Eckart A., Witzel A., Biermann P., et al., 1986, A&A, 168, 17

Guirado J. C., Marcaide J. M., Elosegui P., et al., 1995, A&A, 293, 613

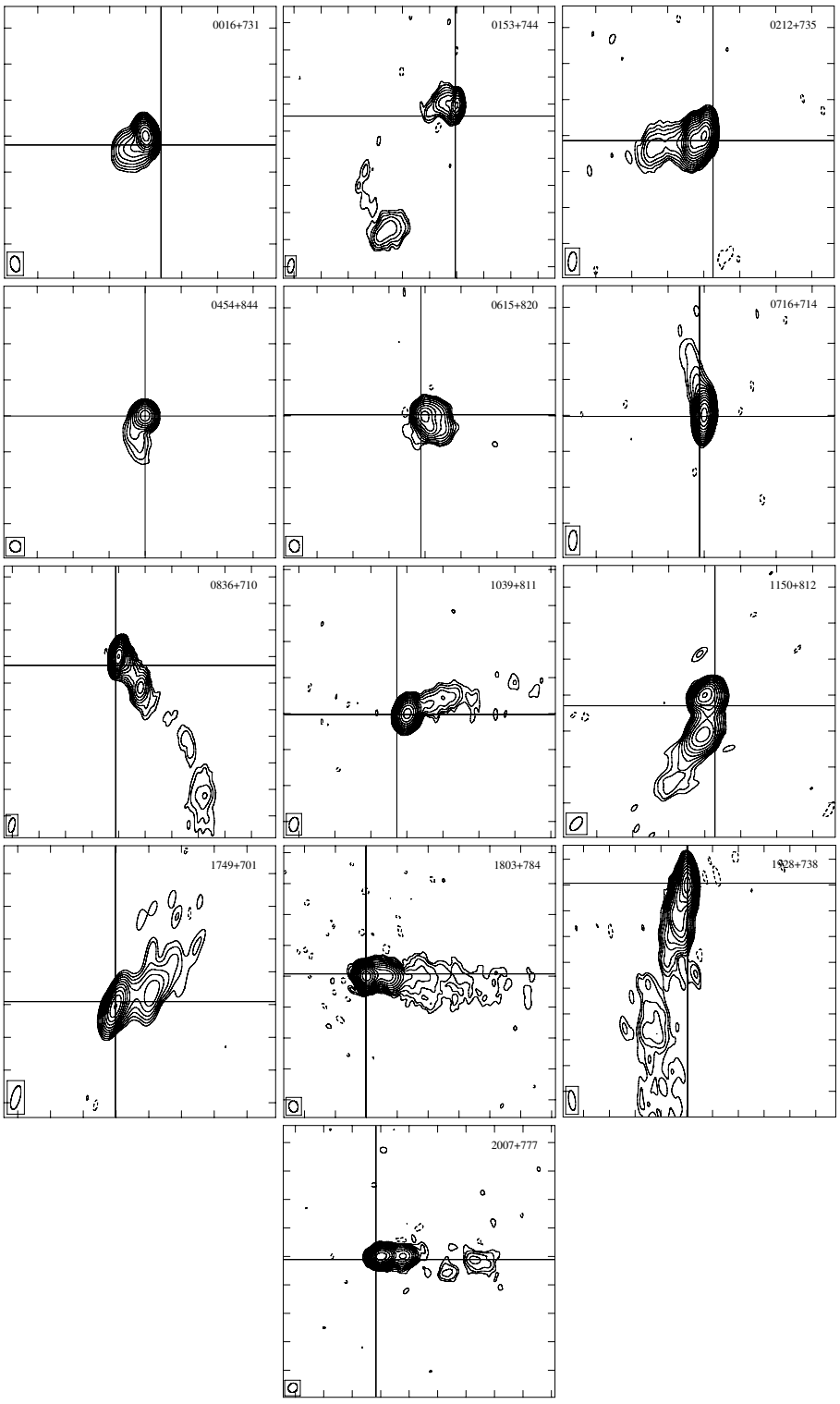

Figure 3. Maps of the S5 polar cap sample sources obtained from our 15.4 GHz observations. The phase center of each map correspond to the peak of brightness of each source. The crosses mark the astrometric corrections with respect to the IERS source positions. The separations of the peaks of brightness from the crosses correspond, then, to our astrometric corrections. Tick marks are separated by 2 mas. Horizontal and vertical axes are relative α and δ, respectively. FWHM of convolving beams are shown at botton-left of each map. Contours are at -3, 3, $3\sqrt{3}$, 9, ... times the rms of the map residuals.

Kühr H., Witzel A., Pauliny-Toth I. I. K., et al., 1981, A&AS, 45, 367

Marcaide J. M., Elósegui P., & Shapiro I. I., 1994, AJ, 108, 368

Martí-Vidal I., Marcaide J.M., Guirado J.C. et al., 2007, in preparation

Pérez-Torres M. A., Marcaide J. M., Guirado J. C., et al., 2004, A&A, 428, 847

Pradel N., Charlot P., & Lestrade J.-F., 2006, A&A, 452, 1099

Robertson D. S., 1975, "Geodetic and astrometric measurements with Very Long Baseline Interferometry", Ph. D. Thesis, MIT

Ros E., Marcaide J. M., Guirado J. C., et al., 1999, A&A, 348, 381

Ros E., Marcaide J. M., Guirado J. C., et al., 2001, A&A, 376, 1090

Shapiro I.I., Wittels J.J., Counselman C.C. et al., 1979, AJ, 84, 1459

Comparison and Cut off Angle Tests for Observed and Simulated CONT05 Sessions

K. Teke[1,2], J. Wresnik[1], J. Boehm[1], H. Schuh[1]

(1) IGG, Vienna University of Technology,
IGG, Vienna University of Technology, Austria

(2) Dept. of Geodesy and Photogrammetry Engineering,
Dept. of Geodesy and Photogrammetry Engineering, Karadeniz Technical University, Turkey

Abstract. Baseline length repeatabilities can be taken as accuracy criteria of the VLBI network, because they are independent of rotations of the polyhedron formed by several VLBI stations.

In the first part of this study, baseline length repeatabilities of 15 sessions of the VLBI CONT05 campaign were investigated for certain mapping functions (VMF1, GMF, NMF) and cut off elevation angles (5°, 6°, 7°, 8°, 9°, 10°, 12°, 15°, 20° and 30°). From the analysis with the VLBI software OCCAM 6.1, the following conclusions can be drawn: All three mapping functions yield about similar baseline length repeatabilities for cut off angles 5° to 10°, but significantly larger repeatabilities for 12° to 30°. The cut off angle of 7° gives the best results for all mapping functions, and baseline length repeatabilities obtained with VMF1 are slightly better than those with NMF and GMF.

In the second part of this study, the observations of the VLBI sessions (NGS files) were simulated and compared with the real observations in terms of baseline length repeatabilities. For the cut off angle 7° the simulated observations for CONT05 yielded approximately the same baseline length repeatabilities as the real observations. One of the main conclusions from the simulation study is that there is no need to observe radio sources below the cut off angle 7° unless the modelling of wet delay parameters is improved.

Keywords. VLBI, CONT05, mapping function, cut off angle, baseline length repeatability, simulation.

1 Introduction

The term “mapping function” is used to describe the relation between the tropospheric delay at zenith direction and an arbitrary angle above the horizon. Throughout the history of VLBI, extensive attention has been paid to tropospheric mapping functions, in view of the dominance of tropospheric delay mismodelling in the error budget.

The baseline length is independent of rotations of the polyhedron formed by several VLBI stations. Thus, baseline length repeatability is a good measure of the accuracy achieved for geodetic VLBI (Niell, 2006). For each baseline, the repeatability σ can be determined as the standard deviation of the n estimates L_i with regard to the corresponding value L_0 on a regression polynomial of first order as e.g. given by (Boehm et al., 2006a),

$$\sigma = \sqrt{\frac{\sum_{i=1}^{n}(L_i - L_0)^2}{n-2}} \tag{1}$$

To describe the increase of the baseline length repeatability with increasing baseline length, Equation (2) can be used,

$$y = a^2 + b^2\, ppb^2 L^2 \tag{2}$$

where a and b are the parameters to be estimated by least-squares method (LSM), y are the repeatability values (σ) w.r.t. baseline lengths (L) (Niell, 2006).

Baseline length repeatability can be taken as criterion for evaluating the accuracy of the mapping functions which changes with cut off angle.

In the first part of this study, based on Eq. (1) and (2), baseline length repeatabilities of 15 sessions of the VLBI CONT05 campaign were investigated for the mapping functions VMF1 (Boehm et al., 2006a), GMF (Boehm et al. 2006b), and NMF (Niell 1996) and the cut off elevation angles 5°, 6°, 7°, 8°, 9°, 10°, 12°, 15°, 20° and 30°.

In the second part of this study, the observations of the VLBI sessions were simulated. Then observed and simulated CONT05 NGS files were compared based on baseline length repeatabilities.

2 Baseline Length Repeatabilities Derived from Different Mapping Functions and Cut off Angles

The CONT05 sessions were processed with the software OCCAM 6.1 for different mapping functions (VM1, GMF, NMF) and for the different cut off angles. The parameters a and b of the regression function given in Eq. (2) were obtained by Least Squares (LS) adjustment as follows:

$$x = (A^T W A)^{-} A^T W\, y \tag{3}$$

where the measurement vector (y) and the vector of unknown parameters (x) were formed as shown in Eq. (4).

$$y = \begin{bmatrix} rms_1^2 \\ rms_2^2 \\ \vdots \\ rms_n^2 \end{bmatrix}; x = \begin{bmatrix} a^2 \\ b^2 \end{bmatrix} \tag{4}$$

The design matrix (A) and the weight matrix of the adjusted baselines (W) were set up according to Eq. (5)

$$A = \begin{bmatrix} 1 & ppb^2 L_1^2 \\ 1 & ppb^2 L_2^2 \\ \vdots & \vdots \\ 1 & ppb^2 L_n^2 \end{bmatrix}; W = \begin{bmatrix} 1/s_1^2 & & & \\ & 1/s_2^2 & & \underline{0} \\ & & \ddots & \\ & \underline{0} & & 1/s_n^2 \end{bmatrix} \tag{5}$$

where s is the mean value of the standard deviations of the adjusted baselines estimated from the 15 CONT05 sessions. The parameters of the regression function for different mapping functions and cut off angles are shown in Table 1. Also the number of the observations that were included for each cut off angle are added. From Table 1 it can be seen that the parameters of the regression function computed from the data of GMF and NMF are nearly the same for all cut off angles. However VMF1 yielded better results for cut off angle 5° to 10°. From 10° to 30° all mapping functions approximately produce the same outcomes w.r.t. baseline length repeatabilities.

Table 1. The parameters of the regression function for each mapping function and cut off angle. The numbers of observables available for each solution are given in parentheses.

Mapping Functions	*Parameters of the function for different cut off angles*									
	5° (6156)		*6°(6028)*		*7°(5907)*		*8°(5818)*		*9°(5646)*	
	a (cm)	*b*	*a (cm)*	*b*	*a (cm)*	*b*	*a (cm)*	*b*	*a (cm)*	*b*
VM1	0,505	0,853	0,515	0,817	0,517	0,801	0,523	0,796	0,510	0,836
GMF	0,524	0,879	0,521	0,844	0,521	0,823	0,522	0,806	0,512	0,844
NMF	0,528	0,879	0,520	0,844	0,521	0,826	0,522	0,808	0,512	0,845
Mapping	*10°(5502)*		*12°(5207)*		*15°(4730)*		*20°(3906)*		*30°(2491)*	
Functions	*a (cm)*	*b*	*a (cm)*	*b*	*a (cm)*	*b*	*a (cm)*	*b*	*a (cm)*	*b*
VM1	0,501	0,859	0,489	0,927	0,428	1,078	0,404	1,229	0,657	1,542
GMF	0,500	0,866	0,488	0,931	0,426	1,081	0,403	1,229	0,656	1,542
IMF	0,500	0,867	0,489	0,931	0,428	1,081	0,404	1,228	0,655	1,543

When Table 1 is investigated an unambiguous comparison cannot be achieved. For that reason the value of the initial parameter a of the regression function is fixed to 0.5 cm in the adjustment stage. So parameter b can be used to find the optimal mapping function and cut off angle w.r.t. baseline length repeatability.

Table 2. The parameters of the regression function for each mapping function and cut off angle (parameter of the regression function fixed to 0.5 cm in order to ensure an unambiguous comparability between mapping functions and cut off angles). The numbers of observables available for each solution are given in parentheses.

Mapping Functions	*Parameters of the function for different cut off angles*									
	5°(6156)		*6°(6028)*		*7°(5907)*		*8°(5818)*		*9°(5646)*	
	a (cm)	*b*	*a (cm)*	*b*	*a (cm)*	*b*	*a (cm)*	*b*	*a (cm)*	*b*
VM1	0,5	0,597	0,5	0,559	0,5	0,537	0,5	0,540	0,5	0,582
GMF	0,5	0,657	0,5	0,605	0,5	0,577	0,5	0,554	0,5	0,595
NMF	0,5	0,660	0,5	0,605	0,5	0,580	0,5	0,558	0,5	0,597
Mapping Functions	*10°(5502)*		*12°(5207)*		*15°(4730)*		*20°(3906)*		*30°(2491)*	
	a (cm)	*b*	*a (cm)*	*b*	*a (cm)*	*b*	*a (cm)*	*b*	*a (cm)*	*b*
VM1	0,5	0,600	0,5	0,680	0,5	0,823	0,5	0,994	0,5	1,506
GMF	0,5	0,610	0,5	0,685	0,5	0,824	0,5	0,993	0,5	1,506
IMF	0,5	0,611	0,5	0,686	0,5	0,826	0,5	0,992	0,5	1,506

From Table 2 the following can be concluded:

- The Vienna Mapping Function VMF1 gives the best baseline length repeatabilities for all cut off angles.
- The cut off angle 7° gives the best baseline length repeatabilities for all mapping functions w.r.t. baseline length repeatabilities.
- From the investigations of CONT05 sessions the optimal tropospheric mapping function was found to be VMF1 with the optimal cut off angle at 7°.
- On the other hand it must be highlighted that this conclusion can only be drawn for CONT05 sessions and when the baseline length repeatabilities are chosen as accuracy criterion.

The scattered data of the baseline length repeatabilities for different mapping functions and cut off angles with their fitted curves are given in the graph below.

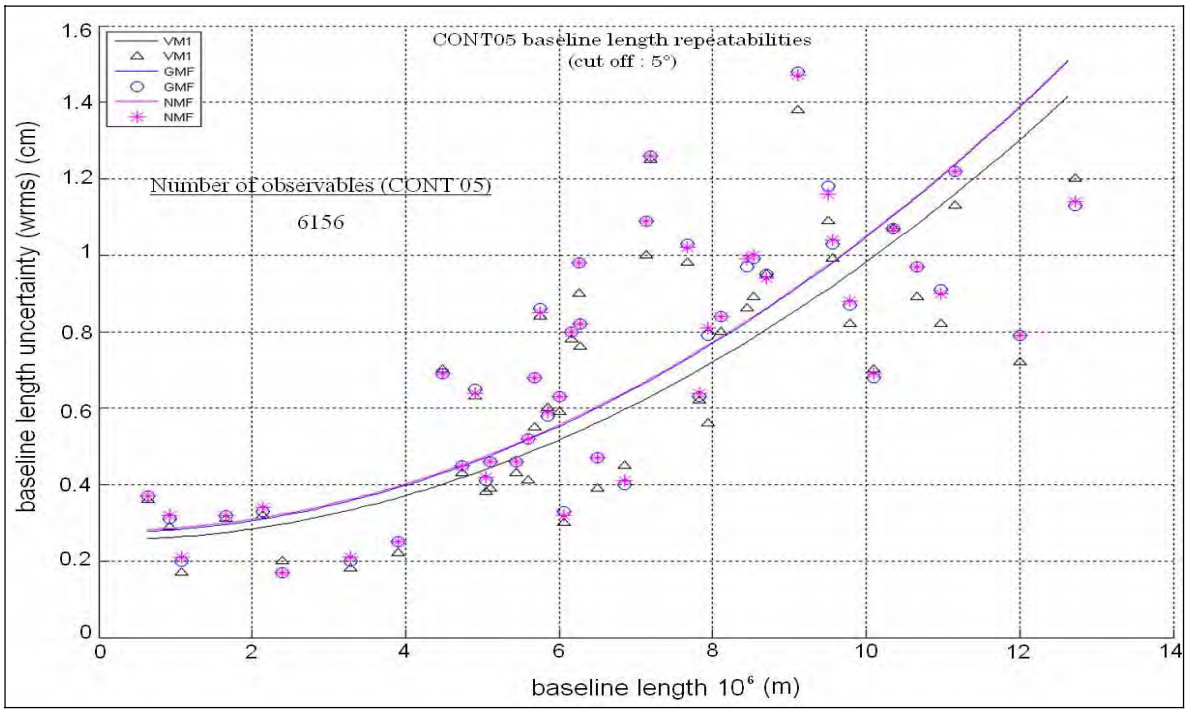

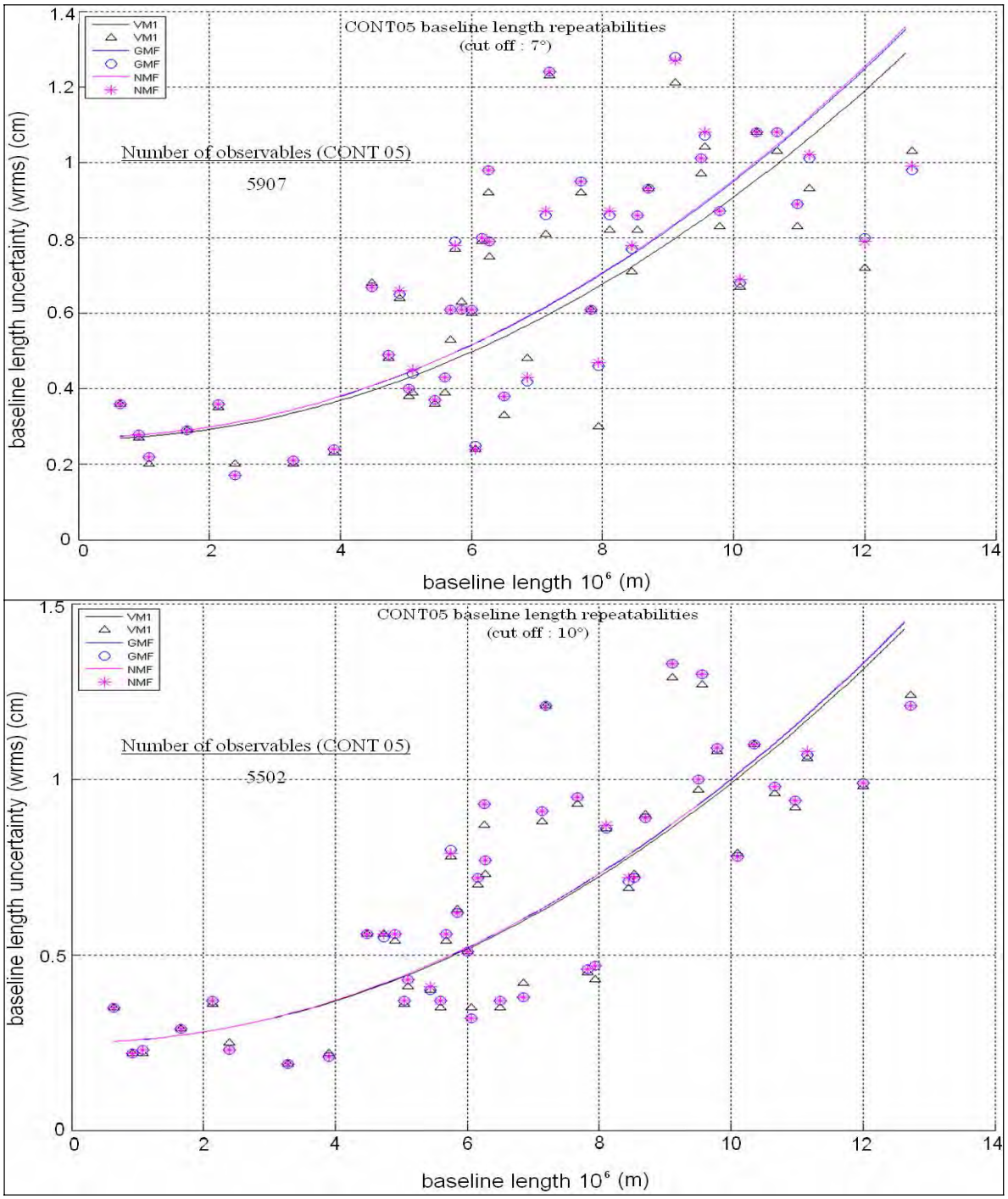

Fig. 1 Baseline length repeatability values provided by the tropospheric mapping functions VMF1, GMF, and NMF for cut off angles 5°, 7°, and 10°.

As it can be seen in Fig. 1 VMF1 produces better results w.r.t. baseline length repeatabilities than NMF and GMF for the cut off angle 5°. From cut off angle 5° to 20° the differences decrease between VMF1 and the other mapping functions. For cut off angles 20° and higher all mapping functions yield approximately the same baseline length repeatabilities.

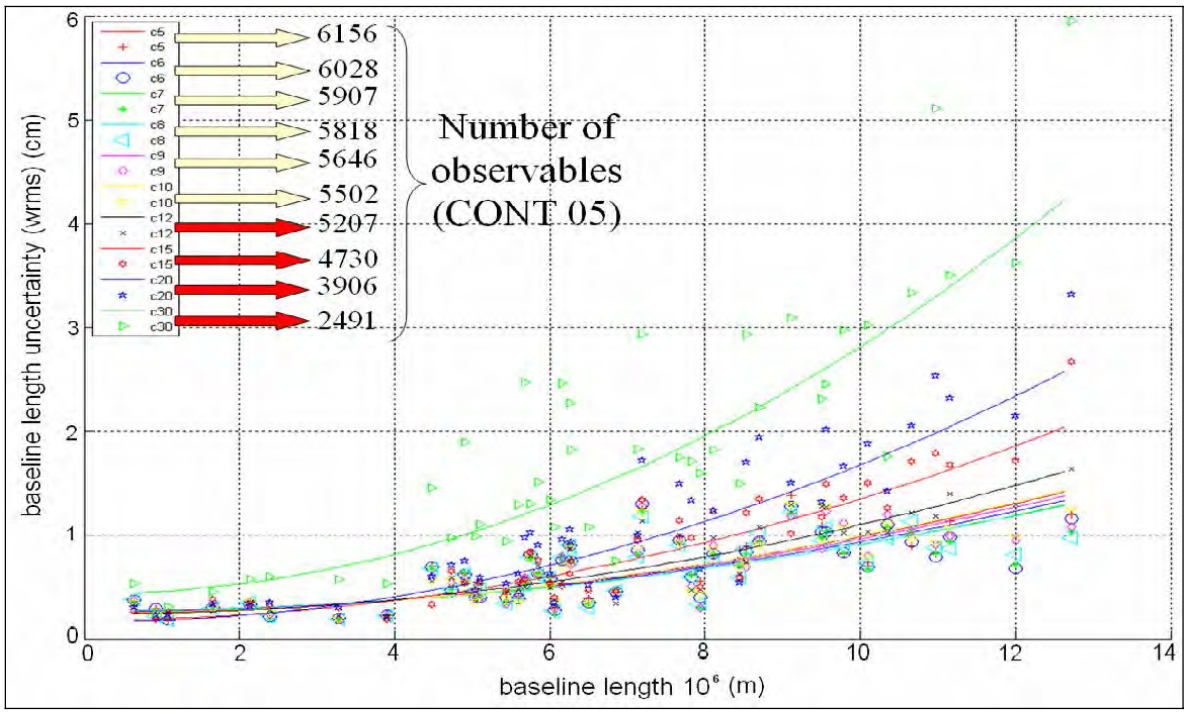

Fig. 2 Baseline length repeatabilities obtained with Vienna Mapping Function (VMF1) for different cut off angles. Also added is the number of observables in CONT05.

Figure 2 shows that the number of observations is significantly decreasing with increasing elevation cutoff angle. This is mainly due to the fact that the CONT05 sessions were scheduled for a cut off angle of 5°; with higher cut off angles several observations were simply discarded. Thus, this comparison is not fully objective because the schedule should have been determined for each cutoff angle separately.

In Section 3 schedules were created for each cut off angle and the observations were filled with simulated values.

3 Comparison of Simulated and Observed CONT05 Sessions derived from Different Mapping Functions and Cut off Angles

The main idea of simulation methods in an optimization procedure is to catch the maximum or minimum value of a mathematical function by trial and error. In geodesy, most of the statistical functions are used to find out the accuracy of the measurements and the unknowns. The values obtained from these statistical accuracy functions are desired to be a minimum. Simulation methods such as Monte Carlo and Sequential Least Squares are effective methods as to reach the accuracy objective functions. Simulation methods are not rigid as analytical optimization methods and more suitable for computer programming.

The simulated and observed NGS files of CONT05 sessions were compared w.r.t. baseline length repeatabilities. It is important to emphasize that these comparisons were based on baseline length repeatabilities.

The group delay ($\Delta\tau$) is simulated according to Eq. (6),

$$\Delta\tau = \Delta\tau_{comp} + (WZD_2\ mfw_2(e) + cl_2) - (WZD_1\ mfw_1(e) + cl_1) + wn_{bsl(1-2)} \quad (6)$$

where WZD denotes to wet zenith delay, mfw is the wet mapping function (NMF was used here), cl is the clock error, wn is the white noise added to the baselines. The simulated NGS files have been processed by the OCCAM 6.1 software for the cut off angles 5°, 7°, 10°, 15° and 20°. The objective function for the optimization is shown in Eq. (7).

$$\sum_{j=1}^{m}(rep_{observed} - rep_{simulated})^2 \Rightarrow \min \qquad (7)$$

After varying the driving parameters for the wet zenith delays, the clocks and the white noise, the best agreement with real observations was found with a power spectrum density of 0.5 psec^2/sec for the wet zenith delay (except for Kokee Park with 0.8, HartRAO with 0.1, and Tsukuba with 0.6 psec^2/sec), an Allan standard deviation of $2 \cdot 10^{-15}$@15 min for all clocks and a white noise of 12 psec for all baselines.

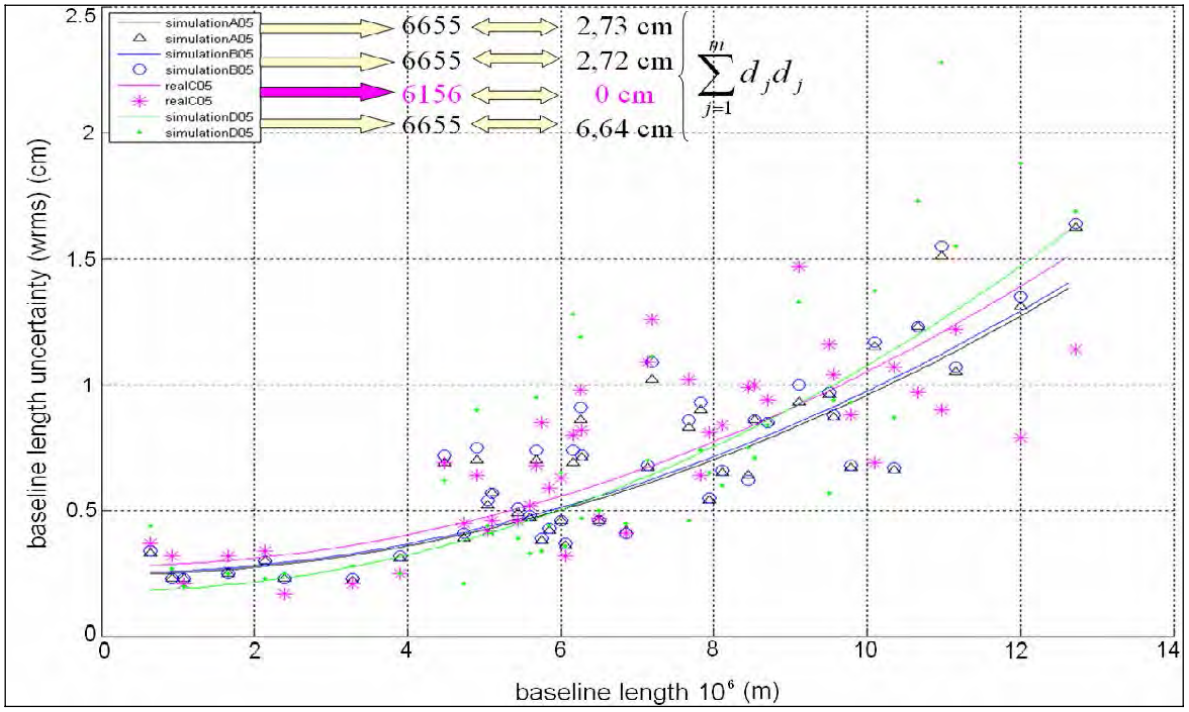

Fig. 3 Comparison of baseline length repeatabilities derived from simulated CONT05 NGS files with respect to real values and a cut off angle of 5°.

In Figure 3 the abbreviation "simulationA05" denotes the first attempt of the creation of simulated NGS files. Then the other attempts were carried out which were named as "simulationB05" and "simulationD05". It can be seen that in Figure 3 the number of the observables in simulated sessions is nearly the same as in the observed sessions. After applying all the procedures which were done for cut off angle 5° also for the cut off angle 7° an excellent agreement was found with the observed NGS files (Figure 4). "Simulated C07" NGS file succeeded to fit to the "Real C07" NGS file w.r.t. baseline length repeatabilities.

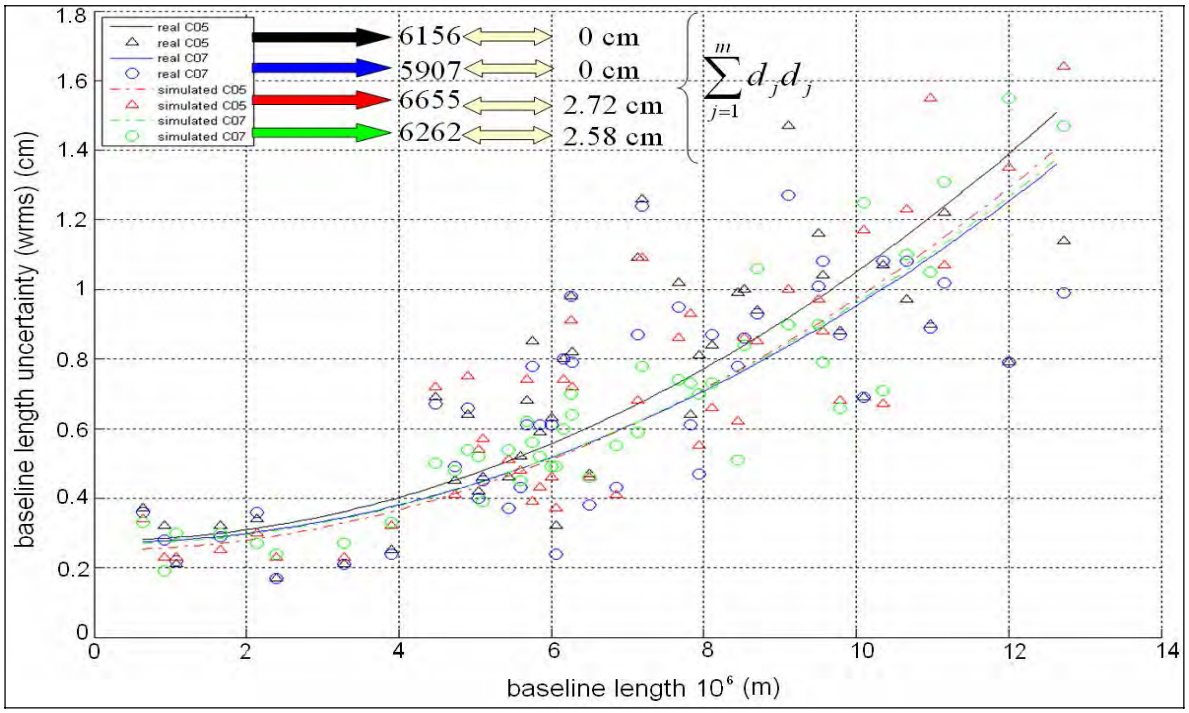

Fig. 4 Comparison of baseline length repeatabilities derived from simulated and observed CONT05 NGS files

4 Conclusions and Outlook

From the investigations of CONT05 baseline repeatabilities for different mapping functions (VMF1, GMF, NMF) and cut off angles (5°, 6°, 7°, 8°, 9°, 10°, 12°, 15°, 20° and 30°) the following conclusions can be drawn:

- The mapping functions produced rather similar baseline uncertainty values for cut off angles 5° to 10° but not for 12° to 30°. This difference occurred because of the various numbers of observables and their distribution on the sky.
- In spite of the small differences, the mapping function VMF1 gives always the best baseline length repeatabilities for all cut off angles.

From the comparison of simulated and observed CONT05 sessions the following conclusions can be drawn,

- For the cut off angle 7° the simulated observations for CONT05 yielded approximately the same baseline length repeatabilities as the real observations.
- No need to observe radio sources below a cut off angle 7° unless the wet zenith delay parameters will be measured more accurately and the related mapping function models will be improved.

Acknowledgments This work was sponsored by the Austrian Science Fund (FWF) (Project: P18404-N10) and we are grateful to the International VLBI Service for Geodesy and Astrometry (IVS) for providing the observations and to the EU Socrates-Erasmus Program for funding one of the authors (K. Teke).

References

Boehm, J., B. Werl, and H. Schuh (2006a) Troposphere mapping functions for GPS and very long baseline interferometry from European Centre for Medium-Range Weather Forecasts operational analysis data, J. Geophys. Res., 111, B02406, doi:10.1029/2005JB003629.

Boehm, J., Niell, A., Tregoning, P., and Schuh, H. (2006b) Global Mapping Function (GMF): A new empirical mapping function based on numerical weather model data, Geophysical Research Letters, 33: L07304, doi:10.1029/2005GL025546.

Niell, A. (1996) Global mapping functions for the atmosphere delay at radio wavelengths, J. Geophys. Res., 101, B2, 3227-3246.

Niell, A. (2006) Baseline Length Repeatability, Report, MIT Haystack Observatory.

Incorporating Correlated Station Dependent Noise Improves VLBI Estimates

John M. Gipson
NVI, Inc./NASA GSFC, Code 698, Greenbelt, 20771 MD, USA

Abstract. I studied the effects of including station dependent delay noise in the analysis of geodetic VLBI data. Such terms increase the observational noise, and introduce correlation between observations. Using the CONT05 sessions, I demonstrate that introducing such noise terms reduces baseline scatter, gives more realistic formal errors, and improves agreement between VLBI and GPS estimates of Polar Motion and LOD.

1 Introduction

The VLBI observable, colloquially called the "delay", is the difference in arrival time of a signal at two different stations. Roughly speaking, the delay is measured by cross-correlating the signals received at the two stations and searching for a peak. This process has an uncertainty associated with it which, for clarity, I call *measurement* noise and denote by σ_{meas}. This noise is inherent to the correlation process and depends only on the signal strength, sensitivity of the antennas, frequency sequence, and number of bits recorded. One can show, assuming SNRs commonly used in VLBI, that the measurement noise on different baselines is uncorrelated. The standard assumption in VLBI processing is that the *observational* noise in VLBI is just the measurement noise. This has the corrolary that the VLBI observations are independent.

There are several indications that this assumption is false. First, χ^2 from individual session solutions is much larger than it should be if $\sigma_{meas} = \sigma_{obs}$. Second, baseline length scatter is larger than it should be based on the formal errors. Third, comparison of EOP measurements from simultaneous VLBI sessions are inconsistent with the formal errors. All of these are indicative of unmodeled error sources and/or incorrect modeling.

There are many other error sources besides measurement noise: 1) Phase cal errors; 2) RF interference in the signals; 3) Other correlator related errors; 4) Source structure; 5) Source position errors; 6) Errors in geophysical models; 7) Mismodeling clocks and/or atmospheres; 8) Underparametrizing the time variation of clocks and/or atmospheres; etc. All of these increase the noise of individual observations. Many also introduce correlation between observations.

In this note, I look at the special case of error sources which are manifest as station dependent changes in the measured delay. Examples are cable calibration errors, and atmosphere calibration or modeling errors. Since, at any instant, these errors are the same for all observations involving a station, these observations are not independent, and the observation covariance matrix is no longer diagonal. Neglecting these correlations leads to formal errors which are too small, and incorrect estimates of parameters.

Other scientists have studied the stochastic model used in VLBI. In a prescient paper Qian (1985) discussed the effect of correlation between observations, suggested a method for estimating these correlations empirically, and demonstrated that these correlations can significantly change EOP estimates. Schuh and Wilkin (1989) derived empirical correlation coefficients from 19 VLBI sessions, but did not take the next step of modifying the normal equations. Schuh and Tesmer (2000) derived empirical correlation coefficients, and, together with the a priori variance, σ^2_{meas}, constructed the covariance matrix. They demonstrated that this improved repeatability on 36 IRIS-S sessions from December 1994 through December 1998. Tesmer (2003a) (2003b), and Tesmer and Kutterer (2004) modified the covariance matrix by inflating the diagonal terms with additional contributions which were source, station and elevation dependent.

They found a reduction in the scatter of station position of a few percent. Gipson (2006) presented an earlier stage of this research at the 2006 IVS General Meeting.

In the next section, I present the least squares equations for VLBI. In Section 3 I discuss how station dependent delay modifies the covariance matrix. In Section 4, I study the effect of including two such error sources: "Clock-like" errors are observation independent; "Atmosphere-like" errors depend on the elevation. Using the CONT05 data set, I demonstrate that including these terms:

1. Decreases baseline scatter.
2. Gives more realistic formal errors.
3. Improves agreement between VLBI and GPS EOP estimates.

2 VLBI Normal Equations

The VLBI observable $\tau_{ij}(t)$ is the difference in arrival time of a signal at two stations i, j at time t. The delay is a function of various parameters A_a, some of which we are interested in, such as station position and Earth orientation, and other "nuisance" parameters such as clock drift and tropospheric delay.

Let $F_{a,ij}(t)$ be the derivative of the delay with respect to these parameters: $F_{a,ij}(t) \equiv \frac{\partial \tau_{ij}(t)}{\partial A_a}$. In the linear approximation the delay is:

$$\tau_{ij}(t) - \tau_{0,ij}(t) = \sum_a A_a F_{a,ij}(t) + \varepsilon_{ij,obs}(t)$$

Here $\tau_{0,ij}(t)$ is the a priori delay and $\varepsilon_{ij,obs}(t)$ is the noise associated with the observation. The noise term incorporates not only the correlator noise, but other sources of noise due to mis-calibration, mis-modeling, and failure of the linear approximation. This equation can be schematically re-written as:

$$\tau_{o-c} = FA + \varepsilon$$

Let Ω be the observation covariance matrix:

$$\Omega_{ijt,klt'} = < \varepsilon_{ij,obs}(t)\varepsilon_{kl,obs}(t') > \qquad (1)$$

Here the triples ijt and klt' label the observations. The least squares equations are given by:

$$\left(F^T\Omega^{-1}F\right)A = F^T\Omega^{-1}\tau_{o-c} \qquad (2)$$

where

$$F^T\Omega^{-1}F = \sum_{ijt}\sum_{klt'} F_{b,ij}(t)(t')\Omega^{-1}_{ijt,klt'}F_{a,kl}$$

and the sum is over all observations. There is a similar expression, *mutatis mutandis*, for $F^T\Omega^{-1}\tau_{o-c}$. The normal equations can formally be inverted to solve for A_a:

$$A = \left(F^T\Omega^{-1}F\right)^{-1}F^T\Omega^{-1}\tau_{o-c}$$

The usual assumption in VLBI data analysis is that the observations are independent, or, stated differently, the noise on different observations is uncorrelated. This is equivalent to saying that the covariance matrix is diagonal.

$$\Omega_{ijt,klt'} = \sigma^2_{ij}(t) \times \left(\delta^{ij}_{kl}\delta^t_{t'}\right)$$

In this case the normal equations simplify substantially, and we have, e.g.,

$$F^T\Omega^{-1}F = \sum_{ijt} F_{b,ij}(t)F_{a,ij}(t)\frac{1}{\sigma^2_{ij}(t)}$$

3 Effect of Station Dependent Delay Noise on Covariance Matrix

In this section I describe how to incorporate the effect of a particular kind of station dependent delay noise into the normal equations. Assume that the delay τ_i at station i is given by:

$$\tau_i = \tau_{i,geom} + \tau_{i,mod} + \varepsilon_{i,A} + \varepsilon_{i,B} \ldots.$$

$\tau_{i,geom}$ is the geometric delay in a vacuum, and $\tau_{i,mod}$ incorporates additional calibration and modeling terms. The $\varepsilon_{i,A}$ are station dependent delay error terms. The observational noise $\varepsilon_{ij,obs}(t)$ for baseline ij is:

$$\varepsilon_{ij,obs}(t) = \varepsilon_{ij,meas}(t) + \varepsilon_{ij,A}(t) + \varepsilon_{ij,B}(t) + ...$$

where $\varepsilon_{ij,meas}(t)$ is the measurement noise due to the correlation process, and the remaining terms are due to different kinds of station dependent delay error: $\varepsilon_{ij,A}(t) = \varepsilon_{i,A}(t) - \varepsilon_{j,A}(t)$.

The following assumptions simplify the evaluation of the covariance matrix:

1. The additional terms are uncorrelated with the measurement noise: $< \varepsilon_A \varepsilon_{meas} >= 0$
2. Different kinds of delay noise are uncorrelated: $< \varepsilon_A \varepsilon_B >= 0$ for $A \neq B$.

3. Delay errors at different times are uncorrelated: $< \varepsilon_{ij,A}(t)\varepsilon_{kl,A}(t') >= 0$ for $t \neq t'$.

4. Delay errors at different stations are uncorrelated.

In what follows, it is crucial to distinguish between *observations* and *scans*. An observation is the measurement of the delay on an *individual* baseline. A scan is a collection of *simultaneous* observations involving a commmon source.

By assumptions 1 and 2, the cross terms in the covariance matrix vanish:

$$\begin{aligned} \Omega &= < \varepsilon^2_{meas} > + < \varepsilon^2_A > + < \varepsilon^2_B > ... \\ &= \Omega_{meas} + \Omega_A + \Omega_B .... \end{aligned}$$

The first term Ω_{meas} is the (diagonal) covariance matrix associated with the measurement process. This is the the only kind of noise included in the standard analysis. The remaining terms are due to the additional noise sources.

Assumption 3 implies that the covariance matrix is block diagonal, with each block being the covariance matrix for a single scan.

By assumption 4, cross-terms involving different stations vanish. The diagonal elements for baseline ij are:

$$\begin{aligned} \Omega_{A,ij,ij} &= < (\varepsilon_{i,A} - \varepsilon_{j,A})^2 > \\ &= < \varepsilon^2_{i,A} + \varepsilon^2_{j,A} > \\ &= \sigma^2_{i,A} + \sigma^2_{j,A} \end{aligned}$$

i.e., just the sum of the noise terms for each station. This is what you would naively expect. The total diagonal contribution is

$$\begin{aligned} \Omega_{t,ij,ij} &= \sigma^2_{ij,meas} + \sigma^2_{i,A} + \sigma^2_{j,A} + \\ &\quad \sigma^2_{i,B} + \sigma^2_{j,B} + ... \end{aligned}$$

This increase in the diagonal terms of the covariance matrix increases the formal errors of the estimated parameters.

The station dependent noise terms also introduce off-diagonal terms in the covariance matrix which are non-zero *if, and only if* the baselines have a station in common. In this case we have:

$$\begin{aligned} \Omega_{A,ij,il} &= -\Omega_{A,ij,li} \\ &= < (\varepsilon_{i,A} - \varepsilon_{j,A})(\varepsilon_{i,A} - \varepsilon_{l,A}) > \\ &= < \varepsilon^2_{i,A} >= \sigma^2_{i,A} \end{aligned}$$

These off-diagonal terms also increase the formal erorrs of the estimates.

Note that both the diagonal and off-diagonal terms depend *only* on the variance of the noise. Hence station dependent delay noise has two effects: 1) The noise level of the observations is increased; and 2) Observations involving a common station at a given time are correlated. Both effects increase the formal erorrs, and both modify the VLBI estimates.

Since, by assumption 3, the covariance matrix is block diagonal, building up the normal equations given in Eq. (2) is straightforward and done on a scan by scan basis: 1) Compute the covariance matrix for a given scan; 2) Invert it; 3) Compute the contribution of this scan to the normal matrix.

4 Station Dependent Clock and Atmosphere Noise

I modified the VLBI analysis software *solve* to take into account two kinds of correlated station dependent noise. The first kind has a constant variance independent of the observation. This might be due, for example, to short term unmodeled clock variation, or random errors in the cable calibration. I call this kind of error "clock-like". Explicity, for station j the variance is:

$$\sigma^2_{j,clk} = a^2_{j,clk}$$

Another error source is due to mis-modeling the atmosphere. In this case, I assume that the variance takes the form:

$$\sigma^2_{j,atm} = a^2_{j,atm} \times [Map(el_j)]^2$$

where $Map(el_j)$ is the mapping function. Because of the strong elevation dependence of the mapping function, low-elevation points are downweigted. Both kinds of noise introduce correlations between observations.

In this study I make the simplifying assumption that the noise terms are the same for all stations, and do not vary with time. Realistically, of course, both noise sources may be time and station dependent.

I looked at the effect of including these noise sources on 15 CONT05 sessions. This is an example of a very good large network observing over a short period of time. Because the period is short, un-modeled seasonal effects should be small. Because the sessions were good, they should be more sensitive to improvements in the analysis.

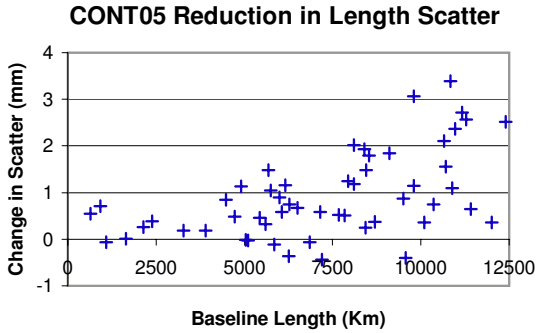

Figure 1. Difference in baseline repeatability for CONT05 data set between the standard solution and one incorporating 10 ps of atmosphere mapping function noise. Points above the x-axis are baselines where the scatter is reduced for the new solution.

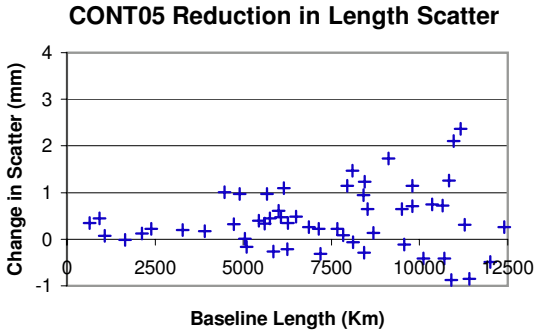

Figure 2. Difference in baseline repeatability for CONT05 data set between the standard solution and one incorporating 10 ps of atmosphere mapping function noise. Only the diagonal terms in the covariance matrix are used in the normal equations.

Figure 1 plots the difference in baseline scatter between the standard solution and a solution using the full covariance matrix where $a_{atm} = 10ps$. The new solution reduces the scatter for the vast majority (46 out of 54) baselines. The average improvement is 0.92 mm, or 12.4%. Generally speaking, the longer the baseline, the greater the improvement. On the few baselines where the scatter is worse, it is only slightly worse, i.e., well under a millimeter.

One possibility is that the improvement is due entirely or predominantly to the increase in the diagonal terms of the covariance matrix. To determine if this is true, I generated a parallel series of solutions where I included only the diagonal terms in the covariance matrix. Figure 2 is the baseline scatter plot for $a_{atm} = 10ps$. The scatter on most baselines (41/54) is improved, but the average improvement is 0.42 mm, less than half that obtained previously. This turns out to be a general feature: Including only the diagonal terms improves the solution, but not as much as including the full covariance matrix.

Table 1 summarizes the results of a series of solutions where I varied a_{atm} and a_{clk} independently. This table lists the results for using both the full covariance matrix and only the diagonal terms. For each pair of solutions the table displays: 1) Average χ^2; 2) RMS scatter; 3) Average improvement in millimeters; 4) Average improvement in percent; 5) Number of baselines where the scatter is reduced.

Introducing a clock-like noise source has little effect on the solutions. Introducing an atmosphere-like noise source generally improves the solutions with a broad peak starting around $a_{atm} = 10ps$. Note that in all instances, the results from the full covariance matrix are better than using just the diagonal terms: Including the correlations is beneficial. The χ^2 in this table is the average value over all baselines. Explictly, I use the formal errors for the baseline lengths given by *solve*, calculate the scatter and the χ^2 for each baseline, and then take the average over all baselines. For the standard solution, $\chi^2_{avg} = 2.16$, which indicates that the formal errors are too optimistic by $\sqrt{2.16} \simeq 1.47$. For the solution with $a_{atm} = 10ps$ $\chi^2_{avg} = 1.03$, indicating that the formal errors are, on average, correct. As the a_{atm} is increased beyond 10 ps, χ^2_{avg} decreases below 1, indicating that we have introduced too much extra noise.

Figure 3 plots the average improvement in baseline scatters a function of a_{atm}. It does this for both cases: full covariance matrix, or only diagonal terms. The greatest reduction in baseline scatter ocurrs around 10ps for both cases. For all values of a_{atm} the scatter is reduced, and for all values the reduction is greater if the full covariance matrix is used instead of the diagonal. Also plotted in this figure is the χ^2_{avg}. This starts at 2.16, and declines as the noise is increased. This is what you would expect. It is interesting to note that $\chi^2_{avg} \simeq 1$ at $a_{atm} = 10ps$: At the value where the baseline scatter has a mininum, the formal errors are, on average, correct.

The above examples show that including station dependent noise improves the consisteny of VLBI sessions. I also looked at the VLBI estimates of EOP, and compared them with GPS results. For this comparison I interpolated the GPS EOP estimates to the epoch of the VLBI estimates using a cubic spline. After removing

Table 1. Effect of Clock and Atmosphere Station Dependent Delay CONT05

		Full Covariance					Diagonal Only				
a_{clk}	a_{atm}	Avg	WRMS	Avg. Imp.		#BL	Avg	WRMS	Avg. Imp.		#BL
ps	ps	χ^2	mm	mm	%	Imp.	χ^2	mm	mm	%	Imp.
0	0	2.16	7.56	-	-	-	2.16	7.56	-	-	-
5	0	1.96	7.53	0.03	0.6%	30	2.07	7.57	-0.01	0.2%	26
10	0	1.65	7.52	0.04	1.0%	30	1.87	7.59	-0.03	0.1%	22
15	0	1.40	7.55	0.01	0.6%	28	1.67	7.65	-0.09	0.2%	21
20	0	1.21	7.62	-0.06	-0.4%	24	1.50	7.72	-0.16	-0.8%	20
25	0	1.07	7.72	-0.16	-1.7%	24	1.35	7.81	-0.25	-1.6%	20
0	1	2.09	7.48	0.08	1.3%	44	2.13	7.54	0.02	0.4%	36
0	2	1.93	7.32	0.24	3.8%	48	2.05	7.48	0.08	1.4%	42
0	3	1.76	7.16	0.40	6.1%	48	1.95	7.42	0.14	2.5%	43
0	4	1.61	7.02	0.54	7.9%	47	1.84	7.35	0.21	3.6%	43
0	5	1.47	6.91	0.65	9.3%	47	1.73	7.29	0.27	4.6%	43
0	6	1.36	6.83	0.73	10.4%	48	1.63	7.24	0.32	5.4%	43
0	7	1.25	6.76	0.80	11.2%	48	1.54	7.20	0.36	6.0%	41
0	8	1.17	6.70	0.86	11.8%	48	1.45	7.17	0.39	6.5%	42
0	9	1.09	6.66	0.90	12.1%	46	1.38	7.15	0.41	7.0%	41
0	10	1.03	6.64	0.92	12.4%	46	1.31	7.13	0.43	7.3%	41
0	11	0.97	6.62	0.94	12.5%	45	1.25	7.12	0.44	7.5%	40
0	12	0.92	6.60	0.96	12.6%	45	1.19	7.11	0.45	7.7%	40
0	13	0.87	6.60	0.96	12.5%	46	1.14	7.10	0.46	7.8%	40
0	14	0.83	6.60	0.96	12.4%	47	1.09	7.10	0.46	7.9%	39
0	15	0.79	6.61	0.95	12.2%	47	1.04	7.10	0.46	7.9%	39
0	20	0.65	6.68	0.88	11.0%	46	0.87	7.13	0.43	7.5%	36
0	25	0.55	6.79	0.77	9.4%	42	0.75	7.19	0.37	6.7%	36

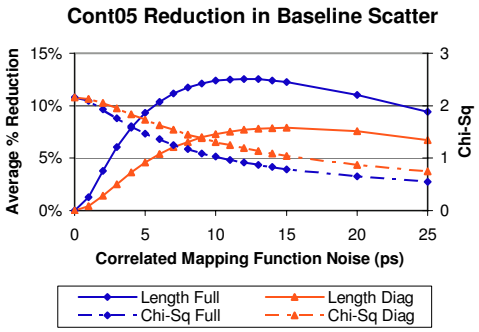

Figure 3. Average percentage improvement in baseline repeatability as a function of mapping function noise. Diamonds indicate the full covariance is used; triangles only the diagonal part of the covariance matrix. Solid lines give the average improvement in repeatability; dashed lines χ^2_{avg}.

an offset, I calculated the WRMS scatter of the difference for X-pole, Y-Pole, and LOD. Table 2 shows the results of this analysis. For each value of a_{atm} I display the WRMS scatter of the difference. For $a_{atm} > 0$, I also indicate the reduction in scatter compared to the $a_{atm} = 0$ solution. These results are presented graphically in Figure 4. As a_{atm} increases to 10 ps, the agreement between VLBI and GPS estimates of EOP improves. Beyond about 12ps there is relatively little change. Relatively speaking, the improvement in Y-Pole and LOD is much less than for X-Pole. The reasons for this are unclear.

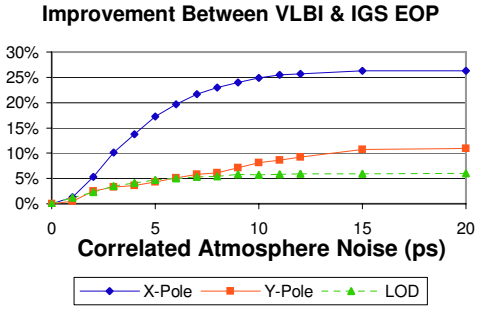

Figure 4. Including correlated atmosphere modeling error improves the agreement between VLBI and GPS estimates for EOP. Most of the improvement occurs in going from 0 ps to 10 ps of correlated noise. After 10 ps the improvement is modest.

Table 2. Comparison of VLBI & GPS EOP

	X-Pole		Y-Pole		LOD	
	RMS	%	RMS	%	RMS	%
a_{atm}	μas	Chg	μas	Chg	μs	Chg
0	60.4	-	39.2	-	17.0	-
1	59.6	1.3	39.0	0.5	16.8	1.2
2	57.2	5.3	38.2	2.6	16.6	2.4
3	54.3	10.1	37.9	3.3	16.4	3.5
4	52.1	13.7	37.8	3.6	16.3	4.1
5	50.0	17.2	37.5	4.3	16.2	4.7
6	48.5	19.7	37.2	5.1	16.1	5.1
7	47.3	21.7	36.9	5.9	16.1	5.4
8	46.5	23.0	36.8	6.1	16.1	5.4
9	45.9	24.0	36.4	7.1	16.0	5.8
10	45.4	24.8	36.0	8.2	16.0	5.8
11	45.0	25.5	35.8	8.7	16.0	5.8
12	44.9	25.7	35.6	9.2	16.0	5.8
15	44.5	26.3	35.0	10.7	16.0	5.8
20	44.5	26.3	34.9	11.0	16.0	5.8

5 Conclusion and Future Work

Using the CONT05 data set, I demonstrated that including station dependent delay noise reduces baseline scatter and results in more realistic formal errors. The effect of including clock-like errors is relatively small. In contrast, including the effect of atmospheric noise results in a dramatic decrease in baseline scatter. This improvement is not due simply to inflating the observational errors, but depends as well on the correlations introduced in the measurement. Including this error makes the VLBI estimates more consistent from day-to-day.

I also compared VLBI and GPS estimates of polar motion and LOD. I found that introducing correlated atmosphere noise improved the repeatability of all three components.

I have performed a similar analysis for other datasets including:

1. The complete set of R1s & R4s.
2. The RDV sessions.
3. High SNR experiments.
4. Sessions in which VLBI was measured by two simultaneous VLBI networks.

Lack of space prevents me from giving a full description of my results. In all instances including the effect of correlated noise reduces baseline scatter, gives more realistic formal errors, and improves the agreement between VLBI and GPS estimates of EOP. For the last data set it also improved the agreement between the VLBI estimates of EOP.

References

Gipson, J.M, (2006). Correlation due to Station Dependent Noise. 2006 IVS General Meeting Proceedings, Concepcion, Chile, D. Behrend and K. Baver (ed), pp 286-290, 2006.

Qian Zhi-han, (1985). The Correlation on VLBI Observables and Its Effects for the Determination of ERP. Shanghai Observatory.

Schuh, H. and Wilkin A. (1989) Determination of Correlation Coefficients between VLBI-Observables., Proc. Of the 7th Working Group Meeting on European VLBI, Madrid, Spain, CSIC, A. Rius Ed pp 79-91.

Schuh, H. & Tesmer, V: (2000) Considering A Priori Correlations in VLBI Data Analysis. 2000 IVS General Meeting Proceedings, p 237.

Tesmer, V. (2003a) Refinement of the Stochastic VLBI Model: First Results. 16th Working Meeting on European VLBI for Geodesy and Astrometry, pp 207-218.

Tesmer, V., Das stochastische Modell bei der VLBI-Anwertung, PhD thesis, University of Munich, Munich, Germany, 2003.

Tesmer, V., and Kutterer, H. (2004). An advanced Stochastic Model for VLBI Observations and its Applications to VLBI Data Analysis. 2004 IVS Generaml Meeting Proceedings, Ottawa, Canada, N. Vandenberg and K. Baver (ed), pp 296-300.

Optimum modeling of troposphere and clock parameters in VLBI

A. Pany, J. Wresnik, J. Boehm, H. Schuh
Vienna University of Technology, Institute of Geodesy and Geophysics, Research Group Advanced Geodesy, Gusshausstr. 27-29, 1040 Vienna

Abstract. Within the IVS (International VLBI Service for Geodesy and Astrometry) there are efforts to significantly improve the existing system of geodetic VLBI (Very Long Baseline Interferometry) ('VLBI2010') [Niell et al. 2004]. To be able to discuss and plan future observing strategies and station networks it is necessary to carry out simulation studies. For these simulations it is of prime importance that stochastic parameters like the tropospheric wet delay or the clock behaviour are realistically simulated and subsequently estimated as good as possible. The work presented here is dealing with the best parameterization of troposphere and clock parameters. Based on the analyses by Treuhaft and Lanyi [1987] and Herring et al. [1990] time series for the wet zenith delay and stochastic clock variations are simulated using distinct variances for these stochastic processes. A cumulative delay time series consisting of wet delay (wet zenith delay mapped to randomly created elevations), station clock and white noise is computed and used as observations to estimate troposphere and clock parameters as well as a station height to investigate the impact of the parameterization of the stochastic parameters on the estimation of geodetic parameters. The estimation of wet zenith delays, clock parameters and heights is performed with a classical least squares adjustment and with Kalman filtering. It can be shown that the limiting factor for VLBI analysis is the variability of the wet troposphere and that the Kalman filter algorithm provides better results than the classical least squares method for white noises of 4 and 8 ps, respectively.

Keywords. VLBI, simulation, VLBI2010, wet zenith delay, clock

1 Introduction

As it is the only measurement technique that provides the link between the celestial and the terrestrial reference system [Brosche and Schuh 1999] VLBI is essential for geosciences and navigation applications. In recent years VLBI has also become more and more important for socially relevant topics like natural hazards or climate research [Niell et al. 2004]. As the parameters of interest, e.g. the sea level rise, are in the order of magnitude of a few millimeters per year, it has become necessary to improve the accuracy and performance of the existing VLBI system in order to be able to meet the demands in the near future. Within the project VLBI2010 the goals of future VLBI have been defined to be [Niell et al. 2004]:

- an accuracy of 1mm on global baselines,
- the performance of continuous measurements for obtaining time series, especially of the earth rotation parameters, and
- the distribution of first geodetic results within 24 hours.

To be able to discuss and plan future observing strategies and station networks it is necessary to carry out simulation studies. For these simulations it is of prime importance that stochastic parameters like the tropospheric wet delay or the clock behaviour are realistically simulated and subsequently estimated as good as possible. Time series for the stochastic variations of wet zenith delay and station clock were simulated for one single station and added together with white noise to account for the inaccuracy of the VLBI receiving system. The troposphere and clock parameters were then estimated testing different parameterizations and two estimation algorithms, classical least squares and Kalman filtering. To investigate the impact of the parameterization on geodetic

parameters the station height was estimated additionally.

The goal of these studies was to optimize the estimation of the parameters of interest, troposphere and clock parameters as well as station height, to figure out how the parameterization of the stochastic parameters influences the estimation of geodetic parameters and to investigate the impact of the parameterization on the correlations between the estimated parameters.

Chapter two deals with the simulation procedure. It is described which parameters were used to compute the time series of wet zenith delay and station clock and how the observations for the adjustment computation were derived. Chapter three explains which estimation algorithms were used and which parameterizations for wet zenith delay and station clock were tested. In chapter four the most important results are presented and chapter five finally gives a brief summary, the conclusions and comments about future perspectives.

2 Simulation of time series

The variations of the wet zenith delay are due to fluctuations of the refractive index n. Assuming the validity of Taylor's theory of frozen-random-medium [Wheelon 2001] the spatial variations of tropospheric wet delay can be described with the structure function [Treuhaft and Lanyi 1987]

$$D_{x,\Theta,\Phi}(\boldsymbol{\rho}) = \mathrm{E}\left(\left(\tau_{\Theta,\Phi}(\mathbf{x}+\boldsymbol{\rho}) - \tau_{\Theta,\Phi}(\mathbf{x})\right)^2\right), \qquad (2.1)$$

where $\mathbf{x}$ denotes the position of a VLBI antenna, $\boldsymbol{\rho}$ the separation to another antenna and τ the group delay. Θ and Φ denote elevation and azimuth of the observed radio source and E is the expectation value. Temporal fluctuations can be calculated by simply substituting $\boldsymbol{\rho}$ by $\mathbf{v}$T where $\mathbf{v}$ is the wind velocity vector and T denotes the time interval for which the structure function is to be evaluated [Treuhaft and Lanyi 1987].

For short time periods it is valid to approximate this structure function with a random walk [Herring et al. 1990]. The structure function of a stochastic process is related to its power spectral density PSD by

$$D(T) = PSD \cdot T\,. \qquad (2.2)$$

Assuming a typical value for the PSD, the time series of the wet zenith delay can be computed with

$$\tau(t+T) = \tau(t) + randn \cdot \sqrt{D(T)}\,, \qquad (2.3)$$

where *randn* can take random values with zero mean and a standard deviation of one. Typical PSD values are between 0.1 ps²/s and 0.7 ps²/s where the first value is rather small and the latter one describes a strongly varying troposphere. These values are commonly used for simulation studies carried out in VLBI2010 [Wresnik and Boehm 2006].

According to Herring et al. [1990] the stochastic variations of the station clock can be described as the sum of a random walk and an integrated random walk. The latter can be ignored for the investigations presented here. The accuracy of a clock is usually given by the Allan Standard Deviation (ASD) which can be converted into a value corresponding to a PSD (when ignoring the integrated random walk) and the simulation can therefore be carried out using equation (2.3).

For the simulations two clocks with an ASD of $2 \cdot 10^{-15}$ @ 15 min and $1 \cdot 10^{-14}$ @ 50 min, respectively were used. The first ASD represents a highly accurate clock whereas the accuracy of the second clock is rather moderate.

In order to be able to separate wet zenith delay, station clock and station height within the estimation procedure it was necessary to create a random sequence of elevation angles. The simulated values of the wet zenith delay were multiplied by a simple mapping function to obtain slant delays. To account for the random delay measurement error, a white noise process was superimposed. Three different values were used for creating the white noise: 4 ps, 8 ps and 16 ps. The final cumulative delay was computed by simply adding the three time series of slant wet delay (*wd*), station clock (*clk*) and white noise (*wn*):

$$delay = wd + clk + wn\,. \qquad (2.4)$$

The time series were computed for 24 hours with a temporal resolution of 30 s. After adding up all time series this resulted in a final number of 2881 observations. The simulations were performed for all possible combinations of PSD, ASD and white noise values.

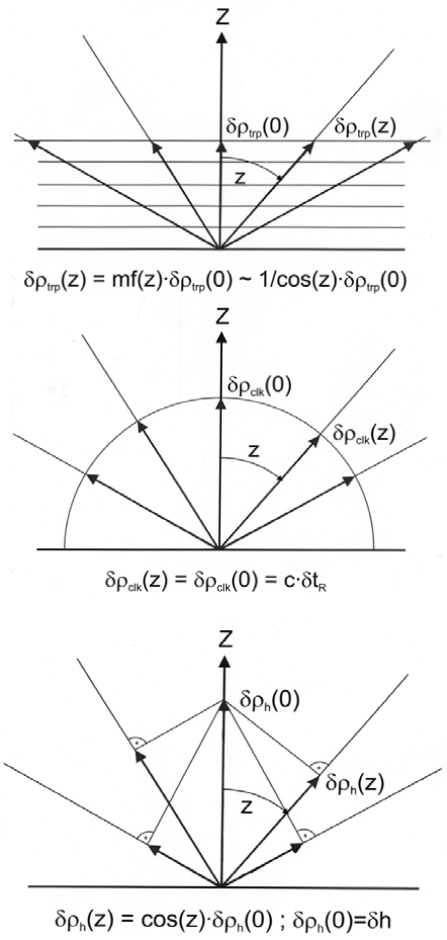

Fig. 1 Dependencies on the zenith distance z: The uppermost figure shows the wet delay (increasing with zenith distance), the middle figure shows the station clock (constant with zenith distance), and the lower plot is for the station height. The influence of the station height error on an observation is decreasing with increasing zenith distances.

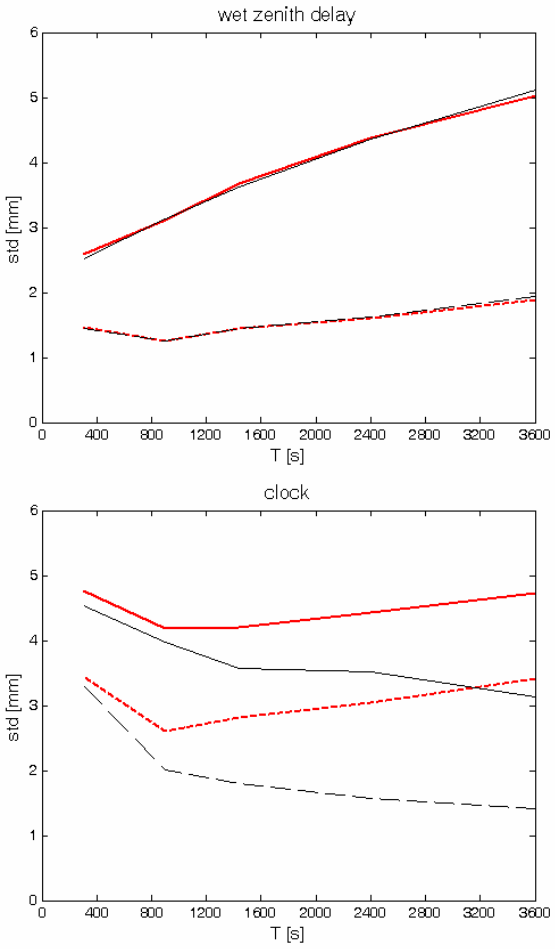

Fig. 2 The upper plot shows the mean standard deviation of wet zenith delay versus the length of estimation interval, the lower plot shows the mean standard deviation of the station clock (dashed: PSD 0.1 ps²/s, solid: PSD 0.7 ps²/s, black (thin lines): ASD $2 \cdot 10^{-15}$ @ 15 min, red (bold lines): ASD $1 \cdot 10^{-14}$ @ 50 min).

3 The estimation procedure

The goal of the estimation procedure was then to calculate troposphere and clock parameters as well as the station height out of the cumulative delay described by equation (2.4). This separation is possible because all of the parameters of interest possess different dependencies on the elevation angle as can be deduced from Figure 1.

The estimation was carried out using two different algorithms, the classical least squares approach and Kalman filtering. Within the scope of the classical least squares algorithm, three functional models for the parameterization of wet zenith delay and station clock were tested: piecewise linear functions, second order polynomials and third order polynomials. The length of the time interval for which the polynomials were estimated was varied between 300, 900, 1440, 2400 and 3600 s. For the piecewise linear functions an offset at the beginning and one rate for each time interval were estimated. Contrarily, for the second and third order polynomials all coefficients were estimated for each time interval. Thus, it was necessary to introduce conditions (matching of the zeroth and first derivative at inner points) in order to obtain continuous functions.

For each model the adjustment computation was performed with the time intervals mentioned above

and using time series of possible combinations of PSD, ASD, and wn. The standard deviations of the wet zenith delay and clock residuals were computed for the 24 hour time series, and to achieve reliable results this procedure was repeated 20 times for wet zenith delay and clock. As the station height was estimated only once per 24 hours, the standard deviation of the station height was determined over 300 estimates.

The Kalman filter was set up as described in Herring et al. [1990]. The station height which is a deterministic parameter was estimated with optimal linear filtering. Wet zenith delay and station clock which are stochastic parameters were estimated with optimal linear smoothing as described in Gelb [1974]. Again residuals and standard deviations were derived for wet zenith delay, clock and station height as described above.

4 Results

Figure 2 (top) shows the mean standard deviation of wet zenith delay in mm versus the length of time interval that was used for the estimation. The two dashed lines at the bottom show results of simulations with a PSD of 0.1 ps²/s but with different clock accuracies. Wet zenith delay and station clock were both modeled with piecewise linear functions. The lines are nearly identical, which indicates that the accuracy of station clock does not significantly affect the estimation of wet zenith delay. The solid lines at the top of the figure show the same results but for a PSD of 0.7 ps²/s. Again it can be seen that the lines are nearly identical. It can also be deduced from this figure that the variability of the troposphere is the dominant effect on the estimation of the wet zenith delay and of the station height (not shown here).

Performing the same investigations on the station clock it can be stated that its estimation is affected by the accuracy of the clock as well as by the PSD that was used for the simulation of the wet zenith delay time series as can be seen in Figure 2 (lower plot). A higher PSD of the wet zenith delay leads the mean standard deviation of station clock to be shifted upwards whereas the clock accuracy determines the slope of the lines. From the bottom plot in Figure 2 it can also be concluded that an estimation interval of 3600 s leads to the best results for the more accurate clock (ASD $2 \cdot 10^{-15}$ @ 15 min) within the tested range of values but for the average clock (ASD $1 \cdot 10^{-14}$ @ 50 min) the best results could be obtained with an estimation interval of 900 s. The statements above lead to the conclusion that the wet zenith delay is the limiting factor in VLBI analysis.

For the Kalman filter algorithm it is necessary to provide a priori values for the process noise variances of the stochastic processes. It was investigated how these values impact the estimation of wet zenith delay and station clock. The results for the wet zenith delay can be seen in the top plots of Figures 3a and 3b, the results for the station clock at the bottom. The thin red lines show the simulated time series, the bold black lines show the estimation.

In Figure 3a the a priori value for the process noise variance of the wet zenith delay was chosen as low as 0.0001 mm². The variation of the wet zenith delay is therefore strongly suppressed in the estimation which leads to huge errors in the estimation of the station clock and to an error in station height of up to 30 mm.

If the a priori process noise variance of the wet zenith delay is chosen too high (1000 mm²), the wet zenith delay estimation is varying too much and the estimation of the station clock is too smooth as can be seen in Figure 3b. In this case the error in height estimation is only 0.8 mm.

In practice the correct process noise variance of the troposphere will not be known and has to be determined. According to Herring et al. [1990] it is possible to determine the PSD of the wet zenith delay out of the VLBI rate observables. However, the question is how accurate the process noise variance has to be determined in order to receive results as good as possible. Figures 3a and 3b indicate that the error in the estimation of geodetic parameters due to an incorrect process noise variance of wet zenith delay is significantly smaller if it is chosen too high than too low.

Very interesting is the comparison of the results obtained by classical least squares adjustment with piecewise linear functions and Kalman filtering. Table 1 shows the standard deviation of station height in terms of the used estimation algorithm and white noise, PSD and ASD of the simulation. Values written in bold letters are results of simulations with a PSD of 0.7 ps²/s, otherwise with a PSD of 0.1 ps²/s. Values written in italic letters

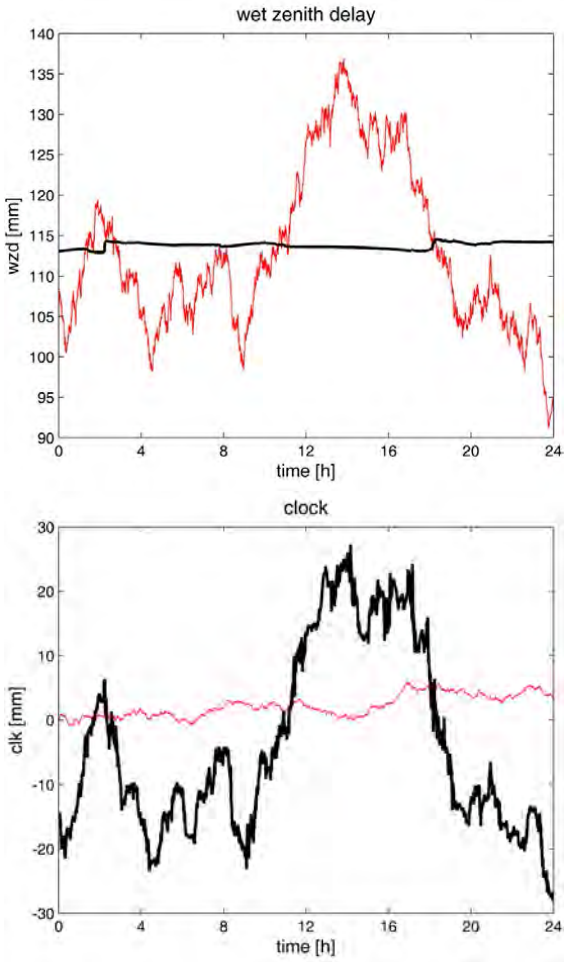

Fig. 3a Impact of the a priori process noise variance of wet zenith delay on the estimation: The upper figure shows the wet zenith delay, the lower figure shows the station clock. The a priori process noise variance of wet zenith delay was chosen as 0.0001 mm² which is too low. Red (thin) lines: simulated data, black (bold) lines: estimation.

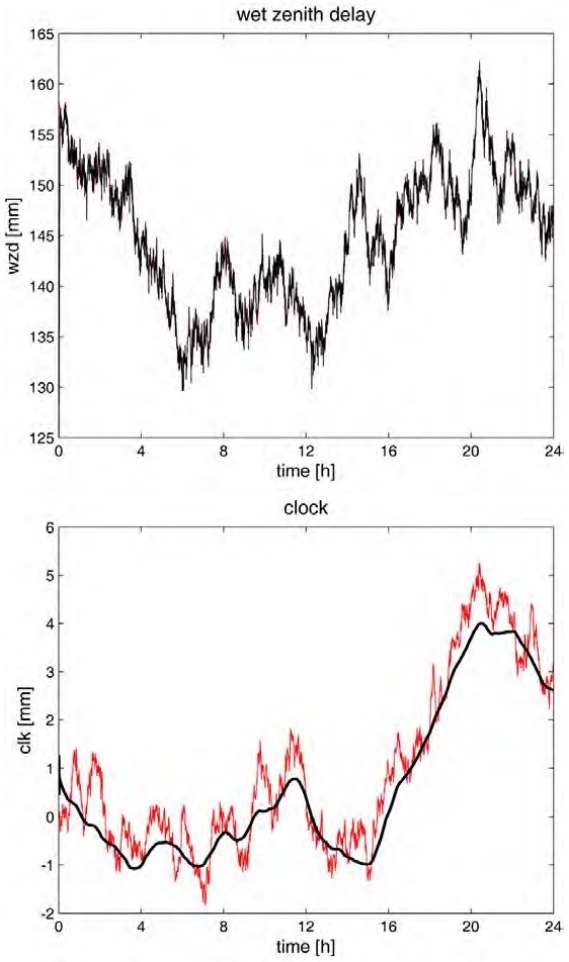

Fig 3b Impact of the a priori process noise variance of wet zenith delay on the estimation: The upper figure shows the wet zenith delay, the lower figure shows the station clock. The a priori process noise variance of wet zenith delay was chosen as 1000 mm² which is much too low. Red (thin) lines: simulated data, black (bold) lines: estimation.

indicate simulations with the more accurate clock (ASD $2 \cdot 10^{-15}$ @ 15 min), otherwise with the less accurate clock (ASD $1 \cdot 10^{-14}$ @ 50 min).

Comparing the first two columns of Table 1 (i.e. for a wn of 4 ps) it can be seen that the difference in height standard deviation due to the different variability of troposphere is 0.5 mm for the classical least squares estimate but only 0.1 to 0.2 mm for the Kalman filter solution. This effect can also be seen for a wn of 8 ps indicating that Kalman filtering is less sensitive to the variability of wet zenith delay than the classical least squares approach. This result seems to be reasonable if one considers that information about process noise variances are a priori included in the Kalman filter. Furthermore, it can be concluded that the impact of white noise is greater for the filter algorithm.

Finally it can be seen that the Kalman filter provides better estimates of station height for a white noise of 4 ps. For a white noise of 8 ps the Kalman filter solution is significantly better for the highly variable troposphere and for a white noise of 16 ps Kalman filter and least squares adjustment with piecewise linear functions are of equal precision.

Table 1 Standard deviation of height residuals in terms of wn, PSD, ASD and the estimation algorithm. Bold numbers: PSD 0.7 ps²/s, non-bold numbers: PSD 0.1 ps²/s, italic numbers: ASD $2 \cdot 10^{-15}$ @ 15 min, non-italic numbers: ASD $1 \cdot 10^{-14}$ @ 50 min.

wn = 4 ps		wn = 8 ps		wn = 16 ps	
PLF	KF	PLF	KF	PLF	KF
0.4	*0.3*	*0.6*	*0.6*	*0.8*	*1.1*
0.4	0.3	0.5	0.7	1.0	1.1
0.9	***0.5***	***1.1***	***0.5***	***1.2***	***1.2***
0.9	**04**	**0.9**	**0.6**	**1.0**	**0.8**

5 Summary and Outlook

Some important conclusions from the investigations described above can be drawn: First of all and most important is that it could be shown that the limiting factor in VLBI analysis clearly is the variability of the wet troposphere. Not shown here but derived in a diploma thesis [Pany 2007] is that the second limiting factor is the white noise. For 4 and 8 ps the variability of wet delay is dominating the estimation accuracy whereas for a white noise of 16 ps it is the white noise which is limiting the accuracy of all results. The accuracy of the station clock is the least important factor for VLBI analysis in this context.

The treatment of the wet zenith delay as stochastic parameter with an update at every observation epoch in the Kalman filter is a very good tool to account for the high variability in the wet troposphere. The variability of the station clock can be deduced from the ASD which is normally known. It has been shown with somewhat extreme values that the a priori value of the process noise variance of wet delay is significantly affecting the estimation which means that this value should be determined properly. Thus, future investigations with focus on the determination of the process noise variance of the wet zenith delay will be necessary.

The direct comparison of the height estimates with both estimation algorithms has proven that the Kalman filter provides better results for small white noise values, especially for a highly variable troposphere. For a white noise of 16 ps it was not possible to draw any conclusions.

One limitation of the approach presented here is the simulation of the wet zenith delay as a random walk. Future simulations will use a turbulence model that provides a more realistic treatment of the variations of wet delay as spatial variations are also taken into account.

References

Brosche, P., Schuh, H. (1990). Neue Entwicklungen in der Astrometrie und ihre Bedeutung für die Geodäsie. *ZfV*, 11/1999, pp 343-349

Gelb, A. (1974). Applied Optimal Estimation. MIT Press, Cambridge Mass.

Herring, T. A., Davis, J. L., Shapiro, I. I. (1990). Geodesy by Radio Interferometry: The Application of Kalman Filtering to the Analysis of Very Long Baseline Interferometry Data. *Journal of Geophysical Research*, Vol. 95, No. 98, pp 12561-12581

Niell, A., Whitney, A., Petrachenko, B., Schlüter, W., Vandenberg, N., Hase, H., Koyama, Y., Ma, C., Schuh, H., Tuccari, G. (2004). VLBI2010: Current and Future Requirements for Geodetic VLBI Systems. *IVS Memorandum*, 2006-008v01, 16. September 2004

Pany, A. (2007). Optimum modeling of troposphere and clock parameters in VLBI, diploma thesis at the Vienna University of Technology, Institute of Geodesy and Geophysics

Treuhaft, R. N., Lanyi, G. E. (1987). The effect of the dynamic wet troposphere on radio interferometric measurements. *Radio Science*, Volume 22, Number 2, pp 251-265

Wheelon, A. D. (2001). Electromagnetic Scintillation – I. Geometrical Optics. Cambridge University Press, Cambridge, pp 242-246

Wresnik, J., Böhm, J. (2006). V2C Simulations at IGG Vienna. *IVS Memorandum*, 2006-010v03, 7 September 2006

Using source maps for scheduling and data analysis: approaches and strategies

L. Petrov
NVI, Inc./NASA GSFC, Code 698, Greenbelt, 20771 MD, USA

Abstract. Since almost all the sources observed with VLBI at intercontinental baselines are resolved, information about source structure should be utilized during scheduling and analysis of geodetic VLBI experiments. I collected the database of images of ~ 4000 sources from analysis of VLBA and Australian LBA array observations. Analysis of images and calibrated visibilities allowed us to select a list of 230 of the best sources for including in geodetic observing schedules. These sources have a) a significant correlated flux density at long baselines, b) a significant compactness index, and c) a least asymmetric core. For these sources the coherence function depends mainly on the length of the projected baseline, and neglecting its dependence on baseline orientation produces errors in the coherence amplitude prediction less than 20%. Usage of source maps in the form of an expansion over a set of δ-functions in data reduction process requires great care. I found that the traditional hybrid CLEAN algorithm produces maps which are not always suitable for reduction of geodetic experiments, since the noise in data makes computation of the contribution of source structure to group delay highly instable.

Keywords. astrometry, data analysis, VLBI

1 Introduction

Almost all the sources observed with VLBI at intercontinental baselines are resolved and cannot be considered as point-like. The presence of detectable source structure affects both prediction of the amplitude of the coherence function and the observed value of group delay.

According to the van Cittert–Zernike theorem, the interferometric coherence function V is related to the source position vector $\vec{s}$, baseline vector $\vec{b}$, the angular frequency of radiation ω through the two-dimensional Fourier-transform of the source brightness distribution $I(\vec{p})$:

$$\begin{aligned} \mathcal{F}(\vec{b},\omega) &= \int\!\!\int I(\vec{p},\omega) e^{-i\frac{\omega}{c}\vec{b}\cdot\vec{p}}\, d\vec{p} \\ V(\vec{b},\omega,\vec{s}) &= e^{i\frac{\omega}{c}\vec{b}\cdot\vec{s}} \times \mathcal{F}(\vec{b},\omega) \end{aligned} \tag{1}$$

The Position of a point in the image plane, which is perpendicular to the direction on the source $\vec{s}$, is designated by a two-dimensional vector $\vec{p}$ which can be expanded at two orthogonal vectors $\vec{p}_x$, $\vec{p}_y$. The second ort, $\vec{p}_y$, is defined as a unit vector laid in the plane of source vector $\vec{s}$ and the celestial pole vector $\vec{z} = (0,0,1)^\top$. The first ort, $\vec{p}_x$, is perpendicular to both $\vec{s}$ and $\vec{p}_y$, so that $(\vec{p}_x, \vec{p}_y, \vec{s})$ forms the right triad. Vector $\vec{p}_x$ points towards the direction of decrease of right ascension, and $\vec{p}_y$ points towards the direction of increase of increase of declination.

$$\begin{aligned} \vec{p}_x &= \frac{\vec{s}\times\vec{z}}{|\vec{s}\times\vec{z}|} \\ \vec{p}_y &= \frac{\vec{s}\times\vec{p}_x}{|\vec{s}\times\vec{p}_x|} \end{aligned} \tag{2}$$

The proof of the van Cittert–Zernike theorem can be found in physics textbooks, for instance in Born & Wolf (2002). The amplitude of the coherence function, phase delay τ_p and group delay τ_g, also depends on the harmonic of the Fourier-transform of the source brightness distribution:

$$\begin{aligned} &\mathrm{Amp}(\vec{b},\omega,\vec{s}) = \sqrt{\mathrm{Re}^2(\mathcal{F}) + \mathrm{Im}^2(\mathcal{F})} \\ &\tau_p = \tfrac{1}{c}\,\vec{b}\cdot\vec{s} + \frac{1}{\omega}\mathrm{arctg}\frac{\mathrm{Im}(\mathcal{F})}{\mathrm{Re}(\mathcal{F})} + O(c^{-2}) \\ &\tau_g = \tfrac{1}{c}\,\vec{b}\cdot\vec{s} + \frac{\mathrm{Re}(\mathcal{F})\frac{\partial}{\partial\omega}\mathrm{Im}(\mathcal{F}) - \mathrm{Im}(\mathcal{F})\frac{\partial}{\partial\omega}\mathrm{Re}(\mathcal{F})}{\mathrm{Re}^2(\mathcal{F}) + \mathrm{Im}^2(\mathcal{F})} \\ &\qquad + O(c^{-2}) \end{aligned} \tag{3}$$

The second term in the expression for delays is zero if the source is point-like, and therefore, it describes the contribution of source structure.

The unmodeled source structure contribution causes both random and systematic errors in VLBI results, so it is desirable that this term should be accounted for in the reduction model. Although the amplitude of the coherence function is not used directly in geodetic VLBI data analysis, it is important to have a realistic prediction of this quantity during scheduling, in order to correctly calculate the integration time required for reaching a targeted signal-to-noise ratio.

It has been demonstrated many times since the 1980s, for instance, Cotton (1980); Zeppenfeld (1993); Sovers (2002), that information from source maps produced by the hybrid mapping algorithm can be applied for solving or at least alleviating the problem. However, using sources maps for scheduling and data reduction did not become a routine analysis procedure, because maps were not available for the majority of the sources. The situation has recently changed dramatically. Long-term projects of producing maps from the current and past VLBA and Australian LBA observations under the RDV, the VLBA Calibrator survey (VCS), and the southern survey projects yielded maps for almost all the sources ever observed under geodetic and astrometric programs. This paper is focused on using this information. In section 2, the image database is described. In section 3, the procedure for creation the new list of geodetic sources is outlined. in section 4, I discuss approaches for using source maps for scheduling. In section 5 problems of using maps for data reduction are mentioned.

2 Image database

Although astronomers have produced images from analysis of VLBI observations from early 1970s, to date there is no a central image repository. Pictures of contour maps of observed sources may be found in literature, however, using source structure information for scheduling and data reduction requires a representation of the two-dimensional function of the brightness distribution in a digital form, not in a form of nice pictures.

I created the image database using maps produced by Dr. Yu. Y. Kovalev, A. Pushkarev, A. Fey, G. Taylor, N. Corey, R. Ojha, members of the MOJAVE team and others who kindly agreed to make results of their work publicly available. These maps were made by analyzing VLBI observations in the framework of the RDV, VCS, MOJAVE, and VIPS projects observed at the VLBA. The database contains 1) images in fits-image format, 2) the visibility data calibrated using both the a priori antenna gains and system temperatures, as well as the a posteriori gain corrections determined by the hybrid image restoration algorithm, 3) auxiliary files.

The database consists of two levels. At the first level, the data are presented in the form at which the analyst has provided them. The data in the `image_orig` directory are split into 63 subdirectories which correspond either to a project or a project segment.

At the second level, the data are re-arranged to the form which is suitable to automatic processing. First, all sources are renamed to 10-character long IAU J2000-names. Second, all files related to a given source are put in the subdirectory which has the same name as the source. Third, the data files are renamed. The data file has name in the form: `SSSSSSSSSS_B_DDDDDDDDDD_AAA_TTT.EEEE`, where `SSSSSSSSSS` is the 10-character long IAU J2000 source name, `B` is the observing band: one of S for 2.2 GHz, C for 5.0 GHz, X for 8.6 GHz, U for 15.0 GHz, K for 22 GHz and Q for 43 GHz; `DDDDDDDDDD` is the nominal start date of the experiment; `AAA` is the analyst code; `TTT` is the data type; and `EEE` is the file extension, which reflects the data format.

There are 5 files for each image with the following combinations of the data type and data format: 1) `uvs.fits` — calibrated visibility data in FITS-format; 2) `map.fits` — an image in the FITS-format. This file keeps both the image in the form of the pixel two-dimensional array and in the form of a an expansion over a set of δ-functions or, using another language, the so-called CLEAN-components. 3) `rad.ps` — a plot in the postscript format of the dependence of the calibrated visibility function, averaged over time within a scan and over intermediate frequencies within a band, as a function of the length of the projected baseline to the plane normal to the source direction. 4) `map.ps` — a contour map in the postscript format of the image convolved with the dirty beam. 5) `cfd.tab` — a table in the ascii format of the correlated flux density estimates: a) the total flux density integrated over the map, b) the median value of the correlated flux density at baselines shorter than 900 km;

Table 1. Statistics of sources in the database per band

Band	# sources	# images
S	3319	7894
C	1119	1119
X	3243	7947
U	299	2072
K	270	890
Q	132	267

Table 2. The number of images at X and S band at each declination zone

Zone	total	X and S		X or S	
$\delta > -45^\circ$	3518	3044	86.5%	3336	94.8%
$\delta < -45^\circ$	143	4	2.7%	26	18.2%

c) the median value of the correlated flux density at baselines longer than 5000 km; d) the rms of the image noise.

Finally, the headers in files with visibilities and images in FITS-format were modified: the verbose history comments are removed and additional meta-information is included: a) precise source position and its errors; b) the Table of estimates of the correlated flux density; c) names of the authors who produced the image; d) the URL of the project; e) references to the papers related to the project.

To date, the database level 2 has 125,126 files of 20189 images of 3991 sources. For about 1/3 of these sources, 1440 objects, images at more than one epoch are available. Several experiments were processed by two independent analysts. Both versions of images are present in the database. The statistics of sources in the databases is presented in Table 1.

Since the vast majority of the maps were produced by analyzing observations at the VLBA, the distribution of sources with available images is quite different in the northern and southern hemispheres. The separate statistics are presented in Table 2. Among sources with declination $> -45^\circ$ that are not imaged, the majority of them are too weak and do not have enough data collected in order to produce a meaningful image.

The first[1] and the second[2] level of the image database is available in the Internet.

[1] `http://lacerta.gsfc.nasa.gov/image_orig/`
[2] `http://lacerta.gsfc.nasa.gov/vlbi/images/`

3 List of geodetic sources

The image database was used for selecting the list of sources best suitable for using in VLBI geodetic observing programs. Three criteria played a role in selection: 1) correlated flux density at long baselines; 2) compactness; 3) low spread with respect to a smooth line at plots of dependence of the correlated flux density on the length of the projected baseline. The rational for excluding weak sources is obvious: the formal uncertainties are reciprocal to the correlated flux density. The sources with extended structure, i.e. low compactness, are avoided, because the maps with high dynamic range are required for adequate modeling source structure effects. The sources with a highly asymmetric core that exhibit a significant spread at plots of dependence of the correlated flux density versus the length of the projected baseline were not selected because their images have a tendency to evolve to double and more complex structure, and remaining errors for correction for source structure using non-perfect maps may still be rather high.

The selection procedure consists of several steps. At the first step, the median correlated flux density at baselines with projected length longer than 5000 km were computed for all the sources using the calibrated visibility data. Then the ratio of the correlated flux density at long baselines to the correlated flux density integrated over the map, the so-called compactness index, was computed for each source. The closer the compactness index is to unity, the greater the share of radiation that comes from the unresolved detail of the source. Finally, the sources that have the median correlated flux density at long baselines > 200 mJy in the declination zone $[+10^\circ, +40^\circ]$ and > 300 mJy at other part of the sky were selected. If images at different epochs were available, the source was selected if it had the correlated flux density greater than the threshold for at least one epoch. In total, 584 objects were selected at the first step.

During the second step, images were scrutinized using a Web-oriented software, and for those objects that had maps from more than one epoch, a "representative image" was manually selected. By default, the last epoch is considered as representative. If the circumstances of observations were not favorable, and the *uv*-coverage was poor, another epoch with an image of better quality was selected using subjective criteria.

Figure 1. Example of the source map with the suitability class 1 ("perfect")

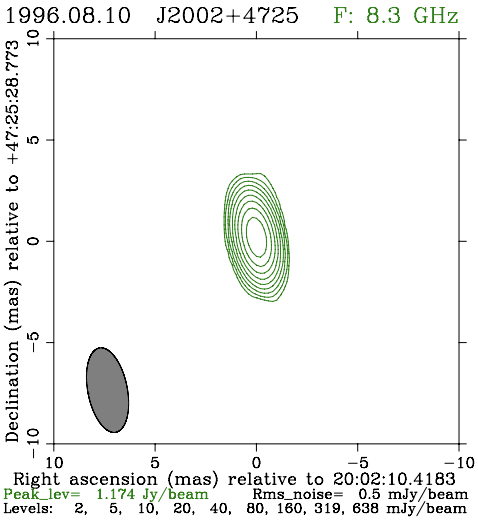

Figure 2. Example of the plot of dependence of the correlated flux density on the length of the projected baseline for a source with the suitability class 1 ("perfect")

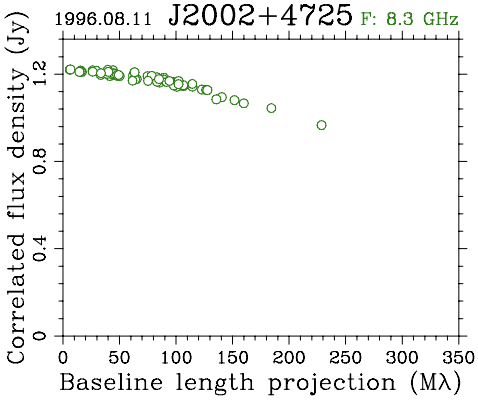

During the third step, a class in the range of 1–4 as a measure of suitability for geodetic observations was assigned to each source.

- Suitability class 1 ("perfect") means that at both bands the source has a compactness index greater than 0.8, and it has a very small spread at plots of calibrated visibilities versus the length of the baseline projected to the plane normal to the source direction, because it does not have image asymmetries (Figures 1–2).

- Suitability class 2 ("good") means that at both bands the source has a compactness index in the range of 0.4–0.8, the scatter of the calibrated visibilities versus the length of the projected baseline about the best fit smooth line is less than 20%, the image does not show significant extended details, and the source core does not have significant deviations from the elliptical structure.

- Suitability class 3 ("bad") means that the source is still detected even at long baselines at both bands, but either has a compactness index is less than 0.4 or has significant image asymmetries that cause a large spread at plots of calibrated visibilities versus the length of the baseline projected to the plane normal to the source direction. (Figures 3–4).

Figure 3. Example of the source map with the suitability class 3 ("bad")

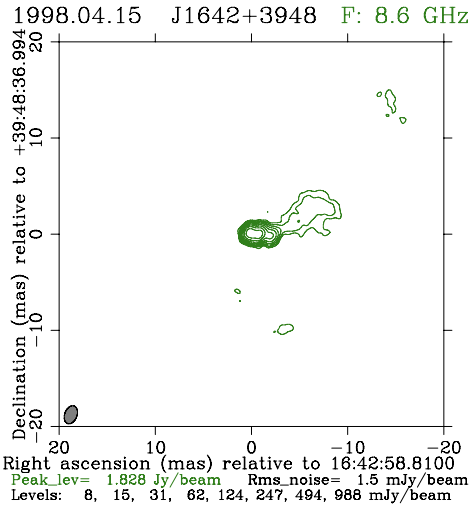

Figure 4. Example of the plot of dependence of the correlated flux density on the length of the projected baseline for a source with suitability class 3 ("bad")

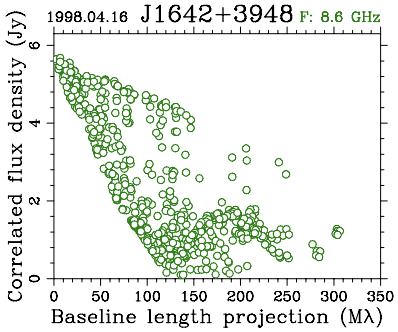

- Suitability class 4 ("unsuitable") means that at least at one band the source is too weak and not compact enough to be even detected

Table 3. The distribution of sources over classes at the old, pre–2007 list and proposed, post–2007 list

Class	pre–2007 list	post–2007 list
1	**4**	**45**
2	**43**	**185**
3	50	0
4	14	0
total	117	230

at baselines longer than 5000 km, i.e. the correlated flux density at long baselines is less than 100 mJy.

The initial classes were assigned automatically, and they were adjusted manually with use of a Web-oriented software. The sources with class 1 and 2, in total 230 objects, are recommended for observing in geodetic programs. The new list is available on the Web[3]. In comparison with the old, pre–2007 list, the total number of sources in the proposed geodetic list is doubled, but many strong asymmetric sources were removed. Approximately 40% of the sources from the old list were retained. Table 3 summarizes the sources distribution over classes.

4 Using maps for scheduling

The preferable way for using source structure information for scheduling is to use images in the form of an expansion over a set of δ-functions. This work is in progress. As an intermediate step, a simplified model of source structure was implemented in the scheduling software SKED. The dependence of the correlated flux density on the length of the projected baseline was approximated by a polynomial of the 3-rd degree using the least squares. These polynomials were used for computing the table of dependence of the correlated flux density on the length of the projected baseline with a step of 1000 km. Since the selection criteria for the proposed list of geodetic sources were developed to avoid sources with a significant spread of visibilities with respect to a smooth line, this simplified approach is expected to have an error of no more than 20–30% for these sources. Precise prediction of the fringe amplitude allows us to reduce the rate of non-detections and further optimize the schedule.

[3] `http://vlbi.gsfc.nasa.gov/pet/discussion/sou_list`

5 Using maps for data reduction

Computation of the contribution of source structure to group delay according to equation 3 is straightforward (Charlot (1990)), provided the two-dimensional Fourier-transform of the image is given. However, the true image of the source is not known, only its approximate model. The hybrid CLEAN method, traditionally used for image restoration in analysis of VLBI data, represents the brightness distribution in the form of the expansion over a set of δ-functions:

$$I(p_x, p_y) = \sum_i^n A_i \, \delta(x - p_{xi}, y - p_{yi}) \qquad (4)$$

The Fourier-transform of the brightness distribution in this form is a sum of sinusoids which fits the visibility data at points of observation. It should be noted that the representation of an image of an active galactic nuclei object in the form of a set of δ-functions is at odds with physical models of these sources that require a certain degree of smoothness in the brightness distribution. Smooth, good-looking images presented in figures 3 and 1 are produced by convolving $I(p_x, p_y)$ with the so-called "clean beam" in the form of a Gaussian function that represents an idealized response of the array with no gaps in the uv-coverage. However, this smoothed image does not fit the visibility data.We need to use images produced in one experiment for calibrating another observing session. The contribution of source structure to group delay is computed at the points at the uv-plane that do not corresponds to the points of visibilities used for producing maps. In fact, maps are used for extrapolation of the phase and amplitude of visibility data. Thus, the mathematical model of the source brightness distribution should correctly represent not only the visibility data at the points at the uv-plane where observations were made, but serve as an adequate approximation of the complex interferometric coherence function at the entire uv-plane. This discussion illustrates the difficulties in using source maps for astronomical reductions.

I attempted to apply group delay source structure contribution to VLBI data. The source brightness distribution was presented in the form of an expansion over a set of δ-functions. The contribution to group delay was computed this way:

$$
\begin{aligned}
B_i &= \vec{b}\,\vec{p_x} p_{xi} + \vec{b}\,\vec{p_x} p_{yi} \\
R &= \sum_i^n A_i \cos\left(\frac{\omega}{c} B_i\right) \\
I &= \sum_i^n A_i \sin\left(\frac{\omega}{c} B_i\right) \\
R' &= -\sum_i^n A_i \frac{B_i}{c} \sin\left(\frac{\omega}{c} B_i\right) \\
I' &= \sum_i^n A_i \frac{B_i}{c} \cos\left(\frac{\omega}{c} B_i\right) \\
\tau_{gr} &= \frac{R\,I' - I\,R'}{R^2 + I^2}
\end{aligned}
\tag{5}
$$

The dependence of brightness distribution on frequency within the observed band was ignored.

I used a short dataset of 89,628 observations of the CONT05 campaign collected at the 11-station network for 15 consecutive days starting from 2005.09.12.

First, I ran the reference solution. Positions of all stations, coordinates of all sources, as well as clock function, atmospheric zenith path delay and troposphere gradients modeled by a linear spline were estimated. No-net-rotation constraints were applied on estimates of site positions and source coordinates. The rms of post-fit residuals for the reference solution was 13.947 ps.

I computed The source structure contribution for X and S bands for each source in that campaign using expression 5 and applied it to data reduction.

Surprisingly, the rms of post-fit residuals increased to 14.204 ps. In order to investigate the problem, I tried an alternative approach. The source structure was not applied to data reduction, but was used as a partial derivative for estimation of the admittance factor, common for all sources. If the model source structure signal is not present in the data the admittance is close to zero. If the model of source structure is perfect, the estimate of the admittance will be close to 1. The estimate was 0.409 ± 0.003 and the rms of post-fit residuals dropped to 13.698 ps. Further analysis showed that the map noise with low spatial frequencies spread over the image and leaks as a noise in group delays with high frequencies in time delay (refer to figure 5). The noise is significantly enhanced for group delay contribution because that contribution depends on the partial derivative of noisy data. Apparently, the high frequency contribution to group delay is an artifact of image restoration.

Figure 5. The contribution to group delay from very compact source J1018+0530 computed using the raw image.

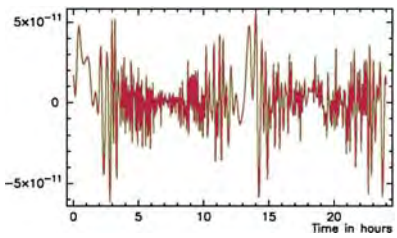

I ran another solution, for which I discarded the components of the image with amplitude less than 2σ of image noise. The admittance factor estimate was 0.482 ± 0.004 and the rms of post-fit residuals was 13.691 ps.

Another way to suppress high frequency noise in structure group delay contribution is to apply a digital diaphragm. I multiplied the image by the circular Gaussian function centered at the phase center of the image with the FWHM 10 mas at X-band and 40 mas at S-band. The admittance factor estimate was 0.652 ± 0.005 and the rms of post-fit residuals was 13.627 ps. Finally, the solution with applied source structure contribution to group delay computed using the map with digital diaphragm applied gave the rms of post-fit residuals 13.716 ps, less than the rms of the reference solution.

A more thorough study of the optimal strategy for computing the contribution of source structure to group delay is necessary.

References

Born, M., E. Wolf, Principles of optics, 1980, Pergamon Press.

Charlot, P., Astron. J., 1990, 99., 1309.

Charlot, P., in IVS General meeting proceedings, 2002, 233.

Cotton, W. D., in Radio interferometry technique for geodesy., p. 193, 1980

Sovers, O.J., P. Charlot, A. Fey, D. Gordon, in IVS General meeting proceedings, 2002, 243.

Zeppenfeld, G. "Einflüsse der Qullenstruktur in der Praxis der geodatischen VLBI, N 80, Mittailungen aus den Geodätischen Instituten der Universität Bonn, 1993.

Studying the geodynamics of the Etnean area by means of VLBI and GPS

S. Di Martino, S. La Delfa, G. Patané
Dipartimento di Scienze Geologiche, Università di Catania, Corso Italia 55, 95129 Catania, Italy

M. Negusini
IRA, Istituto Nazionale di Astrofisica, Via Gobetti 101, 40129 Bologna, Italy

Abstract. VLBI (Very Long Baseline Interferometry) and GPS (Global Positioning System) space geodesy techniques can contribute to the study of crustal deformations in the Mediterranean Sea area. In particular, the correlation between volcanic and seismic activity of Mt. Etna and crustal deformations between Noto and Matera stations was analysed.

By analysing VLBI data we obtained the behaviour of the baseline which crosses the Etnean area, from 1990 to 2004, representing the time variations of the distance between the two stations situated on different plates; the linear trend showed a general increasing, pointing out an extension of the crust between them.

VLBI data are very sparse even if the time series was quite long; therefore, to fill gaps in the information, we analysed GPS data. GPS technique performs continuous observations and we were able to highlight both extensions and compressions in details. We compared the baseline Noto-Matera with the volcanic eruptions of Mt. Etna and we found out a relationship between eruptions and the distance between the two stations: it increases before an eruptive event so there is extension between them; on the contrary, during the eruption it decreases, so emphasizing crust's compression. The comparison with the strain release showed that the main seismic release happens during the extension of the crust before the eruptions so it helps the uplifting and the beginning of the event. The uprising of the mantle occurs before the eruptions and it causes the inflated crust lying over it and the volcanic fractures are opened and the magma up rises inside them.

Moreover, this analysis showed that the crustal deformation of Etnean area is characterized by the geodynamics involving the movements of the plates where all the stations we studied are located.

Keywords. Very Long Baseline Interferometry, Global Positioning System, baseline Noto-Matera, Mt. Etna, strain release curve, volcanic activity, geodynamic processes.

1 Introduction

In this work, we have investigated the crustal deformation between the two station of Noto and Matera. The choice of the baseline Noto-Matera is connected to its crossover of the Etnean area. This region undergoes the convergence between the African and European plates; therefore, the geodetic studies of the crustal deformation between the two stations Noto and Matera can give information about the geodynamic processes of this area (see Figure 1).

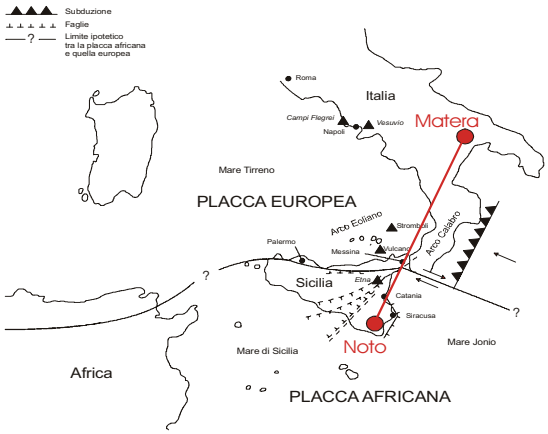

Fig 1 Structural map of the area between Noto and Matera crossing the volcano Mt.Etna. The red solid line shows the baseline Noto-Matera.

The Mediterranean area is constituted by a complex mosaic of plates and micro plates which move each other to arrange the relative movement between the blocks of Africa/Arabia and Eurasia. The Etnean area is an area of convergence between the two plates, Africa and Europe, even if there are some regions of local extension E-O which cause tholeitic and alkaline volcanism of Monti Iblei and Mt.Etna (Barberi et al. (1974)). The two stations of Noto and Matera are situated, respectively, on the Hyblean Plateau of the African plate and on the Adriatic micro plate which is considered by many authors an independent block. Therefore the studies of crustal deformation between the two stations can explain the relative movement and the direction of movement of the plates over they are located. As a matter of fact, progress, in last decades, of the space geodetic techniques (VLBI, SLR, GPS) permits to have precise information about the movement of many sites of Mediterranean Sea.

GPS and VLBI data were processed and the results of their observations were analysed with the purpose of investigate differences in estimated baseline length by both techniques and compare it with the seismic and volcanic activity of Mt.Etna.

15 years of VLBI data acquired within the EUROPE campaign have been analysed to estimate the motion of the stations participating to these experiments. The estimated site velocities and baseline time series are compared to those obtained from the GPS solution, performed in order to have a denser solution. Both the solutions have been expressed in the ITRF00 reference frame in order to compare them in a unique reference system. VLBI coordinates for European stations were obtained from processing of all available experiments collected on European and global VLBI network, GPS data were obtained from processing a regional network acquiring on a daily basis.

2 Geodetic methods

2.1 VLBI data

We have analysed data collected at the stations belonging to the VLBI European network: Noto, Matera and Medicina (Italy), Wettzell and Eflsberg (Germany), Nyales20 (Norway), Onsala60 (Sweden), DSS65 (Spain) and others not very often used, to obtain position and velocity of each VLBI station. All the experiments performed since 1990, when Matera started to record VLBI observations, to 2003, when Matera observations stopped, because of mechanical problems, were selected. The acquired data have been analysed with CALC/SOLVE software package (Caprette et al. (1990)) taking into account the precession's effects, nutation, motion of the pole, UT1, Earth solid tides, ocean loading, polar tides and relativity. By analysing VLBI data we have obtained the time series 1990-2003 of the baseline Noto-Matera (see Figure 2), which represents the time variation of the distance between the two stations; its linear trend shows a general increasing of the length (0.4 ± 0.2 mm/y), thus highlighting an extension of the crust between the two stations.

Looking at baselines Wettzell-Noto and Wettzell-Matera, it's possible to observe that the two Italian stations get nearer to Wettzell; they move with a different velocity from North to South because the African plate drives towards the European plate. Matera moves towards NNE and Noto towards North, with a small component towards West; the geodynamic movements of the two different plates, where the two stations are located, cause these two different directions of movements: Noto is situated on African plate and Matera is situated on Adriatic plate. The movement NNE of the Matera station represents the indentation of the Adriatic plate towards the eastern Alp with a little counter clockwise rotation with respect to Eurasia while, the movement North of Noto, situated on the Hyblean Plateau, represents the convergence between African and European plates and also may be explained by an active extension in the Sicily channel (Mueller et al. (1992); Rebai et al. (1992); Montone et al. (1999)). Therefore, the two different directions of Noto and Matera attest the actual crustal extension between them, according to the geological evidences of the active tectonics in the Calabrian Arc.

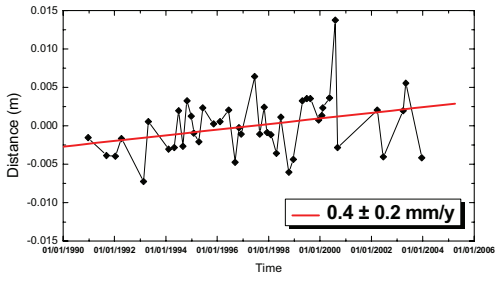

Fig. 2 VLBI baseline Noto-Matera from 1990 to 2003

2.2 GPS data

In addition to the processing of VLBI data, we have computed the daily coordinates of the GPS stations available in the study area, in order to compare, in more detail, the Noto-Matera baseline and the seismic and volcanic activity of Mt.Etna. The regional geodetic network, here considered, was composed of 18 permanent GPS stations: Aquila, Cagliari, Cosenza, Grasse, Graz-Lustbuehel, Elba, Lampedusa, Maratea, Matera, Medicina, Noto, Trapani-Milo, Reggio Calabria, Tito, Perugia, Wettzell, Vallo della Lucania, Zimmerwald; the BPE module of Bernese software V5.0 (Dach et al. (2007)) was used to process the data from 1996 to 2004 to obtain the time series of daily coordinate solutions of the all stations expressed in ITRF2000. IGS final orbits and the Earth rotation parameters have been used; the ambiguities were estimated with the QIF strategy, the estimation of the tropospheric delay for each station was accomplished with the use of Saastamoinen model (1973) and Niell mapping function (Niell (1996)). Absolute antenna phase variations and offset were used (Schmid et al. (2005)). Possible antenna offsets were estimated at discontinuities in the time series related to known equipment change or where a clear discontinuity was observed; moreover, outliers were eliminated.

Thus, by processing of GPS data we have obtained the baseline Noto-Matera. It was carried out a spectral analysis to highlight and thus eliminate the periodic oscillation present within the baseline (annual signal). The linear trend shows, from 1996 to 2004, an increasing of the baseline's length of 0.67±0.01 mm/y, which could mean that an extension of the crust between them occurred (see Figure 3).

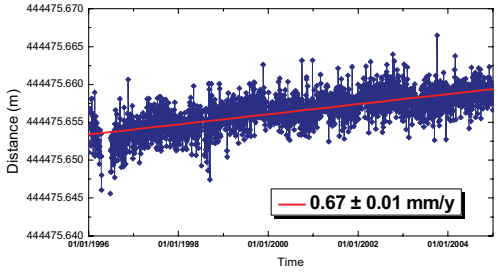

Fig. 3 GPS baseline Noto-Matera from 1996 to 2004.

Moreover, it was computed the value of the displacement, absolute and relative, of each station into ITRF2000 combining together all the daily solutions, at level of Normal Equations. The maps of the absolute and relative velocities (Figure 4 and 5, respectively), in accord with the geological model, indicate the geodynamic movements of the plates. Absolute velocities at all the stations show a movement towards NNE due to the spreading of the Middle Atlantic ridge, while relative velocities show the movement of all the GPS stations respect the reference station of Wettzell which is situated on stable European plate.

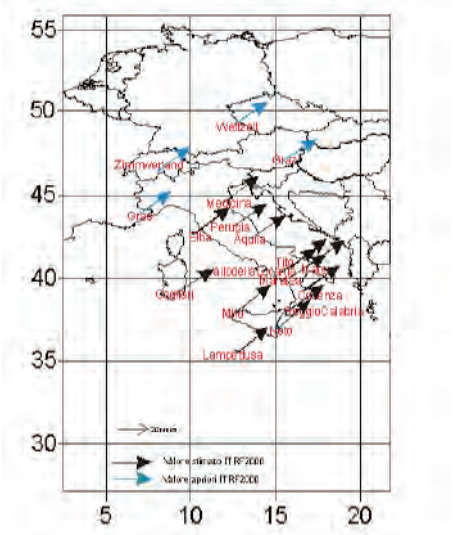

Fig. 4 Map of the absolute movements of the stations into ITRF2000

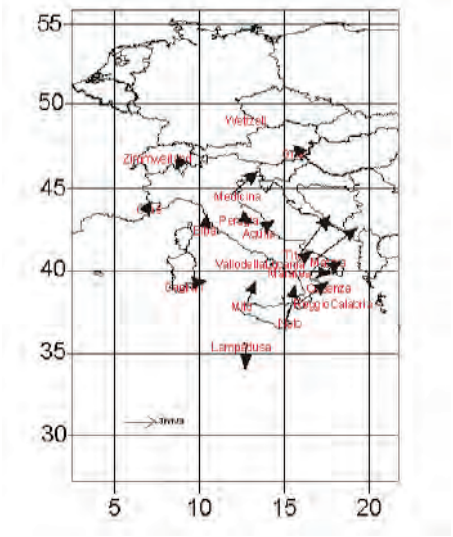

Fig. 5 Map of relative horizontal movements with respect to Wettzell

3 Comparison of geodetic and geophysical data

In this work we have compared the crustal deformations measured by the space geodetic techniques of VLBI and GPS between Noto and Matera stations with the seismic and volcanic activity of Mt.Etna. The two baselines Noto-Matera, obtained with both GPS and VLBI, have a similar linear trend that indicates an increase of the distance between the two stations from 1990 to 2004, translating in crustal extension (see Figure 6). We have compared selected parts of the two curves, noting that, when VLBI registers a crustal extension, the GPS shows the same behaviour; this remark is valid, also, in the case of a compression. Thus, the two curves show the same result even if the magnitude of the displacement is different; actually, the VLBI dataset is poorer than daily GPS observations, because of instrumental problems of the radiotelescopes and especially because of the sparse geodetic VLBI observations, due to the need for radioastronomical experiments.

In the first part of the VLBI curve, from 1990 to 1993, a decrease in the baseline is present and thus, a crustal compression between them coinciding with the eruptive period of Mt.Etna between 1991-1993; however, we cannot make any supposition about the correlation between the crustal deformation and the activity of the volcano in this period because of the very few VLBI measurements and the lack of GPS data to fill the gaps.

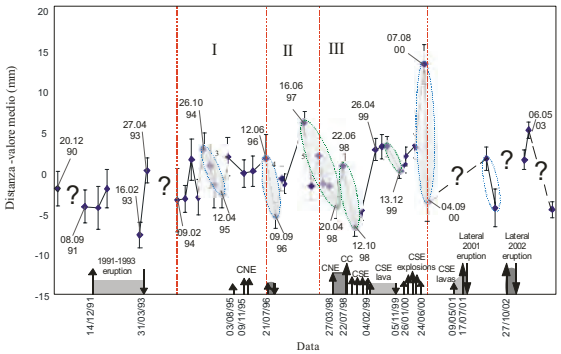

Fig. 6 Comparison of VLBI and volcanic activity of Mt.Etna. At the bottom the arrows show the periods of eruptions

After this first period, it is possible to split up the VLBI curve into three time intervals comparable with the volcanic activity of Mt.Etna: for the first period (02/94-06/96), in which VLBI measures are not statistically significant, it is not possible to point out any movement between the two stations and at the same time there is not any important volcanic event.

The second period (06/96-10/97) is characterized by a sequence of increases and decreases of the Noto-Matera baseline, preceding the third period (10/97-12/2003), when important crustal deformations occurred simultaneously to the sequence of eruptive events concerning Mt.Etna, from 1998 to 2002.

VLBI curve shows two larger values of crustal distension, precisely as regards the measurements of 16/06/97 and 07/08/2000, followed by the strong crustal compression previous and simultaneously to the volcanic activity; this behaviour can be related to the recharge of the volcanic system with the uplift of the mantle and it is followed by the eruptive activity. In fact, the strong distension, present in the second period of VLBI curve, which causes the uplift of the mantle, is the prelude to the compression in the third period when, from 1998 to 2000, there is a sequence of eruptive episodes with the material coming from superficial regions of the volcanic edifice.

Another distension, measured on 07/08/2000 causes a new recharge from the mantle originating the next important volcanic period with the two lateral eruptions of 2001 and 2002. This behaviour of crustal deformation can be explained by a model here proposed: the eruptions are preceded by the uplift of the mantle that determines a bulge of the overlaying crust; the crust is fractured and the magma up rises within the cracks, thus inducing the distension of the crust and then the eruptions. During the eruptions, on the other hand, the crust under the volcanic area is affected by the compressions because the increase of the erupted magma volume cannot be balanced from underneath and so the volcanic system collapses and the fractures close. VLBI data from 2001 and 2003 are very sparse, thus the correlation with volcanic activity occurred during the two important eruptions of 2001 and 2002 is not feasible, in detail.

In order to have a better knowledge of the correlation between geodetic and geophysical observations, GPS daily data are used to study the processes of crustal deformation occurred during these two eruptions (see Figure 7). As a matter of fact, GPS data are able to point out the movements

between the two antennas: the crustal extension is recorded before the two eruptions and the decreasing of the baseline, that means the crustal compression, is recorded during the eruptions in according to the proposed model.

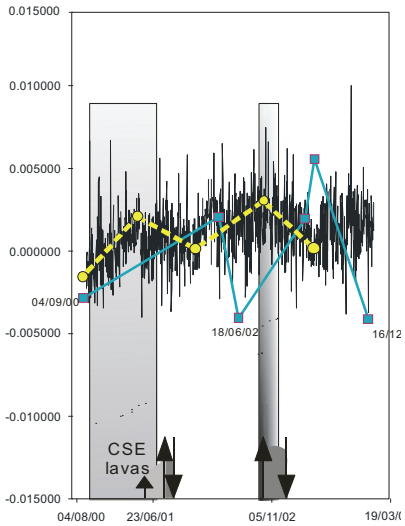

Fig. 7 VLBI baseline (solid blue line) and GPS baseline (dashed yellow line) compared with the eruptions of 2001 and 2002

Correlating VLBI data and the strain release, the larger seismic release is recorded during the distension preceding the eruption because of the opened fractures and the magma up rising easily within them.

As a further outcoming of this work, the vertical components (Up) of the topocentric coordinates of the two GPS antennas located at Reggio Calabria and Noto, the two stations nearer to the volcano, therefore mainly influenced by the geodynamic processes, and the crustal deformations measured with VLBI have been correlated. It's possible to show that, during the crustal extension before an eruption the Up components droop because the magma bulge up rises under the volcano system, while the lateral area undergoes a collapse; during the crustal compression, on the contrary, the Up components increase due to the collapse under the volcano system.

Previous works about GPS-based deformations of Mt.Etna (see e.g. Bonaccorso et al. (2004)), have demonstrated the volcano edifice is characterized by an inflated phase before erupting, while, during the eruptions, the volcano system is deflated in association with the outflow of magma.

4 Discussion and conclusion

The study of the crustal deformations in the Etnean area is inserted in a complex geodynamic setting because of the interactions between the different structural domains in which is divided the central Mediterranean Sea. Therefore, the geodetic measurements are aimed at researching the boundary between Eurasia and Numibia plates to suggest a geological arrangement of the Etnean area. The velocity vectors of the stations, belonging to the regional network, have been estimated by means of GPS technique. The results show the deformation along the boundary of the plate, which is different according to the lithospheric structures. The stations' movements showed in the velocities maps are congruent with the movement of the plates where they are located: from Sicily channel to Calabria and then Puglia, the movement's directions rotate towards East from African plate to Adriatic plate. Lampedusa station drives towards South with the effect of the spreading of Pantelleria ridge, which is also the responsible for the movement of Noto station towards North. All the stations near the Tyrrhenian edge undergo the Tyrrhenian extension and the subduction of the Ionian lithosphere with the roll-back of Calabrian Arc. Matera and Tito stations, which are located on Adriatic plate, show a movement NNE in accord to the geological models that consider the Adriatic plate an independent block from the African plate rotating anti-clockwise. (see Figure 8) (Anderson and Jackson (1987); Westaway (1990); Favali et al. (1993); Console et al. (1993); Oldow et al. (2002)).

Therefore, these studies about the correlation of the VLBI and GPS data with the seismic and volcanic data of Mt.Etna have showed that the crustal deformation of the Etnean area is inserted in a geodynamic contest which determines the movement of the stations, related to the plates over they are located.

The correlation among the crustal deformation between the two stations Noto and Matera and the seismic and volcanic activity of Mt.Etna has proved that the length variation of the baseline Noto-Matera is connected to the eruptive periods. Thus, it was proposed a dynamic model to explain the volcanic processes occurring during the crustal deformation

and to connect the Etnean activity with the geodynamic processes involving all the area between Noto and Matera.

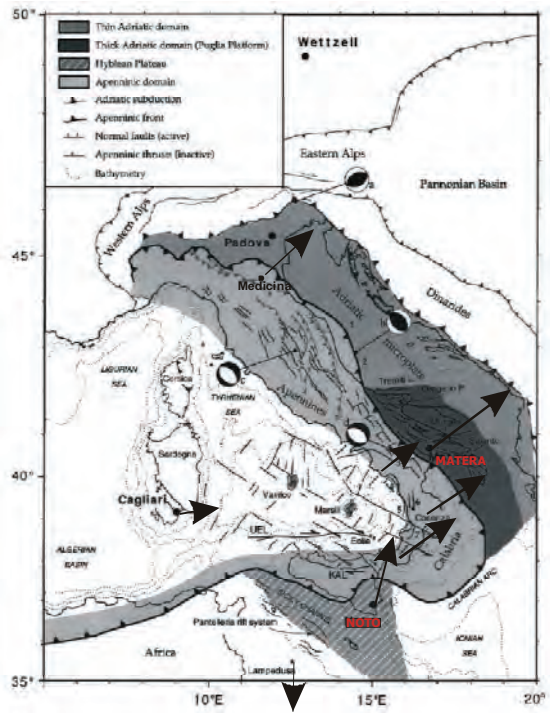

Fig. 8 geological map of Italy and relative movements of the Italian stations

Further GPS and VLBI data will be analysed in order to improve the proposed geodynamic model and to verify if the correlation between crustal deformation and Etnean activity will be still present.

References

Anderson H. and Jackson J. (1987). Active tectonics of the Adriatic region. *Geoph. J.R.ast. Soc*, 91, 937-983.

Barberi F., Civetta L., Gasparini P., Innocenti F., Scandone R., Villari L. (1974). Evolution of a section of the Africa–Europe plate boundary: paleomagnetic and volcanological evidence from Sicily. *Earth Planet. Sci. Lett*. 22, 123–132.

Bonaccorso A., Davis P.M (2004*). Modeling of ground deformation associated with recent lateral eruptions: Mechanics of magma ascent and intermediate storage at Mt.Etna. Volcano Laboratory Geophysical Monograph Series* 143, 2004 by American Geophysical Union.

Caprette D., Ma C., & Ryan J.W (1990). Crustal dynamics project data analysis. *NASA Tech. Mem.* 100765, Goddard Space Flight Center, Greenbelt, Md.

Console R., Di Giovambattista R., Favali P., Presgrave B.W, Smriglio G.(1993). Seismicity of the Adriatic microplate. *Tectonophysics*, 218, 343-354.

Dach R., U. Hugentobler, P. Fridez and M. Meindl (2007), Bernese GPS Software Version 5.0, Astronomical Institute of University of Berne, 640 pp.

Favali P., Funiciello R., Mattietti G., Mele G., Salvini F. (1993). An active margin across the Adriatic sea. *Tectonophysics*, 219, 109-117.

Montone P., Amato A., Pondrelli S. (1999). Active stress map of Italy. *J. Geophys. Res*. 104 (B11), 25595–25610.

Muller B., Zoback M.L., Fuchs K., Mistn L., Gregersen S., Pavoni N., Stephansson O., Ljunggren C. (1992). Regional patterns of tectonic stress in Europe. J.*Geophy.Res*., 97, 11783-11803.

Niell A. E. (1996). Global mapping functions for the atmospheric delay at radio wavelengths. *Journal of Geophysical Research*. Vol. 101, no. B2, pp. 3227-3246.

Oldow J.S et al (2002). Active fragmentation of Adria, the north African promontory, central Mediterranean orogen. *Geology*, 30, 779-782.

Rebai S., Philip H., Taboada A. (1992). Modern tectonic stress field in the Mediterranean region: evidence for variation in stress directions at different scales. *Geophy. Jour.Int.*, 110, 106-140.

Saastamoinen J. (1973). Contributions to the Theory of Atmospheric Refreaction. *Bulletin Geodesique*, 105, pp.279-298, 106, pp. 383-397, 107, pp. 13-34.

Schmid R., Mader G., Herring TA (2005). From relative to absolute antenna phase center corrections. *Proceeding of the IGS Workshop and symposium 2004, ed. Meindl*, pp. 209-219.

Westaway R.(1990). Present-day kinematics of the plate boundary zone between Africa and Europe, from the Azores to the Aegean. *Earth Plan.Sci. Lett*, 96, 393-406.

Forecasting Data of the Troposphere Used for IVS Intensive Sessions

J. Boehm, H. Schuh
Institute of Geodesy and Geophysics,
Vienna University of Technology, Gusshausstrasse 27-29, 1040 Vienna, Austria

Abstract. Troposphere parameters (mapping functions and gradients) determined from analysis and forecasting data of the European Centre for Medium-Range Weather Forecasts are compared and the differences are evaluated. It is shown that hydrostatic parameters are well predictable over four days whereas the wet parameters are more susceptible to forecasting errors. In particular, wet gradients are very sensitive to small differences in the numerical weather model. In the second part of the paper a clear correlation of east gradients vs. estimates of dUT1 from IVS Intensive sessions is pointed out. The influence of the choice of the mapping function w.r.t. dUT1 estimates is negligible.

Keywords. Troposphere mapping functions, troposphere gradients, IVS Intensive sessions

1 Introduction

State-of-the-art analysis of IVS Intensive sessions typically comprises the use of the Niell Mapping Function (NMF, Niell 1996) which only uses station latitude and the day of the year as input parameters. Since 2004 more accurate mapping functions have been made available as 6-hour time series, which are based on data from numerical weather models (NWM), e.g. the Vienna Mapping Functions 1 (VMF1, Boehm et al. 2006) which are provided by the IVS Analysis Center in Vienna with a time delay of about 50 hours. However, if VMF1 should be used for (near) real time analysis of the IVS Intensive sessions, they need to be determined from forecasting data.

In the analysis of IVS Intensive sessions the estimation of troposphere gradients (MacMillan 1995) is not possible because of the sparse amount of observations. Although the Goddard Space Flight Center has recently changed the strategy to non-zero (but still constant) a priori hydrostatic gradients, no analysis center is using total (hydrostatic plus wet) gradients from a numerical weather model with the inherent temporal resolution of 6 hours. Again, the IVS Analysis Center in Vienna is providing such gradient time series (Linear Horizontal Gradients LHG, Boehm and Schuh 2007) with the same time delay of 50 hours as for the VMF1.

This paper mainly consists of two parts: Section 2 investigates the differences between the VMF1 and LHG as determined from analysis data and 10-day forecasting data, respectively, to check whether forecasting data could be used without loss of accuracy. Section 3 focuses on the influence of mapping functions and gradients based on NWM on estimations of dUT1 from IVS Intensive sessions.

2 Troposphere Models from ECMWF Forecasting Data

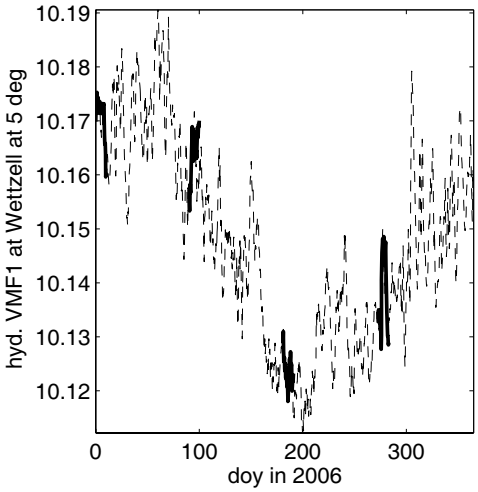

Fig. 1 Day of the year in 2006 versus hydrostatic VMF1 at 5° elevation at Wettzell in 2006 as determined from analysis data (dashed line) and from forecasting data (bold line segments) starting on January 1, April 1, July 1, and September 1.

10-day forecasts from the European Centre for Medium-Range Weather Forecasts (ECMWF) have been retrieved for three stations (Wettzell in Germany, Kokee Park in Hawaii, and Tsukuba in Japan) at four epochs in 2006 (0:00 UT): 1 January, 1 April, 1 July, and 1 September. Figure 1 illustrates the hydrostatic mapping function (VMF1) at Wettzell in 2006 as determined from analysis data (dashed line) and as determined from 10-day forecasting data at the four epochs mentioned above.

2.1 Vienna Mapping Functions 1 (VMF1)

Niell (2006) concluded from comparisons with radiosonde data in 1992 that the VMF1 are as good as 3 mm in terms of equivalent station height errors. Thus, the difference between analysis and forecasting VMF1 should at least stay below this limit. Figure 2 illustrates the equivalent station height errors in mm which correspond to the differences in the hydrostatic mapping functions. They are determined applying a rule of thumb (Boehm et al. 2006): *'The station height error is 1/5 of the error at the lowest elevation.'* It is shown that the agreement during the first three to four days is quite good (better than 2 mm) allowing for enough time to provide hydrostatic mapping functions from forecasting data. Figure 3 shows the same information for the wet VMF1 where the agreement is again sufficient during the first few days after analysis, apart from larger differences at station Tsukuba in Japan. The first significant difference (4 mm) already occurs after one day, which underlines the extreme and hardly predictable (wet) weather conditions at this site in Japan. Analogously, the equivalent station height errors in mm due to different surface pressure values that are used for the determination of the hydrostatic zenith delay are shown in Figure 4. Similar to the hydrostatic mapping functions, analysis and forecasting data agree well for several days.

2.2 Linear Horizontal Gradients (LHG)

Boehm and Schuh (2007) have been determining hydrostatic and wet gradients as 6-hour time series for all IVS stations starting on 1 January 2006, and they showed that the agreement between the gradients rigorously determined from data of the ECMWF and their simple approach is at the level of ±0.2 mm in terms of gradients. Thus, the difference between analysis and forecasting gradients should stay below this level which corresponds to an excess delay of 2 cm at 5° elevation. Figure 5 illustrates the hydrostatic north gradient differences for the three stations and four epochs in 2006. Apart from larger differences at Tsukuba the agreement is sufficiently close. Contrarily, Figure 6 shows the situation for the wet north gradient differences which are significantly larger.

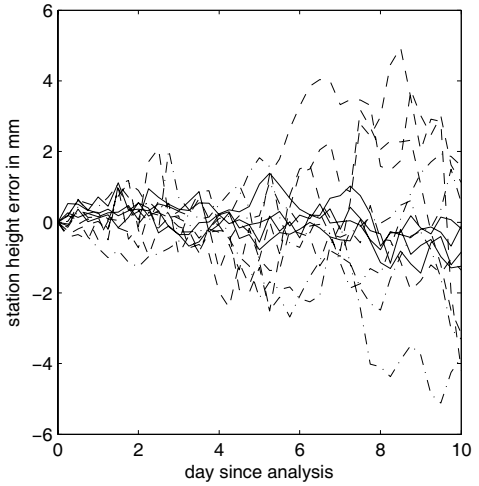

Fig. 2 Equivalent station height errors in mm for the hydrostatic VMF1 differences between analysis and forecasting data. For each of the stations (Kokee Park - solid line, Tsukuba - dashed line, Wettzell - dot-dashed line), four time series are plotted which correspond to the four epochs in 2006.

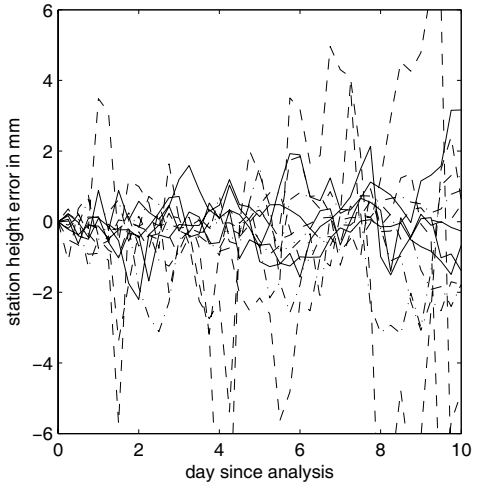

Fig. 3 Equivalent station height errors in mm for the wet VMF1 differences between analysis and forecasting data. For each of the stations (Kokee Park - solid line, Tsukuba - dashed line, Wettzell - dot-dashed line), four time series are plotted which correspond to the four epochs in 2006.

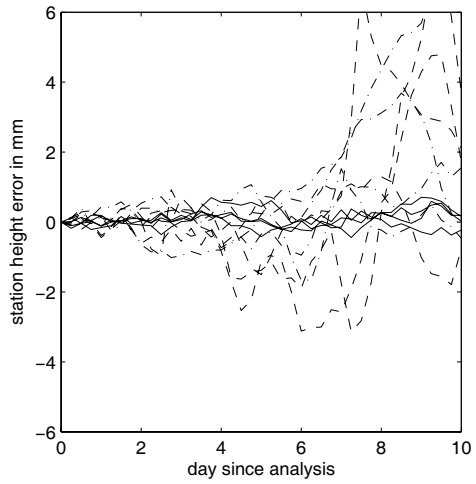

Fig. 4 Equivalent station height errors in mm for the surface pressure differences between analysis and forecasting data. For each of the stations (Kokee Park - solid line, Tsukuba - dashed line, Wettzell - dot-dashed line), four time series are plotted which correspond to the four epochs in 2006.

Moreover, these differences are very large from the beginning, i.e. not even 6-hour or 12-hour forecasts are of reasonable agreement with the gradients derived from analysis data, especially at Tsukuba. Hydrostatic and wet east gradients are not shown here but their behaviour is similar to the respective north gradients. Figure 6 not only shows the differences in wet gradients, it additionally conveys the difficulties to derive wet gradients from numerical weather models.

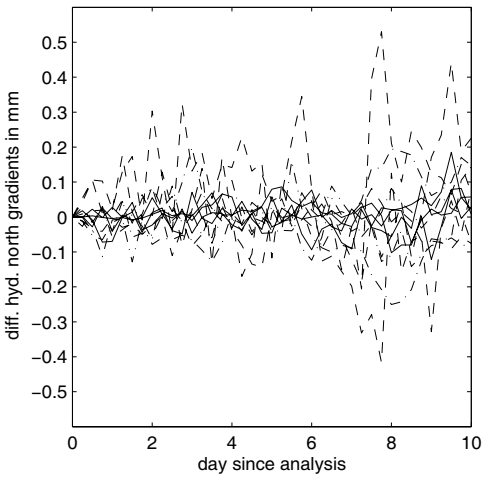

Fig. 5 Hydrostatic north gradients in mm (corresponds to the excess path delay at 5° elevation in dm) between analysis and forecasting gradients. For each of the stations (Kokee Park - solid line, Tsukuba - dashed line, Wettzell - dot-dashed line), four time series are plotted which correspond to the four epochs in 2006.

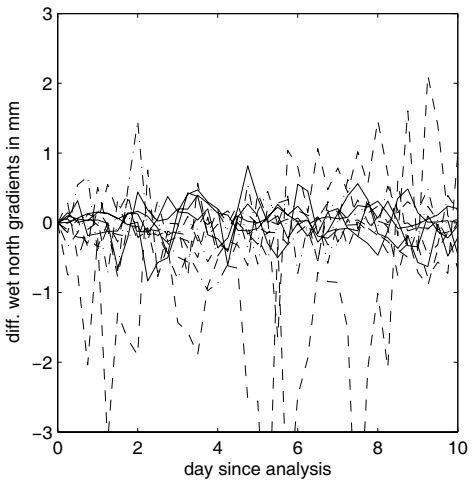

Fig. 6 Hydrostatic north gradients in mm (corresponds to the excess path delay at 5° elevation in dm) between analysis and forecasting gradients. For each of the stations (Kokee Park - solid line, Tsukuba - dashed line, Wettzell - dot-dashed line), four time series are plotted which correspond to the four epochs in 2006.

3 VLBI Analysis of Intensive Sessions

All 1-hour IVS Intensive sessions in 2006 between the stations Kokee Park and Wettzell, and Tsukuba and Wettzell, respectively, are analyzed for the determination of dUT1 with the OCCAM software (Titov et al. 2004). Figure 7 shows the differences in dUT1 in μsec when using VMF1 instead of NMF. Since mapping function errors mainly affect the height component of the stations, the influence on dUT1 is rather small, i.e. below ±1.5 μsec. Figure 8 illustrates the differences in dUT1 when using (non-zero) constant values for the gradients based on data from the Data Assimilation Office (DAO, Schubert et al. 1994) as described by MacMillan and Ma (1997) instead of not using gradients. Although these differences are rather small (< ±4 μsec) there is a systematic variation which might be due to systematic effects in the schedules. Larger differences up to 20 μsec in the estimates of dUT1 can be found when using the gradients as derived by Boehm and Schuh (2007) (Figure 9).

Figure 9 clearly shows that the choice of a priori gradients is more important than the choice of the mapping function for the determination of dUT1 from IVS Intensive sessions. Especially the east gradients at the observing stations have a strong influence as shown in Figure 10. It illustrates that there is a high correlation between dUT1 and the sum of the east gradients at the two sites.

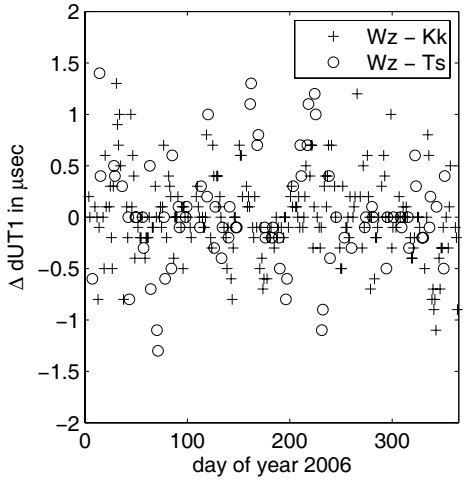

Fig. 7 Differences in dUT1 in μsec when using VMF1 instead of NMF (Kokee Park to Wettzell (+) and Tsukuba to Wettzell (o)).

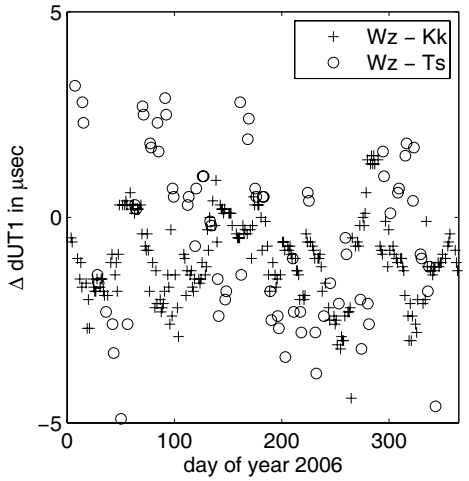

Fig. 8 Differences in dUT1 in μsec when using constant a priori gradients as opposed to not using gradients (Kokee Park to Wettzell (+) and Tsukuba to Wettzell (o)).

This allows another empirical rule of thumb: *'1 mm in the sum of total east gradients corresponds to about 15 μsec change in dUT1.'*

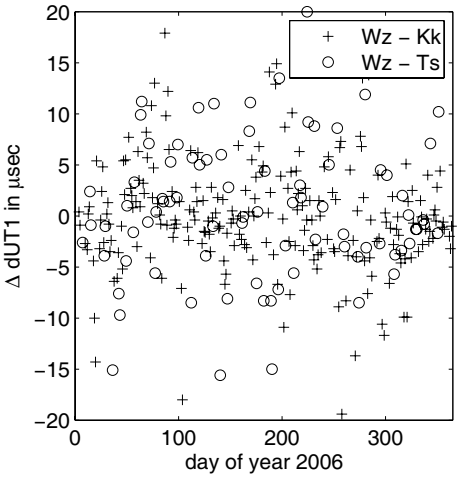

Fig. 9 Differences in dUT1 in μsec when using 6-hour gradients as opposed to not using gradients (Kokee Park to Wettzell (+) and Tsukuba to Wettzell (o)).

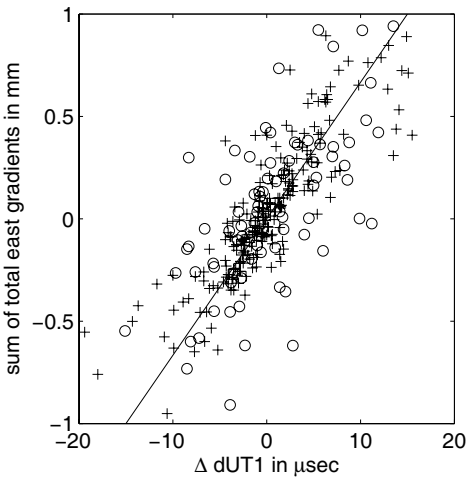

Fig. 10 Sum of east gradients in mm versus dUT1 in μsec (Kokee Park to Wettzell (+) and Tsukuba to Wettzell (o)). Rule of thumb: 15 μsec / mm sum of total east gradients.

4 Conclusions and Recommendations

Hydrostatic mapping functions, (hydrostatic) zenith delays and (hydrostatic) gradients can be determined from (up to) 3 or 4-day forecasts without degradation w.r.t. their counterparts from analysis data. At most sites, also the wet mapping functions can be determined from forecasting data. Contrarily, wet gradients are extremely sensitive to the accuracy of the NWM and therefore might not be determinable from global NWM at all.

Unlike mapping functions, which are of minor importance, gradients are critical for the determination of dUT1 from Intensive sessions (15

μsec per mm sum of total east gradients). The choice of a priori gradients is particularly important for IVS Intensive sessions, consisting of only two (or three) observing stations, for two reasons: First, the dUT1 estimate is roughly dependent on the sum of total east gradients over all stations. With five or more stations observing over 24 hours this sum usually tends to be zero. Second, there is no possibility to estimate gradients from 1-hour sessions.

References

Boehm, J., and H. Schuh (2007). Troposphere gradients from the ECMWF in VLBI analysis. *Journal of Geodesy*, doi:10.1007/s00190-007-0144-2.

Boehm, J., B. Werl, and H. Schuh (2006). Troposphere mapping functions for GPS and very long baseline interferometry from European Centre for Medium-Range Weather Forecasts operational analysis data. *J. Geophys. Res.*, 111, B02406, doi:10.1029/2005JB003629.

MacMillan, D.S. (1995). Atmospheric gradients from very long baseline interferometry observations. *Geophys. Res. Lett.*, 22(9):1041-1044.

MacMillan, D.S., and C. Ma (1997) Atmospheric gradients and the VLBI terrestrial and celestial reference frames. *Geophys. Res. Letters*, 24(4):453-456.

Niell, A.E. (1996). Global mapping functions for the atmosphere delay at radio wavelengths. *J. Geophys. Res.*, 101(B2):3227-3246.

Niell, A.E. (2006). Interaction of Atmosphere Modeling und Analysis Strategy. *IVS 2006 General Meeting Proceedings*, ed. by Behrend D, and Baver KD, NASA/CP-2006.

Schubert, S.D., R.B. Rood, and J. Pfaendtner (1994) An assimilated data set for earth science applications. *Bull. Amer. Meteor. Soc.*, 74:2331-2342.

Titov, O., V. Tesmer, and J. Boehm (2004). OCCAM v. 6.0 software for VLBI data analysis. *International VLBI Service for Geodesy and Astrometry 2004 General Meeting Proceedings*, ed. by Vandenberg NR and Baver KD, NASA/CP-2004-212255.

Twin-Telescope Wettzell (TTW)

H. Hase, R. Dassing, G. Kronschnabl, W. Schlüter, W. Schwarz

Federal Agency for Cartography and Geodesy, Fundamental Station Wettzell, Sackenrieder Str. 25, D-93444 Bad Kötzting, Germany

P. Lauber, R. Kilger
Technical University of Munich, Research Department Satellite Geodesy, Fundamental Station Wettzell, Sackenrieder Str. 25, D-93444 Bad Kötzting, Germany

Abstract. Following the recommendations made by the VLBI2010 vision report of the IVS, a proposal has been made to construct a Twin Telescope for the Fundamental Station Wettzell in order to meet the future requirements of the next VLBI generation. The Twin Telescope consists of two identical radiotelescopes. It is a project of the Federal Agency for Cartography and Geodesy (BKG). This article summarizes the project and some design ideas for the Twin-Telescope.

Keywords. Geodesy, radio telescope, Very Long Baseline Interferometry (VLBI).

1 Introduction

The International VLBI Service for Geodesy and Astrometry (IVS) defined in its vision VLBI2010 the current and future requirements for geodetic VLBI systems (Niell, A. et al (2006)). With this document IVS supports future developments to improve its service functions within the International Association of Geodesy (IAG), in particular to support the IAG project GGOS, aiming in the realisation of a very precise global reference frame (Rothacher (2006)).

The Fundamental Station Wettzell (FSW) hosts the most frequent used VLBI radiotelescope (20m Radiotelescope Wettzell) of the IVS. Nevertheless, facing the future requirements, the VLBI-group of FSW developed a concept of a Twin-Telescope Wettzell (TTW) in order to meet the criteria requested in the VLBI2010 vision.

The Twin-Telescope Wettzell (TTW) is a funded project by the Federal Agency of Cartography and Geodesy (BKG), which aims in supporting the realization of the vision VLBI2010 formulated by the IVS Working Group 3 (WG3). TTW shall consist of two identical radiotelescopes of the 12m class capable to be operated 24h/7days observing more than 1000 radiosources per day in the wide spectrum of 2-18GHz.

The three main goals of the VLBI2010 vision for the IVS are:

- 1mm accuracy in position and 1mm/year accuracy in velocity for ITRF stations (terrestrial reference frame),
- continuous measurements of Earth orientation parameters,
- rapid generation and distribution of the IVS products.

To achieve these goals for the VLBI operations a new class of VLBI instrumentation is needed. To improve the accuracy

- much more observations per time interval will be required; currently 200-400 scans/day are observed during the 24 h sessions, in future 1000-1200scans/day will be observed;
- the SNR of each observation has to be increased, which will be achieved employing higher sample rates and a wider observed frequency spectrum; currently 2.2-2.35GHz + 8-9GHz, future: 2-18Ghz,
- additional information about the atmospheric conditions along the ray path provided by an on-axis radiometer will be helpful.

To guarantee continuous observations the maintenance intervals of the radiotelescope have to be by passed. Failures and maintenance periods force to interrupt the observation series. To overcome such gaps, the idea was born to set up at least two telescopes (Twin).

To provide the data in near-real time, the systems must have e-VLBI capability, in minimum a link with a transmission rate of 1Gbps will be required.

2 TTW-overall plans

The TTW project will be realized at the Fundamental Station in Wettzell. It will be settled on an appropriate ground covering an area of approximately 6000m^2. It consist of the construction of an

- operation building, housing the
  - control and data acquisition,
  - timing devices and of
- two identical radio telescopes, properly founded after soil investigations, housing the
  - digital broadband HF-receivers and properly,
  - water vapour radiometer for deriving atmospheric corrections.

After the planning phase in 2007 the realization of the plan will be carried out from 2008 to 2011 according to the schedule given in the figure 1.

Figure 1, schedule of the BKG Twin Telescope project

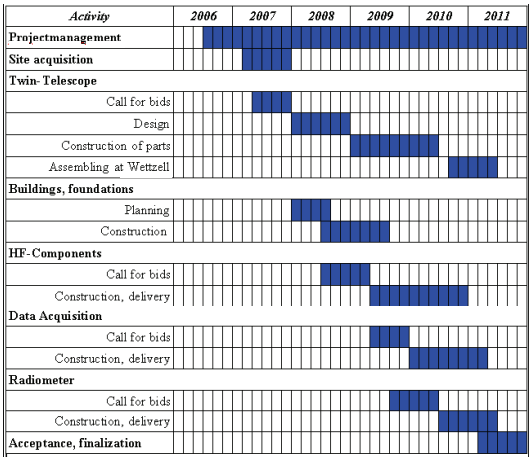

2.1 TTW Key Parameters

Over the last decades the recording systems improved, their memory and recording speed increased, which enable to extend the bandwidth of the observed signal as proposed from 2 to 18GHz without loosing signal quality. The antenna designs have to be layed out for wideband observation, which will be dominated by the flare angle of the feedhorn. So far for the specified frequency range of 2-18 GHz only a few commercial feeds are available, which were not developed for geodetic VLBI applications. Nevertheless it can be assumed, while the feedhorn developments still continue, that a feed with similar features and characteristics compared to the available ones developed by Kildal (Olsson et al. (2006)), Rohde&Schwarz (2004) and Lindgren (2005) will be used for the Twin-Telescopes.
Based on the information about the feeds given by the manufacturer, the layout of a radiotelescope for VLBI has been started. It is characterized by the overall parameter summarized in table 1.

Table 1. Key Parameters.

#alt.-azimuth antennas	2
antenna diameter	≥12 m
f/D, telescope design	t.b.d.
intersection of axis (invariant point)	0.3mm
azimuth velocity	12°/s
elevation velocity	6°/s
acceleration of the Az-El axis	3°/s^2
receiver frequency range	2..18 GHz
frequency bands	4
antenna efficiency	50 %
system noise/temperature	50 K
#observations	1000/day

The arguments for the parameters given in Table 1 are the following:

#Antennas. Two antennas are foreseen to overcome antenna failures – if one antenna needs system maintenance or need to be repaired the second antenna can used to continue the observation program. Moreover, if two antennas are available for observation, the number of observations could be increased approximately by a factor of two or both antennas can observe the same source. Some trade-offs between a single antenna and multiple antennas at a site versus the costs (antenna diameter) and observations are described in Petrachenko (2006).

Antenna diameter. The larger the antenna diameter is, the more is the antenna sensitive to the very weak signal from a quasar. The mechanical stability, the number and speed of motions and finally the price are limiting the size of the antenna. In a study, IVS experienced that 12m should be an appropriate size. World wide 12m antenna designs (e.g. ALMA (2005)) exist already. A design considering ongoing developments of antennas might help to improve the performance and reduce the costs (e.g. Dreher (2001)). The plan for Wettzell is to purchase two antennas (Twin) in minimum with 12 meters

antenna diameter. More than 12m will be considered as long as the costs remain acceptable.

Telescope design, f/D. Due to the broadband requirements a feedhorn with a wide flare angle will dominate the design of the radiotelescopes. Dependant on the feed flare angle the f/D has to be selected, which will affect the antenna geometry and the arrangement of the reflectors (primary or secondary focus system, Cassegrain or Gregorian design, symmetrical or offset antenna).

Mechanical lay out. Geodetic VLBI antennae can be seen as materialized marker for the global reference frames, and as such they have to be designed for a long life cycle, typically for 20 years. Stiffness is one key issue with respect to the intersection of axis, which is the invariant point of the antenna. This point has to be realized with a precision of 0.3mm. The pointing to the quasar should be better than 20" during the observations. To change the pointing from one quasar to the next quasar should be realized within less than 30s with velocities in Azimuth of up to 12°/s and in Elevation with 6°/s. The acceleration should be $3°/s^2$. In summary the requirements to the mechanical lay out are strong. Finally best material and manufacturing will guaranty the long-term stability.

Receiver frequency range and frequency bands. The receiver frequency range is suggested by the VLBI2010 report. So far, the current realizations with existing feeds and low noise amplifiers (LNA) did not cover the total range, but with respect to the latest developments, it is obvious that a feedhorn covering such a range will become available. Due to the increasing RFI in particular within the S-band, this band will be disturbed and will become unusable and the community is forced to go to higher frequencies. As discussed by Kronschnabl (2006), four dedicated bands would be enough within the given overall bandwidth. Feeds with three bands will be available soon and four bands seem to be possible in the future (Petrachenko (2006)).

Antenna efficiency and system noise/ temperature. Virulent visions are promising 75% antenna efficiency, which from the authors point of views seems to be unrealistic. The antenna efficiency including antenna and feed is expected to be about ≤40%, in best case in the future about 50%. The overall system noise should be less than 50°K (Rogers (2006)).

#Observations. At the Radio Telescope Wettzell (RTW), the maximum number of observations per day is 800 for some dedicated measurements, which result in warming up of the gears and motors and in consuming a lot of power. Today the session typically cover 200...400 observations per day. Nevertheless, following the simulations (Behrend, 2006) requesting observations every 30s, more than 1000 observations per day will become a regular number. With respect to a life cycle of the telescopes of 20 years this results in the demands for strong and stiff mechanics.

2.2 Existing Feed Horn and their influence to the telescope design

There exist only few and very different feed horn designs, which can be considered for our purpose. The characteristics of the developments from Olsson, Kildal and Weinreb (2006), ETS-Lindgren (2005) and Rohde&Schwarz (2004) etc. are shown in Table 2. Currently none of these designs achieve the parameters for geodetic VLBI without additional improvements and investigations.

Table 2. Feed horn parameters; α: half angle @10 dB bandwidth.

Feed	Id	Polari-sation	f/GHz	Gain dBi	α
Kildal	Eleven	dual lin.	1..13	-	53..65
Lindgren	3164-05	lin. + circ.	2..18	10..12	45..50
Rohde&S	HL024	lin. + circ.	1..18	7	50..60
Rohde&S	HL050	lin. only	0.9..26	8.5	≈40

The low system noise is mandatory and thus cooling in a cryogenic system is substantially. The Kildal feed isn't tested yet in a cooled environment (Weinreb (2007)). However, the advantage is that the phase centre location is fixed to the ground plane for all frequencies and the centre of the ground plane is the phase reference point (Olsson, Kildal and Weinreb (2006)). The Lindgren feed so far did not provide the demanded low noise temperature over the entire frequency range (Weinreb (2006) and (2007)). An appropriate cooling system for the Lindgren has been developed already. The Rohde&Schwarz feed shows a phase centre change versus the frequency especially for frequencies

below 4 GHz, which can be seen from the data sheets.

In general, feeds for narrow bands have usually a small angle and a good directivity. These broadband feeds mentioned above need a full angle of more than 90 degrees. Their directivity is not as good as it is for the small angle feeds. In order to obtain a good feed gain, the H- and E-field should be congruent. Both, the reflector/s and the feed have to be adapted optimally to achieve a good antenna gain. The f/D will be adopted and optimised for the Twin Telescopes, which is dependent on the chosen design.

3 Antenna designs for TTW

Several designs have been considered:

- Symmetric antenna designs and
- Offset antenna designs

as

- primary focus system,
- Cassegrain type system and
- Gregorian type systems.

Every system has its advantages and disadvantages. Due to a lot of manufacturer dependent mechanical details, no decision on the final constellation could be made until now. A preference would be given to the following designs.

3. 1 "Cascaded" Gregorian Design

The effectiveness of the antenna area/gain can be increased by using the backside of a subreflector as reflecting surface too (Kilger 2007). Usually, the area of a subreflector obstructs the incoming radiation and leads to signal loss of the order of 15 to 20%. The idea is to collect most of this part of the radiation by integrating a small paraboloid of the size of the subreflector of the main system as a collecting mirror at the backside of the subreflector and an additional small subreflector placed on top which focuses the beam through a hole in the primary subreflector directly into the feed horn (figure 2). The advantage is, there is not much obstruction and not much loss due to the subreflector itself. The disadvantage is that this construction is not an antenna standard and the assembly costs might be too high.

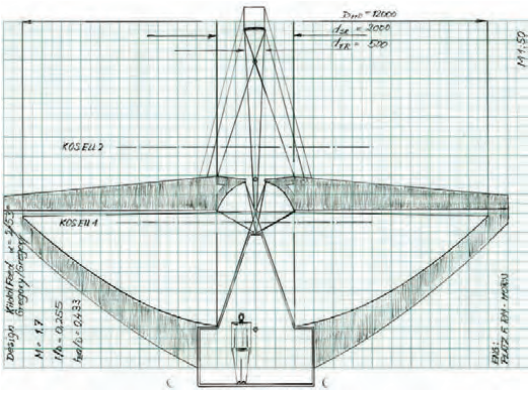

Figure 2: "Cascaded" antenna system. Principle outline by Kilger (2007).

The path lengths for both cascaded antenna systems can be adjusted to be identical and constant from a plain wavefront to the focus where the feed is located. Using the Gregorian antenna design for the main system, the hole for the beam from the second cascaded antenna system can be made large enough to allow lower frequencies passing through the hole.

The "cascaded" antenna system can be used to integrate a water vapour radiometer (WVR) into the design. A second feedhorn optimised for the frequencies of 23 and 32 GHZ (water vapour-lines) could be placed next to the main broadband feed. By tilting the small subreflector those frequencies could be guided to the WVR-horn. Such a constellation would allow observations of the water vapour in the atmosphere along the observation path and quasar signals.

3.2 Offset Antenna

A favourite design is the offset antenna with subreflector in the Gregorian design (figure 3). There is no obstruction due to the subreflector. The integration of the feedhorn can be made such that in all directions the view of the feedhorn will point towards the sky. The offset antenna allows high flexibility in the integration of the horns with respect to the view angle. The disadvantages are, that due to the non-symmetric design the polarisation is affected, which will result in some signal loss, that generally the mechanics is unbalanced with respect to the Elevation angle and that the manufacturer will claim the higher effort in the production of the panels. The loss due to polarisation will be overcome by the fact that there is no obstruction by the subreflector. The unbalanced mass structure could be avoided by

employing appropriate counterweights. The panel structure could be organized as shown in figure 3, which will enlarge the reflecting area and minimize the effort in cutting the panels to form a circle.

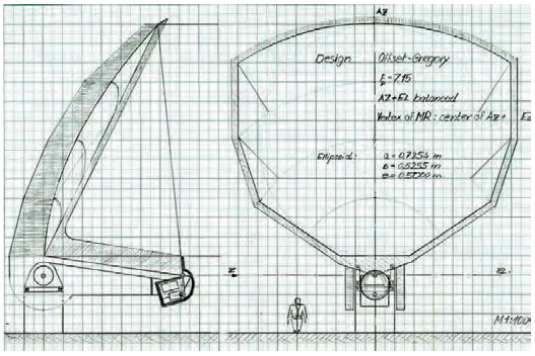

Fig. 3. Offset Antenna, Gregory system. Principle outline by Kilger (2007).

Some interesting offset antenna design studies can be found around the Allen Telescope Array (ATA) project (e.g. Welch (2005)). As in DeBoer (2001) described, the polarization deformations of the offset antenna can be reduced by adapting the subreflector.

References

ALMA (2005). Technical Specification for Design, Manufacturing, Transport and Integration on Site of the ALMA ANTENNAS, Doc. ALMA-34.00.00.00.006-B-SPE.

Behrend, D. (2006). VLBI2010 Antenna Specs, Data sheet.

DeBoer, D. (2001). The ATA Offset Gregorian Antenna, ATA Memo #16, February 10.

Imbriale, W.A. (2006). Design of a Wideband Radio Telescope, Jet Propulsion Laboratory and S. Weinreb and H. Mandi, California Institute of Technology.

Kilger, R. (2007). TWIN-Design studies, Presentation for the IVS board members (internal document), Wettzell.

Kronschnabl, G. (2006). Subject: Memo from Bill Petrachenko, E-mail to the Twin-Working Group (in German), July.

Lindgren, ETS-Lindgren (2005). The Model 3164-05 Open Boundary Quadridge Horn, Data Sheet.

Niell, A., A. Whitney, W. Petrachenko, W. Schlüter, N. Vandenberg, H.Hase, Y. Koyama, C. Ma, H. Schuh, G. Tucari (2006). VLBI2010: Current and Future Requirements for Geodetic VLBI Systems, in: *IVS Annual Report 2005*, pg. 13-40, NASA/TP-2006-214136, April.

Olsson, R., Kildal, P.-S., and Weinreb, S. (2006). The Eleven Antenna: A Compact Low-Profile Decade Bandwidth Dual Polarized Feed for Reflector Antennas, *IEEE Transactions on Antennas and Propagation*, Vol. 54, No. 2, February.

Petrachenko, B. (2006). The Case For and Against Multiple Antennas at a Site, *IVS Memorandum*, 2006-019v01.

Petrachenko, B. (2006). Performance Comparison between Traditional S/X and X/Ka Systems and a Broadband S-Ku System, *IVS Memorandum*, 2006-016v01.

RFSpin (2004). Double Ridged Waveguide Horn-Model DRH20, Antenna Specifications, Data Sheet.

Rohde&Schwarz (2004). SHF Antennas Crossed Log-Periodic Antennas HL024A1/S1, Data Sheet.

Rohde&Schwarz (2004). SHF Antennas Log-Periodic Antennas HL050/HL050S1, Data Sheet.

Rogers, A.E.E. (2006). Simulations of broadband delay measurements, Mark 5 Memo #043, MIT Haystack Observatory.

Rogers, A.E.E. (2006). Some thoughts on the calibration of broadband geodetic VLBI, Mark 5 Memo #044, MIT Haystack Observatory.

Rothacher M. (2006). GGOS: the IAG contribution to Earth observation, IGS Workshop 2006 "Perspectives and Visions for 2010 and beyond", May 8-12, Darmstadt, Germany

Weinreb, S., Mandi, H. (2006). Pattern and Noise Tests of ETS-Lindgren 3164-05 Quadridge/Vivaldi Antenna, California Institute of Technology.

Weinreb, S. (2007). Broadband feeds, E-mail, January.

Welch, Wm. J. (2005). The Allen Telescope Array, URSI, UC Berkeley, January.

VLBI2010 Simulations Using SOLVE

D.S. MacMillan
NVI, Inc. and NASA Goddard Space Flight Center
Greenbelt, Maryland USA 20002

Abstract. To design the future VLBI2010 system, the IVS is performing simulations to determine optimal network antenna locations, antenna sensitivities, slew rates, and observing schedules. I am developing a simulation procedure for testing different observing system parameters using the SOLVE VLBI analysis system. Here I describe the general procedure that is followed, validation and calibration of the simulation procedure, and simulation results for networks of increasing number of antennas.

Keywords. VLBI, simulation, VLBI2010

1 Introduction

The IVS is engaged in the design of a new observing system VLBI2010 (Niell et al., (2005)) that will consist of small (at least 12 m diameter) fast-slewing antennas. The goal is to choose antennas that are mechanically reliable and that can be reproduced economically to allow more international VLBI groups to be able to afford to install antennas. The result would be a superior global coverage with VLBI antennas which currently has poor Southern Hemisphere coverage. The smaller collecting area of the envisioned VLBI2010 antennas will be compensated for with data sampling over 3 or 4 continuous frequency bands from 2 to 15 GHz at a much higher data rate, for example, 8 to 32 Gbps, compared to the current operational rates of 128 or 256 Mbps. As part of the development of specifications for VLBI2010, it is necessary to investigate the geodetic performance of networks of nominal VLBI2010 antennas. To do this, I am developing a Monte Carlo procedure for simulating the performance of a specific observing scenario. In this paper, I describe the procedure, provide some examples of simulation validations where simulation results are compared with results from actual observations, and discuss results of network simulations.

2 Simulation Procedure

The first step in the simulation procedure is to specify the network site locations, antenna sensitivities, antenna slew rates, and observation SNR requirements. We then run the SKED (xxxx) program to generate an observation schedule for a 24-hour VLBI experiment session and a simulation observation file corresponding to the schedule. The next step is to run the VLBI SOLVE (Ma et al. (1990)) analysis program with a simulation data file to estimate parameters (for example, Earth orientation parameters (EOP) and site positions) in the same way as in the analysis of observed data.

To determine the precision (repeatability) of estimated parameters, a Monte Carlo simulation is performed by making repeated VLBI SOLVE runs with the same 24-hour observation file but with different input simulated observed delays. In the current simulation procedure, we generate simulate wet zenith delays and clock delays for each station as random walk processes. It is also possible to add gradient or turbulence (as equivalent wet zenith) delay contributions. Summarizing, the current model for the observed simulation delay is

$$[m_w(\varepsilon_2)\tau_{wz2} + clk_2] - [m_w(\varepsilon_1)\tau_{wz1} + clk_1] + \sigma_{obs} \qquad (1)$$

where m_w is the wet mapping function and ε_1 and ε_2 are the observation angles at sites 1 and 2. The τ_{wz} and *clk* terms are the wet zenith and clock delays at the two sites. To model, observation uncertainty, we add a corresponding white noise contribution, σ_{obs}

3 Simulation Validation

In order to see how simulation results compare with observed results, I have run simulated observations through SOLVE using observing schedules that were used for actual VLBI experiments. We believe that the dominant VLBI errors are a combination of atmospheric and clocklike (maser + instrumental)

errors. To simulate these errors, I generated wet zenith delays and clock delays as random walk processes as described above.

3.1 CONT05 Test

In September 2005, the IVS conducted a series of experiment sessions called CONT05 for a period of 15 consecutive days. These sessions were scheduled with nearly the same observing schedule. To test the simulation procedure, I generated simulated observed delays as random walk processes with typical expected atmosphere and clock variances. In previous work, we found that atmospheric variances computed from delay rate residuals using the Kalman filter procedure KALAN (Herring et al., (1990)) are in the range from 0.1 to 0.6 ps^2/s but are usually less than 0.3 ps^2/s (MacMillan, (1992)). Three simulations were run. In the first case, for all sites random walk variances were 0.1 ps^2/s for the wet zenith troposphere and 0.3 ps^2/s for the clock, which corresponds to an Allan standard deviation of 10^{-14} @ 50 minutes. In the second, the random walk variances were 0.3 ps^2/s for the atmosphere and 1.2 ps^2/s for the clock, which corresponds to $2x10^{-14}$ @ 50 minutes. In the third, random walk variances were increased to 0.5 ps^2/s. For each case, 15 ps was added to observation uncertainties and random noise with standard deviation equal to observation uncertainty was added. In our standard processing with SOLVE, this is about the level of noise that is added to observation uncertainties in reweighting of observations to make the solution χ^2 per degree of freedom unity.

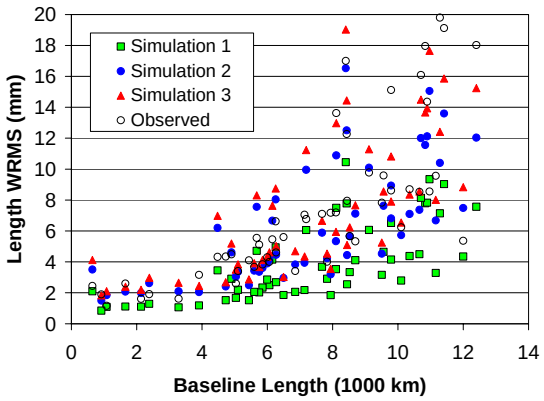

Fig. 1. Comparison of simulated versus observed CONT05 baseline length WRMS. Simulation 1: atmos 0.1 ps^2/s, clock 0.3 ps^2/s; Simulation 2: atmos 0.3 ps^2/s, clock 1.2 ps^2/s, Simulation 3: 0.5 ps^2/s, clock 1.2 ps^2/s.

Figure 1 compares the WRMS (weighted root mean square) baseline length repeatability from simulations with the observed repeatability. The last two simulations yield repeatabilities that are reasonably close to the observed values.

Another test that can be made is to look at the precision of EOP estimates. For this simulation, I computed the repeatability of EOP estimates over the sequence of 15 CONT05 sessions. Table 1 provides a comparison of the simulation EOP precision, the formal EOP uncertainty, and the WRMS difference between VLBI and IGS (International GNSS Service) EOP estimates.

Table 1. Simulation EOP precision for CONT05

Parameter	Simulation Precision	Formal Error	VLBI-IGS WRMS
X (μas)	54	30	55
Y (μas)	69	30	36
UT1 (μs)	3.7	1.3	---
Xr (μas/d)	277	92	198
Yr (μas/d)	178	87	158
LOD (μs/d)	6.4	3	16

In our geodetic analysis with the SOLVE program, we generally find that our parameter formal uncertainties underestimate observed precision by a factor of 1.5 to 2. The simulation precision values tend to be larger than the formal uncertainties by a somewhat larger factor. Except for LOD, the WRMS differences between observed VLBI and IGS EOP during the CONT05 period are comparable to the simulation precision. It is not understood why the simulation precision for Y-pole estimates is somewhat worse than for X-pole; whereas, it is significantly better in the observed data. Network geometry should be reflected in the formal uncertainties, which for CONT05 indicate that the X and Y precision are equal and therefore more consistent with the simulation.

3.2 CORE-NEOS Test

One of the ways that we can measure the accuracy of VLBI EOP estimates is by analyzing the differences between EOP estimated from two independent VLBI networks that observed simultaneously on the same days. From 1997 to 2000, a bi-monthly series of 80 24-hour VLBI experiments, the CORE-A series, were conducted on the same day as a corresponding weekly operational NEOS-A experiment. To see how consistent simulated data is with observed data, we

ran a Monte Carlo solution in which simulated data was run through all of the CORE-NEOS session observing schedules. In this case we used random walk variances of 0.5 ps^2/s for the atmosphere and 0.3 ps^2/s for clocks. I estimated EOP for all sessions and computed the RMS difference between simulated EOP from the 80 simultaneous pairs of 24-hour experiments. Table 2 shows the results from the simulation along with differences for observed data. The CORE-NEOS differences are remarkably similar to the observed differences.

Table 2. WRMS differences between EOP determined by the CORE-A and NEOS-A simultaneous experiment sessions

Parameter	Simulation	Observed
X (μas)	191	203
Y (μas)	223	151
UT1 (μs)	9.4	8.6
Psi (μas)	326	367
Eps (μas)	110	142
Xr (μas/d)	462	523
Yr (μas/d)	542	544
LOD (μs/d)	23	19

4 Recovery of Input Noise

The network simulations reported in this paper used simulated input atmospheric delay based on a random walk wet zenith troposphere model.

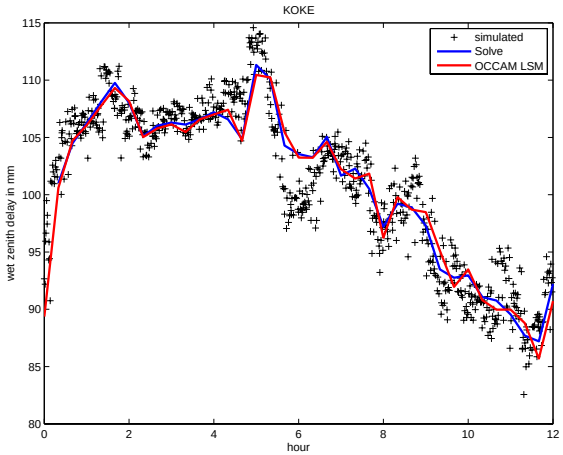

Fig. 2. Comparison of input equivalent wet zenith delay in mm at Kokee Park (Hawaii) (crosses) from a turbulence model with recovered wet zenith delay estimates using the SOLVE (solid blue line) and OCCAM (solid red line) analysis programs. (Figure courtesy of J. Böhm)

One of the issues investigated by the IVS VLBI2010 committee is what is the effect of using turbulent model delays in simulations rather than the simple wet zenith delay random walk. To obtain realistic simulations, we clearly need to use realistic tropospheric delays. T. Nilsson at Chalmers University of Technology (Onsala) generated turbulent delays for given observing schedules assuming Kolomogorov turbulence. Previous work on this was described in Nilsson et al. (2005).

Comparisons in Figure 2 between the input equivalent wet zenith delay input from the turbulence model and the estimated wet zenith delay using SOLVE or OCCAM shows that there are periods of time where recovery of the input model is poor. This implies that the delay from the turbulent model is not well-modeled as the product of an azimuthally symmetric wet mapping function and a wet zenith delay as given by equation (1). On the other hand, if the model input (for example, wet zenith delay random walk) has the same form as the estimation model as in equation (1), we may get unrealistic results that underestimate the atmospheric delay error.

5 Network Simulations

For VLBI2010, we would like to design a global network of antennas to optimize the precision of estimated parameters. Here, I will discuss simulations to determine the dependence of EOP and reference frame scale precision on the number of sites in the network. Simulations were run for the network of 32 sites shown in Figure 3 and then for a sequence of subset networks of 24, 16, and 8 sites. These networks were chosen to provide better global coverage than current VLBI networks and approximately even distribution of sites between the Northern and Southern hemispheres. The antennas used in the simulation were nominal VLBI2010 12-meter antennas with system equivalent flux density (SEFD) of 2500 Jy. The data rate was chosen to be 8 Gbps. For the simulation runs, the wet zenith delays and clock delays were generated with random walk variance of 0.5 ps^2/s and 0.3 ps^2/s.

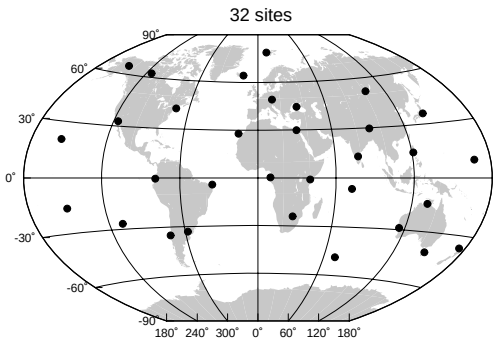

Fig. 3. Global network of 32 sites used for simulations

To estimate the precision of EOP, I ran a solution to estimate EOP in a Monte Carlo run in which the 24-hour simulation observation file was run with different input simulated delays for each of 25 repetitions. The WRMS of the estimated EOPs was taken to be the simulated EOP precision. As a function of network size, Figure 4 shows the EOP precision relative to the 8-station network precision. This relative precision improves by about a factor of two in going from 8 sites to 32 sites, but tends to level off for networks with more than 16 sites.

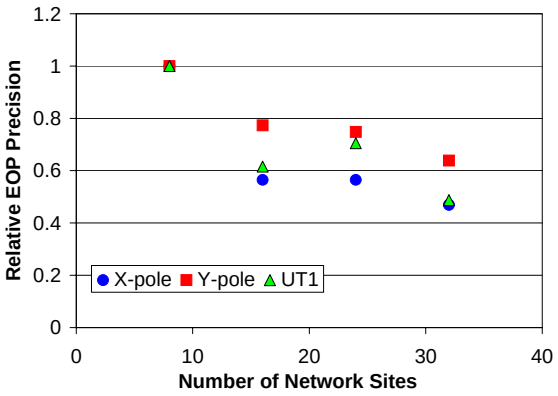

Fig. 4. EOP precision improvement with a larger network size based on Monte-Carlo simulations. Precision is given relative to the 8-site network precision for X-pole (circle), Y-pole (square), and UT1 (triangle).

To obtain an estimate of the terrestrial reference frame scale precision for a given network, I estimated a scale parameter for each of 25 solution repetitions. In this solution, site positions were not estimated so that any residual motion resulting from simulated delays would be propagated only to the estimated network scale parameter. Scale precision from the simulation is the WRMS of the scale

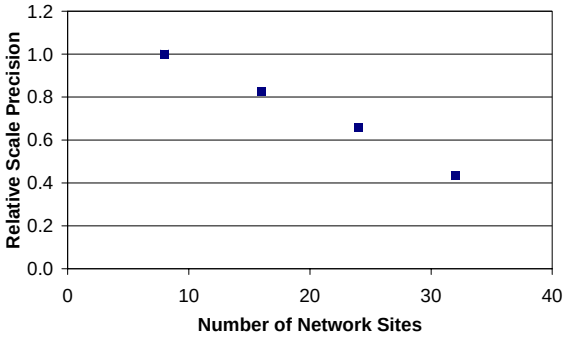

Fig. 5. Reference frame scale parameter precision from Monte-Carlo simulations. Precision is expressed relative to the precision of the 8-site network.

parameter estimates over the series of 25 repetitions. As illustrated in Fig. 5, scale precision improves with network size, where precision is given relative to the 8-site precision. As for EOP, precision improves by about a factor of two with a 32-site network. In contrast, the improvement appears to be nearly linear and does not level off for networks with more than 16 sites.

6 Summary

I have used the Monte Carlo method to determine expected precision of estimated geodetic parameters for global networks of VLBI2010 antennas. Comparisons between statistics of the simulation estimates and estimates from actually observed VLBI sessions show reasonably good agreement. Simulations of global networks of VLBI2010 antennas show that EOP and TRF scale precision improves by about a factor of 2 if the number of network sites increases from the current typical number of 8 sites up to 32 sites. For EOP, most of this improvement occurs in moving up to about 20 sites.

References

Herring, T.A., J.L. Davis, and I.I. Shapiro (1990). Geodesy by Radio Interferometry: The Application of Kalman Filtering to the Analysis of VLBI Data. *Journal of Geophysical Research*, 95(B8), pp. 12561-12582.

Ma, C, J.M. Sauber, L.J. Bell, T.A. Clark, D. Gordon, W.E. Himwich, and J.W. Ryan (1990). Measurement of Horizontal Motions in Alaska Using Very Long Baseline Interferometry. *Journal of Geophysical Research*, 95(B13), pp. 21991-22011.

MacMillan, D.S. and J.R. Ray (1991). Current Precision of VLBI Vertical Determinations. In: *Proceedings of the AGU Chapman Conference on Geodetic VLBI: Monitoring Global Change*, pp. 428-436.

Niell, A., A. Whitney, B. Petrachenko, W. Schlüter, N. Vandenberg, H. Hase, Y. Koyama, C. Ma, H. Schuh, and G. Tucari (2005). VLBI2010: Current and Future Requirements for Geodetic VLBI Systems, Report of Working Group 3 to the IVS Directing Board.

Nilsson, T. and L. Gradinarsky, and G. Elgered (2005). Correlations Between Slant Wet Path Delays Measured by Microwave Radiometry. *IEEE Transactions on Geoscience and Remote Sensing*, 43(5), pp. 1028-1035.

Monte Carlo Simulations for VLBI2010

Jörg Wresnik, Johannes Böhm, Harald Schuh
Institute of Geodesy and Geophysics (IGG),
Vienna University of Technology, Gusshausstr. 27-29, A-1040 Wien, Austria

Abstract. Monte Carlo simulations are carried out at the Institute of Geodesy and Geophysics (IGG), Vienna, and at Goddard Space Flight Center (GSFC), Greenbelt (USA), with the goal to design a new geodetic Very Long Baseline Interferometry (VLBI) system. Influences of the schedule, the network geometry and the main stochastic processes on the geodetic results are investigated. Therefore schedules are prepared with the software package SKED (Vandenberg 1999), and different strategies are applied to produce temporally very dense schedules which are compared in terms of baseline length repeatabilities. For the simulation of VLBI observations a Monte Carlo Simulator was set up which creates artificial observations by randomly simulating wet zenith delay and clock values as well as additive white noise representing the antenna errors. For the simulation at IGG the VLBI analysis software OCCAM (Titov et al. 2004) was adapted. Random walk processes with power spectrum densities of 0.7 and 0.1 $psec^2/sec$ are used for the simulation of wet zenith delays. The clocks are simulated with Allan Standard Deviations of $1 \cdot 10^{-14}$@50min and $2 \cdot 10^{-15}$@15min and three levels of white noise, 4 psec, 8 psec and, 16 psec, are added to the artificial observations. The variations of the power spectrum densities of the clocks and wet zenith delays, and the application of different white noise levels show clearly that the wet delay is the critical factor for the improvement of the geodetic VLBI system. At GSFC the software CalcSolve is used for the VLBI analysis, therefore a comparison between the software packages OCCAM and CalcSolve was done with simulated data. For further simulations the wet zenith delay was modeled by a turbulence model. This data was provided by Nilsson T. and was added to the simulation work. Different schedules have been run.

Keywords. VLBI, Monte Carlo simulation, baseline length repeatability, turbulence model

1 Introduction

Within the frame of IAG's (International Association of Geodesy) flagship project GGOS (Global Geodetic Observing System) it has become clear that modern space geodetic techniques should provide station coordinates and/or baseline length time series with an accuracy better than 1 mm. Only then, subtle effects such as non-linear station motions or sea level rise can be detected.

There has been a lot of discussion in recent years how Very Long Baseline Interferometry (VLBI) could exploit its present resources more efficiently and how future VLBI networks should look like to achieve this general goal of sub-mm accuracy. In October 2003 the International VLBI Service for Geodesy and Astrometry (IVS) installed Working Group 3 (WG3) 'VLBI 2010' to examine current and future requirements for geodetic VLBI systems. Based on the final report of WG3 (Niell et al. 2005) and in particular on the requests defined by the subgroup on 'observing strategies' of WG3, thorough and systematic simulation studies are carried out now. At the Institute of Geodesy and Geophysics (IGG), Vienna, different simulations are done to evaluate new observing strategies and schedules, to improve the modeling of troposphere refraction and clocks, to find the best antenna configuration and to optimize the network geometry.

A sequence of software programs is used for the simulations: after scheduling the observations with SKED (Vandenberg, 1999), they are transformed to NGS format and used as input for the VLBI analysis software package OCCAM (Titov et al. 2004), which was adapted for the simulations. Main part of the simulation studies is a so-called Monte Carlo simulator which creates the artificial observations based on realistic properties of the wet zenith delays and clocks. A description of the Monte Carlo simulator is provided in Section 2.

Possible criteria to evaluate the potential of the VLBI-system are: baseline length repeatabilities, formal errors of the Earth Orientation Parameters (EOP), or the standard deviation between the

simulated stochastic processes (troposphere, clocks) and their estimates. In this paper we focus on the baseline length repeatabilities which are obtained from different observing schedules with different observation densities. Section 4 describes the influence of the wet zenith delays (random walk model and turbulence model) and clocks at three different levels of white noise with respect to baseline length repeatabilities. Section 5 describes the comparison between the two software packages CalcSolve and OCCAM for VLBI analysis.

2 Monte Carlo Simulator

In VLBI analysis the stochastic processes related to clocks and wet delays play a key role. Thus, the basis for predicative (Monte Carlo) simulations is the creation of realistic clock values and wet zenith delays at the stations.

Treuhaft and Lanyi (1987) derived the variation of the wet zenith delay from turbulence theory, and Herring et al. (1990) used random walk processes for the simulation of clocks and wet zenith delays in Kalman filter solutions. For the wet zenith delay Herring et al. (1990) assumed a power spectrum density (PSD) of 0.75 psec^2/sec and for the clocks 0.15 psec^2/sec.

For simulations the o-c vector (observed minus computed) of the least-squares adjustment has to be set up with simulated values of wet zenith delay, clocks and white noise (Equation 1).

$$o - c = (WZD_2 \cdot mfw_2(e) + CL_2 + WN_2) - (WZD_1 \cdot mfw_2(e) + CL_1 + WN_1) \quad (1)$$

$WZD_{1,2}$ and $CL_{1,2}$ are the simulated wet zenith delay and clock values at station 1 and 2 of each observable, and $mfw_{1,2}(e)$ are the wet mapping functions for the elevation angle e which are assumed to be error free in our studies. For each station white noise $WN_{1,2}$ is added individually. The Monte Carlo simulator is implemented in OCCAM and creates values for the wet zenith delays, clocks and white noises at each epoch.

The different power spectrum densities (PSD) used for the simulation of clocks and wet zenith delay are shown in Table 1. The Allan Standard Deviation (ASD) of the clocks is converted to the PSD of a random walk ignoring the integrated random walk. The white noise which corresponds to the performance of the antenna is 4, 8, and 16 psec, with e.g. 4 psec white noise corresponding to an antenna system with an accuracy of approxi-mately 1.2 mm. The white noise covers all instru-menttal errors of the antenna system.

The values given in Table 1 were chosen by the VLBI2010 committee to provide comparability between the simulations done at IGG Vienna and at Goddard Space Flight Center (Greenbelt, USA).

Table 1. Different power spectrum densities (PSD) used for simulation of CL and wet zenith delay, and different values for the white noise.

WZD	0.1 [psec^2/sec]	0.7 [psec^2/sec]	turbulence model
clocks	$2 \cdot 10^{-15}$@15min (ASD) 0.0036 [psec^2/sec] (PSD)	$1 \cdot 10^{-14}$@50min (ASD) 0.3 [psec^2/sec] (PSD)	
WN	4 psec	8 psec	16 psec

The VLBI analysis is carried out with the Kalman filter of OCCAM estimating wet zenith delays and clocks at each observation epoch. The Kalman filter seems to be advantageous for simulations because the time resolution of the wet zenith delay and clock parameters depends on the observation density only and does not have to be adjusted for each schedule as with the Gauss-Markov model.

For the calculation of realistic baseline length repeatabilities the simulation process is repeated 25 times, each time creating new values for wet zenith delay, clocks, and white noise. The baseline length repeatability corresponds to the standard deviation of the 25 determinations of the baseline lengths. In the following analyses, not only the PSD of the wet zenith delay and clocks, and the white noise levels are varied, but also the underlying schedule is changed to assess its influence on the baseline length repeatabilities.

3 Schedule

Three different schedules for exactly the same network (Figure 1) are used for this analysis (Table 2). The network contains 16 stations, including the CONT02 (Thomas et al. 2003) network configu-ration and 8 fictitious stations. The selection of the

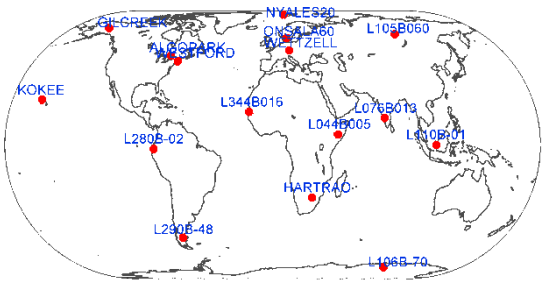

Fig. 1. 16 station network used for the simulations. In addition to the 8 stations from CONT02, 8 fictitious stations have been added to provide a good global coverage.

additional stations was not opti-mized by political, infrastructural, and economical aspects. Further networks are designed as so-called test networks. The selection of additional stations was driven by a good coverage of stations on all major tectonic plates (3 stations on each plate), and for the location IGS sites were picked. The size of the test networks are 16, 24, 32, and up to 40 stations. Schedules for the networks have been created by John Gipson (N.V.I.) and simulations for the different network sizes are in progress.

The schedules were created with different strategies and different scan lengths yielding different num-bers of scans per hour per station and consequently different observation densities for the 24 hour session. The first schedule (sked1) has an inhomo-geneous distribution of observations at the stations.

Table 2. Parameters of the three different schedules (sked1, sked2, sked3) used for the simulation. A schedule is considered as homogenous (last row of the table) if the number of observations at each site is about the same.

	sked1	sked2	sked3
scan length [sec]	5 - 60	5	5
scans/h/stat	45	100	171
scans	2737	5760	9386
observations	57595	116308	226639
homogeneous	no	yes	yes

The baseline length repeatabilities for all three schedules (Figure 2) were calculated with simulated wet zenith delay based on a PSD of 0.1 psec^2/sec, clocks which correspond to an ASD of $2{\cdot}10^{-15}$@15min, and a white noise of 4 psec. These values represent the lower limit of the variations of the stochastic processes, thus giving the possibility to see the influence of the different schedules. Figure 2 gives clearly worse repeatabilities for a couple of baselines of sked1 compared to the other baselines and the other schedules. A closer look shows that all of the "bad" baselines contain the far South station L106B-70 which in the first schedule gets 2703 observations only compared to 9754 observations at Wettzell.

Unlike sked1, sked2 improves the baseline repeatability as the effect of the inhomogeneous schedule is eliminated. There is another slight improvement from sked2 to sked3. The viability of a schedule with more than 170 scans per hour per station has to be proven with respect to the antenna construction, because such a schedule needs very fast slewing rates and accelerations. For these schedules the slewing rates for all 16 antennas were set to 18 deg/sec in azimuth and 4.5 deg/sec in elevation, the acceleration in azimuth is 3.6 deg/sec^2 and 0.9 deg/sec^2 in elevation, which shortens the antenna life time and causes frequent maintenance periods not allowing continuous VLBI observations for a longer time period. This problem could be overcome by a so-called twin telescope at a site, which means that two (or more) identical antennas will be put at one site nearby with the possibility to observe simultaneously or to observe with one antenna while the other one is repaired. Twin telescopes offer additional chances like observing double differences. Nevertheless, the cost efficiency

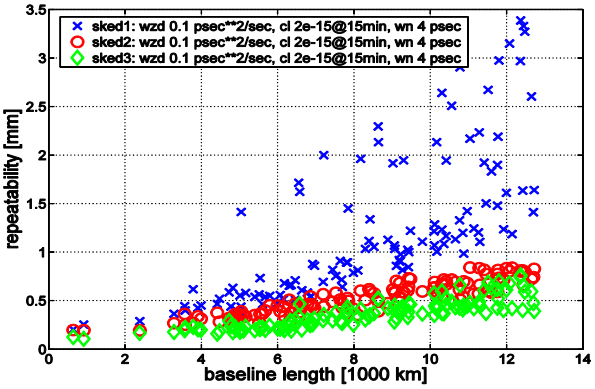

Fig. 2. Baseline length repeatabilities comparing three different schedules (sked1: 57595 observations (x), sked2: 116308 observations (○), and sked3: 226639 observations (◊)).

of twin telescopes and the additional observing options need to be investigated in detail. A rough cost analysis is given in the IVS Memorandum 2006-019v01: The Case For and Against Multiple Antennas at a Site (Petrachenko 2006). The fundamental station Wettzell (Germany) plans to install a twin telescope in the near future (Schlüter 2006, personal communication).

4 Baseline length repeatabilities for different wet zenith delays and clock values

All further analyses with the random walk model for WZD were carried out with the highly dense schedule sked3 so that the influence of wet zenith delays and clocks at different noise levels can be seen more clearly. The baseline length repeatabilities shown in Figure 3 are calculated for simulated wet zenith delay with a PSD of 0.7 psec^2/sec and clocks with an ASD of $2\cdot10^{-15}$@15min. This ASD corresponds to a very small PSD for the random walk of the clock (see Table 1), thus simulating a 'perfect' clock. The baseline length repeatabilities do not reveal a clear difference between the 4 and 8 psec white noise levels; in fact the PSD of the wet zenith delays dominates the baseline length repeatability. With this particular combination an antenna with an accuracy of 4 psec will give nearly the same results as an '8 psec antenna'.

The dominating effect of the wet zenith delay is also shown in Figure 4, where the two different PSD for the wet zenith delay (0.1 and 0.7 psec^2/sec) are compared at 4 psec and 16 psec noise levels. A PSD of 0.7 psec^2/sec for the wet zenith delay and 4 psec antennas give about the same result as 16 psec antennas and wet zenith delays with a PSD of 0.1 psec^2/sec, if the clocks correspond to an ASD of $2\cdot10^{-15}$@15min in both cases.

To compare the effect of different ASD of the clocks, Figure 5 shows two different levels of white noise (4 and 16 psec) and two ASD for the clocks ($2\cdot10^{-15}$@15min and $1\cdot10^{-14}$@50min). The PSD of the wet zenith delay was set to 0.1 psec^2/sec. In general very small differences of the baseline length repeatability can be seen if decreasing the ASD from $2\cdot10^{-15}$@15min to $1\cdot10^{-14}$@50min.

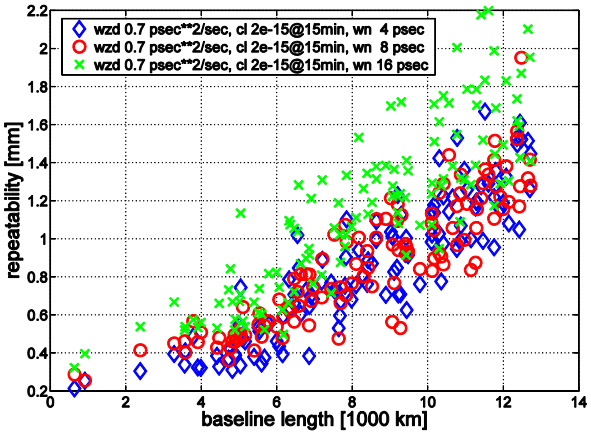

Fig. 3. Baseline length repeatabilities for three different levels of white noise: 4 (◊), 8 (○), and 16 psec (x). Clocks are simulated having an ASD of $2\cdot10^{-15}$@15min and wet zenith delays having a PSD of 0.7 psec^2/sec.

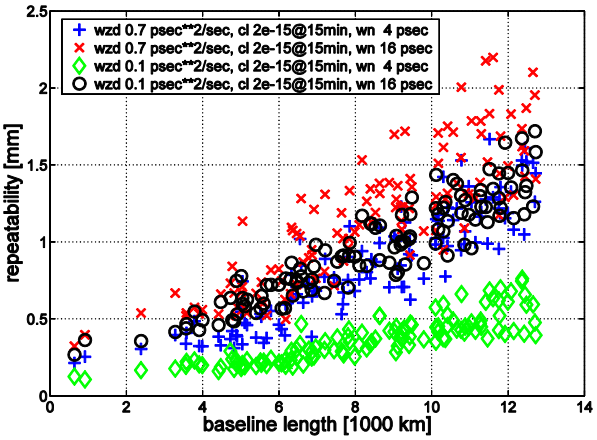

Fig. 4. Baseline length repeatabilities with clocks that correspond to an ASD of $2\cdot10^{-15}$@15min: 4 psec white noise and 0.7 psec^2/sec PSD of wet zenith delay (+); 4 psec white noise and 0.1 psec^2/sec PSD of wet zenith delay (◊); 16 psec white noise and 0.7 psec^2/sec PSD of wet zenith delay (x); 16 psec white noise and 0.1 psec^2/sec PSD of wet zenith delay (○).

To compare the WZD models based on random walk and the turbulence model baseline length repeatabilities for the sked1 have been analyzed. Figure 6 shows that the turbulence model is between the random walk models.

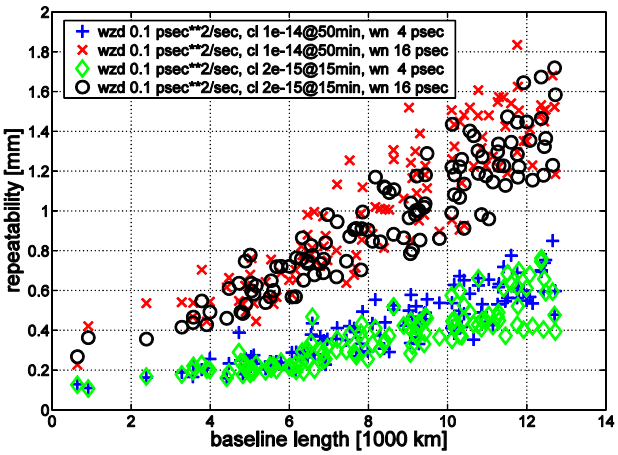

Fig. 5. Baseline length repeatabilities with wet zenith delays that correspond to a PSD of 0.1 psec^2/sec: 4 psec white noise and an ASD of $1{\cdot}10^{-14}$@50min for clocks (+); 4 psec white noise and an ASD of $2{\cdot}10^{-15}$@15min for clocks (◊); 16 psec white noise and an ASD of $1{\cdot}10^{-14}$@50min for clocks (x); 16 psec white noise and an ASD of $2{\cdot}10^{-15}$@15min for clocks (○).

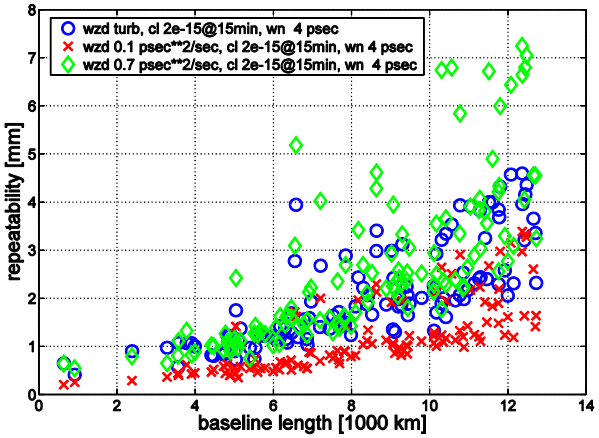

Fig. 6. Baseline length repeatabilities with 4 psec white noise and an ASD of $2{\cdot}10^{-15}$@15min for clocks with WZD from the turbulence model (○), with WZD from the random walk model that correspond to a PSD of 0.1 psec^2/sec (x) and a PSD of 0.7 psec^2/sec (◊).

5 Comparison of CalcSolve and OCCAM

For the comparison between the two VLBI analysis software packages CalcSolve and OCCAM LSM a parameterization as similar as possible is used:

- NNR/NNT for a priori station coordinates, ICRF fixed.
- EOP offsets for the 12 hour session.
- 20 min piecewise linear function for wet zenith delays with 15 mm/hour constraints.
- quadratic function plus 60 min piecewise linear function for clocks with 54 mm/hour constraints.
- 6 hour piecewise linear function for gradients with 2 mm/day constraints, 0.5 mm constraint on gradient offset.

Because the vector (o-c) is set to the sum of stochastic parameters, the expectation value for the unknowns (adjustments) is zero. OCCAM LSM has limitations in terms of size of design matrix. Thus, the Monte Carlo simulation was set up for a 12 h schedule with 37230 observations of a 16 station network, which contains existing VLBI sites and simulated ones (Figure 7). The wet Niell Mapping Function NMF (Niell, 1996) was used to set up (o-c), and it was also used as partial derivative to estimate the WZD in the adjustment.

The o-c vector was build up in the same way as shown before, but the decision was taken to add the white noise to each baseline observation instead of a station dependent white noise. So Equation (1) is changed as follow:

$$o-c = (WZD_2 \cdot mfw_2(e) + CL_2) - (WZD_1 \cdot mfw_2(e) + CL_1) + WN_{BSL} \quad (2)$$

The parameters used for the simulation are listed in Table 3:

Table 3. Parameter used for the simulation of WZD, clocks and the WN.

WZD	0.5 [psec^2/sec]
clocks	$2{\cdot}10^{-15}$@15min (ASD) 0.0036 [psec^2/sec] (PSD)
WN	8 psec

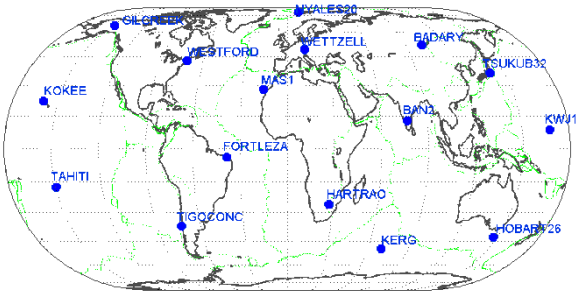

Fig.7. 16 station test-network

The results of different parameters of the CalcSolve and OCCAM resolutions are listed below:

5.1 Earth orientation parameters

The results for Earth orientation parameters are given in Table 4.

Table 4. Earth orientation parameters.

	xp [uas]	yp [uas]	dut1 [us]	psi [uas]	eps [uas]
OCCAM	-0.1	-9.2	0.7	12.6	34.9
LSM	± 3.4	± 3.5	± 0.2	± 3.3	± 7.9
CalcSolve	-0.5	-12.6	0.9	37.0	11.0
	± 3.9	± 4.1	± 0.2	± 8.1	± 3.3

5.2 Station heights and estimation of wet zenith delays

The sigmas of the station heights from CalcSolve are about 0.1 mm, from LSM about 0.7 mm, from the Kalman Filter about 0.5 mm. The sigmas from CalcSolve of the wet zenith delays are about 0.3 mm, from LSM about 0.6 mm.

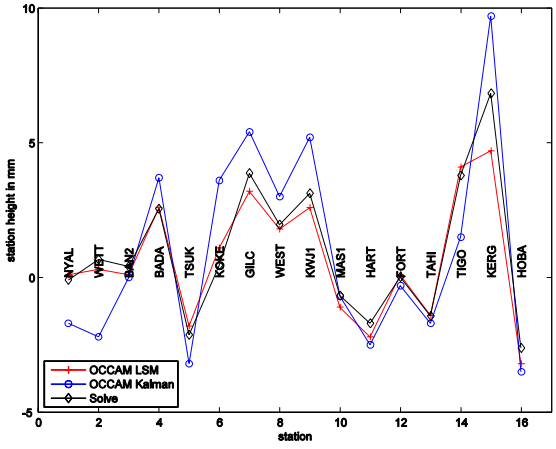

Fig. 8. Adjustments for the station heights in mm

5.3 Baseline lengths

The derived baseline lengths are shown in Figure 10. The comparison between the two software packages shows a good agreement. All baselines with the station KERG show a rather high difference between the estimated and adjusted baseline length. For baselines with this station also the agreement between CalcSolve and OCCAM LSM is not as good as for all other baselines. The disagreement between the two solutions is in a range of about ±2 mm.

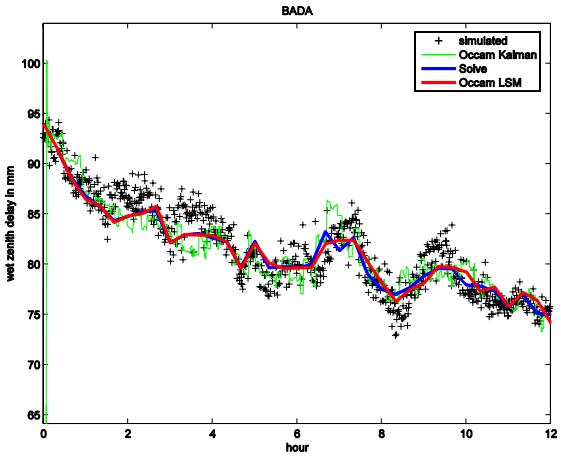

Fig. 9. Estimated wet zenith delays for station BADA

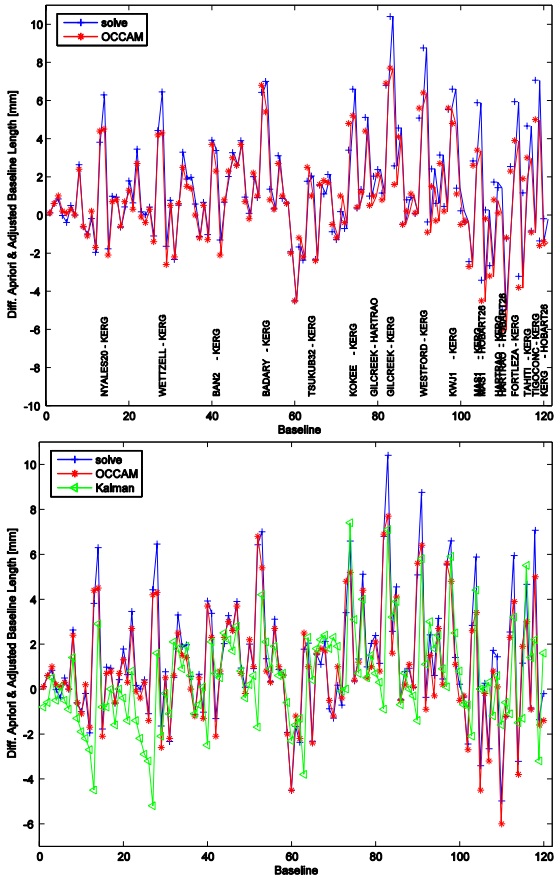

Fig. 10. Adjustments for the baseline lengths in mm,(upper plot) CalcSolve and LSM solutions and (lower plot) CalcSolve, LSM and Kalman solutions

6 Conclusions

The Monte Carlo Simulator produces wet zenith delay and clock values as well as white noise for each individual station at each scheduled epoch, so that the o-c vector can be calculated for all observations of a VLBI session. For the same schedule the Monte Carlo Simulator is creating 25 different 24 hour sessions, which can be used to determine baseline length repeatabilities. The comparison of three different schedules (same network but different number of observations) shows that sked1 with the lowest observation density (57595 observations in 24 hours) and an inhomogeneous schedule (different number of observations at the stations) yields the worst baseline length repeatabilities. Sked2 with 116308 observations significantly improves the baseline repeatabilities, and very dense schedules like sked3 further improve the repeatabilities but hold a problem for the antenna life time as the slewing rates and the accelerations of the antennas have to be very high. This may cause frequent maintenance periods, which is in contradiction to the plan of continuous VLBI observations. The problem could be overcome by twin telescopes.

The simulation points out clearly that the wet zenith delay is the limiting factor for the accuracy of the VLBI system. The baseline length repeatabilities are dominated by the PSD of the wet zenith delay, e.g. if the wet zenith delay is assumed with a PSD of 0.7 psec^2/sec the 4 psec antennas give very similar results in terms of baseline length repeatability as the 16 psec antennas and a wet zenith delay with a PSD of 0.1 psec^2/sec. To reduce the influence of wet zenith delay in the VLBI analysis, the use of Water Vapor Radiometers (WVR) in VLBI analysis has to be further investigated. Changing the ASD of the clocks from $2\cdot10^{-15}$@15min to $1\cdot10^{-14}$@50min shows in general very small differences of the baseline length repeatabilities and it can be assumed that clocks more precise than $2\cdot10^{-15}$@15min will only marginally improve the results. Thus, VLBI station clocks with $2\cdot10^{-15}$@15min seem to be good enough to profit from new and more accurate antenna systems.

The comparison between the two VLBI analysis softwares CalcSolve and OCCAM showed a good agreement for station heights as well as for the adjustments of baseline lengths. The estimation of wzd parameters shows the same result for both software packages.The next development of the Monte Carlo simulation will include a turbulence driven simulation of wet zenith delay. Furthermore, simulations will be carried out for different network geometries with networks of up to 40 stations. The benefit from twin antennas has to be proven, too, which seem to provide interesting new applications of geodetic and astrometric VLBI.

References

Herring, T.A., J.L. Davis, and I.I. Shapiro (1990). Geodesy by Radio Interferometry: The Application of Kalman Filtering to the Analysis of Very Long Baseline Interferometry Data. Journal of Geophysical Research, Volume 95, No. B8, pp 12561-12581.

Niell, A., A. Whitney, B. Petrachenko, W. Schlüter, N. Vandenberg, H. Hase, Y. Koyama, C. Ma, H. Schuh, G. Tuccari (2005). VLBI2010: Current and Future Requirements for Geodetic VLBI Systems. Report of Working Group3 to the IVS Directing Board

Petrachenko B. (2006). The Case For and Against Multiple Antennas at a Site. IVS Memorandum 2006-019v01, 01SEP2006

Treuhaft, R.N., and G.E. Lanyi (1987). The effect of the dynamic wet troposphere on radio interferometric measurements. Radio Science, Volume 22, No. 2, pp 251-265.

Titov, O., V. Tesmer, and J. Boehm (2004). OCCAM v. 6.0 software for VLBI data analysis, in International VLBI Service for Geodesy and Astrometry. In: Vandenberg NR, Baver KD (eds.): Proceedings of the third IVS General Meeting, Ottawa, Canada, February, 267–271.

Thomas, C., D.S. MacMillan (2003). Core operation center report. In: Vandenberg NR, Baver KD (eds): International VLBI Service for Geodesy and Astrometry 2002 Annual Report, NASA/TP-2003–211619. Goddard Space Flight Center, Maryland, USA

Simulations of atmospheric path delays using turbulence models

T. Nilsson, R. Haas, G. Elgered
Department of Radio and Space Science, Chalmers University of Technology, Onsala Space Observatory, SE-43992 Onsala, Sweden

Abstract. In many space geodetic applications, like VLBI and GPS, the atmospheric path delay is an error source which needs to be modelled. A problem when modelling this delay is the turbulent behaviour of the atmosphere. Simulations can be used to investigate this error. In this paper we describe how to simulate the path delay through a turbulent atmosphere. Delays are simulated to vary both as function of observation direction and time.

Keywords. Space geodesy, simulation, atmospheric turbulence, wet delay

1 Introduction

The signals used in space geodetic techniques, like VLBI (Very Long Baseline Interferometry) and GPS (Global Positioning System) are delayed in the atmosphere of the Earth. This delay needs to be properly modelled in order to derive accurate results using these techniques, e.g. estimates of station position etc. However, the turbulent nature of the atmosphere will cause the atmospheric delays to vary both as function of direction and time. The models used for the atmospheric delay in analyses of space geodetic data usually cannot completely describe all these variations. Hence, the results of such analyses will contain errors.

Typically the error caused by atmospheric turbulence will be small and will only be important for high accuracy applications (i.e. mm-level accuracy). One example where turbulence needs to be considered is when designing the next generation geodetic VLBI system, VLBI2010 (Niell et al., 2005). The goal of this system is to reach a global baseline length repeatability of 1 mm.

Simulations can be used in order to investigate how much the atmospheric turbulence degrades the accuracy of space geodetic techniques. This requires simulating the propagation delay of radio signals through a turbulent atmosphere. This work describes how such simulated delays can be obtained. We concentrate on the simulations of the wet part of the atmospheric delays since this part typically gives the largest variations. The described method could however fairy easy be extended to also describe variations in the hydrostatic delay.

The simulations use the theory of Treuhaft and Lanyi (1987) to describe variations in wet delay, which is based on the Kolmogorov turbulence theory (Tatarskii, 1971). The theory has been tested in many different works: The variations as function of time were investigated in e.g. Keihm (1995) and the correlations between the delay in different directions was studied by Nilsson et al. (2005) and Nilsson et al. (2006). Mostly these investigations showed that the basic characteristics of the measurement time series were in agreement with the turbulence theory.

2 Theory

The slant wet delay l_i in direction $\mathbf{r}_i$ at time t_i is given by:

$$l_i = \int_{S_i} (n_w(\mathbf{r}_i(z), t_i) - 1)\, ds_i \qquad (1)$$

where S_i is the slant path, n_w the wet part of the refractive index, and z the height. For simplicity, we refer all wet delays to the zenith direction by introducing the equivalent zenith wet delay (EZWD) l_i^z as:

$$l_i^z = \int_0^\infty (n_w(\mathbf{r}_i(z), t_i) - 1)\, dz = \frac{l_i}{m_i} \qquad (2)$$

where m_i is a mapping function.

To simulate a set of EZWDs we start with an a priori delay l_0^z in some direction at some

time epoch t_0. Then we calculate the covariance matrix C for which element (i,j) is given by:

$$\begin{aligned}[C]_{ij} &= \left\langle (l_i^z - l_0^z)\,(l_j^z - l_0^z) \right\rangle \\ &= \left\langle \iint [n_i(z) - n_0(z)]\,[n_j(z') - n_0(z')]\,dz\,dz' \right\rangle \\ &= \frac{1}{2}\iint \Big[\left\langle (n_i(z) - n_0(z'))^2 \right\rangle \\ &\quad + \left\langle (n_j(z) - n_0(z'))^2 \right\rangle \\ &\quad - \left\langle (n_i(z) - n_j(z'))^2 \right\rangle \\ &\quad - \left\langle (n_0(z) - n_0(z'))^2 \right\rangle \Big]\,dz\,dz' \end{aligned} \tag{3}$$

where $\langle \dots \rangle$ denotes expectation value and the notation $n_i(z) = n_w(\mathbf{r}_i(z), t_i)$ has been introduced. Knowing the covariance matrix C, simulated EZWDs can be obtained simply by generating a series of random numbers with covariance matrix C, and then adding these to the initial EZWD l_0^z.

A simple case is when the EZWDs are described by a Gaussian distribution. This may not correspond to how real EZWDs are distributed, but it is a good approximation in most cases. Since C is a symmetric matrix it can be decomposed as:

$$C = D\,D^T \tag{4}$$

where ^{T} denotes transpose. This decomposition can for example be a Cholesky decomposition (Press et al., 1992). Then the vector of simulated EZWDs, $\mathbf{l}^z = [l_i^z, l_2^z, \dots]^T$, can be generated by:

$$\mathbf{l}^z = l_0^z + D\mathbf{x} \tag{5}$$

where $\mathbf{x}$ is a vector of zero mean white Gaussian random numbers with variance one.

Once the simulated EZWDs have been obtained these need to be mapped back to the slant directions in order to get slant wet delays. In order to do this the wet mapping functions must be known. This is not the case since a mapping function (as defined by (2)) will depend upon the wet part of the refractive index profile along the slant direction. However, the variations in the mapping function are normally small, especially for high elevation angles. In the case when the variations in the wet delays are caused by turbulence, we can divide a slant wet delay into two parts: a homogeneous part which we assume to be constant and a turbulent part which is varying. If the turbulent part is much smaller than the homogenous part the mapping function of a slant wet delay would be very close to the mapping function describing the homogenous part of the delay. Hence we can approximate the mapping functions by those of the homogeneous part.

2.1 Calculating the covariance matrix

In order to calculate the integrals in (3) the correlations between the refractivity at two different locations and/or two different time instants need to be known. Such correlations can be obtained from the theory of atmospheric turbulence. According to Treuhaft and Lanyi (1987):

$$\left\langle (n_w(\mathbf{r}_i) - n_w(\mathbf{r}_j))^2 \right\rangle = C_n^2 \frac{\|\mathbf{r}_i - \mathbf{r}_j\|^{2/3}}{1 + \dfrac{\|\mathbf{r}_i - \mathbf{r}_j\|^{2/3}}{L^{2/3}}} \tag{6}$$

where C_n is called the refractive index structure constant (Tatarskii, 1971) and L is the turbulence saturation scale length. Here, $\|\dots\|$ denotes the norm defined by $\|\mathbf{x}\| = \sqrt{\mathbf{x}^T\mathbf{x}}$. Equation (6) only gives the correlation between spatial locations at the same time instant. Temporal variations can be modelled by the same equation by assuming that these are caused by the air-masses moving with the wind. With this assumption (6) can be generalised to describe both spatial and temporal variations:

$$\left\langle (n_i - n_j)^2 \right\rangle = C_n^2 \frac{\|\mathbf{r}_i - \mathbf{r}_j + \mathbf{v}\delta t_{ij}\|^{2/3}}{1 + \dfrac{\|\mathbf{r}_i - \mathbf{r}_j + \mathbf{v}\delta t_{ij}\|^{2/3}}{L^{2/3}}} \tag{7}$$

where $\mathbf{v}$ is the wind speed and $\delta t_{ij} = t_i - t_j$. Using this expression (3) becomes:

$$\begin{aligned}[C]_{ij} = \frac{C_n^2}{2}\iint \Bigg[& \frac{\|\mathbf{r}_i(z) - \mathbf{r}_0(z') + \mathbf{v}\delta t_{i0}\|^{2/3}}{1 + \dfrac{\|\mathbf{r}_i(z) - \mathbf{r}_0(z') + \mathbf{v}\delta t_{i0}\|^{2/3}}{L^{2/3}}} \\ & + \frac{\|\mathbf{r}_j(z) - \mathbf{r}_0(z') + \mathbf{v}\delta t_{j0}\|^{2/3}}{1 + \dfrac{\|\mathbf{r}_j(z) - \mathbf{r}_0(z') + \mathbf{v}\delta t_{j0}\|^{2/3}}{L^{2/3}}} \\ & - \frac{\|\mathbf{r}_i(z) - \mathbf{r}_j(z') + \mathbf{v}\delta t_{ij}\|^{2/3}}{1 + \dfrac{\|\mathbf{r}_i(z) - \mathbf{r}_j(z') + \mathbf{v}\delta t_{ij}\|^{2/3}}{L^{2/3}}} \\ & - \frac{\|\mathbf{r}_0(z) - \mathbf{r}_0(z')\|^{2/3}}{1 + \dfrac{\|\mathbf{r}_0(z) - \mathbf{r}_0(z')\|^{2/3}}{L^{2/3}}} \Bigg]\,dz dz' \end{aligned} \tag{8}$$

The double integral can be evaluated using numerical integration.

2.2 Optimisation

If the number of EZWDs that needs to be simulated is high the covariance matrix will be large and a lot of calculations are required in order to do the simulations. However, it may not be necessary to consider all correlations. For example, the correlation between two EZWDs can be ignored if the correlation is small (i.e. over large time scales). One possible way to reduce the number of needed calculations is to do the simulations step by step. This could be done by dividing the time period of the simulation into smaller parts, each part having a length of e.g. a few hours. First the EZWDs of the first part can be simulated using (5). The EZWDs of each other part of the simulation period are then simulated using only the correlation between the delays in that part and the delays in the previous part. This is done by first calculating the covariance matrix C for the set of observations consisting of the EZWDs in the part that is to be simulated ($\mathbf{l}_2$) and those of the previous part ($\mathbf{l}_1$) (which has already been simulated). If the decomposition in (4) is a Cholesky decomposition, D will be a lower triangular matrix. This could be divided into sub-matrices as:

$$D = \begin{bmatrix} D_{11} & 0 \\ D_{21} & D_{22} \end{bmatrix} \qquad (9)$$

where D_{11} and D_{22} are lower triangular matrices. D_{11} has the same number of rows and columns as the number of elements in $\mathbf{l}_1$, and D_{22} has the same number of rows and columns as there are elements in $\mathbf{l}_2$. Then, simulated $\mathbf{l}_2$ values can be obtained by:

$$\mathbf{l}_2 = D_{21}\, D_{11}^{-1}\, \mathbf{l}_1 + D_{22}\, \mathbf{x} \qquad (10)$$

An EZWD simulated in this way will have the correct correlation with all other EZWDs in the same part and with the EZWDs in the previous and next part of the simulation period. However, the correlations with the EZWDs in all other parts of the simulation period will not necessarily be correct; hence the length of each part needs to be long enough for those correlations to be negligible. The length needed will be dependent on the wind speed and the C_n profile, with longer periods needed for low wind speeds and/or large C_n values at high altitudes. However, typically a period of a couple of hours should be enough.

2.3 Parameters needed for simulation

Several parameter values are needed in order to simulate the slant wet delays. These are the initial EZWD l_0^z, the structure constant C_n, the saturation length scale L and the wind speed $\mathbf{v}$. Also the mapping function m needs to be specified in order to map the EZWDs to the slant directions.

In order to get realistic delays these parametersshould have values typical for the site of interest. For example, l_0^z and the wind velocity could be obtained from numerical weather prediction models, and C_n could be estimated using high resolution radiosonde data (Tatarskii, 1971; VanZandt et al., 1978; d'Auria et al., 1993). In general C_n will be dependent on height. Treuhaft and Lanyi (1987) used the approximation that C_n is constant up to an effective tropospheric height h and zero above. For Goldstone, California they estimated $C_n = 2.4 \cdot 10^{-7}$ m$^{-1/3}$, $h = 1000$ m, and $L = 3000$ km, using water vapour radiometer data. In later works C_n and h were modified to $C_n = 0.7 \cdot 10^{-7}$ m$^{-1/3}$ and $h = 2000$ m (Keihm, 1995; Linfield, 1996) since these values showed better agreement with radiometer data.

3 Examples of simulated delays

Fig. 1–4 show examples (using (5)) that visualise the temporal and spatial variations of the simulated delays. In Fig. 1 the zenith wet delay is simulated for a one day period. In these simulations $l_0^z = 10$ cm (zenith wet delay at time zero), $h = 2000$ m, $L = 3000$ km, and the wind velocity 8 m/s were used. Simulations for $C_n = 0.3 \cdot 10^{-7}$ m$^{-1/3}$, $C_n = 1 \cdot 10^{-7}$ m$^{-1/3}$, and $C_n = 3 \cdot 10^{-7}$ m$^{-1/3}$ are shown, five different simulations for each value of C_n. As expected the simulated zenith wet delays show larger variations for higher C_n values, i.e. when the atmosphere is more turbulent. The case $C_n = 1 \cdot 10^{-7}$ m$^{-1/3}$ corresponds to typical atmospheric conditions at mid-latitudes. For example, Nilsson et al. (2005) estimated as scale factor proportional to $C_n^2\, h^{4/3}$ using the correlations between equivalent zenith wet delays of different direction as measured by a water vapour radiometer. Assuming $h = 2000$ m, the obtained scale factor values corresponds to C_n values in the range 0.5–2.5 $\cdot 10^{-7}$ m$^{-1/3}$ for the Onsala site on the Swedish west coast.

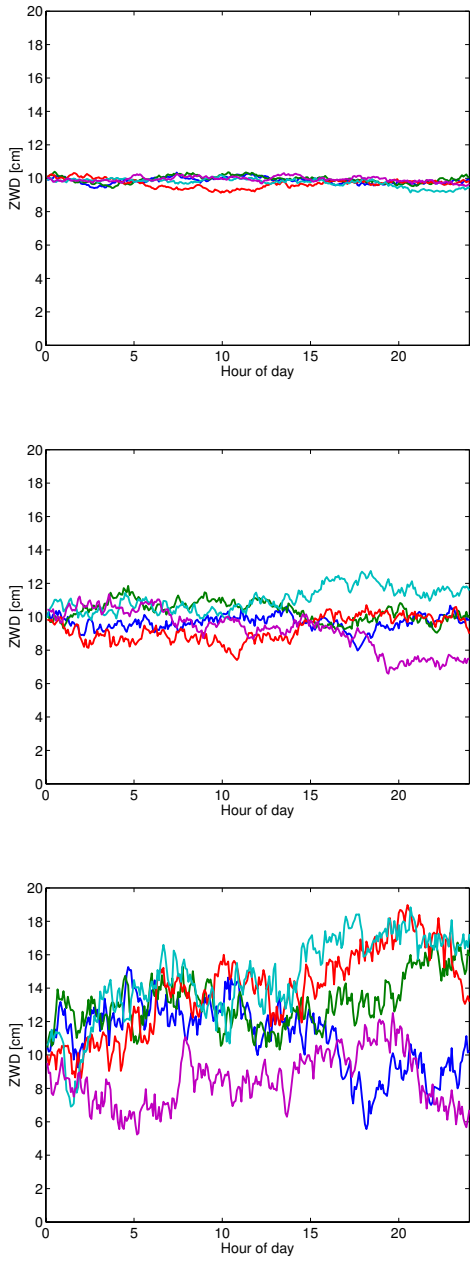

Figure 1. Examples of simulated zenith wet delays for a one day period. Shown are the cases $C_n = 0.3 \cdot 10^{-7}$ m$^{-1/3}$ (top), $C_n = 1 \cdot 10^{-7}$ m$^{-1/3}$ (middle), and $C_n = 3 \cdot 10^{-7}$ m$^{-1/3}$ (bottom). The results of five different simulations are shown for each C_n value, represented by the different lines.

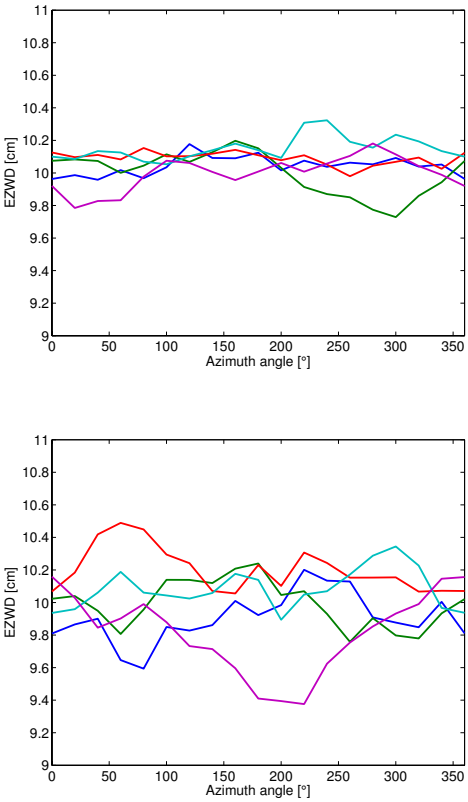

Figure 2. Simulated EZWDs for elevation angle 45° (top) and 10° (bottom) as function of azimuth angle. The results of five different simulations are shown for each elevation angle, represented by the different lines. Note that the variations seen along the simulated azimuth scan in the actual direction of observation is approximately 1.4 and 6 times larger at the 45° and the 10° elevation angle, respectively.

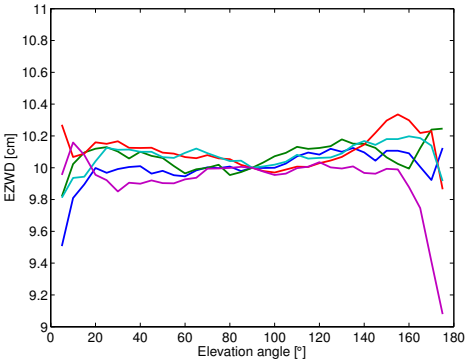

Figure 3. Simulated EZWDs as function of elevation angle when the azimuth angle is 0°. The results of five different simulations are shown, represented by the different lines.

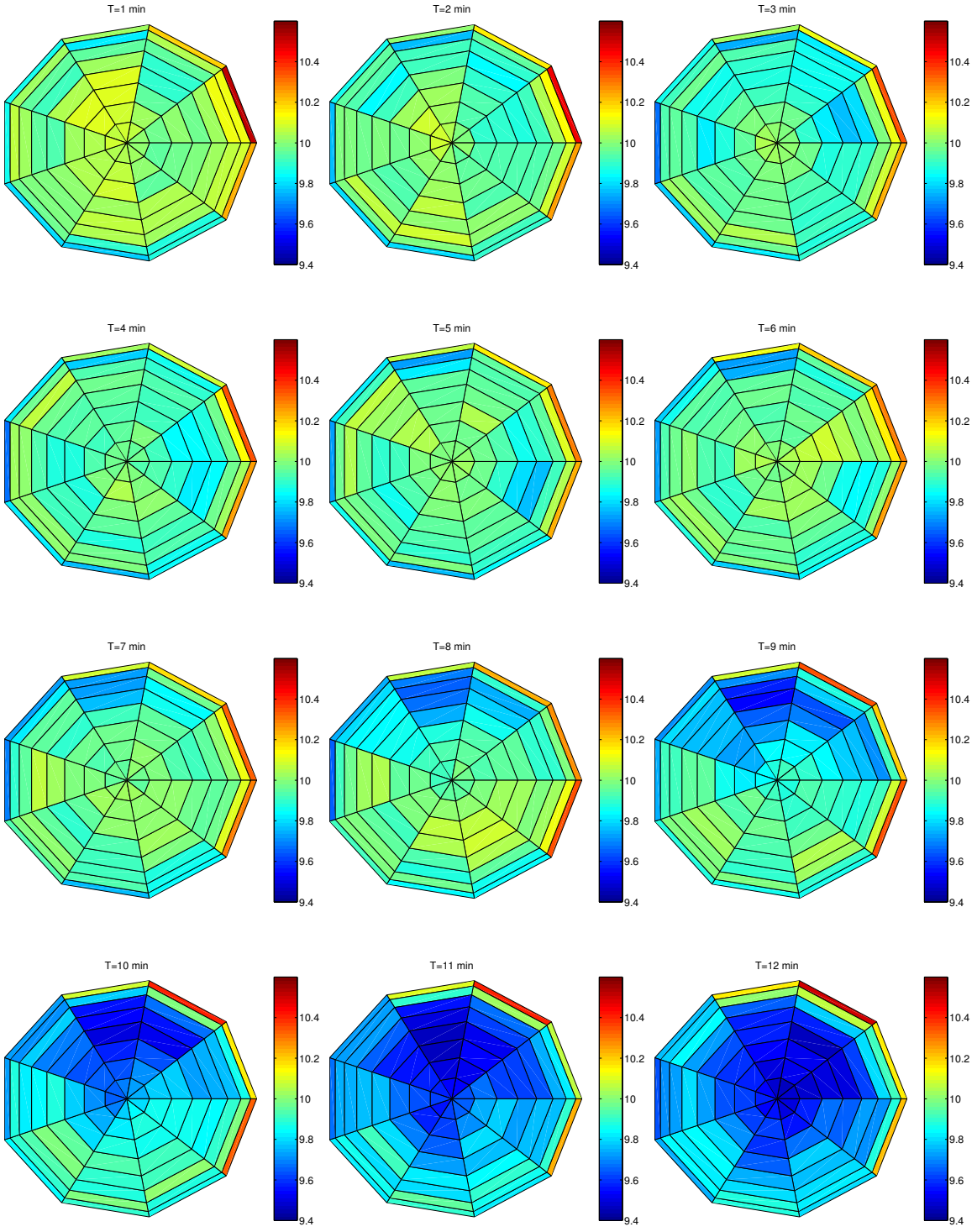

Figure 4. Skyplot of simulated EZWDs for a 12 minute period. East direction is to the right and north direction is upwards. The colour denotes the EZWD in cm. The rotation in azimuth angle is divided into steps of 40° and the elevation angle ranges from 10° in the outer cells to 90° in the middle divided into steps of 10°.

Fig. 2 shows simulated EZWD in different directions at the same time epoch. Shown are EZWD as function of azimuth angle for elevation angles 45° and 10°. Here $C_n = 1 \cdot 10^{-7}$ m$^{-1/3}$ and the other parameters as before. It is clearly visible that the variations as function of azimuth angle are larger for lower elevation angles.

Fig. 3 shows simulated EZWDs as function of elevation angle for the same time epoch and a fixed azimuth direction. The simulation parameters are as in Fig. 2. As could be expected, the difference between a EZWD and the zenith delay is larger for lower elevation angles.

Fig. 4 shows the variations both in time and with direction of observation. This is the result of a 12 minute simulation where the EZWDs of 90 different directions are simulated at each time epoch (separated by 1 minute). In this simulation the wind was in the north-south direction. It can be seen in the plots how the air is moving, especially how an area of lower refractive index is moving across the sky above the station during the second half of the simulation period.

4 Conclusions

We have shown how the wet path delay through a turbulent atmosphere can be simulated. The simulated delays will vary both as a function of the direction of the observation and time. Delays simulated in this way are more realistic than delays simulated by simpler methods, such as a random walk.

The simulations described in this work only consider variations caused by atmospheric turbulence. Other variations caused by, e.g. evaporation, condensation, precipitation, and changes associated with the passage of weather fronts are not considered. However, if there is no complex correlation between these variations and those caused by turbulence, they can be simulated using other methods. Thereafter, this time series could be added to the wet delay time series obtained from the turbulence model.

References

d'Auria, G., F. S. Marzano, and U. Merlo (1993). Model for estimating the refractive-index stucture constant in clear-air intermittent turbulence. *Applied Optics*, 32, pp. 2674–2680.

Keihm, S. J. (1995). Water Vapor Radiometer Measurements of the Tropospheric Delay Fluctuations at Goldstone Over a Full Year. *Telecommunications and Data Acquisition Progress Report*, 42-122J, April, pp. 1–11,. URL `http://tmo.jpl.nasa.gov/tmo/progress_report/42-122/122J.pdf`.

Linfield, R. (1996). The effect of aperture averaging upon tropospheric delay fluctuations seen with a DSN antenna. *Telecommunications and Data Acquisition Progress Report*, 42-124A, February, pp. 1–7. URL `http://tmo.jpl.nasa.gov/tmo/progress_report/42-124/124A.pdf`.

Niell, A., A. Whitney, B. Petrachenko, W. Schlüter, N. Vandenberg, H. Hase, Y. Koyama, C. Ma, H. Schuh, and G. Tuccari (2005). VLBI2010: Current and future requirements for geodetic VLBI systems. Technical report, International VLBI Service for Geodesy and Astrometry. URL `http://ivscc.gsfc.nasa.gov/about/wg/wg3/IVS_WG3_report_050916.pdf`.

Nilsson, T., G. Elgered, and L. Gradinarsky (2006). Characterizing atmospheric turbulence and instrumental noise using two simultaneously operating microwave radiometers. In *Proc. 9:th Specialist Meeting on Microwave Radiometry and Remote Sensing Applications, MicroRad 2006*, IEEE, pp. 270–275.

Nilsson, T., L. Gradinarsky, and G. Elgered (2005). Correlations between slant wet delays measured by microwave radiometry. *IEEE Trans. Geosci. Remote Sensing*, 43, pp. 1028–1035.

Press, W. H., S. A. Teukolsky, W. T. Vetterling, and B. P. Flannery (1992). *Numerical Recipies in C: The Art of Scientific Computing*, 2nd edition, Cambridge University Press.

Tatarskii, V. I. (1971). *The Effects of the Turbulent Atmosphere on Wave Propagation.* Israel Program for Scientific Translations, Jerusalem.

Treuhaft, R. N. and G. E. Lanyi (1987). The effect of the dynamic wet troposphere on radio interferometric measurements. *Radio Sci.* , 22 (2), pp. 251–265.

VanZandt, T. E., J. L. Green, K. S. Gage, and W. L. Clark (1978). Vertical profiles of refractivity turbulence structure constant: Comparison of observations by the Sunset Radar with a new theoretical model. *Radio Sci.*, 13 (5), pp. 819–829.

Kashima Ray-Tracing Service (KARATS) — Fast ray-tracing through numerical weather models for real-time positioning applications in East Asia

T. Hobiger, R. Ichikawa, Y. Koyama, and T. Kondo, Kashima Space Research Center, National Institute of Information, and Communications Technology, 893-1 Hirai, Kashima, Ibaraki, Japan

Abstract. Numerical weather models (NWMs) have undergone a significant improvement of accuracy and spatial resolution. Therefore such models can be used to correct for the excess delay which is caused when signals are propagation through the troposphere. The Kashima Ray-Tracing Service (KARATS) is capable of reading, re-griding and ray-tracing NWMs which cover East Asia countries including Japan, Korea, Taiwan and parts of China and Russia. Optimized algorithms and the upcoming multi-core technology permit real-time computation of troposphere corrections. First tests have shown that KARATS is capable to remove nearly all of the tropospheric delay and that precision and accuracy of estimated station coordinates are improved significantly.

Keywords. troposphere, numerical weather model, ray-tracing, parallel computing

1 Introduction

The tropospheric delay is still one of the limiting factors that restricts accuracy of space geodetic techniques. But recent investigations (Hulley & Pavlis, 2007) have shown that the introduction of ray-traced delays from numerical weather models improves the results and helps to remove systematic errors. With the introduction of the 10km mesoscale model by the Japanese Meteorological Agency (JMA) is became feasible to start the development of a ray-tracing service for East Asia which does not only provide tropospheric corrections in real-time but also supports post-processing requests.

2 Ray-tracing through the 10km JMA mesoscale weather model

The 10km JMA mesoscale weather model is utilized to obtain all the necessary information for the correction of tropospheric delays using ray-tracing techniques.

2.1 Tropospheric delay

Electromagnetic signals propagating through the (neutral) atmosphere are delayed since the refractivity index of the gases inside the media is greater than one. E.g., Smith & Weintraub (1953) report that the atmospheric refractivity N (respectively the index of refractivity n) can be computed by

$$N = (n-1) \cdot 10^{-6} = k_1 \frac{P_d}{T} + k_2 \frac{P_v}{T} + k_3 \frac{P_v}{T^2} \quad (1)$$

where P_d and P_v are the partial pressure of dry air and water vapor and T represents the absolute temperature. The physical constants are set to $k_1 = 77.604$, $k_2 = 70.4$ and $k_3 = 373900$, in accordance with (Bevis et al., 1994). Since numerical weather models provide only values of total pressure P one has to compute the water vapor pressure and thereafter derive the pressure of dry air by applying $P_d = P - P_v$. In an intermediate step the coefficient f, which only depending on the temperature T, can be computed. Finally P_v can be obtained from

$$P_v = \frac{RH}{100} \cdot 10^{f} \quad (2)$$

where RH is the relative humidity (in percent), which is also provided from the numerical weather model. When the index of refractivity $n(\vec{r})$ is known along the the ray-path, the atmo-

spheric delay $\Delta\tau_a$ can be denoted by

$$\Delta\tau_a = \underbrace{\int_{atm} (n(\vec{r}) - 1)\, ds}_{\Delta\tau_e} + \underbrace{\int_{atm} ds - \int_{vac} ds}_{\Delta\tau_g} \quad (3)$$

The first integral in equation 3 is evaluated along the ray from the transmitter through the atmosphere until it reaches the receiver and yields the so-called electromagnetic delay $\Delta\tau_e$. The second term denotes the geometric excess which is caused by a difference of the ray-path when passing the atmosphere compared to vacuum propagation. The integral expression in equation 3 has to be approximated as a finite sum for the case of ray-tracing through a numerical weather model.

2.2 Transformation of the data

Datasets from the JMA are used to compute values of refractivity N at the original grid points. But these points are located on a equally spaced grid whose axes are not parallel to the geographic grid. Moreover a constant grid spacing of about 10km is used, what causes a variation of the geographic distance (in degrees) in dependency of the latitude. Additionally one has to consider that vertical slices of the NWM are provided for constant pressure rather than constant geopotential height. In order to run fast ray-tracing algorithms which utilize these weather models it is necessary to transform, respectively interpolate, the data to an equally spaced geographical grid with height slices given at selected (i.e. constant geopotential) heights. Therefore a sophisticated re-griding algorithm (considering also the ground topography during interpolation) is applied and the data-slices are stored as binary files for follow-on ray-tracing.

2.3 Ray-tracing through the NWM

The ray-tracing class is implemented in C++ and supports two modes. The first one assumes straight propagation of the ray between two consecutive height levels and computes bending only at the intersection with the height slices. The second mode solves the Thayer (1967) partial derivative equations by an iterative algorithm and thus considers bending all along the ray-path. Table 1 summarizes the height levels used for the computation of the delay. Since the JMA model provides only values up to the 10hPa level (i.e. about 32km height) the model is extended by the U.S. Standard Atmosphere (1976) up to 86km. Due to this large number of height-slices the differences between both approaches do not exceed 6 mm at 10 degrees of elevation. Details of the algorithms will be given in Hobiger et al. (2007).

Table 1. Height slices used for ray-tracing computations

from	to	height steps	Lat/Lon res.
topo.	—	—	$0.01^\circ \times 0.01^\circ$
—	3 km	30 m	$0.1^\circ \times 0.1^\circ$
3 km	10 km	100 m	$0.1^\circ \times 0.1^\circ$
10 km	30 km	500 m	$0.1^\circ \times 0.1^\circ$
30 km	86 km	2000 m	$0.1^\circ \times 0.1^\circ$

2.4 Performance and results

All necessary routines are coded in C++ and condensed to a package called Kashima ray-tracing tools (KARAT). It contains all the necessary functions to re-grid the NWM and to carry out the ray-tracing. Moreover a class for manipulating RINEX data has been added and a module for the computation of the observing geometry, using GNSS orbits, has been included. The main ray-tracing class has been prepared for processing on multi-core machines using memory sharing. First tests on a Pentium D, 3GHz using only one core have yielded a ray-tracing thoughput of 1200 observation per second. Additionally the time for reading the binary slices has to be considered,too. At the same machine it takes about 3 seconds to load the re-sampled refractivity grids into memory before the ray-tracing can start.

KARAT does not only provide the ray-traced total delay but also gives total bending angle and ground refractivity as output. Figure 1 shows the ray-traced total zenith delays for a selected region around Japan on July 23rd, 2006 at 0h UT. The obtained delays do not only reflect the complex weather situation (multiple rain-fronts crossing the South of Japan) but also show that the topography is considered well in the ray-tracing process. The latter model refinement has been achieved by introduction the topography from the Space Shuttle Radar Topography Mission (Rabus et al., 2003) instead of the sparse data given from the JMA. In or-

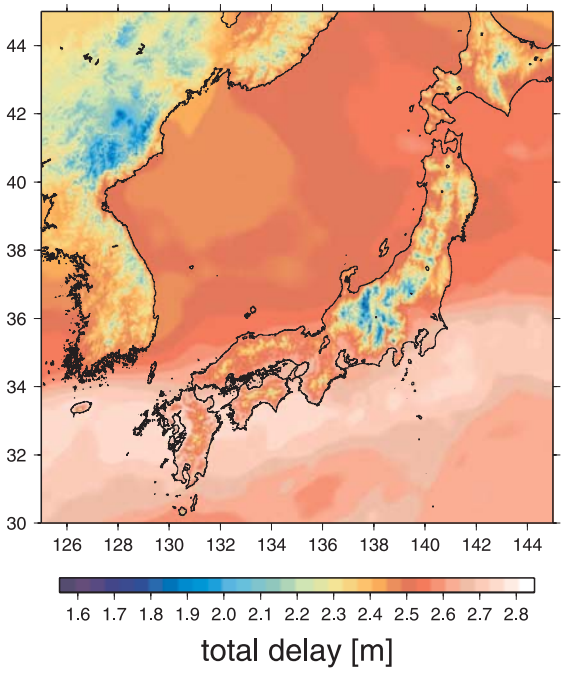

Figure 1. Total zenith delay on July 23, 2006 0UT obtained from ray-tracing through the 10km mesoscale model.

der to reveal how the ray-traced delays differ from model assumptions used in common analysis strategies GPS station AIRA ($\lambda = 130.5996$, $\varphi = 31.8241$) which is located in the center of maximum rainfall has been selected. The residual delay, i.e. the delay differences between the exact ray-tracing and a symmetrical approximation have been computed for all directions on July 23rd, 2006 at 0h UT at that station. Figure 2 shows the result of this evaluation. Due to the fact that there is a strong North-South gradient of water vapor, caused by the rain fields in the Northern parts, the residual delay characteristics are dominated by this behavior too. Thus the excess delay is positive (i.e. the ray-traced delay is larger than the symmetric delay) in North direction and negative when looking Southwards. Since the residual delays reach values up to $\pm$ 25 cm at lowest elevations a noticeable effect of the estimated station coordinates is expected. Ichikawa et al. (2007) have investigated how the site coordinates of AIRA are affected when a symmetrical atmosphere was assumed instead of considering the true weather situation. Thorough investigations about the effect of introduction of ray-traced delays in GNSS

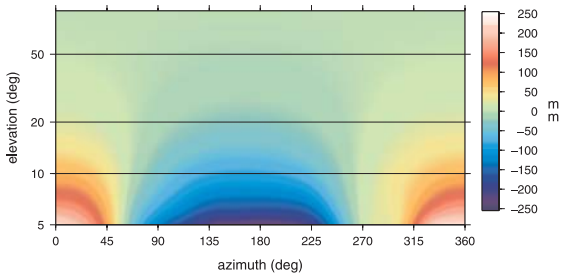

Figure 2. Resid. delay (i.e. the delay excess due to the neglection of asymmetry) at station AIRA on July 23rd, 2006, 0h UT. The elevation axis has been chosen to be of logarithmic scale for better readability.

analysis are currently ongoing.

3 Kashima Ray-Tracing Service – KARATS

Since the first tests with ray-traced slant delays have shown that station position accuracy and precision can be significantly improved it has been decided to open a service that does the ray-tracing for the user. Thus the ray-tracing tools will be embedded in an automatic processing chain, called Kashima Ray-Tracing Service (KARATS), which can be started via a web-interface. Figure 3 shows how KARATS is going to be working. Once a user (from the GPS

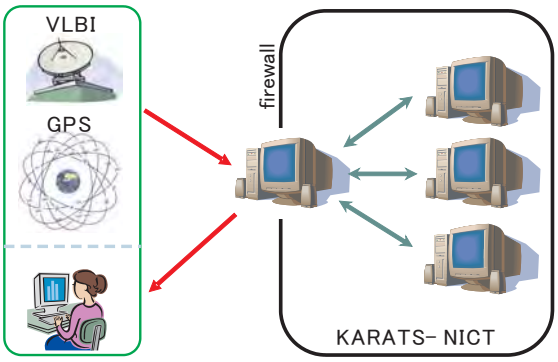

Figure 3. Flow chart of the KARATS processing chain.

or VLBI community) has taken his observations, he can send the data in a common format (which will be RINEX for GPS and MK3/FITS for

VLBI at first) via Internet to KARATS. Thereafter the web-server will do a rough data-check and compute the geometry from the observation file. As soon as a ray-tracing client becomes available it will send the geometry file to that machine. The client performs the ray-tracing through the weather model and sends the tropospheric delays back to the server. Thereafter the ray-traced delays are subtracted from the user's data and a "reduced" observation file is sent back to the user. Thus the analyst can estimate his target parameters without spending too much effort on estimating tropospheric delays. First tests have shown that about 99% of total tropospheric delay are removed by KARATS. Moreover it was found out that it is sufficient to use a simple mapping function, which is independent of any external parameter, to model the remaining atmospheric delay. The KARATS post-processing mode will be free of charge and an turn-around time of one minute per file is aimed at. In the case that VLBI observations are submitted it is checked that both stations lie within the boundaries of the NWM and thereafter the tropospheric delays are computed at each station. In a final step the server will compute the differenced corrections and apply them to the VLBI observations. Up to now it is not planned to support the case that only one station lies within the region supported by KARATS.
Moreover it is planned to run KARATS for real-time applications. Since this mode needs weather prediction data from the JMA it will be limited to a selected user group. In order to determine the maximum load that can be caused by the users it was assumed that 1300 GEONET receivers are streaming their data every second and that on average 12 satellite are tracked by each receiver. This sets the specifications of the data-throughput to about 15000 observations per seconds. Considering that 1200 rays can be computed on a single core machine already, it was concluded that 4 quad-core machines can fulfill the needs of 1Hz GEONET data streams. The real-time mode of KARATS is currently being coded using OpenMP to parallelize the necessary routines. Undertakings to obtain the NWM forecasts from JMA are ongoing.

4 Outlook

KARATS ray-tracing routines are currently going to be optimized to increase the data throughput. Moreover multi-core support via OpenMP is being implemented and the web-interface and the control scripts are being coded. Currently the 10km mesoscale models cover one year of data starting from April, 2006. Before that epoch only models with a coarser grid width are provided for the whole region covered by KARATS. KARATS is already prepared to treat even finer mesh NWMs, if access is granted by JMA. Additionally it is planned to support other observing formats and techniques, as well as offer the user to analyze the data automatically and send back the results.

5 Acknowledgments

The Japan Society for the Promotion of Science (project P06603) is acknowledged for supporting our research.

KARATS post-processing mode is planned to be available in the second half of 2007.

References

Bevis, M., Businger, S., Chiswell, S., Herirng, T.A., Anthes, R.A., Rockmen, C., Ware, R.H., 1994, Mapping zenith wet delays onto perceptible water, GPS Meteorology, J. Appl. Meteoro., 33, pp. 379–386.

Hobiger, T., Ichikawa, R., Koyama, Y., Kondo, T.(2007), Fast ray-tracing for real-time positioning applications using numerical weather models, Earth and Planetary Science letters , in preparation.

Hulley, G., and Pavlis, E. C. (2007), A ray tracing technique for improving satellite laser ranging atmospheric delay corrections, including the effects of horizontal refractivity gradients, J. Geophys. Res., doi:10.1029/2006JB004834, in press.

Ichikawa, R., Hobiger, T., Koyama, Y., Kondo, T.,(2007), An Evaluation of Geodetic Positioning Error Simulated using the Fast Ray Tracing Algorithms through the JMA Mesoscale Numerical Weather Data, IVS TDC News 18 .

Rabus, B., Eineder, M., Roth, A., Bamler, R., (2003), The shuttle radar topography mission- a new class of digital elevation models acquired by spaceborne radar, Photogramm. Rem. Sens., v. 57, pp. 241–262

Smith, E.K., Weintraub, S. (1953), The constants in the equation for atmospheric refractive index at radio frequencies, J. Res. Natl. Bur. Stand., 50, pp.39–41.

Thayer, G. (1967), A rapid and accurate ray tracing algorithm for a horizontally stratified atmosphere, Radio Science 1, pp. 249–252.

U.S. Standard Atmosphere (1976) U.S. Government Printing Office, Washington, D.C.

INTENSIVE – A strategic approach to improve technology and scientific results

Bjørn Engen
Former Director, Geodetic Institute
Norwegian Mapping Authority, N-3507 Honefoss

Abstract. The ambitions for VLBI2010 are very demanding. The technical requirements are covered in many papers, but this paper is looking at the challenges from the management point of view. It points of the INTENSIVE type of observations and eVLBI transfer as the beginning of a stepwise approach to possibly develop and improve both the infrastructure and competence for VLBI2010.

1 VLBI2010 and management challenges

The required investments and increased running costs are very challenging, for some maybe even considered to be impossible to reach. The problems range from even smaller investments for rather short fibre line connections, to enormous running costs for eVLBI based on commercial rates. The achievement with the twin-telescope in Wettzell, adds to the different types of challenges we are facing.

If we look at some of the strategies that has been mentioned in connection with VLBI2010, we could sum them up in 3 strategies, in broad terms as follows:

2 Strategies

2.1 A low cost telescope solution

New telescopes with a smaller diameter eg. 12m will seem to be a favourable solution. But on the other hand, a tremendous increase in observations as close to 24-7-365 as possible, will have an influence on the mechanical specifications and increase the cost. However, various alternative solutions must be tested and kept under investigation as we move forward.

2.2 Possible cooperation with other VLBI users

In sites planning for two or more telescopes, there would be some available time for other VLBI users. The cooperation between geodesy and astronomy is well established, but in some countries there seems to be an increasing interest for cooperation in deep space. This will however require some changes in the traditional thinking. But in times when funds for investments in public sector is limited in most countries, cooperation and joint efforts to optimise both use and operations of infrastructure, will improve the rate of success.

2.3 Successive developments

A possible strategy to reach the ambitious goal is to use a successive development approach. The approach would be

- start from "as is"
- select small data packages for eVLBI in the beginning
- process, analyse and present new achievements
- use the results for new applications for funds
- include good achievements from the community

3 Proposal for INTENSIVE type of observations

Based on strategy 3 a proposal is submitted to the IVS CC/OPC using the INTENSIVE type of observations for testing and improvement of eVLBI. It will also highlight the effect of near real time continuous VLBI time series on VLBI and GNSS combinations. Taking the present INTENSIVE observations –

INT 1
1 h observations Monday to Friday
Wettzell – Kokee Park (partly also including Svetloe and Onsala) correlated at the Washington Correlator

INT 2
During weekends, observing in the morning hours, Wettzell – Tsukuba correlated at the K5 Software Correlator

and additional INTENSIVE type session is proposed:

- 1 h on Mondays, morning hours (to fill the gap between INT 2 and INT 1)
- Network Stations for initial testing
    - Ny Ålesund
    - Wettzell
    - Tsukuba (proposed, to be negosiated)
    - Westford (proposed, to be negosiated)
    - Kokee Park (when connected, to be negosiated)
- To use eVBLI transmission capability
- Correlated at Bonn Correlator at highest priority
- Schedule provided by Operation Center Bonn
- After initial testing, to be extended with more observations per week
- After initial testing, to be open for other eVLBI network stations
- Analysis result should be made available for use in funding applications by VLBI stations

By having such as stepwise approach we will allow ourselves time to improve the infrastructure, carry out testing and troubleshooting on additional equipment and international connections as well as collecting good arguments for new funding and research applications.

PS! The IVS Observing Program Committee (OPC) approved the above proposal in a letter dated May 20th, 2007.

An Analysis of Local Tie Vectors' Temporal Evolution and Site Stability at Medicina Observatory through Terrestrial and GPS-based Observations

C. Abbondanza, L. Vittuari
DISTART Geodesia, Topografia e Rilevamento
Università degli Studi di Bologna, via Risorgimento, 2 40136 Bologna (Italy)

P. Sarti, M. Negusini
Istituto di Radioastronomia (IRA) - Istituto Nazionale di Astrofisica (INAF), via P. Gobetti, 101 40129 Bologna (Italy)

Abstract. The observatory of Medicina (Italy) hosts a co-location between GPS and VLBI, whose eccentricity vector has been re-measured several times once since 2001.
As a result, the co-located site is now provided with a series of nearly annual local tie vectors produced by means of terrestrial and GPS-based observations.

This work aims at summarising the results of a systematic analysis of the whole set of local ties produced so far and highlighting at the same time their temporal evolution.

As such, the application of algebraic tools focussed on deformation detections can benefit the analysis of the local tie temporal variations and at the same time that one of the "geodynamical" stability of the co-located site.

Nevertheless, just like in any other problem of deformation detection, such an analysis would ask for a reproducible local datum, according to which the relative displacements among the points have to be referred to.

The application of algebraic projection theory to the local tie oriented-networks will be carried out in order to select a "common and fully reproducible" datum onto which the network solutions will be projected and discuss possible displacements within the re-measured networks.

Keywords. Local ties**,** Co-location, GPS, VLBI, Inner constraint solution.

---

1 Introduction

Since 2001 a research project at Medicina Observatory has been undertaken with the aim to measure and compute the eccentricity between VLBI and GPS instruments. As a result, the co-located site is now endowed with a series of nearly yearly VLBI-GPS local tie vectors, measured *via* a classical terrestrial approach or a wholly GPS-based one.

This investigation will sum up the results of a consistent analysis of the entire set of local ties performed up to now at Medicina by highlighting their temporal evolution.

In fact, a proper temporal analysis of such eccentricities along with all the network information extracted from the SINEX files might point out possible displacements of the ground control points belonging to the local network, as well as meaningful variations in the Reference Points of the VLBI and GPS techniques.

Nonetheless this investigation is not straightforward at all and it is further complicated by the difficulties in reproducing - epoch by epoch- a stable and consistent local reference frame which the displacements ought to be referred to.

That's the reason why such analysis necessarily have to cope with the attempt of "projecting" all the different realizations of the local reference frame coming from different surveys onto the same space with respect to that they'll be all consistent and comparable.

Once this has been done, an evaluation of displacements in terms of difference of coordinates will be theoretically possible and meaningful.

2 An overview of Inter-Technique eccentricities performed at Medicina

As well known, results in space geodesy claim the necessity of inter-technique eccentricities at 1 mm-level when the definition of a multi-

technique Terrestrial Reference Frame with 1 mm consistency is needed (Ray and Altamimi 2005). In this regard, during the last years, different surveys at the observatory of Medicina were performed aiming at the computation of high precision eccentricities.

2.1 Surveying strategies of tie vectors and connections with the local geodetic network's robustness.

Considering the overall set of VLBI-GPS eccentricities of Medicina, two different groups of local ties can be elected according to the way they were surveyed and the geodetic network's geometry designed as a basis for their processing . The 2 local ties of 2002 and 2006 are completely *GPS-derived*, whereas the 3 local ties of 2001, 2002 and 2003 are computed through *terrestrial* observations.

Terrestrial local ties are typically performed measuring a local geodetic network in the co-located site, according to a scheme of redundant multiple intersections (angles and distances) along with spirit levelling measurements (for further details see Vittuari et al. 2005).

Table 1. Geometrical features of the data sets used: number of azimuthal and elevational surfaces exploited in the local tie computation.

Survey	Azimuthal Surfaces (Nr)	Elevational Surfaces (Nr)
TER 2001	8	3
TER 2002	8	4
TER 2003	10	11
ABS 2002	4	4
ABS 2006	8	14

On the contrary, the basic observables at the root of the GPS derived local ties' computation are represented by baselines bridging the ground fixed points to those traced by moving GPS receivers attached to the VLBI dish. The survey of the VLBI RP (Reference Point) is based on a rapid static approach experienced at Medicina in 2002, whose details are thoroughly discussed in Tomasi et al. (2003).

In both cases (terrestrial and GPS-based) through the observation of the positions of moving targets or GPS receivers fixed on the structure of the VLBI antenna, it is possible to recover circles which are geometrically connected to the VLBI IP.

As showed above, Table 1 details the number of surfaces recovered while the VLBI antenna rotates in azimuth and elevation, during the various surveys.

It's worth noticing that a correlation between the local geodetic network's robustness and the VLBI IP estimation exists : looking at Table 1, a comparison between the ABS 2006 and the ABS 2002 solutions immediately testifies a worst definition of the VLBI IP in the last case.

In spite of the differences in magnitude, an akin behaviour can be inferred from the comparison between TERR 2001 (worst definition) and TERR 2003 (better definition) formal errors in the three geocentric components. In fact a relationship exists between the number of surfaces involved (Table 1) in the VLBI IP geometrical modelling and its accuracy: the higher is the geometrical robustness of the network (number of surfaces exploited), the more accurate is the IP estimation.

2.2 Geometrical and Statistical Indicators

Five GPS-VLBI eccentricities have been computed throughout the period 2001-2006, whose results in terms of moduli are summarized in Table 2; as widely discussed in Sarti et al. (2004) and Dawson et al. (2006), the estimation of each of these local tie vectors relies on an indirect approach entailing a proper geometrical model. Final computation of each eccentricity, provided in a SINEX format, gathers the estimations of the Invariant Points (IP), the ensemble of the points belonging to the local network along with the entire VCV matrix.

Table 2. Moduli and formal errors of the eccentricity vector (values in m).

TER 2001	TER 2002	TER 2003	ABS 2002	ABS 2006
62.7646 (0.0007)	62.7673 (0.0004)	62.7654 (0.0003)	62.7691 (0.0020)	62.7673 (0.0003)

As testified in Table 2, the formal errors (1-σ level) for the local tie moduli can attain sub-

millimetrical values. Analogously, Table 3 displays the formal errors of the VLBI IP coordinates for the same ties, thus bearing out the effectiveness of the indirect approach for the eccentricity computation.

Moreover it's worth noticing that, apart from the 2002 GPS local tie, the accuracies of that one of 2006 are strikingly comparable with those terrestrial; they're even better if compared to the terrestrial eccentricities of 2001. As it's been proved in Dawson et al. (2006) for simulated datasets, such results further confirm that a suitable geometrical modelling can achieve a good level in filtering the noise affecting much more GPS data than the terrestrial ones.

Table 3. Formal errors of the VLBI IP coordinates expressed into ITRF2000 for all the local ties (values in mm)

	TER 2001	TER 2002	TER 2003	ABS 2002	ABS 2006
σ_x	0.45	0.35	0.29	5.27	0.35
σ_y	0.25	0.21	0.15	1.13	0.21
σ_z	0.45	0.36	0.29	5.13	0.35

2.3 The relationship between GPS derived and terrestrial local ties

From an operational point of view, the datum definition for local ties aims at establishing a suitable frame according to which the points of the local networks and the IP may be consistently expressed.
Algebraically speaking, datum definition requires the resolution of the rank deficiency stemming from observations.

Terrestrial tridimensional networks measured with multiple intersections of angles and distances display 4 feasible degrees of freedom: one rotational defect about the Up-axis and three translations which define the frame's origin.

Such a rank-defect is reduced *via* a loosely minimal constrained solution, by fixing three coordinates with a standard deviation of 1 meter and a bearing with a standard deviation of 1.5 gon.

As a consequence of the terrestrial survey procedures, the eccentricity will be always framed into a local reference frame which is topocentric (LTF) and geoid-dependent (Up component normal to the local geoid).

Figure 1 displays the local network of Medicina with the point-to-point connections; in this case the local reference frame, which should be reproduced each time the network is re-measured, originates –for terrestrial eccentricities- in the concrete pillar P3 with orientation along the connection P1-P3.

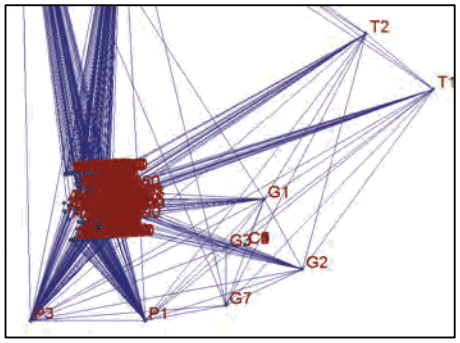

Fig. 1 Terrestrial local geodetic network at Medicina (2001)

If a final alignment into an ITRFyy realization is needed, each terrestrial local tie must be necessarily framed into such a global frame. The passage from LTF to a global frame is typically worked out by means of a rigid transformation (Rototranslation) whose 6 parameters will be stochastically estimated in a Least Square context (Sarti and Angermann 2005).

Such an estimation requires the knowledge of a set of tie points which link the LTF to the ITRFyy: coordinates coming from the GPS-based surveys can be used for this; hence this makes terrestrial eccentricities GPS-dependent as far as the alignment into an ITRFyy is concerned.

3 Is it possible to detect relative site-dependent displacements from multi-temporal realizations of tie vectors?

Despite the fact that local tie vectors are generally regarded as time invariant entities into a terrestrial reference frame combination, the possibility of performing surveys repeated time by time might point out an eccentricity's variation due to local instability related to geophysical phenomena within the co-located site. A correct evaluation of these relative

displacements should be taken into account in order to establish the phenomenon's magnitude and to compare it with the linear temporal evolution impressed to the ITRS realizations.

The local tie surveying strategy aside, each eccentricity we can work out is the result of the processing of a local geodetic network, set up within the co-located site; hence also the adjusted coordinates of reference points, besides the IP involved in the eccentricity, are available whenever the network is re-measured.

For instance, in the case of Medicina, we're provided with multi-temporal network solutions of at least *five points*: three geodetic markers placed on concrete pillars (P1, P3 and G7) and two instrumental reference points. Thus, by exploiting network's solutions, potential relative displacements can be investigated.

3.1 Local datum reproducibility as basic assumption for detecting relative displacements.

Deformations we are going to investigate can be thoroughly defined as a function of the network markers' displacements.

In the case of Medicina, local tie vectors are determined by means of a "relative" geodetic network whose points are assumed to wholly belong to a deformable "area"; thus no point of the network can be theoretically regarded as stable and served as a reference point which the absolute displacements have to be referred to; this makes the geodetic network at a certain extent "relative".

Let $\underline{x}_i(t)$ be the time-dependent position vector of the *i-th* point belonging the local geodetic network expressed with respect to a three dimensional frame; then the displacement undergone by such a point from epoch t_1 to epoch t_2 is itself a 3d vector which can be expressed by differencing:

$$\underline{\delta}_i = \underline{x}_i(t_2) - \underline{x}_i(t_1) \quad (1)$$

Equation (1) clearly shows that the modulus of the point displacement $\underline{\delta}_i$ in a local network is independent from the reference frame definition, providing *it is possible* to define a *datum consistent and repeatable epoch by epoch*.

In fact, if a datum is badly reproducible when passing from epoch t_1 to t_2, such a displacement δ can embed false movements which tend to mask the actual network deformations.

Badly reproducible datum may arise from inconsistencies related to the network repeated in time owing to different reasons; for instance

- changes in network's topology due to the *addition or removal of some points*, which can affect the application of minimal constrained solutions at different epochs;
- a modification in the observation scheme when passing from an epoch to the other (this is the case for our local tie-oriented surveys), which still produces a change in the network's shape.

In all these cases, a projection of the network coordinates onto a new datum free from any error and reference effect (Sillard and Boucher 2001) is mandatory and it represents a valuable tool in order to make the different realizations of our networks comparable. This can be achieved by exploiting the algebraic theory of projectors.

3.2 Datum definition and *Inner constraint solution* for a terrestrial based local tie and its underlying network

When dealing with least square solutions which involve a datum definition problem, the linear system characterizing the observations

$$\underset{m\cdot n}{\mathbf{A}} \cdot \underset{n\cdot 1}{\underline{x}} = \underset{m\cdot 1}{\mathbf{Y}} \quad (2)$$

is obviously *inconsistent* (the solution is not unique) and *not of full rank*; this is formally equivalent to say that:

$$\begin{cases} m > n \\ \rho(\mathbf{A}) < \min\{m, n\} = n \end{cases} \quad (3)$$

where m and n respectively denote the number of observations and the unknown parameters and ρ the rank of $\mathbf{A}$. Being $\mathbf{A}$ a rank deficient matrix, the normal system is not invertible in a classical sense. As it can be inferred by reading Sillard and Boucher (2001), if $\mathbf{W}$ denotes the metric tensor for the dot product onto $\mathbb{R}^m$, each possible least square solution of the not full-rank problem

$$\left(\underset{n\cdot m}{\mathbf{A}^t} \cdot \underset{m\cdot m}{\mathbf{W}} \cdot \underset{m\cdot n}{\mathbf{A}}\right) \cdot \underset{n\cdot 1}{\underline{x}} = \underset{n\cdot m}{\mathbf{A}^t} \cdot \underset{m\cdot m}{\mathbf{W}} \cdot \underset{m\cdot 1}{\mathbf{Y}} \quad (4)$$

lies onto the affine space

$$\Psi = (\underset{n\cdot m}{\mathbf{A}}^{t} \cdot \underset{m\cdot m}{\mathbf{W}} \cdot \underset{m\cdot n}{\mathbf{A}})^{-} (\underset{n\cdot m}{\mathbf{A}}^{t} \cdot \underset{m\cdot m}{\mathbf{W}} \cdot \underset{m\cdot 1}{\mathbf{Y}}) + \underset{m\cdot n}{Ker(\mathbf{A})} \quad (5)$$

where $(\mathbf{H})^{-}$ indicates a generalized inverse for **H** and $Ker(\mathbf{A})$ the null space of **A**.

Whatever the least square solution is, it is unique its projection along the orthogonal direction to Ψ: such solution we're searching for is the inner constraint solution.

As such, the application of projection theory to the local tie-oriented geodetic network allows to define a new datum into which all the different realizations of eccentricities will be framed. From an analytical point of view, let $\underset{3n_p\cdot 1}{\underline{x}_1}$ be a generic realization of a local tie vector issuing from the network observations at epoch t.

Such realization can be connected to another one at the same epoch by means of an equivalence which expresses a similarity transformation:

$$\underset{3n_p}{\underline{x}_1} = \underset{3n_p}{\underline{x}_0} + \underset{3n_P\cdot t}{\mathbf{D}} \cdot \underset{t\cdot 1}{\theta} \quad (6)$$

where the vector θ contains the *t* transformation parameters and **D** is a matrix based on the linearization of the similarity. Such a matrix accounts for the network datum defect: it's got as much columns as the possible degrees of freedom of the network and a number of lines equal to $3 \cdot n_p$ (number of network's points).

Terrestrial geodetic networks underlying eccentricities show a datum defect of 4: 3 translations and 1 rotation about the Up-axis, whose direction is fully determined through the gravity field. In this case the matrix **D** has the following structure:

$$\underset{3n_p\cdot 4}{\mathbf{D}} = \begin{pmatrix} \vdots & \vdots & \vdots & \vdots \\ 1 & 0 & 0 & -y_i^0 \\ 0 & 1 & 0 & x_i^0 \\ 0 & 0 & 1 & 0 \\ \vdots & \vdots & \vdots & \vdots \end{pmatrix} \quad i = 1,..,n_P \quad (7)$$

where the first three columns pertain to the 3 translations and the last one to the unique rotation; the couple (x_i^0, y_i^0) represents the *a priori* coordinates for the *i-th* point.

The problem of projecting the frame realization $\underline{x}_1$ in order to obtain an inner constraint solution $\underline{x}_0$ was widely discussed in geodetic literature; hereafter we propose the solution presented by Sillard and Boucher (2001) relying on the concept of projection onto orthogonal complementary vector spaces. By solving equation (6) in a least square sense with respect to the parameters contained in θ, one can get

$$\begin{cases} \underset{3n_p\cdot 1}{\underline{x}_0} = (\underset{3n_p\cdot 3n_p}{\mathbf{I}} - \underset{3n_p\cdot t}{\mathbf{D}} (\underset{t\cdot 3n_p}{\mathbf{D}^t} \underset{3n_p\cdot 3n_p}{\mathbf{W}} \underset{3n_p\cdot t}{\mathbf{D}})^{-1} \underset{t\cdot 3n_p}{\mathbf{D}^t} \underset{3n_p\cdot 3n_p}{\mathbf{W}}) \cdot \underset{3n_p\cdot 1}{\underline{x}_1} \\ \mathbf{D}\theta = (\mathbf{D}(\mathbf{D}^t\mathbf{W}\mathbf{D})^{-1}\mathbf{D}^t\mathbf{W}) \cdot \underline{x}_1 \end{cases} \quad (8)$$

where $\mathbf{Q} = \mathbf{D}(\mathbf{D}^t\mathbf{W}\mathbf{D})^{-1}\mathbf{D}^t\mathbf{W}$ is, from an algebraic point of view, a projection matrix.

4 Displacement computation and discussion of the results

According to equations (8) projections of each terrestrial network solution onto the normal direction to Ψ have been performed by means of the projector Q, in order to select the inner constraint solution.

At this stage, the approach has been applied only to the terrestrial local ties in such a way that two displacement fields can be evaluated: the first one relevant to the epochs 2001 and 2002, the second one to the epochs 2001 and 2003.

It's worth stressing that, if a network solution was computed by tightly constraining some points to a given value, such constraints have to be removed both from the adjusted coordinates $\underline{x}_1$ and the VCV matrix before the estimation of the inner solution $\underline{x}_0$ (Panafadina et al. 2006)

Conversely, if a loosely constrained solution was performed as in this case, the removal can be limited just to the *a posteriori* VCV network matrix.

The following Table 4 summarizes the results for the two groups of displacements, computed by analysing the 2001, 2002, 2003 terrestrial geodetic networks at Medicina. The first group is relevant to the displacements during the period 2002-2001 whereas the second one to those of 2003-2001; an incremental effect is evident when passing from the first to the second group. Each of these displacements is obviously consistent with the modulus of the

VLBI-GPS eccentricity expressed in the initial realization $\underline{x}_1$ of the local frame: this happens because the inner constraint solution leaves unaltered the geometrical invariants of the network.

Table 4. Displacements for the terrestrial network points related to the *time lag 2002-2001 and 2003-2001*. Shown are the values in mm of the three vector components expressed wrt to the *inner constrained solution*; ***mod*** lines contain the *moduli* of displacements (mm)

		P1	P3	G7	GPS ARP	VLBI IP
2002-2001	X	-1.87	-1.87	3.17	-1.51	2.08
	Y	1.57	-2.85	0.01	-0.81	2.09
	Z	0.57	-2.38	-0.53	2.48	-0.13
	mod	**2.51**	**4.16**	**3.22**	**3.01**	**2.95**
2003-2001	X	-6.32	-6.32	6.45	-3.51	9.69
	Y	4.73	-0.32	0.68	-4.32	-0.77
	Z	0.89	-3.14	0.84	1.83	-0.42
	mod	**7.94**	**7.06**	**6.54**	**5.86**	**9.73**

All the displacements are statistically meaningful: their magnitude is bigger than their formal errors at 1σ value (according to the *VCV* matrix expressed with respect to the inner constraint solution).

Moreover the results deduced by Table 4 suggest relative effects in the displacements among the network's points; in facts P3 and P1, which concur to define the origin and the orientation in the original frame, undergo differential displacements into the new one with respect to all the three components. The point G7 is, on the contrary, fairly stable in the Z and Y components, but shows a significant migration along the X component of about 6 mm. In addition it has to be stressed that the VLBI IP attains the maximum value of local displacement.

5 Conclusions

The inner constraint approach proves to be an effective and highly flexible tool also for tackling the issue of local displacement evaluation within a co-located site.

On the whole such an approach, applied to the terrestrial derived local ties, is capable to highlight local displacements and differential effects within the network which can integrate the description of the co-located site yielded at a global scale by the ITRS realizations.

Concerning local tie vectors, the application of projection theory bears out the idea that an eccentricity cannot be in general regarded as a time invariant entity, since in the case of Medicina its reference points may undergo relative displacements up to 10 mm.

Finally, in order to better describe the magnitude of the phenomenon and to wholly detect eventual deformational patterns, this approach suggests that it is worth widening the investigations by including all the terrestrial surveys executed so far together with the GPS-based solutions.

References

Dawson, J., Sarti, P., Johnston, G.J., Vittuari, L. (2006). *Indirect Approach to Invariant Point Determination for SLR and VLBI Systems: An Assessment*. J Geodesy (av. online, DOY 10.1007/S00190-006-0125-x)

Panafadina, N., Malkin, Z., Weber, R. (2006). *A new combined European permanent network station coordinates solution*. J Geodesy (av. online, DOY 10.1007/s00190-006-0076-2)

Ray, J., Altamimi, Z. (2005). *Evaluation of co-location ties relating the VLBI and GPS reference frames*. J Geodesy (2005) 79: pp. 189-195.

Sarti, P., Angermann, D. (2005). *Terrestrialdata analysisand SINEX generation*. In Proceedings IERS Workshop on Site Co-location. Matera, Italy, 23-24 October 2003 Eds. B. Richter. and Schwegmann W., Dick R.W., IERS Tech. Note 33: pp.118-127.

Sarti, P., Sillard, P., Vittuari, L. (2004). *Surveying co-located space-geodetic instruments for ITRF computation*. J Geodesy, 78: pp. 210-222

Sillard, P., Boucher, C. (2001). *A review of algebraic constraints in terrestrial reference frame datum definition*. J Geodesy 75: pp.63-73.

Tomasi, P., Sarti, P., Vittuari, L., Negusini, M. (2003). *2002 local geodetic survey of VLBI and GPS reference points and ex centre at Medicina*. In Proc. 16th Working Meeting on European VLBI for Geodesy and Astrometry, Leipzig, May 9-10, 2003, W. Schwemann and V. Thorandt Eds, Frankfurt/Leipzig, pp. 91-98.

Vittuari, L., Sarti, P., Sillard, P., Tomasi, P., Negusini, M. (2005). *Surveying the GPS-VLBI eccentricity at Medicina: methodological aspects and practicalities*. In Proc. IERS Workshop on Site Co-location. Matera, Italy, 23-24 October 2003 Eds. B. Richter. and Schwegmann W., Dick R.W.; IERS Tech. Note, 33: pp. 38-48.

MK3TOOLS & NetCDF - storing VLBI data in a machine independent array oriented data format

T. Hobiger, Y. Koyama, and T. Kondo, Kashima Space Research Center, National Institute of Information, and Communications Technology, 893-1 Hirai, Kashima, Ibaraki, Japan

Abstract. In the beginning of 2002 the International VLBI Service (IVS) has agreed to introduce a Platform-independent VLBI exchange format (PIVEX) which permits the exchange of observational data and stimulates the research across different analysis groups. Unfortunately PIVEX has never been implemented and many analysis software packages are still depending on prior processing (e.g. ambiguity resolution and computation of ionosphere corrections) done by CALC/SOLVE. Thus MK3TOOLS which handles MK3 databases without CALC/SOLVE being installed has been developed. It uses the NetCDF format to store the data and since interfaces exist for a variety of programming languages (FORTRAN, C/C++, JAVA, Perl, Python) it can be easily incorporated in existing and upcoming analysis software packages.

Keywords. NetCDF, VLBI, database, correlator output, K5 VSSP

1 MK3TOOLS

Driven by the demand to create a new interface between the K5 correlator and the MK3 format NICT has started in December 2006 to create routines in C++ which allow reading and writing MK3 databases independent of the machines Endianess, without having CALC/SOLVE installed. These routines are pooled under the name MK3TOOLS and are extended with the functionality to translate MK3 databases to/from NetCDF[1] format. In future MK3TOOLS will include small routines for manipulating (adding, multiplying, deleting) MK3 databases directly. Additionally it is planned to add features for reading log-files, which will close the gap in the pipeline between the correlator and the database (version 1).

[1] http://www.unidata.ucar.edu/software/netcdf/

2 NetCDF

The NetCDF (network Common Data Form) is a set of software libraries and machine-independent data formats that support the creation, access and sharing of array-oriented scientific data. Moreover it is freely available and easy to implement in nearly any programming language since interfaces for popular languages are already prepared by the user community. In order to represent the content of the MK3 database the following guidelines have been set-up:

- the full MK3 database name (including the version) is used to name the NetCDF format (without ending)
- each LCODE table (1,2,3) is stored separately in a NetCDF file, (the ending of the file will denote the table number)
- each LCODE is translated to a NetCDF variable, having the same format and dimensions as in the MK3 database
- the LCODE description is added as an attribute to the corresponding variable
- Due to the fact that special characters and blanks can not be used as variable names, the MK3 LCODE name is stored as an additional attribute in the NetCDF database and an internal variable name is used for data management inside NetCDF.

Moreover the usage of NetCDF provides some attractive features:

- the database management is done by NetCDF
- easy and clear interfaces exist for many programming languages (FORTRAN, C/C++, JAVA, Perl, Python, ...)

- an optional flag marks MK3 database consistent data. Thus also additional information (e.g. system temperatures, bandpass filter characteristics, etc.)can be added. Although such information is not supported in analysis packages now, it might be of importance for the future
- the history table is kept in separate file as a text file
- NetCDF viewer and tools exist which allow easy data inspection and manipulation

2.1 Proposed processing chain

Figure 1 shows the proposed processing chain from the correlator to the analyst. The MK3

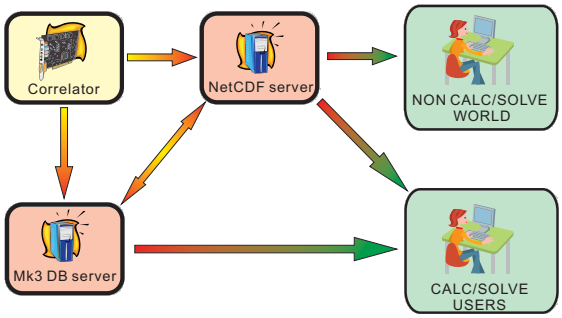

Figure 1. Suggested processing chain when NetCDF is used for geodetic VLBI data representation.

databases can be either generated directly from the correlator or data are written to NetCDF format. In the latter case the MK3 database can be generated from the NetCDF using MK3TOOLS. The user will not be affected by this change, since there is full compatibility between NetCDF and the MK3 database. Thus the analyst can either download the MK3 DB or use the NetCDF files, depending on the choice of his analysis package.

2.2 Outlook

Coding of MK3TOOLS, providing the complete chain from the correlator to the database, is expected to finish end of June. Currently K5 VSSP correlator output is supported only, but an interface to any post-correlator format is possible. Moreover it is planned to open a web-based service that allows the user to convert a MK3 database to NetCDF and vice versa. This might encourage analysts to include more information to their software packages that has not been accessible due to shortened data formats (e.g. the NGS format).

2.3 Acknowledgments

The authors are very grateful to the Japanese Society for the Promotion of Science (project P06603) for supporting our research. National Institute of Information and Communications Technology (NICT) and the Kashima Space Research Center are acknowledged for providing the infrastructure.

A Comparison of intraday variations of the Earth orientation parameters from different VLBI solutions

M. Kudryashova
Sobolev Astronomical Institute,
St. Petersburg State University, 198504, Universitetskii pr. 28, Petrodvorets, St. Petersburg, Russia

D. MacMillan
NVI Inc./ NASA Goddard Space Flight Center, Greenbelt, Maryland, USA

O. Titov
Geoscience Australia, Canberra, Australia

Abstract. It have been shown Kudryashova et.al. (2006), Brzezinski and Bolotin (2006), there can be significant differences between intraday variations seen in intraday EOP series generated by different analysists using different analysis software..In this work we investigate the reason for the differences. To study the differences, we compared several individual time series of intraday Earth Orientation Parameters (EOP) obtained from the CONT02 VLBI campaign. These series are based on the same VLBI observational data but different methods of the parameter estimation were applied.

Keywords. Intraday Earth orientation parameters, VLBI

1 Data description

For our analysis we used several solutions independently obtained by different IVS Analysis Centers (Main Astronomical Observatory of Ukrainian Academy of Science, Goddard Space Flight Center and St. Petersburg University). The Oceanic tide model (IERS Conventions 2003) was first removed from these EOP time series before analyzing them.

Below we give the description of these individual solutions.

1.1 Data obtained in Main Astronomical Observatory

adjustments are with respect to: IERS C04;
method of estimation of unknowns: square-root information filter (SRIF).
a priori information: EOP are modeled as a random walk dynamical process with the following parameters: 1) a priori (initial) standard deviations $\sigma^{PM}_{apriori}$=10000.0 mas, $\sigma^{UT\ 1}_{apriori}$ =10000.0 ms (these values are used for initializing of the information arrays) and 2) power spectral density of ruled white noise S_{PM}=0.6 mas/$\sqrt{hour}$, S_{UT1}=0.04 ms/$\sqrt{hour}$ Bolotin (private communication);
temporal resolution: the resulting EOP series is unevenly sampled with time resolution 3-5 min.

1.2 Data obtained in Goddard Space Flight Center

adjustments are with respect to: smooth a priori spline model (that is a fit to daily EOP offsets);
method of estimation of unknowns: multigroup least-square method (LSM). Each daily experiment is subdivided in hourly bins and EOP is modeled as a piecewise-linear function with rate constraints of 10 mas/day for polar motion and 1 ms/day for UT1;
temporal resolution: the resulting EOP series is evenly sampled with time resolution 1 hour.

1.3 Data obtained in St. Petersburg University

adjustments are with respect to: IERS C04;
method of estimation of unknowns: least-square collocation method (LSCM) (Titov, 2004);
a priori information: EOP are treated as stochastic process with known covariance matrix. Elements of the matrix are calculated in according with the following formula:

$$q_w(\tau) = \sigma^2_{EOP}\, e^{-\alpha|\tau|}\, \frac{\cos(\beta\tau + \varphi)}{\cos(\varphi)}$$

where σ^2_{EOP} is a priori variance of stochastic process, τ - time shift given in parts of day $0 \le \tau \le 1$. Other parameters have the following values: α =50 day^{-1}, β = 1 cycle per day, φ = 0.3 rad. We derive three solutions under different values of a priori variance: series SPU_1 (σ^2_{EOP}=4.4 cm^2); series SPU_2 (σ^2_{EOP}=1 cm^2); series SPU_3 (σ^2_{EOP}=0.44 cm^2);

temporal resolution: the resulting EOP series is unevenly sampled with time resolution 3-5 min.

2 Analysis

Here we focus on the intraday variations of polar motion. Figures 1 and 2 present initial PM series derived by different Analysis Centers. It can be seen that only the MAO series reveals a linear trend. One of the possible reasons for this could be the different separation of 'daily' and stochastic parameters in comparison with GSFC and SPU series. For example, in LSCM and multigroup LSM the expectations of Earth orientation parameters over each 24-hour experiment period are considered as a 'daily' parameter whereas sub-diurnal variations of EOP are supposed to have zero mean values.

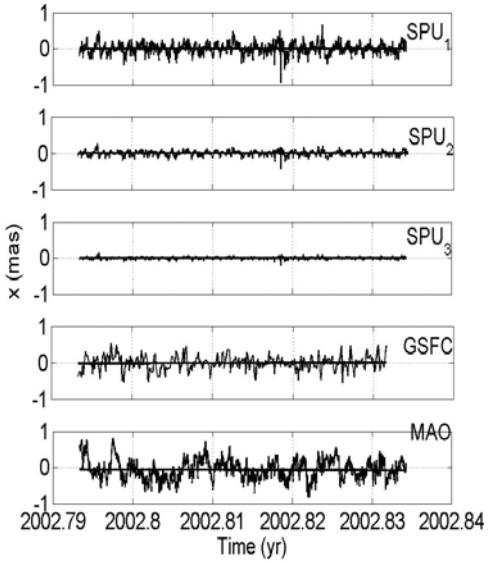

Fig. 1 X-coordinate time series (after removing of the IERS ocean tidal model) and fitted linear function (bold line).

Spectra in figures 3 and 4 show that strong peaks near the frequencies υ==1,2 cpd are still seen in the power spectrum of MAO series though the ocean tidal effects in the diurnal and semi-diurnal bands have been eliminated. The power spectral density of these oscillations is comparable with the PSD of the excluded oceanic tide model. However it seems that the main contribution to these peaks come from broadband noise S. Bolotin (private communication) but from harmonic oscillations with frequencies υ=1,2 cpd. Another distinctive feature of the MAO series is the powerful peaks at low frequencies υ=<0.5 cpd).

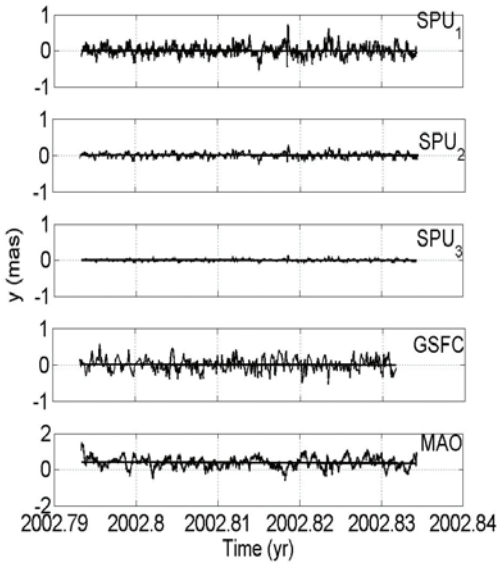

Fig. 2 Y-coordinate time series ((after removing of the IERS ocean tidal model)) and fitted linear function (bold line).

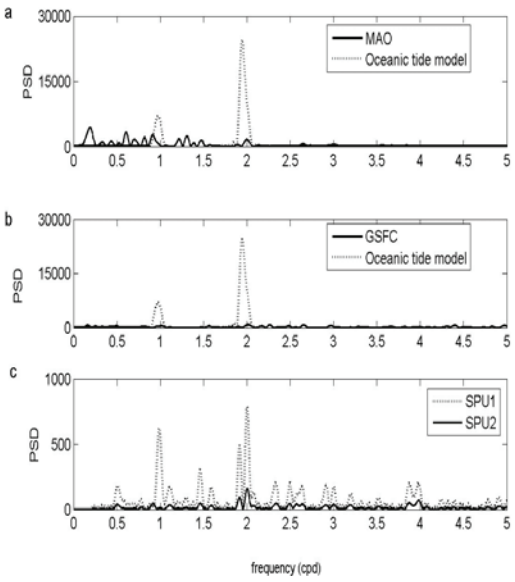

Fig 3. Spectra of individual time series of x-coordinate: a - series obtained in MAO in comparison with the oceanic tide model; b - series obtained in GSFC in comparison with the oceanic tide model; c - series obtained in SPU.

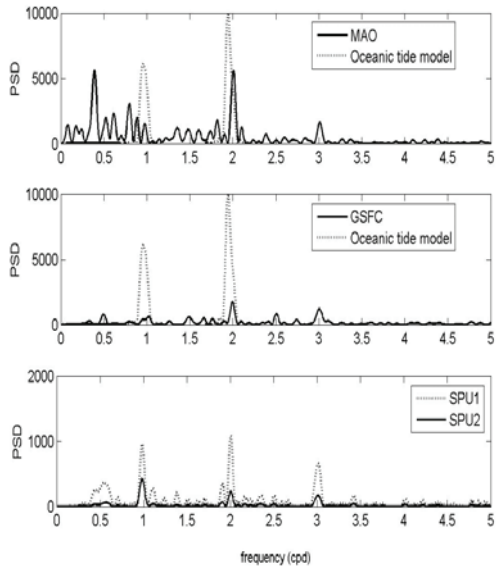

Fig 4. Spectra of individual time series of y-coordinate: a - series obtained in MAO in comparison with the oceanic tide model; b - series obtained in GSFC in comparison with the oceanic tide model; c - series obtained in SPU.

As a quantitative measure of the differences between spectra of the series we use the variance computed according to the following formulas:

$$\sigma^2_{SPU_j-GSFC} = \frac{1}{k-1}\sum_{i=1}^{k}\left[SP_{SPU_j}(\nu_i) - SP_{GSFC}(\nu_i)\right]^2$$

$$\sigma^2_{SPU_j-MAO} = \frac{1}{k-1}\sum_{i=1}^{k}\left[SP_{SPU_j}(\nu_i) - SP_{MAO}(\nu_i)\right]^2$$

where j=1,2,3. From the results given in Table 1 we conclude that agreement between SPU_j and MAO series is not very good and does not depend on a priori EOP dispersion σ^2_{EOP}. On the other hand, SPU_1 and GSFC series provide the best agreement in comparison with other series.

Table 1. Variance (μas) of the differences between spectra of the series SPU_j, GSFC and MAO. In left columns - for x-coordinate of pole and in right one .- for y-coordinate.

difference	σ^2*10^{-4}		difference	σ^2*10^{-4}	
SPU_1-GSFC	1.7	1.7	SPU_1-MAO	6.8	8.3
SPU_2-GSFC	1.8	2.2	SPU_2-MAO	6.8	7.2
SPU_3-GSFC	1.8	2.1	SPU_3-MAO	6.8	8.2

As the oceanic tide model does not include a contribution from the thermal potential the most significant contribution to the residual variations in polar motion should be from the thermal tide S1 Brzezinski and Bolotin (2006). Parameters of the S1 term estimated from different individual time series are compared in Table 2. Agreement between the parameters derived from different series depends on a priori information which is used for obtaining of individual series. For instance, parameters inferred from MAO series are in the best agreement with those one derived from SPU_2 series (a priori dispersion σ^2_{EOP}=1 cm^2). On the other hand, SPU_1 achieves the best agreement with GSFC series (as it have already been shown from spectra comparison).

3 Summary and Conclusions

We compared several individual series of polar motion calculated in MAO, GSFC and SPU analysis centers of VLBI data. It seems that spectrum of MAO series essentially differs from other series spectra. Nevertheless, parameters of the residual variations at the frequency S_1 derived from this series are in agreement with the same parameters derived from SPU_2 series (a priori dispersion 1 cm^2). In contrast, these parameters are underestimated in comparison with those from GSFC polar motion series. In that case when SPU series is calculated with a larger a priori dispersion (4.4 cm^2) it has better agreement with GSFC. In order to obtain the series with better agreement we need to have any constraints on a priori dispersion of EOP.

Table 2. Parameters (μas) of the S1 term in polar motion derived from different VLBI solutions.

amplitude	MAO	GSFC	SPU_1	SPU_2	SPU_3
U_C^x	6.3	17.6	18.7	6.9	3.0
U_S^x	-18.9	-40.7	-45.6	-19.2	-9.0

Acknowledgments. This work has been supported by grant of Ministry of Science and Education of Russian Federation No 2.1.1.5077, Astronomical and Geophysical Research based on VLBI and

GPS/GLONASS observations. The authors want to acknowledge Sergei Bolotin (MAO) for the friendly cooperation.

References

Kudryashova, M. V., A. Brzeziński, S. D. Petrov. On Geophysical Excitation of Prograde Diurnal Polar Motion, to be published in *"Highlights of Astronomy", Vol 14, Proc. of Joint Discussion 16 "Nomenclature, Precession and New Models in Fundamental Astronomy"*, 26th meeting of the IAU, Prague, Czech Republic.

Brzezinski, A., S. Bolotin. Retrieving Diurnal and Semidiurnal Signals in Polar Motion and UT1 from Analysis of the Routine VLBI Observations, to be published in *"Highlights of Astronomy", Vol 14, Proc. of Joint Discussion 16 "Nomenclature, Precession and New Models in Fundamental Astronomy"*, 26th meeting of the IAU, Prague, Czech Republic.

IERS Conventions 2003, eds. D. McCarthy and G.Petit, *IERS Technical Note No.32*, Verlag des Bundesamts für Kartographie und Geodäsie, Frankfurt am Main.

Titov, O. Construction of a Celestial Coordinate Reference Frame from VLBI data, Astron. Reports, 2004, v.48, pp. 941-948.

Effects of Geodetic Datum Definition on the Celestial and Terrestrial Reference Frames determined by VLBI

R. Heinkelmann, J. Böhm, H. Schuh
Institute of Geodesy and Geophysics,
Vienna University of Technology, Gusshausstrasse 27-29, A-1040 Vienna, Austria
rob@mars.hg.tuwien.ac.at

Abstract. We investigate the effects of the selection of reference points on the reference frames determined by global solution of VLBI observables. Effects on the source coordinates and on the station coordinates and velocities are assessed realizing various datum definitions. The celestial datum definitions based on astrometric suitability or time-series stability show no significant systematic effects on the source coordinates. In contrast, the application of various terrestrial datum definitions, taken from IVS Analysis Centers, significantly affects the terrestrial reference frame. The celestial datum shows no measurable effects on the terrestrial reference frame and vice versa.

Keywords. VLBI, datum definition, reference frames

1 Introduction

In case of a 'free' network, the datum is defined by selection of a subset of points. The selection of datum-points depends on a number of criteria, the goal of the particular network, or session, the type, number and quality of measurements, the characteristics of the sources (structure, stability), or stations (ground properties, monumentation, episodic motions etc.). The question is: are there any objective criteria for the quality of a datum? The answer must be given from the network itself, if no validation with a network of higher accuracy is possible. In this preliminary study we simply quantify datum effects. If the effects are significant, it could be worthwhile to extend this kind of investigations.

2 Datum definition in global VLBI solutions

In VLBI analyses the celestial and terrestrial reference frames (CRF, TRF) can be simultaneously determined by accumulating normal equations obtained from the solution of individual sessions (Tesmer et al., 2004). This type of solution is called 'global solution'. However, before the equation system can be solved, it has to be extended by a geodetic datum, i.e. a set of equations coping with the singularity of the equation system. The singularity is due to the fact, that we determine at the same time two frames and the transformations between the two frames.

2.1 The terrestrial datum

2.1.1 *Definition of the terrestrial datum*

Group delays of a VLBI session are observed from baselines, which form a polyhedron, that can be considered as a free network. The scale of the network is given by precise time measurements of H-masers at the stations, expressed in meters by the vacuum speed of light. Thus, in the case of free network adjustment, the inner geometry of the polyhedron is uniquely determined, independent from a datum. The polyhedron can be fixed with respect to an Earth-centered, Earth-fixed system, defining three translations and three rotations referring to all polyhedron points, represented by the geometric center of the polyhedron, or subsets of the polyhedron points. This datum definition does not affect the inner geometry of the polyhedron, thus it is called non-distorting constraint. The datum needs to regard a minimum of two different epochs, because station coordinates are subject to time variations. Alternatively, the datum can be defined using the coordinates at one epoch and the (linear) velocities of the stations.

2.1.2 *Realization and effects of the terrestrial datum*

The terrestrial datum can be realized by no net rotation (NNR) and no net translation (NNT) constraints of station positions and velocities w.r.t.

the Earth-fixed, Earth-centered system, realized by a TRF.

NNT of station positions:

$$\sum_{i=1}^{k} w_i \Delta\vec{r}_i = \vec{0} \quad (1)$$

NNT of station velocities:

$$\sum_{i=1}^{k} w_i \Delta\vec{v}_i = \vec{0} \quad (2)$$

NNR of station positions:

$$\sum_{i=1}^{k} w_i \left(\vec{r}_{0,i} \times \Delta\vec{r}_i\right) = \vec{0} \quad (3)$$

NNR of station velocities:

$$\sum_{i=0}^{k} w_i \left(\vec{r}_{0,i} \times \Delta\vec{v}_i + \Delta\vec{r}_i \times \vec{v}_{0,i}\right) = \vec{0} \quad (4)$$

Here, k = 50 denotes the total number of terrestrial points of solution IGG05R01 (Heinkelmann et al., 2006) and i = 1, 2, …, k is a specific terrestrial point. The [3,1] vector r_i denotes the station positions and the [3,1] vector v_i the station velocities of the specific station. The subscript '0' stands for a-priori values, whereas the symbol 'Δ' denotes adjustments to the a-priori values. With a coefficient w_i = 1 one can select the specific terrestrial point as datum point, whereas with w_i = 0 one can exclude the specific point from the datum definition.

We used the datum definition of some Analysis Centers (Table 1) of the International VLBI Service for Geodesy and Astrometry (IVS, Schlüter et al., 2002) and applied it to the accumulated normal equation system of solution IGG05R01. The a-prioris are taken from VTRF2003 (Nothnagel, 2003).

Table 1. Terrestrial datum realizations

CGS	38 stations of CGS2005A (IVS, 2006) Centro di Geodesia Spaziale, Matera, Italy
GSFC	35 stations of GSF2005B (IVS, 2006) Goddard Space Flight Center, Greenbelt, USA
DGFI	25 stations (Tesmer et al., 2004) Deutsches Geodätisches Forschungsinstitut, Munich, Germany
MAO	8 stations of MAO2003A (IVS, 2006) Main Astronomical Observatory, National Academy of Sciences, Kiev, Ukraine

The datum of Centro di Geodesia Spaziale, Matera, Italy (CGS) includes the stations DSS65, EFLSBERG, GILCREEK, MEDICINA, and MOJAVE12, which show coordinate jumps due to episodic motions, such as earthquakes, rail repairs, etc. Also station HRAS_085, which shows non-linear station motion (Figure 1), is selected as a datum point for this solution. These specific stations are omitted in the other datum subsets. CGS and Goddard Space Flight Center, Greenbelt, USA (GSFC) datum definitions include stations NRAO85_3 and TSUKUB32, which are modelled with episodic motions in ITRF2000 and ITRF2005. In VTRF2003, TSUKUB32 is also modelled with a jump in the up-component due to a repair of the concrete foundation slab. The datum of Deutsches Geodätisches Forschungsinstitut, Munich, Germany (DGFI) is a strict subset of the GSFC datum, including 25 stations. Here, additionally GILCREEK is omitted due to the Denali-fault earthquake in 2002-November-3 (Figure 2). The datum of Main Astronomical Observatory, National Academy of Sciences, Kiev, Ukraine (MAO) consists of only 8 stations and is again a strict subset of DGFI datum.

Position biases between the frames are shown in Table (2). They are at the level of 3.5 mm at epoch 2000.0 and 6.9 mm at epoch 2010.0. The parameters of similarity transformations of the frames into IGG05R01 using DGFI datum are given in Table (3) for epochs 2000.0 and 2010.0. Maximal translations between the frames reach 8.5 mm in X-component between GSFC and DGFI datum definitions. Rotations peak 279.4 μas between MAO and DGFI subsets; both at epoch 2010.0. The scale using different datums shows no significant variation. There is no measurable effect of terrestrial datum definition on the CRF.

Table 2. Station position biases in mm

a) epoch 2000.0

	GSFC	DGFI	MAO
CGS	3.5	2.3	3.1
GSFC	0	4.5	5.3
DGFI		0	2.3
MAO			0

b) epoch 2010.0

	GSFC	DGFI	MAO
CGS	5.3	5.6	7.0
GSFC	0	8.9	8.4
DGFI		0	6.1
MAO			0

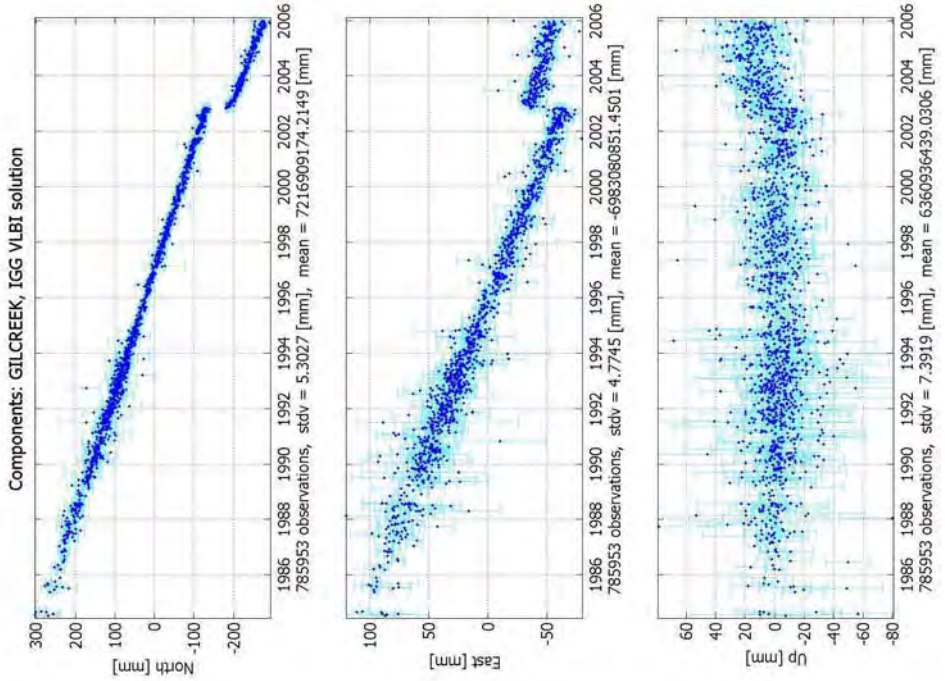

Figure 2. Coordinates of station GILCREEK, an example for episodic station motion

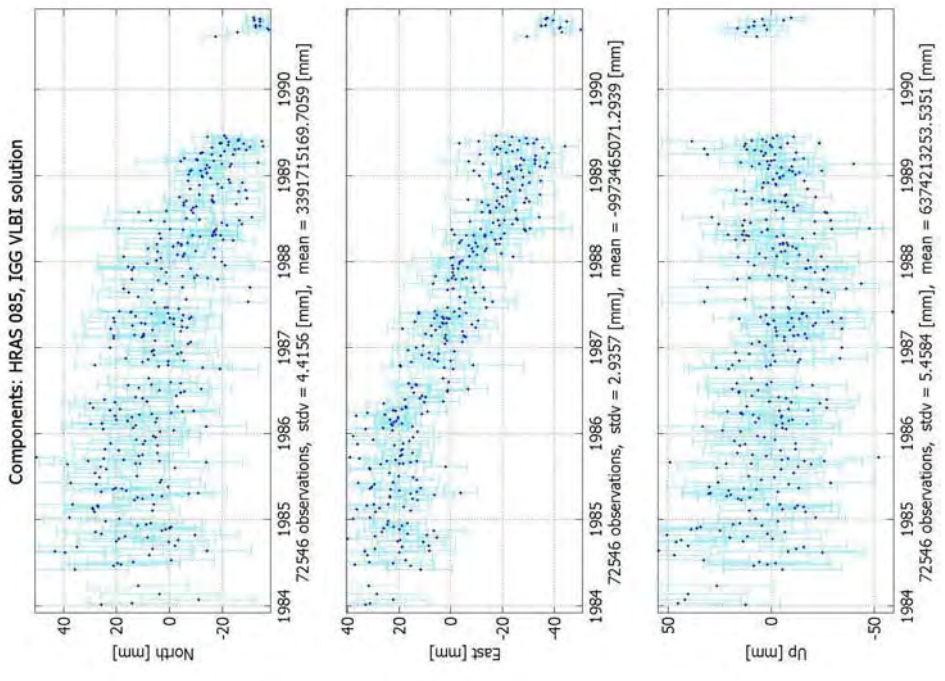

Figure 1. Coordinates of station HRAS 085, an example for non-linear station motion

Table 3. Parameters of a similarity transformation into the frame using DGFI datum
a) epoch 2000.0

	CGS	GSFC	MAO	mean σ
α [μas]	-24.0	9.3	90.6	3.0
β [μas]	-11.0	45.1	-44.5	3.0
γ [μas]	-49.0	-13.4	-5.1	3.0
ΔX [mm]	-0.7	-4.4	1.4	0.1
ΔY [mm]	-0.9	0.6	1.5	0.1
ΔZ [mm]	1.9	1.6	1.3	0.1
scale [ppb]	-0.00	-0.00	-0.00	0.01

b) epoch 2010.0

	CGS	GSFC	MAO	mean σ
α [μas]	2.7	37.0	279.4	4.6
β [μas]	-44.0	39.8	57.5	4.5
γ [μas]	-168.1	-77.7	-13.8	4.5
ΔX [mm]	-3.2	-8.5	-2.3	0.1
ΔY [mm]	-1.7	0.9	5.0	0.1
ΔZ [mm]	2.8	3.2	1.8	0.1
scale [ppb]	-0.01	-0.02	-0.02	0.02

2.2 The celestial datum

2.2.1 *Celestial datum definition*

As the celestial points are assumed to be time-invariant, a second epoch is not regarded. The estimated source coordinates refer to the barycenter and need to be aligned in terms of orientation, only. Here, the two celestial angular arguments, right ascension and declination, have to be fixed. This can be achieved by successive rotations, e.g. described by the three Euler angles, or the three Cardan angles.

2.2.2 *Realization and effects of the celestial datum*

The celestial datum can be NNR of source positions w.r.t. the inertial (translation-invariant) celestial system realized by a CRF.

NNR of source positions:

$$\sum_{j=1}^{l} p_j \left(\vec{s}_{0,j} \times \Delta\vec{s}_j \right) = \vec{0} \qquad (5)$$

Where l = 466 is the total number of sources in solution IGG05R01 and j = 1, 2, … ,l denotes the specific source. The [2,1] vector s_j stands for the coordinates of the specific source and by the coefficient p_j the source can be selected for the celestial datum. The other symbols are used in analogy to Equations (1) to (4).

Since 1998-January-1 the international celestial reference frame (ICRF, Ma et al., 1998) and its current extension (ICRF-Ext.2, Fey et al., 2004) is realized by VLBI. Up to now, there are no celestial reference frames of comparable accuracy. In the context of the determination of a new realization of the ICRS (ICRF2) the selection of sources used for the NNR constraints and the selection of sources estimated as global parameters are important issues. Several studies assess the astrometric suitability of sources, or the stability of source coordinate time-series. Table (4) gives an overview about the various approaches. In order to quantify effects of the celestial datum, we realize subsets based on those approaches and apply them on the accumulated normal equation system of the IGG05R01 solution. A-priori coordinates are taken from ICRF-Ext.2 (Fey et al., 2004). If transforming the various frames into each other by three rotations, we find no significant systematic variations of the orientation (< 1 μas). The coordinate biases are given in Table (5). Average biases of right ascension are on the level of 2.6 μas, and 3.1 μas for declinations. The tested celestial datums have no measurable effects on station coordinates.

Table 4. Celestial datum realizations

DEF	212 sources of category 'defining' of the ICRF (Ma et al., 1998)
ENG	121 sources with normally distributed components (Engelhardt and Thorandt, 2006)
FES	199 sources found to be stable in terms of Allan deviation (Feissel-Vernier, 2003)
FEY	71 sources with structure index 1 in X- and S- bands (Fey and Charlot, 1997)

Table 5. Source coordinate biases in μas
a) right ascension

	ENG	FES	FEY
DEF	0.1	1.3	3.9
ENG	0	1.5	3.8
FES		0	5.2
FEY			0

b) declination

	ENG	FES	FEY
DEF	3.5	1.6	2.1
ENG	0	1.9	5.6
FES		0	3.7
FEY			0

3 Summary of results

The selection coefficients w_i and p_j , Equations (1) to (5), were set either to zero or one, but in principal they can contain any non-negative values. As an alternative approach to the strict selection, or de-selection, of points for the datum, one could also define relative weights of the points for the datum definition.

The largest differences in celestial coordinates can be found w.r.t. the astrometric suitability datum set, where average differences are around 4 μas, about three times larger then the other differences. The structural approach is fundamentally different from the time-series stability assessment methods. It considers astrophysical characteristics of the sources, whereas the time-series stability approaches describe statistical characteristics, such as normal distribution, or Allan deviation of the time-series. The structure indices are obtained by analysing specific VLBA sessions, whereas the stability criteria are based on more or less all available VLBI sessions.

Kutterer (2004) also assessed the uncertainty introduced by the datum. However, his results were based on the analysis of CONT02 sessions, only. He found the uncertainty induced by the celestial datum to be on the level of 10 μas. In our study average source coordinate biases are smaller (3 μas). Since our solution includes much more and in particular older types of sessions, we expected the induced uncertainty to be larger in comparison to CONT02. However, all 466 sources estimated as global parameters in solution IGG05R01 are rather stable. Larger variations may occur if less frequently observed or more unreliable sources are included.

While the selection of celestial datum points has no significant systematic impact on source coordinates determined with solution IGG05R01 the terrestrial datum significantly affects the estimated TRF. In general, there are much less terrestrial points and the celestial points are much more stable than the terrestrial points. It is notable that the selection of stations with episodic motions in CGS datum, such as GILCREEK, and stations showing non-linear motions, such as HRAS 085, does not show larger effects on the TRF than the other datum definitions.

Kutterer (2004) found the coordinate uncertainty induced by terrestrial datum point selection on the level of 2 mm. Our results are about two to four times larger. This is due to the larger number of stations and sessions included in our analyses. In addition CONT02 was observed by a modern network with high quality, whereas our solution contains all type of networks and campaigns starting in 1984. The 2 mm uncertainty found by Kutterer (2004) are valid for coordinates, only. In our investigations we consider epochs outside of the observational epochs of the stations in order to study effects of the coordinate and velocity constraints. Furthermore, Kutterer (2004) investigated effects successively excluding single datum points from the subset. In this study the subsets are significantly variable.

4 Outlook

Since the terrestrial datum definition significantly affects the TRF determined by VLBI, it could be worthwhile to select datum points in an objective way. Reliability, defined as the ability to sense and identify gross errors in the measurements, could be such an objective criterion. The ‘internal reliability’ measures the size of undetectable errors of the measurements, while the ‘external reliability’ quantifies the effects of undetected errors on the parameters. The internal reliability is not affected by the datum definition, but the external reliability depends on it. In absence of errors any arbitrary subset of datum points satisfying minimal conditions, i.e. removing the singularity of the equation system, yields identical results. Then, the optimal datum in terms of external reliability is the one including all points (Even-Tzur, 2006). However, analysing ‘real’ data the optimal subset of datum points has to consider stability and geometry (Papo Haim, 2003) in addition to quantity. In principal it would be possible to find an ‘optimal’ datum in terms of external reliability. However, this optimal datum could be valid for a specific solution, only.

Acknowledgements

We greatly acknowledge the IVS and its components. The authors want to thank the Austrian Science Fund (FWF) for the financial support of project P16992-N10 (VLBI for climate studies).

References

Engelhardt, G., and V. Thorandt (2006). First steps to investigate long-term stability of radio sources in VLBI analysis. In: *International VLBI Service for Geodesy and Astrometry General Meeting Proceedings 2006*. D. Behrend and K.D. Baver (eds) NASA/CP-2006-214140, pp. 281-285

Even-Tzur, G. (2006). Datum definition and its influence on the reliability of geodetic networks. *Zeitschrift für Vermessungswesen* 131. Jg. 2/2006, pp. 87-95

Feissel-Vernier, M. (2003). Selecting stable extragalactic compact radio sources from the permanent astrogeodetic VLBI program. *Astronomy & Astrophysics* 403, pp. 105-110

Fey, A. L., and P. Charlot (1997). VLBA observations of radio reference frame sources. II. Astrometric suitability based on observed structure. *The Astrophysical Journal Supplement Series*. 111, pp. 95-142

Fey, A. L., C. Ma, E. F. Arias, P. Charlot, M. Feissel-Vernier, A.-M. Gontier, C. S. Jacobs, J. Li, D. S. MacMillan (2004). The second extension of the international celestial reference frame: ICRF-Ext.1. *The Astronomical Journal*, Vol. 127, pp. 3587-3608

Heinkelmann, R., J. Böhm, H. Schuh, V. Tesmer (2006). Global VLBI solution IGG05R01. In: *International VLBI Service for Geodesy and Astrometry General Meeting Proceedings 2006*. D. Behrend and K.D. Baver (eds) NASA/CP-2006-214140, pp. 42-46

IVS (2006) web-ressource: ftp://ivs.bkg.bund.de/pub/vlbi/ivsproducts/trf/

Kutterer, H. (2004) Reliability measures for geodetic VLBI products. In: *International VLBI Service for Geodesy and Astrometry General Meeting Proceedings 2004*. D. Behrend and K.D. Baver (eds) NASA/CP-2004-212255, pp. 301-305

Ma, C., E. F. Arias, T. M. Eubanks, A. L. Fey, A.-M. Gontier, C. S. Jacobs, O. J. Sovers, B. A. Archinal, P. Charlot (1998) The international celestial reference frame as realized by very long baseline interferometry. *The Astronomical Journal*. Vol. 116, pp. 516-546

Nothnagel, A. (2003) VTRF2003: a conventional VLBI terrestrial reference frame. In: *Proc. of the 16th working meeting on European VLBI for Geodesy and Astrometry*. W. Schwegmann and V. Thorandt (eds). Bundesamt für Kartographie und Geodäsie, Frankfurt/Leipzig, pp. 195-205

Papo, Haim B. (2003) Datum accuracy and its dependence on network geometry. *Geod. kartogr.*, Springer, Berlin, pp. 379-386

Schlüter, W., E. Himwich, A. Nothnagel, N. Vandenberg, A. Whitney (2002) IVS and its important role in the maintenance of the global reference frames. *Advances in Space Research*, Vol. 30, No. 2, pp. 145-150

Tesmer, V., H. Kutterer, H. Drewes (2004) Simultaneous estimation of a TRF, the EOP and a CRF. In: *International VLBI Service for Geodesy and Astrometry General Meeting Proceedings 2004*. D. Behrend and K.D. Baver (eds) NASA/CP-2004-212255, pp. 311-314

Some issues about the Earth's core and inner core through VLBI

S.B. Lambert, V. Dehant
Royal Observatory of Belgium, 3 Avenue Circulaire, B-1180 Brussels, Belgium

A.-M. Gontier
Département Systèmes de Référence Temps Espace (SYRTE, CNRS/UMR8630)
Observatoire de Paris, 61 avenue de l'Observatoire, F-75014 Paris, France

Abstract. This work addresses some questions about the ability of the current VLBI network and analysis strategies to retrieve the Earth's interior parameters, especially those relevant to the fluid outer and solid inner cores. Especially, how sensitive are the core parameters' estimates to the constraints applied to the celestial reference frame?

Keywords. VLBI, Earth Rotation, Nutation, Outer Core, Inner Core, Celestial Reference Frame, Analysis Strategy

1 Rotation of the core and of the inner core, and nutation

The retrograde free core nutation (RFCN) is a free rotational mode of the Earth, associated with the ellipsoidal liquid core rotating inside the visco-elastic mantle. The signature of this free mode on the Earth's figure axis observed from a space-fixed reference frame is a retrograde motion that reaches an amplitude of about 200 μas, variable in time, and with a variable phase. This signal clearly shows up in VLBI residuals. The apparent period oscillates between 430 and 460 days (Vondrák et al. 2005) and is most likely driven by diurnal atmospheric pressure variations (Gegout et al. 1998, Vondrák & Ron 2006, Lambert 2006). An analogous mode exists for the inner core (free inner core nutation, or FICN). Its signature in the nutation however remains too weak to be observed (Dehant et al. 2005).

Although the apparent periods of the free motions associated with the RFCN and the FICN can fluctuate due to variable excitation, the resonant periods, associated with the flattening of the relevant layers and to other deformability and coupling parameters, are expected to be much stable. These resonant periods can be retrieved observationally considering the effect of the associated resonance on the forced nutations (see Mathews et al. 1991, Mathews et al. 2002, hereafter referred to as MHB). In Lambert & Dehant (2007), we showed that the RFCN resonant period estimated through existing VLBI data sets released by the IVS remains within half a day (the quality factor is stable within ~1500), pointing out that geophysics is sensitive at a significant level to the adopted analysis strategy (including assumptions on the reference frames, selection of sessions, softwares and models). In this study, we restrict the study to the celestial reference frame, since it is well known that different assumptions (or constraints) on the radio source positions lead to different nutation estimates, possibly contaminated by errors due a deficient realization of the celestial frame.

2 Influence of the celestial reference frame realization on the outer and inner core parameters

The realization of the celestial reference system using VLBI observations can be done through many different ways, known to have a substantial influence on the determination of the nutation offsets (see, e.g., Feissel-Vernier et al. 2006, and results here above). The best way to clearly quantify this influence is to generate our own nutation series through several VLBI solutions using exactly the same analysis scheme except for the constraints applied to the radio source coordinates (RSC).

In the following, we use the same method as in Lambert & Dehant (2007) to adjust the RFCN and FICN frequencies on several homemade VLBI nutation series. Only the constraint applied to the radio source coordinates is changed from one to another series. Our solutions take 3,288 sessions,

totalizing 4,488,671 delays. We process the following seven solutions, named A to G:

- A: RSC fixed to their ICRF-Ext. 2 values (Fey et al. 2004), no celestial reference frame estimated;
- B: RSC estimated as global parameters, constrained by a no-net rotation (NNR) condition on the coordinates of the 212 ICRF defining sources (Ma et al. 1998);
- C: same as B, but with NNR on the 247 sources of Feissel-Vernier et al. (2006) wrt ICRF-Ext. 2;
- D: RSC estimated as global parameters for 532 sources, as local parameters for 202 with low observational history, constrained by a NNR on the coordinates of the 212 ICRF defining sources;
- E: same as D but with NNR on the coordinates of the 247 sources of Feissel-Vernier et al. (2006)
- F: same as E but with elevation cut-off at 5° instead of 6°;
- G: RSC estimated as global parameters for the 247 stable sources (also in NNR), all other sources as arc.

The amplitudes of the main tidal terms are reported in Figure 1. It appears that solution B (in green circles) leads to completely different amplitudes than all the other solutions. The reason is unclear.

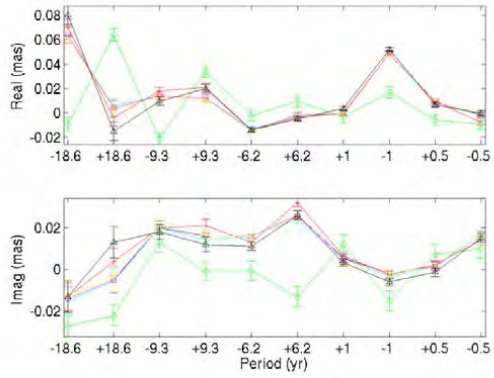

Fig. 1. Amplitudes of the tidal terms adjusted in solutions A to G. The green squares are relative to the solution B.

Figure 2 displays differences between nutation series obtained in solutions A and B. It appears that artifacts completely due to the celestial frame realization can affect determinations of precession and long periodic nutations. Obviously, this imperfect realization of the celestial frame in the early VLBI comes from a deficient network and a rather poor number of sources observed in each session. It is interesting to note that such an artifact can easily mimic a 18.6-yr tidal term that could contribute significantly to constraining the RFCN and FICN frequencies (see Figures 7 and 8 of Dehant et al. 2003).

As in Lambert & Dehant (2007), we base all our analyses on 8 tidally induced nutations (periods from 18.6-yr down to semi-monthly). We proceed consistently with the MHB work by taking the parameter's a priori values in the Table 6 of the MHB paper. Doing so, we basically look for a deviation from the MHB model.

Figure 3 displays the outer core and inner core frequencies and quality factors obtained after a treatment similar to Lambert & Dehant (2007) and removing non tidal contributions (geodesic nutation, atmospheric contribution and non linear effects as computed in Lambert & Mathews 2006). The removal of these non tidal contributions explains the lower quality factor found for the outer core. Except for solution B, the resonant periods appear to stay within ~0.1 day for the RFCN and ~100 days for the FICN, with respective quality factors of ~18000 and ~600.

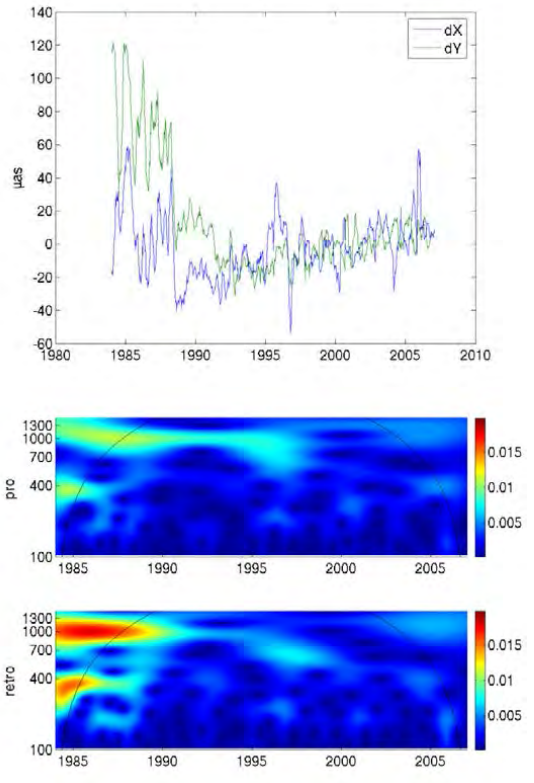

Fig. 2. Differences in nutation offsets obtained with various analysis strategies: A minus B and wavelet spectrum of the prograde and retrograde parts.

4 Concluding remarks

This work shows that the core and inner core parameters can be determined from the current VLBI network and state-of-the-art analysis strategies with a good reliability. Nevertheless, we detected inconsistencies between (i) the various data sets made available in the IVS product centers, and (ii) various analysis strategies concerning the realization of the celestial reference frame applied to a same set of sessions. Although small, these inconsistencies are significant, and reflect strength or deficiencies in the current way of analyzing VLBI observations. If not corrected or considered, they could have an impact on the precision of future geophysical results.

Since the realization of the celestial reference frame is a significant source of errors during global VLBI analysis, the arrival of the second realization of the ICRF, that will replace the current ICRF by 2009, will certainly improve the precision.

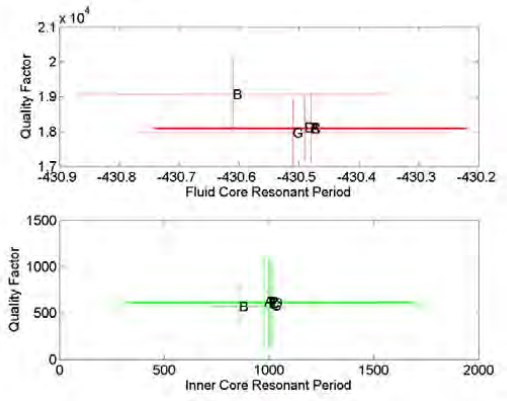

Fig. 3. RFCN and FICN frequencies and quality factors obtained through solutions A to G.

References

Dehant, V., Feissel-Vernier, M., de Viron, O., et al. 2003, J. Geophys. Res., 108(B5), 10.1029/2002JB001763

Dehant, V., de Viron, O., & Greff-Lefftz, M. 2005, A&A, 438, 1149

Feissel-Vernier, M., Ma, C., Gontier, A.-M., & Barache, C. 2006, A&A, 452, 1107

Fey, A.L., Ma, C., Arias, E.F., et al. 2004, AJ, 127, 3584

Gegout, P., Hinderer, J., Legros, H., et al. 1998, PEPI, 106, 337

Lambert, S.B. 2006, A&A, 457, 717

Lambert, S.B., & Mathews, P.M. 2006, A&A, 453, 363

Lambert, S.B., & Dehant, V. 2007, A&A, in press

Ma, C., Arias, E.F., Eubanks, T.M., et al. 1998, AJ, 116, 516

Mathews, P.M., Buffett, B.A., Herring, T.A., & Shapiro, I.I. 1991, J. Geophys. Res., 96(B5), 8219

Mathews, P.M., Herring, T.A., & Buffett, B.A. 2002, J. Geophys. Res., 107(B4), 10.1029/2001JB000390

Vondrák, J., Weber, R., & Ron C. 2005, A&A, 444, 297

Vondrák, J., & Ron, C. 2006, Acta Geodyn. Geomater., 3(143), 53

Datum Deficiency in VLBI Analysis: Case Study of Session 021020XA

P.J. Mendes Cerveira, J. Boehm, E. Tanir, J. Wresnik, H. Schuh
Advanced Geodesy, Institute of Geodesy and Geophysics, Vienna University of Technology, Gusshausstrasse 27-29, 1040 Vienna, Austria

V. Tesmer
Deutsches Geodätisches Forschungsinstitut, Alfons-Goppel-Strasse 11, 80539 Munich, Germany

Abstract. This paper presents the results of a case study analysis applied to the Very Long Baseline Interferometry (VLBI) session 021020XA in terms of datum deficiency. An analysis was performed to determine the number of minimal conditions or constraints necessary to remove the datum deficiency (for various parameter combinations). The respective number of singular values from the normal matrix has been tabulated. Five methods, enabling to remove the rank deficiency of the normal equation system, were tested and compared for the quantitative impact on geodetic parameters. It turns out that the datum definition affects most station coordinates as well as polar motion and universal time, up to the 5 mm level.

Keywords. Reference frames, Very Long Baseline Interferometry (VLBI), Earth rotation, geodetic parameters, datum definition

1 Introduction

We distinguish between conditions and constraints: conditions are fulfilled after the adjustment, while constraints may not (depending on the uncontrollable weighting). To remove the datum defect, many different sets of minimal conditions or constraints are possible for the same problem. The various solutions obtained from different sets of minimal conditions or constraints can be related by similarity transformations (Baarda, 1973; Sillard & Boucher, 2001; Even-Tzur, 2006). The only prerequisite for the minimal condition or constraint matrices is that the rank of the matrix including the design matrix and condition matrix equals the number of unknown parameters. Among all possible minimal condition or constraint solutions, the inner condition solution minimizes the weighted sum of the squares of all estimated parameters and the trace of its cofactor matrix. This paper is a case study for the rank deficiency problem for the VLBI session 021020XA observed during the CONT02 campaign, starting at 18h Coordinated Universal Time (UTC) on October 20^{th} 2002 for nearly 24 hours. The International VLBI Service for Geodesy and Astrometry (IVS) scheduled and led the campaign (Schlueter et al., 2002).

In the past, the no-net-rotation condition NNR1 imposed on corrections of quasar positions was applied for retrieving corrections to quasar positions along with corrections to the deficient a priori precession/nutation model, while the no-net-rotation condition NNR2 was applied to the corrections of a priori station coordinates in order to obtain corrections to the latter along with corrections to the a priori polar motion and universal time parameters. The need and use of the no-net-translation (NNT) on corrections of (a set of) a priori station coordinates is unquestionable. Various implementations of the datum definition were studied w.r.t. their influence on the geodetic parameters, i.e., station coordinates, (five) Earth orientation parameters and wet zenith delays (WZD). Physical parameters should be independent of the choice of the datum.

2 Theoretical background

According to geodetic usage, the datum defining condition matrix $\mathbf{B}$ for the parameter corrections $\mathbf{\Delta x}$ reads:

$$\mathbf{B} \cdot \mathbf{\Delta x} = \mathbf{0} \tag{1}$$

After the successful adjustment, equation (1) must be fulfilled up to numerical accuracy.

2.1 Celestial datum points

For celestial datum points, the NNR1 condition matrix $\mathbf{B}_{\mathrm{cel,NNR1,j}}$ is composed (for quasar j) as,

e.g., by Kutterer (2004):

$$\mathbf{B}_{\mathrm{cel,NNR1,j}} = \begin{bmatrix} \cos\alpha_j \sin\delta_j & -\sin\alpha_j \\ \sin\alpha_j \sin\delta_j & \cos\alpha_j \\ \cos\delta_j & 0 \end{bmatrix} \quad (2)$$

The meaning of equation (2) is that no global rotational mode is allowed w.r.t. the a priori quasar positions, which are given in a specific celestial reference frame.

2.2 Terrestrial datum points

For terrestrial datum points, the NNT condition matrix $\mathbf{B}_{\mathrm{ter,NNT,i}}$ ensures that the origin of the a priori station network (for station i), given in a clearly predefined terrestrial reference frame, equals the origin of the a posteriori network:

$$\mathbf{B}_{\mathrm{ter,NNT,i}} = \begin{bmatrix} 1 & 0 & 0 \\ 0 & 1 & 0 \\ 0 & 0 & 1 \end{bmatrix} \quad (3)$$

Equation (3) can also be fulfilled by fixing one single station, however, with the drawback that this station will lack any information concerning precision.

Apart from the NNT condition, the NNR2 condition matrix $\mathbf{B}_{\mathrm{ter,NNR2,i}}$ enforces the orientation of the adjusted station network to be identical to the one of the a priori network:

$$\mathbf{B}_{\mathrm{ter,NNR2,i}} = \begin{bmatrix} 0 & -z_i & y_i \\ z_i & 0 & -x_i \\ y_i & x_i & 0 \end{bmatrix} \quad (4)$$

A recent review concerning the terrestrial reference frame datum definition is given by Sillard & Boucher (2001).

3 Analysis setup

For the retrieval of the design and weight matrices as well as the reduced observation vector, we used the VLBI software package OCCAM 6.1E (Titov et al., 2004), available at `http://www.hg.tuwien.ac.at/~vlbi`. In addition, the adjusted unknown parameters, as well as their formal errors, served as reference for comparison purposes. The software MATLAB 7.0 was used for testing the impact of the datum on geodetic parameters, i.e., dealing with the datum information w.r.t. the normal matrix.

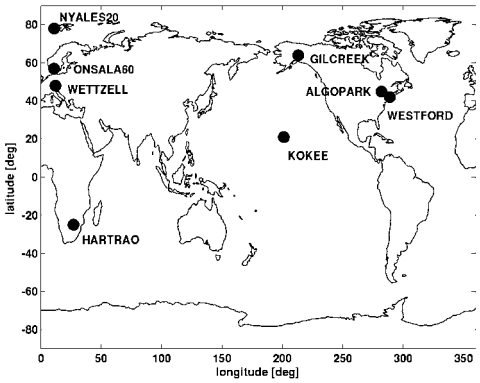

Figure 1. Station network constellation during session 021020XA showing the eight sites.

A short description of the parameterization follows. Station coordinates were estimated once per session for each of the eight sites shown in figure 1. Wet zenith delays were estimated as one offset and hourly piecewise linear functions (PLF) for each of the eight stations. Troposphere gradients were not estimated in order to preserve the present consistent usage of a priori quasar positions and Earth orientation parameters: otherwise the signal of the deficient a priori quasar position model would propagate into the Earth orientation parameters (MacMillan & Ma, 1997). The Earth orientation parameters were parameterized as two nutation offsets (nutation in longitude and in obliquity), two polar motion offsets (x-pole and y-pole), one dUT1 offset and hourly dUT1 rates as PLF. Hourly clock offsets, one 24-hour clock rate and square term were estimated for seven stations. We used hourly clock offsets instead of hourly PLF clock rates because the latter setup is not possible when no constraints are applied. No single loose constraint was used with the exception of defining one condition: the clock of station GILCREEK was fixed as reference. The choice of using GILCREEK instead of, e.g., WETTZELL was motivated by a strong gradient in the clock of the latter. Finally, the elevation cutoff angle was set to 5 degrees. The following a priori models were chosen:

- Terrestrial reference frame (Altamimi et al., 2002) is given by the file ITRF2005.CA1 and includes the source positions according to the ICRF-Ext.2 catalogue (Fey et al., 2004)
- Nutation model IAU2000A (Mathews et al.,

2002)

- IERS C04 polar motion and dUT1 (consistent with ITRF2005)
- Vienna Mapping Functions 1 (Boehm et al., 2006).

The following reduction models were applied:

- Solid Earth tides (McCarthy & Petit, 2004)
- Pole tide (Wahr, 1985; McCarthy & Petit, 2004)
- Ocean tide loading (FES2004)
- Atmospheric pressure loading (Petrov & Boy, 2004)
- Zonal tides on dUT1 (Defraigne & Smits, 1999)
- Diurnal/semidiurnal ocean tidal effects on polar motion and dUT1 (Ray et al., 1994; McCarthy & Petit, 2004)
- IERS 92 relativistic consensus model (McCarthy & Petit, 2004).

4 Rank deficiency in VLBI analysis

VLBI is a differential technique, sensitive to relative translations and rotations. Only the use of a priori models together with additional information relevant to the datum allows for recovering conventional geodetic parameters. The number of additional independent information highly depends on the selection of the unknown parameters.

Table 1 shows the number of singular values depending on the selection of estimated parameters. These values are only true if no further singularities appear, e.g., due to the station network geometry or the quasar constellation. In table 1, the station coordinates are always considered as unknowns. The case of solution S8, having 4 singular values, is particularly interesting when deriving dUT1 estimates from intensive sessions. Apart from the NNT condition, it can be seen from equation (4) that one additional NNR2 condition (line 3), which corresponds to a rotation about the a priori z-axis is sufficient to relieve the rank deficiency. Equivalently, fixing the x- or the y-component of one additional station coordinate would be adequate, while fixing the z-component would still lead to a rank deficiency of 1. Each further datum-related information evidently distorts the network geometry. In case of solution S10, where only station coordinate and nutation parameters are estimated, a NNT condition on station coordinate corrections suffices to get rid of the rank deficiency. In solution S1, quasar positions, nutation, polar motion and universal time, and station coordinate corrections were estimated.

Table 1. Rank deficiency depending on selection of unknown parameters. The cross X marks the estimated parameters in the solutions S1 to S10. The abbreviations are: SOL=solution,QUA=quasar positions, NUT=nutation, PM=polar motion, dUT1= universal time, STA=station coordinates, SV=number of singular values (rank deficiency).

SOL	QUA	NUT	PM	dUT1	STA	SV
S1	X	X	X	X	X	9
S2	X		X	X	X	7
S3	X	X			X	6
S4	X			X	X	5
S5	X				X	4
S6		X	X	X	X	6
S7			X	X	X	6
S8				X	X	4
S9					X	3
S10		X			X	3

5 Handling the datum deficiency

In the following, we applied five strategies for handling the datum deficiency, and will shortly describe them by enumeration:

1. M1: using OCCAM 6.1E, which applies NNR2 and NNT to all station coordinate corrections and NNR1 to all quasar position corrections
2. M2: ident to method M1 except that
   - the station coordinate corrections for NYALES20 and HARTRAO were excluded from NNR2 and NNT conditions
   - the five quasar position corrections 1908-201, 1921-293, 2128-123, 0434-188, and 1034-293 were excluded from the NNR1 condition, i.e., those having been observed less than five times during the session (see figure 2)

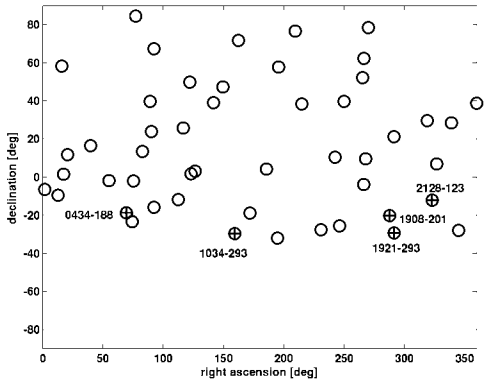

Figure 2. Quasar constellation (49 sources) during session 021020XA. Five sources, removed from NNR1 condition for method M2, are marked by crosses.

3. M3: using the singular value decomposition, following the rank deficiency of table 1

4. M4: using minimal pseudo-observations with robust weighting for station coordinates KOKEE, WESTFORD and the x-component of ONSALA60 as well as for the source position 4C39.25 and the right ascension of source 1357+769

5. M5: ident to method M4, but fixing minimal components, i.e., using minimal conditions instead of constraints.

6 Results

In the following, all results will be shown w.r.t. the ones obtained by method M1 for solution S6, having a rank deficiency of six. Estimating source positions from one single session causes instabilities in, e.g., nutation parameters with the formal errors being multiplied by an order of magnitude. However, in subsections 6.1 and 6.6 the case of solution S1 has been considered, including the quasar positions, and leading to a rank deficiency of nine. The standard deviation of unity weight is 1.24 cm for solution S1, while it is 1.33 cm for solution S6. The improvement of the S1 solution w.r.t. S6 is only about 7% although the $98 = 2 \cdot 49$ additional unknown source position coordinates were estimated. In the S1 solution, station position corrections reach up to 4 cm.

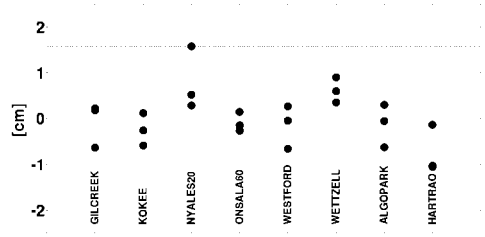

Figure 3. Station coordinate corrections obtained by method M1, solution S6. The three filled circles inherent to one station represent the three geocentric coordinate components x, y, and z.

6.1 Quasar positions

Forty-nine (49) sources have been observed during session 021020XA. Five sources, marked by crosses, have been observed less than five times and were removed from the NNR1 condition for the method M2 (see figure 2). No source with a declination inferior to -40 degrees has been observed.

6.2 Station coordinates

Eight stations observed during session 021020XA (see figure 1). The station coordinate corrections obtained by method M1 for solution S6 are largest (> 1 cm) at the stations NYALES20 and HARTRAO (see figure 3). Both stations were removed from the NNT and NNR2 conditions for the M2 method. These stations were also avoided in the methods M4 and M5. Figure 4 shows the difference in the x-component station coordinates w.r.t. the results obtained by method M1. Differences up to 5 mm do appear w.r.t. method M1, but results do also vary up to 3 mm within the methods M2 to M5. Insufficient modelled or unpredictable station coordinate deformations at specific sites, e.g., due to the incompletely modelled non-tidal ocean/atmoshpere loading effects or displacements induced by minor successive earthquake swarms, do impact the remaining station coordinates at the sub-cm level.

6.3 Nutation, polar motion and universal time corrections

The separation of nutation and polar motion in Very Long Baseline Interferometry (VLBI) is per convention purely frequency-dependent. As we

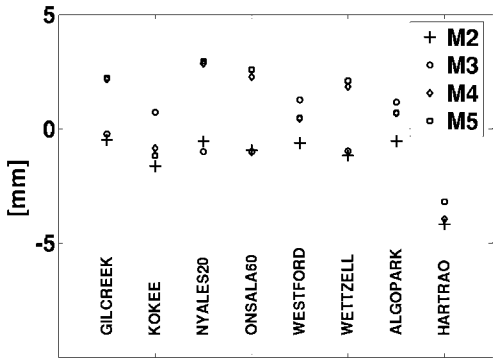

Figure 4. Difference in x-component station coordinates w.r.t. method M1, solution S6.

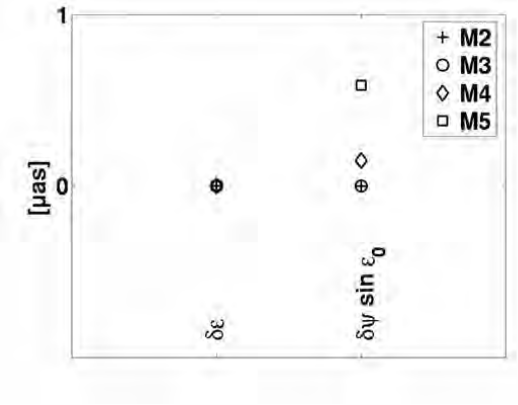

Figure 5. Difference in nutation components w.r.t. method M1, solution S6.

reduced all known diurnal and semi-diurnal effects on polar motion and universal time, we decided to only estimate daily nutation and polar motion parameters. The hourly dUT1 rates by PLF remain greatly unaffected by the choice of parameterization of polar motion and nutation. The differences in nutation (in obliquity $\delta\epsilon$ and longitude $\delta\psi \cdot \sin\epsilon_0$) w.r.t. method M1 are less than 1 μas (see figure 5). The results obtained by methods M1 to M5 are extremely stable for the nutation offset in obliquity $\delta\epsilon$, while the influence of the datum handling is most pronounced for the nutation offset in longitude $\delta\psi \cdot \sin\epsilon_0$. In contrast, the differences in polar motion and universal time between methods M1 and M5 may arise up to 200 μas, which corresponds roughly to 6 mm when projected to Earth surface (see figure 6). Universal time is also given in units of μas for better comparison to polar motion. The x-pole component in polar motion shows the largest variability. Especially the results of method M3 (using the singular value decomposition) differ considerably and systematically w.r.t. method M1.

6.4 Wet zenith delays

We picked out the differences in WZD-rates for station KOKEE w.r.t. method M1 (see figure 7). The x-ticks on the x-axis represent the hourly marks. As expected, WZD should not be affected by how the datum is handled. The differences, which were largest for the station at KOKEE, are less than 4 mm/day, i.e., less than 0.2 mm/hour. The largest variability arises when method M5 is

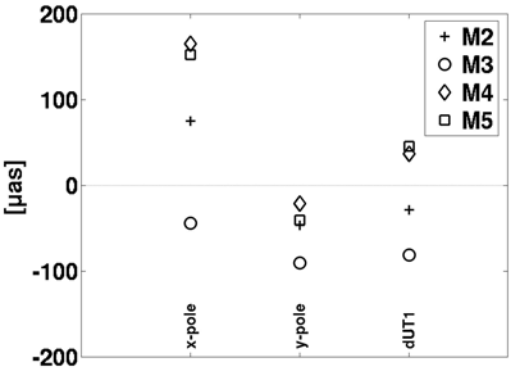

Figure 6. Difference in polar motion and dUT1 w.r.t. method M1, solution S6.

applied. Only methods M1, M2 and M3 provide identical results up to numerical accuracy.

6.5 Clock offsets

The largest differences also arise at station KOKEE for hourly clock offsets (see figure 8). Again, the largest variability (0.5 mm) is obtained when method M5 is used. Here too, only methods M1, M2 and M3 provide stable and identical results.

6.6 Correlation matrix

Figure 9 shows the correlation matrix obtained for solution S1 by method M2. High positive correlations (in white) are visible in hourly clock off-

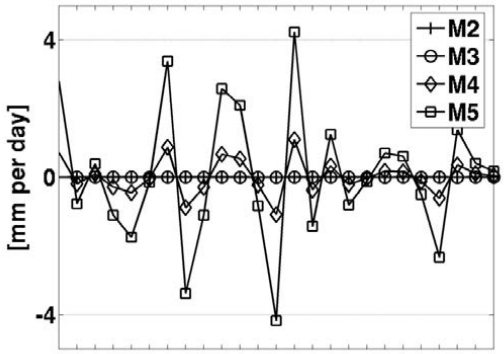

Figure 7. Difference of hourly WZD-rates for station KOKEE w.r.t. method M1, solution S6.

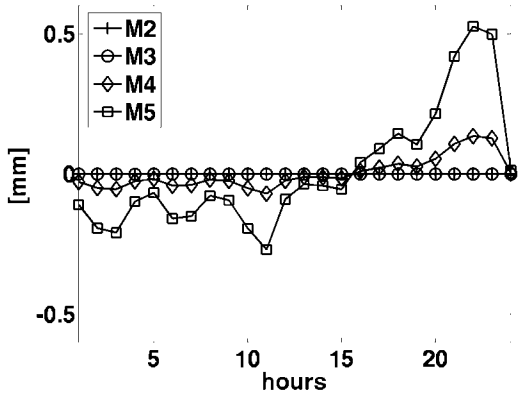

Figure 8. Differences of hourly clock offsets for station KOKEE w.r.t. method M1, solution S6.

sets for individual stations primarily because of the daily estimated rate and square terms in the clocks parameterization, but also due to the presence of station coordinates. If only hourly clock offsets are estimated, then the correlation coefficients between those hourly parameters for each single station will be zero. A cross-correlation of these parameters between stations does of course exist. Non-zero correlation coefficients, in hourly clock offsets within individual stations, are a clear indication of a deficiency in available observations to separate these parameters from station coordinates, especially heights.

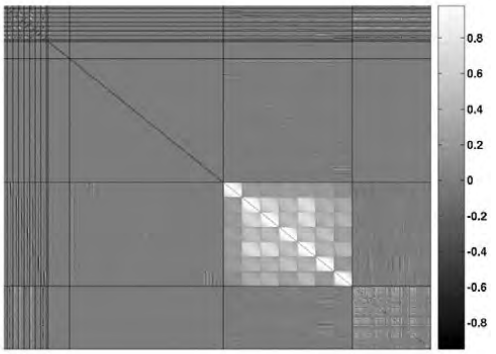

Figure 9. Correlation matrix obtained from solution S1 by method M2.

7 Conclusions

In VLBI analysis, station coordinates, polar motion and universal time corrections are principally affected by the way the datum definition is applied. This is especially true, if displacements in station coordinates arise due to, e.g., the discarding of non-tidal ocean/atmospheric loading effects or minor earthquakes. Auxiliary parameters (WZD and clock offsets) remain highly unaffected by the choice of the datum definition, especially if the datum is handled following the methods M1 to M3.

Acknowledgments

The first author is particularly indebted to the German Science Foundation (DFG, Deutsche ForschungsGemeinschaft) for funding this work within the Research Unit FOR584 'Earth Rotation and Global Dynamic Processes'.

References

Altamimi, Z., P. Sillard, & C. Boucher, (2002). ITRF2000: A New Release of the International Terrestrial Reference Frame for Earth Science Applications, J. Geophys. Res., 107 (B10), 2214, doi: 10.1029/2001JB000561.

Baarda, J., (1973). S-transformations and criterion matrices, Netherlands Geodetic Commission, Vol. 5 (1), Delft University of Technology.

Boehm, J., B. Werl, & H. Schuh, (2006). Troposphere mapping functions for GPS and very long baseline interferometry from European Centre for Medium-Range Weather Forecasts opera-

tional analysis data, J. Geophys. Res., Vol. 111, L07304, doi:10.1029/2005JB003629.

Defraigne, P., & I. Smits, (1999). Length of day variations due to zonal tides for an elastic earth in non-hydrostatic equilibrium, Geophys. J. Int., Vol. 139, pp. 448-572.

Even-Tzur, G., (2006). Datum definition and its influence on the reliability of geodetic networks, ZfV: Zeitschrift für Geodäsie, Geoinformation und Landmanagement, Augsburg, Vol. 131 (2), pp. 87-95.

Fey, A.L., C. Ma, E.F. Arias, P. Charlot, M. Feissel-Vernier, A.M. Gontier, C.S. Jacobs, J. Li, & D.S. MacMillan, (2004). The second extension of the international celestial reference frame: ICRF-Ext.2, Astron. J., Vol. 127, pp. 3587-3608.

Kutterer, H., (2004). Reliability Measures for Geodetic VLBI Products. In: Vandenberg, N., K. Baver (Eds.): IVS 2004 General Meeting Proceedings, NASA/CP-2004-212255, pp. 301-305.

MacMillan, D.S., C. Ma, (1997). Atmospheric gradients and the VLBI terrestrial and celestial reference frames, Geophys. Res. Lett., Vol. 24(4), doi: 10.1029/97GL00143, pp. 453-456.

Mathews, P.M., T.A. Herring, & B.A. Buffett, (2002). Modelling of Nutation and Precession: New Nutation Series for Non-Rigid Earth and Insights into the Earth Interior, J. Geophys. Res., Vol. 107 (B4), doi: 10.1029/2001JB000390.

McCarthy, D.D., & G. Petit, (2004), (Eds.), IERS Conventions 2003, IERS technical note No. 32, Verlag des Bundesamtes fuer Kartografie und Geodäsie, Frankfurt am Main.

Petrov, L., & J.-P. Boy, (2004). Study of the atmospheric loading signal in very long baseline interferometry observations, J. Geophys. Res., Vol. 109 (B03405), doi: 10.1029/2003JB002500.

Ray, R.D., D.J. Steinberg, B.F. Chao, & D.E. Cartwright, (1994). Diurnal and Semidiurnal Variations in the Earth's Rotation Rate Induced by Oceanic Tides, Science, Vol. 264, pp. 830-832.

Schlueter, W., E. Himwich, A. Nothnagel, N. Vandenberg, & A. Whitney, (2002). IVS and Its Important Role in the Maintenance of the Global Reference Systems, Advances in Space Research, Vol. 30, No. 2, pp. 145-150.

Sillard, P., & C. Boucher, (2001). A review of algebraic constraints in terrestrial reference frame datum definition, Journal of Geodesy, Vol. 75, pp. 63-73.

Titov, O.A., V. Tesmer, & J. Boehm, (2004). OCCAM V 6.0 software for VLBI data analysis, In: Vandenberg N, Baver K (eds.) IVS 2004 General meeting proceedings, NASA/CP-2004-212255, NASA Goddard Space Flight Center, Greenbelt, MD.

Wahr, J.M., (1985). Deformation Induced by Polar Motion, J. Geophys. Res., Vol. 90, pp. 9363-9368.

VLBI Intra-technique Combination for Kalman Filter and Least-Squares Solutions

E. Tanir, J. Boehm, H. Schuh
Institute of Geodesy and Geophysics (IGG)
Vienna University of Technology, Vienna, Austria

V. Tornatore
DIIAR, Sez. Rilevamento, Politecnico di Milano, Milano, Italy

K. Felsenstein,
Institute of Statistics and Probability Theory
Vienna University of Technology, Vienna, Austria

Abstract. The VLBI software packages for the data analysis which are used by different IVS (International VLBI Service for Geodesy and Astrometry) Analysis Centers applying various statistical methods. These statistical methods are the Least-Squares (LSQ) method, the Kalman filter (KF) method, the Square-Root Information Filter (SRIF) and the Least-Squares Collocation (LSQC) method which consider the behaviour of stochastic parameters in different ways. For the intra-technique combination of different VLBI Analysis Center solutions, the effect of using different stochastic models on the estimates of geodetic parameters should be taken into account. In this study, we consider the combination of Kalman Filter and LSQ solutions in our VLBI intra-technique combination algorithm. With the KF method, the use of polynomials to model the effect of the clocks and atmospheric delays are replaced by stochastic models. The implementation of the Kalman Filter estimator to account for the stochastic behavior on those parameters which vary during a VLBI experiment will be discussed.

Keywords. VLBI intra-technique combination, Kalman Filter, Least-Squares estimation.

1 Introduction

Different statistical approaches used in VLBI data analysis differ in the propagation of variance-covariance information and the behaviour of the stochastic parameters. However, it cannot be stated that one solution is better than the other. The quality of products of geodetic Very Long Baseline Interferometry (VLBI) observations is improved in terms of reliability, robustness and accuracy if the results of different analysis software packages are combined using a suitable combination process (intra-technique combination). In our previous combination algorithm (Tanir et al. 2006a; 2006b), the normal equations in SINEX format were taken on a session-by-session basis from five different IVS Analysis Centers (BKG (Federal Agency for Cartography and Geodesy), NASA GSFC (Goddard Space Flight Center), DGFI (Deutsches Geodaetisches Forschungsinstitut), SHA (Shanghai Astronomical Observatory), USNO (U.S. Naval Observatory)) which apply only Least-Squares (LSQ) solutions. We consider the combination of Kalman Filter (e.g., AUS (Geoscience Australia)) and LSQ solutions (e.g., BKG, GSFC, DGFI, SHA, USNO) in our VLBI intra-technique combination algorithm. In order to start such a combination, we should firstly understand the effect of different statistical models on the estimates of geodetic parameters and the quality of these estimates compared to the conventional LSQ method.

In this study, we make first comparisons of Kalman Filter (KF) and LSQ solutions in OCCAM software to evaluate how estimation of some parameters of interest varies in different adjustment methods. We have performed this comparison on real data of regular VLBI observations and also on simulated data for the same sessions with all geophysical effects set to zero.

The second step of our study will be to combine two solutions writing the proper formulation of combination in a way similar to normal equation level combination and using not only LSQ solutions, but Kalman Filter, too.

2 VLBI Analysis Basics

The basic principle of geodetic VLBI is the measurement of the group delay originating from an extra-galactic point like a radio source and receiving the signals at two separate radio telescopes forming a baseline. This group delay contains information on the geometric situation during the observation and additional atmospheric and also instrumental effects. Thus, positions of radio telescopes and radio sources, Earth orientation parameters, atmospheric parameters and additional parameters can be determined. In order to estimate different parameters from geometric delay observables a large number of delay observations on different baselines are necessary. The observation equation for VLBI geometric delay (τ) is following

$$\tau = -\frac{1}{c} b\, k \tag{1}$$

where c is the speed of light; b is the baseline vector between radio telescopes; k is the source vector. These two vectors are defined in two different reference frames. Transformation between the terrestrial geocentric system and the celestial geocentric system for baseline vector b are formulated as

$$b_C(t) = P\,N\,U\,X\,Y b_T(t) \tag{2}$$

with (P, N, U, X, Y) transformation term w.r.t. the Earth orientation parameters i.e. precession and nutation model, apriori information for Earth rotation ($UT1$) and polar motion (x_p, y_p). In eq. (2) b_C is the baseline vector in the celestial system; b_T the baseline vector in the terrestrial system. The baseline vector in the terrestrial reference frame has some corrections, i.e. τ_{tides} for solid Earth tides (several dm per day); $\tau_{p.tect}$ for plate tectonics (some mm per year); $\tau_{o.load}$ for ocean tide loading (several mm per day); $\tau_{a.load}$ for atmospheric loading (some mm to cm per day); $\tau_{h.load}$ for hydrological loading (several mm per year); τ_{ion} for ionospheric correction; τ_{trop} for tropospheric correction; τ_{clock} for clock correction. Eq. (1) can be rewritten by taking into consideration these corrections for geometric delay and transformation between celestial and terrestrial system which is given in eq. (2) as following

$$\begin{aligned}\tau_{obs} &= -\frac{1}{c} b_t\, Y\,X\,U\,N\,P\,k_c \\ &+ \tau_{tides} + \tau_{p.tect} + \tau_{o.load} + \tau_{a.load} \\ &+ \tau_{h.load} + \tau_{ion} + \tau_{trop} + \tau_{clock} \ldots\end{aligned} \tag{3}$$

where τ_{obs} is the observed geometric delay, b_t the baseline vector in the terrestrial system, k_c source vector in the celestial system. The observation equation given in eq.(3) can be used for parameter estimation with e.g. the LSQ method, the Kalman Filter (KF) method, the Square-Root Information Filter (SRIF) and the Least-Squares Collocation (LSQC) method. These statistical approaches differ in the propagation of variance-covariance information and the behaviour of the stochastic parameters (Haas 2004; 2006).
The linearized observation equation can be given in detail with respect to parameters of interest as following

$$\begin{aligned}\tau = \tau_0 &+ \frac{\partial\tau}{\partial x_1}\Delta X_1 + \frac{\partial\tau}{\partial y_1}\Delta Y_1 + \frac{\partial\tau}{\partial z_1}\Delta Z_1 \\ &+ \frac{\partial\tau}{\partial clock_1}\Delta clock_1 + \frac{\partial\tau}{\partial atm_1}\Delta atm_1 \\ &+ \frac{\partial\tau}{\partial x_p}\Delta x_p + \frac{\partial\tau}{\partial y_p}\Delta y_p + \frac{\partial\tau}{\partial UT1}\Delta UT1 \\ &+ \ldots\end{aligned} \tag{4}$$

where τ_0 is the a priori delay calculated with a priori parameters, $\Delta X_1, \Delta Y_1, \Delta Z_1$ the station coordinates, $\Delta clock_1, \Delta atm_1$ the clock and atmosphere corrections, and $\Delta x_p, \Delta y_p, \Delta UT1$ the Earth rotation parameters. The design matrix for the linearized observation equation in eq. (4) consists of blocks for the parameter groups,

$$A = \begin{vmatrix} (X,Y,Z) & clock & atm. & (x_p, y_p, UT1) & \dots \\ \vdots & & & & \vdots \\ \vdots & & & & \vdots \\ \vdots & & & & \vdots \\ \vdots & & & & \vdots \end{vmatrix} \quad (5)$$

and the parameter vector for station coordinates, clocks, atmospheric parameters, and Earth rotation parameters are as following:

$$x = \begin{vmatrix} \Delta(X,Y,Z) \\ \Delta clock \\ \Delta atm \\ \Delta(x_p, y_p, UT1) \\ \dots \end{vmatrix} \quad (6)$$

The observation vector consists of the observed delays minus the modelled delays based on a priori values.

$$l = \begin{vmatrix} (\tau_{obs} - \tau_0)_i \\ \\ \\ \end{vmatrix} \quad (7)$$

2.1 Kalman Filter in VLBI Data Analysis

The Kalman Filter was developed in the early 1960s as an efficient method to produce an estimate of variables during the interval in which data is collected in a condition that the error is minimized statistically. For such an estimation procedure, Kalman Filter processes are available measurements to estimate those parameters of which the values changed during the interval over which data were collected by using knowledge of the system, statistical description of the system noise, measurement errors and information about initial conditions of the parameters. In this procedure, the stochastic process models are used to predict the changes of the stochastic parameter values between epochs of data and to determine constraints to be placed on their changes. The constraints placed on the changes in the stochastic parameters by covariance matrix and the information about these parameters contained in the observations enable estimates of the stochastic and non-stochastic parameters to be made. Three types of stochastic processes are used to represent the variations of clocks and atmospheric delays: white noise, random walks, and integrated random walks.

The linearized form of equations which relates VLBI observables to the parameters to be estimated is

$$l_t = A_t x_t + v_t \quad (8)$$

where all quantities refer to epoch t and l_t is the vector of differences between the observations and their theoretical values calculated from a priori values of parameters in eq. (7); x_t is the vector of adjustments to the a priori values of the parameters in eq. (6); A_t is the matrix of partial derivatives (design matrix) which relate the changes in parameters values to changes in the values of the observables in eq. (5); and v_t is a vector of residuals which represent the noise in the observations. The dynamics of the parameters are represented by the state transition equations

$$x_{t+1} = T_t x_t \quad (9)$$

where x_{t+1} is the vector of values of the parameters at epoch $t+1$; T_t is the transition matrix at epoch t which gives the expected state at epoch $t+1$. These parameters are the positions of radio telescopes, the radio sources, and the Earth orientation parameters.

The Kalman Filter is carried out sequentially. The sequence of adding the observations at epoch $t+1$ to the estimation, given the estimated state, $\hat{x}_t^{t=0}$ and its covariance matrix $C_t^{t=0}$ at epoch t is given following:

Prediction for $t+1$

$$\begin{aligned} \hat{x}_{t+1}^{p} &= T_t \hat{x}_t^{t=0} \\ C_{t+1}^{p} &= T_t C_t^{t=0} T_t^T + w_t \end{aligned} \quad (10)$$

Updating for $t+1$

$$\begin{aligned} \hat{x}_{t+1}^{u} &= \hat{x}_{t+1}^{p} + K(l_{t+1} - A_{t+1}\hat{x}_{t+t}^{p}) \\ C_{t+1}^{u} &= C_{t+1}^{p} - KA_{t+1}C_{t+1}^{p} \end{aligned} \quad (11)$$

where w_t is the system noise during the interval between epochs t and $t+1$, $\hat{x}_{t+1}^{p}$ and $\hat{x}_{t+1}^{u}$ are solution vectors from prediction and updating and C_{t+1}^{p} and C_{t+1}^{u} covariance matrices of estimated

parameters from prediction and updating. For non-stochastic parameters, w_t is defined to be zero, i.e., there are no random noise of the state with time. K is the Kalman gain given by

$$K = C_{t+1}^{p} A_{t+1}^{T} (v_{t+1} + A_{t+1} C_{t+1}^{p} A_{t+1}^{T})^{-1} \qquad (12)$$

When the computations of prediction and filtering at epoch $t+1$ are completed, the sequence is repeated with quantities at epoch $t+2$. At this step, $t+i$ substituted for those at epoch $t+(i-1)$. This procedure is repeated until all observations have been included. To start the filter, a priori values for the parameters and their covariance matrix i.e. $\hat{x}_t^{t=0}$ and $C_t^{t=0}$ in eq. (10) have to be taken. This sequence is called forward Kalman Filter (Kalman 1960; Herring et al. 1990; Maybeck 1999; Welch and Bishop 2004). After all observations have been added to the forward Kalman Filter, the estimate of non-stochastic parameters is obtained. To determine the estimates of the stochastic parameters, a backward Kalman Filter solution is performed.
A backward Kalman Filter is not used as often as a forward Kalman Filter because Kalman Filter is mostly used in real time applications, when only the values of the parameters at the current epoch are of interest. Backward Kalman Filter applying the same procedure as described in (10), (11) and (12). The final estimates of parameters are a priori values for backward Kalman Filter. After forward and backward Kalman Filter, smoothing is applied to get estimates of stochastic parameters at each epoch as a weighted mean of forward and backward estimate. The estimate of parameters and its covariance matrix for each epoch can be shown as $x_F(i), C_F(i,i)$ for forward Kalman Filter and $x_B(i), C_B(i,i)$ for backward Kalman Filter. The estimation results for parameter and its covariance matrix $x_S(i), C_S(i,i)$ from smoothing can be calculated as following

$$x_S = x_F + C'(x_B - x_F) \qquad (13)$$

$$C' = I - C = C_F (C_F + C_B)^{-1} \qquad (14)$$

$$C_S = (C_F^{-1} + C_B^{-1})^{-1} \qquad (15)$$

Albertella et al. (2005) demonstrated an alternative method to obtain a rigorous solution with a numerical effort comparable with the solution of forward plus backward Kalman Filter. This method allows deriving LSQ solutions equivalent to Kalman Filter solutions.
In VLBI analysis, Kalman Filter (KF) is used to account for stochastic behavior of the clocks and the atmosphere parameters which vary during a VLBI session. Local parameters e.g. clocks, atmospheres, and EOP are estimated with KF by forward and backward applications in case more than one estimation are applied within a 24h-period. However, for the global parameters, e.g. station coordinates, station velocities, radio source coordinates, only the forward solution is applied.

2.2 Equivalence of Kalman Filter and Least Squares

The optimal solution of KF has to be derived taking into account all the observations. Under the same starting hypotheses describing the dynamic of a system, the LSQ parameter estimate is equivalent to what in Kalman Filter literature is called the final estimate or optimal estimate obtained with the full data set by applying the forward and backward Kalman filtering and then Kalman smoothing. The equivalence of the two procedures has been verified by some simulated numerical examples (Albertella et al. 2005).
It has to be noticed that many softwares do not implement the Kalman smoothing at all, or if it is applied, it is not implemented in a rigorous way especially for the computation of the variance/covariance matrix of the final estimates. Moreover, one could have a different approach in the rejection of outliers used by LSQ and KF and therefore obtain different results. It is useful to understand firstly the different effect of using KF or LSQ on the geodetic parameter estimation (baselines, coordinates, or EOP).

3 Results

The property of offering estimation results with different adjustment methods within the OCCAM software is an efficient tool for make a comparison of data analysis methods. Within this study, simulated VLBI NGS files for CONT05 sessions created by Joerg Wresnik at IGG setting the geophysical effects to zero are analyzed with the OCCAM software using KF and LSQ adjustment methods.

For the simulated observations the observed group delays were set up as shown in Eq. (16)

$$o = c + (\Delta L_w^z \, mf_w + dk + w_n) \qquad (16)$$

where c is the computed group delay, ΔL_w^z denotes the wet zenith delay, mf_w is the mapping function, dk is the time delay of the signal (clock) and w_n is the white noise. The mapping function for the simulated files is fixed to the wet Niell Mapping Function.

The wet zenith delay is created with a random walk with a Power Spectrum Density of 0.5 psec^2/sec and the clocks are created with a random walk and an integrated random walk corresponding to an Allan standard deviation of $2 \cdot 10^{-15}$@15min. The white noise is created with a standard deviation of 8 psec. The formal errors (uncertainty) of the estimated baseline lengths are used as an accuracy measure for the comparison between results obtained from KF and LSQ within the VLBI software OCCAM. The formal errors of the baseline lengths estimated by Kalman Filter are always smaller than those estimated by Least-Squares method for all VLBI sessions examined. We get the uncertainties for estimated baseline lengths around 0.4 cm by LSQ and around 0.3 cm by KF (see Figure 1).

To understand the reason of this effect, it is necessary to go into detail in the implemented algorithm for the Kalman Filter solution.

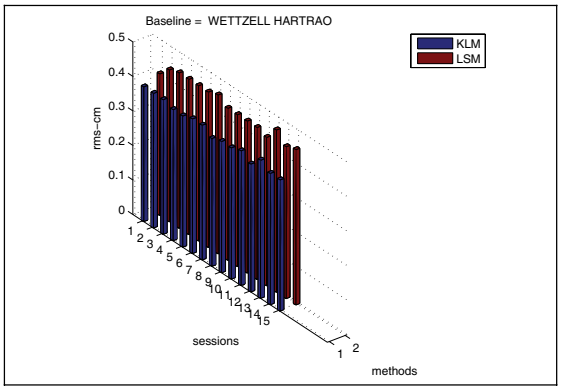

Figure 1. Formal errors for estimated baseline lengths for simulated CONT05 sessions

One of the measures of the overall accuracy of space geodesy techniques is baseline length repeatability. The smaller the value of the repeatability is the better the result is.

$$\sigma = \sqrt{\frac{\sum_{i=1}^{n} (L_i - L_0)^2}{n-2}} \qquad (17)$$

where L_i is the estimated baseline length, L_0 is the mean value of the estimated baseline length on a regression polynomial of first order, n is the number of estimated baseline lengths. Baseline length repeatability is consistent for KF and LSQ solutions for real CONT05 sessions. The same values of KF solutions are smaller than of LSQ solutions for simulated CONT05 sessions (see Figure 2).

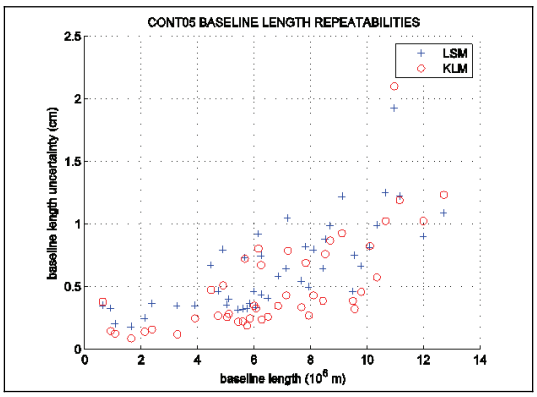

Figure 2. Repeatability of estimated baseline lengths for simulated CONT05 sessions

As we already know there are some important aspects in combination:

- quality check of solutions from individual Analysis Centers (AC);
- make sure that the individual solutions are datum free;
- proper scaling of the individual solutions within the combination;
- usage of rigorous combination methods;
- quality check of the final combined solution.

In case of using individual AC solutions taken from different adjustment methods (e.g., KF and LSQ), we should also take into account the effect of using different adjustment methods on the parameter estimation in individual solutions.

4 Conclusions

From this study we get a first impression of how the parameter estimation differs in different adjustment methods. The second step of our study will be to

combine two solutions writing the proper formulation of combination in a way similar to normal equation level combination but using not only LSQ solutions, but KF, too. In order to do this, it should be understood what is implemented in OCCAM for the filtering. Once the filtering algorithm is clear we should implement the smoother. After getting results with filtering and smoothing, we can start to think how the proper output (the equivalent matrix and vector of normal equation) of the filtering plus smoothing that can be combined with the LSQ solution can be written.

Acknowledgments Thanks to the International VLBI Service for Geodesy and Astrometry (IVS) for providing their data and to Joerg Wresnik from IGG for providing simulated data for the CONT05 sessions.

References

Albertella A., Betti B., Sansò F., Tornatore V., (2005) Real time batch navigation solutions: alternative approaches, Arti Grafiche Pisano (Cagliari), Cagliari, Bollettino SIFET, ISSN 1721-971X, page 82-99, Vol. n.4/2005, No.1.

Haas R., (2004) Analysis Strategies and Software for geodetic VLBI, Proceedings of the 7th European VLBI network Symposium, Bachiller R., Colomer F., Desmurs J.F., de Vicente P. (eds.), October 12th-15th 2004, Toledo, Spain.

Haas R. (2006). ERR 170 Interferometry in Astronomy, Lecture Notes Geodesy 2005/2006 GEO-VLBI-5,GEO-VLBI-6, http://www.oso.chalmers.se/~haas/ERR170/.

Herring T., Davis J.L., Shapiro I.I. (1990) Geodesy by radio Interferometry: The Application of Kalman Filtering to the Analysis of Very Long Baseline Interferometry data, Journal of Geophysical Research, Vol. 95, No. B8, 12,561-12,581.

Kalman R.E., (1960) A New Approach to Linear Filtering and Prediction Problems, Journal of Basic Engineering, 82 (series D), 35-45.

Tanir E., Heinkelmann R., Schuh H., Kusche J., (2006a) Determination of Regularization Parameters for VLBI Intra-technique Combination, Geodätische Woche 2006, October 10-12, 2006, Munich, Germany.

Tanir E., Heinkelmann R., Schuh H., Kusche J., van Loon J.P., (2006b) Assessment of the Results of VLBI Intra-technique Combination Using Regularization Methods, IAG-Symposium on Geodetic Reference Frames (GRF), 2006, October 09-13, 2006, Munich, Germany, Springer-Verlag.

Welch G., Bishop G., (2004). An Introduction to the Kalman Filter, TR 95-041, Department of Computer Science, UNC at Chapel Hill, NC 27599-3175.

Maybeck P.S., (1999) Stochastic Models, Estimation and Control, Vol.1, Department of Electrical Engineering, Air Force Institute of Technology, Wright-Patterson Air Force Base, Ohio.

VLBI Terminal in Badary Observatory

L. V. Fedotov
Institute of Applied Astronomy, Russian Academy of Sciences,
nab. Kutuzova 10, St. Petersburg, 191187 Russia

Abstract. The new VLBI terminal is developed at IAA RAS. It has been installed in Badary Observatory and used in observations. The terminal consists of 14-chanel R1000 Data Acquisition System (DAS), R4103 system for interface to recording equipment, Mark 5B and S2-RT recording terminals. Input IF is from 100 MHz to 1000 MHz. Bandwidths are 0.25 MHz, 2 MHz, 8 MHz or 16 MHz. There are 16 two-bit samplers, the device for formation 32 MHz clock and one per second impulses (1 PPS) synchronizer. All devices of terminal are controlled by means of Mark IV Field System computer. On March 1-2, 2007 this terminal took part in VLBI observation in structure of the international network under the program R4265.

Keywords. VLBI terminal, Data Acquisition System (DAS), recording terminal, samplers

1 Introduction

Badary VLBI Observatory was installed in 2005. The radio telescope of this station is equipped with 32 m quasi-paraboloid main dish, 5 low-noise cooled receivers with HEMT amplifiers for wavelengths 1.35, 3.5, 6.0, 13 and 18/21 cm for observations in the left and right circular polarizations. VLBI Terminal was installed at Badary Observatory in 2006-2007. It is intended for observations under national and international programs. This Terminal consists of multichannel R1000 DAS, R4103 interfacing system for recording equipment, S2-RT recording terminal and Mark 5B recording terminal (Figure 1). All this equipment is incorporated to system which is controlled from the Field System central operating computer of the radio telescope and synchronized from time-and-frequency synchronization system of the radio telescope.

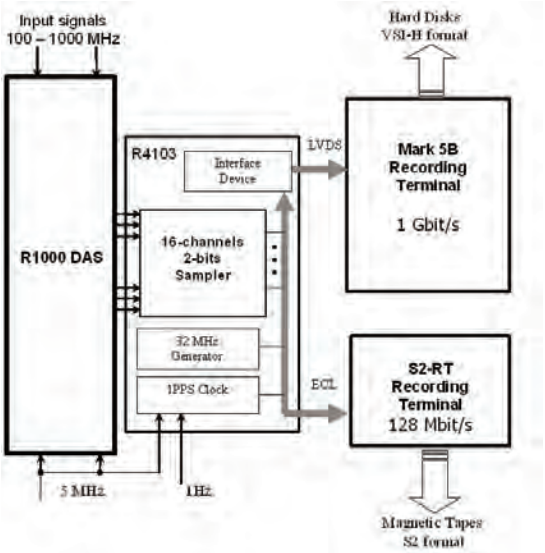

Fig. 1. Block diagram of the VLBI Terminal in Badary Observatory.

The R1000 DAS has been developed at IAA RAS on the basis of developed before the experimental sample. Positive results of tests and pre-production operation of this sample in Svetloe and Zelenchukskaya observatories in 2004-2005 have enabled to organize industrial production of the multichannel R1000 DAS together with "RELTA" firm. This DAS was installed in Badary Observatory in 2006. R1000 DAS (Figure 2) consists of 5 data acquisition modules with dimension of 450×360×300 mm. Each module has on board a power supply unit and can work independently. One of them is the head module (R1103). It contains IF signals distributor together with IF signals power meters and two R1200 Base Band Converters (BBC). Two equivalent inputs of system allow processing simultaneously signals from two receivers or different polarization signals. The wide band IF distributor enables to switch DAS converters on any of two inputs of system.

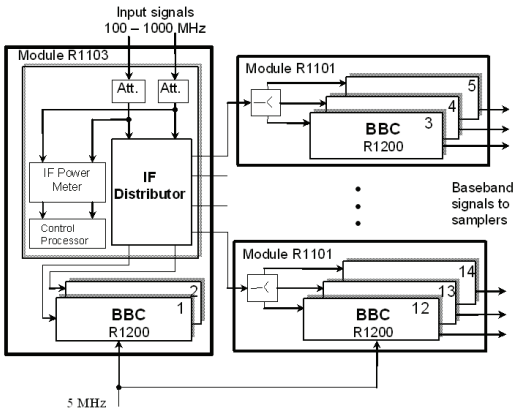

Fig.2. Block diagram of the R1000 DAS.

Besides for the head module the system contains 4 base modules (R1101), in each of which there are 3 converters having one general input (Figure 3).

Fig.3. R1101 base module of the R1000 DAS.

From outputs of converters the upper-side-band or lower-side-band signals act on R4103 interfacing system.

The R1200 BBC is a basic element of DAS. It represents compact unit with the dimension of 330×85×265 mm and consists of 3 printed-circuit-boards: Sideband Separation Mixer Board (SSM Board) with switch able preselector filters and controlled attenuator, Local Oscillator Board with control processor, Base Band Board with video frequency amplifiers and filters for upper-side-band signals and lower-side-band signals separately (Figure 4).

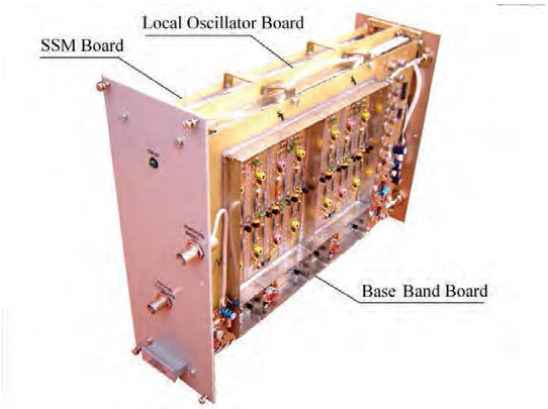

Fig.4. R1200 Base Band Converter.

In 2006 comparative tests of the Mark 4 DAS and R1000 systems were held in Svetloe observatory. Tests have shown full compatibility of these systems. Pre-production operation of R1000 DAS in Badary observatory has confirmed its high parameters which provide for the full functions of the VLBI terminal (Table 1).

Table 1. Parameters of the VLBI Terminal in Badary Observatory

Type of DAS	R1000
Input frequency range	100 – 1000 MHz
Number of IF inputs	2
Number of base band converters	14
Connection of base band converters to IF inputs	Electronic switch
Sidebands	Upper and lower
Image rejection	More then 26 dB
Bandwidths	0.25, 2, 8 and 16 MHz
IF attenuator's range on distributor inputs	0 – 18 dB
IF attenuator's range on base band converter's input	0 – 15 dB
Phase noise of local oscillator	Less then 2 degree rms
Error of signal level measure	0.1%
Number of 2-bits samplers	16
Clock frequency for signal's record	32 MHz
Type of recording terminal	Mark 5B and S2-RT
System's software	Mark 4 Field System

R4103 interfacing system (Figure 5) consists of the samplers unit (R4101) and the interface device (R4102).

Fig.5. R4103 interfacing system.

The samplers unit includes 16 two-bit signal samplers, 32 MHz clock generator and 1 PPS clock. The interface device unites the bit streams, converts the levels to form output bit streams according to VSI-H standard and encodes the sign and magnitude bit streams to make them compatible with the bit-streams produced by the samplers. The system has the special output for the S2 format bit-stream to connect the S2-RT recording terminal.

Now 13 converters of R1000 system have been installed and operated in Badary observatory (Figure 6).

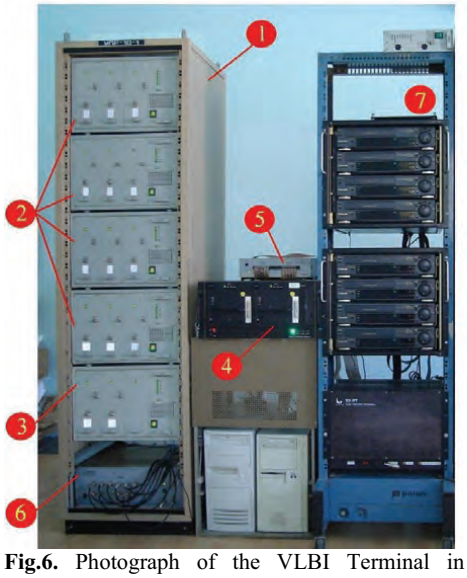

Fig.6. Photograph of the VLBI Terminal in Badary Observatory: 1 – R1000 DAS, R1101 modules, 3 – R1103 module, 4 – Mark 5B Recording Terminal, 5 – interface device of R4103 system, 6 – samplers and clock of R4103 system, 7 – S2-rt Recording Terminal.

Also we installed the simplified variant of the broadband IF signals distributor which does not allow to switch inputs of converters in the electronic way yet. The upgrade of recording terminal Mark 5A up to Mark 5B has been made in IAA RAS last year. In 2007 this recording terminal was installed in Badary Observatory.

On March 1-2, 2007 the radio telescope in Badary took part in VLBI observation in structure of the international network under the program R4265. This session became the first experiment which took place in Badary Observatory under the IVS international program. Also it was one of the first experiments of application of the new recording terminal Mark 5B in geodetic VLBI observations. Primary processing of this session has been successfully made on Haystack correlator. On all baselines with participation of Badary radio telescope precise fringes have been received (Figure 7). The amplitude and phase of correlation responses of all channels are stable during the all period of accumulation. Data of this observation have been estimated by the maximum estimation. Participation of Badary Observatory in other sessions of IVS observations is planned.

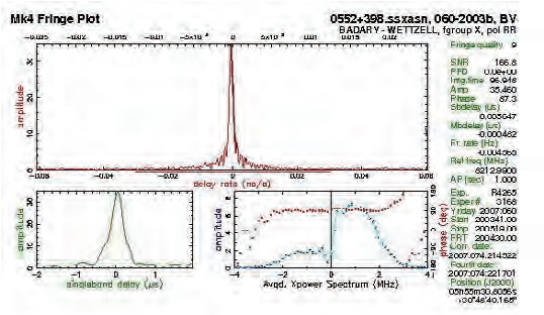

Fig.7. Example of the fringe on Badary – Wettzel baseline at observation of 0552+398 radio source in 3,5 cm band.

This year the complete set of R1000 system will be established in Badary observatory. Besides that it is planned in 2008 the replacement of the S2-RT by the modern national computer recording terminal (RDR-1) which is developed in Astro Space Center (Moscow).

References

Ipatov A.V., Koltsov N.E., Fedotov L.V. (2003). A Data Acquisition System for Very-Long-Baseline Interferometers. *Instruments and Experimental Techniques*. Vol. 46, No.6, pp 787-797.

Agenda of the 18th EVGA Working Meeting

2007.04.12 ***Thursday***

12:00 – 13:00	**Registration**		
13:00 – 13:30	**Opening**		
13:00 – 13:10		**Harald Schuh**	*IVS Chair*
13:10 – 13:20		**August Hochwartner**	*President of the BEV - Federal Office of Metrology and Surveying*
13:20 – 13:30		**Axel Nothnagel**	*EVGA Chair*

13:30 – 15:30	***Session 1***		***Schuh H***
13:30 – 13:45	S1-1	Russian VLBI network Quasar: international and domestic observational programs	Finkelstein A, Ipatov A, Smolentsev S
13:45 – 14:00	S1-2	Status of geodetic application research in KASI	Kwak Y, Cho J, Park J
14:00 – 14:15	S1-3	Medicina VLBI RadioTelescope: gravitational deformations estimated through a terrestrial laser scanning survey	Montaguti S, Negusini M, Sarti P, Vittuari L
14:15 – 14:30	S1-4	IAA RAS Radio Telescope Monitoring System	Lavrov A, Mikhailov A
14:30 – 14:45	S1-5	JIVE Correlator Report:: Astronomy Projects, Aspiring EVN Stations, e-VLBI, & Software Correlation	Campbell RM, Szomoru A
14:45 – 15:00	S1-6	Bonn correlator report	Alef W, Müskens A, Bertarini A
15:00 – 15:15	S1-7	Status report on the software correlator	Bertarini A, Alef W, Deller A T, Graham D, Rottmann H, Roy A L, Tingay S J
15:15 – 15:30	S1-8	e-VLBI data transfer from Onsala and Metsähovi to the Bonn correlator	Haas R, Müskens A, Wagner J, Dulfer Ch, Mujunen A, Ritakari J

15:30 – 16:00 **Coffee**

16:00 – 18:00	***Session 2***		***Tuccari G***
16:00 – 16:15	S2-1	Mark 5 Data System Status and Developments	Whitney A
16:15 – 16:30	S2-2	Development of Digital Back End System for VLBI	Whitney A
16:30 – 16:45	S2-3	DBBC - A Flexible Environment for VLBI and Space Research: Digital Receiver and Back-end Systems	Tuccari G, Alef W, Buttaccio S, Keller R, Nalbach M, Nicotra G, Wunderlich M
16:45 – 17:00	S2-4	Effect on geodetic-VLBI measurables due to polarization leakage in the S-band and X-band receivers	Bertarini A, Nothnagel A, Alef W, Corey B, Walker R C
17:00 – 17:15	S2-5	SATTRACK - A satellite tracking module for the VLBI Field system	Moya Espinosa M, Haas R
17:15 – 17:30	S2-6	GINS: a new tool for VLBI Geodesy and Astrometry	Bourda G, Charlot P, Biancale R
17:30 – 17:45	S2-7	Site reliability in VLBI sessions of the Europe series	Nothnagel A, Müskens A
17:45 – 18:00	S2-8	Baseline length repeatability	Titov O

18:30 – … **Welcome Dinner**

2007.04.13 ***Friday***

08:30 – 10:00	***Session 3***		***Böhm J***
08:30 – 08:45	S3-1	ERP timeseries with daily and subdaily resolution determined from CONT05	Artz T, Böckmann S, Nothnagel A, Tesmer V
08:45 – 09:00	S3-2	On dependence of EOP derived from VLBI observations on network	Malkin Z
09:00 – 09:15	S3-3	QUASAR software in IAA EOP service: Global Solution and Daily SINEX	Kurdubov S
09:15 – 09:30	S3-4	Comparisons and combination of consistent VLBI solutions	Böckmann S, Artz T, Nothnagel A, Tesmer V
09:30 – 09:45	S3-5	Long-term trends of water vapour from VLBI observations	Heinkelmann R, Schmidt M, Böhm J, Schuh H
09:45 – 10:00	S3-6	An investigation and empirical modeling of the Free Core Nutation	Malkin Z, Miller N
10:00 – 10:30	**Coffee**		
10:30 – 12:30	***Session 4***		***Haas R***
10:30 – 10:45	S4-1	On comparison and combination of radio source catalogues	Sokolova J, Malkin Z
10:45 – 11:00	S4-2	Effect of various analysis options on VLBI-determined CRF	Tesmer V
11:00 – 11:15	S4-3	Extending the ICRF to Higher Radio Frequencies: 32/8.4 GHz Global Astrometry	Jacobs Ch S, Sovers O J
11:15 – 11:30	S4-4	Linking Deep Astrometric Standards to the ICRF	Frey S, Platais I Fey A L
11:30 – 11:45	S4-5	First-Time Differential Phase-Delay Astrometry of a Complete Radio Sample	Marti-Vidal I, Marcaide J M, Guirado J C
11:45 – 12:00	S4-6	Comparison and cutoff-angle tests for observed and simulated CONT05 sessions	Teke K, Wresnik J, Böhm J, Schuh H
12:00 – 12:15	S4-7	Comparison of different models to estimate nutation and polar motion rates	Tesmer V, Böckmann S
12:15 – 12:30	**Posterpresentation** short presentation of the 12 posters		Nothnagel A
12:30 – 13:30	**Lunch**		
13:30 – 14:45	***Session 5***		***MacMillan D***
13:30 – 13:45	S5-1	Incorporating Station Dependent Correlation Improves VLBI Estimates	Gipson J
13:45 – 14:00	S5-2	Optimum modeling of troposphere and clock parameters in VLBI	Pany A, Wresnik J, Böhm J, Schuh H
14:00 – 14:15	S5-3	Using source maps for scheduling and data analysis: strategies, approaches	Petrov L
14:15 – 14:30	S5-4	Studying the geodynamics of the Etnean area by means of VLBI and GPS	Di Martino S, Negusini M, La Delfa S, Patanè G
14:30 – 14:45	S5-5	Forecasting data of the troposphere used for IVS Intensive sessions	Böhm J, Schuh, H
14:45 – 15:15	**Coffee**		
15:15 – 16:30	***Poster Session***		

16:30 – 18:00	***Session 6***		***Nothnagel A***
16:30 – 16:45	S6-1	Twin-Telescope Wettzell TTW	Lauber P, Kilger R, Hase H, Schlüter W, Kronschnabl G, Schwarz W, Dassing R
16:45 – 17:00	S6-2	VLBI2010 Simulations Using SOLVE	MacMillan D
17:00 – 17:15	S6-3	Monte Carlo Simulations for VLBI2010	Wresnik J, Böhm J, Schuh H
17:15 – 17:30	S6-4	Simulations of atmospheric path delays using turbulence models	Nilsson T, Haas R, Elgered G
17:30 – 17:45	S6-5	Kashima Ray-Tracing Service (KARTAS) - Fast ray-tracing algorithms through numerical weather models for real-time positioning applications in East Asia	Hobiger Th, Ichikawa R, Koyama Y, Kondo T
17:45 – 18:00	S6-6	INTENSIVE - as a strategic approach to improve technology and scientific results	Engen B

POSTER

P-01	Update of activities at OAN-IGN	Colomer F
P-02	Temporal evolution of local tie vectors at Medicina's observatory from terrestrial and GPS observations	Abbondanza C, Negusini M, Sarti P, Vittuari L
P-03	NetCDF - a machine-independent array-oriented format for storing VLBI data	Hobiger Th, Kondo T, Koyama Y
P-04	Comparison of sub-diurnal variations of the ERP from different VLBI solutions	Kudryashova M, MacMillan D, Titov O
P-05	Effects of datum definition on CRF and TRF	Heinkelmann R, Böhm J, Schuh H
P-06	Some issues about the Earth's core through VLBI	Lambert S, Dehant V, Gontier A-M
P-07	Datum deficiency in VLBI analysis	Mendes Cerveira P J , Tanir E, Wresnik J, Böhm J, Tesmer V, Schuh H
P-08	Intraday variation of EOP and Tropospheric parameters from CONTs	Skurikhina E A, Kurdubov S L, Finkelstein A M, Ipatov A V, Rakhimov I A
P-09	VLBI Intra-technique Combination for Kalman Filter and Least Squares Solutions	Tanir E, Tornatore V, Böhm J, Felsenstein K, Schuh H
P-10	On using cable delay measurements in VLBI data processing	Malkin Z
P-11	Statistical analysis of long-time zenith path delay time series	Malkin Z
P-12	VLBI Terminal in Badary Observatory	Fedotov L

List of participants

Last Name	Affiliation	Country	e-mail
Alef, Walter	MPIfR, Bonn	Germany	walef@mpifr-bonn.mpg.de
Arsov, Kirco	FGI, Masala	Finland	arsovk@yahoo.com
Artz, Thomas	GIB, Univ of Bonn	Germany	thomas.artz@uni-bonn.de
Bertarini, Alessandra	GIB, Univ of Bonn	Germany	abertari@mpifr-bonn.mpg.de
Boboltz, David	USNO, Washington	U.S.A.	dboboltz@usno.navy.mil
Böckmann, Sarah	GIB, Univ of Bonn	Germany	boeckmann@uni-bonn.de
Boehm, Johannes	IGG, TU Vienna	Austria	johannes.boehm@tuwien.ac.at
Bourda, Geraldine	LAB, Bordeaux	France	Geraldine.Bourda@obs.u-bordeaux1.fr
Campbell, Bob	JIVE, Dwingeloo	the Netherlands	campbell@jive.nl
Charlot, Patrick	LAB, Bordeaux	France	charlot@obs.u-bordeaux1.fr
Cho, Jungho	KASI, Daejeon	South Korea	jojh@kasi.re.kr
Colomer, Francisco	IGN/OAN	Spain	f.colomer@oan.es
Engen, Bjørn	NMA, Hønefoss	Norway	bjorn.engen@statkart.no
Fedotov, Leonid	IAA RAS, St. Petersburg	Russia	flv@ipa.rssi.ru
Fey, Alan	USNO, Washington	U.S.A.	afey@usno.navy.mil
Frey, Sándor	FÖMI/SGO, Budapest	Hungary	frey@sgo.fomi.hu
Fubara, DMJ	NASRDA	Nigeria	karialaconsult@yhoo.com
Gipson, John	NVI/NASA GSFC	U.S.A.	jmg@gemini.gsfc.nasa.gov
Gontier, Anne-Marie	OBSPM/SYRTE, Paris	France	Anne-Marie.Gontier@obspm.fr
Guirado, Jose Carlos	Univ of Valencia	Spain	Jose.C.Guirado@uv.es
Haas, Rüdiger	OSO, Onsala	Sweden	rudiger.haas@chalmers.se
Hobiger, Thomas	NICT/KSRC, Kashima	Japan	hobiger@nict.go.jp
Jacobs, Christopher	JPL, Pasadena	U.S.A.	Chris.Jacobs@jpl.nasa.gov
Klioner, Sergei	LO, TU Dresden	Germany	Sergei.Klioner@tu-dresden.de
Kurdubov, Sergey	IAA RAS St. Petersburg	Russia	ksl@quasar.ipa.nw.ru
Kwak, Younghee	KASI, Daejeon	South Korea	bgirl02@kasi.re.kr
Lambert, Sebastien	ROB, Brussels	Belgium	s.lambert@oma.be
Lanotte, Roberto	Telespazio	Italy	roberto.lanotte@asi.it
Lauber, Pierre	TU Munich	Germany	lauber@fs.wettzell.de
Lavrov, Alexey	IAA RAS, St. Petersburg	Russia	lexslavrov@yandex.ru
Loesler, Michael	GIK, Univ Karlsruhe	Germany	loesler@gik.uni-karlsruhe.de
Ma, Chopo	NASA/GSCF, Washington	U.S.A.	cma@gemini.gsfc.nasa.gov
Malkin, Zinovy	CAO RAS, St. Petersburg	Russia	malkin@gao.spb.ru
Marti-Vidal, Ivan	Univ of Valencia	Spain	I.Marti-Vidal@uv.es
McMillan, Dan	NVI/NASA GSFC, Washington	U.S.A.	dsm@leo.gsfc.nasa.gov
Montaguti, Simonetta	DISTART, Univ of Bologna	Italy	montaguti@ira.inaf.it
Mueskens, Arno	GIB, Univ of Bonn	Germany	mueskens@mpifr-bonn.mpg.de
Negusini, Monia	IRA INAF, Bologna	Italy	m.negusini@ira.inaf.it
Niell, Arthur	MIT Haystack Observatory	U.S.A.	aniell@haystack.mit.edu
Nilsson, Tobias	OSO, Onsala	Sweden	tobias.nilsson@chalmers.se
Nothnagel, Axel	GIB, Univ of Bonn	Germany	nothnagel@uni-bonn.de
Petrachenko, Bill	NRCan, Penticton	Canada	Bill.Petrachenko@nrc.gc.ca
Petrov, Leonid	NVI/NASA GSFC, Washington	U.S.A.	Leonid.Petrov@lpetrov.net
Poutanen, Markku	FGI, Masala	Finland	Markku.Poutanen@fgi.fi
Sohn, Bong Won	KVN/KASI, Seoul	Korea	bwsohn@kasi.re.kr
Sokolova, Yulia	CAO RAS, St. Petersburg	Russia	jrs@ipa.nw.ru
Sovers, Ojars	RSA Systems/JPL	U.S.A.	ojars@rsasys.com
Tesmer, Volker	DGFI, Munich	Germany	tesmer@dgfi.badw.de
Thorandt, Volkmar	BKG, Branch Leipzig	Germany	volkmar.thorandt@bkg.bund.de
Titov, Oleg	Geoscience Australia, Canberra	Australia	oleg.titov@ga.gov.au
Tornatore, Vincenza	DIIAR Politecnico di Milano	Italy	vincenza.tornatore@polimi.it
Tuccari, Gino	IRA INAF, Bologna	Italy	g.tuccari@ira.inaf.it
Ullrich, Dieter	BKG, Branch Leipzig	Germany	dieter.ullrich@bkg.bund.de
Vennebusch, Markus	GIB, Univ of Bonn	Germany	Vennebusch@uni-bonn.de
Wang, Guangli	SHAO, Shanghai	China	wgl@shao.ac.cn
Whitney, Alan	MIT Haystack Observatory	U.S.A.	awhitney@haystack.mit.edu

Last Name	Affiliation	Country	e-mail
Wresnik, Joerg	IGG, TU Vienna	Austria	wresnik@mars.hg.tuwien.ac.at
Yatskiv, Ya. S.	MAO, Kiev	Ukraine	yatskiv@MAO.Kiev.UA
Gaume, Ralph	USNO, Washington	USA	rgaume@usno.navy.mil

GEOWISSENSCHAFTLICHE MITTEILUNGEN

Bisher erschienen:

Heft 1 Kolloquium der Assistenten der Studienrichtung Vermessungswesen. 1970 - 1973, Dezember 1973.

Heft 2 EGGER-PERDICH-PLACH-WAGENSOMMERER, Taschenrechner HP 45 und HP 65, Programme und Anwendungen im Vermessungswesen. 1. Auflage, März 1974, Special Edition in English, Juli 1974, 2. verbesserte Auflage, November 1974.

Heft 3 Kolloquium der Assistenten der Studienrichtung Vermessungswesen 1973 - 1974, September 1974.

Heft 4 EGGER-PALFINGER-PERDICH-PLACH-WAGENSOMMERER, Tektronix-Tischrechner TEK 31, Programmbibliothek für den Einsatz im Vermessungswesen, November 1974.

Heft 5 K.LEDERSTEGER, Die horizontale Isostasie und das isostatische Geoid, Februar 1975.

Heft 6 F.REINHART, Katalog von FK4 Horrebow-Paaren für Breiten von +30 bis +60, Oktober 1975.

Heft 7 Arbeiten aus dem Institut für Höhere Geodäsie, Wien, Dezember 1975.

Heft 8 Veröffentlichungen des Instituts für Photogrammetrie zum XIII. Internationalen Kongreß für Photogrammetrie in Helsinki 1976, Wien, Juli 1976.

Heft 9 W.PILLEWIZER, Felsdarstellung aus Orthophotos, Wien, Juni 1976.

Heft 10 PERDICH-PLACH-WAGENSOMMERER, Der Einsatz des programmierbaren Taschenrechners Texas Instruments SR-52 mit Drucker PC100 in ingenieurgeodätischen Rechentechnik, Wien, Mai 1976.

Heft 11 Kolloquium der Assistenten der Studienrichtung Vermessungswesen 1974 - 1976, November 1976.

Heft 12 Kartographische Vorträge der Geodätischen Informationstage 1976, Wien, Mai 1977.

Heft 13 Veröffentlichung des Instituts für Photogrammetrie anläßlich des 80. Geburtstages von Prof.Dr.h.c.K.Neumaier, Wien, Januar 1978.

Heft 14 L.MOLNAR, Self Checking Analytical Relative Orientation and Strip Formation, Wien, Dezember 1978.

Heft 15 Veröffentlichung des Instituts für Landesvermessung anläßlich des 80. Geburtstages von Prof.Dr.Alois Bavir, Wien, Januar 1979.

Heft 16 Kolloquium der Assistenten der Studienrichtung Vermessungswesen 1976 - 1978, Wien, November 1979.

Heft 17 E.VOZIKIS, Die photographische Differentialumbildung gekrümmter Flächen mit Beispielen aus der Architekturbildmessung, Wien, Dezember 1979.

Heft 18 Veröffentlichung des Instituts für Allgemeine Geodäsie anläßlich des 75. Geburtstages von Prof.Dipl.Ing.Dr.F.Hauer, Die Höhe des Großglockners, Wien, 1981.

Heft 19 H.KAGER, Bündeltriangulation mit indirekt beobachteten Kreiszentren, Wien, April 1981.

Heft 20 Kartrographische Vorträge der Geodätischen Informationstage 1980, Wien, Mai 1982.

Heft 21 Veröffentlichung des Instituts für Kartographie anläßlich des 70. Geburtstages von Prof.Dr.Wolfgang Pillewizer: Glaziologie und Kartographie, Wien, Dezember 1982.

Heft 22 K.TEMPFLI, Genauigkeitsschätzung digitaler Höhenmodelle mittels Spektralanalyse, Wien, Mai 1982.

Heft 23 E.CSAPLOVICS, Interpretation von Farbinfrarotbildern, Wien, November 1982.

Heft 24 J.JANSA, Rektifizierung von Multispektral-Scanneraufnahmen - Entwicklung und Erprobung eines EDV-Programms, Wien, Mai 1983.

Heft 25 Zusammenfassung der Diplomarbeiten, Dissertationen und Habilitationen an den geodätischen Instituten der TU Wien, Wien, November 1984.

Heft 26 T.WUNDERLICH, Die voraussetzungsfreie Bestimmung von Refraktionswinkeln, Wien, August 1985.

Heft 27 G.GERSTBACH (Hrsg.), Geowissenschaftliche/geotechnische Daten in Landinformationssystemen - Bedarf und Möglichkeiten in Österreich, Juni 1986.

Heft 28 K.NOVAK, Orientierung von Amateuraufnahmen ohne Paßpunkte, Wien, August 1986.

Heft 29 Veröffentlichung des Instituts für Landesvermessung und Ingenieurgeodäsie, Abt. Ingenieurgeodäsie, anläßlich des 80. Geburtstages von Prof.Dipl.Ing.Dr.F.Hauer, Wien, Oktober 1986.

Heft 30 K.-H.ROCH, Über die Bedeutung dynamisch ermittelter Parameter für die Bestimmung von Gesteins- und Gebirgseigenschaften, Wien, Februar 1987.

Heft 31 G. HE, Bildverbesserung mittels digitaler Filterung, Wien, April 1989.

Heft 32 F.SCHLÖGELHOFER, Qualitäts- und Wirtschaftlichkeitsmodelle für die Ingenieurphotogrammetrie, Wien, April 1989.

Heft 33 G.GERSTBACH (Hrsg.), Geowissenschaftliche/geotechnische Daten in Landinformationssystemen - Datenbestände und Datenaustausch in Österreich, Wien, Juni 1989.

Heft 34 F.HOCHSTÖGER, Ein Beitrag zur Anwendung und Visualisierung digitaler Geländemodelle, Wien, Dezember 1989.

Heft 35 R.WEBER, Lokale Schwerefeldmodellierung unter Berücksichtigung spektraler Methoden zur Geländereduktion, Wien, April 1990.

Heft 36 o.Prof.Dr.Hans Schmid zum 70. Geburtstag. Veröffentlichung der Abteilung für Landesvermessung, Wien, Oktober 1990.

Heft 37 G.GERSTBACH, H.P.HÖLLRIEGL und R.WEBER, Geowissenschaftliche Informationsbörse - Eine Nachlese zu GeoLIS II, Wien, Oktober 1990.

Heft 38 R.ECKER, Rastergraphische Visualisierungen mittels digitaler Geländemodelle, Wien, August 1991.

Heft 39 Kartographische Forschungen und Anwendungsorientierte Entwicklungen, herausgegeben von W.Stams und F.Kelnhofer zum 80. Geburtstag von Prof.Dr.W.Pillewizer, Wien, Juli 1991.

Heft 39a W.RIEGER, Hydrologische Anwendungen des digitalen Geländemodelles, Wien, Juli 1992.

Heft 40 K.STEINNOCHER, Methodische Erweiterungen der Landnutzungsklassifikation und Implementierung auf einem Transputernetzwerk, Wien, Juli 1994.

Heft 41 G.FORKERT, Die Lösung photogrammetrischer Orientierungs- und Rekonstruktionsaufgaben mittels allgemeiner kurvenförmiger Elemente, Wien, Juli 1994.

Heft 42 M.SCHÖNER, W.SCHÖNER, Photogrammetrische und glaziologische Untersuchungen am Gàsbre (Ergebnisse der Spitzbergenexpedition 1991), Wien, Mai 1996.

Heft 43 M.ROIC. Erfassung von nicht signalisierten 3D-Strukturen mit Videotheodoliten, Wien, April 1996.

Heft 44 G.RETSCHER, 3D-Gleiserfassung mit einem Multisensorsystem und linearen Filterverfahren, Wien, April 1996.

Heft 45 W.DAXINGER, Astrogravimetrische Geoidbestimmung für Ingenieurprojekte, Wien, Juli 1996.

Heft 46 M.PLONER, CCD-Astrometrie von Objekten des geostationären Ringes, Wien, November 1996.

Heft 47 Zum Gedenken an Karl Killian "Ingenieur" und "Geodät" 1903-1991, Veröffentlichung der Fachgruppe Geowissenschaften, Wien, Februar 1997.

Heft 48 A.SINDHUBER, Ergänzung und Fortführung eines digitalen Landschaftsmodelles mit multispektralen und hochauflösenden Fernerkundungsaufnahmen, Wien, Mai 1998.

Heft 49 W.WAGNER, Soil Moisture Retrieval from ERS Scatterometer Data, Wien, Dezember 1998.

Heft 50 R.WEBER, E.FRAGNER (Editoren),Prof.Bretterbauer, Festschrift zum 70.Geburtstag, Wien, Juli 1999.

Heft 51 Ch.ÖHRENEDER, A Similarity Measure for Global Image Matching Based on The Forward Modeling Principle, Wien, April 1999.

Heft 52 M.LECHTHALER, G.GARTNER, Per Aspera ad Astra, Festschrift für Fritz Kelnhofer zum 60. Geburtstag, Wien, Jänner 2000.

Heft 53 F.KELNHOFER, M.LECHTHALER, Interaktive Karten (Atlanten) und Multimedia – Applikationen, Wien, März 2000.

Heft 54 A.MISCHKE, Entwicklung eines Videotheodlit-Meßsystems zur automatischen Richtungsmessung von nicht signalisierten Objektpunkten, Wien, Mai 2000

Heft 55 Veröffentlichung des I.P.F. anlässlich der Emeritierung von Prof.Dr. Peter Waldhäusl, Wien.

Heft 56 F.ROTTENSTEINER, Semi-automatic Extraction of Buildings Based on Hybrid Adjustment Using 3D Surface Models and Management of Building Data in a TIS, Wien, Juni 2001.

Heft 57 D.LEGENSTEIN, Objektrekonstruktion aus perspektiven Bildern unter Einbeziehung von Umrisslinien, Wien, Mai 2001.

Heft 58 F.KELNHOFER, M.LECHTHALER und K.BRUNNER (Hrsg.), Telekartographie und Location Based Services, Wien, Jänner 2002.

Heft 59 K.BRETTERBAUER, Die runde Erde eben dargestellt: Abbildungslehre und sphärische Kartennetzentwürfe, Wien, 2002.

Heft 60 G.GARTNER, Maps and the Internet 2002, Wien 2002.

Heft 61 L.DORFFNER, Erzeugung von qualitativ hochwertigen 3D Photomodellen für Internetbasierte Anwendungen mit besonderem Augenmerk auf Objekte der Nahbereichsphotogrammetrie, Wien, Jänner 2002.

Heft 62 CHMELINA, Wissensbasierte Analyse von Verschiebungsdaten im Tunnelbau Wien 2002

Heft 63 A.NIESSNER, Qualitative Deformationsanalase unter Ausnutzung der Farbinformation, Wien 2002

Heft 64 K.BRETTERBAUER; R.WEBER, A Primer of Geodesy for GIS-Users, Wien im Herbst 2003

Heft 65 N.PFEIFER, 3D Terain Models on the basis of a triangulation, Wien, Jänner 2002.

Heft 66 G.GARTNER (Hrsg), Lacation Based Services & Telecartography, Wien, 2004

Heft 67 I.KABASHI, Gleichzeitig-gegenseitige Zenitwinkelmessung über größere Entfernungen mit automatischen Zielsystemen, Wien, 2004

Heft 68 J.BÖHM, Troposphärische Laufzeitverzögerungen in der VLBI, Wien 2004

Heft 69 R.WEBER, W.SCHLÜTER, U.SCHREIBER, O. TITOV
Evolving Space Geodesy Techniques (EGS XXVII General Assembly, Nice, France, 2002), Wien 2004

Heft 70 G. WEINWURM, Amalthea’s Gravity Field and its Impact on a Spacecraft Trajectory, Wien 2004

Heft 71 Forschungsgruppe Ingenieurgeodäsie, Festschrift anlässlich des 65. Geburtstages von Herrn o.Univ.Prof.Dr.-Ing. Heriber Kahmen, Wien 2005

Heft 72 A. REITERER, A Knowledge-Based Decision System for an On-Line Video-Theodolite-Based Multisensor System, Wien 2005

Heft 73 M. HABERLER, Einsatz von Fuzzy Methoden zur Detektion konsistenter Punktbewegungen, Wien 2005

Heft 74 G. GARTNER, Location Based Services & Telecartography, Proceedings of the Symposium 2005, Wien 2005

Heft 75 Th. HOBIGER, VLBI as a tool to probe the ionosphere, Wien 2006

Heft 76 E. KLAFFENBÖCK, Troposphärische Laufzeitverzögerung von GNSS-Signalen – Nutzen aktiver Referenzstationsnetze für die Meteorologie, Wien 2006

Heft 76a P.J. MENDES-CERVEIRA, Tidal and non-tidal contributions to surface loading processes on station coordinates, Wien 2006

Heft 78 G.KOSTOV, G.BOURDA, L.FERNANDEZ. T.KONDO, Research Projects at IGG – Reports -, Wien 2007